Numerical Investigation of Disturbance Environments in Low Pressure Turbines

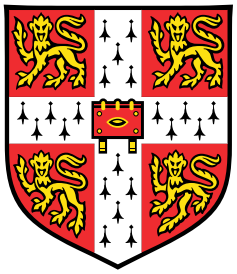

Aditi Sengupta

Department of Engineering
University of Cambridge

This dissertation is submitted for the degree of
Doctor of Philosophy

Churchill College

February 2020

To my loving parents, Tapan and Soma, and brother, Soumyo

Declaration

This thesis is the result of my own work and includes nothing which is the outcome of work done in collaboration except as declared in the Preface and specified in the text. It is not substantially the same as any that I have submitted, or, is being concurrently submitted for a degree or diploma or other qualification at the University of Cambridge or any other University or similar institution except as declared in the Preface and specified in the text. I further state that no substantial part of my thesis has already been submitted, or, is being concurrently submitted for any such degree, diploma or other qualification at the University of Cambridge or any other University or similar institution except as declared in the Preface and specified in the text. It does not exceed the prescribed word limit for the relevant Degree Committee.

This dissertation contains has nine chapters consisting of fewer than 65,000 words including appendices, bibliography, footnotes, tables and equations and has 149 figures.

The work contained within this thesis has, to date, produced the following publications:

Roughness induced transition in low pressure turbines. Proceedings of 55^{th} AIAA Aerospace Sciences Meeting, Grapevine, Texas, 9-13 January 2017.

“An enstrophy based linear and nonlinear receptivity theory". Phys. Fluids, 30, pp. 054106 (2018).

“Direct numerical simulation of vortex-induced instability for a zero pressure gradient boundary layer". Phys. Rev. E., 100, pp. 033118 (2019).

“Tracking disturbances in transitional and turbulent flows: Coherent structures". Phys. Fluids, 31, pp. 124106 (2019).

“Nonmodal nonlinear route of transition to two-dimensional turbulence". Phys. Rev. Research, 2(1), pp. 012033 (2020).

Aditi Sengupta
February 2020

Abstract

Numerical Investigation of Disturbance Environments in Low Pressure Turbines

Aditi Sengupta

Using a series of direct numerical simulations, the individual and cumulative effects of various disturbance environments existing in a low pressure turbine (LPT) are investigated. In particular, the effects of free-stream turbulence (FST), unsteady wakes, roughness and blade oscillations on the separation-induced transition on the suction surface of a low pressure turbine blade are analyzed. Two configurations are considered: (i) a flat plate subjected to streamwise pressure gradient representative of the suction surface of a low pressure turbine blade, (ii) a flat plate subjected to a convecting free-stream vortex of fixed strength and at a fixed height over the plate. The first configuration represents the 'ultra high-lift' blades for the next generation low pressure turbine. The local pressure gradient induced by the convecting vortex in the second configuration is representative of the adverse pressure gradient on the suction surface of a low pressure turbine blade. The results are validated against existing experimental or numerical data and it is demonstrated that the numerical framework has captured most of the phenomena to a reasonable level of accuracy. A kernel experiment for bypass transition is simulated for the vortex-induced instability. The effect of the convection speed and strength of the vortex are discussed and the paths of transition adopted are distinguished.

At low disturbance levels, the transition to turbulence is primarily due to the breakdown of 'Kelvin-Helmholtz' roll up vortices. In the presence of aeroelastic blade oscillations, unsteady wakes, free-stream turbulence and roughness, transition takes the bypass route and the results show evidence of streamwise streaks. These streaks impart spanwise waviness to the separated shear layer and cause early destabilisation. The blade oscillation has an effect in reducing the separated region and hence, the profile loss, which is further accentuated in the presence of free-stream turbulence. A blade fluctuating at higher reduced frequency is found to be more effective in shrinking the separation region. Blade vibration is found to increase the level of pre-transitional fluctuations, without having a significant influence on the growth beyond separation. There is a cumulative effect in suppressing the separation

region when blade oscillation and free-stream turbulence are studied in conjunction, although the additional effect of free-stream turbulence is marginal. A secondary separation bubble, noted in the unperturbed flow, is reduced in size with blade oscillation and further reduced in the presence of free-stream turbulence.

The vortex-induced instability has been proposed to be a unit process of free-stream turbulence, the effect of which is studied in the presence of a discrete roughness element (similar in functionality to a trip wire). The roughness element triggers early transition by destabilizing the mean flow. Streaks are observed in the presence of the convecting and rotating cylinder, generating a vortex of fixed strength, and are enhanced by the presence of roughness in the pre-transitional zone. Enhanced spanwise waviness is noted with the roughness, leading to earlier breakdown to turbulence. The route of transition and the origin of three-dimensionality marked by the prominence of the vortex stretching is shown. An optimum range of convection speeds of the free-stream vortex is obtained and the maximum receptivity is noted at a speed of 0.386, which concurs with prior experiments on a periodic convecting vortex (Kendall, 1987).

The unsteady wake has a direct effect on the velocity profile. A lag is noted between the wake passing and transition. While the wake convects at the local free-stream velocity, its impression in the boundary layer convects much slower, between 50% and 70% of the local free-stream velocity. Both unsteady wakes and blade oscillation promote near-wall mixing. The unsteady wakes and blade oscillations have a conjunctive effect on reducing the size of separation bubble. The secondary separation bubble observed in the unperturbed flow is reduced with the presence of wakes and is completely suppressed with the addition of the blade oscillation. Turbulent kinetic energy production increases with increasing perturbation levels, with the maximum effect seen for the combination of wakes and oscillation.

A receptivity method based on disturbance enstrophy transport equation (DETE) is proposed. The disturbance enstrophy is evaluated as the difference between the instantaneous and mean enstrophies, and while these are positive definite quantities, the difference may not be so. This aspect of disturbance enstrophy has been used meaningfully to obtain new information about the flow instability, such as segmenting regions of flow instabilities into those dictated by positive growth rates of disturbance enstrophy, and those due to its negative counterpart. The positive growth rates are associated with large scale coherence in the free-stream whereas the negative growth rates are found to be arising in near-wall viscous structures (Sengupta et al., 2019a,b). The extension of this method to structure detection and comparison against existing vortex identification methods, indicates the ability of the DETE method to capture small-scale structures induced by the viscous term of the Navier-Stokes equation. DETE has been used for the two configurations operating with varying

perturbation levels and valuable insight pertaining to the flow dynamics has been attained with respect to its budget terms. In particular, the role of vortex stretching in leading the flow to three-dimensionality is highlighted.

The global and local spatio-temporal receptivity analysis of flows perturbed by plate oscillations, wakes and free-stream excitation yields a spatio-temporal wave front to be the causal mechanism for flow transition. This is essentially representative of the nonmodal part of the disturbance spectrum. While this flow instability has already been established for geophysical flows such as tsunami and other fluid dynamical problems such as for zero pressure gradient boundary layer formed over a semi-infinite flat plate excited from inside the shear layer, its role for pressure gradient dominated flows (such as in LPTs) is shown for the first time. The importance of nonlinearity and its dispersion effects is shown, specifically for flows excited at the free stream, even when the onset of disturbances follows a linear mechanism. The need for using a global, nonlinear, spatio-temporal setup is established in order to capture all pertinent flow physics.

Acknowledgements

Without the support of a great number of people the work reported in the thesis would not have been possible.

Firstly, I am indebted to Dr. Ricardo Garcia-Mayoral for his guidance and the opportunities he has afforded me throughout his supervision of this work, while providing me the freedom to pursue my own ideas. I have gained further insight and greater understanding under his counsel. I also express my gratitude to Prof. Paul Tucker for his technical advice and guidance from the inception of my thesis work. He has provided me with prompt and invaluable guidance at crucial stages of my thesis work.

I am thankful for the financial support provided by the Cambridge Trust and the Department of Science and Technology, India through the Cambridge India Ramanujan Scholarship.

My sincere gratitude to Dr. Swagata Bhaumik for providing the velocity-vorticity based incompressible Navier-Stokes solver used in chapters 4 and 6 of the thesis and to Dr. Nagabhushana Rao Vadlamani for providing the pressure-velocity based compressible Navier-Stokes solver used in chapters 5 and 7 of the thesis. I would also like to thank Dr. Tapan Kumar Sengupta and Dr. Swagata Bhaumik for their expertise and insights into the research problem in chapters 4 and 6. Their time and patience in answering my questions is greatly acknowledged. I am especially indebted to Mr. V. K. Suman for his valuable input and for running a part of two of the simulations in chapter 6 at the supercomputing facility in National Aerospace Laboratory, India. The computational time from the supercomputing facility, Darwin at the Department of Engineering and from the UK Turbulence Consortium through Archer supercomputer is also greatly appreciated.

I would like to thank Mr. Prasannabalaji Sundaram and Mr. Pushpender Sharma for their technical insights which helped me in preparing the revised version of my thesis.

Colleagues at the department have been a valuable source of assistance, encouragement and friendship.

It is only right that the ultimate acknowledgement be to my parents and my brother, for their unending love and support.

Table of contents

List of figures

List of tables

Nomenclature

Roman Symbols

a	Amplitude of imposed blade oscillation
a_w	Amplitude of imposed unsteady wake
c	Convection speed of free-stream vortex
C_f	Skin friction coefficient = $\tau_w / \frac{1}{2}\rho {U_\infty}^2$
k	Turbulent kinetic energy
k_{osc}	Reduced frequency
Ma	Mach number
Q	Second invariant of velocity gradient tensor
Re	Reynolds number
St	Strouhal number
t_o	Time period of imposed blade oscillation
Tu	Turbulence intensity
t_w	Time period of wake passing
u, U	Streamwise velocity
u'	Streamwise fluctuating velocity
v, V	Wall-normal velocity
w, W	Spanwise velocity

Greek Symbols

Γ	Strength of free-stream vortex
λ_2	Second eigenvalue of characteristic equation for velocity gradient tensor
π	$\simeq 3.14\ldots$
ρ	Density
Ω	Enstrophy $\omega \cdot \omega$
ω	Vorticity

Superscripts

$\rightarrow$	Vector quantity

Subscripts

d	Disturbance component
∞	Free-stream component
m	Mean/equilibrium component
x	Streamwise component
y	Wall-normal component
z	Spanwise component

Acronyms / Abbreviations

CFD	Computational Fluid Dynamics
DETE	Disturbance Enstrophy Transport Equation
DME	Disturbance Mechanical Energy
DNS	Direct Numerical Simulation
FFT	Fast Fourier Transform
FST	Free-Stream Turbulence
LES	Large Eddy Simulation

LNSE Linearised Navier-Stokes Equation

LPT Low Pressure Turbine

NNSE Nonlinear Navier-Stokes Equation

NSE Navier-Stokes Equation

OSE Orr Sommerfeld Equation

STWF Spatio temporal wave front

TKE Turbulent Kinetic Energy

ZPG Zero Pressure Gradient

Chapter 1

Introduction

1.1 Motivation

Turbomachines are complex systems which operate with the sole purpose of converting the energy contained in a working fluid into useful work. It has been projected that 84% of the world's total electricity consumption will be provided by turbomachines by 2040, despite the availability of renewable energy sources (EIA, 2013). Gas turbines are used for electrical power generation and to power most modern aircraft. The fan of the turbofan engine, driven by the low pressure turbine (LPT), produces around 80% of the forward thrust required in modern high bypass ratio engines. Halstead et al. (1997) determined that, a 1% increase in LPT efficiency gives rise to 0.7% increase in overall engine efficiency. There is a direct correlation between the efficiency of a LPT and the overall specific fuel consumption. The weight of the engine is detrimental to fuel consumption and manufacturing costs. An improved efficiency requires a reduction in weight of the LPT by reducing the number of blades and increasing the effective loading per blade. As a result, high-lift and ultra high-lift blade designs are becoming increasingly popular.

Transition is a feature of most external aerodynamic and turbomachinery flows and it has a detrimental effect on the operational characteristics. In low pressure stages of a turbomachine, the Reynolds number (Re) is usually modest for the accelerating flow and thus, the flow is transitional over a significant portion of the blade, especially in the turbine stage. The higher loading on each highly cambered LPT blade makes it more susceptible to separation on the suction surface. There are losses associated with flow separation, especially at low Reynolds numbers. Banieghbal et al. (1996) showed that 60% of the loss on the suction surface can be attributed to that occurring in the boundary layer. The boundary layer and subsequent losses are sensitive to the external environment of the blade. Thus, studying the flow physics governing the transition process in LPT under the influence of various

disturbance environments viz. aeroelastic flutter, free-stream turbulence (FST) and surface roughness, is of interest to designers looking to improve engine efficiency via improving LPT efficiency. The various processes taking place on the suction and pressure sides of a LPT blade, during boundary layer transition are indicated in Fig. 1.1.

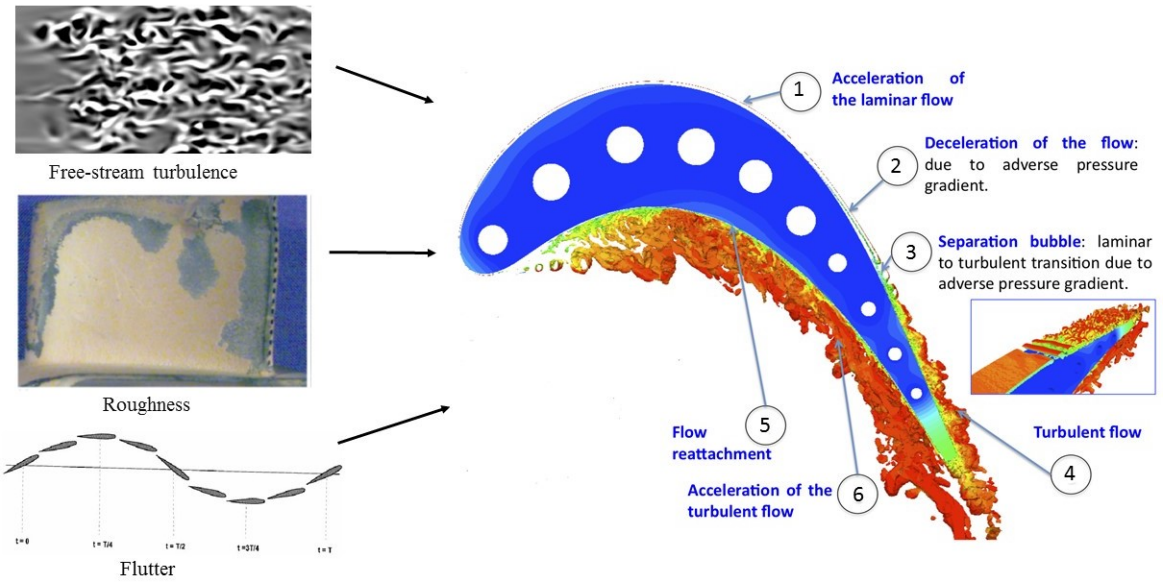

Fig. 1.1 Features of boundary layer transition to turbulence, relaminarization process and reattachment of flow in a LPT blade.

The classical definition of various routes of transition to turbulence are primarily noted according to Morkovin (1991) as: (i) the classical route associated with the presence of Tollmien-Schlichting waves at the onset, shown in the controlled experiment for zero pressure gradient (ZPG) boundary layer flow by Schubauer and Skramstad (1947) and (ii) all other mechanisms as bypass routes for any flow. Since then, there are many complementary schools of thought which try to address the receptivity at different spatial and temporal scales (Reshotko, 2001; Saric et al., 2002; Schmid, 2007; Trefethen et al., 1993) and provide a definition of bypass transition. For example, even for the same flow type, depending upon the amplitude of background disturbances, one can observe either Tollmien-Schlichting waves as the dominant underlying mechanism governing the transition or transition can take place by a bypass route, for higher amplitude background disturbances (Cherubini et al., 2012; Saric et al., 2002). Another definition is based on the concept of “transient growth" involving interplay between nonnormal eigenvectors (obtained from modal analysis), which may be overlooked by traditional spatial or temporal receptivity theories. Other practitioners such as Eckhardt et al. (2007); Kawahara et al. (2012); Kerswell (2018) give prominence to a nonlinear mechanism by which bypass transition takes place. Wu et al. (2014) define bypass

transition as *"similar to the secondary instability.*" The narrow definition of bypass transition as being caused by free-stream excitation is not rigorous, as researchers have been able to create Tollmien-Schlichting waves by vibrating a ribbon in the free stream (Dietz, 1999; Leib et al., 1999), which is explained by linear theory governed by the Orr-Sommerfeld equation (Sengupta, 2012). In the context of turbomachines for laminar flows, the dominant transition mechanism is considered to be the one governing Kelvin-Helmholtz instability in free-shear layers, i.e. associated with the inflectional profile in the early stage of the separation (Dovgal et al., 1994). When free-stream disturbances are introduced, the transition process in the separated shear layer is altered. Hairpin or Λ-vortices appear early in the separated region (Alam and Sandham, 2000), even at low free-stream turbulence levels. For higher values of the free-stream turbulence intensity, the transition in the separated shear-layer is preceded by a bypass transition process in the attached boundary layer.

Vortex-induced instability: One reason for the lack of consensus in the causality of bypass transition is due to the absence of definitive kernel experiments for bypass transition (Smith, 1993). A bypass mechanism for transition has been experimentally studied by Lim et al. (2004) as the vortex-induced instability problem for a ZPG boundary layer caused by a convecting vortex in the free stream, and the bypass mechanism has been identified theoretically by Sengupta et al. (2003). Vortex-induced instability has been noted earlier by Doligalski et al. (1994) *"as one of the most important unsolved problems of fluid dynamics.*" It has been proposed that the convecting vortex can be approximated as a unit process of the background free-stream turbulence. The primary instability is triggered by a convecting vortex over ZPG boundary layer, with the same mechanism noted in unsteady flow separation (Degani et al., 1998) and near-wall eddy formation in turbulent boundary layers (Brinckman and Walker, 2001). Hairpin vortices are formed in the near-wall region of turbulent flows and are discussed by previous researchers (Robinson (1991) and Smith et al. (1991)). The experiment for vortex-induced instability (Lim et al., 2004), was designed to test the hypothesis that a distant vortex can induce a small longitudinal adverse pressure gradient to destabilize a wall-bounded flow causing unsteady separation. This is comparable to the suction surface of a LPT blade where an adverse pressure gradient leads to flow separation. A compact vortex is created in the experiment (Lim et al., 2004) by a spinning and translating cylinder above a ZPG boundary layer. As the spin rate and height of the cylinder can be controlled with precision, the bypass mechanism can be reproduced at will. The only unknown in this experiment is the magnitude of circulation of the convecting vortex, yet its strength can be correlated with the spin rate. The physical mechanism for this bypass transition has been explained previously with the help of an equation based on disturbance mechanical

energy (DME), derived from the incompressible Navier-Stokes equation (NSE) without any underlying assumptions (Sengupta et al., 2003).

Roughness effects: Surfaces of aircraft wings, turbine or compressor blades are irregular due to the nature of the processes by which they are created. Due to a multitude of factors such as corrosion, sand, combustion products, erosion and airborne dust deposit, degradation of gas turbine components takes place and the surfaces progressively roughen (Bons, 2010). Some of these factors causing surface roughness have been illustrated for a gas turbine blade in Fig. 1.2. This has a direct effect on the performance and stability of the engine. Bhaganagar et al. (2004) state that *"turbulent boundary layers within turbomachinery is a case for which smooth wall idealization rarely applies.*" In transitional and turbulent boundary layers observed on the suction surface of low pressure turbines, the processes involved are laminar separation, separation-induced transition and reattachment of the flow; while on the pressure surface, relaminarization of the turbulent flow is observed, as shown in Fig. 1.1. When surface roughness interacts with the aforementioned complex flow processes, it may lead a significant alteration in the transition and turbulence process and operability. Hence, it is important to study the effects of surface roughness to determine its influence on performance.

For the bypass transition during vortex-induced instability under the influence of surface roughness, a set of important results for roughness effects have been reported for a 2D (Klebanoff and Tidstrom, 1972) and a 3D (Klebanoff et al., 1992) roughness element on the surface of a flat plate. Klebanoff and Tidstrom (1972), experimented with 2D discrete roughness on a ZPG boundary layer and investigated the effects of FST as a rate of strain to destabilize the equilibrium flow. The focus in the study was more on aspects of classical linear stability theory for the interactions between the equilibrium flow (comprising of discrete roughness) and FST. The experimental evidence was summarized by the authors to be sufficient to conclude that *"the effect of a two-dimensional roughness element on boundary layer transition can be regarded as a stability governed phenomenon.*" It was concluded that *"the basic mechanism by which a two-dimensional roughness element induces earlier transition is by the destabilizing influence of the flow in the recovery zone on existing disturbances which hastens the downstream development of the instability.*" While the authors did not state explicitly whether the transition follows the classical route via growth of Tollmien-Schlichting waves or via the bypass route, an illuminating discussion on the topic was provided by Klebanoff et al. (1992) with respect to the nature of existing disturbance of FST and the route of transition for 2D roughness effects. Despite the common perception that the FST is stochastic in nature, Klebanoff et al. (1992) demonstrated that

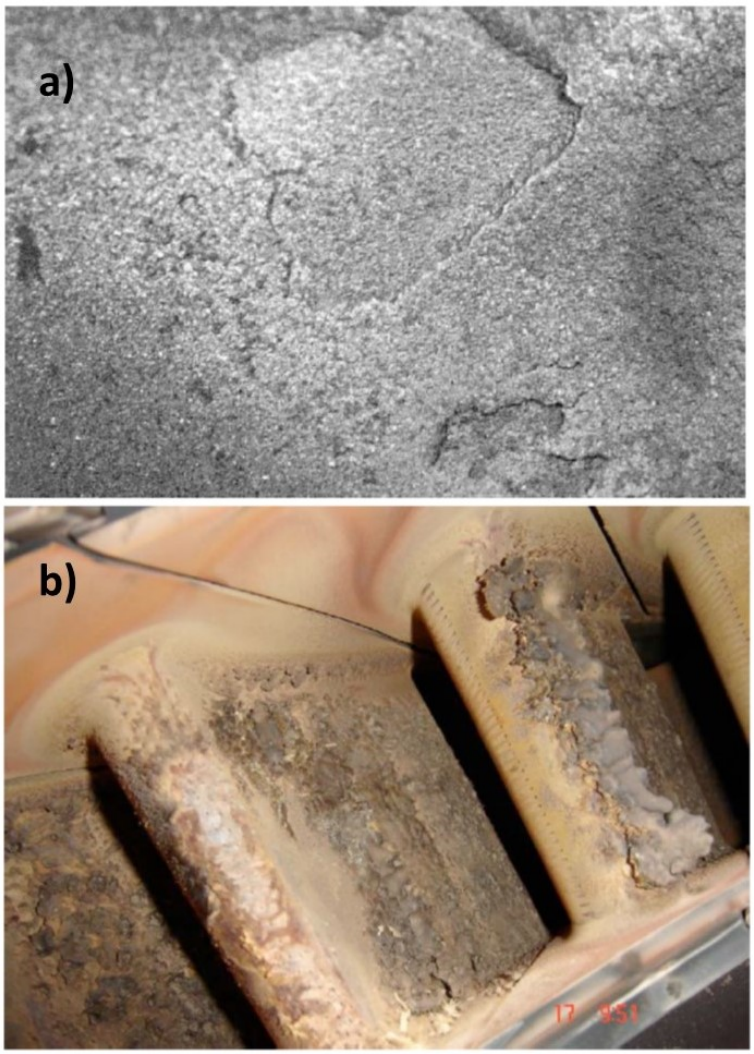

Fig. 1.2 a) Sample of erosion from suction surface leading edge region, b) Deposition on gas turbine vane after 8000 hours service. (From Bons (2010))

the wind tunnel used in the experiments has a very distinctive spectrum with discrete peaks for FST. The authors also stated that the *"source of the spectral peaks is attributed to the wind tunnel fan. The peak at 20Hz, as alluded to previously, corresponds to the fan motor r.p.m. The peaks at 180Hz and the higher harmonics of 180Hz are a consequence of the passage frequency of a 9-bladed fan.*" It was furthermore emphasized with the help of a measured spectrum by an accelerometer attached to the fan housing, that the peaks of FST correlated perfectly with it. This tunnel was used for the experiments on 2D roughness (Klebanoff and Tidstrom, 1972) also. Klebanoff et al. (1992) specifically discussed about the route of transition by FST on the flat plate without roughness. It was stated that, *"the disturbance level is a consequence of variations of boundary-layer thickness in space and*

time associated with free-stream turbulence effects as proposed in Klebanoff (1971) and not as a result of a Tollmien-Schlichting type of instability." It is furthermore emphasized that the *"peak in the spectral intensity at 20Hz should not be interpreted as being due to a Tollmien-Schlichting instability. It is a consequence of vibration induced by the fan motor and is accentuated by the velocity gradient in the boundary layer.*" All these observations, establish two aspects: one, that the effect of FST observed in a real flow application (the wind tunnel in the experiments) is equivalent to free-stream excitation at discrete frequencies and secondly, the transition caused by FST is via the bypass route.

Flutter in LPTs: Flutter is an unstable, self-sustained aeroelastic instability phenomenon that is associated with coupling of aerodynamic forces and structural vibration of blades. In contrast to this classical definition of flutter, stall flutter is a phenomenon observed during separation of flow occurring periodically during the oscillation. Dowell et al. (2004) state that *"the number and classes of structures that potentially could experience stall flutter are very great, and include such diverse examples as suspension bridges, helicopter rotors and turbomachinery blades.*" Safety and economic aspects motivate the assessment of the flutter phenomenon. In the context of aircraft wings, Sieg (2000) determined that 46% of fighter aircraft are inoperable due to high cycle fatigue associated with flutter. A paramount task in engine design is to achieve aerodynamic stability by assessment of the unsteady aerodynamic field created by the flutter process. Fans, front compressor stages and aft turbine stages are locations which are sensitive to flutter occurrence (Srinivasan, 1997). LPT blades, with their high aspect ratios and higher effective loading per blade exacerbated by the modern trend of high lift blade designs, have an unfavourable aeroelastic ratio of aerodynamic force to structural stiffness. This makes the later LPT stages highly prone to flutter. The ultra-high bypass ratio engines are more prone to the flutter phenomenon. Flutter is a high risk event in LPT blades, thus a physical understanding of how operating conditions affect aeroelastic behaviour is important.

Wakes in LPTs: Most current turbine design methods rely on the flow, impinging on a blade row, being steady. However, this assumption holds true only for the fan and first stator stage of the high pressure turbine. Other blade rows experience the effects due to a number of upstream blade rows. Upstream blades shed wakes which contribute to the overall flow conditions on downstream blades. A wake is a periodic disturbance of high turbulence fluid and velocity defect on the downstream blade. The transition process is complex due to the inherent unsteadiness of multi-stage turbomachines, the wakes shed by one blade row convect through the downstream blade passages, periodically disturbing the boundary

layer. This periodic passing of turbulent wakes affects the separation bubble observed on a modern LPT blade and a reduction in the profile loss is seen due to the wake passing for some flow conditions (Schulte and Hodson, 1998). An overall repressed separation region is observed due to turbulent wakes, which can be attributed to the turbulent spots induced by wake upstream of the separation point, preventing boundary layer separation. The calmed region following after the wake passing is also a contributor in suppressing separation due to elevated shear and full velocity profiles. The interaction between the turbulent wake and the unsteady separation bubble that re-establishes between wake passing events has to be investigated in detail. Here, bounded within the permissible wake-passing frequencies (Tucker, 2014) for a row of upstream blade-induced wakes, we study the effect of wakes on the separation-induced transition in low pressure turbines.

1.1.1 Numerical Tools for Flow Characterization

Turbulent and transitional flows are dominated by spatially coherent and temporally evolving vortical motions, referred to as coherent structures. The genesis and propagation of these structures are essential features to be traced in transitional and turbulent flows. Identifying coherent structures is not straight forward and can be seen as a tool for understanding complex flow phenomena. The vortical structures existing within turbulent flows have been a subject of study for decades, and some strategies for their identification are the λ_2-criterion (Jeong and Hussain, 1995), based on tracking the pressure minima and Q-criterion (Perry and Chong, 1987), based on velocity gradient tensor calculations. The λ_2-criterion involves approximation of the incompressible Navier-Stokes equation (NSE), by neglecting unsteady and viscous terms (Jeong and Hussain, 1995). Both these methods have been used to identify vortical structures characterizing the flow. Two alternative structure detection methods derived directly from the incompressible NSE are based on the disturbance components of mechanical energy and enstrophy. A method based on disturbance enstrophy transport equation (DETE) has been developed and it has been applied to a periodic flow (Sengupta et al., 2018b) and the inhomogeneous flow of vortex-induced instability (Sengupta et al., 2018a). The DETE method demonstrates the creation and growth of rotationality, while DME helps in explaining the nonlinear instability developed as a result of the interacting velocity and vorticity fields from the convective acceleration term. As, the application of DME involves taking the divergence of the incompressible NSE, it causes dropping of viscous and unsteady terms from the NSE. Unlike Q-criterion and λ_2-criterion which are derived from the velocity field, it is obtained through rearrangement of the rotational form of NSE, and has a direct correlation with the vorticity field. DME can be considered as a sub case

of the DETE analysis, where the unsteady and viscous terms have not been accounted for. DME operates in outer inviscid flow, while the added function of DETE is more evident in near-wall viscous part of the flow. The discerning feature of disturbance enstrophy is that it is not always necessarily a positive definite quantity which deviates from the traditional analogy drawn between enstrophy and dissipation (Doering and Gibbon, 1995) for 2D periodic flows. By the rudimentary definition of disturbance components obtained by subtracting mean quantities from instantaneous ones, we end up with a definition of disturbance enstrophy which can either be positive or negative. This information is used meaningfully to identify patterns in the flow about the sign and source of disturbance during different stages of the evolving flow field, as demonstrated for vortex-induced instability in Sengupta et al. (2019a). The application of DME and DETE in capturing and tracking coherent structures has been demonstrated for the ZPG boundary layer excited from inside the shear layer and from the free stream in Sengupta et al. (2019b).

Low pressure turbine flows are comparatively simple, compared to fans and compressors, thus, there is a good understanding of turbine aerodynamics and the response of LPT to FST, blade roughness, unsteady wakes and flutter can be computationally predicted with reasonable accuracy. However, the unpredictable nature of blade flutter, is the source of incidents in industry. Commercial computational fluid dynamics (CFD) codes depend on empirical correlations and simplified models and thus, these tools inaccurately assess the flow under unanticipated dynamics. Additionally, reproducing the conditions associated with FST, roughness, flutter, wakes etc. in LPTs to validate blade designs by experimentation may prove to be an expensive venture. Understanding the flow physics governing the various perturbation environments in a LPT is thus, of paramount importance. Using high fidelity CFD, parameters pertaining to transitional LPT flow will be studied for various airfoil geometries and operating conditions. The configurations used in the current study involve a flat plate subjected to a pressure gradient representative of the suction surface of a low pressure turbine blade and a flat plate over which a convecting free-stream vortex with counterclockwise rotation induces local pressure gradient similar to that seen for suction surface of a LPT blade

1.2 Objectives and Outline of the Thesis

The current study aims to achieve the following objectives:
(i) Understanding the physics governing LPT flutter, effects of free-stream turbulence, unsteady wakes and surface roughness on separation-induced transition on the suction surface

of LPT blades.

(ii) Determining whether an analogy to the 'roughness benefit' associated with rough blade surfaces in low Re flows can be extended to aeroelastic flutter of blades, wherein the laminar separation region was suppressed by the introduction of roughness, and hence leading to a reduction in the net profile loss associated with the LPT blade.

(iii) Characterizing the bypass transition of a free-stream convecting vortex, under the influence of a discrete roughness element, using various linear and nonlinear receptivity mechanisms.

(iv) Studying the effect of aeroelastic blade vibration on the wake-induced transition on the suction surface of ultra high-lift blade profiles.

(v) Using classical and recently developed theories of stability and receptivity to highlight the underlying mechanisms in the presence of various disturbance environments.

(vi) Demonstrating the use of the theory based on disturbance enstrophy transport equation in tracking and identifying coherent structures for transitional flows excited in the free stream.

The next chapter will present a literature review of turbomachinery flutter, free-stream turbulence effects, unsteady wake effects and surface roughness effects on the boundary layer transition in LPT blades. A discussion on classical and recent developments in boundary layer receptivity and in structure detection will also be provided. In chapter 3, the numerical methods employed in the CFD solvers, the inflow conditions and governing equations for the various test cases will be introduced. In chapter 4, a correlation between well-established vortex identification techniques and the proposed DETE method is obtained and application of the proposed methods in tracking a structure from its nascent stage to a fully developed turbulent flow structure is shown. Chapter 5 will focus on the results establishing the relationship between LPT flutter and FST on the transitional flow on the suction surface of LPT blade. Chapter 6 will focus on the 2D and 3D results obtained for the vortex-induced instability mechanism with and without roughness, through various linear and nonlinear receptivity theories for the canonical ZPG boundary layer. Chapter 7 will present the results pertaining to the separation-induced transition on the ultra high-lift blade profile in the presence of unsteady wakes and aeroelastic vibration of the blade. In chapter 8, the nonlinear receptivity methods of DME and DETE are put in context with classical linear

receptivity methods. Further insight into the DNS results of chapters 5 to 7 is obtained and the underlying mechanism is brought to the forefront. The final chapter summarizes the key points determined and remarks on avenues for future work.

Chapter 2

Literature Review

In literature, several researchers have experimentally and numerically investigated the separation-induced transition mechanisms governing the boundary layer separation on the suction surface of a LPT blade. The configurations used primarily involve a flat plate subjected to a streamwise pressure gradient representative of cascade geometries. This chapter includes the relevant literature explaining the transition mechanisms of boundary layer separation and effect of aeroelastic oscillations, free-stream turbulence, unsteady wakes and surface roughness on the laminar separation bubble that arises during separation-induced transition on LPT. The relevant literature for bypass transition arising from a free-stream convecting vortex, modelled as a unit process of FST, propagating at a constant height and speed over a discrete roughness element, is detailed next. A discourse on various vortex and coherent structure identification methods is provided, which highlights the need for a more generic method for tracking the instability from its inception, to turbulent stage. Finally, based on the gaps in the existing literature, objectives of the current research are established.

2.1 Separated Flow Transition

On highly loaded LPT blades, the aft portion of the suction surface is prone to separation (Bons, 2010). A thin pre-transitional boundary layer commences from the leading edge. At low Reynolds numbers (Re), beyond the leading edge, the flow is unable to overcome a strong adverse pressure gradient due to lack of momentum. The flow separates from the wall forcing the streamlines away from the surface at an angle, as has been seen in previous large eddy simulation (LES) studies of Lardeau et al. (2012) and Vadlamani (2015). If the separated shear layer does not reattach to the surface before the trailing edge, then it is referred to as open separation. If it reattaches to the surface before the trailing edge, a laminar separation bubble is formed. At a location downstream of separation, the fluid

trapped under the shear layer is stagnant and the pressure remains constant. This has been termed as the 'dead-air region' by Himmel (2010). This is the scenario for low Re where one encounters steady separation. In an actual moderate to high Re case, the separation bubble is unsteady, and one often studies such phenomenon in phase-averaged or time-averaged sense. Unsteady separation is a subject of research for several decades, accounts of which are provided by Telionis (1981) and Haller (2004). The separated shear layer is unstable due to inflectional velocity profiles and sheds Kelvin-Helmholtz vortices. The Kelvin-Helmholtz vortices further break down due to the action of secondary instability and transition of flow to turbulence occurs. This is marked by an increased wall-normal mixing, and hence leads to flow reattachment. Jahanmiri (2011) provides a detailed account of boundary layer transition mechanisms in gas turbines. The flow features surrounding a laminar separation bubble have been described by Horton (1968) and marked in Fig. 2.1. It must be pointed out that the figure shows a time-averaged structure of the bubble. The instantaneous flow field is highly unsteady and three-dimensional. The separation bubble decreases the effect of the adverse pressure gradient either by affecting the local pressure gradient or due to a prolonged interaction with the free-stream flow.

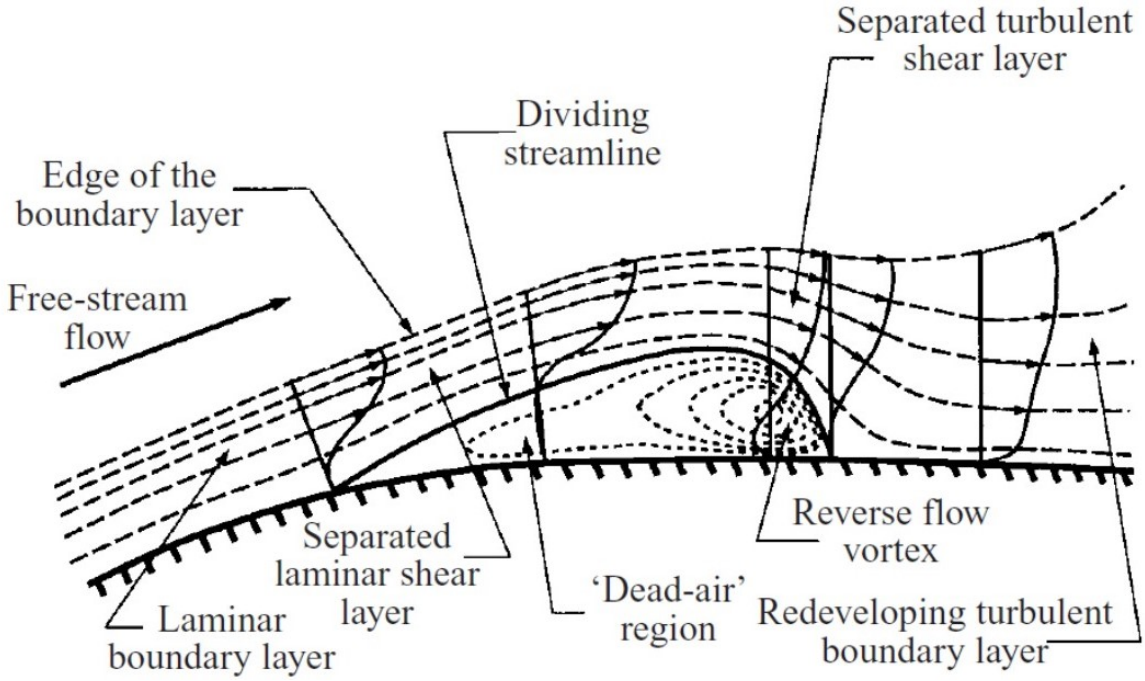

Fig. 2.1 Flow structure of a time-averaged laminar separation bubble. (From Horton (1968)).

The paths to transition followed on the suction surface of a LPT blade as a response to various disturbance environments existing for a LPT have been clearly distinguished by Coull and Hodson (2011), and have been illustrated in Fig. 2.2.

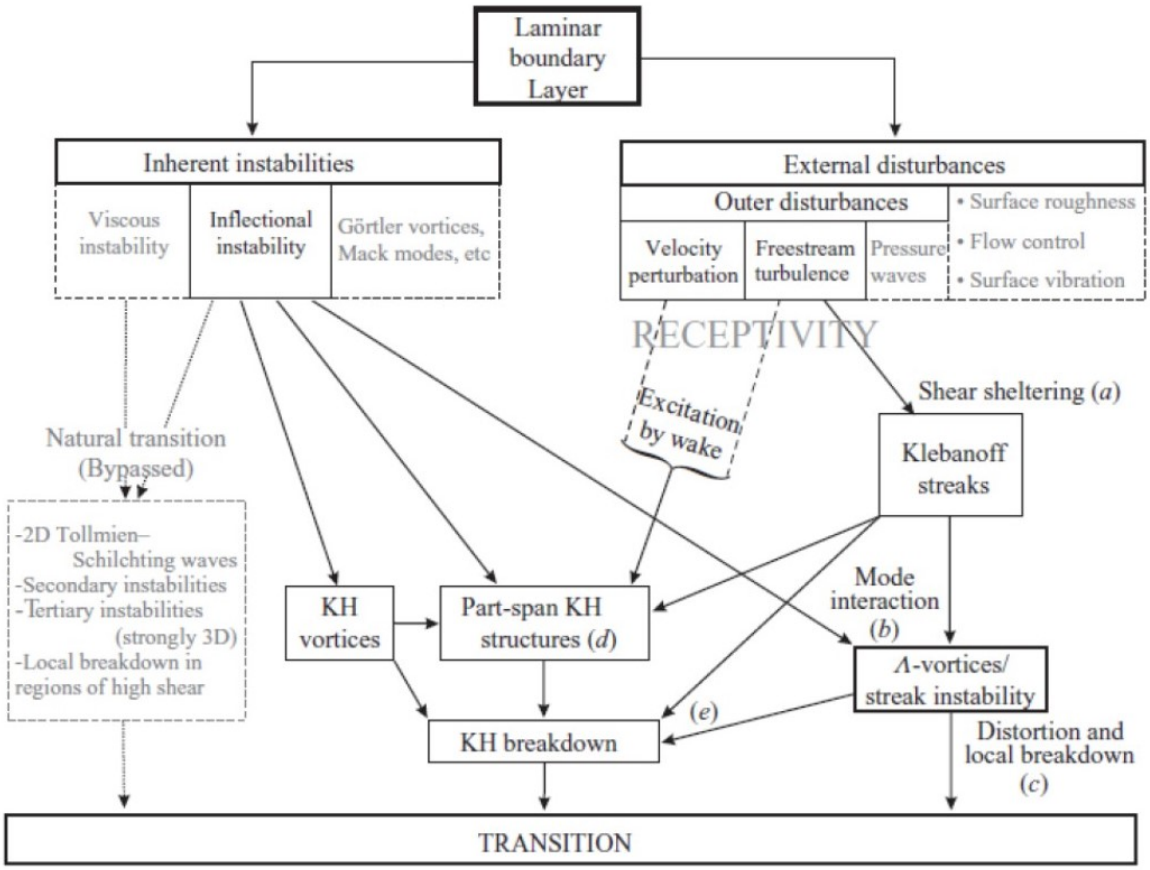

Fig. 2.2 Paths to transition from the laminar boundary layer. (From Coull and Hodson (2011)).

2.1.1 Low FST Levels

At low levels of FST, most researchers advocated for inviscid instability of the free shear layer as the dominant governing mechanism for transition in a laminar separation bubble. Watmuff (1999) performed flying hot-wire measurements to document flow separation downstream of the adverse pressure gradient. The maximum disturbance amplitude was found to be at the inflection point and Kelvin-Helmholtz instability was the primary transition mechanism at play. This observation was supported by direct numerical simulations (DNS) of Spalart and Strelets (2000), Wissink and Rodi (2004), Simens (2008) and experiments of Häggmark (2000). DNS of 'short' laminar separation bubbles was performed by Alam and Sandham (2000). The bubbles were classified as 'short', as the pressure gradient of the flow was affected only in the immediate vicinity of the bubble. 'Long' bubbles have significant effects on the pressure distribution. The authors observed transition of separated shear layer via oblique modes and Λ-vortices-induced breakdown.

In experimental investigations of Diwan and Ramesh (2009), Simoni et al. (2012) and DNS by Brinkerhoff and Yaras (2011), it was observed that although the Tollmien Schlichting instability has a role in promoting transition, it is the Kelvin-Helmholtz instability which dominated the transition mechanism. LES studies of Vadlamani et al. (2013) and Vadlamani (2015) found interactions of Tollmien-Schlichting waves with Kelvin-Helmholtz instability to promote transition at low levels of FST. The origin of the inflectional instability is associated with the generation and amplification of Tollmien-Schlichting waves, upstream of the separation point by a viscous instability, in the adverse pressure gradient region of the attached boundary layer.

2.1.2 High FST Levels

At high levels of FST, bypass transition is observed. The Klebanoff streaks observed at elevated FST levels interact with the separated shear layer, and either reduce the size of the separation bubble or completely suppress the separation region. Jacobs and Durbin (2001) carried out DNS to explain the mechanism of bypass transition. Streamwise streaks were observed as an evidence of the Klebanoff mode. A phenomenon called shear sheltering was also observed. Disturbances are of two kinds, identified by the spectrum of solution of the Orr-Sommerfeld equation (OSE): a) one developing as a consequence of the free-stream mode, and b) the other developing from the wall mode. Alternatively, Jacobs and Durbin (1998) termed these as discrete modes and continuous modes. The free-stream modes fail to penetrate significantly into the region of shear. The shear layer suppresses the disturbances from crossing into the sheared region. This phenomenon is called shear sheltering (Hunt and Durbin, 1999). In the free stream, the free-stream modes encounter damping from the viscous stresses only. However, the wall modes decay by inviscid shearing and viscous dissipation. This results in free-stream disturbances being confined in a region outside the shear layer. The high frequency perturbations of FST are damped by the mean shear of boundary layer, whereas low frequency perturbations penetrate through boundary layer and are amplified. DNS studies of Durbin et al. (2009) demonstrated the interaction between the Klebanoff modes with viscous Tollmien-Schlichting instability, causing bypass transition. The interaction between the modes led to Λ-vortices.

The interaction of the Klebanoff streaks with the separated shear layer can either suppress the separation bubble or reduce its size. This was seen experimentally by Häggmark (2000) and on a LPT blade by Volino (2002). McAuliffe and Yaras (2010) explored the transition mechanisms at two FST levels (0.1% and 1.45%). Using spectral analysis, a Kelvin-Helmholtz mechanism was shown to dominate at low levels of FST. At high FST levels, the transition process was quicker due to the formation of Klebanoff streaks, which

increased the energy content at all frequencies. The streaks interact with pre-transitional boundary layer and lead to earlier reattachment and shorter separation bubble due to the creation of turbulent spots. Coull and Hodson (2011) described the unsteady boundary layer transition in LPTs experimentally, for FST levels representative of a typical LPT, in the presence of unsteady wakes. Numerical simulations studying the effect of high levels of FST include DNS performed by Karaca and Gungor (2003), Wissink and Rodi (2004) and Balzer and Fasel (2016) and LES by Lardeau et al. (2012), Vadlamani et al. (2013) and Vadlamani (2015). As discussed in the introduction, Klebanoff et al. (1992) noted discrete peaks for FST associated with the wind tunnel used for experiments. They commented on the disturbance environment, and attributed it to bypass route due to FST effects rather than a Tollmien-Schlichting instability.

2.1.3 Effect of Roughness on Separation-Induced Transition

Blade surfaces progressively roughen due to various damage mechanisms, despite being hydrodynamically smooth during deployment (Licari and Christensen, 2011). A review of surface roughness effects in gas turbines was carried out by Bons (2010). Aerodynamic loss studies allowed Bons (2010) to conclude that the suction surface of a blade is the region most susceptible to roughness effects. Roughness eliminates suction side separation via bypass transition. Bons (2010) states that *"for some low Re cases, roughness induced transition actually prevented laminar boundary layer separation on suction surface thus lowering the overall vane losses compared with the smooth wall case. The low Re benefit only occurs if a smooth-wall laminar separation is prevented by roughness-induced transition, which depends strongly on the airfoil profile and loading. Low pressure turbine airfoils are more prone to experience this benefit.*"

Artificial roughness elements were used in the experimental works of Roman (2002), Vera (2004) and Zhang (2005) to investigate the effect of flow control in ultra high-lift devices. Roughness benefits were observed for a Re range of 1×10^5 to 2×10^5. Experiments by Himmel (2010) utilised a backward facing step on the suction surface to considerably reduce loss at low Reynolds numbers. Realistic roughness configurations were employed by Roberts and Yaras (2005) and Montomoli et al. (2010). Roberts and Yaras (2005) noted that roughness promoted earlier transition in separated shear layers and hence reduced the size of the separation bubble. Simens and Gungor (2013) employed DNS to study the correlation between height and location of discrete roughness elements and the transition of the separated shear layer. The roughness was modeled using an immersed boundary method, however only the adverse pressure gradient part of the blade was taken. Vadlamani et al. (2013) performed

LES to study the individual and synergistic effects of FST and roughness. They observed a shift in the inflection point of the velocity profile towards the wall, with combined FST and roughness. The authors observed from their results that, the streaks due to roughness were steady, whereas those arising from FST were intermittent. In recent numerical investigation of Sengupta et al. (2017), the individual and cumulative effects of free-stream turbulence and roughness have been studied and the contributions on net turbulent kinetic energy production and other flow parameters have been described. It is found that while FST had an effect in suppressing the laminar separation bubble via the Reynolds stress, surface roughness has a direct effect on mean velocity, promoting enhanced wall-normal mixing and thus led to effective suppression of the separation region. This was also noted in the experiments of Klebanoff et al. (1992). Recent DNS of Abderrahaman-Elena et al. (2019) for a turbulent channel with rough walls studied the effects of the roughness on overlying turbulence using a modified triple decomposition of the flow.

2.1.4 LPT Blade Flutter and Control Parameters

Flutter is an aeroelastic instability which occurs when positive aerodynamic work (i.e. work exerted by the fluid on the blade) exceeds damping mechanisms inherent in the structure. Thus, the objective of designers is to have the blade performing net work on the fluid to ensure stability. The unsteady parameters related to the aerodynamic stability have been found to be the reduced frequency and mode shapes. Stall flutter, which is the type of flutter studied here, differs from classical flutter in terms of the mechanism for energy transfer from flow to the oscillating structure. In classical flutter, the mechanism relies on the coupling of elastic and/or aerodynamic coupling between two modes, such as the bending mode or torsion mode. Whereas for stall flutter, Dowell et al. (2004) state that *"the essential feature of stall flutter is the nonlinear aerodynamic reaction to the motion of the airfoil/structure. Thus, although coupling and phase lag may alter the results somewhat, the basic instability and its principal features must be explained in terms of nonlinear normal force and moment characteristics.*" Thus, here the full NSE is solved to provide an accurate estimate of the nonlinear dynamics governing LPT flutter. The flow field during stall flutter is characterized by the generation of free vortices near the separation points, which are shed periodically creating regions of reversed flow in the vicinity of the blade.

An important parameter for studying blade flutter is the reduced frequency (k_{osc}) and its effects on stability are well documented by Bendiksen and Friedmann (1980), Nowinski and Panovsky (2000), Panovsky and Kielb (2000) and Vogt (2005). It is defined as,

$$k_{osc} = \frac{\omega_{osc} L}{U} \tag{2.1}$$

where ω_{osc} is the angular frequency ($\omega_{osc} = 2\pi f$, f is the frequency of oscillation), L is the reference length scale, usually taken to be the chord length, and U is the inlet flow velocity. Small values of the reduced frequency ($k_{osc} < 0.1$) indicate a 'quasi-steady' situation, where the flow is allowed to settle to the changed conditions (Logan and Roy, 2003). A typical reduced frequency associated with the first bending mode is 0.3, while the first torsional mode is observed at a higher reduced frequency of 1 for a low pressure turbine (Vogt, 2005). A lower structural reduced frequency indicates a higher tendency to flutter. The low pressure turbine consists of high aspect-ratio blades which are subjected to high subsonic relative velocities, which tend to yield airfoil oscillations in the low reduced frequency regime. Additionally, there is the modern trend of weight saving for engine manufacturers focused on increasing fuel efficiency. By reducing the blade chord or thickness, a lighter, lower-reduced frequency blade results. This has a cumulative effect in lowering the reduced frequency. The aeroelastic engineer strives to design blades with higher reduced frequencies to avoid unwanted vibrational instabilities (Waite, 2016). The present investigation aims at studying aerodynamic space-time variation and one can similarly study reduced frequency related to fluid dynamics. Prevention of flutter would require safe separation of structural and fluid dynamic reduced frequencies.

Another parameter of importance is the blade's vibratory mode shape. This has more prominence for studies focusing on the structural dynamics of the blade. The two types of turbine mode shapes are (i) blade-dominated (bending, torsion etc.) wherein mode shapes arise from studying a single blade experiencing vibration; (ii) disk-dominated wherein mode shapes are based on considering the blade to be mounted on a disk-like assembly. Kirschner et al. (1976) experimentally highlighted the importance of mode shape on aerodynamic damping. Panovsky and Kielb (2000) created the design tool, Tie-Dye plot, to map the critical reduced frequency corresponding to neutral aerodynamic damping, as a function of mode at various inter-blade phase angles. Peng and Vahdati (2002) performed a similar study replacing the varying parameter, as the ratio of leading edge to trailing edge displacements. The cumulative effects of reduced frequency and mode shape have been undertaken by Panovsky and Kielb (2000) and Vega and Corral (2013).

Szèchènyi (1985), performed experimental studies on compressor blade flutter, and stated that *"contrary to widespread practice, the fundamental approach to flutter problems should lie at least as much in the study of single blade flutter as in that of unsteady cascade effects.*" He (1996) experimentally studied the unsteady flow in oscillating LPT blade cascade. A short separation bubble was observed near the trailing edge on the suction surface. He

(1996) observed that *"the short bubble on the suction surface seemed to follow closely a laminar bubble transition model in a quasi-steady manner, and had a localized effect.*" The suction surface bubble had a stabilizing effect despite the unsteady pressure variation at 75-85 % axial chord, showing a tendency toward a negative damping. This was due to the dominance of the stabilizing effect, as a result of abrupt phase increase and the high amplitude of pressure variation around the reattachment point of the suction surface separation bubble. Hack (2014) showed that a spanwise time-harmonic wall excitation led to the suppression of bypass breakdown. Buffum et al. (1998) experimentally investigated the aerodynamics of an oscillating cascade of airfoils in torsion. At an angle of incidence of 10^o, Mach number = 0.5 and $Re = 9 \times 10^5$, they observed a separation bubble on the suction surface at the leading edge. Panovsky and Kielb (2000) conducted a linearized Euler analysis on LPT blade flutter with an emphasis on designing methods to prevent flutter in LPT blades. Vogt (2005) performed an experimental investigation of three-dimensional mechanisms in LPT flutter. Barbarossa et al. (2016) used analytical models based on potential flow theory to study LPT bending flutter. Wissink and Rodi (2003) carried out a 3D DNS of a laminar separation bubble in the presence of an oscillating flow, which induces a streamwise pressure gradient varying in time. Wu et al. (2003) performed an investigation of blade flutter pertaining to fans for high bypass ratio engines. Corral and Vega (2015) studied lightly and highly loaded airfoils in the low reduced frequency range ($k_{osc} < 0.05$) and noted a linear variation of stability with reduced frequency for highly loaded airfoils. Waite (2016) explored the physical mechanisms pertaining to flutter in LPTs and the effect of steady aerodynamic loading, offering design tools to control LPT flutter. Onoue and Breuer (2016) analyzed the vortex evolution over a controlled pitching flat plate in stall flutter. They used an oscillation over a flat plate subjected to appropriate pressure gradient distribution that is atypical of a wind tunnel. Culler et al. (2017) used a similar configuration to demonstrate that stall flutter oscillation of torsionally flexible structure comprised of two harmonic motion analogous to cantilevered beam eigenmodes.

2.1.5 Wake-Induced Transition

Wake-induced transition measured for Reynolds numbers ($2.5 \times 10^5 - 3 \times 10^5$) by Schulte and Hodson (1998) showed that the incoming wakes induced bypass transition upstream of the separation location. The wake-induced turbulent spots prevented the boundary layer from separating while the ensuing calmed regions also led to suppression of the separation bubble due to higher shear and fuller velocity profiles. A net reduction in the profile loss was observed due to the incoming wakes. This benefit was prominent at lower Reynolds numbers. Stieger and Hodson (2004) experimentally investigated wake-induced transition on

the T106A cascade for Reynolds numbers of 1.6×10^5 and at a low FST level ($Tu = 0.5\%$). Although transition was not observed upstream of separation location (suggesting a total suppression of the separation region), the convecting wake perturbed the separated shear layer due to increased shear, which intensified the growth of Kelvin-Helmholtz instability. The subsequent vortices and their breakdown triggered transition of the boundary layer. Unsteady measurements on the blade surface recorded large pressure fluctuations due to the convection of the wake-intensified Kelvin-Helmholtz vortices. Large scale velocity perturbations induced by the wake were found to intensify the Kelvin-Helmholtz vortices, and their breakdown was accentuated by small scale turbulence in the wake, noted in the DNS studies of Wissink et al. (2006) and in the LES studies of Michelassi et al. (2003) and Sarkar (2008). Coull and Hodson (2011) in their experimental observations for wake-induced transition at elevated FST levels, showed that the wakes perturb the boundary layer by initially accelerating the boundary layer and then decelerating it. They also found that the small scale turbulence in the wake-induced streaks in the boundary layer were stronger than those due to FST. DNS studies of Gungor et al. (2012) showed the relationship between the separation bubble and different wake passing frequencies and profiles. The frequency of wake passing showed a strong effect on the time dependent location of separation and reattachment. However, the wake shape and its velocity deficit didn't have a considerable effect on the flow development. Recent DNS studies of Karaca and Gungor (2016) investigated the combined effects of discrete surface roughness elements and periodic large scale wake forcing on the separation bubble transition. They observed the dominance of wake effects compared to those due to roughness.

In the experimental investigations of Lou and Hourmouziadis (2000), the unsteadiness was introduced by a sinusoidal perturbation to the free-stream. A similar approach will be used in the present wake-induced transition study, where a periodic Gaussian will be used to introduce unsteadiness in the free-stream. A sample of the unsteady results reported by Lou and Hourmouziadis (2000) is reproduced in Fig. 2.3. At a location upstream of the separation bubble (A), the sinusoidal velocity profile shows no turbulent fluctuations. Along the separated shear layer (B), waves evolve prior to the minimum velocity in the cycle. The packets of instability grow in amplitude and occupy an increasing portion of the sinusoidal cycle (B – E) until the velocity signals are turbulent throughout the cycle after the reattachment location (F). The 'dead air' region of the separation bubble (G) is characterised by intermittently turbulent flow with velocity traces similar to what would be expected for the passing of turbulent spots. The transition onset, reattachment locations and size of the bubble were found to vary with the free-stream oscillation induced by the sinusoidal perturbation.

To the author's knowledge, there have not been any numerical simulations which have studied the effect of blade vibration of LPT blades on the wake-induced transition of the separated shear layer in LPTs and the present study attempts to bridge this gap in our understanding.

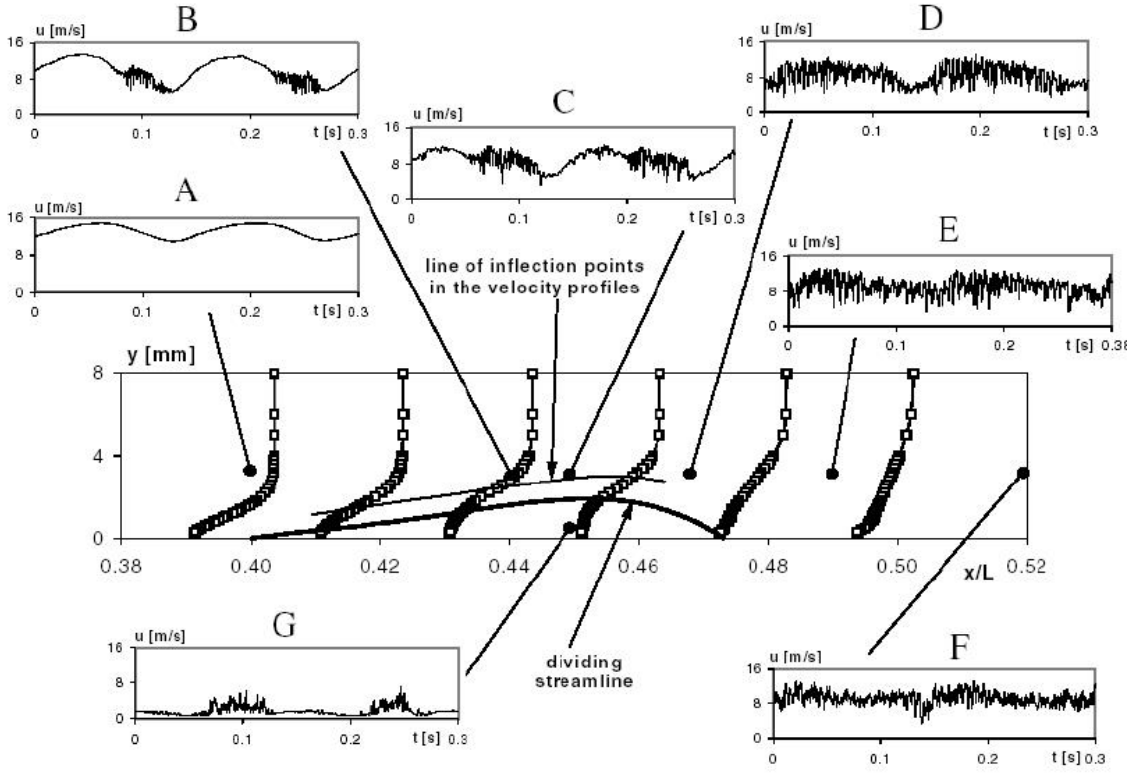

Fig. 2.3 Velocity measured during transition of separation bubble impinged by sinusoidal free-stream unsteadiness (From Lou and Hourmouziadis (2000)).

2.2 Bypass Transition Caused by Vortex-Induced Instability

The process of transition for boundary layers in external flows can be qualitatively described using the block diagram in Fig. 2.4 of Morkovin (1991), wherein he questioned whether bypass transition was arising as a consequence of some nonlinear or nonparallel effects or due to some unknown mechanisms altogether. Distinction is made between surface excitation (excitation inside the shear layer, whose instability is to be studied) and other excitations originating from the outside of the shear layer in Fig. 2.4. This distinction was prompted

by the observation in the vibrating ribbon experiment of Schubauer and Skramstad (1947). The experimentalists noted that they could create the elusive Tollmien-Schlichting waves when the ZPG boundary layer was excited by a vibrating ribbon, thereby creating a vortical excitation inside the boundary layer. However, they also noted that acoustic excitation from the roof of the tunnel did not create Tollmien-Schlichting waves. This prompted Morkovin (1969) to coin the term receptivity. In the receptivity analysis, a deterministic perturbation is fed as an input to the system and the response or sensitivity of the system to such an excitation is analysed. In the experiment, the boundary layer was receptive to vortical excitation from within the boundary layer but not receptive to acoustic excitation in the free stream. However, Dietz (1999) created Tollmien-Schlichting wave in a boundary layer by vibrating ribbon in the free stream. So it is important to distinguish the qualitative natures of input while discussing receptivity, rather than whether the source is located inside or outside the boundary layer. Although Hunt and Durbin (1999) have shown that free-stream disturbances remain sheltered from the boundary layer, and enter the boundary layer as steady and/or unsteady fluctuations of the base state. Receptivity provides a coupling between the external ambient disturbances and the boundary layer instabilities.

Morkovin (1991) demarcated transition to follow two principal routes: one that will be created by Tollmien-Schlichting waves, thought to be for natural transition and rest of the cases which could not be explained by linear stability theory with normal mode analysis. These last events are clubbed together as the bypass transition routes (as seen in Fig. 2.4).

Saric et al. (2002) provided another "roadmap"of various transition routes which has been shown here in Fig. 2.5. The amplitude of the disturbance increases from left to right (paths A to E in Fig. 2.5). The authors report that if a weak disturbance initiates the flow (as in path A in Fig. 2.5), the initial growth rate of the disturbance can be described by linear stability theories. As the amplitude of the disturbance grows, nonlinear interactions occur in the form of secondary instabilities. The path A in Fig. 2.5 assumes that the free-stream disturbances are weak. However, the situation is different when the free-stream disturbances are so strong that the growth of linear disturbances is bypassed (Morkovin, 1993) and turbulent spots or subcritical instabilities arise. This situation is shown by path E in Fig. 2.5. This phenomenon has been documented for high FST levels by Reshotko (1976, 1994, 1997, 2001). Saric et al. (2002) state that *"bypass refers to a transition process whose initial growth is not described by the primary modes of the OSE. "*

Of the various cases classified as bypass transition, two flows, namely the pipe flow and Couette flow show unconditional stability with respect to linear theory. The plane channel flow or plane Poiseuille flow exhibit subcritical transition and thus, cannot be easily explained by linear normal modes. In this context, the concept of transient growth of disturbances was

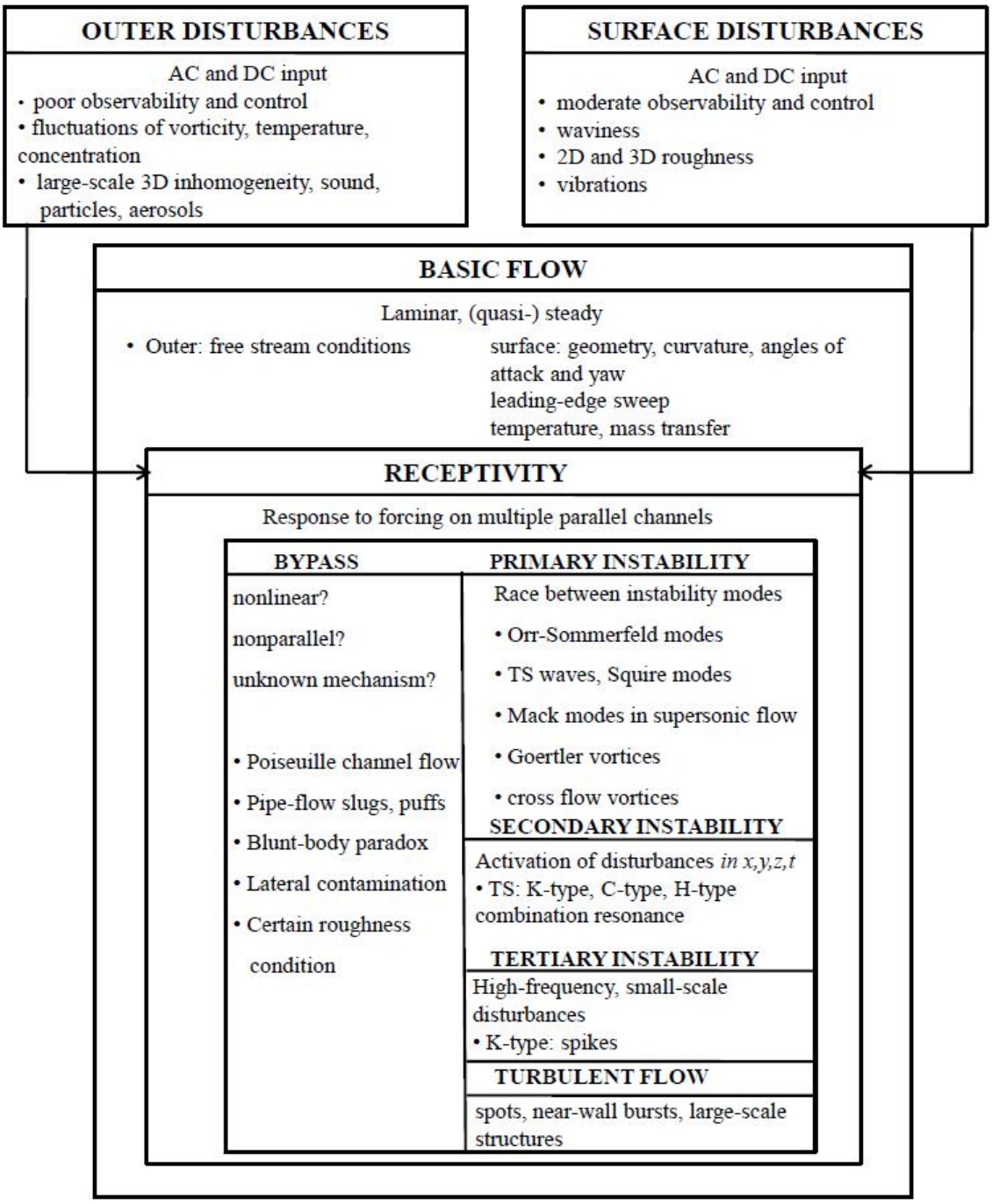

Fig. 2.4 Various routes to turbulence from receptivity stage. (From Morkovin (1991)).

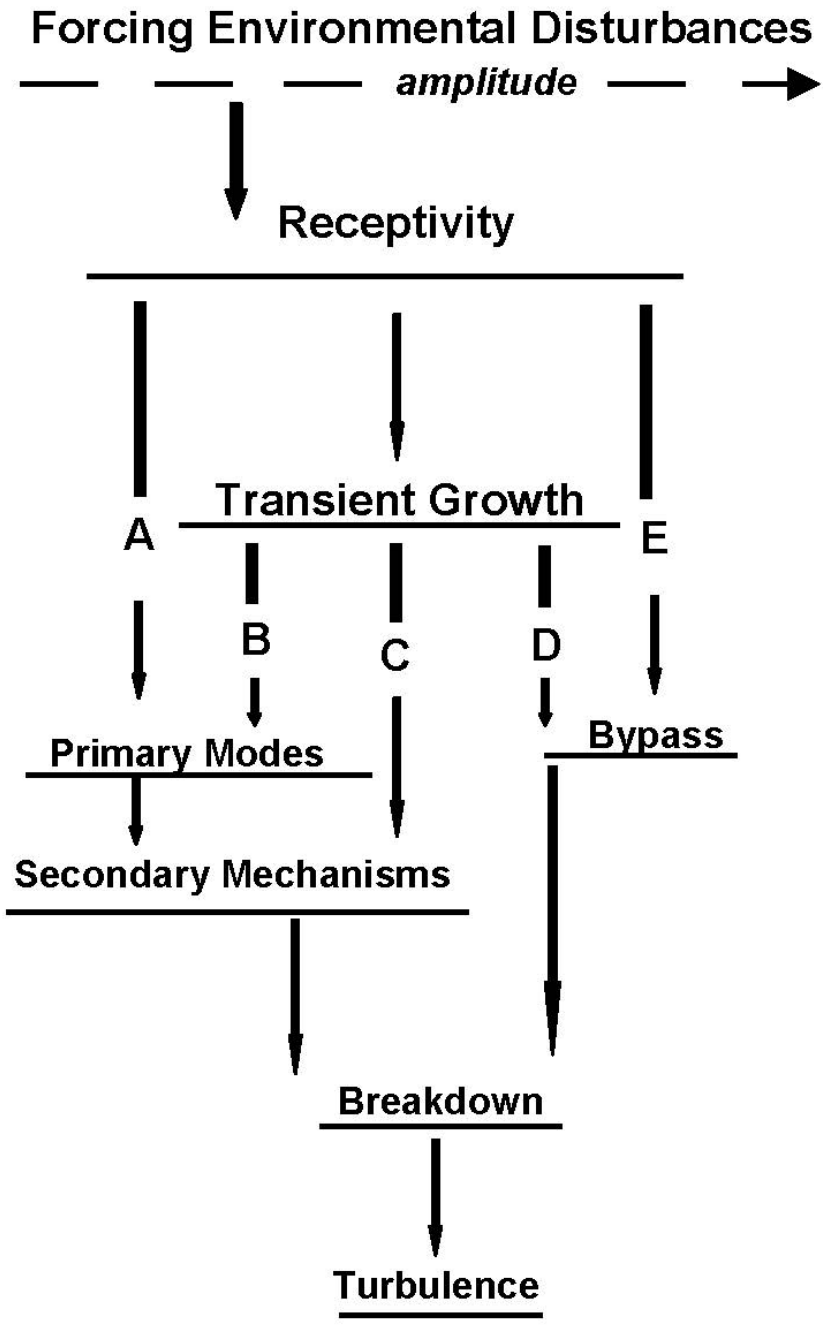

Fig. 2.5 Various paths from receptivity stage to transition. (From Saric et al. (2002)).

sought by invoking the concept of non-normality or non-orthogonality of the modes by Reddy et al. (1993) for Poiseuille and Couette flow. Transition initiated by transient growth can also be termed as bypass transition. Transient growth occurs when two, nonorthogonal, stable modes interact, undergo algebraic growth, and then decay exponentially. This mechanism

was first elucidated by Landahl (1980) and then by Hultgren and Gustavsson (1981) and has since then been used by Boberg and Brosa (1988); Butler and Farrell (1992); Farrell (1988); Gustavsson (1991); Reddy and Henningson (1993). Reshotko (2001); Schmid (2007); Schmid and Brandt (2014); Schmid and Henningson (2001) have provided a review of transient growth and its role in bypass transition. The remaining paths in Fig. 2.5 can be explained by this concept of transient growth. Depending on the disturbance amplitude, transient growth can lead to spanwise modulations of 2D waves (path B), direct distortion of the base state that leads to secondary or subcritical instabilities (path C), or a direct bypass route (path D). In some studies (Biau and Bottaro, 2008; Bottaro et al., 2003) sensitivity of the bypass transition process to the variations in the base flow are reported. The researchers found that the initial stages of the transition process offer a combination of algebraic and exponential growth of disturbances, with the latter having a direct correlation with the base flow variation.

Wu et al. (2014) have defined bypass transition in the narrow sense as *"a superposition of the Blasius layer with free stream continuous isotropic turbulence at an initial intensity level (FST) between approximately 1% and 4% "*. Schlatter et al. (2008) noted bypass transition to develop its own primary instability in the form of long-streaks whose algebraic/transient growth led to secondary instability (streak meandering or streak interaction with free-stream eddy). Matsubara and Alfredsson (2001) have reported experimental results for boundary layer flow subjected to free stream turbulence in the range of 1-6% which showed initial growth of streaky structures to be closely related to algebraic or transient growth theory. Westin et al. (1994) have experimentally studied modification of flat plate boundary layer subjected to nearly isotropic free-stream turbulence and reported that the fluctuations inside the boundary layer are dominated by streaky flow structures which grow downstream both in amplitude and length.

Cherubini et al. (2012) proposed various transition scenarios for a boundary layer flow, which have been shown in Fig. 2.6. The authors showed that apart from primary instability and transient growth-initiated bypass transition, there is also possibility of nonlinear route of transition caused by finite-amplitude disturbances taking the laminar flow to chaotic state via triggering a regeneration cycle of Λ and hairpin vortical structures. The transient growth itself can be considered to be a primary growth stage of disturbance field. The nonlinear route adopted is very different to the classical route initiated by perturbation in the form of streamwise vortices or Tollmien-Schlichting waves, as has been shown in Fig. 2.6. A similar nonlinear approach was adopted by Eckhardt et al. (2007); Waleffe (1998) wherein transition and turbulence were envisioned as *"random walk of the system's trajectory "* employing the exact unstable solutions of the NSE. Recently, in a review paper by Kerswell (2018), a

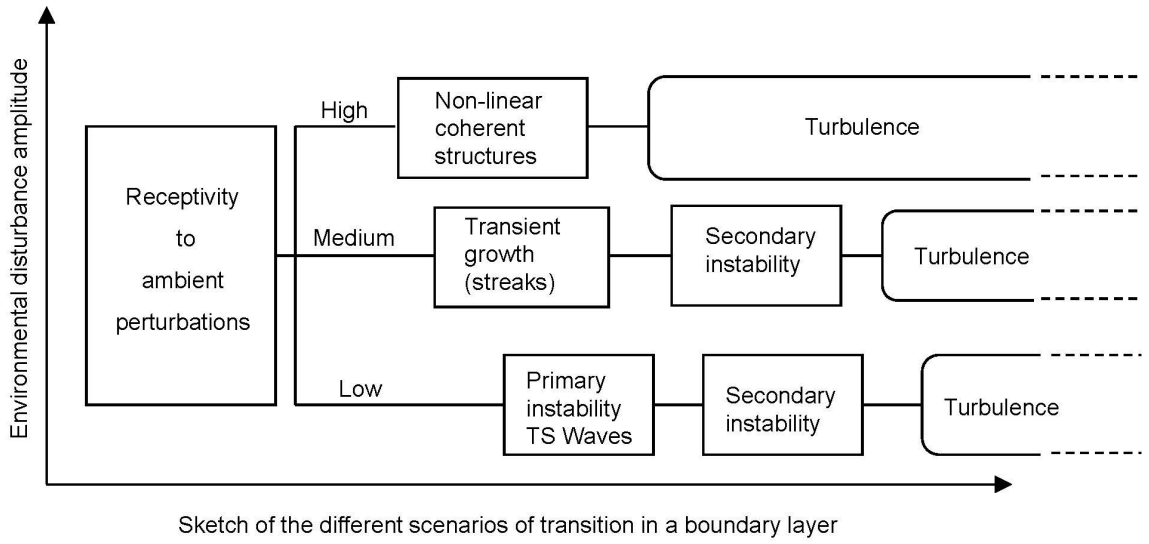

Fig. 2.6 Different transition scenarios in a boundary layer. (From Cherubini et al. (2012)).

nonlinear nonmodal strategy of stability and receptivity study has been provided. In this approach, not only is the transient growth obtained by considering the contributions from non-normality of eigenmodes, but also nonlinear terms from the solution of the NSE are incorporated by a direct adjoint-looping technique (Cherubini et al., 2010; Juniper and Sujith, 2018; Monokrousos et al., 2011). Interestingly, Kerswell (2018) notes that one of the avenues for future development in the field of nonlinear stability is the *"treatment of time-periodic states"* and *"aperiodic flows like an impulsively started flow"*. This is one of the features of the DETE analysis (discussed later) wherein a time-varying base state has been studied and information about its stability (such as saddle points) has been obtained for the Taylor-Green vortex problem (Sengupta et al., 2018b). Impulsive start experiments have been performed by Gaster and Grant (1975) wherein a wavepacket is created from a single hole on the surface of a flat plate over which a ZPG boundary layer exists. The resultant disturbance field in the form of a spatio-temporal wave packet was traced to turbulent spot stage. There are two corresponding 3D nonlinear simulations (Bhaumik and Sengupta, 2017; Sundaram et al., 2018) where the primacy of spatio-temporal wave front (STWF) has been shown in creating transition to turbulence. In the experiments and computations, no Tollmien-Schlichting waves were observed.

Other attempts have been made by researchers to understand the physical mechanisms causing bypass transition. These broadly fall under the categories of streak instabilities as given by Brandt et al. (2003), Brandt and de Lange (2008), Brandt et al. (2004), Monokrousos et al. (2008) and Schlatter et al. (2008) and interaction between continuous and discrete

modes as given by Durbin et al. (2009), Jacobs and Durbin (2001), Liu et al. (2008), Zaki and Durbin (2005) and Zaki and Durbin (2006).

In the former, bypass transition is characterized by the appearance inside the boundary layer of streamwise elongated streaky structures of alternating high and low streamwise velocity. The non-normality of the linearized operator of the Navier-Stokes equations, causes some disturbances to experience a significant transient energy growth. For the case of boundary layers, they consist of streamwise counter-rotating vortex pairs. The vortices lift low-momentum fluid from the wall and push high-momentum fluid from the outer parts towards the plate, thus creating elongated regions of alternating accelerated and decelerated streaks. This is also known as lift-up effect. Once the streaks are formed, the boundary layer becomes susceptible to high-frequency secondary instabilities due to the presence of both wall-normal and spanwise inflectional velocity profiles. These secondary instabilities manifest themselves in symmetric and antisymmetric streak oscillations, finally leading to the formation of turbulent spots.

Brandt et al. (2003) studied the nature of the secondary instability experienced by finite-amplitude streaks in the flat-plate boundary layer with high levels of free-stream turbulence. This led them to conclude that the bypass transition studied by them is essentially noise-driven. The authors further noted that the perturbations considered represent one of several plausible approximations of the streaks observed in boundary layers subject to relatively high free-stream turbulence. Brandt et al. (2004) studied the effect of high levels of FST on bypass transition in a Blasius boundary layer by DNS. The authors used a synthetic turbulent inflow obtained as a superposition of modes of the continuous spectrum of the Orr-Sommerfeld and Squire operators which constitute an optimal set in the linear stage. These perturbations were found to become unstable via sinuous/varicose breakdown which the authors identified as the underlying mechanism triggering bypass transition phenomena. Further this led to their identification of two distinct physical mechanisms depending on the energy content of the external disturbance: (i) a linear mechanism if the free-stream turbulence contains low-frequency disturbances, and (ii) a nonlinear process if the free-stream turbulence mainly contains high-frequency disturbances.

Schlatter et al. (2008) explained the role of the boundary-layer streaks and their instability with respect to turbulent breakdown in bypass transition on a boundary layer subject to free-stream turbulence. The authors concluded that the similarity with the flow structures observed in the transitioning wave packet is evidence for the role of the streak secondary instability in bypass transition. Although the authors claimed that the inclusion of the leading-edge is important for the free-stream disturbances to enter the boundary layer, it is not clear whether it has been accounted for. Brandt and de Lange (2008) showed that the turbulent breakdown

in the flat-plate boundary layer flow is due to streamwise velocity streaks of finite amplitude. The authors showed the importance of unsteadiness and interaction among streaks to be an important triggering mechanism of the breakdown. Monokrousos et al. (2008) studied the transition to turbulence occurring in a flat-plate boundary-layer flow subjected to high levels of free-stream turbulence and noted formation of streamwise streaks.

In the other scenario, bypass transition is explained as a consequence of interaction between continuous and discrete modes, i.e. the Orr-Sommerfeld modes. Jacobs and Durbin (2001) performed DNS of bypass transition of a ZPG boundary layer forced by a fully turbulent free-stream. The turbulent inflow was constructed from Orr-Sommerfeld continuous modes. Zaki and Durbin (2005) studied the manner by which external vortical disturbances penetrate the laminar boundary layer and induce transition. They showed that the entire transition process is realizable through the interaction of only two Orr-Sommerfeld continuous mode eigenfunctions: one low-frequency, strong coupling disturbance which generates Klebanoff streaks, and one high-frequency mode. The former penetrates the boundary layer and induces the forward and backward perturbation jets. The latter high-frequency disturbance is filtered by the shear, and hence exists solely in the free-stream. This mode interacts with the lifted backward jets only near the top of the boundary layer, causing an inflectional type of instability. The instability was found to intensify downstream, leading to breakdown into a turbulent spot.

Zaki and Durbin (2006) investigated the continuous mode transition in the presence of adverse pressure gradients. The influence of pressure gradient in the bypass regime was found to be not due to the inflectional mean velocity profile, but instead due to the coupling of the free-stream vortical disturbances to the boundary-layer shear and the intensity of the streaks. It is interesting to note that the authors support the fact that there is no leading-edge effect due to insensitivity of bypass transition on it. Liu et al. (2008) performed numerical simulations to study the interaction of Tollmien-Schlichting waves and boundary-layer streaks.

It can be inferred from the above discussion that the two theories portray different mechanisms for bypass transition. Researchers such as Wu (2010), Wu and Moin (2009) and Wu et al. (2017) studied bypass transition by introducing patches of isotropic turbulence periodically from the free-stream at the inflow. They observed the mechanism to bear similarity to the secondary instabilities in boundary layer natural transition studies of Herbert (1998) i.e. bypass transition defined as the primary instability in natural transition. They further stated that "*a well-controlled bypass transition will proceed along a path broadly resembling one of the secondary instabilities in natural transition.*" Wu (2010) showed a forest of hairpin vortices in both the transitional and turbulent regions of the boundary

layer. Recently, Wu et al. (2017) studied the transitional-turbulent spots in bypass transition and found that the spot inception mechanism is analogous to the secondary instability of boundary-layer natural transition.

Some researchers such as Cherubini et al. (2011), Cherubini et al. (2012) and Cherubini et al. (2010) presented an interesting transition scenario connecting two different views of transition- 1) transient growth and secondary instability of the streaks (Brandt et al., 2004) and 2) the one describing breakdown via the continuous regeneration of vortices (Wu and Moin, 2009). This connection was obtained by finding a global optimal disturbance via non-linear optimization which they termed as "*the minimal seed*" or "*the most dangerous disturbance.*" According to the authors, the global optimal disturbance is a pair of streamwise-modulated counter-rotating vortices, tilted upstream.

In the laser doppler anemometry measurements of Stieger and Hodson (2004) studying the wake-induced transition process on the T106 LPT cascade, the authors noted that the separated shear layer was associated with inflectional velocity profiles forming roll-up vortices beneath the passing wake. The roll-up vortices were found to breakdown to turbulent spots. Opoka and Hodson (2008) observed inflectional velocity profiles at elevated FST eventually leading to formation of turbulent spots, in their experimental investigation of a high-lift T106A turbine blade. Garai et al. (2018) in their numerical simulation of a high pressure turbine cascade, observed formation of streamwise Klebanoff modes in the presence of FST with $Tu = 7\%$, similar to the bypass transition mechanism noted by Zaki and Durbin (2005). Mao et al. (2017) studied the flow around a NACA 65 airfoil in a compressor passage. On the pressure side, two types of optimal perturbations were obtained: (i) Λ structures stretched to hairpin vortices before breaking down to turbulence (ii) high and low speed streaks generated through a lift-up mechanism. Davide et al. (2017) analyzed the coherent structures formed during wake-boundary layer interaction in a LPT. The authors observed low and high speed streaks penetrating the boundary layer at elevated FST levels. Scillitoe et al. (2019) performed LES of a gas turbine compressor cascade. At $Tu = 10\%$, the authors noted "*classical bypass transition*" with Klebanoff streaks incepting turbulent spots.

Receptivity to free-stream excitation in vortex-induced instability

Experiments on flow instability and receptivity are carefully designed, as in Schubauer and Skramstad (1947), to show the existence of Tollmien-Schlichting waves predicted by spatial instability theory. Thus, one has to excite the system at a fixed single frequency to create Tollmien-Schlichting waves. However in a natural transition by wall excitation, the background disturbances are never at a single frequency, and it is next to impossible to clearly

identify Tollmien-Schlichting waves for natural transition. It was the same for the receptivity experiment of Klebanoff et al. (1962) for 3D route of transition, with the equilibrium flow as the ZPG boundary layer. The ZPG boundary layer is known for its neutrally stable response to very small background disturbances. This was the rationale for the design of a very low-noise wind tunnel at NBS, Washington DC, where Tollmien-Schlichting waves were detected for the first time, by exciting the ZPG boundary layer by a monochromatic vibrating source. The use of ZPG boundary layer to study transition to turbulence is an example of performing controlled experiment, so that a vibrating vortical disturbance at a fixed frequency excited Tollmien-Schlichting wave. This aspect of using specific equilibrium flow has been emphasized in Smith (1993) to design such 'kernel' experiments to study transitional and turbulent flows. For this reason, in receptivity experiments and DNS of transitional flows, a ZPG boundary layer is always preferred, as in the experiment of Liu and Rodi (1991) to simulate transition in a turbomachine. As the vortices were given a downward wall-normal velocity towards the plate, that showed violent transition. This experimental flow field was simulated by Wu et al. (1999). While the above studies presented mechanisms to study bypass transition, there are some uncertainties/questions regarding the mechanisms. Few such mechanisms are described in the following, which helps in deciding how to study the mechanism(s) computationally and experimentally.

Monin and Yaglom (1971) noted that free stream excitation can cause "separation of the boundary layer under the action of a negative longitudinal pressure gradient", which explains "the effect of disturbances in the ambient flow", and "is connected with the generation of fluctuations of the longitudinal pressure gradient by these disturbances, leading to the random formation of individual spots of unstable S-shaped velocity profiles .... and hence, to separation and transition of the boundary layer. On the basis of this hypothesis, Taylor (1936) tried to estimate theoretically the dependance of the critical Reynolds number on the initial turbulence level of the ambient flow". Taylor also proposed that critical Reynolds number is determined by the modified Pohlhausen parameter $\Lambda = -\frac{\delta^2}{\mu U}\frac{\partial p}{\partial x}$, where δ is the boundary layer thickness. However, it is noted that in a ZPG boundary layer, $\frac{\partial p}{\partial x} = 0$, and yet there may exist fluctuations in pressure. "Thus, Taylor proposed that the character of the motion in a fixed section is determined here by the parameter $\Lambda = -\frac{\delta^2}{\mu U}\frac{\delta p'}{\delta x}$ (where p' is the pressure fluctuation and $\delta/\delta x$ signifies a typical value of the derivative $\partial/\partial x$). In other words, according to Taylor, the point of transition from laminar to turbulent flow is determined by the parameter Λ attaining some critical value"(Monin and Yaglom, 1971). This provides a justification for the study of effect of free stream disturbances on a ZPG boundary layer, provided one can create controlled pressure fluctuations, as have been reported in the experiments Kendall (1987); Lim et al. (2004); Sengupta et al. (2019a).

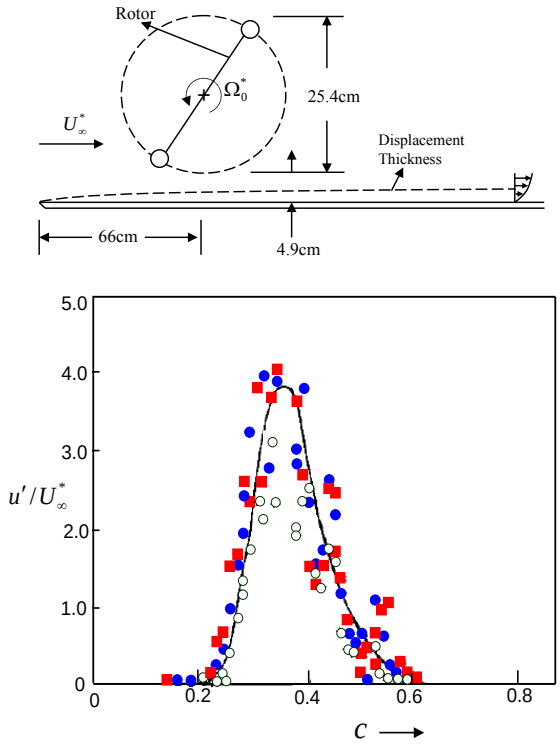

Fig. 2.7 Schematic of the experimental setup used by Kendall (1987) for the periodic free stream vortex excitation problem over a ZPG boundary layer (top); Peak response of streamwise disturbance velocity (u') measured for different rotor speeds as obtained by Kendall (1987).

The experiments of Kendall (1987) show the boundary layer to be excited by periodic free stream disturbances, in which the disturbances were not introduced inside the boundary layer. The schematic of the experimental apparatus and a typical set of results reported in Kendall (1987) are shown in Fig. 2.7. In the top panel of the figure, the test configuration shows a rotor with two cylinders placed at a distance R from the axis of rotation, rotating with a rate Ω_0 in an anti-clockwise direction. The translation speed of the periodic pulse is given by $c \simeq \Omega_0 R$. It is noted that this setup creates disturbances which remain distinctly outside the boundary layer. In the bottom frame of Fig. 2.7, it is evident that the induced streamwise fluctuations display strong receptivity for speeds c in the range 0.2 to 0.6, with a maximum receptivity for $c = 0.35$, and which falls off rapidly on either side. For this periodic excitation, the induced pressure field ahead of the rotor creates an adverse pressure gradient. In the computations reported in Sengupta et al. (2002) for the case of periodic free stream excitation a similar trend was noted. For vortex speed $c = 0.3$, a rapid growth of disturbances was reported (Fig. 10 in Sengupta et al. (2002)), whereas for the higher speed $c = 1$, the flow was not at all receptive (see Fig. 9 in Sengupta et al. (2002)). Also, the stability diagram in Fig. 6 of Sengupta et al. (2002) clearly shows the linear disturbance growth to occur in the speed range 0.26 to 0.39 for spatio-temporal growth. In Fig. 11 of Kendall (1987), it is noted that when the rotor rotated in the clockwise direction (thereby creating a favourable pressure gradient ahead of the rotor), the flow was not at all receptive.

We note that the effects of FST bears local resemblance to the effects created by free stream convecting vortex. If a free stream vortex is in isolation far away from any wall, then it will convect at the local speed dictated by vorticity transport equation. However, when the vortex is placed above a flat plate, it will not do so, due to Biot-Savart interactions among the free stream vortex, its image system and the boundary layer forming over the flat plate. For the case of FST, this situation is further complicated as FST is an ensemble of many vortices, which interact continually leading to individual vortex to travel at changing local speed, which is distinctly different from the free stream speed. One of the goals of the study on vortex-induced instability is to find out which local speed of translating vortex has a higher receptivity. This was the basis of design for the experiments in Lim et al. (2004), where control over the fluctuating pressure was exercised via the speed, strength and sign of the circulation. This was achieved with the help of a translating and a rotating cylinder, moving at a fixed height, constant rotation rate and a constant translational speed. By rotating a cylinder at a high rotation rate, a stable, compact and constant strength captive vortex in the free stream was created, and which was constrained to move at a fixed speed and height while it translated. The idea of creating a captive vortex by a rotating cylinder is supported by the experimental and computational work reported by White (2008) for super-critical rotation

rates, for which vortex shedding is suppressed for moderate Reynolds numbers. Also, it has been shown in Lim et al. (2004) that if there are any shed vortices behind the rotating cylinder then those will not affect the boundary layer below it, as the strength of such vortices will be orders of magnitude lower than the captive vortex associated with the rotating cylinder. If the cylinder was not rotated and simply translated in the experiment, then the boundary layer was not perturbed Lim et al. (2004). Thus, the carefully designed experiment isolates the effects of the free stream vortex on the boundary layer.

The shear layer is destabilized by the propagation of the free-stream vortex via the creation of an adverse pressure gradient. As the spin rate and the height of the cylinder can be controlled with precision, any vortex-induced instability created in the experiment can be repeated as and when required. The schematic and experimental apparatus used is provided in Fig. 2.8.

The ZPG boundary layer under investigation was allowed to form over a vertically held flat plate. The plate had a rounded leading edge and an adjustable trailing edge flap used to create a ZPG boundary layer in the absence of excitation. A rotating cylinder, whose axis was parallel and along the spanwise direction of the plate, was used to create the vortex. Visualizations were captured through dye-lines emerging from six dye ports located at a downstream location from the leading edge. The disturbance source was, by design, kept significantly outside the shear layer to mimic the unit process of FST. From the visualizations, the authors noted that, for a convection speed (with respect to free-stream velocity) of $0.39U_\infty$ and anticlockwise rotation, the dye filaments were initially parallel, indicating a 2D primary flow. As the vortex propagated, each dye filament split into two, with one part lifting off with small spanwise spreading and the other part staying its course. Disturbances amplified ahead of the cylinder leading to violent breakdown of dye-lines. This indicated a strong unsteadiness due to instability caused by translating vortex. At a higher convection speed of $0.77U_\infty$, there was no violent breakdown of flow indicating absence of instability. This can be qualitatively explained by the expression of the disturbance stream function ψ induced by the free-stream vortex convecting over the flat plate, given in Eq. (6.2) in Chapter 6.

Sengupta et al. (2003) solved 2D NSE for the vortex-induced instability using the stream function-vorticity formulation. The instability mechanism was tracked and explained by the disturbance mechanical energy and exchange of energy from mean and disturbance fields was brought out. The study of the vortex-induced instability, under the influence of a discrete roughness element has not been attempted previously, and is one of the objectives of the current research. However, there are are other studies by Goldstein (1985) and Ruban (1985) related to roughness effects on boundary layers, such as, the generation of Tollmien-Schlichting waves in the presence of 2D roughness by acoustic waves studied by triple deck

theory. Recently, DNS results have been reported on 3D roughness-induced transition by Bucci et al. (2018) and effects of 3D roughness on separating turbulent boundary layer by Wu and Piomelli (2018). The present focus on roughness is based on effects of 2D and 3D roughness elements on bypass transition caused by free-stream convecting vortex. The 2D vortex-induced instability studied in isolation by the nonlinear instability mechanism based on the DETE has been attempted by Sengupta et al. (2018a). Recently, the effects of varying translation speeds, vortex strength and direction of rotation of the vortex on the receptivity of ZPG boundary layer have been investigated (Sengupta et al., 2019a) by solving the full 3D NSE for the vortex-induced instability. The reported results use the nonlinear theory of DETE (Sengupta et al., 2018a) and its budget terms to reinforce the role of vortex stretching in the evolving 3D disturbance field.

2.3 Coherent Structure and Vortex Identification Methods

A coherent structure was originally introduced when discussing turbulence. There are many definitions of a coherent structure which exist in literature. Robinson (1991) defined a coherent structure as "*a three-dimensional region of the flow over which at least one fundamental flow variable (velocity component, density, temperature, etc.) exhibits significant correlation with itself or with another variable over a range of space and/or time that is significantly larger than the smallest local scales of the flow*." While defining a coherent structure, Jeong and Hussain (1995) stated that "*turbulent shear flows have been found to be dominated by spatially coherent, temporally evolving vortical motions, popularly called coherent structures*." Holmén (2012) consider coherent structure as "*regions in the flow field where there is less mixing or movement than would be otherwise expected considering the velocity field, that means that a section of the fluid remains roughly together (coherent) while moving in the fluid*." To distinguish between vortices and coherent structures, Holmén (2012) stated that "*vortices are coherent structures, and while the inverse is generally true, it is not necessarily so.*"

A wide variety of coherent structures have been reported in the literature. Some of these structures are: (i) low speed streaks in the near-wall region, (ii) ejections of low-speed fluid outward from the wall, (iii) sweeps of high-speed fluid inward toward the wall, (iv) vortical structures, (v) large scale motions in the form of three-dimensional bulges in outer regions. A very good perspective on the topic is given by Jiménez (2018) and Robinson (1991). Some of the early works on these structures have been reported for some specific flows by Brown and Roshko (1974), Kline et al. (1967), Robinson (1991) and Smith et al. (1991). It is the coherent structures which are responsible for the maintenance of turbulence in a boundary

layer (Robinson, 1991). Thus, identifying and tracking coherent structures from their nascent stage is pertinent for understanding the dynamics of the boundary layer. Some aspects of coherent structures are also described by Hussain (1983) and Hussain (1986). There is a growing realization that coherent structures which are formed during late-transitional stages, can be related to coherent structures reported for fully developed turbulent flows. This is supported by the observation that features in the transitional regime of the flow such as spanwise rolls eventually acquire spanwise waviness and break down to turbulence, as we will observe in spanwise vorticity contours of chapter 7. Coherent structures in fully developed turbulent flows have been subject of many publications (Chong et al., 1990; Haller, 2005; Hunt et al., 1988; Jeong and Hussain, 1995; Robinson, 1991; Smith et al., 1991; Zhou et al., 1999).

A significant portion of coherent structure literature is devoted to the detection and characterization of vortical elements and structures. The vortex identification schemes are classified into two types based on the Eulerian or Lagrangian approach. In the Eulerian approach, detection criteria are evaluated using spatial derivatives of the velocity field, such as closed or spiraling streamlines, iso-surfaces of vorticity, pressure minima etc., while in the Lagrangian approach, coherent structures (also called Lagrangian coherent structures) are identified by studying the stability of fluid trajectories. In the Lagrangian approach, Haller (2015) identified processes of repelling, attracting, and shearing of material surfaces to understand the flow geometry, while allowing exact quantification of material transport to provide a tool to predict large-scale flow features and mixing events. However, computationally the Lagrangian approach is expensive, as compared to Eulerian approaches. We will mostly focus on Eulerian approach in the present investigation.

Several definitions of a vortex exist in literature which are largely based on an intuitive understanding. A vortex is often defined as a region of fluid rotating about an axis (Lugt, 1979). Infact, three intuitive definitions of a vortex are based on (Jeong and Hussain, 1995): (i) closed circular streamlines and pathlines (ii) magnitude of vorticity and (iii) region of pressure minimum. The detection of vortices based on spiraling or closed pathlines was proposed by Lugt (1979) due to the tendency of material particles to rotate about a common centre. A major drawback of this definition is that a particle may not complete a full circulation about the axis of rotation during the time span of the vortex and thus will not form a closed pathline around the axis. The vortex may also breakdown because of transition triggered by nonlinear processes before particles complete a pathline. Definitions based on vorticity magnitude consider the presence of vorticity in the absence of shear as a sufficient criterion for a vortex. It was initially thought that instantaneous vorticity was necessary for the eduction of vortical structures (Bisset et al., 1990; Hussain and Hayakawa, 1987).

However, Robinson (1991) showed that instantaneous vorticity by itself is inadequate despite having success for free shear flows. In cases where background shear is comparable to voticity magnitude, vortex cores cannot be unambiguously identified. Some definitions of vortices consider a local pressure minimum to exist at the core of the vortex. This is based on the understanding that a fluid particle in circular motion about an axis experiences centrifugal force balanced by the pressure force on the particle. However, in some scenarios centrifugal force may be balanced by viscous forces such as in Karman viscous pumps (Karman, 1921) and low Reynolds number Stokes flow. There may be regions in the flow where pressure minima exist without the presence of vorticity. For example, planar source/sink flows do not have any rotationality at all, although they do have a pressure minimum at the point of origin. This leads Holmén (2012) to state *"the presence of pressure minimum in a flow is neither a sufficient nor a necessary condition for the existence of a vortex."* Despite this, pressure minima based vortex detection are commonly used.

The two most popular detection schemes are the λ_2-criterion developed by Jeong and Hussain (1995) and the Q-criterion developed by Hunt et al. (1988) for detection using Eulerian approach. These methods are very effective, when vortical structures dominate the disturbance field, such as during late stage of transition and in fully developed turbulent flows (Sengupta et al., 2019b).

According to previous researchers in the field such as Chakraborty et al. (2005), Hussain (1986), McWilliams (1984), some coherent structures in the boundary layer are indicated by localized regions of high vorticity and they emulate characteristics of flow induced by interacting vortex filaments, sheets or blobs. The structure detection schemes are based on defining and evaluating a function at each point in the flow field, and all points are classified as being inside or outside a vortex, according to a criterion based on the function values as explained by Chakraborty et al. (2005). It is noted that most vortex identification criteria are derived from the velocity gradient tensor ($\nabla\vec{V}$). The most popular local criteria are:

1) The Q-criterion has been determined by Kolár (2007) to define a vortex as a "*connected fluid region with a positive second invariant of* $\nabla\vec{V}$," i.e $Q > 0$. This criterion adds a secondary condition on the pressure, requiring it to be lower than ambient pressure in the vortex. From the definition of the second invariant of the velocity gradient tensor, Q represents the local balance between shear strain rate and vorticity magnitude, defining vortices as areas where the vorticity magnitude is greater than the magnitude of rate-of-strain (Perry and Chong (1987) and Kolár (2007)). A modification of the Q-criterion looks for pressure minima at cores of vortical structures, as has been shown by Hunt et al. (1988). Q can also be interpreted as the source term of pressure in the Navier-Stokes equation as (Jeong and Hussain, 1995),

$$\nabla^2 p = 2\rho Q \tag{2.2}$$

where $Q = \frac{1}{2}[|\bar{\Omega}|^2 - |S|^2]$; while $S = (\nabla\vec{V} + (\nabla\vec{V})^T)/2$ and $\bar{\Omega} = (\nabla\vec{V} - (\nabla\vec{V})^T)/2$, are the symmetric and anti-symmetric parts of $\nabla\vec{V}$. The properties of Poisson equation, given in Eq. (2.2), state that the positive value of Q is related to the sink of pressure (or minimum of pressure). One can arrive at the expression given in Eq. (2.2) by starting from the definition of S and $\bar{\Omega}$.

$S = \frac{1}{2}(\nabla\vec{V} + (\nabla\vec{V})^T)$ or $S_{i,j} = \frac{1}{2}\left(\frac{\partial u_i}{\partial x_j} + \frac{\partial u_i}{\partial x_j}\right)$

Similarly,

$\bar{\Omega} = \frac{1}{2}(\nabla\vec{V} - (\nabla\vec{V})^T)$ or $\bar{\Omega}_{i,j} = \frac{1}{2}\left(\frac{\partial u_i}{\partial x_j} - \frac{\partial u_i}{\partial x_j}\right)$

Using these, we can show that $\text{trace}(S^2 + \bar{\Omega}^2) = u_{i,j}u_{j,i}$. Thus, Q can be written as

$$Q = -\frac{1}{2}trace(S^2 + \bar{\Omega}^2) = -\frac{1}{2}u_{i,j}u_{j,i} \tag{2.3}$$

For an incompressible flow, pressure is related to the velocity field through a Poisson equation, obtained by taking divergence of the NSE (Pope, 2000) as,

$$\nabla^2 p = -\rho u_{i,j}u_{j,i} \tag{2.4}$$

It can be seen from Eq. (2.2) that the Q-criterion is independent of the effects of unsteady and viscous terms of the NSE. It should be noted that a pressure minimum may not always be inside the pressure sink region, it can even occur at the boundary of the region of $Q > 0$. Thus, there is not a direct connection between a pressure minimum and pressure sink region.

2) λ_2 is the second eigenvalue solution of the characteristic equation, given by Eq. (2.7), for the velocity gradient tensor. In λ_2-criterion of Jeong and Hussain (1995), pressure minimum detection is the starting point for the definition of vortex, but the kinematic swirl of a vortex is also accounted for. The unsteady and viscous terms of the incompressible NSE are not accounted for in this method (Holmén, 2012). A pressure Hessian ($p_{,ij}$) is obtained by taking gradient of the NSE for detecting local pressure extrema. The symmetric part of the expression obtained after taking gradient of NSE and decomposing the acceleration gradient into symmetric and antisymmetric parts is,

$$\frac{DS_{ij}}{Dt} - \nu S_{ij,kk} + S_{ik}S_{kj} + \bar{\Omega}_{ik}\bar{\Omega}_{kj} = -\frac{1}{\rho}p_{,ij} \tag{2.5}$$

After neglecting the first two terms on the left hand side which represent unsteady irrotational straining and viscous effects, respectively, we get the following,

$$-\frac{1}{\rho}p_{,ij} = S_{ik}S_{kj} + \bar{\Omega}_{ik}\bar{\Omega}_{kj} \tag{2.6}$$

Only $S^2 + \bar{\Omega}^2$ is considered to determine if there is a local pressure minimum that entails a vortex. A vortex is defined as "*connected region with two negative eigenvalues of* $S^2 + \bar{\Omega}^2$." by Jeong and Hussain (1995). Here λ_2 is the second eigenvalue of the right hand side matrix, with $\lambda_2 < 0$ signifying a vortex. This is substantiated by the observation that $S^2 + \bar{\Omega}^2$ is symmetric and thus, it has real eigenvalues only. By ordering the eigenvalues $\lambda_1 < \lambda_2 < \lambda_3$ the necessary condition for a vortex is $\lambda_2 < 0$. The trace of Eq. (2.6), produces the pressure Poisson equation, Eq. (2.2). Thus, we note that λ_2-criterion is obtained by neglecting the unsteady and viscous terms of the NSE, while Q-criterion is exact but the unsteady and viscous terms are not retained due to the divergence free condition for velocity for incompressible flows, i.e. $S_{ii} = 0$. Structures identified by both these methods appear more coherent, neglecting small scale structures. Jeong et al. (1997) noted mismatch between the low pressure regions and λ_2-isocontours near the wall of a turbulent channel flow. Often, the pressure minima identified do not fulfill the negative λ_2 requirement, shown in Sengupta et al. (2019b).

3) The Δ-criterion of Chong et al. (1990) is defined by Kolár (2007) as "*regions in which two of the eigenvalues of the velocity gradient are complex and the streamline pattern is spiralling or closed.*" Chong et al. (1990) used eigenvalues of the velocity gradient tensor to classify the local streamline pattern around any point in the flow. The vortex core was defined as a region with complex eigenvalues of the velocity gradient tensor, as these imply that the local streamline pattern is closed or spiral.

The characteristic equation for $\nabla\vec{V}$ is given by,

$$\lambda^3 + P\lambda^2 + Q\lambda + R = 0 \tag{2.7}$$

where P, Q and R are the three invariants of the velocity gradient tensor. The discriminant of the Eq. (2.7) is

$$\Delta = \left(\frac{Q}{3}\right)^3 + \left(\frac{R}{2}\right)^2$$

for incompressible flows ($P = 0$). The streamlines are closed or spiralling if two of the eigenvalues form a complex conjugate pair, thus, $\Delta > 0$ criterion must be followed (Holmén, 2012).

4) The swirling strength, λ_{ci}^2-criterion given by Zhou et al. (1999), is based on the Δ-criterion, but uses the imaginary part of the complex conjugate eigenvalues of $\nabla\vec{V}$ to identify vortices. It is based on the notion that the velocity gradient tensor can be decomposed into its real eigenvalues and corresponding eigenvectors. The threshold for this method is not well-defined (Holmén, 2012).

While the vortical structures identified by the above approaches are useful for turbulent flows, these provide a posteriori episodic description and do not inform how structures evolve from the nascent stage, which in most cases is strongly coupled to the dynamics of the event. Thus, the kinematic being linked to the dynamics, focusing only on the former does not provide the causality of the physical processes. Coherent structures are linked to instabilities, and the genesis and evolution of disturbances are essential pathways to be followed. The flow features observed during the secondary stages of instability evolve to produce the coherent structures for fully developed turbulent flows. This will be seen in chapter 4 while tracking an isolated structure back in time and also seen in chapter 7 in the iso-surfaces of spanwise vorticity showing the secondary stage of instability breaking down to turbulence. To improve our understanding of transition from laminar to turbulent stage, we use two complementary approaches based on disturbance mechanical energy (DME) developed by Sengupta et al. (2003) and disturbance enstrophy transport equation (DETE) developed and applied by Sengupta et al. (2018a) and Sengupta et al. (2018b) to follow both linear and nonlinear routes of disturbance evolution, with the evolving disturbances due to instability of incompressible NSE.

Here, subscripts m, d represent equilibrium and disturbance quantities, respectively. As the total mechanical energy is defined as $E = \frac{p}{\rho} + \frac{1}{2}V^2$ (Landahl and Mollo-Christensen (1992) and Sengupta et al. (2003)), the DME is given by, $E_d = E - E_m$. The equation for the distribution of E_d is as follows (Sengupta et al., 2003),

$$\nabla^2 E_d = \Big[\nabla\cdot(\vec{V}\times\vec{\omega})\Big] - \Big[\nabla\cdot(\vec{V}_m\times\vec{\omega}_m)\Big] \tag{2.8}$$

where, $\vec{\omega} = \vec{\omega}_m + \vec{\omega}_d$ and $\vec{V} = \vec{V}_m + \vec{V}_d$, with $\vec{\omega}$ being the vorticity. This being a Poisson equation, a negative right hand side represents source of E_d, while a positive right hand side indicates a sink of E_d. The detailed derivation starting from the incompressible NSE is provided in appendix A. It is important to note here, that the DME method also provides a kinematic quantity, similar to Q and λ_2-criterion.

Finally we show the evolution of disturbance enstrophy given by, $\Omega_d = \vec{\omega}_m \cdot \vec{\omega}_d$. The DETE is given here, with the complete derivation provided in appendix B,

$$\frac{D\Omega_d}{Dt} = \overbrace{\left(2\omega_i\omega_j\frac{\partial u_i}{\partial x_j} - 2\omega_{mi}\omega_{mj}\frac{\partial u_{mi}}{\partial x_j}\right)}^{\textbf{Term1}} + \overbrace{\left(\frac{1}{Re}\frac{\partial^2\Omega_1}{\partial x_j\partial x_j} - \frac{1}{Re}\frac{\partial^2\Omega_m}{\partial x_j\partial x_j}\right)}^{\textbf{Term2}} + \overbrace{\left(-\frac{2}{Re}\frac{\partial\omega_i}{\partial x_j}\frac{\partial\omega_i}{\partial x_j} + \frac{2}{Re}\frac{\partial\omega_{mi}}{\partial x_j}\frac{\partial\omega_{mi}}{\partial x_j}\right)}^{\textbf{Term3}} \tag{2.9}$$

The above equation is the non-linearized version of the DETE and has been used throughout the thesis unless specifically mentioned otherwise. The linearized version of DETE has been derived in appendix B. The first, second and third terms on the right hand side of Eq. (2.9) are the contributions from the stretching, diffusion and the dissipation terms of the enstrophy transport equation, respectively. Both the DME equation and DETE are derived from the NSE without any approximations, and are unlike other theories developed with restrictive assumptions of linearity, parallel flow (Sengupta, 2012). In principle, DME which is based on total pressure and Q-criterion which is based on static pressure, are similar. Structures identified by DME are smoother as they also account for the dynamic pressure, $V^2/2$. These methods cannot account for viscous terms due to the incompressibility condition.

Recently, DETE has been developed and implemented by Sengupta et al. (2018a) and Sengupta et al. (2018b) where it has been shown that Ω_d can trace instability and rotationality. As Ω_d can be of either sign, it is not necessary to associate it with dissipation, as it is done with the instantaneous enstrophy, Ω_1 (Pope (2000) and Yeung et al. (2012)). The condition of instability is

$$\frac{D\Omega_d}{Dt} \lessgtr 0 \ \text{ for } \ \Omega_d \lessgtr 0 \tag{2.10}$$

Both DME and DETE have been developed from the NSE to track nonlinear instability and can also be used to detect patterns and coherent structures in any flow. The choice of the equilibrium flow for calculating the disturbance fields for these methods is an important one. This has been discussed in chapter 6 for the vortex-induced instability. A comparative study between different structure tracking strategies has been attempted here in the present study for vortex-induced instability.

2.4 Boundary layer stability and receptivity theory

The fact that some of the exact solutions of Navier-Stokes equation (subject to simplifications) did not match with the actual flows led the early pioneers to link this mismatch with flow instability (Rayleigh, 1880; Thomson, 1887). The mathematical view of this has been stated lucidly by Landau and Lifshitz (1959), as that a unique solution of the governing equation of motion may be shown to exist and it is unique, yet this solution will not be observable because the exact solution (which we will call as the equilibrium solution, obtained by solving the governing equation by embedding the conservation laws) is not stable with respect to omnipresent background disturbances. Implicit in this introductory definition of instability is the fact that the perturbations are infinitesimally small. This is the most well-known reason for adopting linear theory of instability. There is also the complementary point of view where Schmid and Brandt (2014) have stated: *"It is easy to verify that the nonlinear terms of the incompressible Navier-Stokes equation are energy preserving: the role of the nonlinear terms is the distribution, scattering and transfer of energy, but this reorganization is accomplished in a conservative manner. Energy growth or decay can only come from linear processes. "* This is another reason for performing linear instability theory studies to trace the onset of disturbance field. In fact, in the global receptivity studies of the vortex-induced instability in Chapter 8, energy dispersion effects (due to nonlinearity) lead to formation of turbulent spots and subsequent transition to fully developed turbulence.

Therefore, the above discussion tells us that the study of flow instability can be performed by considering vanishingly small perturbations. In fact, these perturbations are deemed so small, that mathematically in an instability study, the boundary conditions are considered as homogeneous. If the governing equation for the perturbation field is also homogeneous, then this constitutes the well-known eigenvalue problem. Once an instability is predicted, it is incumbent that one can also understand the physical manifestation of the same experimentally. However, in an experiment it is not a viable situation where the demonstration of the physical instability depends upon imperceptible background disturbances. Experimental verification of instability theory demands that such background disturbances are removed, as much as possible, and then one imposes different types of deterministic inputs to record the response of the fluid dynamical system. For the same reason, computational verification of instability theory can follow the same procedure. Computationally, using deterministic input for the dynamical system is equivalent to solving the receptivity problem. In receptivity studies, imposed auxiliary conditions (i.e. boundary and initial conditions) provide the corresponding responses of the dynamical system. Thus, in experiments and computations, this is the preferred approach, where cause and effects can be correlated. We must also note that apart from small perturbations, one may be interested in finding the response of large perturbations

also, to perform nonlinear instability/ receptivity studies, as noted in Fig. 2.6 from Cherubini et al. (2010).

In performing receptivity studies for a dynamical system, two factors are important: first, the equilibrium flow characterizes the transfer function of the dynamical system, which can become unstable. Secondly, the background disturbance is capable of exciting instability to cause growth of disturbances. In this context, the famous pipe flow experiments of Reynolds (1883) should be kept in mind. Reynolds performed his experiments by taking pipes of different diameters (d) with a trumpet shaped mouth-piece or a bell-mouth, so that the water on entry in the pipe experienced acceleration. It is now known that a favourable pressure gradient attenuates disturbances and this was the reason for the design of the inlet in the experiment. It was found that the injected dye along the center of the pipe diffused rapidly, when the non-dimensional parameter (now known as the Reynolds number) given by $Re = \frac{Vd}{\nu}$, exceeded some critical value. Reynolds (1883) noted in his carefully conducted experiment that the critical value could be extended all the way up to 12,830, which led him to state in his paper: *"This at once suggested the idea that the condition might be one of instability for disturbance of a certain magnitude and stable for smaller disturbances."* It can therefore be noted that the instability in pipe flow depends upon the amplitude of input perturbation, which is an attribute of nonlinear instability. It is now well known that pipe flow and Couette flow are two prime examples of flows which are found to be unconditionally stable, when their linear dynamics are studied by solving OSE. There is also the interesting example of plane Poiseuille flow, for which the linear theory predicts a critical Reynolds number of 5772, while the flow is noted experimentally to suffer instability for Reynolds number as low as 1000 by Davies and White (1928). There are complementary points of view of how such flows become turbulent via different mechanisms and these are discussed next.

As we are interested here in instability of boundary layer flows, there is another interesting aspect of linear theory that needs to be addressed. For such a flow, Rayleigh and other contemporary scientists conjectured that the flow governing the equation of motion for the disturbances can be viewed by studying inviscid dynamics, as any present viscous terms will attenuate the disturbance field. Such an inviscid disturbance field only can support temporal growth, as shown in Betchov and Criminale Jr. (1967). Rayleigh (1880, 1889, 1890) while proposing the governing Rayleigh's equation for the inviscid stability equation. Rayleigh's inflection point theorem (Drazin and Reid, 1981; Schmid and Henningson, 2001) states that a parallel flow with inflection points for the velocity profile in the interior, is unstable. This theorem was further improved by Fjørtoft (1950). However, both these theorems provide necessary, but insufficient conditions for instability. Furthermore, a flat plate placed at zero angle of attack in a uniform flow does not exhibit any internal inflection points and hence

should be temporally stable as per Rayleigh's theorem. However, in other boundary layer flows with adverse pressure gradient, as is the case of flows in turbomachines, one notices velocity profiles with inflection points, and these are prime cases which display violent temporal growth of disturbances. This is also the case for many free shear layer flows, where the presence of inflectional velocity profile displays temporal growth of disturbances.

The ZPG boundary layer flow has achieved canonical status, as this flow is sensitive to various disturbances which lead to flow transition. The failure of inviscid disturbance fields in demonstrating growth in space and time, led researchers to look for spatial growth instead for this canonical flow. Orr (1907) and Sommerfeld (1908) proposed an alternate equation for viscous disturbance flow field which is the famous OSE. This equation is the linearized Navier-Stokes equation for disturbances, for which the equilibrium flow is assumed to be parallel and the variables are traced in spectral plane, i.e. in wavenumber and frequency plane. When this is solved as an eigenvalue problem, one notes that the satisfaction of homogeneous boundary condition leads to the requirement of relating spatial scale(s) (wavenumber) with the temporal scale (circular frequency). This relation is the dispersion relation, also known as the characteristic determinant of the eigenvalue problem. The OSE has been used extensively to study flow instability in early decades of last century, including those reported by Heisenberg (1924); Schlichting (1933); Tollmien (1931). In these studies, the authors adopted spatial growth of disturbances, for which the time scale is fixed. One of the distinct features of these early attempts has been the announcement of the spatially growing waves inside the boundary layer. These are known as the Tollmien-Schlichting (TS) waves. However, in the absence of immediate experimental verifications, the linear spatial theory was not accepted. The situation changed, with the publication of the results showing the experimental verification of TS waves by Schubauer and Skramstad (1947), and a series of studies and eigenvalue analysis followed.

While the receptivity experiment by Schubauer and Skramstad (1947) verified the stability aspect of TS wave, there were many features of the experiment that stability theory could not explain. In the experiment, a ribbon was vibrated inside the boundary layer at a single frequency, in the same way as it was posed in the spatial theory. While the subject benefitted from this success, the question of whether the TS waves were amplifying and causing eventual transition was raised by Mack (1984), who stated that such a theory: *"tells nothing about turbulence, or about the details of its initial appearance, but it does explain why the original laminar flow can no longer exist. "*

There have been attempts where the experimental set up of Schubauer and Skramstad (1947) have been formulated, as in Ashpis and Reshotko (1990); Gaster (1965), i.e. the experiment being posed as a receptivity problem. A specific assumption is often made in

these formulations that the response is strictly at the input frequency. One of the justifications for this assumption is given in Schmid and Brandt (2014) where it is noted that: *"Due to the linearity of the governing equation, the output responds with the same frequency"* – this is the signal problem assumption. Despite the discussion in Huerre and Monkewitz (1985), about dispersion relation showing the disturbance field to represent either a convective instability or an absolute instability, there have been no prior attempts to study the general instability and receptivity problems to represent spatio-temporal growth of the flow field. The appearance of the work reported in Sengupta et al. (1994) for flow instability was perhaps the first application of spatio-temporal growth of disturbance for the ZPG boundary layer. In the present study, this spatio-temporal approach has been used. Before we explain this, it is pertinent to discuss about other complementary approaches, where temporal or spatial growth is attempted to be studied via new concepts.

2.4.1 Transient growth by linear theory using (i) non-orthogonality/ non-normality (ii) non-modal approach (iii) pseudo-spectra of matrix approach (iv) mean flow distortion

The concept of energy growth (Reddy and Henningson, 1993), pseudospectra of the Orr-Sommerfeld operator (Reddy et al., 1993), instability without eigenvalues (Trefethen et al., 1993) appeared with the idea that linear stability theory with signal problem assumption is not adequate. This was also noted recently by (Kerswell, 2018) that *"linear stability analysis says nothing about the short term behaviour of the linearized initial value problem which it was realized much later, could be very different (Boberg & Brosa 1988, Farrell 1988, Gustavsson 1991, Butler & Farell 1992). "* The concept of transient growth via a nonmodal stability theory is discussed in the reviews of Schmid (2007), Schmid and Brandt (2014), Kerswell (2018) and in the textbook by Schmid and Henningson (2001). It is conceived that due to the non-normality/ nonorthogonality of the modes obtained from eigenvalue analysis, a short-term growth is often overlooked, but this can have implications on the long-term dynamics of the disturbance field.

The nonmodal approach reviewed in Schmid (2007) involves beginning from the linearized incompressible Navier-Stokes equation and finding the evolution equations for infinitesimal three-dimensional perturbations. The governing equations, solving a system of two evolution equations; one for wall-normal velocity and another for wall-normal vorticity, are written in the form

$$\frac{\partial}{\partial t}\begin{bmatrix} v \\ \eta \end{bmatrix} = \underbrace{\begin{bmatrix} L_{OS} & 0 \\ L_C & L_{SQ} \end{bmatrix}}_{A}\begin{bmatrix} v \\ \eta \end{bmatrix} + \underbrace{\begin{bmatrix} i\alpha M^{-1}D & M^{-1}k^2 & i\beta M^{-1}D \\ i\beta & 0 & -i\alpha \end{bmatrix}}_{B}\begin{bmatrix} u_{in}(t) \\ v_{in}(t) \\ w_{in}(t) \end{bmatrix}$$

$$\begin{bmatrix} u_{out} \\ v_{out} \\ w_{out} \end{bmatrix} = \underbrace{\begin{bmatrix} i\alpha/k^2 D & -i\beta/k^2 \\ 1 & 0 \\ i\beta/k^2 D & i\alpha/k^2 \end{bmatrix}}_{C}\begin{bmatrix} v \\ \eta \end{bmatrix}, \begin{bmatrix} u \\ v \\ w \end{bmatrix}_{t=0} = \begin{bmatrix} u_o \\ v_o \\ w_o \end{bmatrix} \tag{2.11}$$

where v and η are the wall-normal components of velocity and vorticity, and u, w are the velocity components in the streamwise and spanwise directions. The streamwise wavenumber is α and the spanwise wavenumber is β. Matrix M is given as $k^2 - D^2$ where the differentiation matrix with respect to wall-normal direction, y is D and $k = \sqrt{\alpha^2 + \beta^2}$ is the total wavenumber. L_{OS}, L_{SQ} and L_C are the Orr-Sommerfeld, Squire and coupling operators which are given as

$$L_{OS} = M^{-1}(-i - i'' - \frac{1}{Re}M^2)\; L_{SQ} = -i - \frac{M}{Re}\; L_C = -i\beta U' \tag{2.12}$$

The evolution of the disturbances is influenced by the initial conditions (u_0, v_0, w_0) as well as by the external forcing functions (u_{in}, v_{in}, w_{in}), which are functions of time. The output variables are given by $(u_{out}, v_{out}, w_{out})$. The quantity of interest is the kinetic energy (E) of the perturbation given by the state vector $q = (u, v, w)^T$ as $E = q^H W q$ with W containing the weights of different modes.

The maximum amplification of this kinetic energy is considered as a measure of the maximum response to varying initial conditions and is a quantity of interest in hydrodynamic stability theories. The maximum amplification $G(t)$ of initial energy is expressed as

$$G(t) = max\frac{||q(t)||^2}{||q_0||^2} = ||Cexp(tA)B||^2 \tag{2.13}$$

This is the optimization function over all initial conditions, and the maximum amplification corresponding to an initial condition for some time t, that provides the choice of the "optimal" initial condition. In the review of nonmodal analysis, Schmid (2007) observed that *"systems governed by non-normal matrices can exhibit a large transient amplification of energy contained in the initial condition."* According to Trefethen et al. (1993), the *"essential feature of this nonmodal amplification is that it applies to three-dimensional perturbations*

of the laminar flow...the growing attention to 3D linear, nonmodal phenomena represents significant change in traditional conception of problem of hydrodynamic stability."

For the energy growth at $t = 0^+$(short time energy growth), using matrix exponential solution, an expression (Schmid and Henningson, 2001; Trefethen and Embree, 2005) for the amplification is provided as

$$max\frac{1}{||q||^2}\frac{d||q||^2}{dt} = max\frac{1}{||q||^2}\frac{d}{dt}||C(I+At+A^2\frac{t^2}{2!}+...)Bq_o||^2 \tag{2.14}$$

In the study of transient growth by nonmodal stability theory, Trefethen (1997); Trefethen and Embree (2005) introduce a concept of pseudo-spectra, which are considered as extensions of eigenvalues, giving information about the limits of the maximum transient growth by calculating the resolvent norm of the amplification matrix. Using this concept, Schmid (2007) was able to show small time energy growth for eigenvalues confined to a stable region obtained by normal modal analysis and provide an estimate for the maximum attainable transient growth.

The major observation in Schmid (2007) is that *"the linear theory ... for most wall-bounded shear flows ... is a poor proxy for the disturbance behaviour as it only describes the asymptotic ($t \to \infty$) fate of the perturbation and fails to capture short-term characteristics."* This observation is perhaps due to the way classical linear theory works by looking at individual modes in isolation, and all these transient growth studies suggest that instead action of all the modes should be studied together. Most of these studies relate to Poiseuille and Couette flows for the growth of three-dimensional perturbation field. Reddy et al. (1993) noted that the operators that arise in Poiseuille and Couette flows are far from normal. The resultant effects of the non-normal stable modes of these flows can interact to provide constituent modes to interfere constructively for transient growth. In Fig. 4 of Schmid and Brandt (2014) the eigenspectrum of these two flows are shown along with the transient amplification rates, which show an order of magnitude growth in a short time of $t \sim 10$. In a similar way, Sengupta et al. (2006a) observed in their spatio-temporal receptivity analysis of boundary layer disturbances that by considering modes obtained from OSE, they found a cumulative stabilizing effect, while each mode was found to be unstable, inspected in isolation. Thus, this is a complementary effort, which also highlights that the interactions among all the modes are very important. This was explained by the fact that there were pairwise modes, which were nearly out of phase, nullifying the growth rate of the individual unstable modes. This suggests that not only the amplitude of the growing modes is important, but rather the phase relations among these modes are more important, when studying the stabilizing/destabilizing effect in a boundary layer. It is to be noted that the proposed spatio-

temporal receptivity theory accounts for all the modes together, unlike the normal mode approach used in linear instability studies.

A variation of the nonmodal stability theory has been used by Bottaro et al. (2003), wherein the sensitivity of eigenvalues to variations of the mean flow is computed through sensitivity functions, which are combinations of the Orr-Sommerfeld eigenfunctions and those obtained from the adjoint Orr-Sommerfeld eigenfunctions. The authors propose a pseudospectrum based on base flow variations and suggest it as an alternative to the pseudospectrum proposed earlier by Trefethen (1997); Trefethen and Embree (2005), where perturbations are restricted to the Orr-Sommerfeld operator. Bottaro et al. (2003), furthermore noted that *"such a disturbance operator is meant to characterize very general perturbations to the system, whose physical origin is unspecified."* Biau and Bottaro (2008) extended the use of mean flow distortion-based nonmodal stability theory to obtain an "optimal" path to transition in square duct. Brandt et al. (2011) considered the effect of mean flow distortion on exponentially growing TS waves and transiently growing streaks in a Blasius boundary layer. The authors found that base flow modifications provided a strong impact on modal growth, leading to more unstable states for smaller perturbations, whereas nonmodal amplification was marginally affected. The sensitivity was found to be strongest near the leading edge of the flat plate.

2.4.2 Nonlinear Stability Theory and Nonmodal, Nonlinear Approaches

A fully nonlinear dynamical systems approach emerged in the early 1990s, which found finite amplitude solutions (disjointed from the base state). This approach has been reviewed by Eckhardt et al. (2007); Kawahara et al. (2012); Kerswell (2005). In this approach, the flow is considered as a "huge dynamical system" wherein a finite amplitude disturbance takes the flow from its reference state to a state beyond the reference state's basin of attraction in phase space, which is the case when transition to turbulence by nonlinear instability occurs. While distinguishing between this nonlinear dynamical systems approach and the linear nonmodal approach, Kerswell (2018) noted that *"the dynamical systems approach to transition focuses on fully nonlinear structures like basin boundaries and what happens beyond them, whereas nonmodal analysis describes how infinitesimal disturbances can grow temporarily in the immediate neighbourhood of the reference state deep within the basin of attraction."*

A nonlinear extension of the nonmodal analysis has been developed for transitional flows by Cherubini et al. (2012, 2010); Kerswell (2018); Monokrousos et al. (2011); Pringle and Kerswell (2010). These researchers use a direct adjoint-looping approach wherein the full 3D Navier-Stokes equations are incorporated into the nonlinear stability analysis to arrive at an "optimized" initial perturbation. Cherubini et al. (2012) identify flow structures on the edge of

laminar-turbulent boundary, when an initial finite amplitude disturbance was imposed at the inflow and the optimal path to transition was followed. Biau and Bottaro (2008); Bottaro et al. (2003) have noted the importance of a nonlinear strategy for transition by stating that *"the linear optimal disturbances are poor at triggering transition, in this being easily surpassed suboptimal initial conditions. Thus, it appears important to devise a nonlinear strategy capable of yielding the most dangerous shape and amplitude of initial conditions."* The optimal initial condition is also referred to as the minimal seed and Cherubini et al. (2012) discovered that this perturbation evolved towards Λ and hairpin structures. This nonlinear route to turbulence is sharply contrasted by the classical route initiated either by streamwise vortices or Tollmien-Schlichting waves by using an initial perturbation obtained by linear analysis. Researchers in the fields of oceanography (Mu et al., 2004) and in thermoacoustics (Juniper and Sujith, 2018) have also adopted the nonlinear nonmodal analysis for their stability calculations.

As in the linear nonmodal approach (Schmid, 2007), an optimization process is used in the nonlinear nonmodal theory. A logical objective function for the energy at a finite time ($E(t) =< u(t).u(t) >$) and its evolution after some time T is used in this approach. It is assumed that the base state, the disturbance fields and the full fields from the solution of Navier-Stokes equation, (i) satisfy the incompressible condition, (ii) with no forcing imposed and (iii) satisfaction of homogeneous boundary conditions. The process of optimization with the objective function requires the formulation of an initial optimal perturbation by a Lagrange multiplier technique (Pringle and Kerswell, 2010) given by

$$L = \frac{E(T)}{E(0)} - \int_0^T < p^+ \nabla.u > dt - \int_0^T < u^+ . \frac{\partial u}{\partial t} + u.\nabla U + U.\nabla u + u.\nabla u + \nabla p - \frac{\nabla^2 u}{Re} > dt - \lambda(\frac{E_o}{E(0)} - 1) \tag{2.15}$$

The constraints of the above equation are the initial perturbation energy, $E_o =< u_o.u_o >$ and the full nonlinear Navier-Stokes equation for the disturbance quantities. Here, (u^+, p^+, λ) are the Lagrange multipliers, which enforce the constraints. The above equation is integrated by parts and the first variation of L with (u, p) is set to zero to obtain adjoint equations and compatibility conditions. A review of the application of adjoint equations in stability analysis is given by Luchini and Bottaro (2014). The adjoint equations are linked to the Navier-Stokes equation through the advection terms. The adjoint problem is integrated backward in time. The solution obtained at $t = 0$ undergoes consistency check with the initial solution of the Navier-Stokes equation through a conjugate gradient algorithm (Marquet et al., 2008).

The main operating principle of the method is to nonlinearize nonmodal analysis so that disturbances of a fixed finite amplitude are considered to optimize an objective function (obtained from the adjoint analysis) constrained by the notion that each disturbance evolves by considering the full Navier-Stokes equation. This procedure links the linear nonmodal analysis with nonlinear dynamical system approach to flow stability (Kerswell, 2018). The longevity of the "transient" state identified by nonmodal analysis has been studied by probing phase space for unstable solutions near the base state (Olvera and Kerswell, 2017). The review by Kerswell (2018) only features a single finite amplitude disturbance and traces its evolution, however it may be pertinent to study multiple disturbances and how these interact to reach the optimal path of transition to turbulence.

2.4.3 A spatio-temporal linear viscous stability theory via OSE

Spatio-temporal linear stability theory is another way of studying growth of disturbances to provide a general framework in which neither a temporal nor a spatial growth/decay of an instability is imposed on the disturbance field, while solving the OSE. Using this analysis, researchers have identified a wave-packet like structure, and termed it as the "spatio-temporal wave front (STWF)" (Sengupta et al., 2006b). The STWF was proposed as the *"forerunner "* for transition in electromagnetic wave propagation (Brillouin, 1960). This concept has also found applications in the fields of optics (Kondacki and Abouraddy, 2019) and in wave front shaping in microwaves (Hougne et al., 2016). A STWF was noted for strictly spatially stable eigenspectrum of the OSE for the ZPG boundary layer, while studying the problem in spatio-temporal framework developed in Sengupta et al. (1994) by Bromwich contour integral method. This involves solving OSE for complex wavenumber and complex frequency simultaneously following Bromwich contours, as described later. Once the STWF was identified for a spatially stable system, its role in 2D and 3D turbulence was established for transition to turbulence following 2D and 3D routes in Bhaumik and Sengupta (2014); Sengupta and Bhaumik (2011), respectively, by solving the OSE and complete Navier-Stokes equation. The dynamics of the transition to turbulence by the STWF has been followed for ZPG boundary layers excited at the wall by Kang (2015); Kang and Yeo (2013, 2017, 2020); Yeo et al. (2010) and over compliant surfaces by Wang (2003); Wang et al. (2005); Zhao (2007). These are receptivity analysis following the experimental framework of Schubauer and Skramstad (1947). Even though the system is excited at a single frequency, due to its finite start-up, all other frequencies are excited as well, as explained here. A complementary impulse response problem has been studied, where the boundary layer is excited by a localized in space (delta function in space), and as an impulse (delta function) in time, following the experimental arrangement in Gaster and Grant (1975). Linear

(2D OSE) and nonlinear (3D Navier-Stokes equation) simulations show once again the role of the STWF in Bhaumik and Sengupta (2017); Sundaram et al. (2018). Apart from this spatio-temporal approach, transition process over a boundary layer subjected to free-stream turbulence has been provided in Kreilos et al. (2016) by solving full Navier-Stokes equation. The same procedure has been used for transition to turbulence in Rayleigh-Benard convection in Daviaud et al. (1990). As the OSE has been in use, it is first necessary to state its condition of applicability.

Foundations of Fourier-Laplace Transform: Abel and Tauber Theorems:

The theorems by Abel and Tauber provide essential justifications for the use of Fourier-Laplace transforms in calculating the perturbation field from the OSE by providing the relationship between the response field in the physical plane and the image of the transform in the spectral plane. Using these theorems, not only can one obtain near and far-field responses of the dynamical system to a perturbation field for the signal problem, but one can also obtain short time ($t \to 0$) growth (which can be viewed as the transient growth stage), as well the time asymptotic solution ($t \to \infty$). The near-field and transient response created due to a localized-pulsed wall excitation can be directly computed by the integral of the bilateral Laplace transform in space and a Fourier integral in time along suitable Bromwich contours. The corresponding far-field and time-asymptotic response is simultaneously obtained by the same Bromwich contour integral method. Two fundamental theorems, which provide the basis for understanding both near and far-field solutions, are due to Abel and Tauber, which is given in van der Pol and Bremmer (1959), an excerpt of which is provided in Fig. 2.9.

Tauber's theorem states that if we are interested in the near field response (i.e. near the location of the exciter at $\tilde{x} = 0$), then we need to investigate the corresponding image in the spectral plane as $\alpha \to \infty$.

Abel's theorem states that if we are interested in the far field solution ($\tilde{x} \to \infty$), then only the neighbourhood of the origins in spectral planes need to be investigated, i.e. $\alpha \to 0$.

The response field at $t = 0^+$ and as $t \to \infty$ can also be found out from the linear spatio-temporal theory by investigating the corresponding images in the spectral plane for $\omega_o \to \infty$ and $\omega_o \to 0$ respectively. It is to be noted here that response field at $t = 0^+$ is nothing but the transient growth. Here, α and ω_o are the streamwise wavenumber and dimensionless circular frequency, respectively.

Based on the above two theorems, one can now formally state their application to receptivity analysis in fluid flow. We will now provide a detailed formulation of the OSE starting from the incompressible Navier-Stokes equation (NSE).

Starting from the incompressible NSE, if we consider a parallel/quasi-parallel equilibrium flow in the $(\tilde{x},\tilde{z})$-plane (i.e. $U = U(\tilde{y}), V = 0, W = W(\tilde{y})$) and express each flow quantity e into a mean (steady) and an unsteady disturbance term $\varepsilon e'$ given as

$$e(\tilde{x},\tilde{y},\tilde{z},\tilde{t}) = E + \varepsilon e'(\tilde{x},\tilde{y},\tilde{z},\tilde{t}) \tag{2.16}$$

By substituting the above equation into the momentum and continuity equations of NSE, we obtain the disturbance equations as

$$\frac{\partial u'}{\partial \tilde{t}} + U\frac{\partial u'}{\partial \tilde{x}} + W\frac{\partial u'}{\partial \tilde{z}} + v'\frac{dU}{d\tilde{y}} = -\frac{\partial p'}{\partial \tilde{x}} + \frac{1}{Re}\nabla^2 u' \tag{2.17}$$

$$\frac{\partial v'}{\partial \tilde{t}} + U\frac{\partial v'}{\partial \tilde{x}} + W\frac{\partial v'}{\partial \tilde{z}} = -\frac{\partial p'}{\partial \tilde{y}} + \frac{1}{Re}\nabla^2 v' \tag{2.18}$$

$$\frac{\partial w'}{\partial \tilde{t}} + U\frac{\partial w'}{\partial \tilde{x}} + W\frac{\partial w'}{\partial \tilde{z}} + v'\frac{dW}{d\tilde{y}} = -\frac{\partial p'}{\partial \tilde{z}} + \frac{1}{Re}\nabla^2 w' \tag{2.19}$$

$$\frac{\partial u'}{\partial \tilde{x}} + \frac{\partial v'}{\partial \tilde{y}} + \frac{\partial w'}{\partial \tilde{z}} = 0 \tag{2.20}$$

The Eqs. (2.17) to (2.20) are linear partial differential equations with variable coefficients, which are functions of wall-normal coordinate. Thus, the perturbation quantities are alternatively written by Fourier-Laplace transforms as

$$[u', v', w', p']^T = \int\int\int [\upsilon(\tilde{y}), \phi(\tilde{y}), \chi(\tilde{y}), \sigma(\tilde{y})]^T e^{i(\alpha\tilde{x}+\beta\tilde{z}-\omega_o\tilde{t})} d\alpha d\beta d\omega_o \tag{2.21}$$

where υ, ϕ, χ and σ are complex amplitude functions and β is spanwise wavenumber. Here, we have written the most generic disturbance form in Eq. (2.21), which varies with space and time. In the most general case, with variables growing/decaying in space and time, the independent variables α, β and ω_o will be complex. This approach is the spatio-temporal route of describing linear receptivity. Alternative approaches are to study the spatial or temporal growth/decay in isolation. For a temporal theory, α, β are real and ω_o is complex, while for a spatial theory, α, β are complex and ω_o is real.

Substituting Eq. (2.21) into Eqs. (2.17) to (2.20) and reducing to form a single ordinary differential equation for ϕ, we obtain

$$\phi^{iv} - 2(\alpha^2+\beta^2)\phi'' + (\alpha^2+\beta^2)^2\phi = iRe[(\alpha U + \beta W - \omega_o)[\phi'' - (\alpha^2+\beta^2)\phi]$$

$$-(\alpha U'' + \beta W'')\phi] \tag{2.22}$$

This fourth order ordinary differential equation is the OSE and forms the basis for major flow instability analysis. If the flow field and mean flow are 2D, then Eq. (2.22) transforms to

$$\phi^{iv} - 2\alpha^2\phi'' + \alpha^4\phi = iRe[(\alpha U - \omega_o)[\phi'' - \alpha^2\phi] - \alpha U''\phi] \tag{2.23}$$

One can also obtain Rayleigh's inviscid stability equation from the OSE by considering Eq. (2.23) for $Re \to \infty$ as

$$(U - \frac{\omega_o}{\alpha})(\phi'' - \alpha^2\phi) - U''\phi = 0 \tag{2.24}$$

We note here that Rayleigh's inviscid stability equation is usually studied for temporal growth, i.e. α is real and ω_o is complex. The phase speed $C_{ph} = \omega_o/\alpha$ is then written as the sum of its complex and real parts as $C_{ph} = C_{phr} + iC_{phi}$.

To distinguish between stability and receptivity analysis, we classify disturbances into (i) outer disturbances or free-stream excitations (ii) surface disturbances or wall excitation. In the following we study the equivalence of instability and receptivity analysis for a wall excitation problem, using the OSE.

Stability Problem using OSE

The two sets of boundary conditions for the 2D OSE given in Eq. (2.23) are such that one pair can be prescribed at the wall and the other in the free-stream. The no-slip condition at the wall can be transformed in terms of ϕ as

$$At\ y = 0 : v = 0 \implies \phi = 0\ and\ u = 0 \implies \phi' = 0 \tag{2.25}$$

At the free-stream the disturbance velocity components are assigned a boundary condition as,

$$y \to \infty : \phi \to 0, \phi' \to 0 \tag{2.26}$$

Using the mean flow information at the free-stream ($y \to 0$) i.e. $U(\tilde{y}) = 1$ and $U''(\tilde{y}) = 0$ in the OSE given by Eq. (2.23) renders the differential equation at the free-stream as a constant coefficient ordinary differential equation amenable to exact solutions as,

$$\phi^{iv} - 2\alpha^2\phi'' + \alpha^4\phi = iRe[(\alpha - \omega_o)(\phi'' - \alpha^2\phi)] \tag{2.27}$$

The solution of the above equation is obtained as $\phi \sim e^{ry}$ where the roots are $r_{1,2} = \mp\alpha$ and $r_{3,4} = \mp T$ where $T = [\alpha^2 + i\alpha Re(1 - C_{ph})]^{1/2}$. For problems where $Re \to \infty$, $|T| >> |\alpha|$, this makes the OSE a stiff differential equation as the solutions vary by different orders of magnitude depending on the location. This problem of stiffness is counteracted by the compound matrix method (CMM) which is explained in more detail in Chapter 3.

As the OSE is a fourth order ordinary differential equation, it has four fundamental solutions, given as

$$\phi = a_1\phi_1 + a_2\phi_2 + a_3\phi_3 + a_4\phi_4 \tag{2.28}$$

for which at the free-stream: $\phi_{1\infty} \sim e^{-\alpha y}; \phi_{2\infty} \sim e^{\alpha y}; \phi_{3\infty} \sim e^{-Ty}$ and $\phi_{4\infty} \sim e^{Ty}$. To satisfy the boundary condition given in Eq. (2.26) at the free-stream, $a_2 = a_4 = 0$ as the solutions associated with these coefficients are monotonically growing for $real(\alpha, T) > 0$. Thus, the general solution in Eq. (2.28) reduces to

$$\phi = a_1\phi_1 + a_3\phi_3 \tag{2.29}$$

Eigenvalue analysis of the OSE

The no-slip boundary condition given by Eq. (2.25) is applied to the equation showing the general solution of OSE in Eq. (2.29), so that we obtain

$$v = 0 \implies a_1\phi_{10} + a_3\phi_{30} = 0 \tag{2.30}$$

$$u = 0 \implies a_1\phi'_{10} + a_3\phi'_{30} = 0 \tag{2.31}$$

which can be alternatively expressed as

$$[\Phi] \begin{bmatrix} a_1 \\ a_3 \end{bmatrix} = 0 \tag{2.32}$$

A non-trivial solution of the above set of equations exists if and only if the determinant of the associated matrix of the solution is zero, i.e. $Det[\Phi] = 0$ which yields

$$a_1\phi_{10}a_3\phi'_{30} - a_1\phi'_{10}a_3\phi_{30} = 0 \tag{2.33}$$

This is the characteristic eigenvalue equation for the OSE and is also the dispersion relation for the instability problem.

Receptivity analysis for wall excitation using OSE

The process by which disturbances are entrained into the shear layer to produce an instability is at the heart of receptivity studies which correlates the *cause* and *effect(s)*. There have been many studies on various aspects of receptivity for wall and free-stream excitation cases (Buter and Reed, 1993; Butler and Farrell, 1992; Chaudhari, 1996; Cherubini et al., 2010; Collis and Lele, 1996; Crouch, 1992; Diwan and Ramesh, 2009; Goldstein and Hultgren, 1989; Kerswell, 2018; Leib et al., 1999; Lin et al., 1995; Reshotko, 1976; Saric et al., 1999; Schmid and Brandt, 2014; Sengupta et al., 2002). Before, we derive the OSE for a ZPG boundary layer subjected to a wall excitation in the form of a vibrating ribbon, as in the experiments of Schubauer and Skramstad (1947), various types of input responses to a system are categorized and certain mathematical tools are introduced.

The frequency response of a system can be obtained if for any input at some given frequency $\overline{\omega}_o$, the output of the system can be obtained via a transfer function (T) which is also at that frequency, i.e. $T(\overline{\omega}_o)$. If the input to the system is in the form of a Dirac delta function in space and time, then all possible wavenumbers and frequencies are excited simultaneously and the corresponding output is called an impulse response. Since most systems are "causal", i.e. the output of the system does not anticipate the input, and the output and impulse response are one-sided in time. While this may be true for time marching, there is no such constraint in space. Although a signal cannot move backwards in time, spatially it can propagate in any direction. This shows the need for using bilateral Laplace transforms, the application of which is explained next.

A function f_1 in the time domain can be obtained from its Fourier transform as

$$f_1(t) = \frac{1}{2\pi}\int_{-\infty}^{\infty} F(\omega_o)e^{i\omega_o t}d\omega_o \tag{2.34}$$

The unilateral Fourier Transform of the above function is then written as

$$F(\omega_o) = \int_{0}^{\infty} f_1(t)e^{-i\omega_o t}dt \tag{2.35}$$

When we use the bilateral Laplace transform $F_{II}(\alpha)$ to describe the space dependence of the function f_2, we obtain

$$F_{II}(\alpha) = \int_{-\infty}^{\infty} f_2(x)e^{-i\alpha x}dx \tag{2.36}$$

For a complex value of α, with $\alpha = \alpha_r + i\alpha_i$, the bilateral function $F_{II}(\alpha)$ is defined only in a limited range of α_i. There is a strip defined by $gamma_2 < \alpha_i < \gamma_1$ in the complex α plane, where the direct and inverse transforms are defined (see pages 188-189 of Papoulis (1962)).

This is called the strip of convergence and Bromwich contour can be chosen anywhere within this strip of convergence. The diagrammatic description of the bilateral Laplace transform and the subsequent strip of convergence and Bromwich contour is provided in Papoulis (1962); van der Pol and Bremmer (1959). An application of the Bromwich contour integral in solving the receptivity problem using the OSE is provided in Sengupta (2012) which has been summarized here next.

A wall excitation in the form of a vibrating ribbon is embedded on a flat plate over which a ZPG boundary layer is formed, as in experiment of Schubauer and Skramstad (1947). If the disturbance source has an excitation frequency of $\overline{\omega}_o$, then the disturbance stream function is given by

$$\psi_d(\tilde{x},\tilde{y},\tilde{z},\tilde{t}) = \frac{1}{(2\pi)^2}\int\int_{Br}\phi(\tilde{y},\alpha,\omega_o)e^{i(\alpha\tilde{x}-\omega_o\tilde{t})}d\alpha d\omega_o \tag{2.37}$$

where *Br* represents the Bromwich contour integral where the contour is traced simultaneously in the α- and ω_o-planes, as the spatio-temporal linear analysis is employed.

The boundary conditions at the wall are:

$$u = 0 \; and \; \psi_d(\tilde{x},0,\tilde{t}) = U_1(\tilde{t})\delta(\tilde{x})e^{-i\overline{\omega}_o\tilde{t}} \tag{2.38}$$

where $U_1(\tilde{t})$ is the Heaviside function which ensures that excitation begins at $\tilde{t} = 0$. The corresponding spectral plane boundary conditions are

$$\phi'(\alpha,0,\omega_o) = 0 \tag{2.39}$$

$$\phi(\alpha,0,\omega_o) = WBC \tag{2.40}$$

where $WBC = [i(\overline{\omega}_o - \omega_o)]^{-1} + \pi\delta(\omega_o - \overline{\omega}_o)$ is the wall boundary condition. The second part of *WBC* will contribute to the formation of TS wave, while the first part is the source of disturbance field contributed by all other frequencies. This first part produces STWF and will be explained with the help of a demonstration case in Chapter 8. For satisfying the free stream condition, solution of the OSE would reduce to the form given in Eq. (2.29) and the constants a_1 and a_3 are fixed by the wall boundary conditions given in Eqs. (2.39) to (2.40). This gives

$$\psi_d(\tilde{x},\tilde{y},\tilde{t}) = \frac{1}{(2\pi)^2}\int\int_{Br}\frac{\phi_1(\alpha,\tilde{y},\omega_o)\phi'_{30} - \phi'_{10}\phi_3(\alpha,\tilde{y},\omega_o)}{\phi_{10}\phi'_{30} - \phi'_{10}\phi_{30}}WBCe^{i(\alpha\tilde{x}-\omega_o\tilde{t})}d\alpha d\omega_o \tag{2.41}$$

Note the connection between instability and receptivity problems from this expression. The denominator of Eq. (2.41) is the dispersion relation given in Eq. (2.33) for the instability problem. Thus, the eigenvalues of the OSE constitute the poles for the receptivity problem given in Eq. (2.41).

For the signal problem, the disturbance stream function is given by the expression

$$\psi_d(\tilde{x},\tilde{y},\tilde{t}) = \frac{1}{2\pi}\int_{Br} \phi(\alpha,\tilde{y},\overline{\omega}_o)d\alpha \tag{2.42}$$

where Br is in the α-plane, and the wall excitation condition is written as,

$$u = 0 \; and \; \psi_d(\tilde{x},0,\tilde{t}) = \delta(\tilde{x})e^{-i\overline{\omega}_o\tilde{t}} \tag{2.43}$$

Note the absence of the Heaviside function in the above boundary condition (as compared to that in Eq. (2.38)) shows the fixed frequency output at $\omega_o = \overline{\omega}_o$.

Linear Receptivity of General (Free Stream and Wall) Excitation Problem using OSE

We will next explain the stability of the flow field over a ZPG boundary layer, simultaneously excited at the wall and in the free stream. This has been formulated in detail in Sengupta (2012) and here only a brief summary is provided to explain the coupling between the wall and free stream modes of the OSE.

Suppose that the wall excitation ($\tilde{y} = 0$) is in the form of a time-periodic localized excitation at a streamwise station $\tilde{x} = \tilde{x}_o$, such that transverse velocity oscillation is set up as

$$u = 0, v = v_w\delta(\tilde{x}-\tilde{x}_o)e^{-i\overline{\omega}_o\tilde{t}} \tag{2.44}$$

A line vortex in the free stream, of strength Γ, convects at a speed c at a constant height H_1 over the flat plate with an instantaneous location $\bar{x}$ from the leading edge. We note here that H_1 is significantly larger than the boundary layer thickness. The stream function induced by this vortex at $(\tilde{x},\tilde{y})$ is given by

$$\psi_\infty = \frac{\Gamma}{4\pi} ln \frac{(\tilde{x}-\bar{x})^2+(\tilde{y}+H_1)^2}{(\tilde{x}-\bar{x})^2+(\tilde{y}-H_1)^2} \tag{2.45}$$

This is also the excitation used in Chapter 6 for the vortex-induced receptivity study of the thesis. The disturbance stream function is given by Eq. (2.41) for pure wall excitation case. The variable ϕ can be written as the sum of the four fundamental modes of the OSE as

$$\phi(\alpha,\tilde{y},\omega_o) = C_1\phi_1 + C_2\phi_2 + C_3\phi_3 + C_4\phi_4 \tag{2.46}$$

Here, we must retain all the four modes for the case with a free stream excitation. To satisfy the wall boundary condition given in Eq. (2.44), we have

$$C_1\phi'_{10} + C_2\phi'_{20} + C_3\phi'_{30} + C_4\phi'_{40} = 0 \tag{2.47}$$

$$C_1\phi_{10} + C_2\phi_{20} + C_3\phi_{30} + C_4\phi_{40} = \frac{v_w}{i\alpha}e^{-i\alpha\tilde{x}}\delta(\omega_o - \overline{\omega}_o) \tag{2.48}$$

Similarly, the free stream boundary condition ($\tilde{y} \to \infty$) implied by Eq. (2.45) should be satisfied as

$$C_1\phi'_{1\infty} + C_2\phi'_{2\infty} + C_3\phi'_{3\infty} + C_4\phi'_{4\infty} = B(\alpha, \omega_o) \tag{2.49}$$

$$C_1\phi_{1\infty} + C_2\phi_{2\infty} + C_3\phi_{3\infty} + C_4\phi_{4\infty} = D(\alpha, \omega_o) \tag{2.50}$$

Equations (2.47) to (2.50) can be written as a linear algebraic equation

$$[\Phi]C_i = f_i \implies C_i = [\Phi]^{-1} f_i \tag{2.51}$$

where f_i represents the external wall and free stream forcing and the $[\Phi]$ matrix can be obtained as

$$[\Phi] = \begin{bmatrix} \phi'_{10} & \phi'_{20} & \phi'_{30} & \phi'_{40} \\ \phi_{10} & \phi_{20} & \phi_{30} & \phi_{40} \\ -\alpha e^{-\alpha\tilde{y}} & \alpha e^{\alpha\tilde{y}} & -Te^{-T\tilde{y}} & Te^{T\tilde{y}} \\ e^{-\alpha\tilde{y}} & e^{\alpha\tilde{y}} & e^{-T\tilde{y}} & e^{T\tilde{y}} \end{bmatrix} \tag{2.52}$$

Here, the expressions for $\phi_{i\infty}$ and $\phi'_{i\infty}$ are as given following Eq. (2.28) and have been used to construct the last two rows of $[\Phi]$ matrix. Once the constants of Eq. (2.46) are known, these can be replaced in the expression for the disturbance stream function given in Eq. (2.41) for this type of general excitation. One notes that for the general solution of ϕ with free stream excitation, all the modes of the OSE must be retained, contrary to the case of pure wall excitation. We know that the first and third modes decay, while the second and fourth modes increase with $\tilde{y}$ for $real(\alpha, T) > 0$. The decaying modes with wall-normal distance are referred to as wall modes, while the other two modes are called the free stream modes. The free stream modes grow to match the applied free stream disturbance. The far field boundary condition usually assumes that the decaying modes are negligibly small and thus, the disturbance is solely supported by the free stream modes. Fixing the free stream boundary condition leaves the homogeneous boundary conditions at the wall to be satisfied.

Thus, there is a coupling between the free stream and wall modes, as explained above with respect to Eqs. (2.47) to (2.51).

2.5 Concluding Remarks

The combined body of literature leads to the following objectives of the current thesis:

(i) There is an increasing shift towards high-lift blade designs to bring down manufacturing costs by lowering engine weight. It has been found by Sengupta et al. (2017) and Vadlamani (2015) that surface roughness can have a beneficial effect on such blade designs. Although, there have been numerical and experimental studies of the effects of aeroelastic blade vibrations on such configurations, but these are from a structural dynamics point of view. It would be of interest to study whether, oscillation has a beneficial effect on high-lift blade designs akin to roughness, with emphasis on the boundary layer transition process. This is addressed in chapters 5 and 7 for aeroelastic vibration studies in conjunction with FST and unsteady wakes, respectively.

(ii) In literature, most studies of wakes involved isolated analysis or cumulative analysis at varying levels of FST and with surface roughness. The study of the mechanism observed with aeroleastic blade vibration has not been attempted before and is explored here in chapter 7.

(iii) There are contrasting opinions on the nature of bypass transition observed in various canonical fluid dynamical flows, thereby supporting the need for designed kernel experiments for transitional flows which study a singular occurrence of the disturbance field existing in LPT environments. This has been attempted in chapter 6 for the vortex-induced instability under the influence of a discrete roughness element.

(iv) New methods of structure detection and identification have been developed and their calibration with respect to existing methods is pertinent to understanding the broad spectrum application and limitations of the proposed methods in transitional and turbulent flows. This has been shown in chapter 4 for the vortex-induced instability.

(v) Understanding the underlying causal mechanism governing the separation-induced transition process under the influence of various disturbances existing within the low pressure turbine by performing a global, spatio-temporal linear and nonlinear receptivity study.

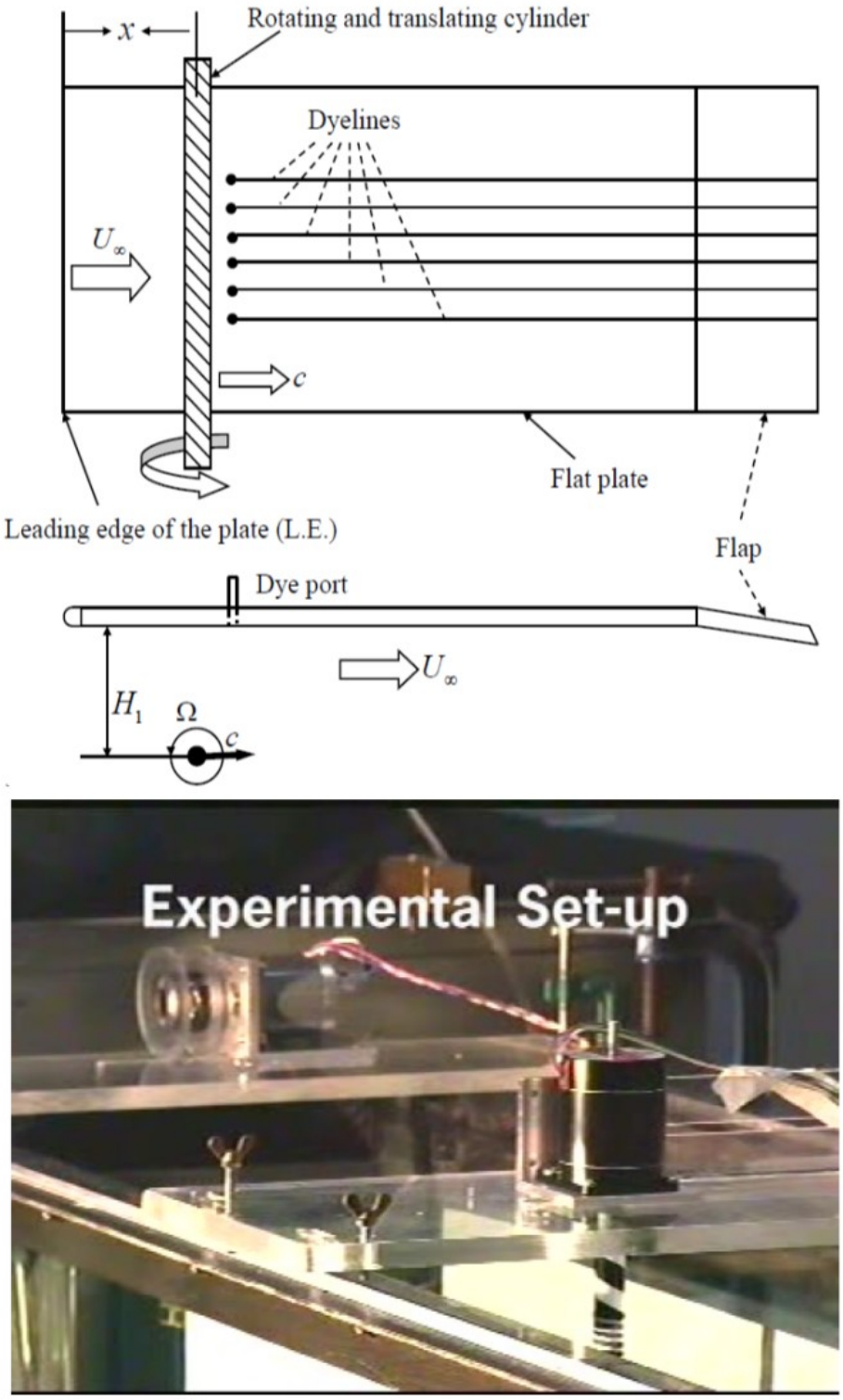

Fig. 2.8 Schematic of the vortex-induced instability experiment and the experimental apparatus used. (From Lim et al. (2004)).

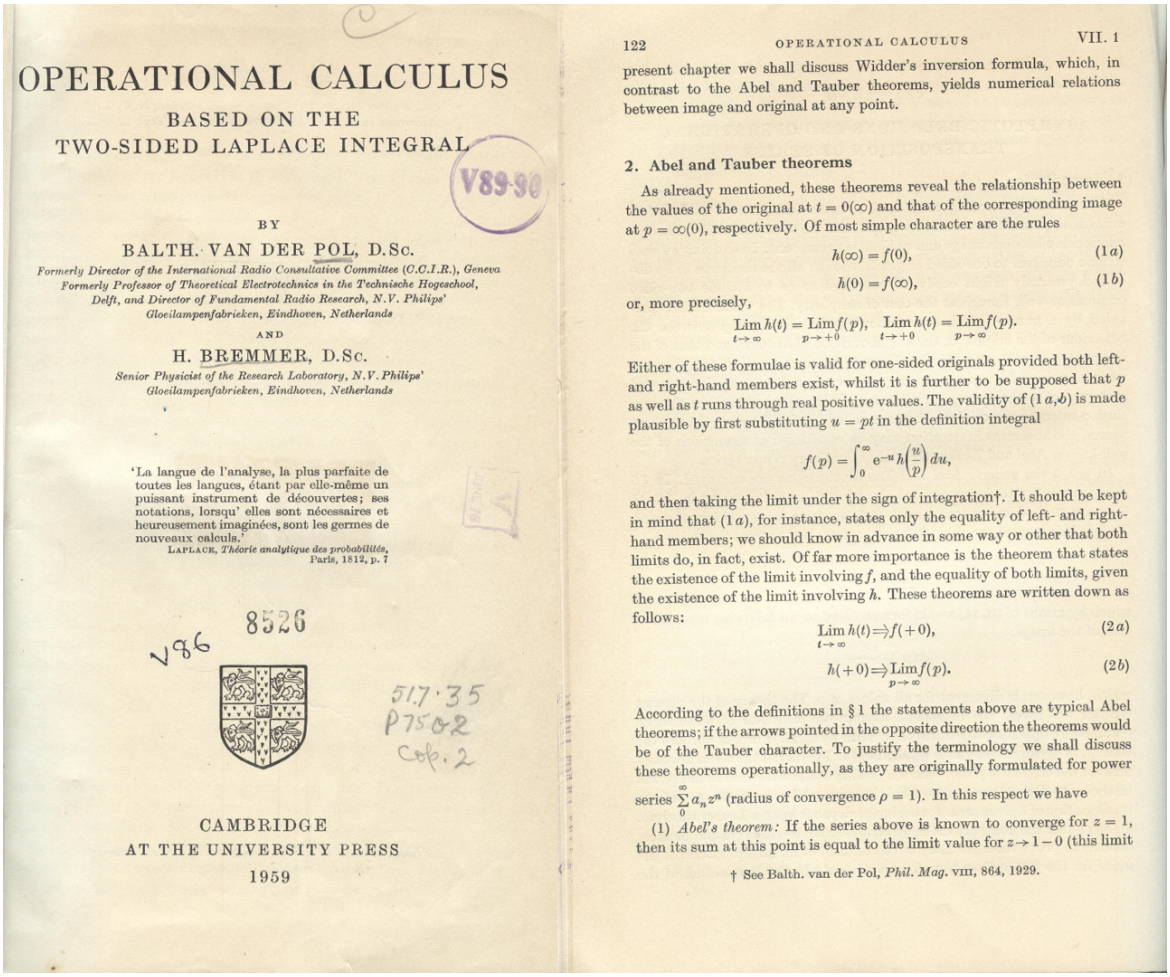

OPERATIONAL CALCULUS

BASED ON THE
TWO-SIDED LAPLACE INTEGRAL

BY

BALTH. VAN DER POL, D.Sc.

Formerly Director of the International Radio Consultative Committee (C.C.I.R.), Geneva
Formerly Professor of Theoretical Electrotechnics in the Technische Hogeschool, Delft, and Director of Fundamental Radio Research, N.V. Philips' Gloeilampenfabrieken, Eindhoven, Netherlands

AND

H. BREMMER, D.Sc.

Senior Physicist of the Research Laboratory, N.V. Philips' Gloeilampenfabrieken, Eindhoven, Netherlands

'La langue de l'analyse, la plus parfaite de toutes les langues, étant par elle-même un puissant instrument de découvertes; ses notations, lorsqu' elles sont nécessaires et heureusement imaginées, sont les germes de nouveaux calculs.'
LAPLACE, *Théorie analytique des probabilités*, Paris, 1812, p. 7

CAMBRIDGE
AT THE UNIVERSITY PRESS
1959

present chapter we shall discuss Widder's inversion formula, which, in contrast to the Abel and Tauber theorems, yields numerical relations between image and original at any point.

2. Abel and Tauber theorems

As already mentioned, these theorems reveal the relationship between the values of the original at $t = 0(\infty)$ and that of the corresponding image at $p = \infty(0)$, respectively. Of most simple character are the rules

$$h(\infty) = f(0), \tag{1a}$$

$$h(0) = f(\infty), \tag{1b}$$

or, more precisely,

$$\operatorname*{Lim}_{t\to\infty} h(t) = \operatorname*{Lim}_{p\to+0} f(p), \quad \operatorname*{Lim}_{t\to+0} h(t) = \operatorname*{Lim}_{p\to\infty} f(p).$$

Either of these formulae is valid for one-sided originals provided both left- and right-hand members exist, whilst it is further to be supposed that p as well as t runs through real positive values. The validity of (1 *a*,*b*) is made plausible by first substituting $u = pt$ in the definition integral

$$f(p) = \int_0^\infty e^{-u} h\left(\frac{u}{p}\right) du,$$

and then taking the limit under the sign of integration†. It should be kept in mind that (1 *a*), for instance, states only the equality of left- and right-hand members; we should know in advance in some way or other that both limits do, in fact, exist. Of far more importance is the theorem that states the existence of the limit involving f, and the equality of both limits, given the existence of the limit involving h. These theorems are written down as follows:

$$\operatorname*{Lim}_{t\to\infty} h(t) \Rightarrow f(+0), \tag{2a}$$

$$h(+0) \Rightarrow \operatorname*{Lim}_{p\to\infty} f(p). \tag{2b}$$

According to the definitions in § 1 the statements above are typical Abel theorems; if the arrows pointed in the opposite direction the theorems would be of the Tauber character. To justify the terminology we shall discuss these theorems operationally, as they are originally formulated for power series $\sum_0^\infty a_n z^n$ (radius of convergence $\rho = 1$). In this respect we have

(1) *Abel's theorem:* If the series above is known to converge for $z = 1$, then its sum at this point is equal to the limit value for $z \to 1 - 0$ (this limit

† See Balth. van der Pol, *Phil. Mag.* VIII, 864, 1929.

Fig. 2.9 Excerpt from *Operational Calculus* by van der Pol and Bremmer (1959) which shows the Abel and Tauber theorems for the justification of use of Fourier-Laplace transform in linear stability.

Chapter 3

Numerical Methods

Two in-house solvers have been used for all the simulations reported here. A compressible flow solver with the pressure-velocity formulation has been developed by Dr. Nagabhushana Rao Vadlamani. This has been used for the simulations reported in chapters 5 and 7. An incompressible flow solver using the velocity-vorticity formulation has been developed by Dr. Swagata Bhaumik. This has been used for the results reported in chapters 4 and 6. The key features of these two solvers will be introduced in this chapter. This is followed by the governing equations for these two solvers. Lastly, a discussion is provided on the various initial conditions and enhancements added to the solver to carry out the simulations reported in the thesis.

3.1 Key Features of Pressure-Velocity Formulation for Compressible NSE

An in-house solver COMP-SQUARE is used for the simulations reported in chapters 5 and 7. It is a high order, structured, multi-block, compressible Navier-Stokes solver which uses high order compact schemes of Gaitonde and Visbal (1998) to evaluate the spatial derivatives and fourth order explicit Runge-Kutta scheme (RK_4) for time integration. Tri-diagonal matrix algorithm is used to solve the matrices of the spatial derivative. The solver has been parallellized to run on distributed memory machines using the message passing interface. The solver has been thoroughly validated on the benchmark test case of the convection of a vortex by Sengupta et al. (2017) and to analyse the transitional flows on the intake lip separating under crosswinds by Vadlamani and Tucker (2016). Pade type formulas of sixth order with a five-point stencil are used for the spatial discretization, termed scheme C_6 by Gaitonde and Visbal (1998). Viscous terms are treated by successive applications of the first

derivative operator. One of the principal problems encountered during the solution of the compressible NSE with centred schemes is the occurrence of numerical instabilities, arising near the boundaries. If these are not handled, the spurious numerical waves contaminate the solution and destroy the accuracy of the simulation. A common method to suppress such instabilities is through the application of a filter. A tenth order central filter of Gaitonde and Visbal (1998) with filter coefficient of 0.49 has been used for the calculations performed in chapters 5 and 7. The spatial discretization for interior points is given by,

$$\alpha u'_{i-1} + u'_i + \alpha u'_{i-1} = b\frac{u_{i+2} - u_{i-2}}{4} + b\frac{u_{i+1} - u_{i-1}}{2} \tag{3.1}$$

where α, a and b are determined by substituting Taylor series approximations about node i in the above equation and terms of various orders are set to zero. Since, the C_6 method is a sixth order scheme, the sixth order is set to zero as,

$$O(h^6) : -a + 10\alpha - 16b = 0 \tag{3.2}$$

The solution of these equations for the sixth order compact scheme, C_6 provide $\alpha = \frac{1}{3}, a = \frac{14}{9}, b = \frac{1}{9}$ and this scheme is the highest order scheme obtainable from Eq. (3.1). The tridiagonal stencil gives rise to the need for two boundary stencils. The first boundary condition is given as,

$$u'_1 + \alpha_1 u'_2 = a_1 u_1 + b_1 u_2 + c_1 u_3 + d_1 u_4 + e_1 u_5 + f_1 u_6 + g_1 u_7 \tag{3.3}$$

The parameters for C_6 are obtained as

$$\alpha_1 = 5, a_1 = \frac{-197}{60}, b_1 = \frac{-5}{12}, c_1 = 5, d_1 = \frac{-5}{3}, e_1 = \frac{5}{12}, f_1 = \frac{-1}{20}, g_1 = 0$$

from the Taylor series approximations. The stencil for the second boundary condition is given as,

$$\alpha_{21} u'_1 + u'_2 + \alpha_{22} u'_3 = a_2 u_1 + b_2 u_2 + c_2 u_3 + d_2 u_4 + e_2 u_5 + f_2 u_6 + g_2 u_7 \tag{3.4}$$

The parameters for C_6 are obtained as

$$\alpha_{21} = 0, \alpha_{22} = 2, a_2 = \frac{-1}{10}, b_2 = \frac{-25}{12}, c_2 = \frac{4}{3}, d_2 = 1, e_2 = \frac{-1}{6}, f_2 = \frac{1}{60}, g_2 = 0$$

from the Taylor series approximations. The same boundary conditions are implemented at the N^{th} and $(N-1)^{th}$ nodes.

3.2 Key Features of Velocity-Vorticity Formulation for Incompressible NSE

For both the 2D and 3D simulations pertaining to the vortex-induced instability problem reported in chapters 4 and 6, a velocity-vorticity formulation based solver has been used. A staggered grid has been used as it has been shown to remove aliasing errors (Sengupta, 2013) for high Reynolds number flows. This role of staggering has been demonstrated for lid driven cavity flows(Sengupta, 2013), where at high wavenumbers, staggering is shown to be equivalent to adding numerical diffusion governed by leading terms of the interpolated velocity at vorticity nodes. However, the use of staggering also incorporates numerical errors due to interpolation. This can be circumvented by developing the equivalent 3D vector potential-vorticity formulation with higher accuracy, as in streamfunction-vorticity formulation for 2D fields. In the presented simulations in chapters 4 and 6, we have used optimized compact schemes for spatial discretization, referred to as optimized staggered compact schemes (OSCS) (Bhaumik and Sengupta, 2015). An optimized third order Runge-Kutta scheme is used for time integration, which is obtained by optimizing three-stage third order Runge-Kutta (RK_3) (Rajpoot et al., 2010). The optimization process is carried out by considering the spatial and temporal discretization schemes together. The combined space-time scheme is optimized for conditions of neutral stability, i.e. when the numerical amplification factor is less than or equal to unity. Additional constraints required for optimization are obtained through the group velocity and phase speed calculations. The same formulation and methodology has been used by Bhaumik and Sengupta (2014) and Bhaumik and Sengupta (2015) on a staggered grid to solve the 3D receptivity to wall excitation problem, from receptivity to fully developed turbulent flow stage. The velocity components, of the staggered grid, shown in Fig. 3.1, are defined at the center of the planes on which the component is perpendicular; while the vorticity components are placed at mid-location on the edges of the cell on which the component is parallel. Such grid staggering for 3D flows requires additional evaluation of derivatives of vorticity components at different nodal locations. For example, if the variables are defined at integral points, *i.e.* at j^{th} nodes, then using staggered arrangement of variables, interpolation or evaluation of derivatives are required at $(j+1/2)^{th}$ nodes. The evaluation of the derivative has been performed with the help of an optimized compact scheme interpolation scheme using a staggered grid. Interpolation of quantities obtained at the nodes to the mid-points is also required which is done by an optimized version of the existing compact interpolation scheme of Nagarajan et al. (2003). Resultant optimized scheme is referred to as optimized staggered compact scheme (OSCS) and is fourth order accurate in space, but is shown to match first and second derivative calculations of the sixth

order scheme (Nagarajan et al., 2003) due to the optimization process. The details of the optimization process for the spatial discretization and time integration schemes are given next.

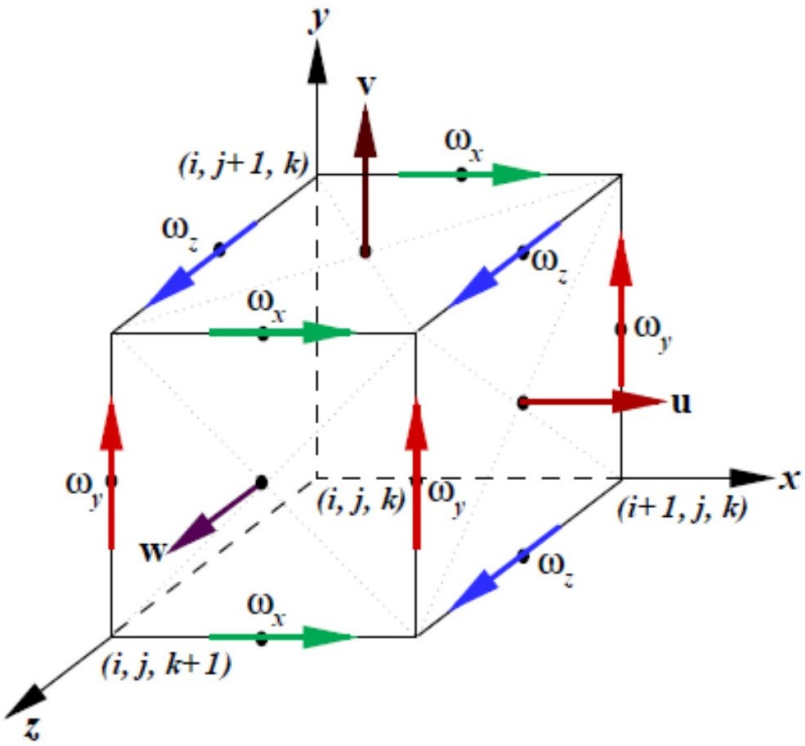

Fig. 3.1 Staggered grid arrangement of velocity and vorticity components for the vortex-induced instability problem in chapters 4 and 6.

The interpolation in staggered grids is carried out by the optimized compact mid-point interpolation scheme. The interpolation scheme is given as

$$\alpha_I \hat{u}_{j-1} + \hat{u}_j + \alpha_I \hat{u}_{j+1} = \frac{a_I}{2}(u_{j-\frac{1}{2}} + u_{j+\frac{1}{2}}) + \frac{b_I}{2}(u_{j-\frac{3}{2}} + u_{j+\frac{3}{2}}) \tag{3.5}$$

where $\hat{u_j}$'s are the interpolated values at the j^{th}-location obtained from the known $u_{j\pm n/2}$ values at the $(j \pm n/2)^{th}$-locations. For fourth order accuracy, one should have $a_I = \frac{1}{8}(9 + 10\alpha_I)$ and $b_I = \frac{1}{8}(6\alpha_I - 1)$, with α_I as a free parameter. A choice of $\alpha_I = \frac{3}{10}$ yields 6^{th} order accuracy for the interpolation scheme. However, here $\alpha_I = 0.42$ is obtained by optimizing the integrated phase error of the scheme in the spectral plane. Using Fourier-Laplace transform one can express, $\hat{u}_j = \int \hat{U}(k)\, e^{ikx_j}\, dk$ and $u_j = \int U(k)\, e^{ikx_j}\, dk$. The resolution properties and the performance of any interpolation scheme can be characterized by a transfer function given by $TF = \hat{U}(k)/U(k)$, which is the ratio of the Fourier amplitude of the interpolated function to that of the original function. From Eq. (3.5), this transfer function is obtained as,

$$TF(kh) = \left[\frac{a_I \cos(kh/2) + b_I \cos(3kh/2)}{1 + 2\alpha_1 \cos(kh)}\right] \tag{3.6}$$

with uniform grid spacing h. Then to minimize the error in the spectral plane, one can define an objective function given as,

$$I_{interp} = \int_0^{\gamma} \left|1 - TF(kh)\right| d(kh) \tag{3.7}$$

which is the error integrated over the range of kh up to γ, which is less than or equal to the Nyquist limit. The transfer function is shown in Fig. 3.2(a) for the indicated values of α_I. The objective function is shown in Fig. 3.2(b). Following the trend shown in the figure, the objective function is found to be minimum at $\alpha_I = 0.42$ for $\gamma = \pi$ (Bhaumik and Sengupta, 2015). This optimized fourth order scheme has been used here, for all the reported computations in chapters 4 and 6.

The evaluation of the first derivative in staggered grids is performed by a variation of the scheme given by Nagarajan et al. (2003) for derivative evaluation in staggered grid. The interior stencil is given by

$$\alpha_{II} u'_{j-1} + u'_j + \alpha_{II} u'_{j+1} = \frac{b_{II}}{3h}(u_{j+3/2} - u_{j-3/2}) + \frac{a_{II}}{h}(u_{j+1/2} - u_{j-1/2}) \tag{3.8}$$

where the first derivatives, u'_j s are defined at the j^{th}-location using the known function $u_{j\pm n/2}$, defined at the $(j \pm n/2)^{th}$-locations. The authors (Nagarajan et al., 2003) considered a fourth-order, single parameter (α_{II}) with $b_{II} = (22\ \alpha_{II} - 1)/8$ and $a_{II} = (9 - 6\ \alpha_{II})/8$. A sixth order version with $\alpha_{II} = 9/62$ was also formulated. To obtain better spectral properties, an optimized version for the stencil in Eq. (3.8) has been developed (Bhaumik and Sengupta, 2015). Using Fourier-Laplace transform, an equivalent wavenumber k_{eq} is defined as

$$k_{eq} = \frac{2}{h}\left[\frac{a_{II} \sin(kh/2) + (b_{II}/3)\ \sin(3kh/2)}{1 + 2\alpha_{II} \cos(kh)}\right] \tag{3.9}$$

Once again, the objective function to be optimized is the error integrated over the range of kh up to γ, which is less than or equal to the Nyquist limit and is defined as

$$I_{comp} = \int_0^{\gamma} \left|1 - \frac{k_{eq}}{k}\right| d(kh) \tag{3.10}$$

This objective function I_{comp} is plotted as a function of α_{II} in Fig. 3.3(b) for the indicated values of γ, while in Fig. 3.3(a), k_{eq}/k as a function of kh is plotted for different indicated values of α_{II}. From Fig. 3.3, the optimum value of $\alpha_{II} = 0.216$ is obtained for $\gamma = \pi$.

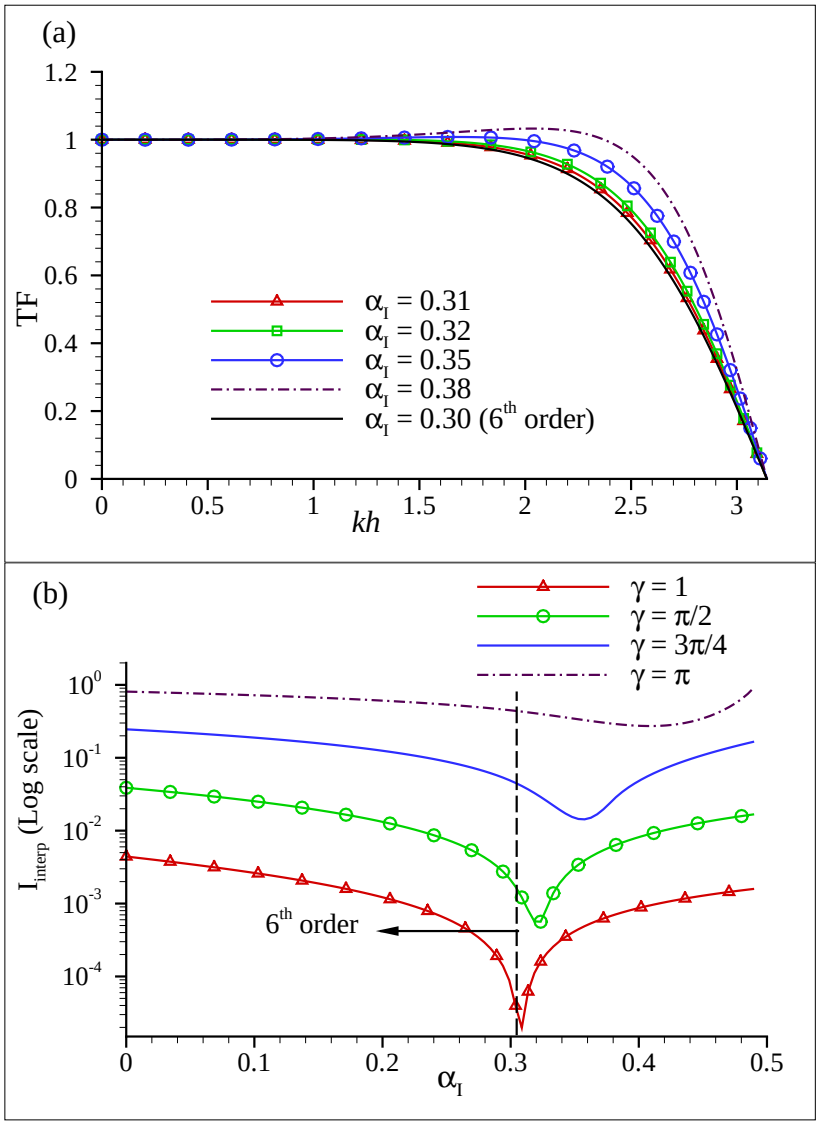

Fig. 3.2 a) Transfer function of staggered interpolation scheme plotted versus kh for indicated values of α_I. (b)Integrated phase error plotted as a function of α_I (From Sengupta and Bhaumik (2019)).

Now that, the coefficients of the optimized spatial discretization (OSCS) have been obtained, we will optimize the combined space-time scheme by considering dispersion relation preserving property of the numerical scheme subjected to a model 1D convection equation. The stencil of the ORK_3 time-integration scheme is given as

$$u^{(1)} = u^{(n)} + (a/b)\Delta t F[u^{(n)}] \tag{3.11}$$

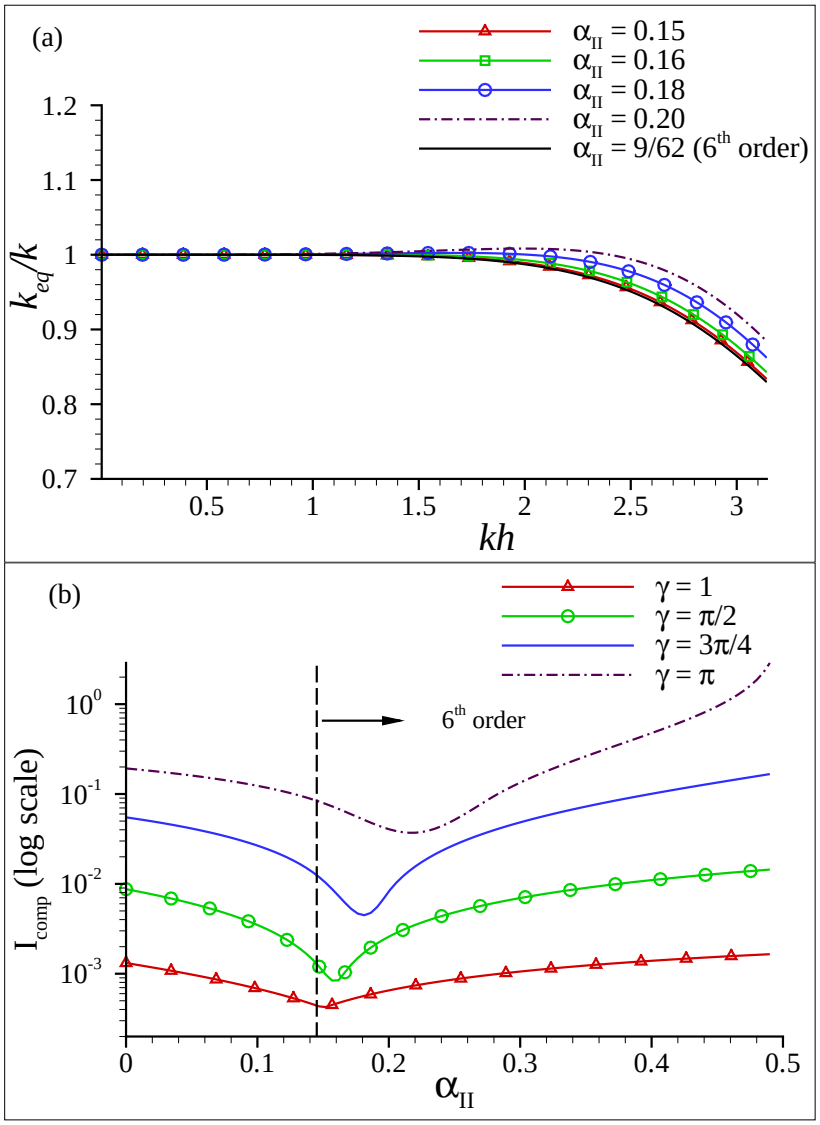

Fig. 3.3 a)Spectral resolution of compact scheme given in Eq. (3.8) plotted versus kh for indicated values of $\alpha_I I$. (b)Integrated phase error plotted as a function of $\alpha_I I$ (From Sengupta and Bhaumik (2019)).

$$u^{(2)} = u^{(n)} + b\Delta t F[u^{(1)}] \tag{3.12}$$

$$u^{(n+1)} = u^{(n)} + \Delta t F[u^{(2)}] \tag{3.13}$$

The numerical amplification factor for the 1D convection equation is obtained for RK_3 time integration method as

$$G_j = 1 - A_j + b\,A_j^2 - a\,A_j^3 \tag{3.14}$$

where a and b are the parameters to be obtained by optimization and $A_j = N_c \sum_{l=1}^{N} C_{jl} e^{ik(x_l - x_j)}$ where N_c is the CFL number and C_{jl} is the coefficient matrix of the [C] matrix used in derivative evaluation such that $u' = \frac{1}{h}[C]u$. The procedure to arrive at Eq. (3.14) and the details of numerical phase and dispersion errors of the model 1D convection equation are provided in Chapter 8 of Sengupta (2013).

The objective function to be minimized to obtain the optimized three stage Runge-Kutta method (ORK_3) is given as

$$F(a,b,N_c) = \int_0^{\gamma} |G_{num} - G_{exact}|^2 \, d(kh) \tag{3.15}$$

where γ is less than or equal to the value of kh at Nyquist limit. In addition to minimizing F, we also explicitly constrain schemes to ensure neutral stability, minimum phase and dispersion errors through satisfaction of following inequalities

$$F_1(a,b,N_c) = \int_0^{\gamma_1} ||G| - 1| \; d(kh) \leq \varepsilon_1 \tag{3.16}$$

$$F_2(a,b,N_c) = \int_0^{\gamma_2} \left| \left(\frac{V_{gN}}{c} \right) - 1 \right| \; d(kh) \leq \varepsilon_2 \tag{3.17}$$

$$F_3(a,b,N_c) = \int_0^{\gamma_3} \left| \left(\frac{c_N}{c} \right) - 1 \right| \; d(kh) \leq \varepsilon_3 \tag{3.18}$$

where γ_i and ε_i are constants chosen to satisfy the numerical properties of the basic space-time method. Although, a small tolerance is prescribed in ε_1, the main aim of this optimization is to look for numerical parameters which ensure neutral stability for large regions of the (N_c, kh)-plane.

To solve this constrained optimization problem, a grid-search technique (Sengupta, 2013) is used to locate the feasible region in (a,b)-plane using constraints given in Eqs. (3.16)-(3.18) for different, but fixed value of N_c. While a and b are functions of N_c, fixed values for the ORK_3 scheme are obtained for a particular N_c, but which could be used over a longer range of CFL numbers. This is shown in Fig. 3.4 where the dotted lines in the figure are the conventional values of a and b for RK_3 method and the optimized values of (a,b) can be chosen depending on the value of N_c to arrive at the optimized ORK_3 method.

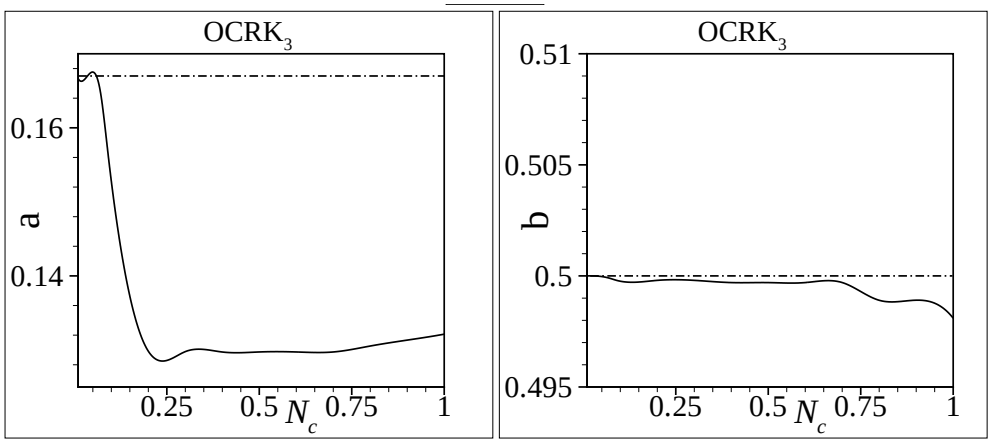

Fig. 3.4 Variation of a and b in Eq. (3.14) with CFL number for ORK_3 scheme. (From Sengupta (2013))

3.3 Governing Equations: Pressure-Velocity Formulation

The full three-dimensional, compressible, unsteady Navier-Stokes equations are solved, which conserve mass, momentum and energy in the pressure-velocity formulation in COMPSQUARE. A set of 5 non linear partial differential equations for flow have been expressed in the divergence form by Hoffman and Chiang (1993) and are as,

$$\frac{\partial \hat{Q}}{\partial t^*}+\frac{\partial \hat{E}}{\partial x^*}+\frac{\partial \hat{F}}{\partial y^*}+\frac{\partial \hat{G}}{\partial z^*}=\frac{\partial \hat{E}_v}{\partial x^*}+\frac{\partial \hat{F}_v}{\partial y^*}+\frac{\partial \hat{G}_v}{\partial z^*}+\rho F_i \tag{3.19}$$

where the conserved variables are given by

$$\hat{Q}=\begin{bmatrix}\rho^*\\ \rho^* u^*\\ \rho^* v^*\\ \rho^* w^*\\ \rho^* e_t^*\end{bmatrix} \tag{3.20}$$

The convective flux variables $\hat{E}$, $\hat{F}$ and $\hat{G}$ are given as

$$\hat{E}=\begin{bmatrix}\rho^* u^*\\ \rho^* u^{*2}+p^*+(\rho^*-\rho_s)g_x x\\ \rho^* u^* v^*\\ \rho^* u^* w^*\\ (\rho^* e_t^*+p^*)u^*\end{bmatrix} \tag{3.21}$$

$$\hat{F} = \begin{bmatrix} \rho^* v^* \\ \rho^* u^* v^* \\ \rho^* v^{*2} + p^* + (\rho^* - \rho_s) g_y y \\ \rho^* v^* w^* \\ (\rho^* e_t^* + p^*) v^* \end{bmatrix} \tag{3.22}$$

$$\hat{G} = \begin{bmatrix} \rho^* w^* \\ \rho^* u^* w^* \\ \rho^* v^* w^* \\ \rho^* w^{*2} + p^* + (\rho^* - \rho_s) g_z z \\ (\rho^* e_t^* + p^*) w^* \end{bmatrix} \tag{3.23}$$

and the viscous fluxes $\hat{E}_v$, $\hat{F}_v$ and $\hat{G}_v$ are

$$\hat{E}_v = \begin{bmatrix} 0 \\ \tau_{xx}^* \\ \tau_{xy}^* \\ \tau_{xz}^* \\ u^* \tau_{xx}^* + v^* \tau_{xy}^* + w^* \tau_{xz} \end{bmatrix} \tag{3.24}$$

$$\hat{F}_v = \begin{bmatrix} 0 \\ \tau_{yx}^* \\ \tau_{yy}^* \\ \tau_{yz}^* \\ u^* \tau_{yx}^* + v^* \tau_{yy}^* + w^* \tau_{yz} \end{bmatrix} \tag{3.25}$$

$$\hat{G}_v = \begin{bmatrix} 0 \\ \tau_{zx}^* \\ \tau_{zy}^* \\ \tau_{zz}^* \\ u^* \tau_{zx}^* + v^* \tau_{zy}^* + w^* \tau_{zz} \end{bmatrix} \tag{3.26}$$

A body force term is added to the right hand side of Eq. (3.19), if vibration of the flat plate is to be included in the simulation. The term F_i has been shown in Eq. (3.48) and is given here as,

$$\rho F_i = \begin{bmatrix} 0 \\ \rho F_1 \\ \rho F_2 \\ \rho F_3 \\ 0 \end{bmatrix} \tag{3.27}$$

The variables ρ^*, p^*, u^*, v^*, w^*, T^* and e_t^* represent the density, the fluid pressure, Cartesian components of fluid velocity, the absolute temperature and the specific internal energy of the fluid, respectively. The specific heat ratio is denoted by γ. τ_{xx}^*, τ_{xy}^*, τ_{xz}^*, τ_{yx}^*, τ_{yy}^*, τ_{yz}^*, τ_{zx}^*, τ_{zy}^*, τ_{zz}^* are the components of the symmetric viscous stress tensor and are related to the rate of strain tensor as

$$\tau_{xx}^* = \left(2\mu \frac{\partial u^*}{\partial x^*} + \lambda \nabla^* \cdot \vec{V}^* \right) \tag{3.28}$$

$$\tau_{yy}^* = \left(2\mu \frac{\partial v^*}{\partial y^*} + \lambda \nabla^* \cdot \vec{V}^* \right) \tag{3.29}$$

$$\tau_{zz}^* = \left(2\mu \frac{\partial w^*}{\partial z^*} + \lambda \nabla^* \cdot \vec{V}^* \right) \tag{3.30}$$

$$\tau_{xy}^* = \tau_{yx}^* = \mu \left(\frac{\partial u^*}{\partial y^*} + \frac{\partial v^*}{\partial x^*} \right) \tag{3.31}$$

$$\tau_{xz}^* = \tau_{zx}^* = \mu \left(\frac{\partial u^*}{\partial z^*} + \frac{\partial w^*}{\partial x^*} \right) \tag{3.32}$$

$$\tau_{yz}^* = \tau_{zy}^* = \mu \left(\frac{\partial v^*}{\partial z^*} + \frac{\partial w^*}{\partial y^*} \right) \tag{3.33}$$

Stokes' hypothesis is used here, which relates μ with λ via the relation: $\lambda = -2\mu/3$. Sutherland's law is used to fix the viscosity as a function of temperature. Closure of system of equations is provided by the ideal gas equation given by,

$$p^* = \rho^* R^* T^* \tag{3.34}$$

and it is used to define specific energy, e_t^* as

$$e_t^* = \frac{p^*}{[\rho^*(\gamma - 1)]} + \frac{(u^{*2} + v^{*2} + w^{*2})}{2} \tag{3.35}$$

The governing equations are non-dimensionalized so that the solution is not restricted to a particular geometry or a set of flow conditions. This involves introduction of *Re* in the viscous stress tensor equations.

3.4 Governing Equations: Velocity-Vorticity Formulation

The simulations for vortex-induced instability, shown in chapters 4 and 6, are performed in the transformed (ξ,η,ζ)-plane, such that $x = x(\xi)$, $y = y(\eta)$ and $z = z(\zeta)$. The rotational variant of the $(\overrightarrow{V},\overrightarrow{\omega})$-formulation of the incompressible NSE is used here, as given by Bhaumik and Sengupta (2015). It is given as,

$$\frac{\partial \omega_\xi}{\partial t} + \left(\frac{1}{h_2}\frac{\partial H_\zeta}{\partial \eta} - \frac{1}{h_3}\frac{\partial H_\eta}{\partial \zeta}\right) = 0 \tag{3.36}$$

$$\frac{\partial \omega_\eta}{\partial t} + \left(\frac{1}{h_3}\frac{\partial H_\xi}{\partial \zeta} - \frac{1}{h_1}\frac{\partial H_\zeta}{\partial \xi}\right) = 0 \tag{3.37}$$

$$\frac{\partial \omega_\zeta}{\partial t} + \left(\frac{1}{h_1}\frac{\partial H_\eta}{\partial \xi} - \frac{1}{h_2}\frac{\partial H_\xi}{\partial \eta}\right) = 0 \tag{3.38}$$

where, $\overrightarrow{\omega} = (\omega_\xi, \omega_\eta, \omega_\zeta)$ and $\overrightarrow{V} = (u, v, w)$ are the vorticity and velocity vectors. The scale factors of the above grid transformations, h_1, h_2 and h_3 are given as $h_1 = \frac{\partial x}{\partial \xi}$, $h_2 = \frac{\partial y}{\partial \eta}$ and $h_3 = \frac{\partial z}{\partial \zeta}$. In Eqs. (3.36) to (3.38), the terms H_ξ, H_η and H_ζ are given as

$$H_\xi = (w\omega_\eta - v\omega_\zeta) + \frac{1}{Re_L}\left(\frac{1}{h_2}\frac{\partial \omega_\zeta}{\partial \eta} - \frac{1}{h_3}\frac{\partial \omega_\eta}{\partial \zeta}\right) \tag{3.39}$$

$$H_\eta = (u\omega_\zeta - w\omega_\xi) + \frac{1}{Re_L}\left(\frac{1}{h_3}\frac{\partial \omega_\xi}{\partial \zeta} - \frac{1}{h_1}\frac{\partial \omega_\zeta}{\partial \xi}\right) \tag{3.40}$$

$$H_\zeta = (v\omega_\xi - u\omega_\eta) + \frac{1}{Re_L}\left(\frac{1}{h_1}\frac{\partial \omega_\eta}{\partial \xi} - \frac{1}{h_2}\frac{\partial \omega_\xi}{\partial \eta}\right) \tag{3.41}$$

For the $(\overrightarrow{V},\overrightarrow{\omega})$-formulation, the corresponding velocity vectors are obtained from the velocity Poisson equations, $\nabla^2\overrightarrow{V} = -\nabla\times\overrightarrow{\omega}$, and in the transformed plane these are given as

$$\nabla^2_{\xi\eta\zeta} u = \left(h_1 h_2 \frac{\partial \omega_\eta}{\partial \zeta} - h_3 h_1 \frac{\partial \omega_\zeta}{\partial \eta}\right) \tag{3.42}$$

$$\nabla^2_{\xi\eta\zeta} v = \left(h_2 h_3 \frac{\partial \omega_\zeta}{\partial \xi} - h_1 h_2 \frac{\partial \omega_\xi}{\partial \zeta}\right) \tag{3.43}$$

$$\nabla^2_{\xi\eta\zeta} w = \left(h_3 h_1 \frac{\partial \omega_\xi}{\partial \eta} - h_2 h_3 \frac{\partial \omega_\eta}{\partial \xi} \right) \tag{3.44}$$

where, the operator $\nabla^2_{\xi\eta\zeta}$ is given for an orthogonal grid previously given by Bhaumik and Sengupta (2015)

$$h_1 h_2 h_3 \, \nabla^2_{\xi\eta\zeta} = \frac{\partial}{\partial \xi}\left(\frac{h_2 h_3}{h_1} \frac{\partial}{\partial \xi} \right) + \frac{\partial}{\partial \eta}\left(\frac{h_3 h_1}{h_2} \frac{\partial}{\partial \eta} \right) + \frac{\partial}{\partial \zeta}\left(\frac{h_1 h_2}{h_3} \frac{\partial}{\partial \zeta} \right)$$

While solving the receptivity problem, the Poisson equations for u and v components of velocity given by Eqs. (3.42) and (3.43) are solved. Explicit satisfaction of divergence free condition for velocity is used for calculating the third velocity component. In a Cartesian framework, where grid transformations are not required the governing equations are derived by making the following substitutions,

$$h_1 = h_2 = h_3 = 1;$$

$$\omega_\xi = \omega_x;$$

$$\omega_\eta = \omega_y;$$

$$\omega_\zeta = \omega_z$$

3.5 Free-stream Turbulence

The velocity fluctuations with the prescribed spectra are imposed at the inflow plane for simulations of chapter 5. Following Brandt et al. (2004), a state of quasi-isotropic and homogeneous perturbations is approximated using the modified von-Kàrmàn energy spectrum given by,

$$E(\kappa) = \frac{2}{3} \frac{a(\kappa L)^4}{[b + (\kappa L)^2]^{17/6}} L \tag{3.45}$$

with $a = 1.606$, $b = 1.35$ and the integral length-scale L given by $L = 1.8/\kappa_p$, with κ_p being the wave number of maximum energy. The generic energy spectrum obtained using Eq. (3.45) is shown in Fig. 3.5.

These are based on a turbulence intensity of 3%. The Fourier-series method preserves the spatial and temporal coherence and includes random sampling in respect of the phase of the Fourier components (Vadlamani, 2015). At each time step, the velocity fluctuations u', v', w' are interpolated onto the inflow plane from a specific location in the synthetic turbulence

box governed by the distance moved into the plane of the box. Once the entire length of the box is exhausted, the process is again started from the first plane. Details of this procedure have been provided by Lardeau et al. (2012).

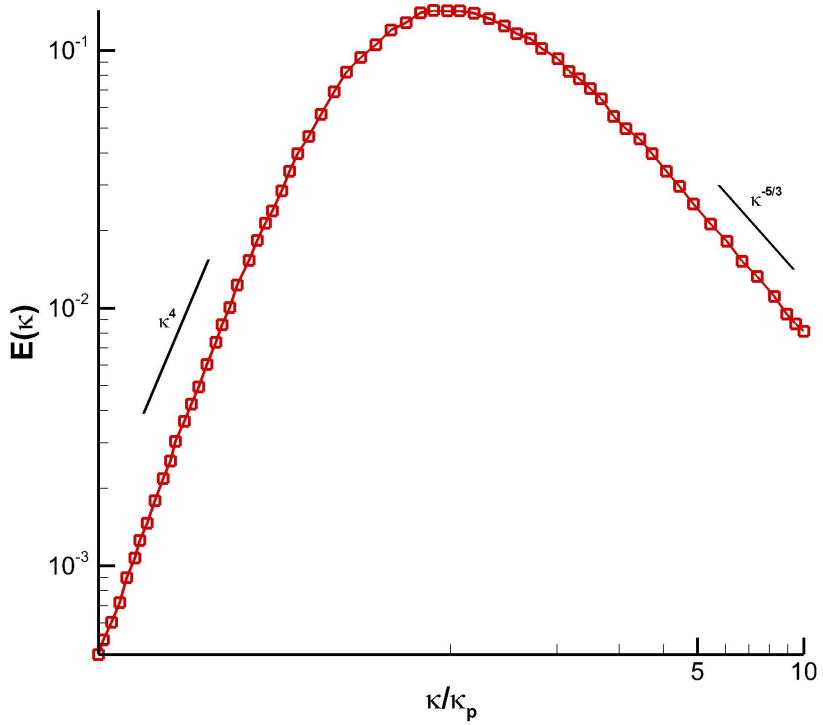

Fig. 3.5 von-Kàrmàn energy spectra of the inflow FST, as prescribed by Eq. (3.45).

3.5.1 kd-tree Search Algorithm

The kd-tree search algorithm (Bentley, 1975) is used at the inflow plane to impose FST by interpolating the velocity fluctuations from a turbulent box (Lardeau et al., 2012). It is used as a preliminary step for the interpolation used here. A search of the nearest neighbouring points to a 'query' point is performed in this algorithm. Based on the distance from the query point, weights are assigned to neighbouring points. This is the basic concept of inverse distance interpolation. The variable at the query point is then updated as a weighted average of the variable values at the neighbouring points.

A k-dimensional tree is created to reduce the time required for the search of the neighbouring points. The algorithm scatters the data of each cell in the domain of interest into a tree-like structure. This significantly brings down the time for the search, and thus, the interpolation time by searching along the 'branches' of the tree.

3.6 Inducing Oscillation

Flat plate oscillations are induced by a body force method used by Sakamoto et al. (1993), where an oscillating prism is subjected to a sinusoidal motion in the lateral direction. The whole computational domain is considered to move with the body. In order to incorporate the influence of the oscillatory motion, an inertia force term is added to the momentum equation in the direction of motion, as an external force at every grid point. This is equivalent to adding the acceleration the body experiences.

The flat plate is subjected to an oscillating velocity field in the wall-normal direction as,

$$v = a\, sin(2\pi\, t/t_o) \tag{3.46}$$

where a is the amplitude and t_o is the time period of oscillation.

3.7 Inducing Gaussian Wake at Inlet

A Gaussian wake is imposed at the inflow of the wake-induced transition simulations in chapter 7, by the following velocity profile which is added to the streamwise inlet velocity at every iteration.

$$u(w) = a_w e^{-\alpha\left[mod\left(\frac{y}{y_{max}}+\frac{2t}{t_w}-1{,}2\right)\right]^2} \tag{3.47}$$

where a_w is the amplitude associated with the wake, α is the exponential constant dictating the width of the Gaussian profile, y_{max} is the maximum wall-normal height of the domain used in chapter 7 and t_w is the time period of wake passing. This equation is used to ensure that during each wake passing cycle the incoming wake accounts for the relative position of the LPT blade with respect to the stator blades as well as the phase shift associated with the wake. A non-dimensional frequency based on the length of the plate and the reference velocity at the inlet defined as $St = f_w L/U_\infty$, is the Strouhal number where, $f_w = \frac{1}{t_w}$ is the wake passing frequency.

3.8 Immersed Boundary Method

In many industrial applications, geometric complexity in CFD is found in conjunction with moving boundaries, irregular surfaces and high Reynolds numbers. This has brought in a need for regeneration and deformation of grid during the computations. Pressure on existing

CFD tools to accurately simulate canonical flows, in terms of finite memory and speed of computations is very high. In view of this, to use regular Cartesian-like meshes, the requirement of grid conforming to the domain boundary is relaxed in immersed boundary method. Immersed boundary method allows the solution of complex geometrical features on simple meshes by introducing forcing conditions on certain surfaces corresponding to the physical location of the complex boundaries. It has been used extensively to model roughness.

The immersed boundary method was developed by Peskin (1977) to study blood flow in the heart. One of the first examples of application of immersed boundary method, was due to Vieceli (1969) where an extension of the marker-and-cell method was developed to account for the moving boundaries by assigning pressure boundary conditions along the interface. The first applications of immersed boundary method to solid, non-deformable surfaces was performed by Briscolini and Santangelo (1989) and Goldstein et al. (1993). Reviews written by Iaccarino and Verzicco (2003) and Mittal and Iaccarino (2005) provide detailed accounts of applications of immersed boundary method to various canonical flows. Bhaganagar et al. (2004) conducted DNS of channel flow with 3D roughness elements to study the alterations in the inner and outer layers and subsequent interactions, with the introduction of roughness elements modeled by immersed boundary method. Leonardi et al. (2006) performed DNS and LES of turbulent channel flow with transverse square bars on a wall. They used immersed boundary method to treat the roughness. Busse et al. (2015) executed DNS of turbulent flow over a rough surface based on a scan of a rough graphite surface. An embedded boundary method was employed which accounted for the rough boundaries by introducing a force term in the Navier-Stokes equation. The effect of surface filtering on turbulent rough wall channel flow was studied. Simens and Gungor (2013) employed DNS to study the correlation between height and location of discrete roughness elements and the transition of the separated shear layer. The roughness was modelled using an immersed boundary method, however only the adverse pressure gradient part of the blade was considered.

A volume of fluid approach was used by Yuan and Piomelli (2014) to impose no slip boundary conditions at rough surfaces, using an immersed boundary method. The method used will be adopted for roughness calculations via immersed boundary method calculations. The volume fraction occupied by fluid $\psi_{vi}(x,y,z)$ of each cell is calculated in the pre-processing step. $\psi_{vi} = 1$ for the grid points outside the roughness elements and $0 < \psi_{vi} < 1$ on the physical boundary of the roughness element. A body force F_i is obtained from the i^{th} component of velocity predicted ($\hat{u}_i$) with the help of a forcing term per unit volume.

$$F_i(x,y,z) = -(1-\psi_{vi}(x,y,z))\frac{\hat{u}_i(x,y,z)}{\Delta t} \tag{3.48}$$

The body force is included on the right hand side of the momentum equation for all successive iterations in the pressure-velocity formulation of COMP-SQUARE in Eq. (3.19). This enables one to account for the physical boundary of the roughness element, while solving a simple mesh without the roughness element. The curl of the body force, $\Delta \times F_i$ is added to the right hand side of the vorticity transport equation for all successive iterations in the velocity-vorticity formulation used for vortex-induced instability problem in chapter 6.

Immersed boundary method has been used to impose the no-slip boundary condition of the flat plate in configurations of chapters 5 and 7 using the compressible solver, COMP-SQUARE. The boundary condition has been implemented to machine level accuracy for this compressible flow. The boundary of a discrete roughness element has been imposed by immersed boundary method in chapter 6 using the velocity-vorticity formulation to solve the incompressible NSE. The no-slip condition inside the solid boundary has been implemented with an order of accuracy of 10^{-4}. The maximum error has been observed to be ≈ 0.0007. The Gaussian bump obtained via the application of immersed boundary method has been shown in Fig. 3.6. This has been used for the roughness studies of chapter 6 for vortex-induced instability.

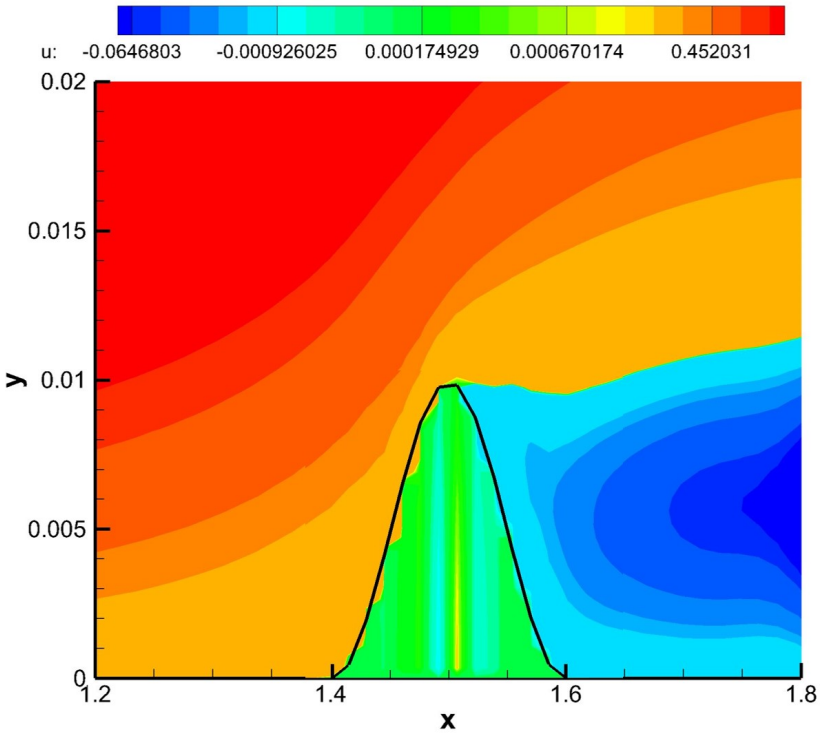

Fig. 3.6 Discrete roughness element (Gaussian bump) obtained through the application of an immersed boundary method. The boundary of the Gaussian bump is given by Eq. (6.1) and is shown by the solid line in the figure.

3.9 Compound Matrix Method for Solution of Stiff Partial Differential Equations

The compound matrix method (CMM) (Ng and Reid, 1980, 1985) is used in solving the stiff Orr-Sommerfeld equation (OSE) for both stability as well as receptivity problems, as shown in chapter 8. According to Bridges and Morris (1984), there are three methods for solving linear stability problems: (i) matrix method based on finite difference and spectral discretization, (ii) shooting methods based on orthogonalization and (iii) shooting with CMM. Allen and Bridges (2002) found that for eigenvalue problems in an infinite domain, matrix methods based on spectral collocations produced spurious eigenvalues due to fracturing of the continuous spectra while satisfying boundary conditions. Shooting methods based on orthogonalization have large memory requirements and thus, CMM is a viable candidate for hydrodynamic stability calculations and has been used here. There are other methods such as one based on solving the ordinary differential equation in physical space (SUPORT)(Scott and Watts, 1977) and spectral collocation methods involving Chebyshev discretization of OSE (Schmid and Henningson, 2001). In the CMM, we work with a new set of variables which are combinations of the fundamental solutions ϕ_1 and ϕ_3 instead of ϕ (the complex wall-normal amplitude of the Fourier-Laplace transform). The problem of stiffness in the OSE is removed here due to the new proposed variables which vary with wall-normal coordinate at identical rates. The new variables for the OSE are

$$\begin{aligned} q_1 &= \phi_1\phi_3' - \phi_1'\phi_3 \\ q_2 &= \phi_1\phi_3'' - \phi_1''\phi_3 \\ q_3 &= \phi_1\phi_3''' - \phi_1'''\phi_3 \\ q_4 &= \phi_1'\phi_3'' - \phi_1''\phi_3' \\ q_5 &= \phi_1'\phi_3''' - \phi_1'''\phi_3' \\ q_6 &= \phi_1''\phi_3''' - \phi_1'''\phi_3'' \end{aligned} \tag{3.49}$$

These six variables can be rearranged to get six first order ordinary differential equations of the new variables as

$$
\begin{aligned}
q_1' &= \phi_1'\phi_3' + \phi_1\phi_3'' - \phi_1'\phi_3' - \phi_1''\phi_3 = q_2 \\
q_2' &= (\phi_1\phi_3''' - \phi_1'''\phi_3) + (\phi_1'\phi_3'' - \phi_1''\phi_3') = q_3 + q_4 \\
q_3' &= d_1 q_2 + q_5 \\
q_4' &= q_5 \\
q_5' &= q_6 + d_1 q_4 + d_2 q_1 \\
q_6' &= d_2 y_2
\end{aligned} \tag{3.50}
$$

where $d_1 = 2\alpha^2 + i\alpha Re(U - C_{ph})$ and $d_2 = \alpha^4 + i\alpha^3 Re(U - C_{ph}) + i\alpha ReU''$. The new variables change the order of the system from four (in the OSE) to six (in CMM), while the governing equation is transformed from a boundary value problem to an initial value problem, removing the stiffness of the OSE altogether. Subsequently, any standard time integration scheme, such as four stage Runge-Kutta ($RK4$) method can be used. The free-stream property of the fundamental solution is used to generate initial conditions for q_1 to q_6 as

$$
\begin{aligned}
q_1 &\sim (-T + \alpha)e^{-(T+\alpha)y} \\
q_2 &\sim (T^2 - \alpha^2)e^{-(T+\alpha)y} \\
q_3 &\sim (-T^3 + \alpha^3)e^{-(T+\alpha)y} \\
q_4 &\sim (-\alpha T^2 + \alpha^2 T)e^{-(T+\alpha)y} \\
q_5 &\sim (\alpha T^3 - \alpha^3 T)e^{-(T+\alpha)y} \\
q_6 &\sim (-\alpha^2 T^3 + \alpha^3 T^2)e^{-(T+\alpha)y}
\end{aligned} \tag{3.51}
$$

We note from the set of above equations that all the variables have the same exponential growth rate i.e. the problem of stiffness has been removed. Next, we normalize the initial conditions given in Eq. (3.51) with the value of q_1. The six ordinary differential equations of q_1 to q_6 are solved from the free-stream to the wall starting from the normalized initial conditions. At the wall, we ensure that the dispersion relation obtained from the stability analysis of the OSE in Eq. (2.33) is satisfied which is equivalent to enforcing $q_1 = 0$ at $\tilde{y} = 0$. The eigenvalues are calculated with ease using the new variables and the eigenvector ϕ is solved from the differential equations given as

$$
\begin{aligned}
q_1\phi'' - q_2\phi' + q_4\phi &= 0 \\
q_1\phi''' - q_3\phi' + q_5\phi &= 0 \\
q_2\phi''' - q_3\phi'' + q_6\phi &= 0 \\
q_4\phi''' - q_5\phi'' + q_6\phi' &= 0
\end{aligned} \tag{3.52}
$$

Thus, there are four equations which provide the solution of the eigenvalue problem and the receptivity problem. It can be shown that only the first or the fourth equation is suitable, while the other two provide spurious modes which will cause the solution to become unstable during integration. A more detailed explanation of choice between these four alternatives is provided by Sengupta (1992). The CMM in conjunction with an iterative numerical method such as Newton Raphson method is used to find the eigenvalues of the stability/receptivity problem. Time marching from the free-stream to the wall and then from the wall to the free-stream is performed with $RK4$ time integration method.

Chapter 4

Identification and Evolution of Coherent Structures in Transitional Flows

The coherent structure identification methods used in the subsequent chapters have been briefly introduced in the literature review. The application of the two new methods derived from the incompressible Navier-Stokes equation, namely, the DETE and DME methods, is demonstrated in this chapter and correlations are drawn with respect to the well-established vortex identification methods: Q- and λ_2-criteria. It is well known that the methods based on Q- and λ_2-criteria are effective in identifying vortical coherent structures during the late transitional stages, where aligned and staggered Λ- and hairpin-vortices are present in the flow. Coherent structures are traced back in time to show the process of growth of disturbances from their onset, and comparisons are drawn between the structures identified by DETE method and λ_2-criterion, as also demonstrated by Sengupta et al. (2019b) while tracking coherent structures in their receptivity studies to wall and free-stream excitation. The results displayed in this chapter are evaluated for the bypass transition in the vortex-induced instability in Chapter 6 for two convection speeds of free-stream vortex: $c = 0.3$ and 0.386 non-dimensionalized with respect to the free-stream velocity. The computational details, boundary conditions and flow parameters of the problem are provided in Sengupta et al. (2019a).

4.1 Correlating Coherent Structure Detection Methods with Magnitude of Vorticity

In this section, the steps involved in a statistical correlation method used to correlate the positive and negative growth rates of Ω_d in DETE method, λ_2-, Q-criteria and DME with respect to a reference vorticity magnitude value $|\vec{\omega}|$, are provided.

The first step in this is to identify a particular region in space, which shows significant disturbance activity. Next, we extract the values of the criteria at the grid points in the selected region, which assume the value of $|\vec{\omega}|$ within a small tolerance of the reference value. Here, we have used a tolerance of 0.1 for $|\vec{\omega}| = 10$. Using the DNS data in the selected region of enquiry, we calculate the mean and variance of each structure detection criteria for a specific time. Thus, the mean and variance refer to spatial distribution of the values within the interrogation box chosen. This process is repeated for each reference value of $|\vec{\omega}|$. In the plots shown in this and following sections, we compare different criteria, with respect to spatial mean value with and without standard deviation, for the particular criterion used to plot the iso-surfaces and compare with the chosen reference value of $|\vec{\omega}|$. The procedure has been applied in Sengupta et al. (2019b) to demonstrate and compare the application of DME- and DETE-criteria for wall and free-stream excitations imposed on a ZPG flat plate geometry.

In Fig. 4.1, the correlations obtained between $|\vec{\omega}|$ and vortex identification methods based on DETE and λ_2-criteria are shown for a free-stream convecting vortex with translation speed, $c = 0.3$ and strength, $\Gamma = 2$, at the indicated times. Results are shown following the primary instability for $t = 34$ and beyond, as indicated in the frames of Fig. 4.1. A tolerance limit of ± 0.1 is used for the calculation of the spatial mean and standard deviation for $|\vec{\omega}|$. In the top frame, the spatial mean of positive growth rate of Ω_d with $|\vec{\omega}|$ is shown to increase, with increasing $|\vec{\omega}|$ for the times considered. Here, one notices significant disturbance growth for $\Omega_d > 0$ for larger values of $|\vec{\omega}|$ at $t = 34$. In contrast, the growth rates for $\Omega_d < 0$ are lower by at least one order of magnitude for all times. At the later times, $t = 43$ and 45, one notices monotonic growth of positive-Ω_d, as $|\vec{\omega}|$ takes higher and higher values. This quantity for all the four time instants show an increasing trend, at late transition stages for $t = 43$ and 45, when larger $|\vec{\omega}|$ dominates the flow. In the second frame, the mean, the difference between the sum and standard deviation are shown for the λ_2-criterion. As λ_2 has to be a negative quantity (Jeong and Hussain, 1995), the standard deviation is subtracted from the mean (which is a negative quantity). There is a large region of positive-λ_2 for low values of $|\vec{\omega}|$ at later times, which does not follow the requirement of negative-λ_2. For the λ_2-criterion, one notices a significantly large negative value of this eigenvalue for $|\vec{\omega}| \sim 20$ at

$t = 34$. At later times also, this same vorticity magnitude value shows large negative value of λ_2. Other than this spike, the other $|\vec{\omega}|$ values do not display negative values for λ_2 at $t = 34$. However, for $t = 43$ and 45, one notices negative values of λ_2 for all values of $|\vec{\omega}|$, except for very small values of vorticity. The bottom frame in Fig. 4.1, shows the magnitude of growth of disturbance enstrophy, for $\Omega_d < 0$. At earlier times of $t = 34$ and 39.6, the sources of negative disturbance enstrophy are larger noted by the logarithmic ordinate, while at the later times, due to growth of ω_d the nonlinear contribution of Ω_d is more dominant.

In Fig. 4.2, the DME method and Q-criterion are investigated for the same free-stream excitation case. For the Q-criterion, presence of a coherent structures requires this quantity to be positive for the static pressure to be a minimum (Jeong and Hussain, 1995) whereas for the DME method, disturbance sources are present for a negative RHS of the equation. The Q-criterion correlation shows large positive value of Q, for $|\vec{\omega}| \sim 20$. Higher values of $|\vec{\omega}|$ show negative values of Q, and thus, those values cannot be associated with coherent structures at $t = 34$. At later times, those higher values have positive values of Q, and could be related to coherent structures. In comparison, the RHS of the DME method alternates in sign at $t = 34$, implying strong unsteadiness and therefore growth of disturbances. At later times, the fluctuations reduce for lower to moderate values, but negative values are seen for $|\vec{\omega}| \sim 25$. The higher values of $|\vec{\omega}|$ show stronger fluctuations of signs implying very high unsteadiness.

4.1.1 Example of Free Stream Excitation Case: Comparing DETE Method and λ_2-criterion

In Figs. 4.1 and 4.2, we have correlated various Eulerian methods for tracking disturbances and coherent structures. Within those correlation curves, we will present some specific cases marked in the figures as $A1$ to $D2$.

In Figs. 4.3 and 4.4, the λ_2-criterion and DETE method for $\Omega_d > 0$, are compared for the cases shown in Figs. 4.1 and 4.2. In Fig. 4.3, comparison is shown between these two methods at $t = 34$ for $|\vec{\omega}| = 14.6$, 15.8 and 17.4, with these points marked in Fig. 4.1 in the middle frame, for which λ_2 takes negative values. For this case, the vorticity contours shown in the bottom frames of Fig. 4.3 are compared with the λ_2-criterion, along with DETE methods for both $\Omega_d > 0$ and $\Omega_d < 0$. The complementary nature of $\Omega_d > 0$ and $\Omega_d < 0$ is clearly evident, with the detected structure matching very well with the vorticity contours. It is observed that the λ_2-criterion displays exaggerated structures, with the DETE method producing smoother and larger rolled-up structures.

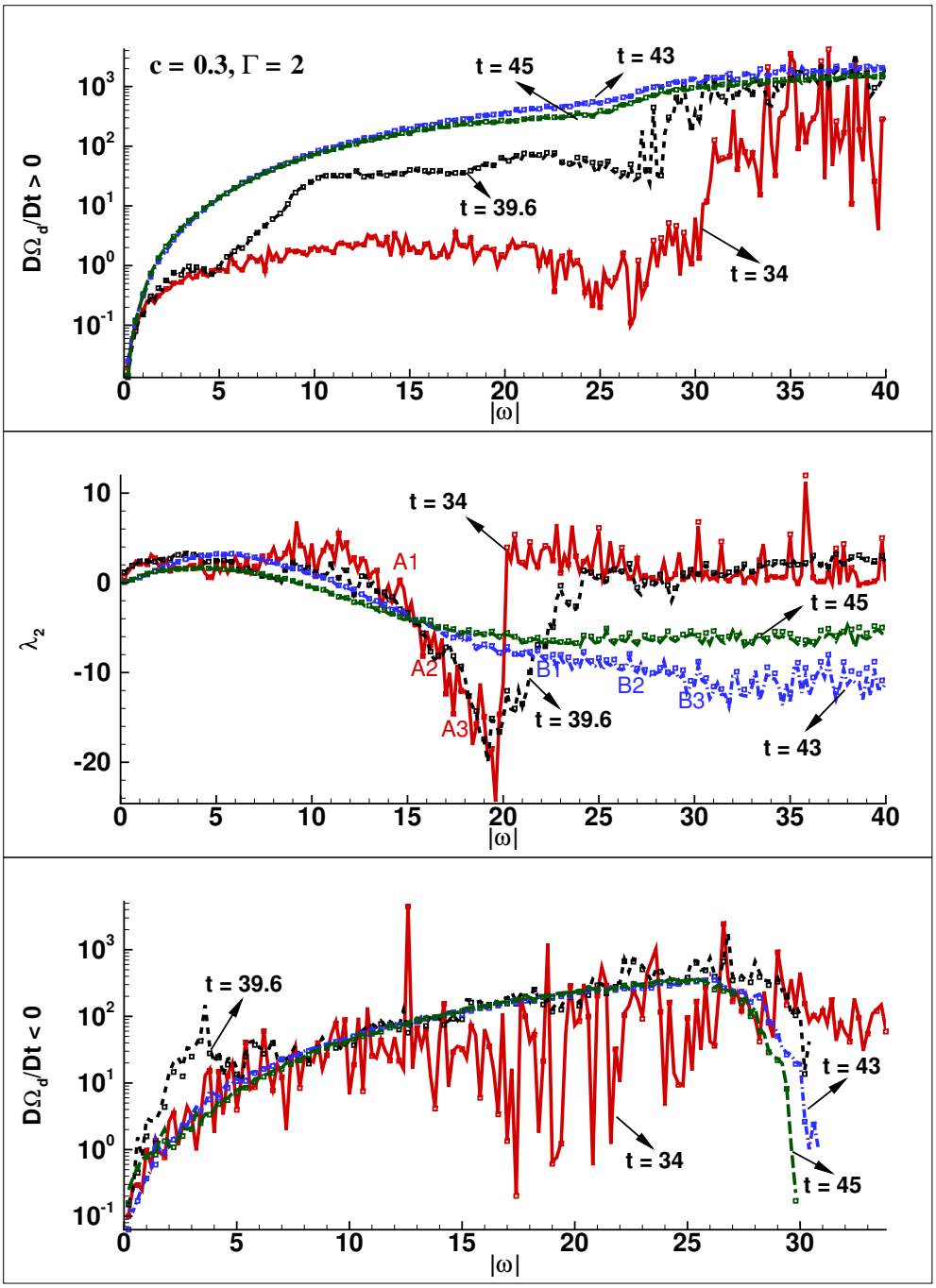

Fig. 4.1 Correlation curve showing DETE criteria for positive and negative Ω_d and λ_2 with $|\vec{\omega}|$, for free stream excitation case with $c = 0.3$ and $\Gamma = 2$.

In Fig. 4.4, the methods are compared at the later time, $t = 43$ for the three $|\vec{\omega}|$ values identified as $B1, B2$ and $B3$ in the middle frame of Fig. 4.1. At this later time, a disturbance packet termed as the STWF is identified, and which displays much smaller structures in the

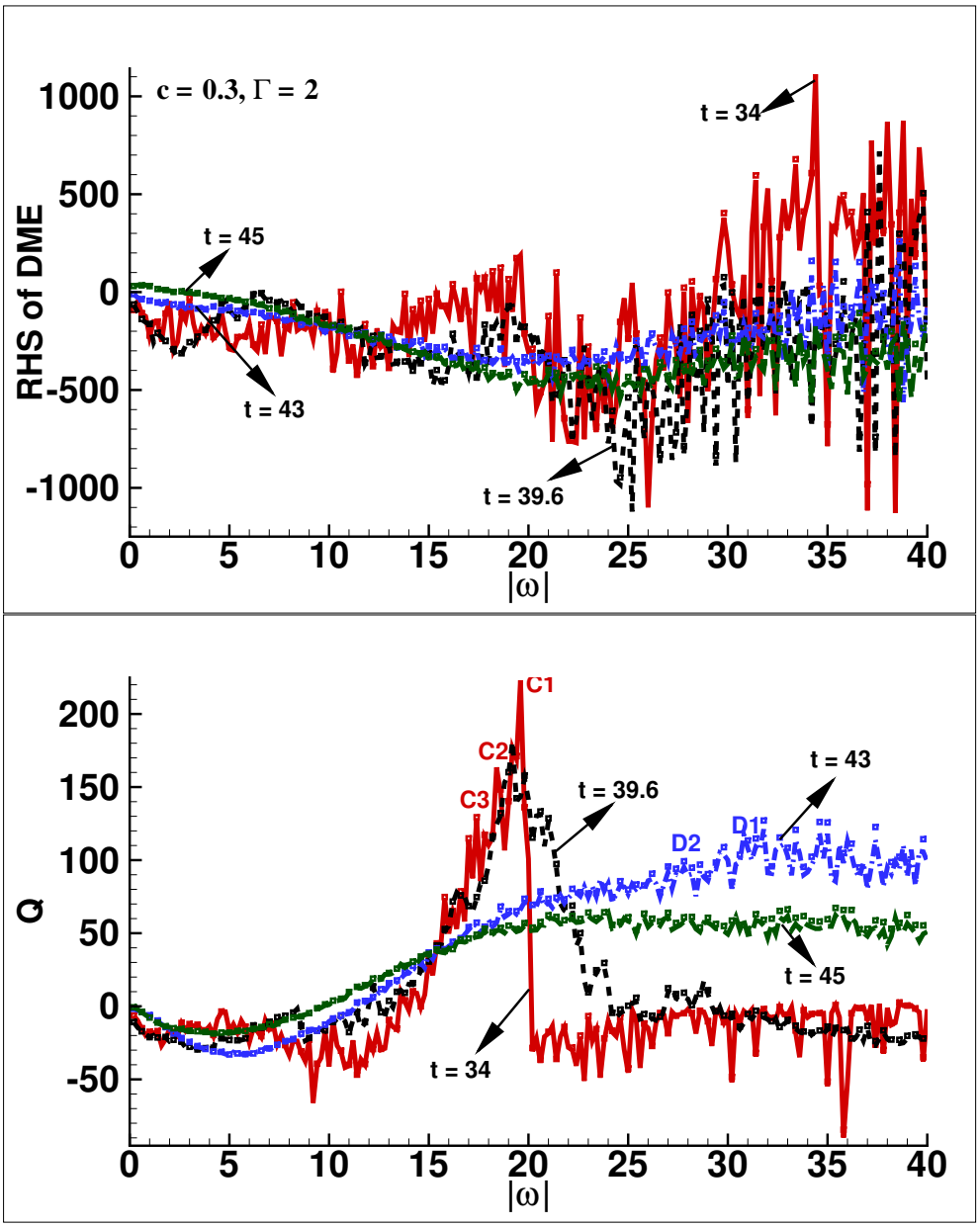

Fig. 4.2 Correlation curve showing Q- and DME-criteria with $|\vec{\omega}|$, for free stream excitation case with $c = 0.3$ and $\Gamma = 2$.

vorticity contours. This is captured with the DETE method and λ_2-criterion equally. The near-wall, small scale structures are captured well with DETE method for $\Omega_d < 0$, while the outer bigger structures are captured well by $\Omega_d > 0$. The corresponding figures comparing the two structure detection methods for a case with a time-harmonic wall excitation on the flat plate are shown in Sengupta et al. (2019b), wherein a good match is obtained by both methods for early and late times. This suggests that the free-stream excitation case is a more

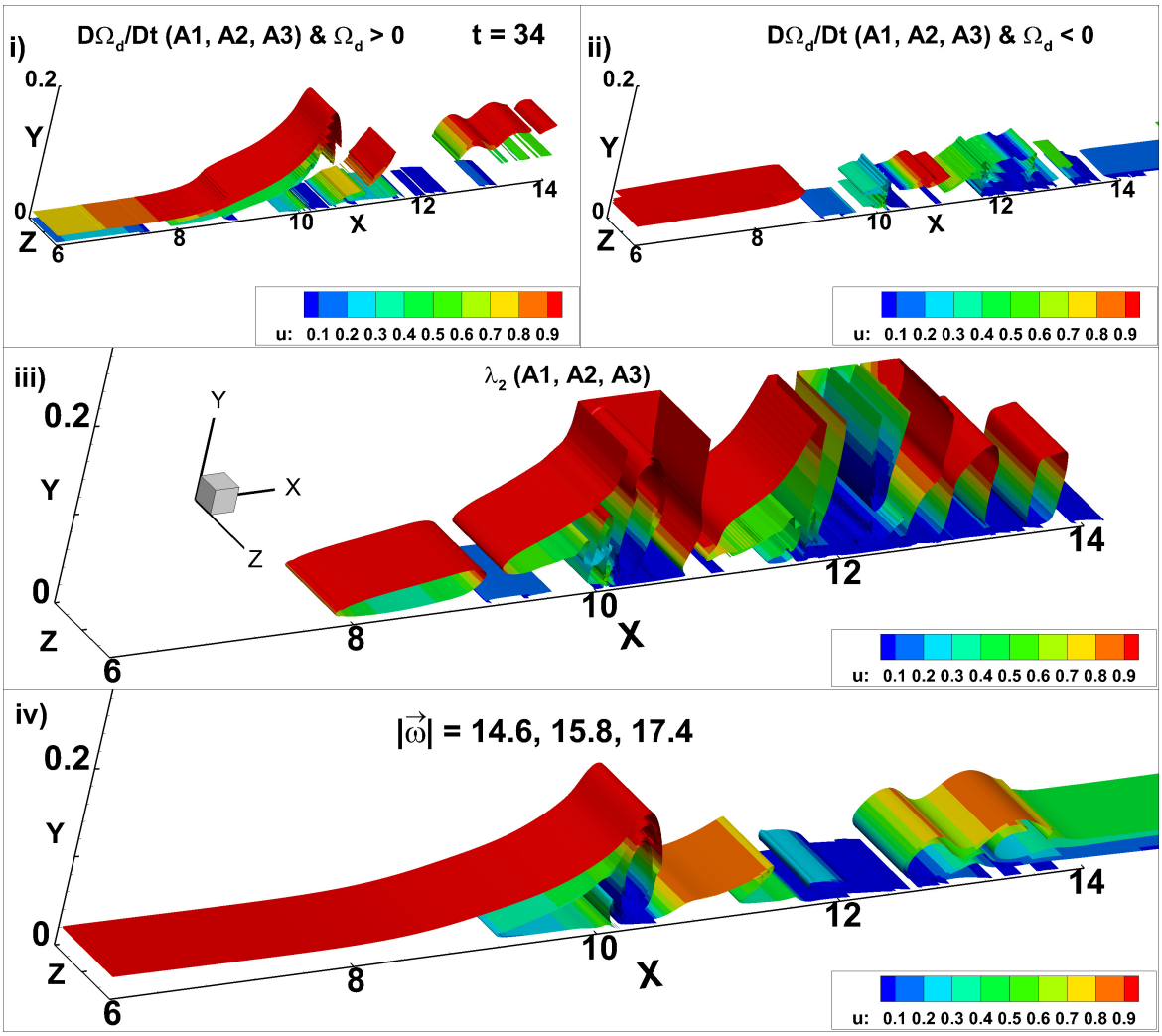

Fig. 4.3 Iso-surfaces of (i) $\frac{D\Omega_d}{Dt} > 0$, (ii) $\frac{D\Omega_d}{Dt} < 0$ (iii) λ_2, calibrated against (iv) vorticity magnitude, $|\vec{\omega}|$ at $t = 34$, for the free stream excitation case with $c = 0.3$ and $\Gamma = 2$.

critical one, which requires the nuances of the unsteady and viscous terms in the DETE method, specifically for the early stages of disturbance evolution.

4.1.2 Example of Free Stream Excitation: Comparing DME Method and Q-criterion

In Fig. 4.5, the DME- and Q-criteria are compared for the free-stream excitation case noted at $t = 34$ and 43, tracking the points $(C1, C2, C3)$ for the earlier time and $(D1, D2)$ for the later time, as marked in Fig. 4.2. For both these times, it is noted that the Q-criterion fares poorly, as compared to the method based on DME, specially at the earlier time. The reason

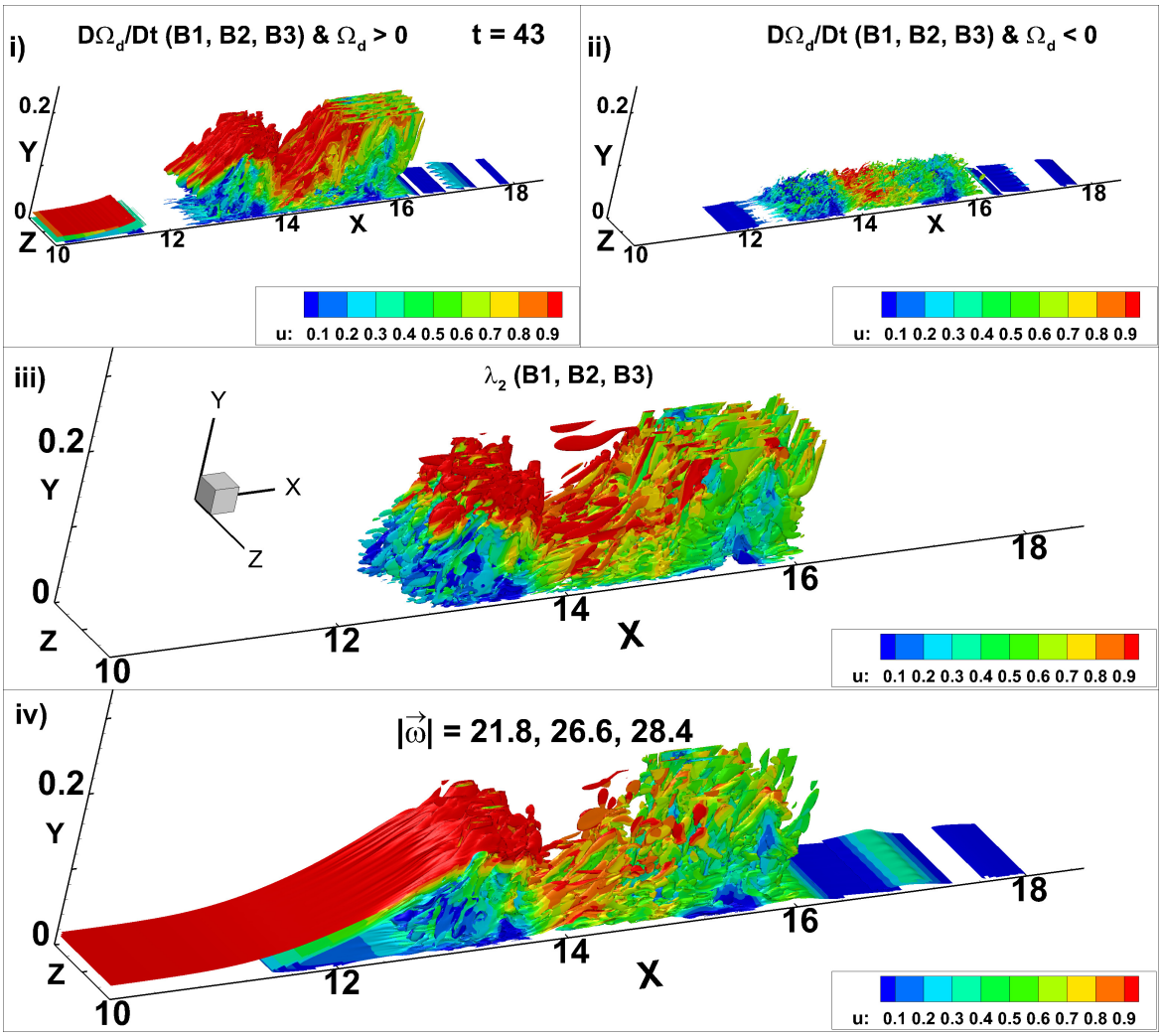

Fig. 4.4 Iso-surfaces of (i) $\frac{D\Omega_d}{Dt} > 0$, (ii) $\frac{D\Omega_d}{Dt} < 0$ (iii) λ_2, calibrated against (iv) vorticity magnitude, $|\vec{\omega}|$ at $t = 43$ for the free stream excitation case with $c = 0.3$ and $\Gamma = 2$.

for this is on the fundamental basis of the Q-criterion which considers the vortex core to be at a pressure minima, but all vortical structures in transitional and turbulent flows are not always related with pressure minimum. This enables methods based on the NSE using physical disturbance quantities like DME to perform better when such requirements are not met by the earlier stages of disturbance growth.

4.2 Tracking Coherent Structures Backwards in Time

Our discussion so far demonstrates that the DETE method and λ_2-criterion perform relatively better in identifying disturbance structures, with λ_2-criterion performing well in the presence

of pressure minima. From the results reported in Sengupta et al. (2019b), it can be inferred that the wall excitation case demonstrates a better match. Here, we would like to trace the coherent structures backwards in time for the free-stream excitation case with $c = 0.386$ and $\Gamma = 2$.

In Fig. 4.6, we trace back the disturbance vorticity from $t = 34.4$ backward in time up to $t = 32$, shown on the right column for $|\vec{\omega}| = 10$. The DETE method for $\Omega_d > 0$ results are shown in the left column, while the results for λ_2-criterion are shown in the frames in the middle. For the vortex-induced primary instability, onset causes unsteady separation (Sengupta et al., 2019a) and the recirculation zone with associated pressure minimum is seen in the vorticity contour and is identified by the λ_2-criterion and DETE method. However,

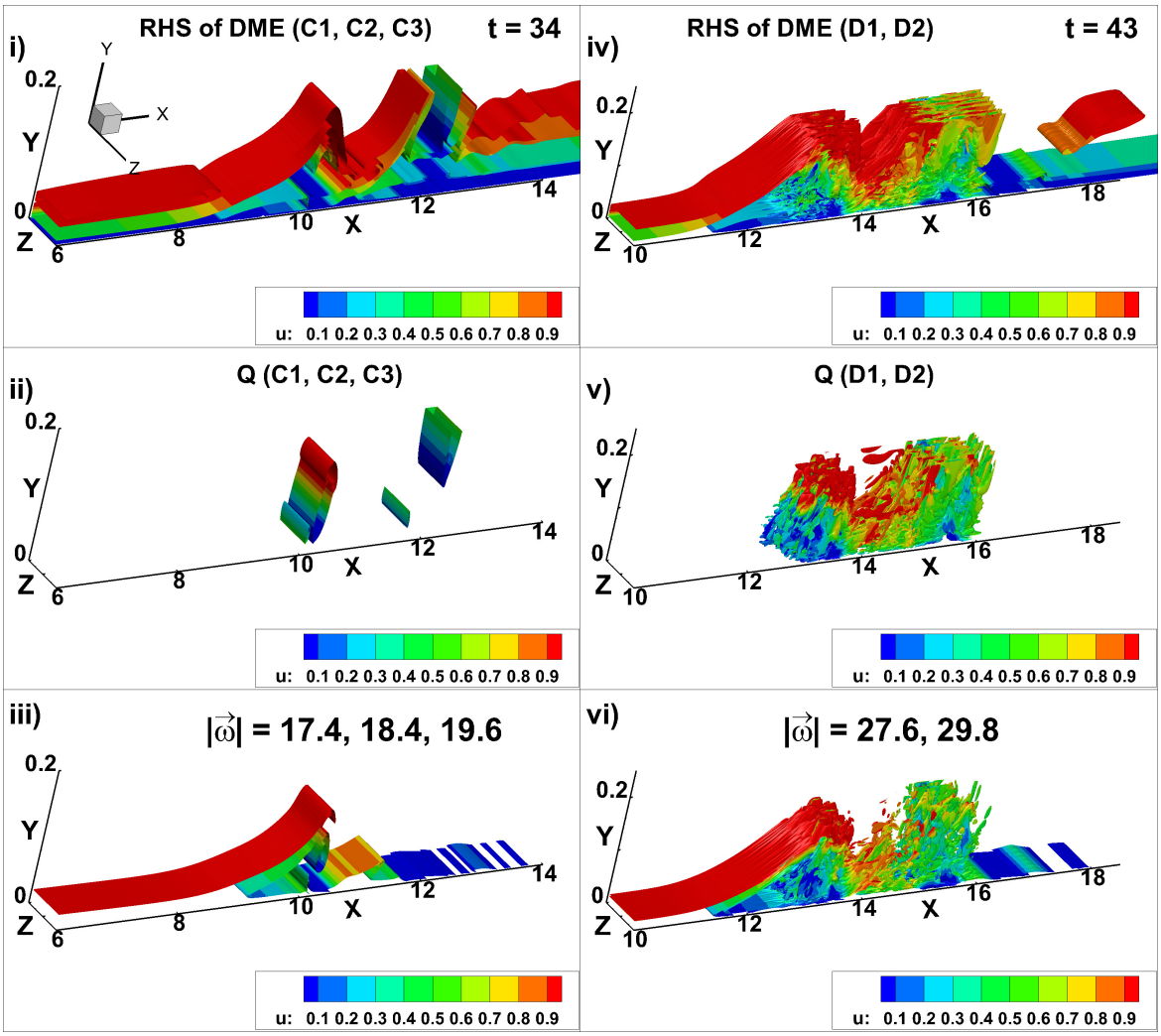

Fig. 4.5 Iso-surfaces of (i,iv) DME- (ii,v) Q-criterion, calibrated with (iii,vi) vorticity magnitude, $|\vec{\omega}|$ at $t = 34$ and 43, for free stream excitation case with $c = 0.3$ and $\Gamma = 2$.

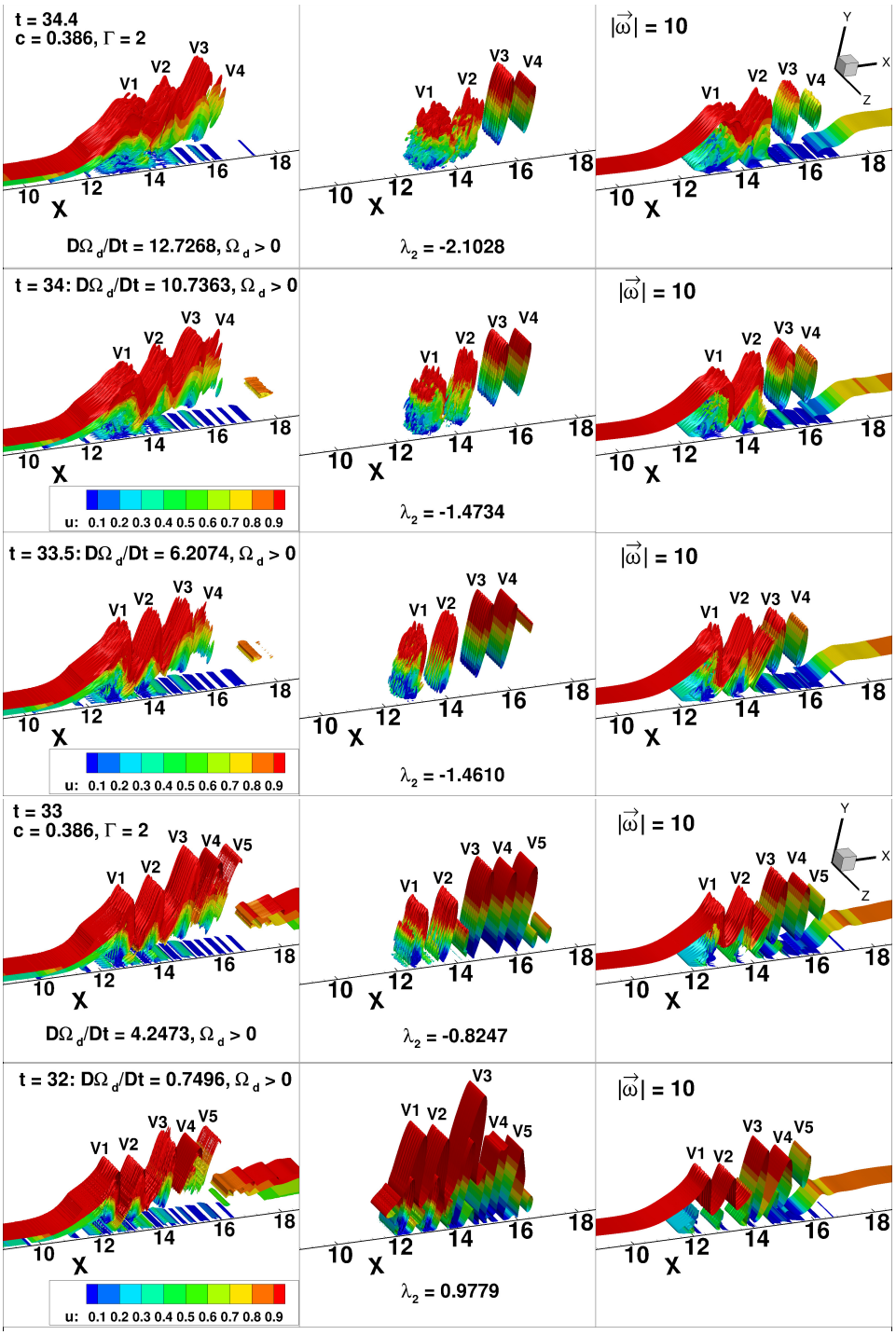

Fig. 4.6 Iso-surfaces of $\frac{D\Omega_d}{Dt} > 0$ and λ_2-criterion for $|\vec{\omega}| = 10$ starting at $t = 34.4$, and moving backward in time at $t = 34, 33.5, 33$ and 32, for free stream excitation case with $c = 0.386$ and $\Gamma = 2$.

the other vortical structures which do not roll up to form vortices are completely missed by λ_2-criterion. These are captured by the DETE methods with higher fidelity. One also notices that the λ_2-criterion exaggerates the captured recirculating bubbles in the wall-normal direction. Thus, for the free stream excitation case, the DETE method performs better in capturing and tracking the vortical structures. This may not strictly be the case for the wall excitation case shown by Sengupta et al. (2019b) wherein both DETE and λ_2-criteria provide an adequate comparison with the reference $\vec{\omega}$-isosurface.

4.3 Conclusions

The new proposed methods of structure visualization which are derived directly from the incompressible Navier-Stokes equation and based on disturbance mechanical energy (DME) and disturbance enstrophy transport equation (DETE), respectively are qualitatively and quantitatively compared with established methods of vortex detection, namely the Q- and λ_2-criteria. A canonical fluid dynamical problem of vortex-induced instability (Sengupta et al., 2019a, 2018a) has been chosen to track the evolving disturbance field from the receptivity stage to fully developed turbulent stage. The flow parameters and numerical details for this problem will be provided in Chapter 6.

The DETE approach is rooted to a developed transport equation for the incompressible Navier-Stokes equation, without making any assumption. Unlike the other three methods discussed here, both the unsteady and viscous terms are accounted for in the DETE method, and as a consequence small scales in the flow are identified by this method, as shown in Figs. 4.3 and 4.4. The λ_2-criterion and Q-criterion are tools for identifying vortical structures and are effective in the outer inviscid part of the flow, where the source terms of the governing Poisson equation are active and non-negligible and where the flow is dominated by vortical motion. The procedure here has been applied to a small range of iso-surface values of Q or λ_2, but there have been attempts to account for the effect of wall-normal distance for a fully developed turbulent channel flow by including a threshold value (of these methods) which is a function of the wall-normal distance (del Álamo et al., 2006).

A statistical correlation methodology adopted in the present study to correlate different methods has been presented, and it will be used in all subsequent comparisons made between various structure detection methods. The four methods are correlated with a chosen reference value of vorticity magnitude. The generic comparison among the four methods is shown as a function of vorticity magnitude at two time instants in the evolving flow field with the primary aim in providing basis for chosing values for Q-criterion and DME, and λ_2 and DETE criteria, respectively. We have tracked identifiable coherent structure of the STWF

backwards in time. It is observed that coherent structures mature very quickly from late transitional stage. The tracking of coherent structures by the DETE method is found to capture near-wall coherent structures in addition to the vortical motions within the perturbed flow. The λ_2-criterion has been designed to demonstrate vortical coherence in turbulent flows and it has shown a good match when calibrating with the vorticity field containing pressure minima (Jeong and Hussain, 1995; Kolár, 2007; Sengupta et al., 2019b).

The feature of the DETE method based on disturbance enstrophy, is that it can take both signs. These two different signs of disturbance enstrophy and their corresponding growth rates provide different physical mechanisms of disturbance growth. It is noted that the growth rates of positive disturbance enstrophy iso-contours are associated with large scale coherence inside the disturbance packet, whereas the negative disturbance enstrophy growth rates are associated with unsteady separation noted at the wall, which induces locally an adverse pressure gradient in the neighbourhood of each separation bubble. This will be demonstrated in Chapter 6 for the vortex-induced instability. The downstream migration of such bubbles affects larger streamwise extent, and since these bubbles are confined near the wall, they are dominated by viscous action, giving rise to fine scale structures. Overall, the DME and DETE methods have been shown to provide a favourable agreement with flow structures noted for an incompressible flow excited at the wall (in Sengupta et al. (2019b)) and from the free-stream. It will be worthwhile to extend this exercise for compressible flow applications such as for stratified buoyancy driven flows where the flow evolves due to a baroclinic vorticity such as in Rayleigh-Taylor instability. Such flows will not be governed by pressure considerations alone, and application of Q or λ_2-criteria may not be viable.

Chapter 5

Aeroelastic Effects on Transition on Ultra High-Lift Blades

In this chapter, the individual and coupled effects of the incoming free-stream turbulence (FST) and blade oscillations on the transition of a separated shear layer is presented. The numerical investigations are carried out using a series of DNS over a flat plate subjected to a streamwise pressure gradient representative of an 'ultra high-lift' blade loading. The computational domain, boundary conditions imposed, the characteristics of the test cases are introduced first. This is followed by a detailed analysis of the instantaneous and time-averaged quantities; and a discussion on the mechanisms by which blade oscillation and FST alter the transition process. Further insight into the flow physics is gained using turbulent kinetic energy budgets and phase-averaged plots. Finally, nonlinear instability tracking mechanisms developed directly from the full 3D incompressible Navier-Stokes equation (NSE) are applied to distinguish the transition mechanisms governing the flow.

5.1 Computational domain and boundary conditions

The computational domain considered in the present study is shown in Fig. 5.1. It consists of a flat plate with finite thickness and a rounded leading edge, subjected to a streamwise pressure gradient by virtue of the contoured upper wall. The given configuration has been studied experimentally at higher Reynolds numbers by Lou and Hourmouziadis (2000) and numerically at lower Reynolds numbers by Lardeau et al. (2012), Vadlamani et al. (2013) and Wissink and Rodi (2004). The geometry has been mirrored about the $y^* = 0$ line to remove the need for prescribing a free-slip boundary condition in the region upstream of the flat plate ($x^* < 0$) in the original configuration, which has a time varying angle of attack, for

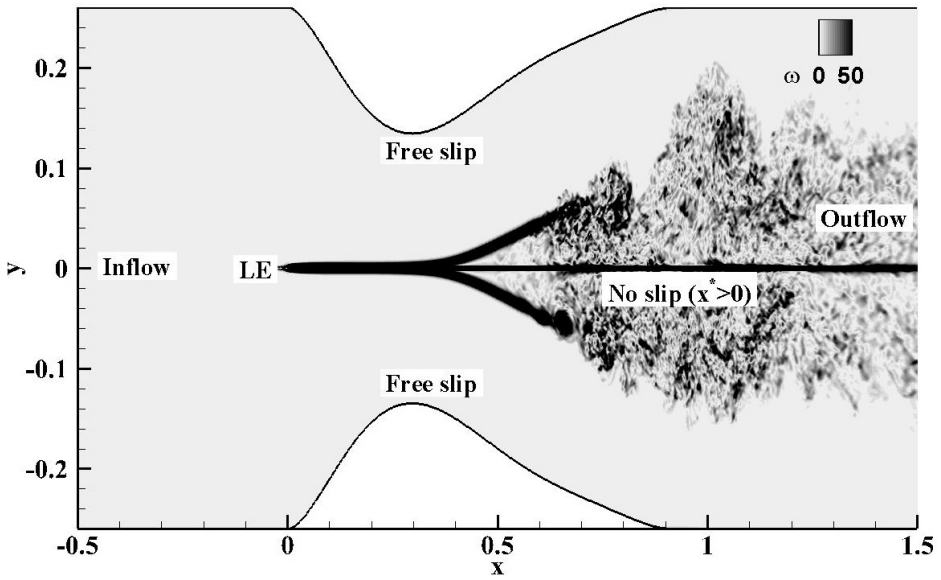

Fig. 5.1 Computational framework and boundary conditions implemented. The magnitude of vorticity has been shown in the figure.

the oscillating flat plate. The pressure distribution over the flat plate is representative of the loading on a ultra high-lift low pressure turbine blade.

Free-slip boundary conditions are imposed on the contoured walls at the top and bottom. As shown in Fig. 5.1, a no-slip condition is imposed on the flat plate downstream of the sharp leading edge ($x^* > 0$) with the help of an immersed boundary method used by Yuan and Piomelli (2014). Periodic boundary conditions are imposed in spanwise direction. A spanwise width of 12% of chord length is used. The size of the span is sufficient to accommodate all dominant modes as reported for the LES of Lardeau et al. (2012) and DNS of Wissink and Rodi (2004).

For the outflow, static pressure at the exit is specified and the velocities are extrapolated from interior nodes. Riemann boundary condition has been imposed at the inflow along with the incoming FST to prevent reflections for low amplitude acoustics. FST has been modeled by synthetic box turbulence which follows the modified von-Kàrmàn spectrum, as previously reported by Lardeau et al. (2012) and Vadlamani (2015), and described in chapter 3.

For the present computations a mesh of 52 million points is considered, with 787 points in the streamwise direction resolving $-0.5 < x^* < 2$. There is an additional buffer zone in the streamwise direction beyond $x^* > 2$ to avoid reflections from the outflow, applied through enhanced filtering in this zone. In the wall-normal direction, there are 513 points resolving $-0.26 < y^* < 0.26$, while the periodic spanwise length, $0 < z^* < 0.12$ is resolved with 128 points. Figure 5.2 shows the streamwise variation for near wall spacing in terms of wall

units x^+, y^+, z^+. In the separated region (0.4 < x < 0.6), absolute friction velocity is used to calculate the wall units due to negative shear stress values. It is crucial to capture the separated shear layer. The grid spacing in the wall-normal direction in the separated region varies from 4×10^{-4} near the wall to 2×10^{-3} at the upper slip-wall. The height of the duct varies from 0.13 at the throat to 0.18 at the location of reattachment. With 513 points in the wall normal direction, the separated shear layer is resolved using 70-80 points.

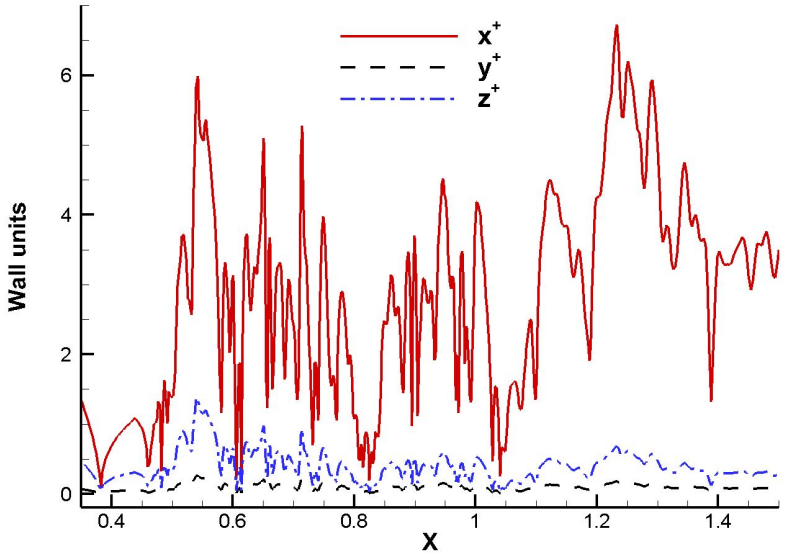

Fig. 5.2 Streamwise variation of wall-units near the wall for test cases simulated.

Computations are carried out at a Reynolds number of 60000, based on the reference inlet velocity and flat plate length. Here, the flow has a Mach number (Ma) of 0.1, because of this low value of Ma, one can safely operate in the incompressible limit, thereby enabling one to use instability receptivity mechanisms (derived from the incompressible NSE and shown in appendices A and B) in characterizing the disturbance field in later sections.

5.1.1 Test Cases

The descriptions of the four different test cases simulated are provided in Table 5.1, where k_{osc} is the reduced frequency given by Eq. (2.1), t_o is the time period and a is the amplitude of imposed oscillation given in Eq. (3.46) and p_o is the blade pitch. The reduced frequency has been chosen within the reference values usually observed for turbomachines (Vogt, 2005).

Table 5.1 Details of the test cases simulated. Here, k_{osc} is the reduced frequency given by Eq. (2.1), t_o is the time period and a is the amplitude of forced oscillation given in Eq. (3.46) and p_o is the blade pitch.

Case	k_{osc}	t_o	a
LI: Laminar inlet	NA	NA	NA
WS: Forced oscillation case 1	0.1	0.0775	0.031 (p_o/30)
HWS: Forced oscillation case 2	0.05	0.1551	0.031 (p_o/30)
WSF: Forced oscillation case 1 + FST at inlet	0.1	0.0775	0.031 (p_o/30)

5.2 Numerical Validation

The current computational framework is validated in Fig. 5.3 by comparing the present simulation results against the DNS results of Wissink and Rodi (2004) where the Reynolds numbers for the flows are the same. The validation study focuses on effects of FST with turbulent intensity, $Tu = 3\%$ on the laminar separation bubble created on the suction surface. The mean streamwise velocity profiles and the corresponding Reynolds stresses are shown in Fig. 5.3 at eight streamwise locations. Even though a coarser resolution (47 %) simulation is performed here, when compared to the DNS of Wissink and Rodi (2004), the results show a reasonable quantitative agreement. The pre-transitional region has been predicted accurately. Deviations from the DNS observable beyond $x^* = 0.7$, are due to the early reattachment of the flow which was also seen by Lardeau et al. (2012) in their LES studies.

In Fig. 5.4, the evolution of FST imposed at inlet is quantified in terms of the streamwise velocity fluctuations, u'. Elongated streamwise structures appear in the separated shear layer ($x^* > 0.4$), and the separation becomes irregular in the spanwise direction. This irregularity is attributed to the Klebanoff mode arising at high FST levels. This process of implementing FST has been used for test case WSF, as given in Table 5.1. In comparing the vortical structures in Figs. 5.5 and 5.6, it is observed that the Q-criterion produces smoother and more coherent features as compared to the instantaneous vorticity field. This is in consonance with the description provided in chapter 2, where we noted that the Q-criterion does not include the unsteady and viscous terms of the NSE (Perry and Chong, 1987) due to divergence free velocity condition for the incompressibility of the present flow (Ma = 0.1).

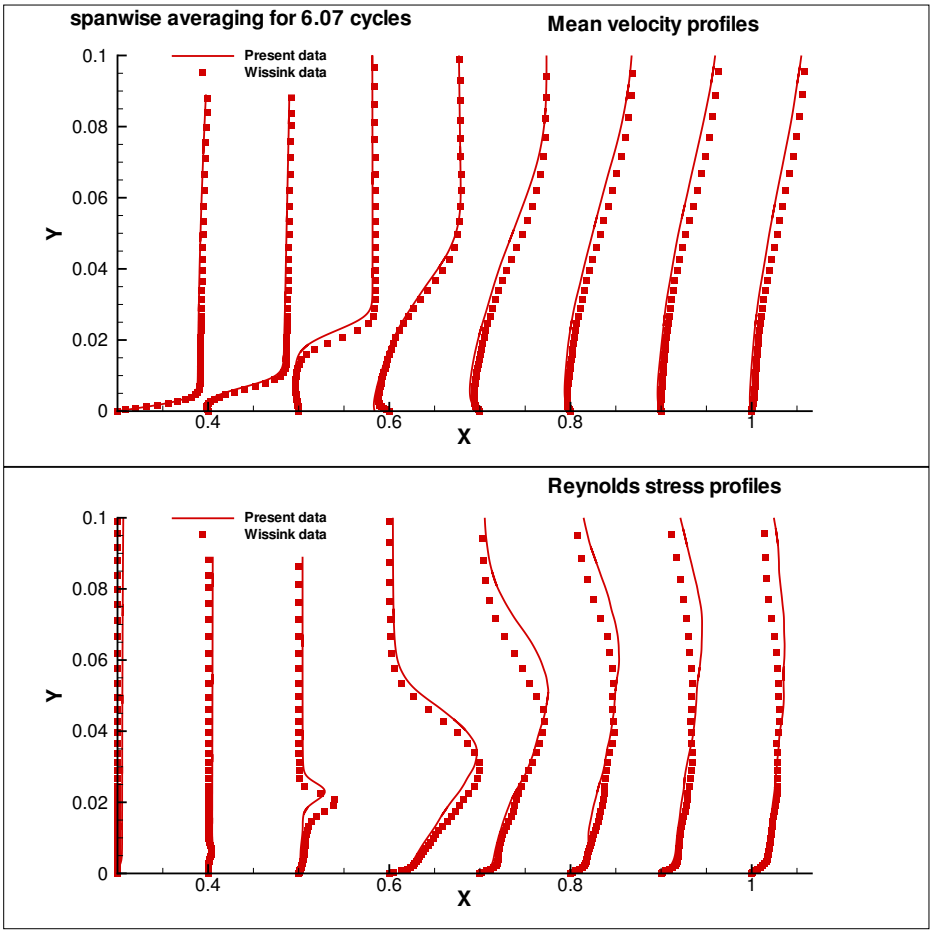

Fig. 5.3 Comparison of streamwise mean velocity profiles and Reynolds stresses with DNS results of Wissink and Rodi (2004).

5.3 Initializing the Flow

The laminar case, LI is computed first, which acts as the equilibrium flow for the other oscillation cases in disturbance quantity calculations. The flow is allowed to settle after flushing off the transients, after five through-flows in the computation. The mean statistics are recorded after this time for another six through-flows. For the test cases with oscillation, the flow is initiated with oscillation at t = 0, by including the body force term as described in chapter 3. The probe data for calculation of time period of the flow is stored at every time-step for ten time periods of oscillation. The statistics for phase-averaging are collected during five time periods of oscillation.

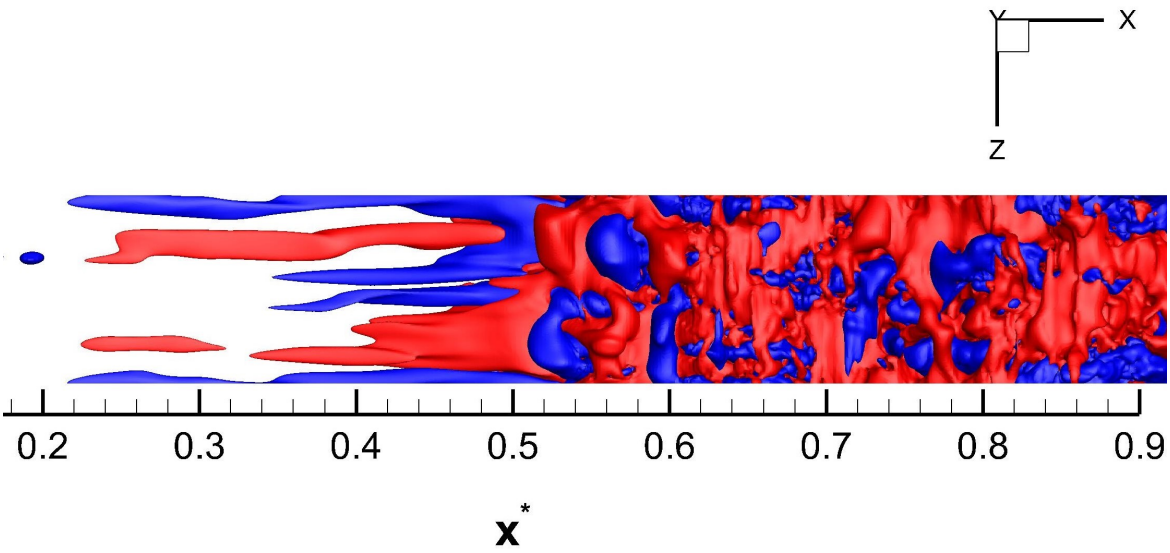

Fig. 5.4 Iso-surface of $u' = \pm 0.1 U_\infty$ for Tu = 3 %. The motions faster than the mean velocity are given by the red (lighter shade) structures, while the slower ones are provided by blue (darker) structures.

5.4 Instantaneous Flow Features

The present flow is dominated by coherent vortical structures and it is true for all transitional/turbulent flows dominated by structures created near the wall. In a LPT, small-scale boundary layer structures and vortices are created by FST and wall vibration. The vortical structures are usually visualized by Q-criterion (Perry and Chong (1987), Hunt et al. (1988)) and λ_2-criteria (Jeong and Hussain, 1995).

In Fig. 5.5, iso-surfaces of Q-criterion ($Q = 40$), given by Eq. (2.2), coloured by streamwise velocity are shown for the test cases LI, WS, HWS and WSF described in Table 5.1. Predominant convecting 2D spanwise vortices are observed near $x \approx 0.5$, for LI, WS and HWS cases, originating from the separated shear layer. For case LI, two such vortices are observed, while for cases WS and HWS, there is only one such vortex. In all the cases, there are two sites of spanwise vortices, which can be attributed to two localized regions of adverse pressure gradient. However, as the level of wall disturbance increases with blade vibration and FST from cases WS to WSF, it leads to the breakdown of the two-dimensionality of the vortices and elongates the structure in the streamwise direction. These vortices interact downstream at later times, with the underlying hairpin vortices to create strong three-dimensionality noted by spanwise waviness of these vortices as also seen by Brinkerhoff and Yaras (2011). For the case WSF (with FST), the spanwise waviness is noted for the vortex created by the separated shear layer. This waviness accentuates further as it

convects downstream, as noted in the Fig 5.5. Only for the case LI, the two dominant spanwise vortices are lifted off the plate as they convect downstream. Progressive distortion of the second vortex is observed, as the disturbance levels are increased from test case WS to WSF in Fig. 5.5. A reduction in reverse flow, indicated by the blue contours, is also noted for cases WS, HWS and WSF. The eddies from FST are present for WSF case in the bottom frame of Fig. 5.5. An upstream shift in the location of the commencement of three-dimensionality is observed, as perturbations are increased progressively from LI to WSF case. The presence of oscillation makes the rolled up vortex more susceptible to transition, and which rapidly breaks down to turbulence, as noted beyond $x = 0.55$ for the cases WS, HWS and WSF. Case LI is more transitional than the other cases under consideration.

In Fig. 5.6, iso-surfaces of spanwise vorticity ($\omega_z = -50$) coloured by wall-normal component of vorticity, ω_y are shown for the test cases given in Table 5.1. For the case LI shown in the top frame, a detached vortical sheet is seen which rolls into a vortical structure, and thereafter, small-scale vortical structures are present. Therefore, this sheet can be viewed as the pre-transitional boundary layer for case LI.

The two predominant spanwise structures shown in the top frame of Fig. 5.5 are not seen here, as these rolls are located below the smooth separated shear layer. For the other three cases in Fig. 5.6, presence of higher fluctuating wall-normal velocity disturbs the smooth separated shear layer noted in LI case. For the same reason, the second spanwise vortical roll loses its coherence for these three cases, and this is noted by uneven leading edge of the separated shear layer for the higher oscillation frequency case. In contrast to the lower oscillation frequency case, HWS, the separated shear layer has a longer streamwise extent, and the spanwise undulations are correspondingly less. For the WSF case, presence of additional rate of strain is noted via the creation of streamwise streaks, referred to as Klebanoff streaks, as noted by Lardeau et al. (2012) and Vadlamani (2015) in their LES on the effect of FST on the separated shear layer in LPTs. These streaks are associated with streamwise vorticity, and whose presence intensifies the vortex stretching mechanism. These streaks induce local perturbations in the flow relative to the mean flow. There is clear evidence of the high speed and low speed longitudinal streaks. As noted previously in Fig. 5.5, there is an upstream shift in the transition point with the introduction of oscillation and FST, seen in cases WS, HWS and WSF.

5.5 Time-Averaged Flow Field

In the previous section, while describing the instantaneous flow field, recirculating regions were observed near the plate, with and without oscillation. This is the result of the imposed adverse pressure gradient which provokes separation of the flow. Thus, it is relevant to investigate whether such signatures are also retained in the time-averaged flow field.

In Fig. 5.7, the outline of the laminar separation bubble is noted by stream-traces drawn in the mid-span plane ($z = 0.06$) for this 3D flow field. Ideally, one defines the vector potential for the 3D flow field (Batchelor, 1988), and the present stream-trace is the spanwise component of it. In the background of the stream-trace, the contours of the streamwise velocity are given for test cases LI, WS, HWS and WSF, described in Table 5.1. In the top frame, a pair of laminar separation bubbles are observed which extend beyond $x = 1$. When the plate is oscillated and FST is imposed at the inlet, the separation bubble's size is significantly reduced. We emphasize again that the features noted in this figure are for the time-averaged field with data averaged over six through-flows, and these are not the instantaneous snapshots. The streamwise extent of the separation region is also reduced for cases WS, HWS and WSF. The most significant reduction ($\approx 33\%$) of size of separation bubble is noted for case WSF, compared to LI case. A secondary separation bubble is noted for cases LI and HWS upstream of the primary bubble. For the other two cases, WS and WSF, the secondary separation bubble is negligibly small. For case LI and HWS, the core of the secondary bubble is closer to the plate as compared to the core of the primary bubble. This was clearly noted in Figs. 5.5 and 5.6. Thus, the imposed adverse pressure gradient creates a separation bubble, whose presence and effects are diminished by the imposed oscillation and FST. From Fig. 5.7, it is noted that the higher frequency oscillation with FST, (WSF case) is the most effective in controlling Kelvin-Helmholtz vortices and would thus improve the performance of the LPT.

In Fig. 5.8, the streamwise variation of skin friction coefficient is shown for the test cases given in Table 5.1, where the skin friction is evaluated as

$$C_f = \frac{\tau_w}{\frac{1}{2}\rho U_\infty^2} \tag{5.1}$$

with τ_w as the wall shear stress and U_∞ is the free-stream velocity.

From the point of view of steady flow, the zero crossings of C_f are inferred as the locations of separation and reattachment. It is also conjectured that the global minimum is the location of transition. However, for an unsteady case, the flow is more resistant to separation, as given by the empirical criterion of zero crossing by Prandtl (Schlichting and Gersten, 2017). Although the present case correspond to unsteady flow, the trend shown in

Fig. 5.8 provides the signature of the primary and secondary bubbles as noted in Fig 5.7. With oscillation and FST, additional disturbance levels are introduced, which significantly alter the flow topology in the form of slightly delayed separation and significant precedence of the location of transition and reattachment. Another observation to be made is that HWS case, with lower reduced frequency and which has more tendency to flutter (Dowell et al. (2004) and Vogt (2005)), has a smaller effect in suppressing the laminar separation bubble. The cumulative effects of FST and blade oscillation in case WSF, do not show a marked disparity from the WS case without FST at inlet, however, it does have an additive effect leading to further suppression of the laminar separation bubble, as shown in Fig. 5.8. A prominent secondary separation bubble is observed for test cases LI and HWS, which is attributed to the local separation of the reverse flow as it approaches the 'dead-air' region, (signified by positive C_f region between $0.5 < x < 0.6$). Increasing the imposed oscillation frequency in cases WS and WSF suppressed the secondary separation bubble, due to lower magnitude of reverse flow. A similar result was noted by Vadlamani (2015) and Sengupta et al. (2017) with the introduction of roughness on the blade surface.

In Fig. 5.9, the rms u-velocity contours are shown for the test cases, given in Table 5.1. The wall-normal location for the peak value shifts closer to the wall, with the introduction of oscillation in the cases HWS, WS and WSF. This effect is more prominent at higher reduced frequency, in cases WS and WSF, and the lowest wall-normal location is noted for the WSF case with FST at inlet. Also, the intermittent streaks induced by FST increases the rms fluctuations, noted in the bottom frame, as compared to the cases without FST. Presence of the Klebanoff streaks introduces streamwise vortices and induces peak-valley structure in the flow field by inducing local high and low velocity perturbations, which in turn increases fluctuating component of velocities, as seen in Fig. 5.6. An upstream shift in the peak location is noted with higher reduced frequency. Thus, the reduced frequency has an effect on the separated boundary layer which is similar to the effect surface roughness has. Both blade vibration and surface roughness promote near-wall mixing, which was observed for roughness by Vadlamani (2015) and Sengupta et al. (2017).

Another way of looking at the fluctuating components of the flow is by studying the evolution of turbulent kinetic energy (TKE). This is also a key step in proposing any modifications for turbulence modelling. The transport equation for the turbulent kinetic energy is given by

$$\frac{\partial k}{\partial t} + C = P - \varepsilon + PD + TD + VD \tag{5.2}$$

where:

$$C = U_j \frac{\partial k}{\partial x_j},\ P = -\overline{u_i' u_j'} \frac{\partial U_i}{\partial x_j},\ \varepsilon = \nu \left\langle \frac{\partial u_i'}{\partial x_j} \left(\frac{\partial u_i'}{\partial x_j} + \frac{\partial u_j'}{\partial x_i} \right) \right\rangle$$

$$TD = \frac{\partial}{\partial x_i} \left(0.5 \left\langle u_i' u_j' u_j' \right\rangle \right),\ PD = \frac{\partial}{\partial x_i} \left(\left\langle p' u_i' \right\rangle \right),\ VD = \frac{\partial}{\partial x_i} \left(-\nu \frac{\partial k}{\partial x_j} \right)$$

P, ε, C, PD, TD and VD are the turbulent production, dissipation, convection, pressure diffusion, turbulent diffusion and viscous diffusion, respectively. The net diffusion involves an interchange between pressure diffusion, turbulent diffusion and viscous diffusion.

In Fig. 5.10, the TKE budget is shown by the contour plots for the production term for test cases LI, WS, HWS and WSF. Similar to the streamwise rms contours, the wall-normal location of the peak production value shifts closer to the wall with increase in reduced frequency. An upstream shift in the streamwise location of the peak positions is also noted progressively from LI to HWS to WS to WSF. Additionally, for HWS case, at $x = 0.55$ a new peak in the production is observed close to the wall, which can be attributed to the secondary separation bubble and the associated separation of reversed flow. This is indicative of the emergence of near wall turbulence, which possesses both the characteristics of a free shear flow and a newly formed turbulent layer. A similar new peak was observed by Alam and Sandham (2000) in their DNS of a laminar separation bubble. The convection contribution to TKE are shown by the contours in Fig. 5.11 from which it is evident that production is predominantly counter-balanced by convection in providing the TKE budget.

In Fig. 5.12, the profiles of TKE production term for the cases LI, WS, HWS and WSF are extracted at $x = 0.55$. As compared to case LI, the peak production value is significantly higher for cases with oscillation, WS, HWS and WSF. As a consequence the wall-normal location of the peak value also has a tendency to shift towards the wall, with higher reduced frequency and addition of FST. The maximum TKE production is noted for WSF case. For the HWS case, as noted previously in the production contours of Fig. 5.10, a new production peak is noted at $y = 0.003$. This is attributed to the effects of secondary bubble. This once again shows that there is an analogy between reduced frequency of oscillation and roughness, with respect to the wall-normal shift of peak position.

5.6 Calculating the Time Period

The time period of flow in test cases WS, HWS and WSF is evaluated by collecting data over 20 time periods of imposed oscillation at six varying streamwise and wall-normal locations

on the transitional boundary layer, as shown in Fig. 5.13.

The fast Fourier transform (FFT) of these time series, stored at the six locations (shown in Fig. 5.13), is performed for the test cases WS, HWS and WSF to determine the predominant time scales in the flow and its dependence on oscillation and frequency and FST. In Fig. 5.14, the FFT of the streamwise velocity fluctuations is plotted against the frequency of the probe data for the WS case. For this case, the frequency of imposed oscillation is 12.91Hz, whereas the frequency determined from the FFT in Fig. 5.14 is 13.56Hz for points A, C, D, E and F. The point B coincides with the exact location of zero time-averaged C_f and thus, the time series retains zero velocity components, as this turns out to be also a half-saddle point (Telionis (1981) and Tobak and Peake (1982)). In Fig. 5.15, the corresponding FFT of u-velocity fluctuations versus frequency plot is shown for test case HWS at the six locations identified in Fig. 5.13. Apart from the half-saddle point B, the other points show a peak value at frequency, 6.84 Hz, while the frequency of imposed oscillation is 6.45Hz. Thus the system responds within reasonable limits of the imposed frequency. For case WSF, FFT plots are shown in Fig. 5.16, one has an additional source of disturbance in the form of FST at the inlet. In this figure, at points C and F, which are located near the commencement of the thin boundary layer and at the centre of the hump created at the edge of the boundary layer as seen in Fig. 5.13, the maximum peak is not associated with the imposed frequency of 12.91 Hz. This can be explained by the observation that points C and F are influenced by the FST imposed. Point F is located outside the separated shear layer and is dominated by mean flow, which is reflected by zero frequency component of the spectrum. Point C, which is near the thin leading edge is an ideal location for penetration of low frequency component of FST. Thus the flow dynamics is not only determined by the blade vibrations at these points, but also due to the FST.

To understand the variation of the frequency of the probed data from the frequency of imposed oscillation, for the cases WS and HWS, the ratio of the frequency obtained from the solution to the frequency imposed, as given by Eq. (3.46), is plotted against multiple time periods of imposed oscillation in Fig. 5.17. It is observed that the frequency obtained from the solution is equal to the imposed frequency, when an integer number of the time periods of oscillation is considered. This suggests that the frequency obtained from the solution exactly corresponds to the imposed frequency. Thus, the flow surrounding the blade shows a perfectly linear response to the imposed frequency of blade vibration in the absence of added FST.

5.7 Phase-Averaged Flow Field

Having noted the predominant time scale in Figs. 5.14 to 5.16, the next logical step is to study the phase-averaged flow field for a selected blade oscillation without the cumulative effect of FST. Phase-averaged statistics for the flow are gathered during five cycles of oscillation. Each period t_o from Table 5.1 is divided into 64 intervals. The phase ϕ is defined by $\phi = t/t_o - n$ where n is an integer such that $0 \leq \phi \leq 1$.

In Fig. 5.18, a series of profiles of streamwise velocity, for the test case WS, are shown at various locations in and around the time-averaged separation bubble to study the recirculating flow. The magnitude of the reverse flow at $x = 0.52$ is found to increase from $0.15U_\infty$ at $\phi = 40/64$ (top left) to $0.3U_\infty$ for $\phi = 47/64$ (bottom right). With increasing phase, the profile of u-velocity shifts closer to the wall with two inflection points noted. This is due to a change in the centre of the recirculation zone. It is also of interest that the profile at $x = 0.50$, which shows a marked reverse flow for $\phi = 40/64$, however, by $\phi = 47/64$, the reverse flow is almost negligible. This observation seems to agree with the unsteady nature of separation observed for the instantaneous flow field, which occurs on the suction surface of a LPT blade due to adverse pressure gradient. The events described in Fig. 5.18 is for $1/8^{th}$ of the cycle of imposed oscillation. This is one of the most eventful periods within the phase-averaged cycle.

In Fig. 5.19, contours of the fluctuating kinetic energy, k in Eq. (5.2), are shown at four different phases for test case WS spanning the complete phase cycle. At the beginning ($\phi = 0$), the maximum of k is noted at a wall-normal location of $y = 0.03$ and a streamwise location of $x = 0.55$. There is a second zone of maximum fluctuation at $x = 0.75$, and these are mostly noted near the edge of the unsteady boundary layer. In the next frame ($\phi = 0.25$), these energetic zones in the outer layer are seen to connect together. The role of the second energetic zone diminishes as time increases during the cycle, which is seen to be at its peak at the beginning at $\phi = 0$. We note that the fluctuating kinetic energy contributes to the variation of total mechanical energy, which is discussed next.

5.8 Disturbance Flow Mechanisms explained through DME and DETE

Evolution of disturbance which leads to formation of coherent vortical structures is at the heart of the transition process. In the literature, vortex identification schemes such as λ_2-

and Q-criterion, are widely used for detecting such structures in terms of the velocity stress gradient and as a consequence the pressure minima (Holmén, 2012) as shown in chapter 2.

Earlier, we have described two methods for tracing the disturbance field in chapter 2, the detailed derivations of which are provided in appendix A for the DME method and in appendix B for the DETE method. The DME equation has a source of instability appearing as a negative right hand side of the equation, whereas a positive right hand side of the equation is considered a sink of instability. The simultaneous presence of such sources and sinks give rise to secondary flows, leading to enhanced unsteadiness in the disturbance field. As explained in chapter 2, this equation does not have contributions coming from unsteady and viscous terms. It is important to note that to compute the disturbance field mechanisms via DME and DETE, an appropriate equilibrium flow is essential. For flows with adverse pressure gradient, obtaining an equilibrium flow is not a simple task. Even when a similarity profile is obtained as the equilibrium flow numerically, it is not always possible to obtain the same flow experimentally. In the results reported here, the effects of perturbations in the form of blade vibrations (cases HWS and WS) and FST (case WSF) are studied by considering the test case LI with laminar inflow as the equilibrium flow.

In Fig. 5.20, the iso-surfaces of the right hand side of the DME equation for the test cases WS, HWS and WSF of Table 5.1 are shown. The iso-surface value has been chosen on the basis of the statistical correlation previously described in chapter 4, by chosing the iso-surface of $\omega_z = -50$, shown in Fig. 5.6, as the reference value. Here, the right hand side has the physical implication of variations of total mechanical energy comprising of fluctuating pressure and the fluctuating kinetic energy. The equilibrium flow for the study of instability is as given by test case LI. However, the coherent structures observed are distinctly different from those observed by Q-criterion in Fig. 5.5, which can be attributed to the additional effect of the fluctuating kinetic energy shown in Fig. 5.19 such that $\nabla^2 E_d = 2Q + \nabla^2[\frac{1}{2}(V^2 - V_m^2)]$. Since DME accounts for the Q-criterion along with a velocity head, it not only is able to detect vortical motions (similar to Q-criterion), but also is able to detect streak-like instabilities due to the velocity head. For the case WS, coherent hairpin vortices are observed which interact with the Kelvin-Helmholtz vortices and break down to three-dimensional structures. Additionally, the shed spanwise vortex shows waviness in the spanwise direction compared to the 2D nature of the shed vortex in LI case of Fig. 5.5. DME emphasizes stronger three-dimensionality as compared to Q-criterion. The structures have evolved from the nascent disturbance field observable in the upstream part of frame WS. In the other two cases shown in Fig. 5.20, a similar enhanced three-dimensionality, the hairpin vortices and their interactions are observed. The effect of eddies due to FST are more pronounced for frame WSF, when compared with the corresponding frame for Q-criterion in Fig. 5.5. As the DME

equation does not have any contribution from viscous terms, the visible structures do not show the small-scale structures. Additionally, DME is a direct evolution from the rotational form of NSE (as seen in appendix A) and shows more direct correspondence with the vorticity field in Fig. 5.6 and hence is more effective in capturing the Klebanoff streaks for WSF case, whereas Q-criterion is based on the velocity gradient calculations and is used for vortex detection only.

The second method is based on disturbance enstrophy which helps explain the creation and growth of rotationality in the flow. The DETE is described briefly in chapter 2, given in Eq. (2.9), with the condition for instability provided by Eq. (2.10). The detailed derivation of this equation is provided in appendix B.

The first, second and third set of terms in Eq. (2.9) are the respective contributions from vortex stretching, diffusion and dissipation of the enstrophy transport equation. The vortex stretching term is absent for 2D flows and plays a major role in 3D flows. Here, an attempt to understand the contributions arising from the various constituent terms of DETE are provided for the test case WS in Figs. 5.21 and 5.22 for Ω_d taking negative and positive values respectively. As Ω_d can be of either sign, it is not necessary to consider it analogous to dissipation as it is done with enstrophy, Ω_1 (Pope, 2000).

In Fig. 5.21, the terms comprising the growth rate of disturbance enstrophy, namely, the vortex stretching term (term 1 of Eq. (2.9)), the term due to diffusion (term 2 of Eq. (2.9)) and the term due to dissipation (term 3 of Eq. (2.9)) are shown at the same instantaneous time. From the condition for instability given by Eq. (2.10), here, the instability structures associated with negative Ω_d are shown for three different iso-contour levels. Here, for diffusion, dissipation and DETE, it is observed that there is a small but net contribution from the upstream part of the flow before separation. This is indicated by the near-wall strip ($x < 0.4$). However, the order of magnitude of each term, when compared with its counterpart for positive Ω_d, shows it to be lower. This information is provided only by the DETE, wherein classification of instabilities into positive/negative Ω_d can be carried out. It is also pertinent to understand which sign of Ω_d originates from the inviscid/viscous and separated/unseparated part of the flow.

In Fig. 5.22, the corresponding terms from DETE are shown for instabilities with positive Ω_d. The vortex stretching term, shown in the top frame, is an order of magnitude higher than the diffusion term, and two orders of magnitude higher than the dissipation term. The total of these terms provided in the last frame, shows a strong correlation with the structures identified as being due to the vortex stretching term. An important observation to be made here is that, the vortex stretching term (and hence DETE) gains relevance only after flow

separation, for positive Ω_d instabilities. The contribution from dissipation is insignificant in comparison to the other two terms. The most significant contributions from the vortex stretching term, indicated by the blue (dark) contours arise and propagate near the wall. For the test case, WS shown in Figs. 5.21 and 5.22, where a wall excitation in the form of blade vibration is imposed on the flow, the contributions from positive Ω_d are significantly higher than for negative Ω_d. Overall, the instability has more large scale structures with positive Ω_d than small scale viscous structures with negative Ω_d. Also, the instability is driven mostly by stretching and diffusion term, though dissipation term also surprisingly contributes to the instability for the both of the signs of Ω_d. For an instability with negative Ω_d, the dissipation term has a higher contribution to the growth of the instability, whereas for the positive Ω_d instabilities, the diffusion term has precedence over the dissipation term.

In Fig. 5.23, iso-surfaces of positive and negative growth rate of disturbance enstrophy, $|\frac{D\Omega_d}{Dt}|$ are shown for the test cases WS, HWS and WSF, with the equilibrium solution taken as the test case LI. The iso-surface values have been chosen by taking the $\omega_z = -50$ iso-surface shown in Fig. 5.6 as the reference and following the method of statistical correlation shown in chapter 4. The structures identified by DETE vary from those identified by DME in Fig. 5.20, which can be attributed to the absence of unsteady and viscous terms in the equation for DME. DETE is a reasonable representation of the flow operating across all scales present in the solution of NSE, as it is obtained without making any assumptions. In WS case, positive and negative streamwise streaks are observed which were not discernible by Q-criterion, as it is used for detecting only vortical structures. The DETE method is capable of discerning structures in the evolving vorticity field shown in Fig. 5.6. For HWS case, the flow undergoes transition by the evolution of $\Lambda-$vortices. Looking at the $\Lambda-$vortices, the flow is identified as a combination of K- and H-type transitions, noted in transition experiments for wall excitation on a flat plate geometry by Bhaumik and Sengupta (2015). For the WSF case, simultaneous presence of FST and high frequency oscillations causes near wall structures whose sign is also detectable by this method unlike any other methods. The large scale structures in the free-stream are detected in regions of positive growth rate and disturbance enstrophy whereas, the near-wall viscous structures have negative growth rates and disturbance enstrophy.

5.9 Conclusions

The individual and coupled effects of incoming free-stream turbulence and aeroelastic blade oscillations on the separation of the suction surface boundary layer over a flat plate is numerically investigated. Four different direct numerical simulations have been performed for distinguishing between the individual and cumulative effects of the imposed disturbance

fields and to establish the mean flow required for all disturbance calculations. The upper wall of the test section is specifically contoured to simulate the pressure gradient on the suction surface of a 'ultra high-lift' low pressure turbine (LPT) blade. The oscillation on the blade surface is imposed by a sinusoidal wall-normal perturbation and parameters have been chosen to simulate blade flutter in real LPT blades. An effort has been made to study the response of the system to varying frequencies of blade oscillation and a relationship is established between the reduced frequency and the profile loss attributed to the separation bubble on the suction surface. The FST at the inlet is prescribed with a synthetic turbulence box which uses the modified von Kàrmàn spectrum to generate the correlated perturbation field.

The results show the evidence of enhanced spanwise undulations in the separated shear layer in the presence of blade oscillations when compared with the baseline laminar inflow. The destabilization of the shear layer by the spanwise waviness is found to be an increasing function of the reduced frequency. The introduction of free-stream turbulence significantly altered the bypass transition mechanism by propagation of unsteady, intermittent Klebanoff streaks along the span. It is found that free-stream turbulence has a cumulative effect on the boundary layer in suppressing the separation bubble, when compared to the corresponding isolated oscillation case. Both free-stream turbulence and blade oscillation promoted near-wall mixing. This resulted in the upstream shift of the transition point and a significant reduction in the size of the separation bubble. The combined effect of free-stream turbulence and blade oscillations further reduced the size of separation bubble. The secondary separation bubble observed in the unperturbed flow was reduced with the presence of blade oscillation. The effect was more pronounced at higher reduced frequencies while the flow with free-stream turbulence as an added perturbation was most effective in bringing down the secondary separation bubble size. The net effect of mixing was to shift the inflection point of the velocity profile towards the wall. The system was found to exhibit a linear response to the imposed frequency of blade oscillation through time period and phase averaged calculations. This was altered in the case where free-stream turbulence introduces another time scale in the form of unsteady fluctuations of the velocity profile. The budgets of turbulent kinetic energy showed that the production term largely dominates with higher level of disturbance in the separated shear layer. The largest production values were found for the highest perturbation level of the free-stream turbulence and blade oscillation. The structures identified by various coherent structure detection methods are compared and the source of the instability is traced back. Smoother structures are noted for Q-criterion and disturbance mechanical energy, whereas the additional structures observed through the disturbance enstrophy transport equation are the small-scale structures arising due to unsteady and viscous terms of the Navier-Stokes

equation. The structures indicate a smaller extent of reversed flow with added disturbance, with the least seen with the cumulative effect of free-stream turbulence and blade oscillations. The budget of the disturbance enstrophy provided insight into the regions of flow where three-dimensionality indicated by the presence of the vortex stretching term, becomes prominent. The most significant contributions were found downstream of the separation region and in regions near the wall. The large scale structures in the free-stream are detected in regions of positive growth rate and disturbance enstrophy whereas, the near-wall viscous structures have negative growth rates and disturbance enstrophy.

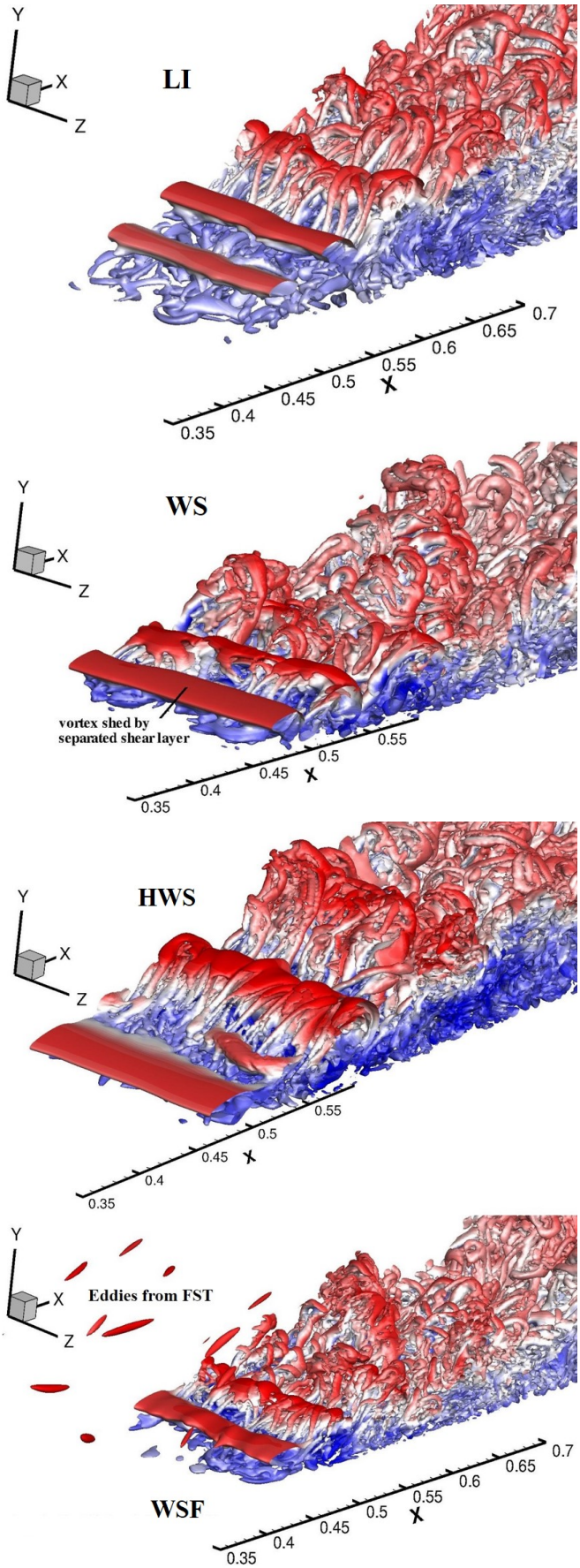

Fig. 5.5 Iso-surfaces of Q criterion (Q = 40) contoured with streamwise velocity for test cases LI, WS, HWS & WSF.

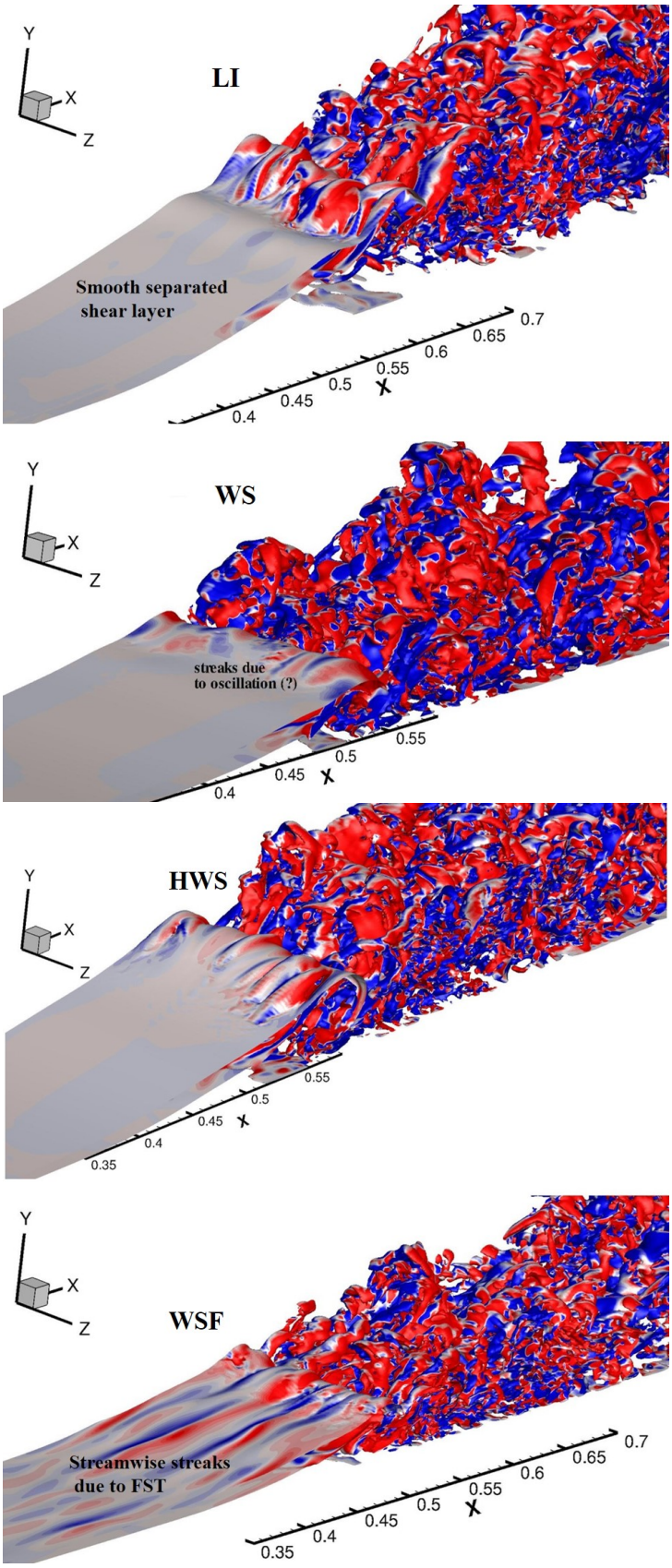

Fig. 5.6 Iso-surfaces of spanwise vorticity (ω_z = -50) contoured with y-vorticity for test cases LI, WS, HWS & WSF.

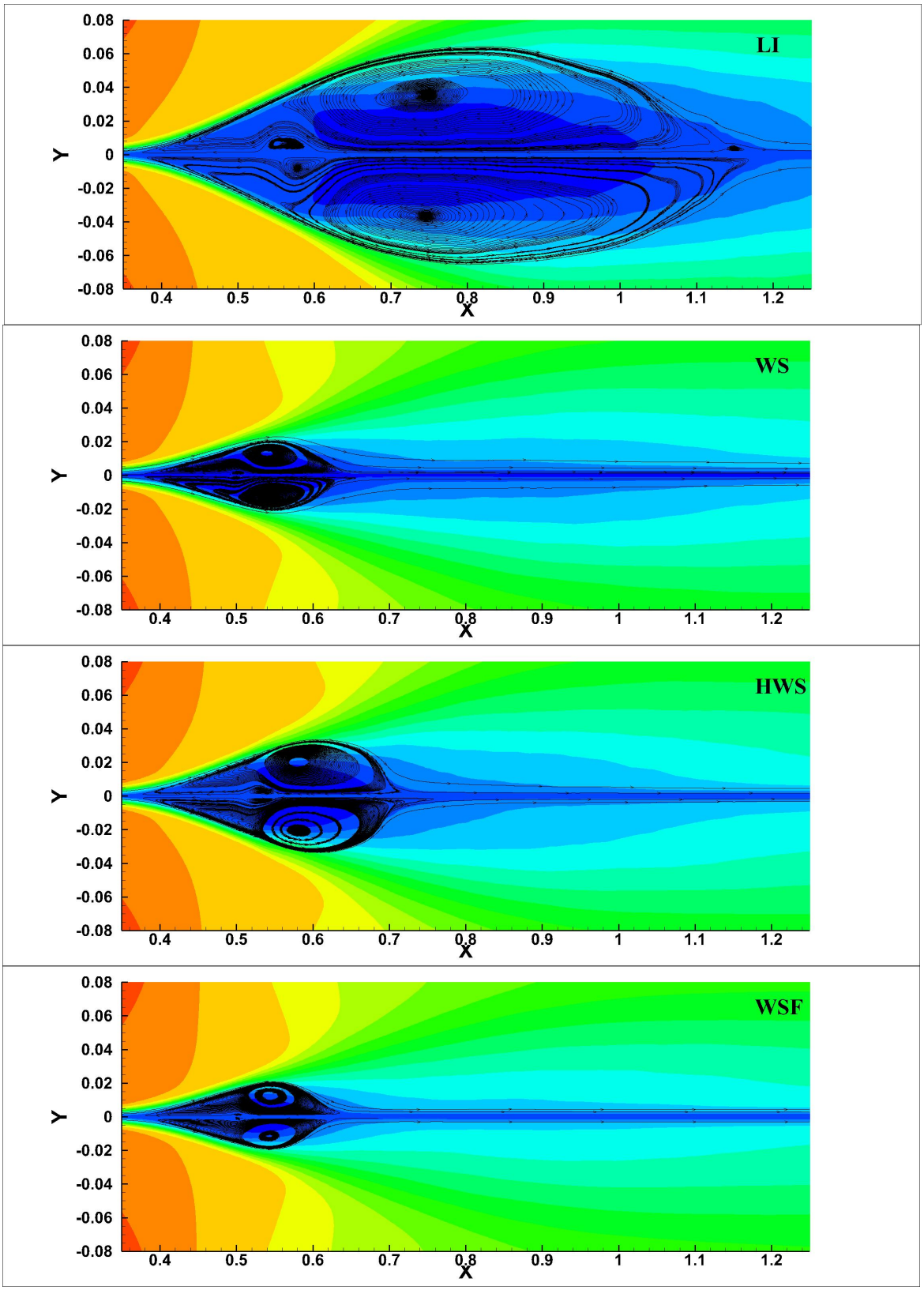

Fig. 5.7 Laminar separation bubble shown by streamlines in u-velocity contours for test cases LI, WS, HWS and WSF.

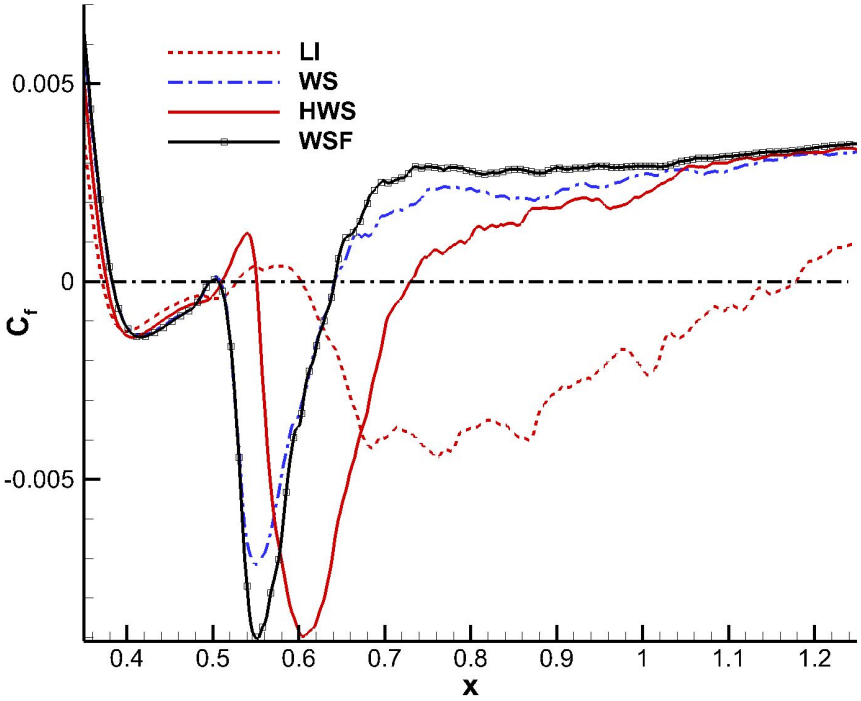

Fig. 5.8 Skin friction lines extracted at $y = 0.0018$ for test cases LI, WS, HWS and WSF showing the separation, transition and reattachment points in the flow.

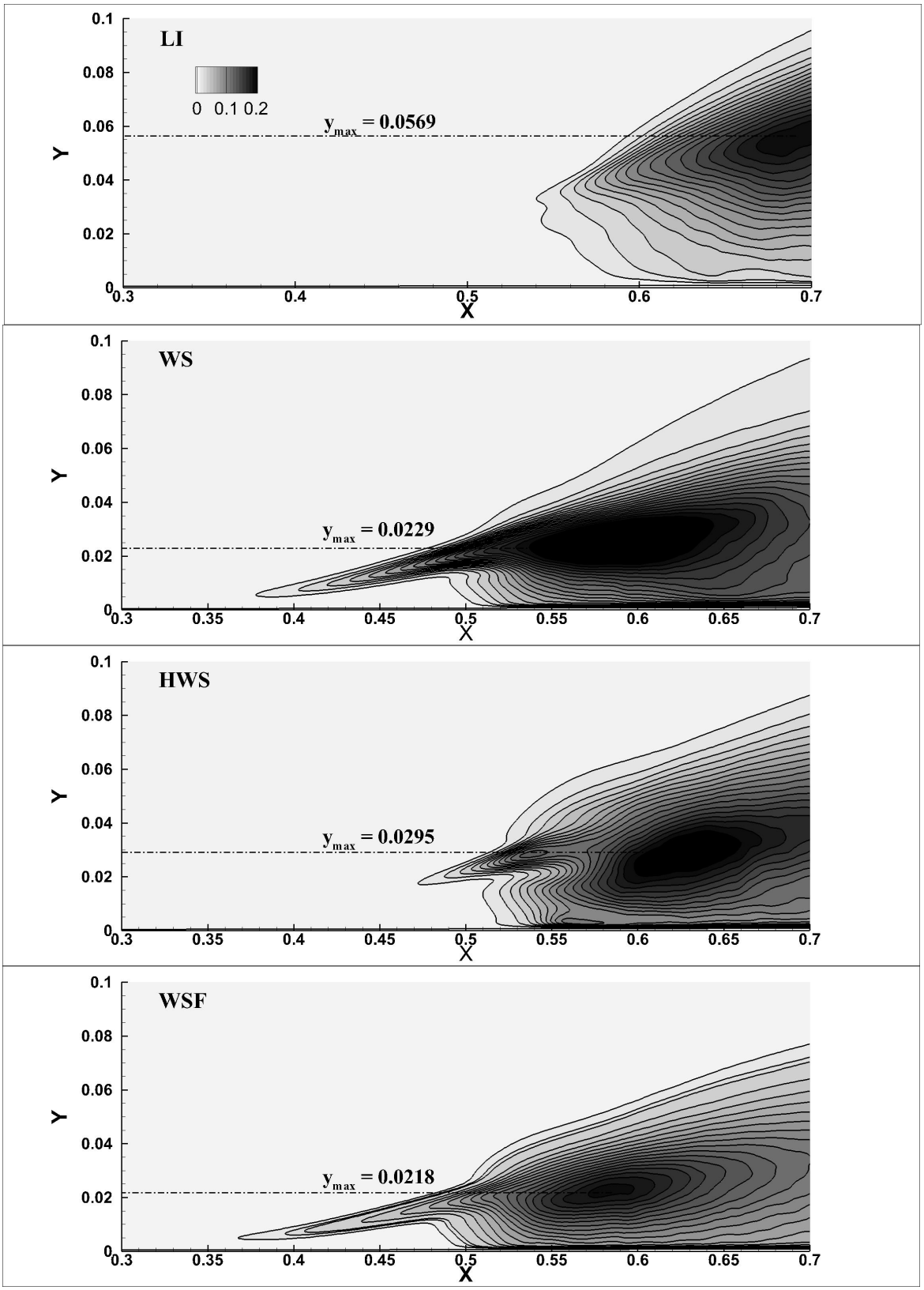

Fig. 5.9 Root mean square u-velocity contours for test cases LI, WS, HWS and WSF showing the wall normal location of the peak value.

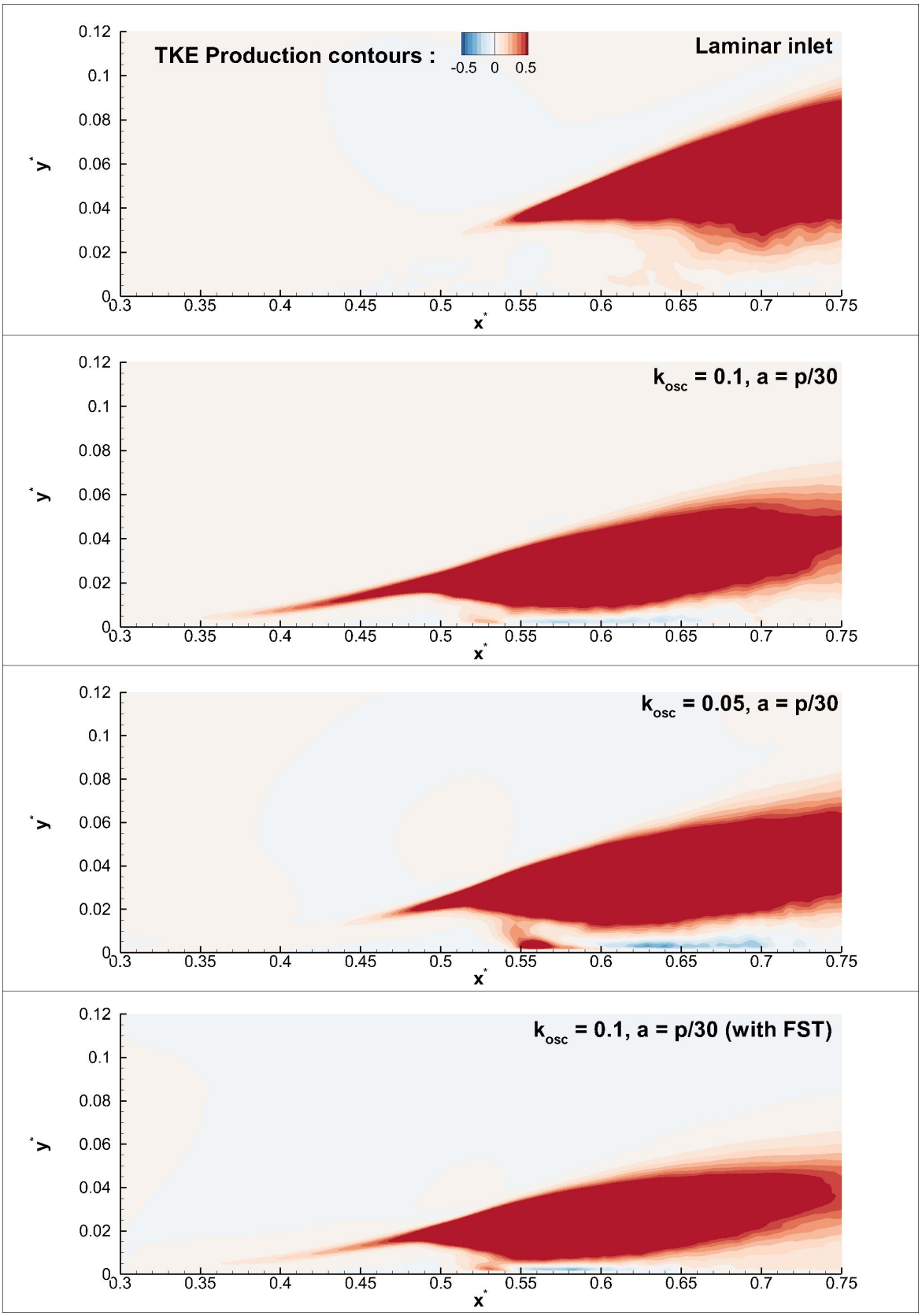

Fig. 5.10 TKE production contours for test cases LI, WS, HWS and WSF.

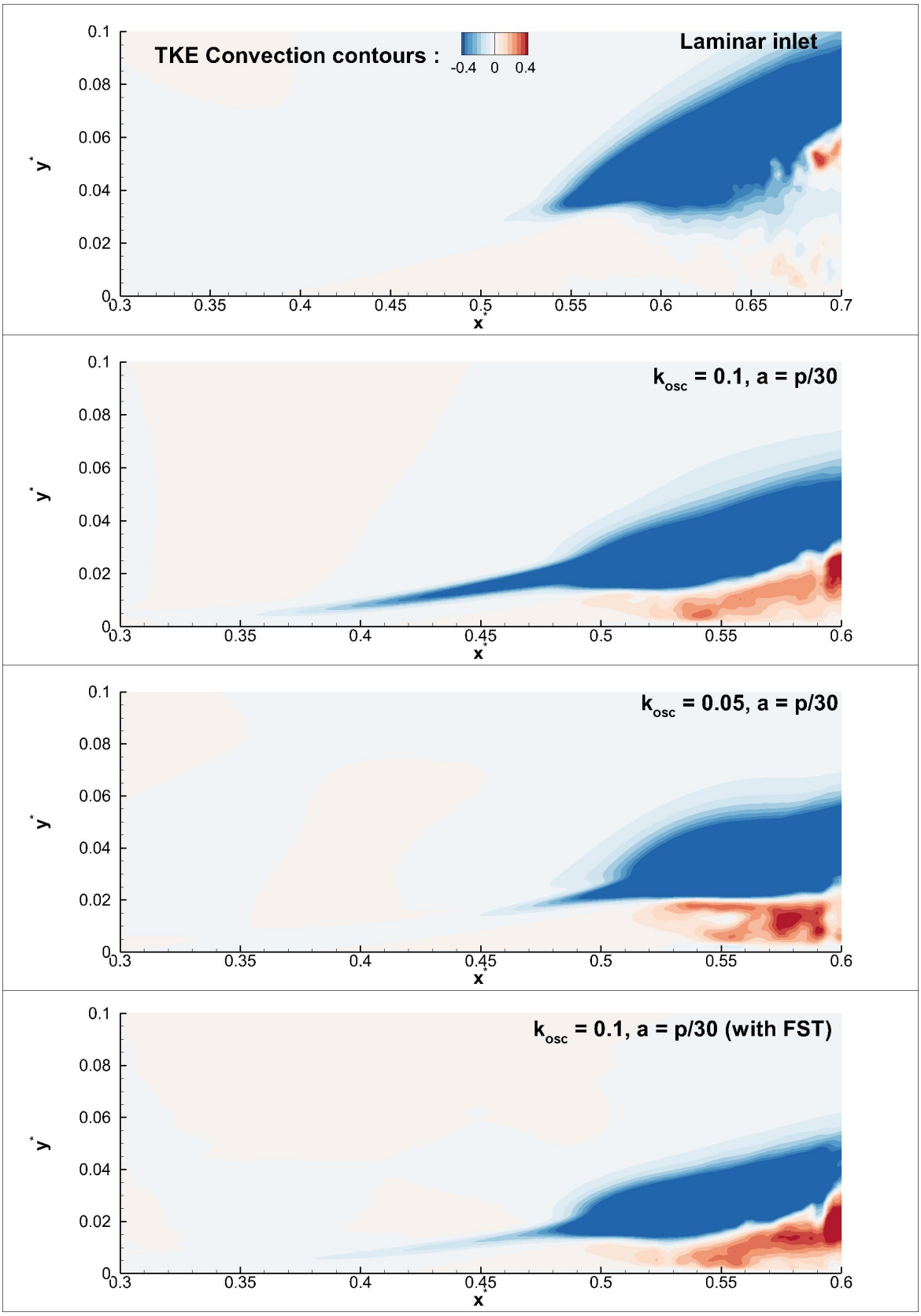

Fig. 5.11 TKE convection contours for test cases LI, WS, HWS and WSF.

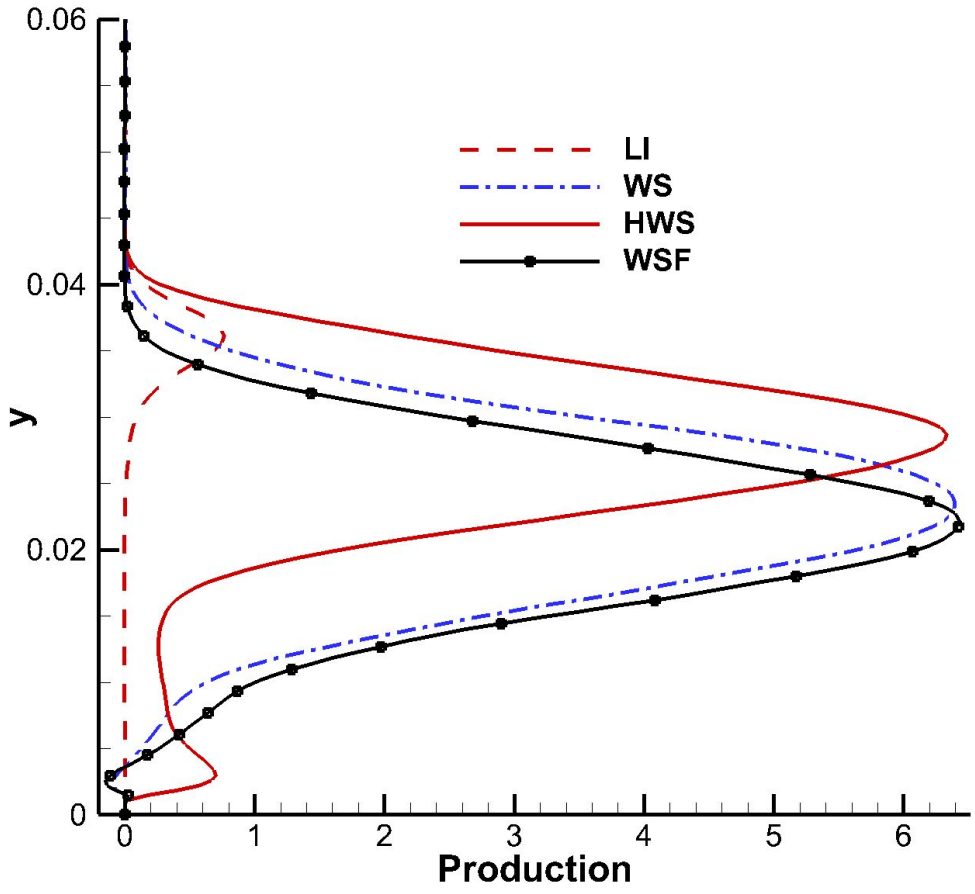

Fig. 5.12 TKE production extracted at $x = 0.55$ for test cases LI, WS, HWS and WSF.

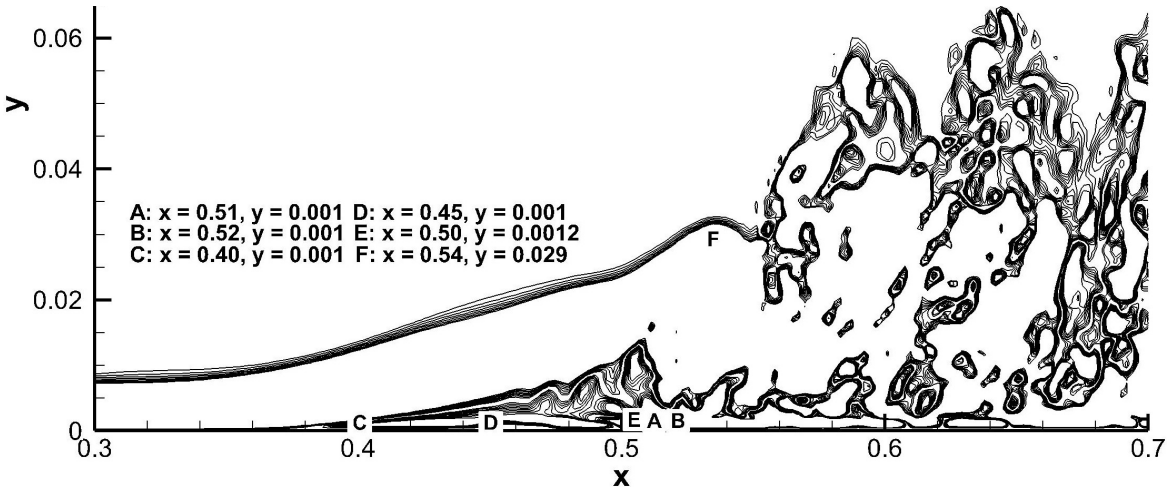

Fig. 5.13 Locations for storage of probe data for calculation of time period of flow for test cases WS, HWS and WSF.

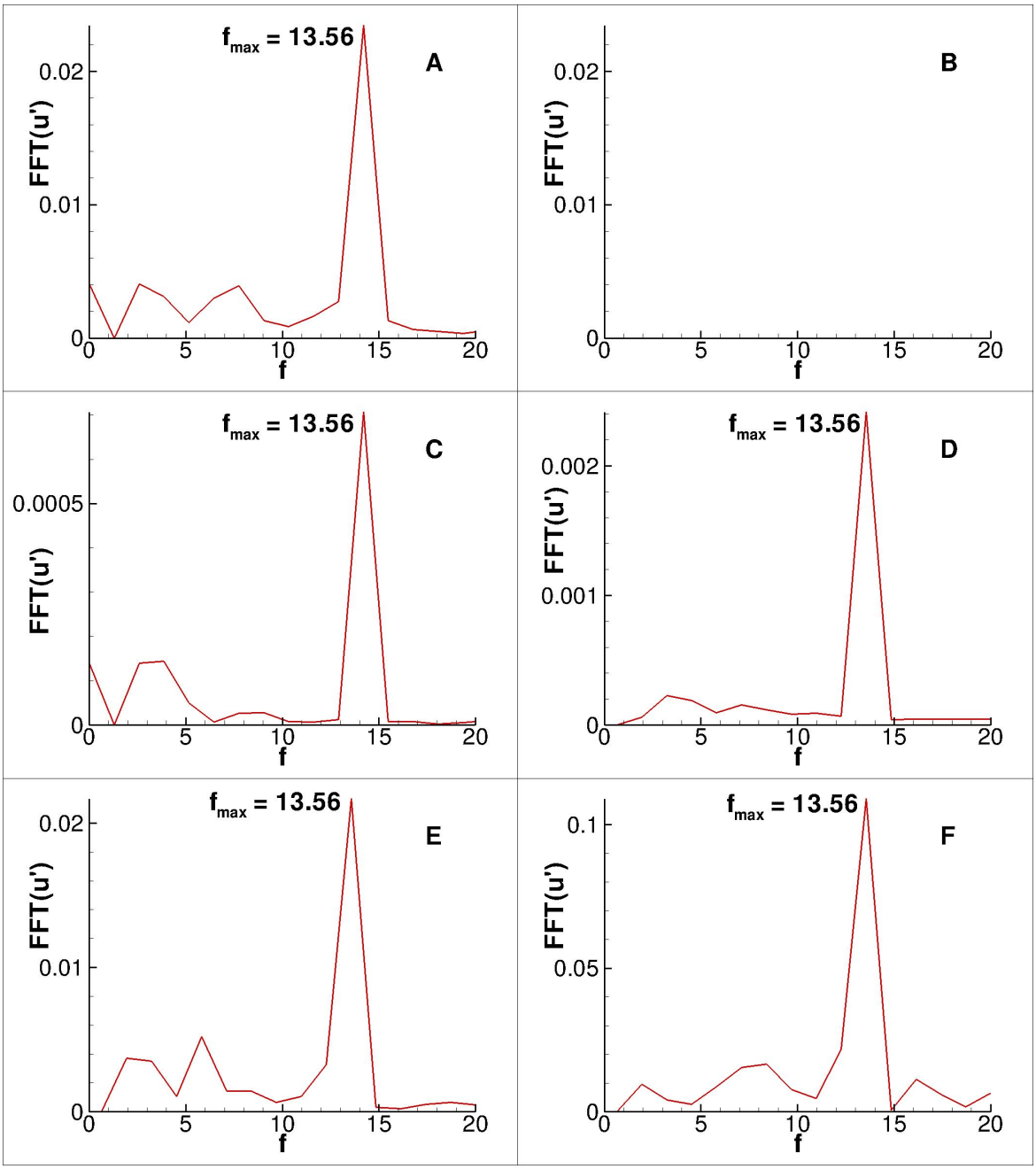

Fig. 5.14 FFT of u-velocity fluctuations plotted against frequency for test case WS at six locations shown in Fig. 5.13.

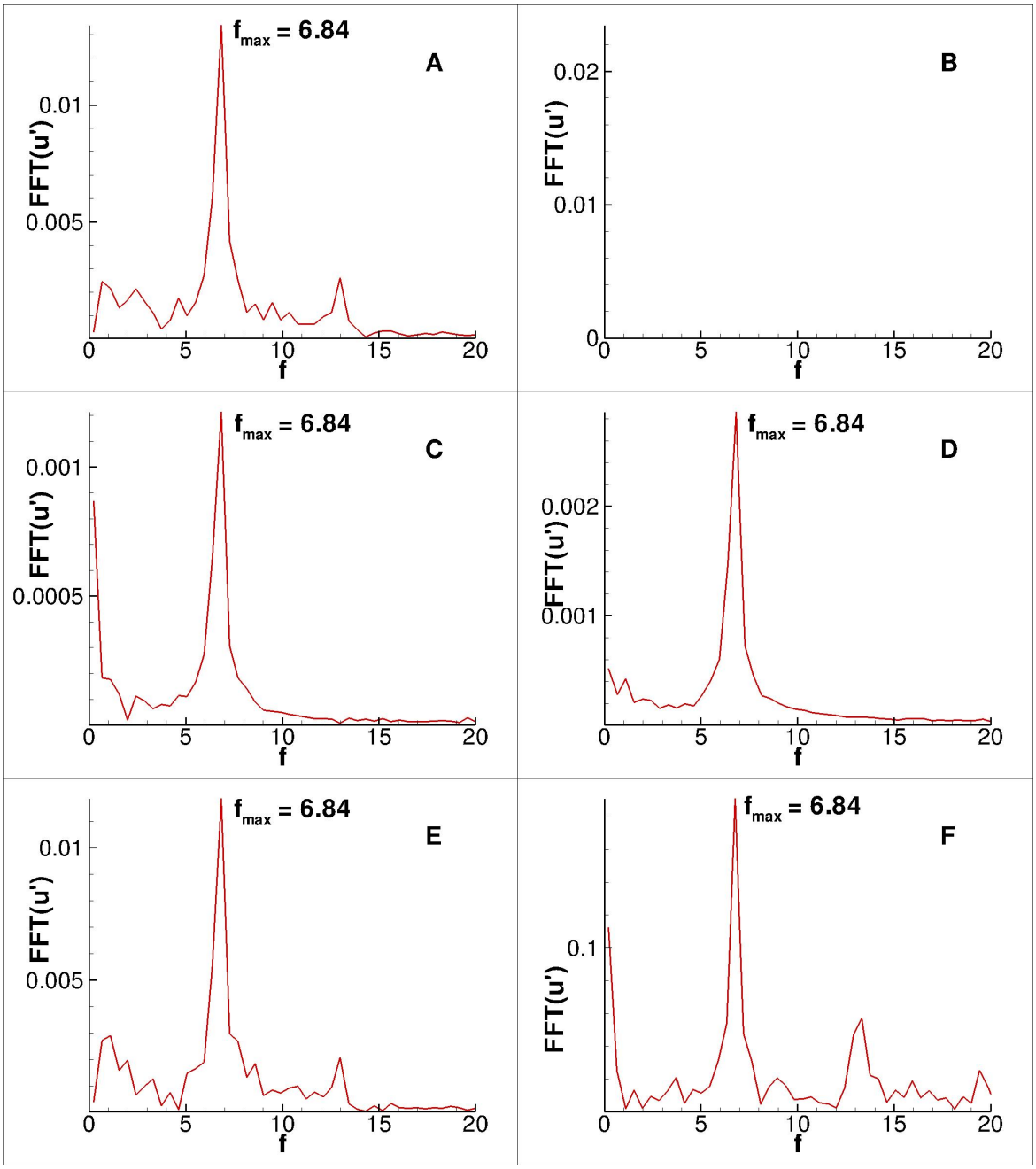

Fig. 5.15 FFT of u-velocity fluctuations plotted against frequency for test case HWS at six locations shown in Fig. 5.13.

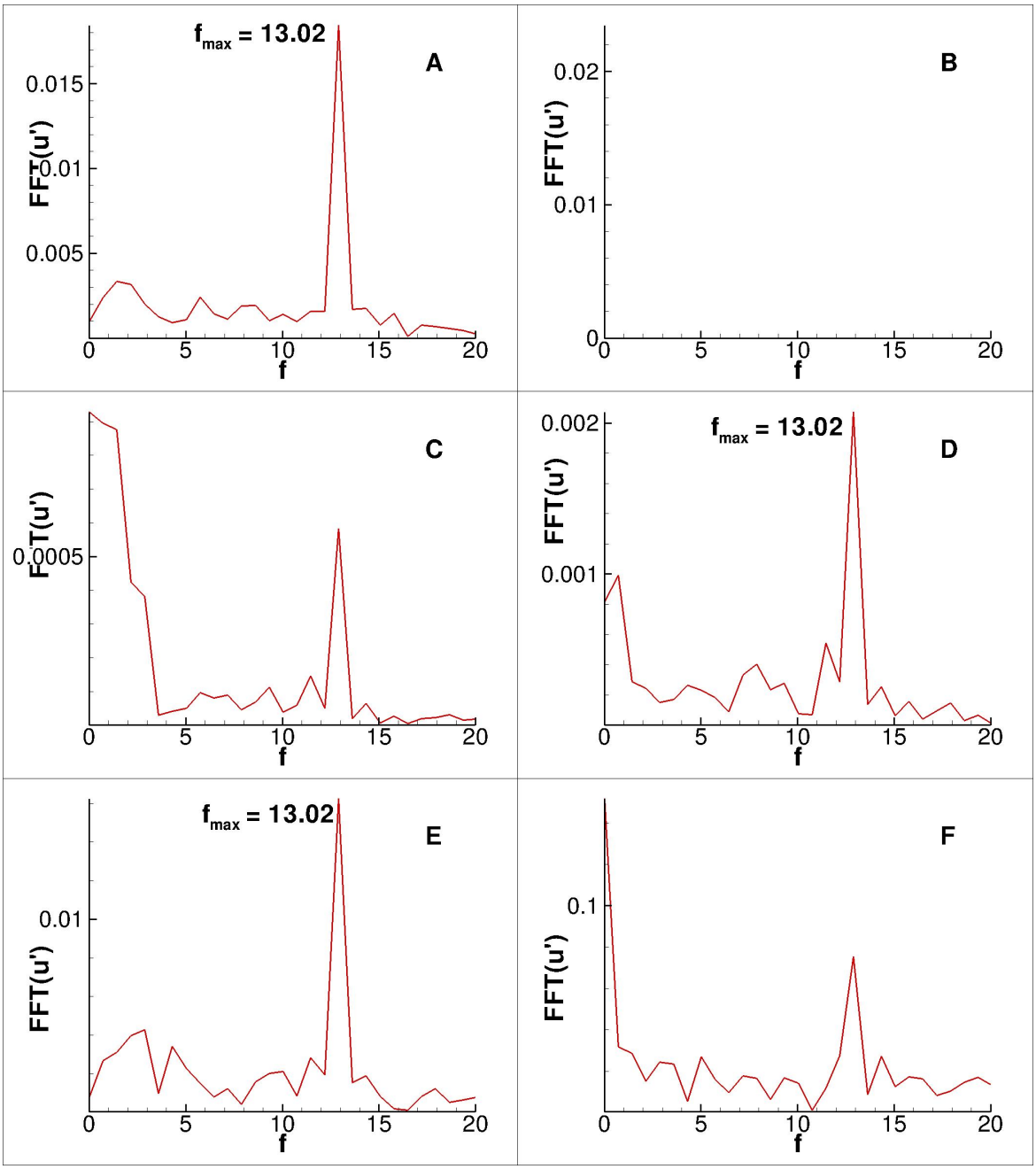

Fig. 5.16 FFT of u-velocity fluctuations plotted against frequency for test case WSF at six locations shown in Fig. 5.13.

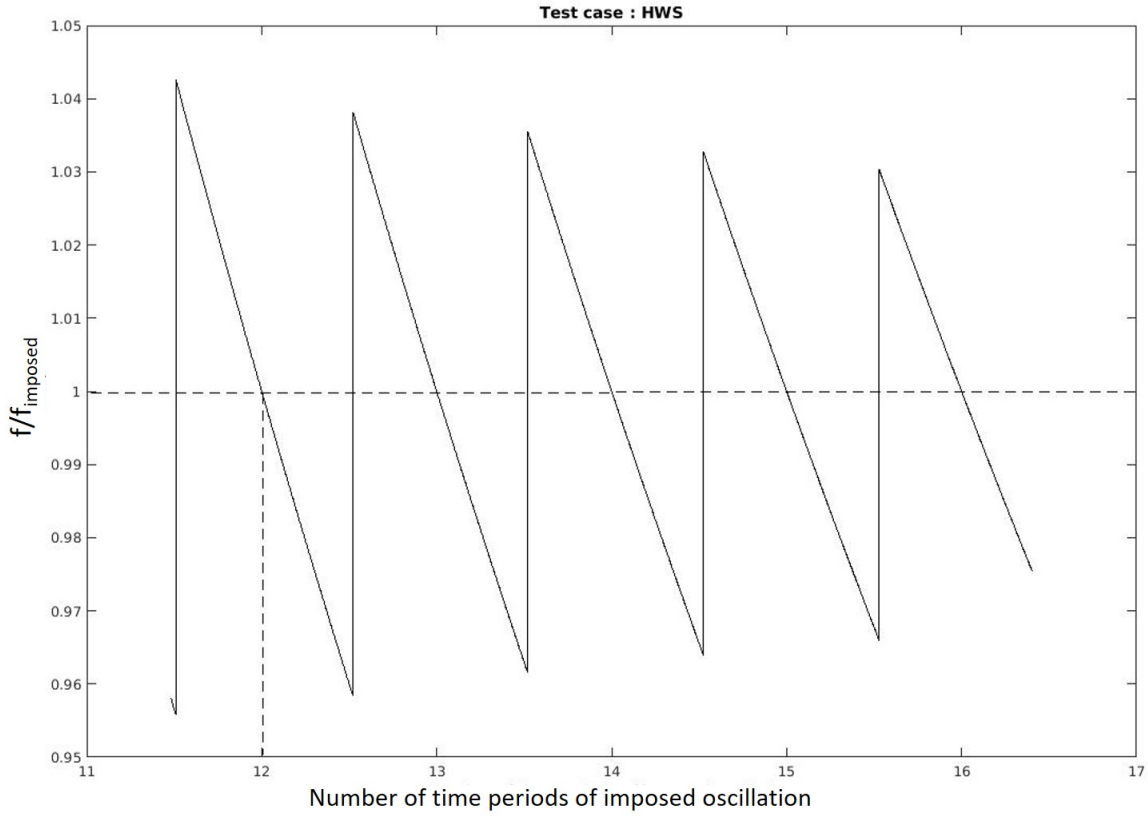

Fig. 5.17 Ratio of frequency of time series stored to frequency of imposed oscillation, plotted against the number of time periods of imposed oscillation for case HWS.

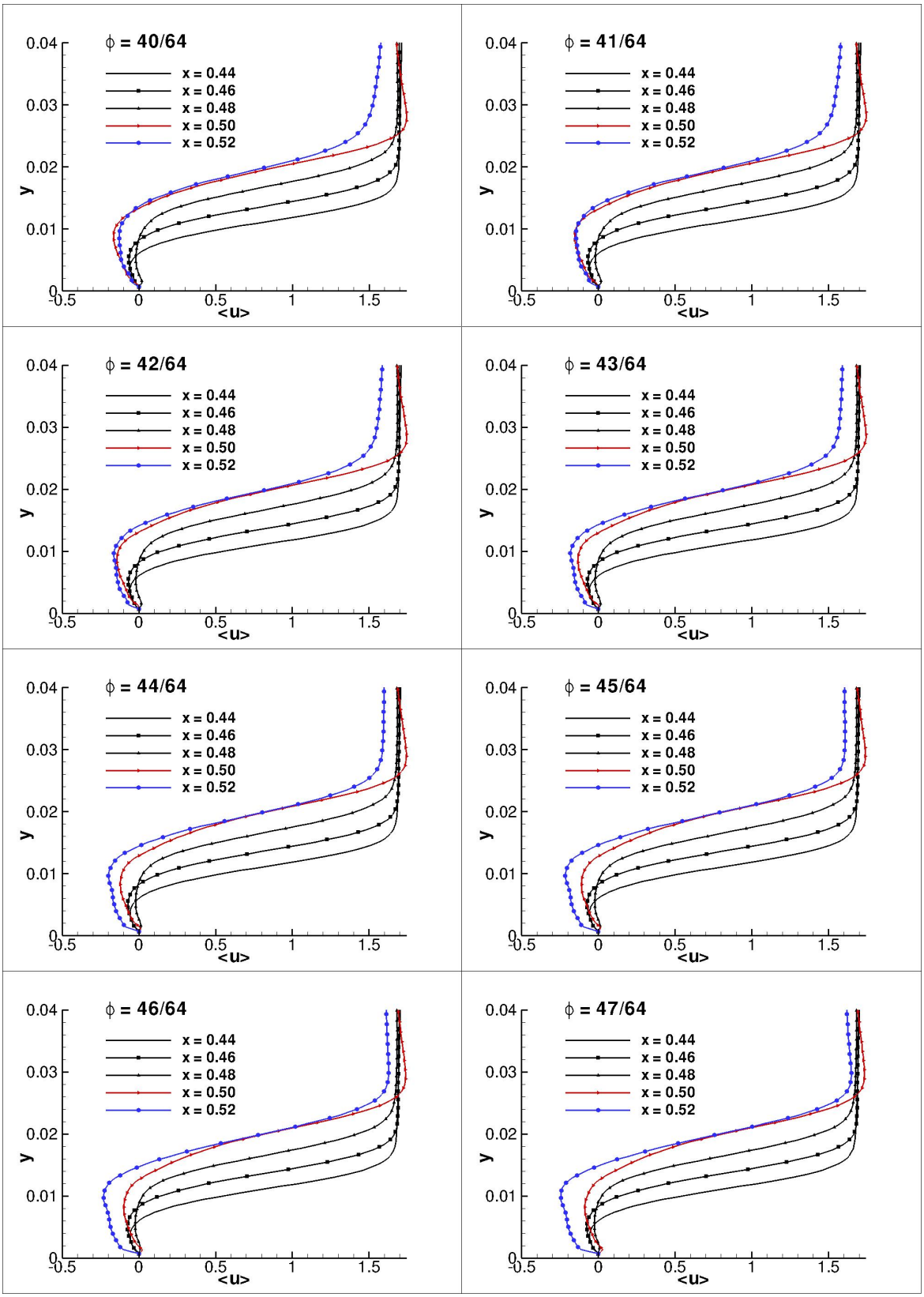

Fig. 5.18 Profiles of phase-averaged u-velocity at various locations in the proximity of the separation region for test case WS.

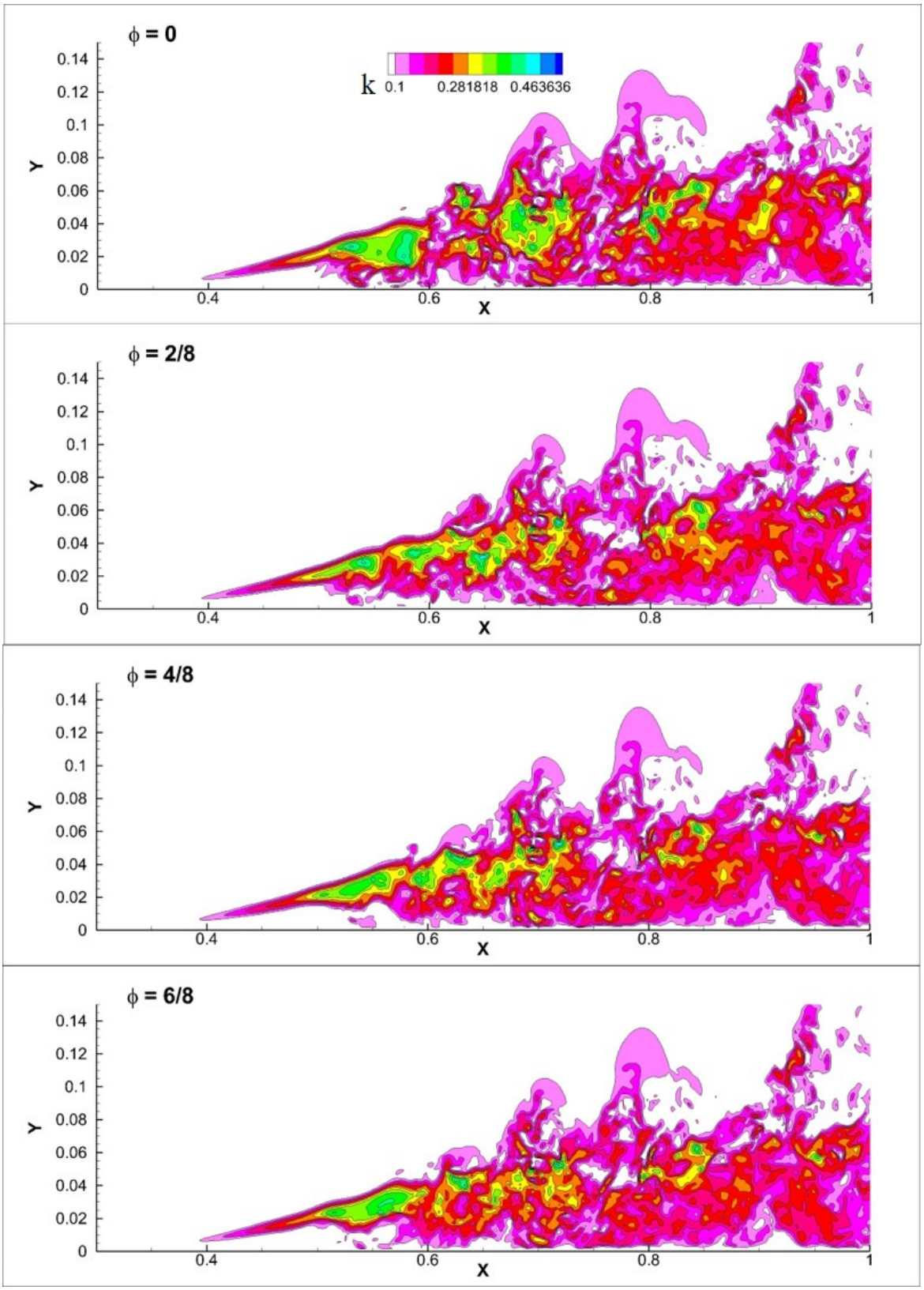

Fig. 5.19 The phase-averaged fluctuating kinetic energy, k shown at four different phases for test case WS.

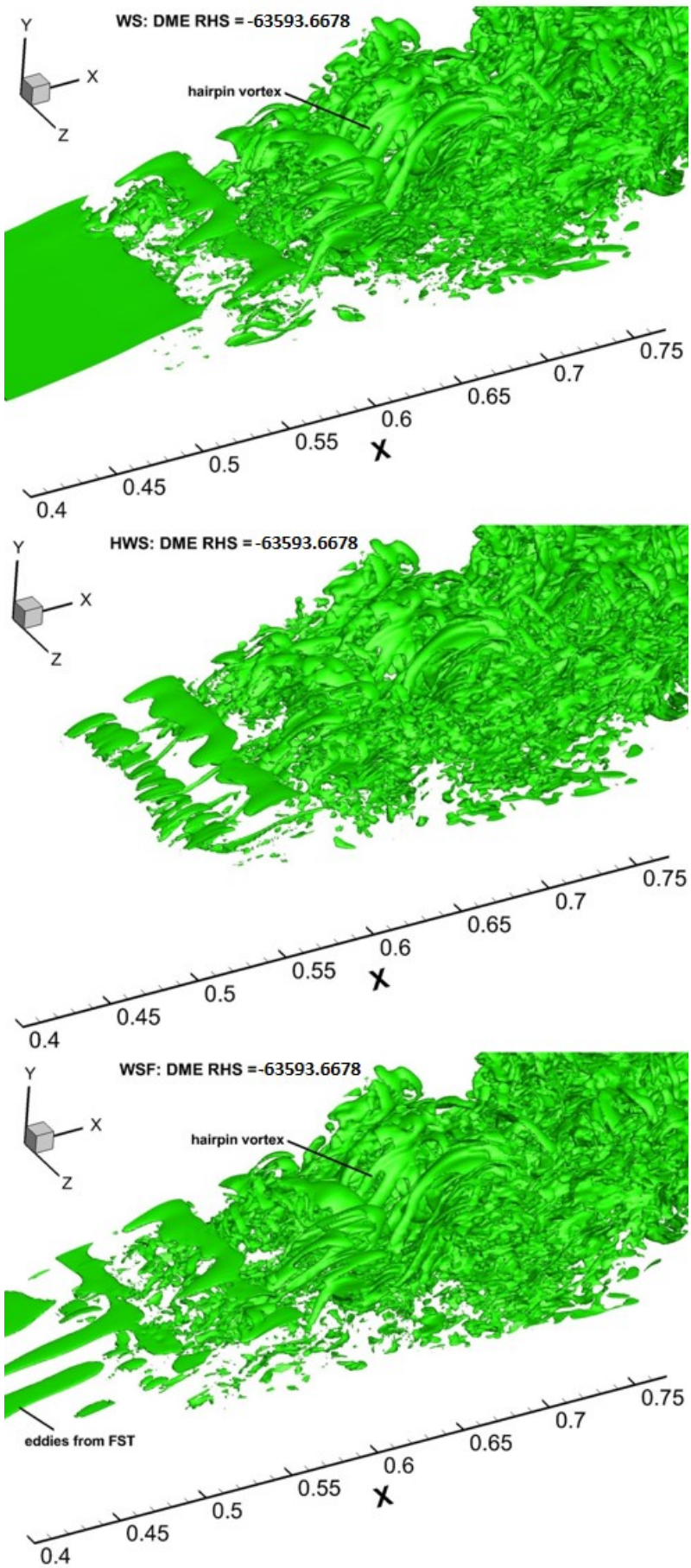

Fig. 5.20 Iso-surfaces of right hand side of DME ($\nabla^2 E_d$=-63593.6678) given by Eq. (2.8) for test cases WS, HWS and WSF.

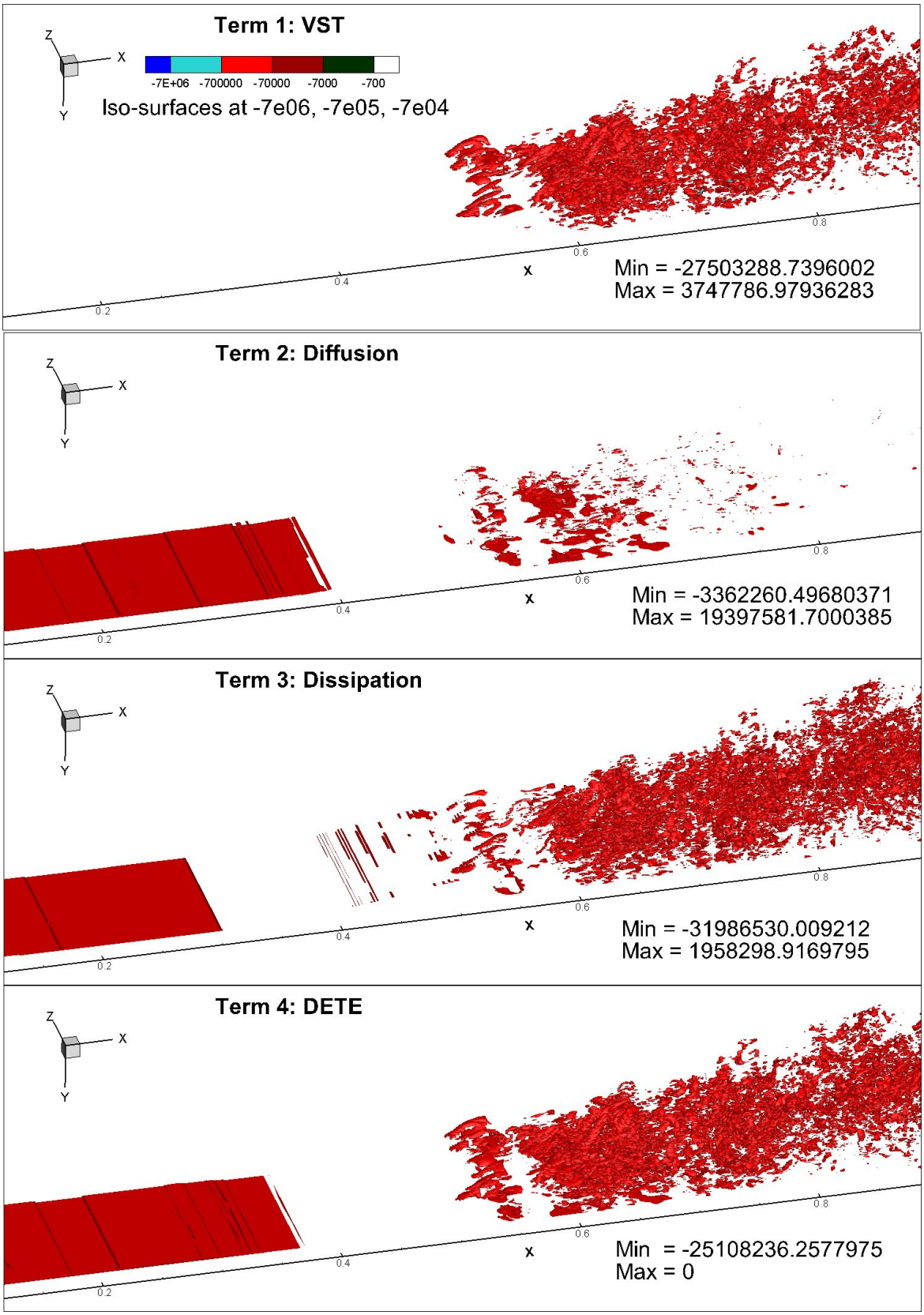

Fig. 5.21 Iso-surfaces of constituent terms of DETE given by Eq. (2.9) shown for test case WS, when $\frac{D\Omega_d}{Dt} < 0$ and $\Omega_d < 0$. Three iso-surface levels are shown: $-7 \times 10^6, -7 \times 10^5$ and -7×10^4.

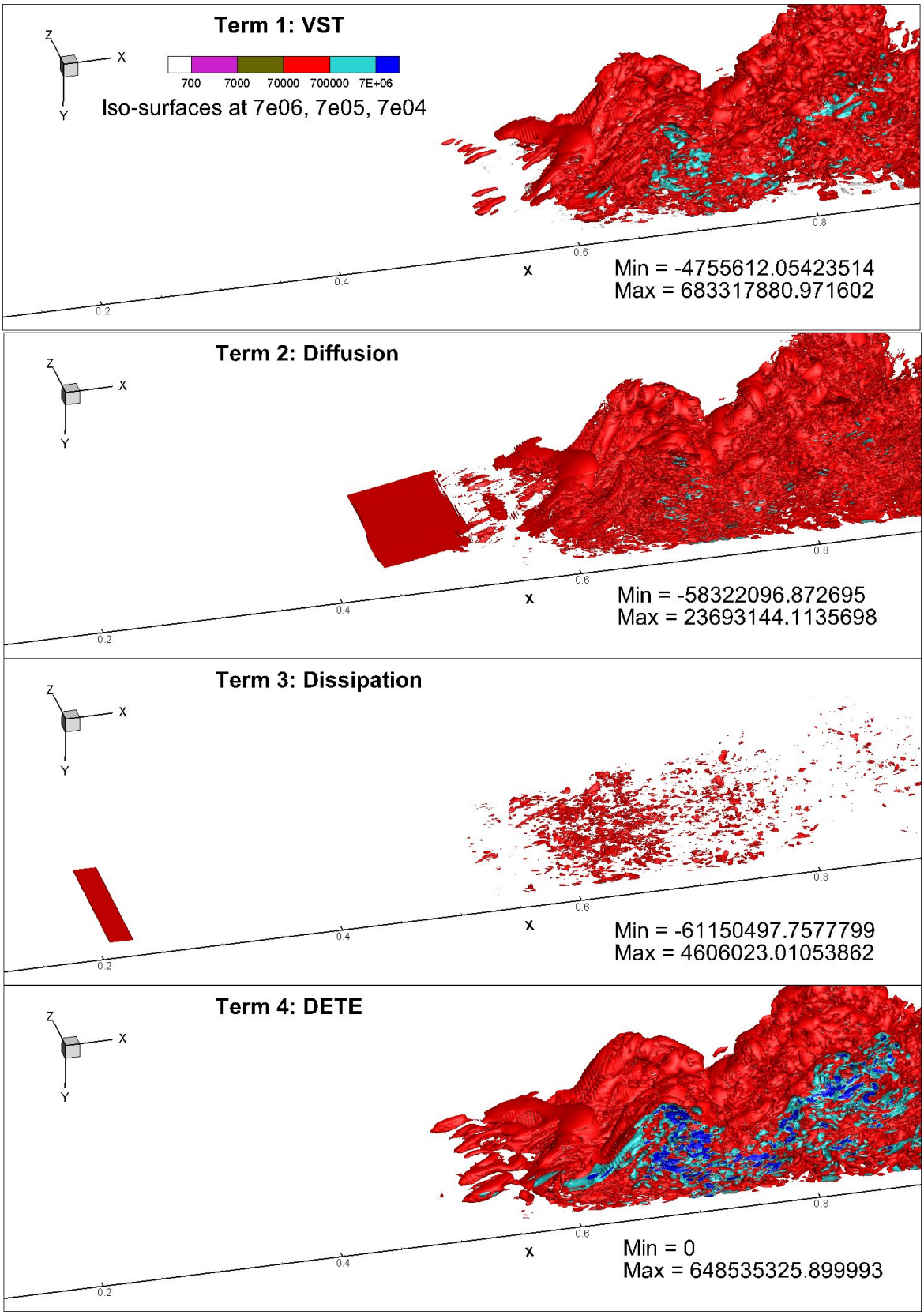

Fig. 5.22 Iso-surfaces of constituent terms of DETE given by Eq. (2.9) for test case WS, when $\frac{D\Omega_d}{Dt} > 0$ and $\Omega_d > 0$. Three iso-surface levels are shown: $7 \times 10^6, 7 \times 10^5$ and 7×10^4.

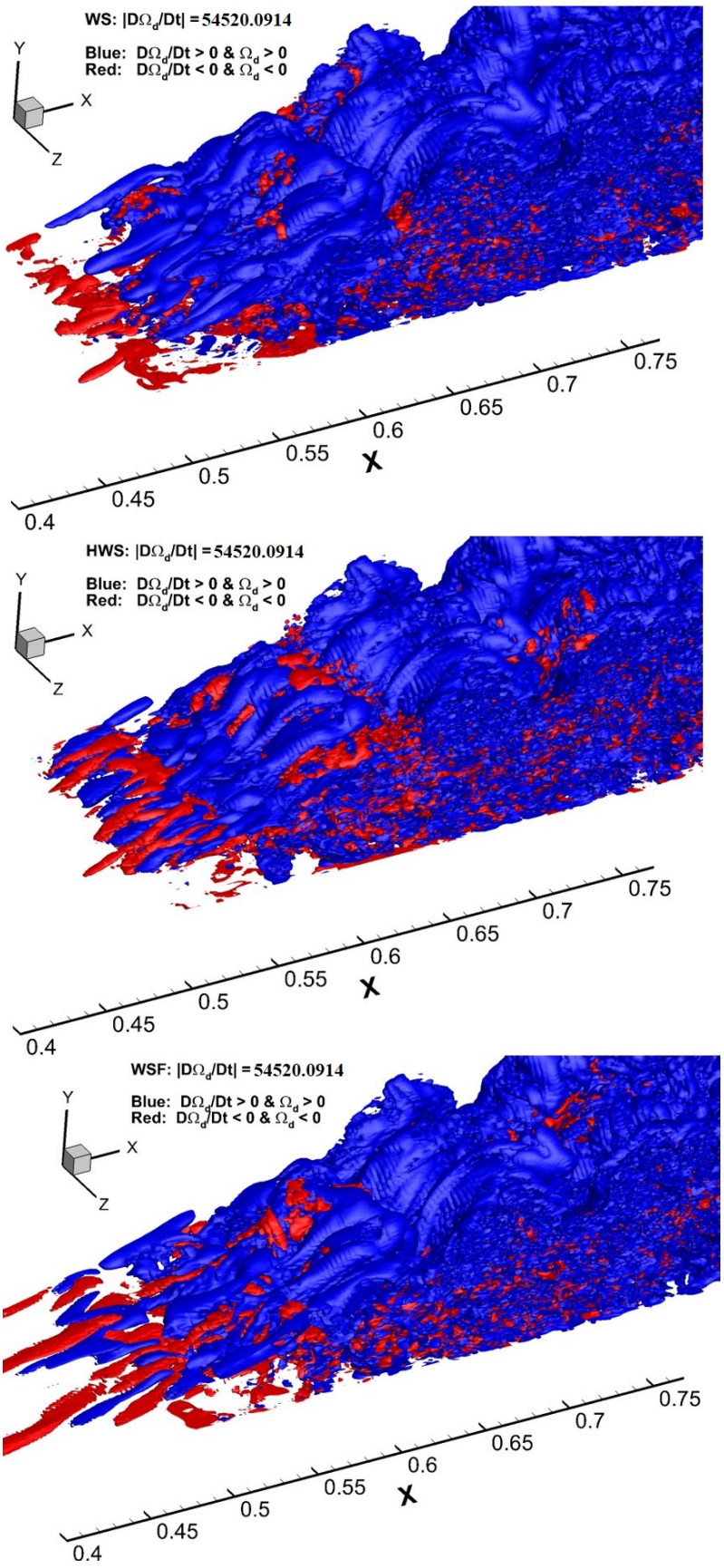

Fig. 5.23 Iso-surfaces of $\frac{D\Omega_d}{Dt}$ ($|\frac{D\Omega_d}{Dt}| = 54520.0914$) for test cases WS, HWS and WSF. The red (lighter) contours are for negative growth rate and for negative disturbance enstrophy, whereas the blue (darker) contours indicate positive growth rate for positive disturbance enstrophy.

Chapter 6

Bypass Transition Mechanism via Vortex-Induced Instability

The aim of this chapter is to study the basic mechanisms of what is termed as bypass transition in the literature, for a free-stream convecting vortex over a ZPG boundary layer, and the modifications induced by a discrete roughness element on the surface of the flat plate over which the boundary layer forms. There are many reasons for conducting the present investigation over a ZPG boundary layer. For all receptivity and instability studies, one must identify an equilibrium state, whose properties are assessed with respect to various forms of imposed disturbances. In search of basic mechanisms for instabilities and transition, one of the prime requirements is reproducibility of the study by the imposed disturbance. In this context, ZPG boundary layer has provided a framework for instability studies from the beginning. There is also a computational reason, which is very important in the present context, in obtaining the correct equilibrium flow. In many reported numerical studies of instability, researchers use similarity profiles, like the Blasius profile as the equilibrium flow. To compute such a flow to compare with the experimental results, one must get the appropriate equilibrium flow first. This is very much possible for ZPG boundary layer to include the effects of boundary layer growth near the leading edge of the plate, as shown by Sengupta et al. (2019a, 2018a). For flows with adverse pressure gradient, obtaining the equilibrium flow is not trivial. Even when such a similarity profile is obtained as the equilibrium flow numerically, it is not always possible to obtain the same flow experimentally. A simple non-trivial example will be flow past a circular cylinder, where the computed flows are always affected by background disturbances. While the flow field inside the LPT experiences wide range of pressure gradients, any mechanism established for ZPG boundary layer associated with a semi-infinite flat plate will be further accentuated for flows with adverse pressure gradient. From now on, reference to ZPG boundary layer will imply the equilibrium flow over

a semi-infinite flat plate. In designing receptivity experiments, one of the main requirement is the ability to reproduce the experiment, correlating cause with effects, as has been reported in Schubauer and Skramstad (1947) for the classical vibrating ribbon experiment. Similarly, to understand the basic mechanisms of bypass transition one must design an experiment, where all the essential parameters can be controlled independently. This was achieved in the reported experiment on vortex-induced instability by Lim et al. (2004), performed on a sub-critical (with respect to exciting Tollmien-Schlichting wave-packets) ZPG boundary layer.

In the previous chapter, the effects of blade vibration and FST have been studied on a representative suction surface of a LPT blade. In this chapter, the physical mechanisms underlying the various disturbance environments often encountered in a LPT are studied through controlled computations of a ZPG boundary layer subjected to a free-stream convecting vortex traversing over a flat plate with a discrete roughness element. The root causes of bypass transition are identified more effectively for a flow experiencing pressure gradient. With this aim, a series of computations studying the effects of a free-stream convecting vortex (approximated as a unit process of FST) over a discrete roughness element (considered as a unit process of roughness) are carried out. A series of 2D and 3D simulations are performed for the incompressible NSE, to compare with the experimental results of Lim et al. (2004), carried out for vortex-induced instability. The computational domain, boundary conditions, initial conditions and features of the test cases under consideration are introduced. The computations are validated with the experimental results of Lim et al. (2004) and the effect of 2D roughness element is validated against experimental work of Klebanoff and Tidstrom (1972). This is followed by some representative 2D results comparing the effects of different convecting speeds of the free-stream vortex and additional effects brought about by the introduction of a 2D bump-like roughness element. A similar analysis in 3D is performed and results are presented using iso-surfaces of vorticity and instability mechanisms introduced earlier. The effects of the strength of the vortex and direction of rotation are also described by computing cases at other convecting speeds and comparing with corresponding experimental results of Lim et al. (2004).

6.1 Formulation of the Problem

Vortex-induced instability is used here as a prototypical example of bypass transition caused by a convecting vortex in the free stream. As we have discussed, the definition of bypass transition involves many aspects other than the mere absence of natural transition caused by Tollmien Schlichting waves (Morkovin, 1993). The scenario of the receptivity experiment

of vortex-induced instability in Lim et al. (2004) is replicated with the intention of showing modifications in the mechanism by the presence of a discrete 2D roughness element. The computed flow fields are shown in Fig. 6.1, to study the receptivity of ZPG boundary layer to convecting vortex in the free stream, with and without the bump on the plate.

In this numerical setup, all physical lengths are nondimensionalized with respect to the plate length, L. A potential line-vortex with circulation (Γ), translates from left to right with a constant speed, c, at a constant height, $H_1 = 2$, above the plate in Fig. 6.1(a). The vortex is initiated from the location: $x = -1, y = 2$, upstream of the leading edge for all the simulations reported here. This potential vortex convecting in the inviscid part of the flow, imposes an image vortex below the plate, to ensure zero wall-normal velocity boundary condition. For the case with the bump, it is placed at a distance of $x_b = 1.5$ from the sharp leading edge of the flat plate, as shown in Fig. 6.1(b). The height of the bump is $h_b = 0.01$, while its width is $w_b = 0.2$, also shown in Fig. 6.1(b). The equation for this 2D roughness element is given by,

$$y(x) = \frac{h_b}{2}\left(1+\cos\left(\frac{2\pi(x-x_b)}{w_b}\right)\right) \quad \text{for } x_b - w_b/2 \leq x \leq x_b + w_b/2 \tag{6.1}$$

Time-dependent boundary forcing by the convecting vortex excites the physical disturbances during the receptivity stage. The leading edge of the plate is retained inside the computational domain. The origin of the reference co-ordinate system is located at the mid-point of the spanwise edge of the plate. The computational domain is given as $x_{in} \leq x \leq x_{out}$ along the streamwise direction with $x_{in} = -0.05$ and $x_{out} = 20$. Along the wall-normal direction the domain is given by, $0 \leq y \leq y_{max}$, with $y_{max} = 0.75$ for all the 2D and 3D computations except for the 3D case of $c = 0.386$, where $y_{max} = 1.5$ is used. The domain extends along the spanwise direction as, $-z_{max}/2 \leq z \leq z_{max}/2$, where $z_{max} = 1.6$ is used. In all the simulations reported here, velocity is referred with respect to the free stream speed, U_∞, and all lengths by plate length L, such that a Reynolds number is used here as, $Re_L = U_\infty L/\nu = 10^5$, where ν is the kinematic viscosity. The details of the test cases simulated here are given in Table 6.1.

The resolution in wall-normal direction is given by $\Delta y = 3.688 \times 10^{-4}$, which is half the wall resolution taken by Sengupta et al. (2003) for 2D simulations. The spacing in the wall-normal direction is stretched following a hyperbolic tangent distribution given by,

$$y_j = 1 - \frac{tanh[\beta_y(1-j/N_j)]}{tanh\beta_y}$$

with the stretching parameter of $\beta_y = 2.0$. The maximum spacing is 5.186497×10^{-3} in the wall-normal direction. The first grid point in the streamwise direction, from the inflow is

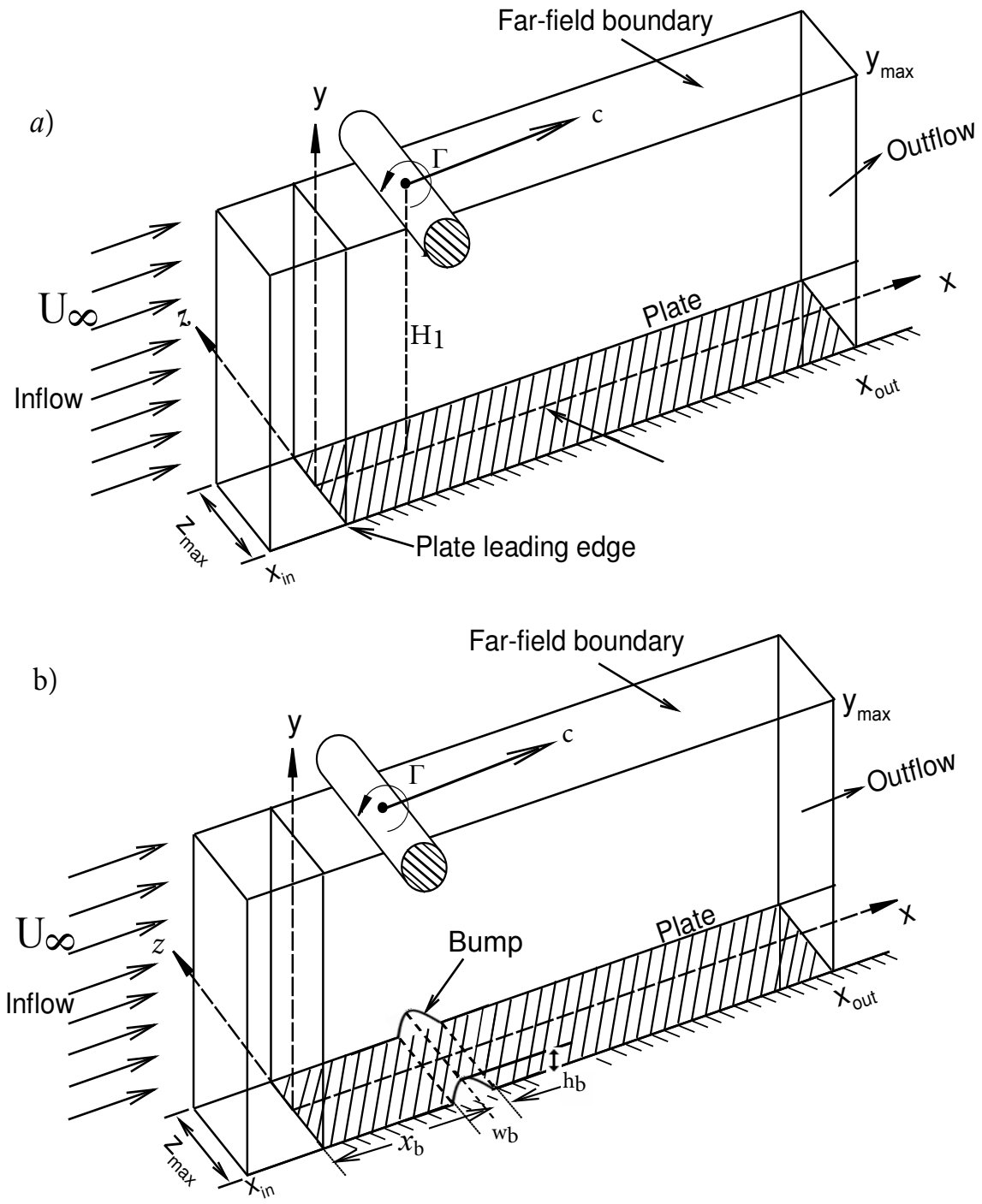

Fig. 6.1 Schematic for vortex-induced instability due to a) an isolated vortex of circulation Γ, convecting at speed c in the free stream, at a constant height H_1 over a ZPG boundary layer (b) in conjunction with a 2D bump of height h_b, width w_b centred at x_b from the leading edge of the plate.

Table 6.1 Details of the 2D and 3D test cases simulated. Here, c is the convection speed of the free-stream vortex, Γ is the strength of the vortex and Δt is the time-step for computations.

Case	c	Γ	Δt	Mesh
2D1: Isolated vortex	0.3	+2.0	8×10^{-5}	1001×301
2D2: Isolated vortex	0.386	+2.0	8×10^{-5}	1001×301
2D3: Vortex with bump	0.3	+2.0	8×10^{-5}	1001×301
3D1: Isolated vortex	0.3	+2.0	1×10^{-5}	$1001 \times 301 \times 129$
3D2: Isolated vortex	0.386	+2.0	1×10^{-5}	$1001 \times 351 \times 129$
3D3: Vortex with bump	0.3	+2.0	4×10^{-5}	$1001 \times 301 \times 129$
3D4: Isolated vortex	0.19	-0.5	8×10^{-5}	$1001 \times 301 \times 129$
3D5: Isolated vortex	0.77	+2.0	8×10^{-5}	$1001 \times 301 \times 129$
3D6: Isolated vortex	0.77	+0.5	8×10^{-5}	$1001 \times 301 \times 129$

$\Delta x_i = 0.009106986$, with spacing reducing up to the leading edge of the plate, following hyperbolic tangent distribution with a stretching parameter, $\beta_x = 2.0$. From the leading edge of the flat plate, up to a streamwise distance of a quarter of plate length ($x = 5$) the grid is stretched with identical value of β_x. From $x = 5$ to the outflow of the computational domain ($x = 20$), a uniform grid is used with the nondimensional spacing of $\Delta x_f = 0.021630828$. Altogether there are 1001 points in the streamwise direction. Reynolds number based on displacement thickness at the outflow is 2432.44, and this domain is five times longer than that was taken by previous simulations of Sengupta et al. (2003). For cases 2D3 and 3D3, the roughness is imposed by an immersed boundary method based on the volume of fluid approach shown by Yuan and Piomelli (2014), explained in chapter 3.

6.1.1 Boundary Conditions

A velocity-vorticity formulation developed by Bhaumik and Sengupta (2015), details of which are provided in chapter 3 for a 3D formulation, has been used on a staggered grid for all the simulations reported here. The governing equations for 2D and 3D flows in velocity-vorticity formulation have also been provided in Sengupta et al. (2019a, 2018a). The boundary conditions used in solving the vortex-induced instability problem are listed as follows,

(i) At the inflow, uniform inlet velocity U_∞ is imposed, along with the contributions imposed by the free-stream vortex and its image. Similarly, the boundary condition for

v-velocity is calculated as caused by the convecting vortex and its image. The induced stream function created by the finite-core line vortex in the inviscid part of the flow is given by,

$$\psi = (U_\infty - c)\left[y - \frac{(y-H_1)(d/2)^2}{\bar{x}^2+(y-H_1)^2} + \frac{(y+H_1)(d/2)^2}{\bar{x}^2+(y+H_1)^2}\right] + \frac{\Gamma}{4\pi} Ln \frac{\bar{x}^2+(y+H_1)^2}{\bar{x}^2+(y-H_1)^2} \tag{6.2}$$

where d is the diameter of the cylinder, Γ is the strength of the vortex and $\bar{x}$ is the current streamwise location of the vortex. The sign of the vortex is considered as positive, if the action of the vortex on the underlying boundary layer is to scour it ahead of the cylinder. From Eq. (6.2), it can be seen that: (i) the displacement effects of convecting vortex with c, d and H_1 as one set of control parameters, and (ii) the circulatory effects caused by the convecting vortex with c, H_1 and Γ acting as the other set of control parameters.

(ii) At the far-field boundary: $\omega = 0$ and (u, v) are calculated by the Biot-Savart law caused by the free stream vortex and its image.

(iii) At the spanwise boundaries: Periodic condition on all the six variables (three components of velocity and three components of vorticity) are used.

(iv) At the wall: No-slip boundary conditions on u, v and w components are used. The boundary conditions on the vorticity components on the plate surface are given as

$$\omega_y = 0 \tag{6.3}$$

$$\omega_x = \left(\frac{\partial w}{\partial y} - \frac{\partial v}{\partial z}\right) \text{ and } \omega_z = \left(\frac{\partial v}{\partial x} - \frac{\partial u}{\partial y}\right) \tag{6.4}$$

(v) The sharp leading edge of the flat plate is taken as the locus of stagnation points for this flow and hence, at the bottom plane ahead of the leading edge (as shown in Fig. 6.1) symmetry conditions are used on all the six variables given by

$$\frac{\partial u}{\partial y} = v = \frac{\partial w}{\partial y} = \omega_x = \frac{\partial \omega_y}{\partial y} = \omega_z = 0 \tag{6.5}$$

(vi) At the outflow: Convective Sommerfeld boundary conditions are applied on the variables u, ω_y and ω_z as

$$\frac{\partial u}{\partial t} + U_c \frac{\partial u}{\partial x} = 0 \tag{6.6}$$

$$\frac{\partial \omega_y}{\partial t} + U_c \frac{\partial \omega_y}{\partial x} = 0 \tag{6.7}$$

$$\frac{\partial \omega_z}{\partial t} + U_c \frac{\partial \omega_z}{\partial x} = 0 \tag{6.8}$$

where, U_c is chosen as U_∞. The boundary condition on ω_x at the outflow boundary is derived from the solenoidality condition of vorticity as

$$\frac{\partial \omega_x}{\partial x} = -\left(\frac{\partial \omega_y}{\partial y} + \frac{\partial \omega_z}{\partial z} \right) \tag{6.9}$$

The boundary conditions for the v- and w-components of velocity at the outflow boundary are derived from the definition of the vorticity components ω_y and ω_z as

$$\frac{\partial v}{\partial x} = \frac{\partial u}{\partial y} + \omega_z \tag{6.10}$$

$$\frac{\partial w}{\partial x} = \frac{\partial u}{\partial y} - \omega_y \tag{6.11}$$

6.1.2 Initial Conditions

The equilibrium flow for 2D cases is calculated by solving the NSE without the free-stream convecting vortex, before solving the receptivity problem. For case 2D3, the equilibrium flow is calculated with the roughness element imposed by immersed boundary method, but without the convecting vortex. Once the 2D equilibrium flow is established, the 3D equilibrium flow is obtained by specifying u, v and ω_z variables at all the discrete spanwise stations, while prescribing other variables, *i.e.* w, ω_x and ω_y as zero at all locations at $t = 0$. With these initial conditions, the 3D solver is run till the unsteady terms fall below a prescribed small value, so that the flow field adjusts itself to the 3D domain and boundary conditions. Subsequently, 2D free-stream excitation by the convecting vortex is initiated to study various receptivity cases.

6.2 Characterizing the Equilibrium Flow

The equilibrium flow for receptivity studies of the vortex-induced instability is characterized here for 2D test cases, with and without the roughness element, by solving 2D NSE without the external excitation, which is in the form of the free-stream convecting vortex. The 3D equilibrium flow field is evaluated thereafter from the 2D field by projecting it in the 3D grid as initial condition, as described in the previous subsection.

In Fig. 6.2, equilibrium flow for the cases of an isolated vortex (2D1 and 2D2), and for a vortex with 2D bump (2D3), are shown with the help of contour plots drawn for the

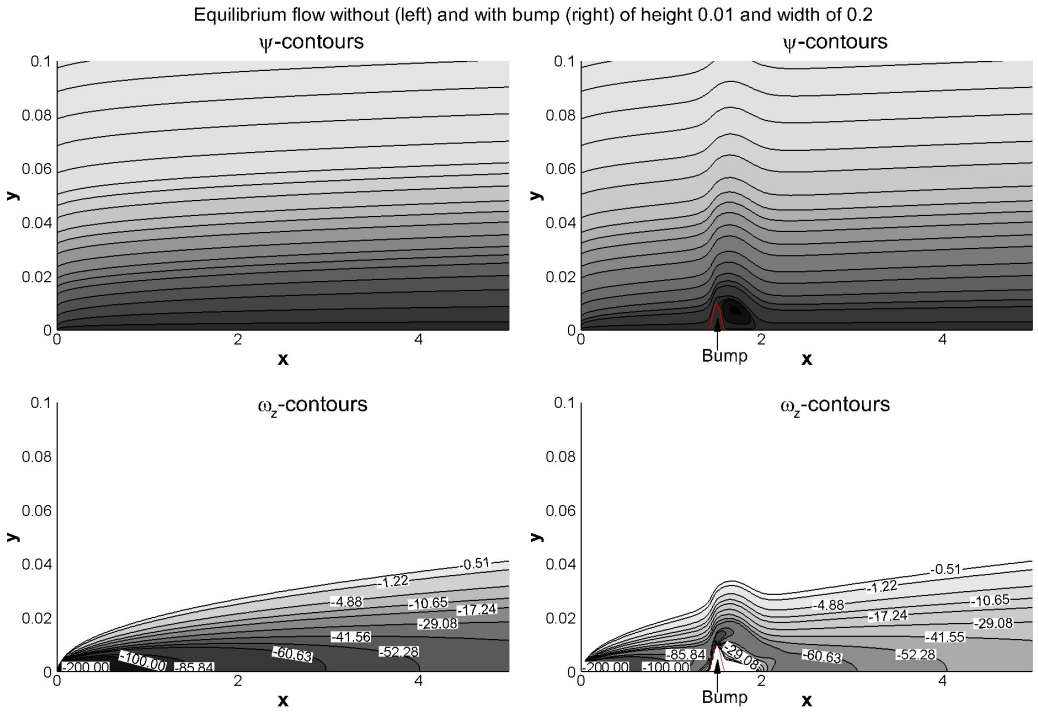

Fig. 6.2 Equilibrium flow solution for flow over a flat plate, for test cases without and with bump evaluated by stream function (top) and vorticity (bottom).

stream function and vorticity. The time dependent vorticity transport equation is solved till the maximum local time rate of spanwise vorticity in the full domain is below a prescribed limit of $\frac{\partial \omega_z}{\partial t} \leq 10^{-5}$ for a steady state of the equilibrium flow. The order of magnitude of the maximum spanwise vorticity observed is of the order 10^3 and thus a change in order of its residual by eight orders has been considered as the steady state of the equilibrium flow. On the top right frame showing the equilibrium flow for the case with bump, the flow downstream of the bump is seen as separated. This is the case of steady separation and is different from the unsteady separation noted for bypass transition in Lim et al. (2004) and Sengupta et al. (2003). This is also noted in the vorticity contours shown in the bottom frames. When one compares the cases with and without the bump, the flow separation is indicated by the zero-contour for the vorticity.

6.3 Validation with Experiments

The vortex-induced instability 3D test cases with an isolated vortex, i.e. cases 3D2, 3D4 and 3D6 are validated with experimental results presented in Lim et al. (2004) for the convection

speeds, $c = 0.386, 0.19$ and 0.77, respectively, in this section. Additionally, validation of the effects of a 2D roughness element for test case, 2D3 is performed and compared with the experimental results in Klebanoff and Tidstrom (1972) for a 2D roughness element on a flat plate tested in a wind tunnel in the presence of FST. In the following subsections, vortex-induced instability created by counter-clockwise and clockwise rotations of the convecting vortex is computed and compared with experimental results. The effects of the strength of the induced vortex on the flow features are also studied. First, a brief description of the experimental observations of Lim et al. (2004), and the parameters affecting the flow are identified. A similar description is provided for the experimental parameters of Klebanoff and Tidstrom (1972).

Experimental study of effects of convecting vortex: In the experiments, flow visualization images are captured by tracking food-dye released from six dye ports located on the surface of the plate, and at a location downstream from the leading edge of the plate as shown in Fig. 2.4. The free-stream vortex was simulated by the rotating and translating cylinder for which the Reynolds number was found to be about 3000 based on the diameter (15mm) and the free stream speed was $U_\infty = 163$ mm/s, which is used as the velocity scale. The turbulent intensity in the test section of the water tunnel was significantly lower than one percent. The physical distance between the cylinder and plate was equivalent to a distance of about twenty eight times the displacement thickness of the ZPG boundary layer at the streamwise location of the dye-ports. Further details of the experimental set-up, the water tunnel and various cases studied experimentally are to be found in Lim et al. (2004).

Experimental details to study effects of a 2D roughness element with a free-stream convecting vortex: An experimental investigation on the effects of 2D roughness elements on boundary layer transition was carried out by Klebanoff and Tidstrom (1972). The boundary layer on a plate with a symmetrically tapered and sharpened leading edge, was mounted vertically in the centre of the wind tunnel used for the investigations. The required pressure gradient was achieved by a false wall on the working side of the plate, mounted on the tunnel wall, while the required angle of attack was achieved by displacing the leading edge and blocking the air passage downstream on the working side of the plate. The 2D roughness elements were in the form of cylindrical rods placed at a streamwise distance from the leading edge of the plate, along its length. Measurements of mean velocity distributions, disturbance spectra and intensity, growth and decay of disturbances within the recovery zone were made, for a unit Reynolds number of 1.42×10^5 per foot. The FST existing in the wind tunnel has been described in chapter 1, and a detailed spectrum was provided in Figs. 6 and 7 in the experimental work of Klebanoff et al. (1992) on 3D roughness elements, where the same

wind tunnel was used, as in the experiments for a 2D roughness element as in Klebanoff and Tidstrom (1972).

6.3.1 Strong Vortex-Induced Instability by Counter-clockwise Free-stream Vortex

The experimental case for the cylinder rotating in counter-clockwise direction with a convection speed $c = 0.386$ in Lim et al. (2004) (whose effect due to Biot-Savart interaction is to scour out the boundary layer off the plate ahead of the vortex) is detailed in this subsection. This action of scouring is equivalent to boundary layer thickening, which is also akin to exposing the equilibrium boundary layer to adverse pressure gradient, and is explained quantitatively in Fig. 2 of Sengupta et al. (2018a). The corresponding flow visualization images are shown in Fig. 6.3(a), where the cylinder is translating from left to right, so that the relative speed of the cylinder is $(U_\infty - c)$. The ZPG boundary layer is seen to remain unperturbed in the top frame of experimental results in Fig. 6.3(a), while a nascent disturbance in the wall-normal direction is perceived immediately downstream of the convecting vortex location by the third frame from the top in Fig. 6.3(a). The interaction between the free stream vortex and the vorticity field in the boundary layer is such that the latter is stabilized upstream of the counter-clockwise vortex, while the boundary layer is destabilized downstream of the convecting counter-clockwise vortex. This is clearly visible in the corresponding computational results shown in Fig. 6.3(b), on the right column. The computed results obtained by solving 3D NSE show a qualitative agreement with the experimental visualizations. Strong interaction via the scouring action of the imposed adverse pressure gradient is observed from the time indicated in the bottom three frames of Fig. 6.3(b). While in the top three frames, the induced perturbation field causes very strong spanwise vorticity (ω_z) with negligible spanwise movement, the other two components of vorticity (ω_x, ω_y) slowly evolve due to vortex-stretching term in the enstrophy transport equation (Raudkivi and Callander (1975) and Sengupta et al. (2013)). Recently, the role of vortex stretching has been shown for 3D vortex-induced instability in Sengupta et al. (2019a) via the budget terms of disturbance enstrophy. The strong 3D nature of the flow is seen at later times, for both experimental and computational frames. In flow visualization pictures, this is visible as dye streaks diffusing, caused by strong eddy diffusivity of the created turbulence, ahead of the convecting vortex. This is despite the fact that the boundary layer on the flat plate was essentially sub-critical in the experiment of Lim et al. (2004). Thus, vortex-induced instability is a perfect example of bypass transition, as growing Tollmien-Schlichting wave or wavepacket was not created in the experiment.

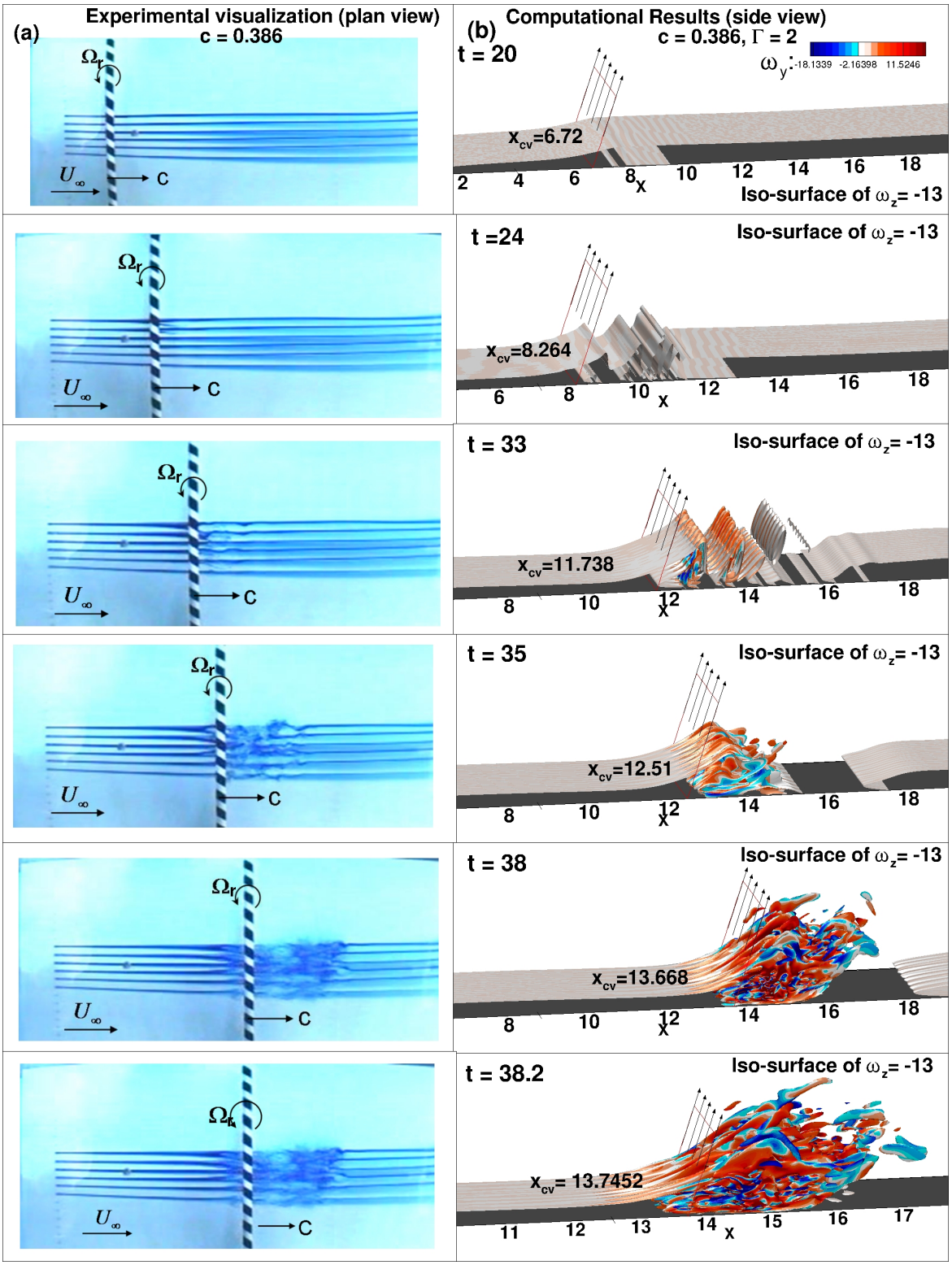

Fig. 6.3 Comparison between a) experimental results of Lim et al. (2004) (left) and b) computational results (right) for the receptivity experiment for the counter-clockwise rotating vortex case, 3D2 with $c = 0.386$. The instantaneous location of the free stream convecting vortex are indicated by x_{CV} in each frame. The inclined frame, with arrowheads on top, shows the location of the free stream vortex, with respect to the disturbance field.

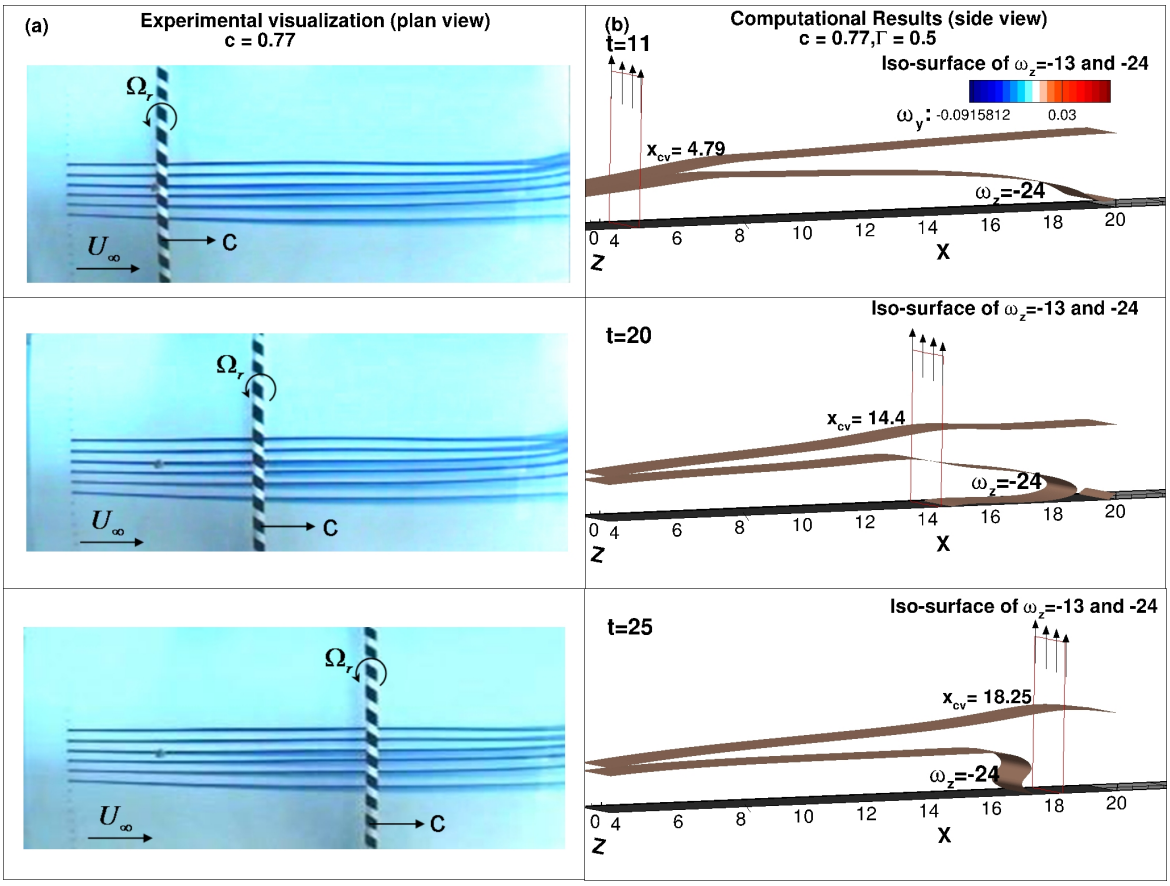

Fig. 6.4 Comparison between a) experimental results of Lim et al. (2004) (left) and b) computational results (right) for the receptivity experiment for the counter-clockwise rotating vortex case 3D6, with $c = 0.77$. The instantaneous location of the free stream convecting vortex are indicated by x_{CV} in each frame.

6.3.2 Weaker Vortex-Induced Instability by Counter-clockwise Free-stream Vortex

In the experimental results reported by Kendall (1987), it was noted that periodic free stream vortical excitation shows a preferential peak for vortex-induced instability at a convection speed around, $c \sim 0.35$. At higher speeds of convection, the receptivity decreased for the experiments of Kendall (1987). Similarly, for a free stream vortex, reduced receptivity is computationally and experimentally noted with increased convection speed. A higher convection speed case with $c = 0.77$, was studied experimentally in Lim et al. (2004), and is shown here in Fig. 6.4(a). It can be discerned that the equilibrium ZPG boundary layer is insensitive to the imposed perturbation by the convecting vortex for this experimental case. The very weak receptivity for this case can be understood from the expression of induced

perturbation, given by Eq. (6.2). The displacement effect in Eq. (6.2) is directly affected by the reduction of the input perturbation at the higher convection speed, as given by reduced $(U_\infty - c)$. It is also noted that the strength of the captive vortex (Γ) is also related to the effective speed of the flow over the cylinder, $(U_\infty - c)$, along with the rotation rate of the cylinder. Lim et al. (2004) observed that when the cylinder is translated at a lower speed of $c = 0.39$ without any rotation i.e. with $\Gamma = 0$, there was negligible receptivity. Thus, it was concluded from the expression of the input stream function, that the relative speed plays a stronger role in determining the circulation effect, and which is the main driver in providing receptivity to the boundary layer via larger input to the fluid dynamical system.

In Fig. 6.4(b), the corresponding computational results are shown at the indicated times, with the following vortical parameters: $x_0 = -1.0$; $c = 0.77$ and $\Gamma = 0.5$. The side view is on display for the computational results at $t = 11$, 20 and 25 for the spanwise component of vorticity (ω_z), which indicates that a very mild perturbation is induced in this case. It is clearly evident that the flow remains 2D for this case up to $t = 25$ and beyond, as the input perturbation is also 2D.

6.3.3 Vortex-Induced Instability by Clockwise Free-stream Vortex

Figure 6.5 shows the results for the case where the cylinder is rotating in clockwise direction, and moving with a slower convection speed $c = 0.19$. This case does not exhibit the same type of instability, which has been observed for the counter-clockwise vortex cases. For this case, the shear layer is seen to be perturbed as a bulge of the dye-line upstream of the convecting vortex. For the case of a counter-clockwise vortex on the other hand, the instability onset is with the appearance of a bulge of the dye-line, which leads to a separation bubble on the wall as the primary instability. For the clockwise rotating vortex, the bubble does not form on the wall and does not burst, because the adverse pressure gradient, which is formed upstream of the vortex, is weaker. Here, instead the following are observed in the experimental results shown in Fig. 6.5(a):

(i) The disturbances trail upstream of the convecting vortex and (ii) the growth of the disturbance is insufficient to cause transition to turbulence. The reason for the former is due to lower input disturbance, which creates an adverse pressure gradient upstream of the vortex. In the downstream direction, the imposed pressure gradient is favourable. Apart from the weaker disturbance field, there is also very little spanwise mixing of the disturbance field. All of these can be graphically demonstrated from the 3D simulation of the flow field in Fig. 6.5(b). In the displayed three frames, it is noted that the vorticity field is demarcated into two zones about the marked point A, with the upstream part showing a bulge, and the downstream

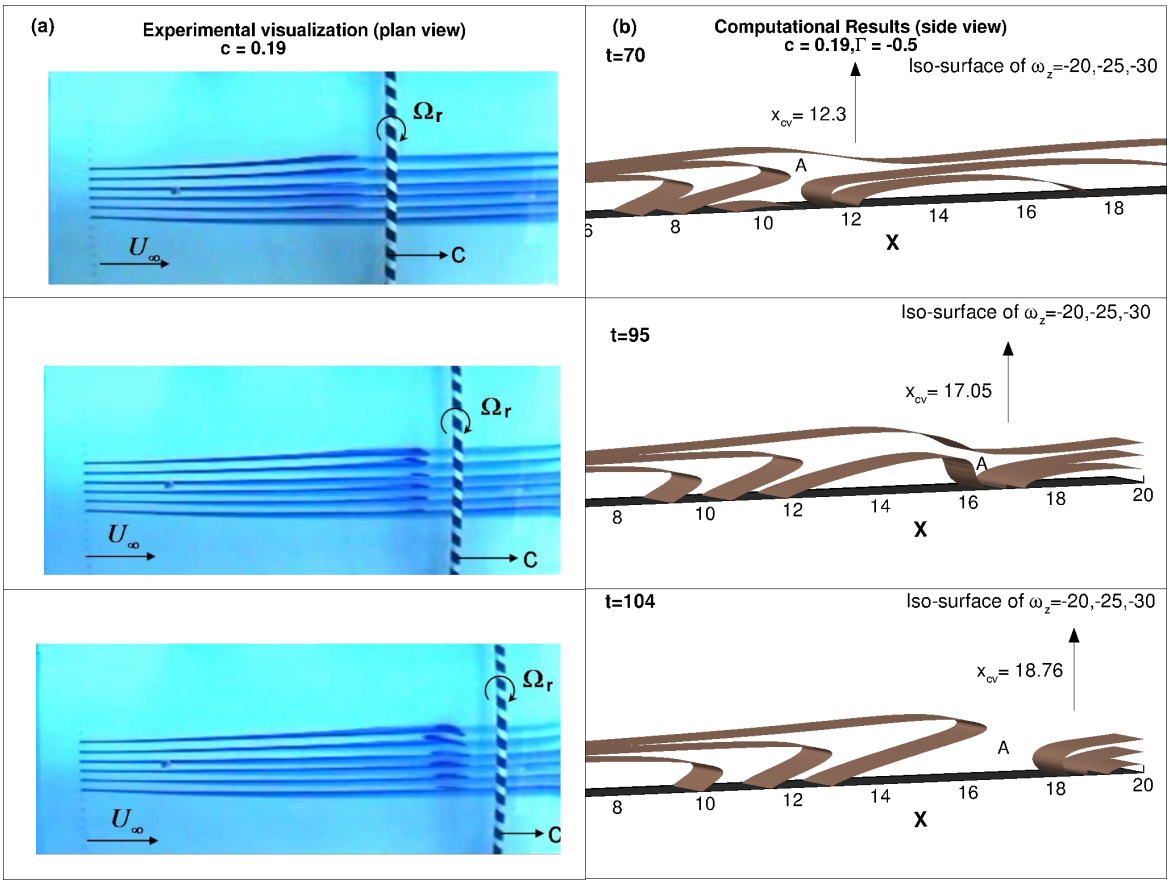

Fig. 6.5 Comparison between a) experimental results of Lim et al. (2004) (left) and b) computational results (right) for the receptivity experiment for the clockwise rotating vortex case, 3D4 with $c = 0.19$. The instantaneous location of the free stream convecting vortex are indicated by x_{CV} in each frame.

part showing a compressed vortical layer. This feature is also noted in the corresponding experimental frames.

6.3.4 Vortex-Induced Instability under the Influence of Surface Roughness

In the experimental setup of Klebanoff and Tidstrom (1972), the FST in the wind tunnel acted as the trigger for instability and transition, which was then modified by the introduction of the 2D surface roughness element.

In Fig. 6.6, the computed spectra for the 2D velocity components are shown. Apart from showing the mean components, smoothened peaks are observed in the spectra with continuous variations. In these frames, both the cases of $c = 0.3$ and 0.386 are considered,

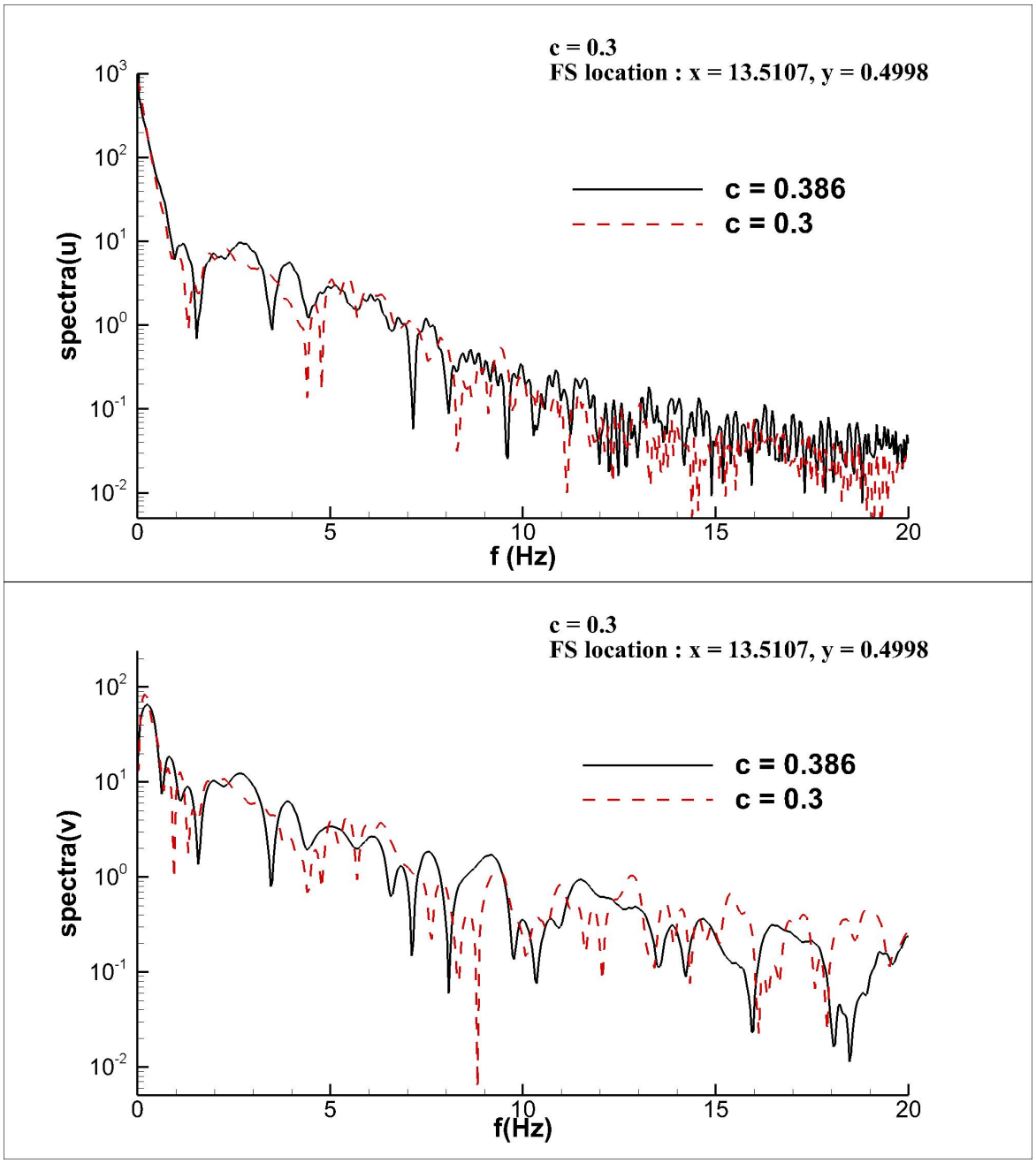

Fig. 6.6 Spectrum of imposed streamwise and wall-normal velocity components at ($x = 13.5107$, $y = 0.4998$) for test cases 2D1 and 2D2.

and similar variation of spectral amplitude with the frequency is observed, even though some variations are noted at higher frequencies for wall-normal component of velocity for the case of $c = 0.3$. It can be understood that such pronounced effects on v at higher frequencies will cause higher vortical ejection in wall-normal direction during vortex-induced instability. However, the mean flow perturbation is stronger for the higher speed of convection cases. These spectra can be contrasted with Fig. 6 of experimental results in Klebanoff et al. (1992) for the FST of the empty wind tunnel with discrete spectral peaks. Thus, the effects of the free-stream convecting vortex is qualitatively similar to effects of actual FST in a wind tunnel. This is the reason for using vortex-induced instability caused by convecting free-stream vortex as a representative case of bypass transition, which also mimics the effects of FST. Thus, the present study can be viewed as a unit process of FST-induced bypass transition. The additional effects of 2D discrete roughness in the presence of FST are analysed next through validation of test case 2D3 against few representative experimental results provided in Figs. 4 and 8 of Klebanoff and Tidstrom (1972). Another aspect to be highlighted here is that the vortices comprising FST are not passive scalars, and there are Biot-Savart interactions among the vortices within FST. The boundary layer forming over the turbine blade/flat plate also interacts with the elements of FST. These vortices do not propagate in the flow with free-stream velocity. Schlichting and Gersten (2017) state that "*vortex street moves with a velocity, v, which is smaller than the flow velocity U in front of the body ..... the velocity ratio u/U must be known from experiment.*" This is the reason different values of the convection speed have been considered, which are not equal to the free-stream velocity. While the convection speeds $c = 0.3$ and 0.386 may not be an accurate assessment of FST profiles for all the vortical elements in the ensemble, the local adverse pressure gradient downstream of the vortex is representative of the pressure gradient on suction surface of a LPT blade. The maximum receptivity was observed for $c \sim 0.35$ in the experiments of Kendall (1987) for periodic convecting vortices. Computations have also been performed at higher convection speeds, such as $c = 0.77$, and lower speeds, such as $c = 0.19$. The main aim here is to study receptivity as a function of convection speed.

In Fig. 6.7, the spectra for streamwise velocity fluctuations are shown for case 2D3, when the 2D roughness element is centered around a nondimensional streamwise location, $x_b = 1.5$, for vortex-induced instability triggered by free-stream convecting vortex at a speed of $c = 0.3$. These are shown for different locations downstream of the 2D roughness element. For the nearest station from the bump at a nondimensional streamwise location $x = 1.633$, a typical spectrum of a bump at around 180 Hz is observed, as was also the case for Fig. 4 of Klebanoff and Tidstrom (1972) for a corresponding station 0.5 inch downstream of the roughness element. To compare with the experimental results of Klebanoff and Tidstrom

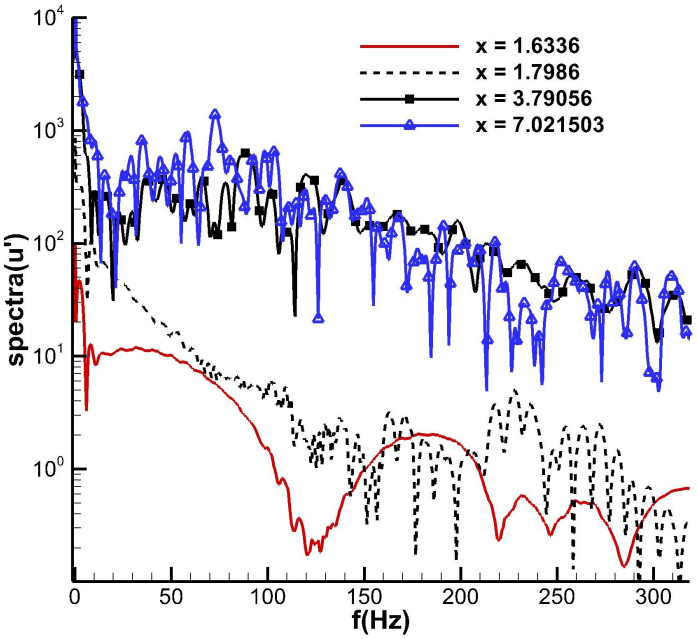

Fig. 6.7 Spectra of streamwise disturbance velocity, computed at the indicated streamwise stations. The time series is logged at the height, $y = 0.00909$.

(1972), the frequencies in the computations have been dimensionalized with a time scale (L/U_∞). For the experiments of Klebanoff and Tidstrom (1972), it was observed that lower frequency component in the spectrum represents the FST of the wind tunnel. For the present case, apart from a very low frequency (which can give rise to Klebanoff mode), there are no distinct peaks. It was noted in Fig. 7 of Klebanoff et al. (1992), that the spectrum in the free stream had multiple discrete peaks. In our case, no such peaks are noted and the hump in the low frequency part of the spectrum is understood to be due to the alteration of mean flow by the presence of steady separation for the equilibrium flow. For the other downstream stations in Fig. 6.7, higher amplitude wide-band spectrum are observed which are different from the ones noted by Klebanoff and Tidstrom (1972). This is due to the discrete peaks of FST in the wind tunnel, which are not present for the case of vortex-induced instability caused by a single convecting vortex. Discrete peaks are a consequence of train of vortices caused by the fan in the tunnel, decided by the number of such blades and the rpm of the fan (Klebanoff et al., 1992).

In Fig. 6.8, the streamwise velocity fluctuations are shown as a function of wall-normal distance at a streamwise location, $x = 1.633$, which is downstream of the roughness element centered at $x_b = 1.5$, for the test case 2D3 with the free-stream vortex convecting with a speed of $c = 0.3$. The fluctuations are time-averaged during the period $0 \leq t \leq 119$. A

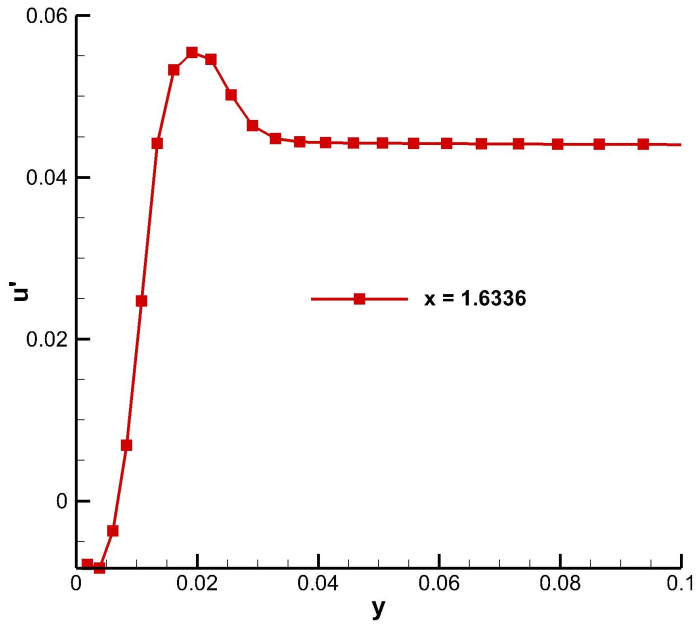

Fig. 6.8 Streamwise disturbance velocity profile computed at streamwise station, $x = 1.6336$ and time-averaged in the interval $0 \leq t \leq 119$, for test case 2D3.

comparison is attempted with Fig. 8 of Klebanoff and Tidstrom (1972), wherein the intensity of streamwise fluctuations are measured downstream of the roughness element, with the wall-normal distance. The distinctive features of this disturbance velocity component are, (i) unlike streamwise disturbance fields created by classical Tollmien-Schlichting wave route having an inner and an outer maximum, here only a single peak is observed and (ii) the disturbance amplitude is far higher than the one observed in experiments of Klebanoff and Tidstrom (1972) with wind tunnel FST, implying that vortex-induced instability triggered by a single convecting vortex creates a higher level of perturbation.

6.4 2D Vortex-Induced Instability Results

The results for test cases 2D1, 2D2 and 2D3 are provided in this subsection to facilitate comparison between effects of different convecting speeds on the receptivity of the boundary layer. Modifications to transition mechanisms with the introduction of a discrete 2D bump will also be analysed using the contours of spanwise vorticity (ω_z); the distribution of DME created for the disturbance field and the DETE for tracking creation of rotationality, as indicated by linear-nonlinear receptivity theory developed in Sengupta et al. (2018a).

6.4.1 Receptivity of Zero Pressure Gradient Boundary Layer: Spanwise Vorticity

In Fig. 6.9, the contours of spanwise vorticity are plotted for two convecting speeds $c = 0.3$ (left) and 0.386 (right), at representative times to compare the test cases 2D1 and 2D2. The free-stream vortex, for both the cases, convects at a constant height, $H_1 = 2$ with a fixed strength, $\Gamma = +2$. In frames (a) and (b) at $t = 5$ and 10, for the initial stages of vortex propagation, the contours are similar for the two convecting speed cases. As noted earlier that a vortex with counter-clockwise circulation lifts up the boundary layer in the downstream, and such action is equivalent to creating an adverse pressure gradient, promoting increase in boundary layer thickness and eventually creating nascent separation bubble, enclosing vortical structures. At the same time, at upstream locations of the free-stream vortex, a favourable pressure gradient is created. These simultaneous actions of thickening and thinning of the underlying boundary layer are noted in frames from $t = 15$ onwards. For frames (c) at $t = 15$, the vortical structures created for case 2D2 (for vortex convecting at higher speed $c = 0.386$), have a larger streamwise and wall-normal extent, implying higher receptivity for this convection speed, as compared to the other case of $c = 0.3$. Such a delayed growth for $c = 0.3$ is also noted for the following frame at $t = 20$. By $t = 30$, the disturbance packet for the case 2D2, spreads in the streamwise and wall-normal directions by a higher degree than that is noted for the case 2D1. Also, due to higher convection speed of the disturbance wave-packet, its leading edge crosses the exit plane of the computational domain. This state of growth and propagation continues further with time, as noted in frames (f) at $t = 40$, where the peak of the disturbance wave-packet has almost convected out of the domain for case 2D2. This figure shows the higher receptivity for the case of $c = 0.386$, as compared to the case for $c = 0.3$. Different dispersion effects are observed on the wave-packet for the two cases of different convection speed. For the higher speed of convection, the wave-packet disperses rapidly, while the eruptions are noted to achieve higher height for the peak. In comparison, the wave-packet for $c = 0.3$ case, the wave-packet is more compact in the streamwise direction.

In Fig. 6.10, the contours of spanwise vorticity are plotted for the convecting speed, $c = 0.3$, at the indicated times for test cases 2D1 and 2D3, to understand the additional role played by a surface-bump in case 2D3, as compared to the case of an isolated vortex convecting in the free-stream alone for the case 2D1. In frames (a) at $t = 5$, the flow is quiescent for both the cases. But the effect of the bump is observed in this contour plot for vorticity, in the form of disturbance in the neighbourhood of the bump and another packet which is downstream of the bump, little ahead of $x = 5$. By $t = 10$ in frames (b), the quasi-steady nature of vorticity field is noted for the case 2D1, while due to the presence of

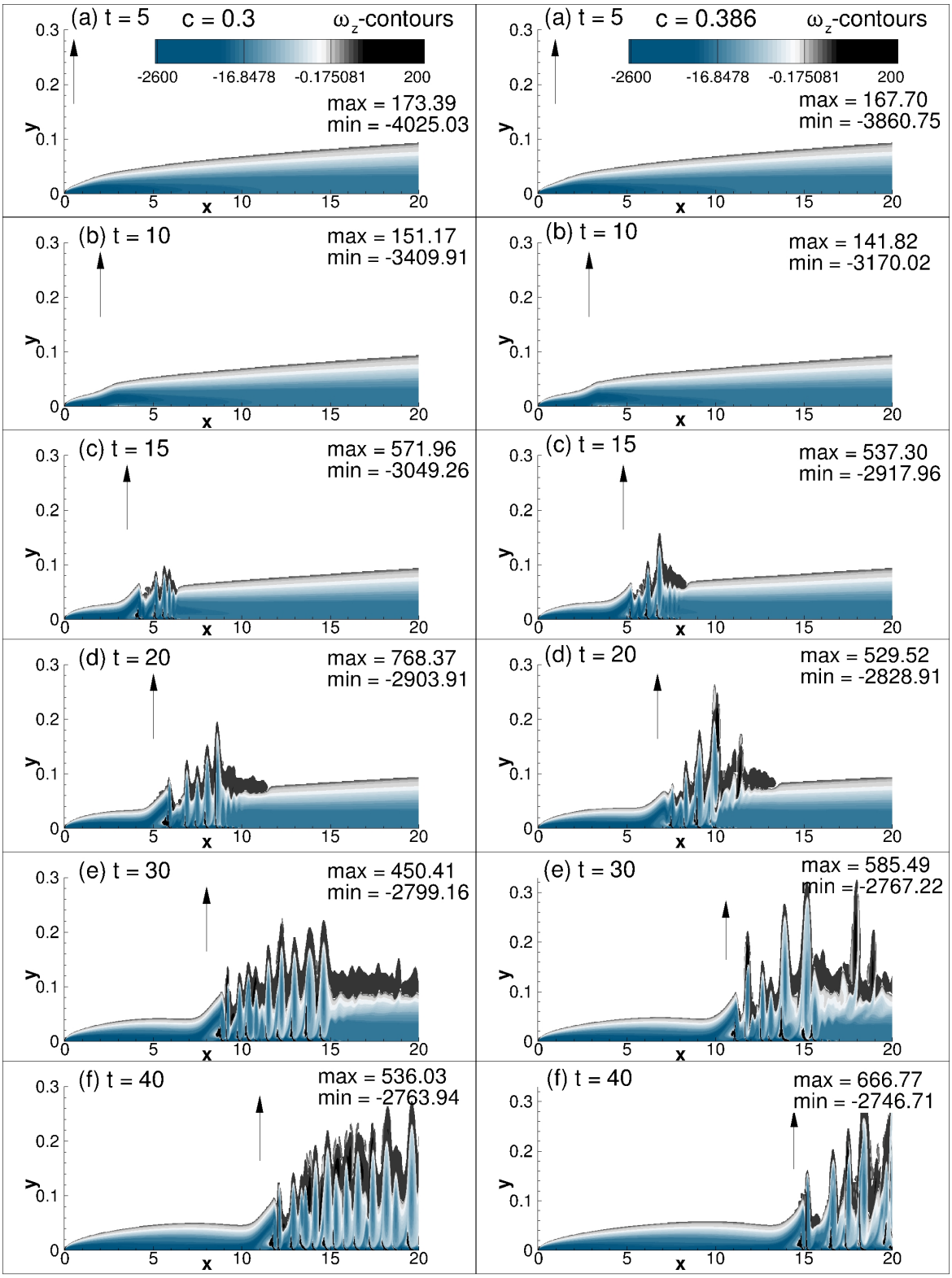

Fig. 6.9 ω_z contours at indicated times for cases 2D1 and 2D2, at convecting speeds $c = 0.3$ and 0.386, respectively. Arrowheads at the top show the streamwise location of the convecting vortex.

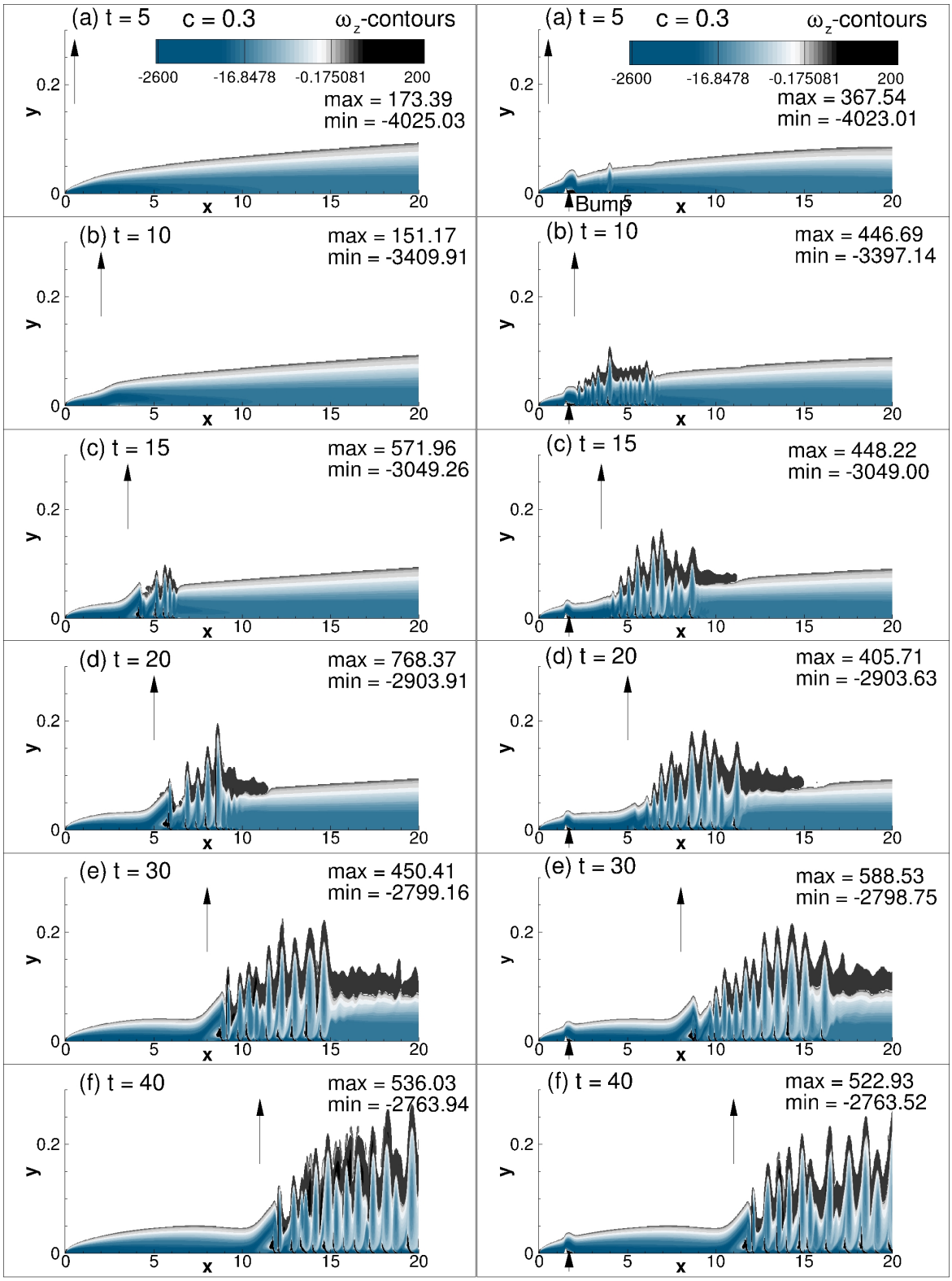

Fig. 6.10 ω_z contours at indicated times for cases 2D1 and 2D3, at convecting speed $c = 0.3$, with and without the bump. Arrowheads at the top show the streamwise location of the convecting vortex.

bump in case 2D3, a sequence of unsteady separation bubbles are noted, which are capped by opposite signed vorticity at the edge of the perturbed shear layer. A well spread out disturbance packet is noted downstream of the bump. Thus, the presence of the bump is noted to accelerate the vortex-induced instability by the convecting free-stream vortex. However by $t = 15$, the free-stream vortex moves further downstream, and as a consequence separation has commenced for the case 2D1 near $x = 5$. By this time, the disturbance packet for 2D3 has gained sufficient traction in the streamwise and wall-normal directions. The moment vortex-induced instability comes into play, the negative vorticity in the domain reduces, while the positive vorticity increases. Despite larger dispersion of the disturbance packet for the case with bump, the maximum positive vorticity value is higher for the case of 2D1, as compared to the case of 2D3, till $t = 20$.

In subsequent frames at $t = 30$ and 40, the presence of roughness in case 2D3 allows the disturbance packet to propagate over a larger streamwise extent, which is comparable to case 2D2 at a higher convection speed. As the speeds of convection are similar for cases 2D1 and 2D3, the packet does not convect out of the domain for case 2D3, as we had observed for the case of 2D2. In fact, at streamwise locations which are much further downstream of the bump location, the flows in cases 2D1 and 2D3 are similar, and so is the minimum vorticity noted for both the cases at $t = 30$. By this time, vortex-induced instability becomes stronger for the case with the bump, but thereafter it relaxes back to a state where the effect of the bump is seen to be of the same order, as it is for the case 2D1. This can be associated with the flow reaching a 'recovery zone', as also mentioned by Klebanoff and Tidstrom (1972), i.e. the downstream location beyond the roughness element where the effect of the roughness is no longer felt in the flow, while the bump is in a location of favourable pressure gradient, imposed by the free-stream vortex. In case 2D3, the bump of height 0.01, which is $1/10^{th}$ the boundary layer thickness, essentially acts like a trip wire to trigger early bypass transition. Apart from hastening the onset of bypass transition, the effect of bump is not seen to bring significant effects on bypass transition, for these parameters.

6.4.2 Instability Mechanism Explained by DME Equation

Studying the disturbance field and underlying instability mechanisms through total mechanical energy has been developed by Sengupta et al. (2003) directly from the incompressible NSE, as detailed in appendix A. The developed equation for the disturbance component is due to interactions between the equilibrium and disturbance fields via the DME equation (E_d), given by Eq. (2.8). This equation can be contrasted with the similar Poisson equation derived for static pressure to identify coherent structures in the method of Q-criterion (Hunt et al., 1988), as shown in chapter 2. Without solving Eq. (2.8), one can qualify the solution

by the right hand side of the Poisson equation, as is explained by Sommerfeld (1949). It indicates the presence of a source or a sink of E_d, with a negative/positive sign of the right hand side of the equation, respectively.

Growth of DME is due to interactions of velocity and vorticity field, creating terms which act as source on the right hand side of Eq. (2.8). The leading term on the right hand side of Eq. (A.7) is nothing but the disturbance enstrophy, $\Omega_d = 2\vec{\omega}_m \cdot \vec{\omega}_d + \omega_d \cdot \omega_d$, which can be either positive or negative, with negative sign implying a source of DME. Thus, the evolution of E_d is governed by Ω_d, which is a source for positive value or a sink for negative value. The growth is indicated when there is a transfer of energy from the equilibrium to the disturbance flow fields.

In Fig. 6.11, the right hand side of DME is evaluated at the given times for the test cases 2D1 and 2D2, with identical equilibrium flows, but with dissimilar convection speeds. From the plotted contours, there are two sources of disturbances, one originating from the leading edge and the other originating deep inside the boundary layer. These have been interpreted as free-stream and wall modes (Sengupta, 2012), respectively. At $t = 20$, for the case 2D1, the interaction between disturbances originating from these two sites is seen to occur at a location of $x = 6$. For case 2D2 ($c = 0.386$), there are multiple locations, where the wall-mode disturbances erupt in wall-normal direction to penetrate into the free-stream mode, originating from the leading edge. Additionally, like the vorticity contours in Fig. 6.9, the streamwise and wall-normal extents of disturbances for case 2D2 is larger than that is for the case 2D1. By $t = 30$, the leading part of disturbances have propagated out of the domain for the case 2D2, due to higher convection speed. For the case 2D1 at the corresponding time, the separation structures appear to be much more regular than those observed for the higher receptivity case. By $t = 40$, leading part of disturbances have propagated out of the domain for both the test cases 2D1 and 2D2.

In Fig. 6.12, the sources of E_d are compared with negative contour values for $c = 0.3$, for the test cases 2D1 and 2D3. It can be observed that the presence of the bump enhances the growth of instability via DME at early times. Even up to the intermediate time, $t = 30$, this is noted from the magnitude of the source term for E_d, given in each frame. However by $t = 40$, both the cases show similar disturbance levels, as was also noted in the vorticity contour plots. For the top frame at $t = 10$, for the case 2D1 on the left, there is only one source of instability arising from the leading edge, while for the case 2D3 on the right, an additional site for disturbance origin is observed immediately downstream of the bump. At $t = 20$, apart from the leading edge instability, there is another instability starting downstream of the leading edge of the plate ($x = 5$ for the case 2D1). It is seen that the instability at the leading edge continues to remain outside the boundary layer due to the shear sheltering effect

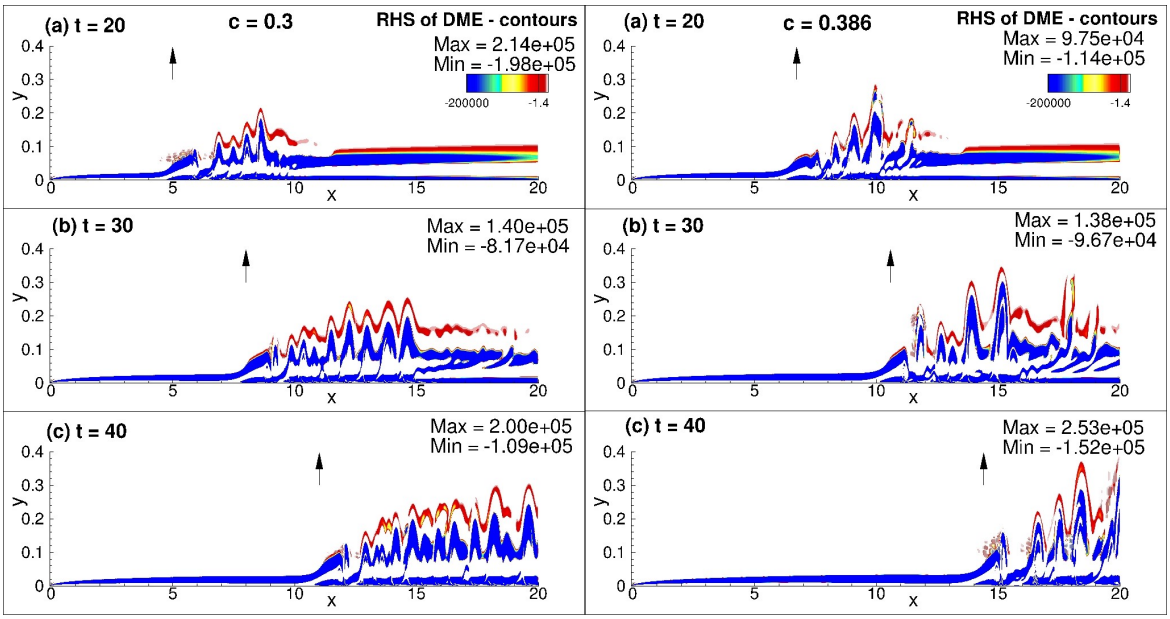

Fig. 6.11 Contours of right hand side of DME at indicated times for cases 2D1 and 2D2, at convecting speeds $c = 0.3$ and 0.386, respectively. Arrowheads at the top show the streamwise location of the convecting vortex.

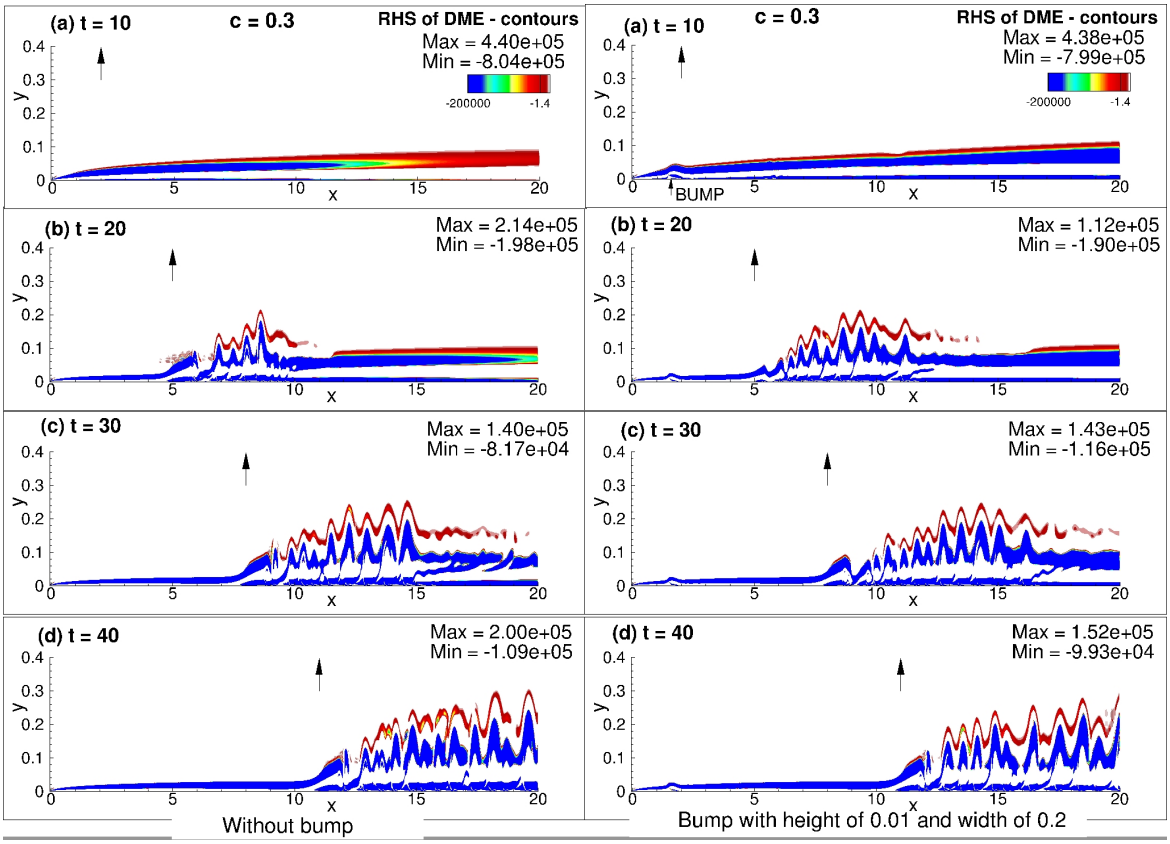

Fig. 6.12 Contours of right hand side of DME at indicated times for cases 2D1 and 2D3, at convecting speed $c = 0.3$, with and without the bump. Arrowheads at the top show the streamwise location of the convecting vortex.

(Hunt and Durbin, 1999). Despite the larger extent of outer source, it does not contribute to instability inside the shear layer. The major instability inside the shear layer originates near $x = 2.4$ (seen at $t = 20$) for case 2D3, which matches with the vorticity contours in Fig. 6.10. For case 2D3, it is noted that the wall source of disturbance has a longer streamwise extent due to the bump. Disturbance energy structures from these two sites start interacting early, and is seen in the frame at $t = 20$ for the 2D1 case, while these two disturbances remain distinct for the 2D3 case at this time. For the frame at $t = 30$, it is seen that these two sources of E_d interact for the 2D3 case, as well and from this time onwards, these two sources remain merged together.

6.4.3 Instability Mechanism Explained by DETE

The growth/decay rate of disturbance enstrophy (Ω_d) is determined by the vortex stretching terms given on the right hand side of Eq. (2.9) (derived in appendix B) inside the first set of curly brackets. These will not be present for 2D disturbance fields. The term that is identified as strictly dissipative term for enstrophy Ω_1, can contribute to growth of Ω_d, as shown by the last term on the right hand side. We note that, unlike Ω_1, Ω_d can be either positive or negative, as this is given as $(2\vec{\overline{\omega}}_m \cdot \vec{\overline{\omega}}_d)$.

Instability for Ω_d can arise for Ω_d being either positive or negative. The growth rate for positive Ω_d will indicate instability when $D\Omega_d/Dt > 0$, and for negative Ω_d, its amplitude will grow, when $D\Omega_d/Dt < 0$. These conditions are investigated in this section for vortex-induced instability affected by the presence or absence of 2D surface roughness.

In Figs. 6.13 and 6.14, the linearized growth rates of positive and negative disturbance enstrophy (Ω_d) are shown, respectively. This follows the linearized version of the DETE given by Eq. (B.10) in appendix B. In both these figures, a comparison is made between the test cases 2D1 and 2D2. The coloured regions indicate the regions where the condition for an instability are met. In Fig. 6.13, there are two sources for instability, one originating from the leading edge and lifting off into the free stream, and the other which originates from the wall. The structures observed for the test cases 2D1 and 2D2 are similar to the ones observed for DME in Fig. 6.11. The structures in the free stream are far more ordered for the test case 2D1, than those noted for the case 2D2. In Fig. 6.14, there is an oblong shaped instability structure arising from the leading edge and a series of smaller instabilities are noted away from the wall. A comparison between instabilities noted in Figs. 6.13 and 6.14, shows that the structures identified are complementary. In fact, the oblong negative instabilities lie above the leading edge positive instabilities while the near-wall instabilities for $\Omega_d > 0$ fill in the spaces beneath the instabilities for $\Omega_d < 0$, lifted off from the wall. For the test case 2D2, in Fig. 6.14 at $t = 40$, the instabilities lifted off from the wall penetrate

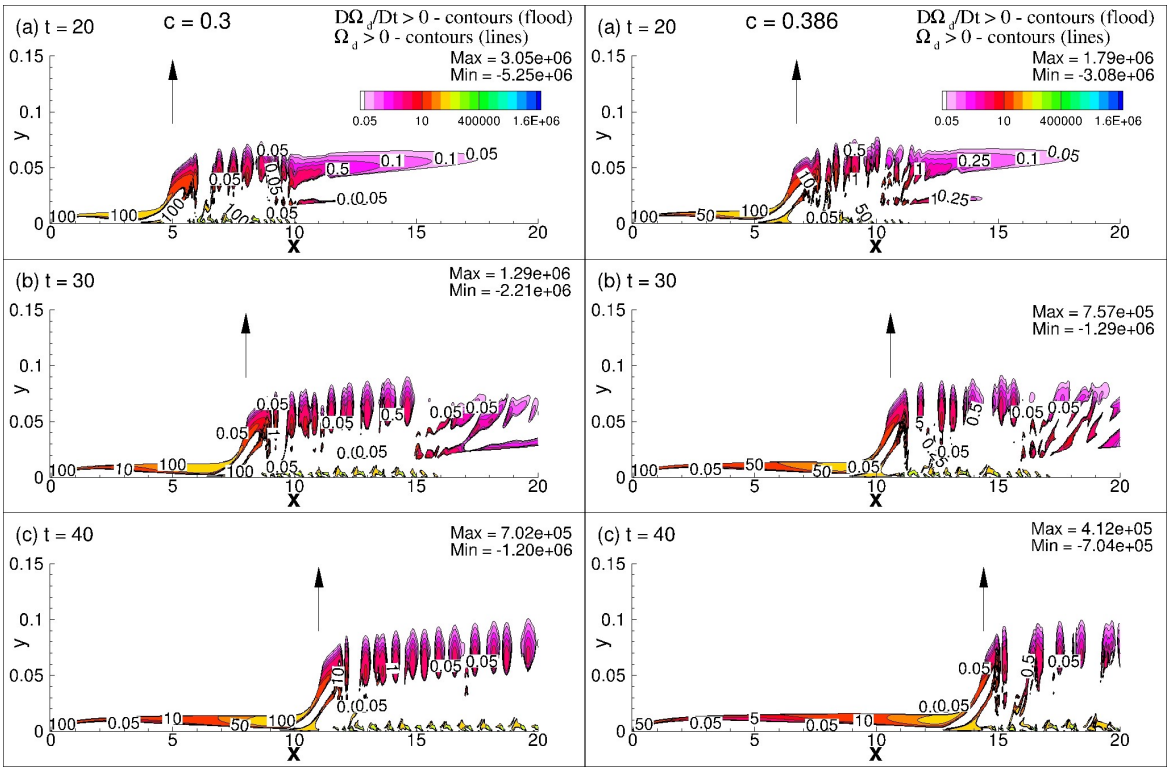

Fig. 6.13 Linearized growth rates of Ω_d are compared for test cases 2D1 and 2D2, for positive Ω_d at the indicated time instants for $c = 0.3$ and 0.386, respectively.

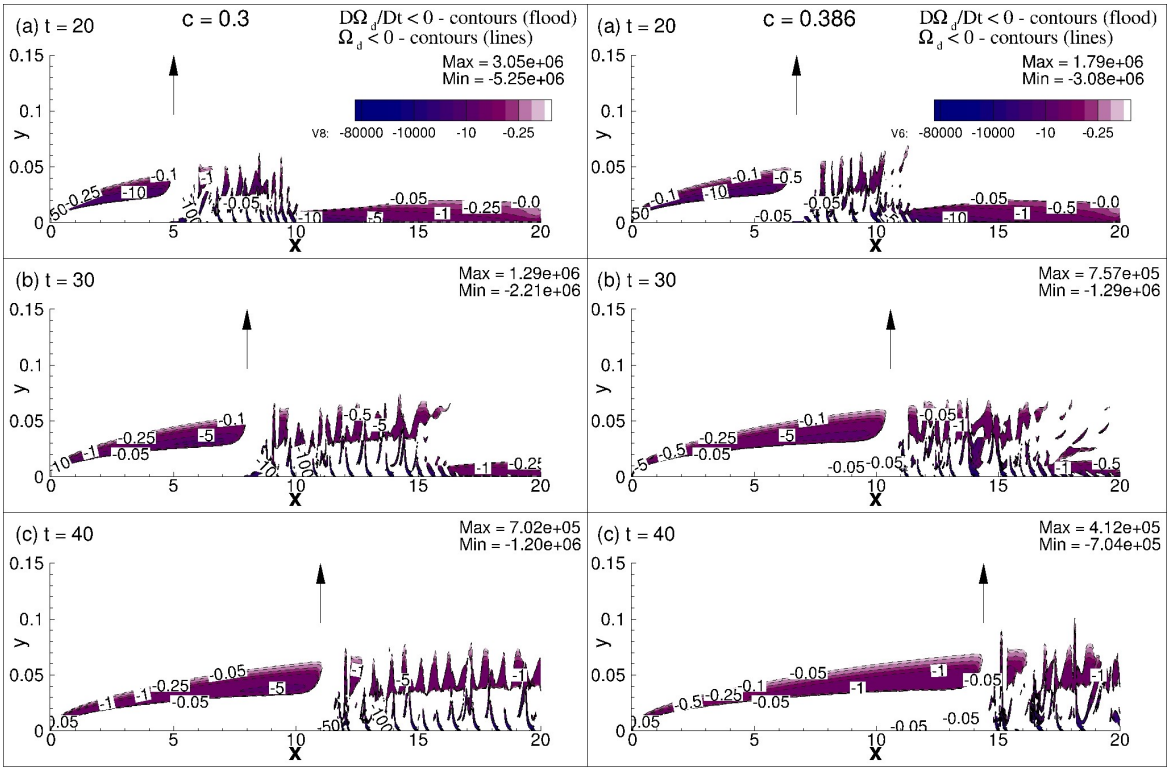

Fig. 6.14 Linearized growth rates of Ω_d are compared for test cases 2D1 and 2D2, for negative Ω_d at the indicated time instants for $c = 0.3$ and 0.386, respectively.

into the oblong structure arising from the leading edge, which is not seen for any frame for case 2D1.

In Figs. 6.15 and 6.16, the linearized growth rate contours of $D\Omega_d/Dt$ are plotted in the domain, for $\Omega_d > 0$, and for $\Omega_d < 0$, respectively for the test cases 2D1 and 2D3, for the convecting vortex with $c = 0.3$. This follows the linearized version of the DETE given by Eq. (B.10) in appendix B. In both these figures, the vortex-induced instability with and without the 2D surface roughness cases are compared. The region of instabilities are qualitatively different for the positive and negative values of Ω_d. It appears that the regions are complementary, i.e. where instabilities are noted for $\Omega_d < 0$, the same region indicates no instability for the case of $\Omega_d > 0$, and vice versa. For the positive values, disturbances originate outside the shear layer, and those are affected by the vortex-induced wall-normal eruptions, as shown for $t = 20$ for both the cases 2D1 and 2D3. As a consequence of these eruptions starting from the wall, the formation of oblong vortical structures is observed, as indicated by the disturbance enstrophy contours. At downstream locations, these vortical structures are followed by less strong horizontal streaky disturbance growth region. For the case of bump, this streaky region is more elongated. However by $t = 30$, the growth rates weaken for both the cases (as noted by the maximum value), but the oblong vortical structures are more numerous and the horizontal structures are punctuated by the formation of inclined growth regions. It is noted that the presence of wall bump reduces the growth in all the frames of case 2D3, as compared to the case 2D1. In the frame at $t = 40$, the maximum growth rates come down even further, and convection of vortical structures is observed. One significant difference for test case 2D3 with a bump is the creation of unsteady separation on the wall, immediately downstream of the physical bump and the region is elongated more with time. In Fig. 6.16 at $t = 20$, larger growth rates are seen near the wall, i.e. a predominance of wall mode as compared to the free-stream mode noted for $\Omega_d > 0$. With time, the wall modes are shown to eject vortical structures in the wall-normal direction, as seen at $t = 30$. By the later time, large growth rates are seen to be confined inside the shear layer, while the outer disturbances for later streamwise stations have smaller growth rates. In Figs. 6.15 and 6.16, the linearized growth rate contours are thus, seen to create multiple decks.

In Figs. 6.17 and 6.18, we show the nonlinear growth rates for positive and negative Ω_d, respectively for the test cases 2D1 and 2D3. This involves accounting for all linearized and nonlinear terms of $\Omega_d = 2\omega_m \cdot \omega_d + \omega_d \cdot \omega_d$. As we noted for the linear growth rates, here also we see similar qualitative features for the nonlinear growth rates. However, the nonlinear growth rates for disturbance enstrophy are significantly higher than the corresponding linear growth rates shown in Figs. 6.15 and 6.16. We note that the nonlinear growth rates for disturbance enstrophy are compatible with the computed vorticity contours, specifically

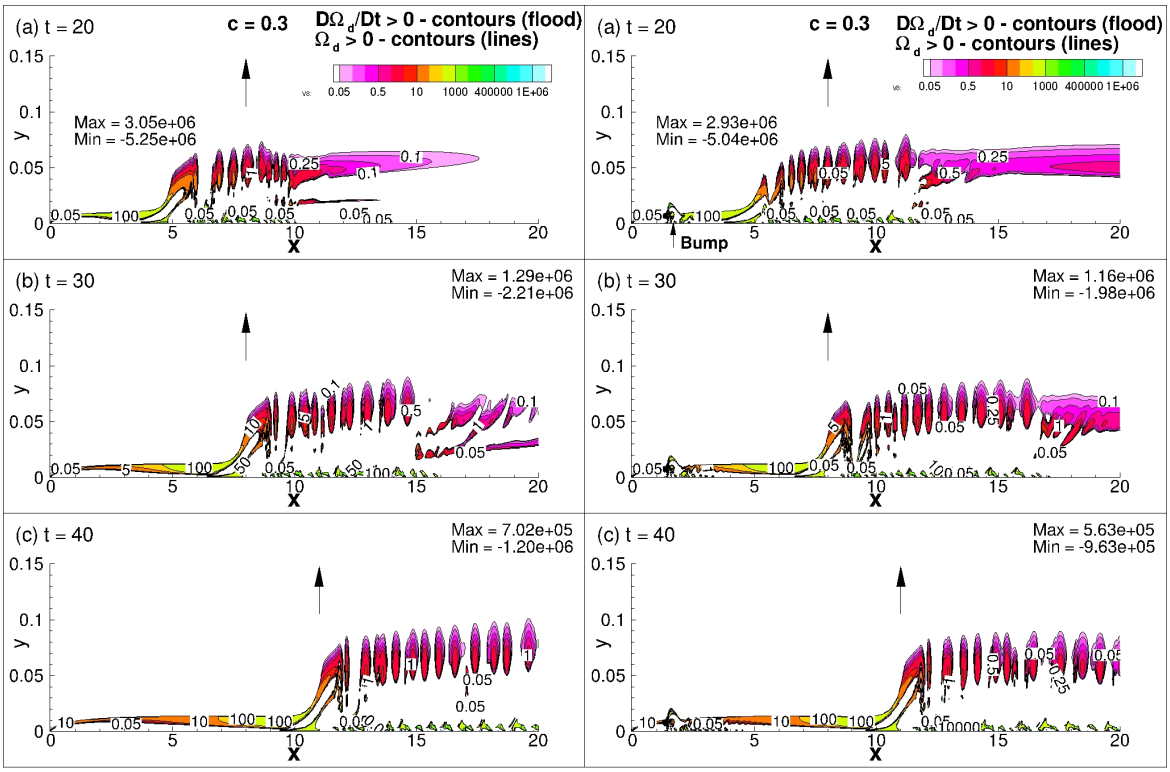

Fig. 6.15 Linearized growth rates of Ω_d are compared for test cases 2D1 and 2D3, for positive Ω_d at the indicated time instants for $c = 0.3$.

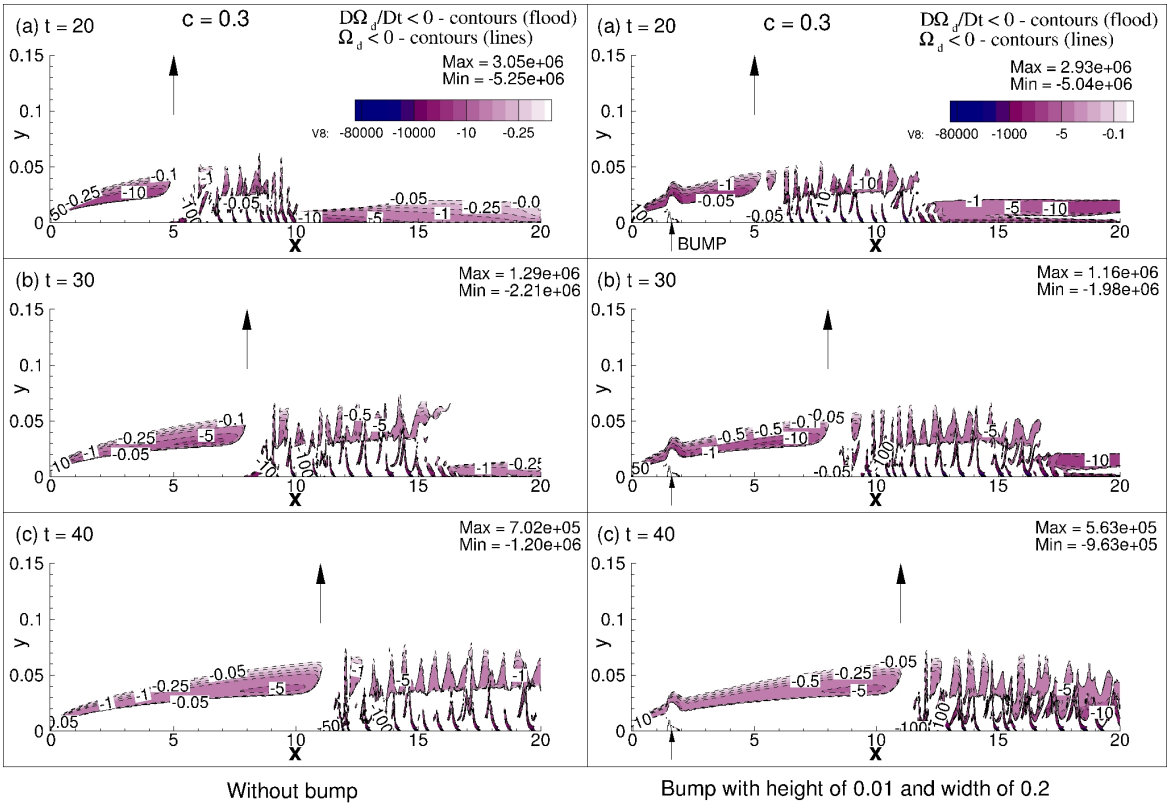

Fig. 6.16 Linearized growth rates of Ω_d are compared for test cases 2D1 and 2D3, for negative Ω_d at the indicated time instants for $c = 0.3$.

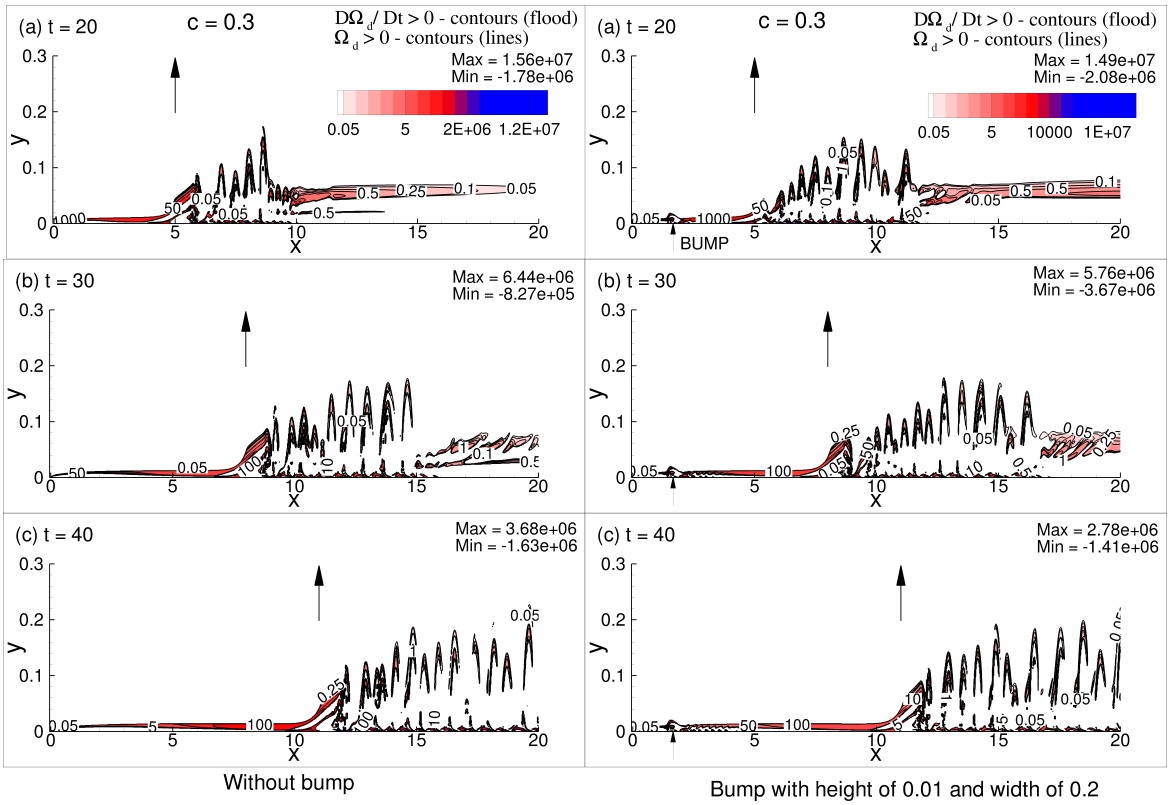

Fig. 6.17 Nonlinear growth rates of Ω_d are compared for test cases 2D1 and 2D3, for positive Ω_d at the indicated time instants for $c = 0.3$.

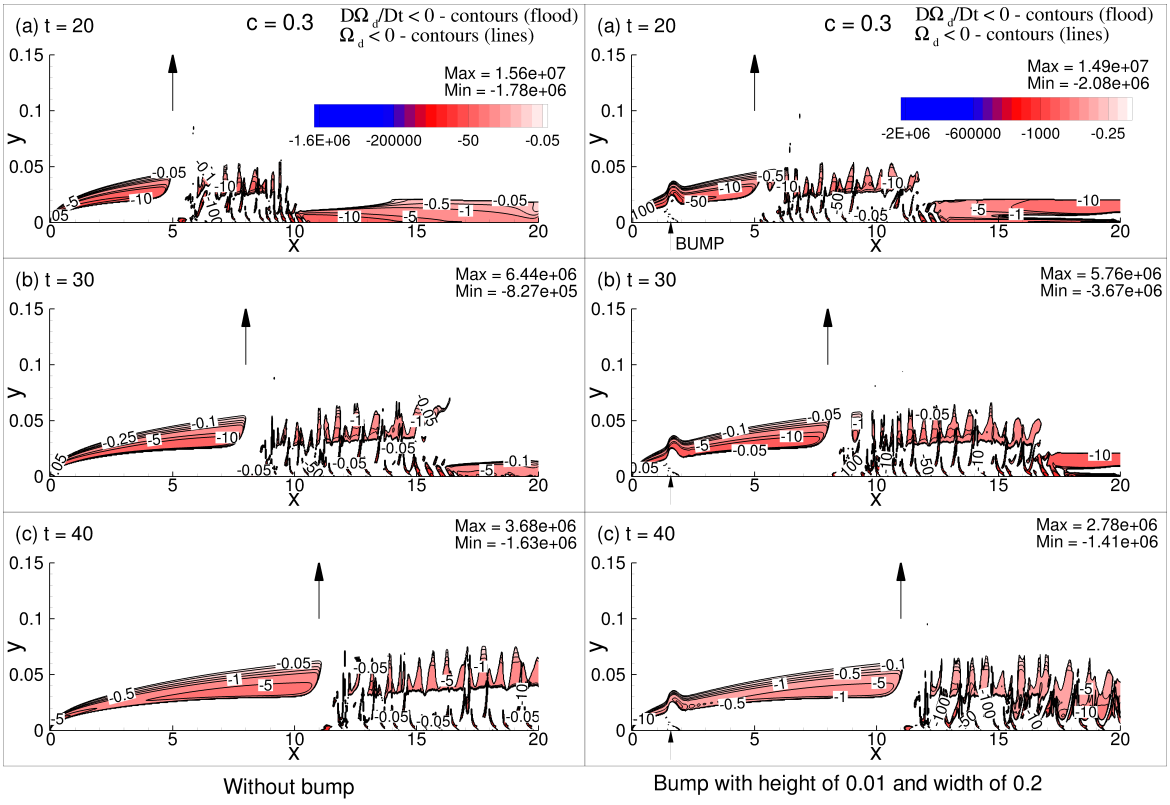

Fig. 6.18 Nonlinear growth rates of Ω_d are compared for test cases 2D1 and 2D3, for negative Ω_d at the indicated time instants for $c = 0.3$.

in capturing the vortical eruptions associated with the unsteady separation. This implies that nonlinear disturbance enstrophy equation provides a more accurate description of the instability while linearized equation provides a qualitative trend.

6.5 Characterizing the Flow Fields of 3D Vortex-Induced Instability

The differences among the flow fields depicted in Figs. 6.3 to 6.5 can be explained with the help of sketched inviscid streamlines for the case of counter-clockwise and clockwise vortex in Fig. 6.19, as created by the convecting free-stream vortex. These are the streamlines in the inviscid part of the flow, which are created by the rotating and translating cylinder for both the cases of rotation direction. The straight line at the bottom depicts the flat plate and in frame (a), the stagnation points are located below the mid-plane for the case of clockwise rotating vortex. The flow enclosed between the stagnation streamline and the flat plate, suggests that the imposed pressure gradient is favourable, ahead of the finite core vortex. While the flow upstream of the vortex experiences milder adverse pressure gradient, with maximum streamline divergence just behind the vortex. These regions of adverse pressure gradient are marked in both the frames by cross hatches. One can perform the Fourier transform of the wall-normal velocity, and the spectrum is shown on top of the streamline plots. For the clockwise rotating case shown in frame (a), two regions of adverse pressure gradient are indicated: one behind the cylinder and the other region is just below the cylinder in the front part of it. For the case of counter-clockwise rotation, adverse pressure gradient is noted in the front half of the region below the cylinder.

For the counter-clockwise rotating case shown in frame (b) of Fig. 6.19, the streamline divergence downstream of the cylinder is more pronounced, than that is noted for the clockwise rotating vortex case in frame (a). Thus, the imposed adverse pressure gradient downstream of the counter-clockwise rotating vortex creates a significantly stronger effect that leads to higher disturbance growth, and this is the key to the vortex-induced instability cases reported in Lim et al. (2004). This finding is also consistent with the 2D computational results reported by Sengupta et al. (2003). The corresponding Fourier spectrum of the wall-normal velocity on top of frame (b) corresponds to the case of Figs. 6.3 and 6.4. The spectrum in this case is significantly broadband, as compared to the clockwise rotating case of frame (a). In both the cases, the zero wavenumber component are almost the same, and the lower wavenumber cases of counter-clockwise cases impose significantly stronger adverse pressure gradient, leading to vortex-induced instability. In the next section, we present

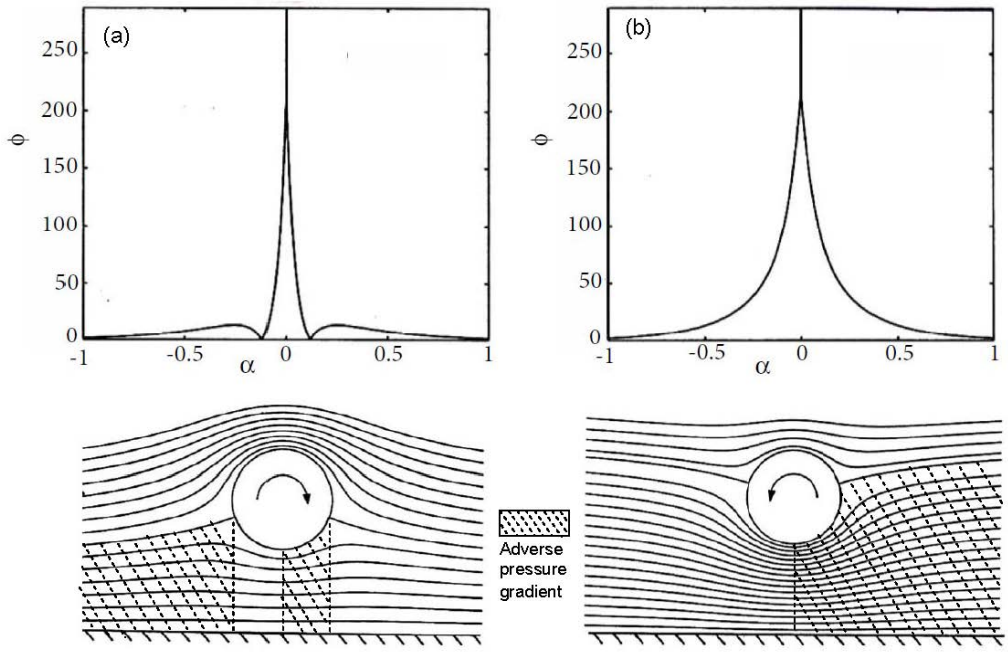

Fig. 6.19 Spectrum of induced flow field (top) and streamlines for translating and rotating cylinder obtained by potential flow model (bottom) for a) clockwise rotating vortex and b) counter-clockwise vortex.

the computed 3D flow field by DNS and provide detailed events leading to vortex-induced instability.

6.6 3D Stage of Vortex-Induced Instability

Some preliminary results for the spanwise vorticity have been shown at selected spanwise planes and times, by solving the 3D receptivity case of the convecting counter-clockwise vortex case with $c = 0.3$ and $\Gamma = 2$ in Sengupta et al. (2018a). The results have clearly shown the primary and secondary vortices forming, with strong similarity with the 2D computational results at early times. In the following, we show computed 3D results for the cases shown in Figs. 6.3 to 6.5. As the free-stream vortical excitation is 2D, the response field reveals the flow field to be 2D during the onset of primary and secondary stages of vortex-induced instability. Similar behavior was recorded also in the experiments by Lim et al. (2004), and some representative results have been shown in Figs. 6.3 to 6.5. The 2D response field becomes 3D as time progresses, by the action of the vortex stretching term of the enstrophy budget, as explained in Sengupta et al. (2019a, 2018a). The transformation of the response field from 2D to 3D stage is explained next.

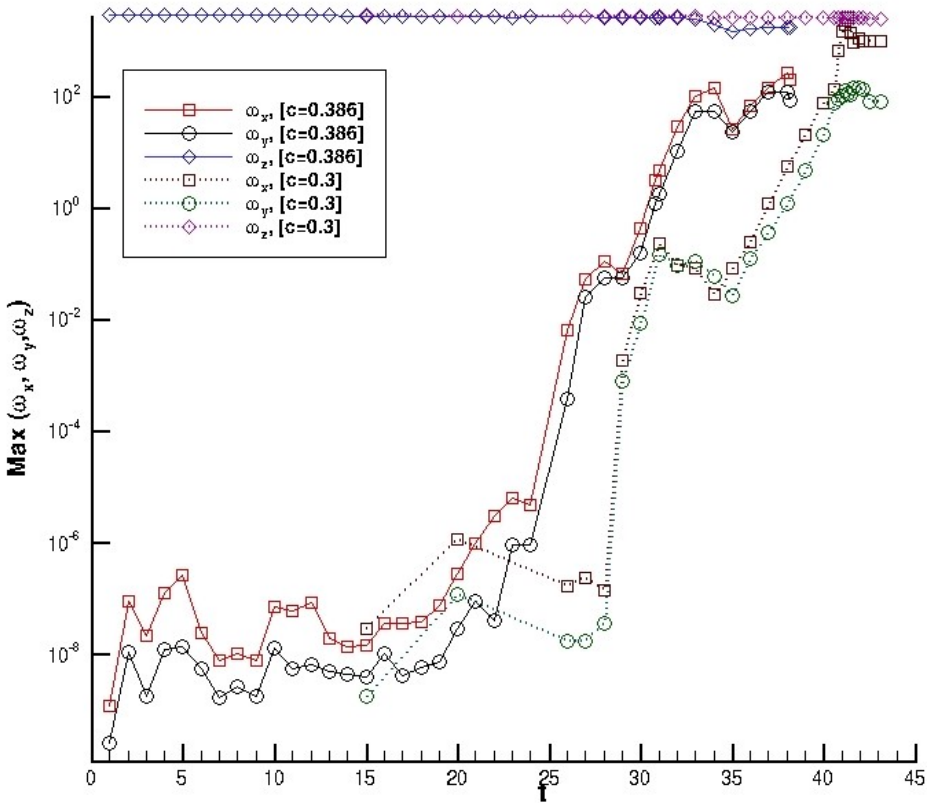

Fig. 6.20 Maximum vorticity components in the flow as function of time, for the test cases 3D1 and 3D2.

6.6.1 Evolution of Three-Dimensionality during Vortex-Induced Instability caused by 2D Free-Stream Vortical Disturbance

In Fig. 6.20, the absolute value of vorticity components, as obtained by solving NSE for the test cases 3D1 and 3D2 with $\Gamma = 2$ and $c = 0.3$, $c = 0.386$, are compared. It is noted that both the convection speed cases are equally receptive to vortex-induced instability by the convecting free-stream vortex. The application of 2D excitation creates a 2D response field initially, as ω_x, ω_y are seen to have values which are eleven orders of magnitude smaller than ω_z (spanwise vorticity). Interestingly, even when the streamwise and wall-normal components of vorticity rapidly grow, ω_z retains the same value for both the convection speed cases. Thus, the evolution from 2D to 3D disturbance field is noticeable more with respect to the streamwise and wall-normal components of vorticity, and not the spanwise component, which remains virtually invariant with time.

For both the cases 3D1 and 3D2, the streamwise and wall-normal vorticity components are seen to grow by more than six orders of magnitude during a small interval of time due

to the presence of vortex stretching term in the vorticity transport equation. This vortex stretching stage is followed by a further growth, but at a lower rate during the phase of three-dimensionalization. This is graphically seen in Figs. 6.21 to 6.24 for test cases 3D1 and 3D2, where a single iso-contour of ω_z is shown at the indicated times. The iso-contours are coloured with ω_y, whose colour map is shown in the top frames in these figures.

In Figs. 6.21 and 6.22 the iso-contours of $\omega_z = -13$ are plotted during the primary and secondary instabilities. In Fig. 6.21, the onset of primary instability is observed in the frame at $t = 16$, where the free-stream convecting vortex is located at $x_{cv} = 5.176$, while the disturbance field is noted to be 2D (without any spanwise variation), and a bubble-like structure is noted between $x = 6$ and 8. The $\omega_z = -13$ iso-contour is coloured with ω_y in the range of -18.1339 to +16.0874. Absence of any spanwise variations in the other two frames at $t = 24$ and 25 also testifies the 2D nature of the perturbation field. With time, the iso-contour of ω_z shows the evolution of the spanwise vorticity at early times, even though the maximum value of this component is shown to be invariant in Fig. 6.20 for a long time, while the other two components start growing from completely negligible to significantly higher values.

In Fig. 6.22 for the frame at $t = 28$, quasi-2D nature of the flow is maintained. At the same time, mild spanwise variation is noted in the form of faint streamwise streaks, along with very coherent ω_z contours, which are lifted off from the boundary layer. In the next frame at $t = 34$, one can not only see the growth of primary instability, but also a secondary instability with spanwise variation, with varying strength of instability in the streamwise range of $x = 12$ to 15. The evolution of two distinct sites, over which vortex-induced instability is formed, is observed at this time, centered at $x = 13$ and $x = 14$. In the bottom frame of Fig. 6.22, the interaction and amalgamation of these two sites into a single strong and longer perturbed region is observed. The effects of evolving perturbation field can also be seen to move upstream of the location of the free-stream vortex at $x = 13.668$. From the frames at $t = 35$ to 38 (not all shown), it is observed that the maximum ω_z is about 30 times larger as compared to the maximum ω_x at $t = 35$, and by $t = 37$, this ratio reduces to about 12 times. This flow is still in transitional stage, with progress towards homogenization of the vortical components by the action of further vortex stretching and diffusion mechanisms.

Another case has been computed for a reduced convection speed of $c = 0.3$ with $\Gamma = 2$, to show the similarity with the vortex-induced instabilities shown in Figs. 6.21 and 6.22. In Figs. 6.23 and 6.24 the iso-contours of $\omega_z = -13$ are plotted for primary and secondary instabilities, for $c = 0.3$ case. In Fig. 6.23, one again observes the primary stage of vortex-induced instability, with the position of free-stream convecting vortex indicated by x_{cv}.

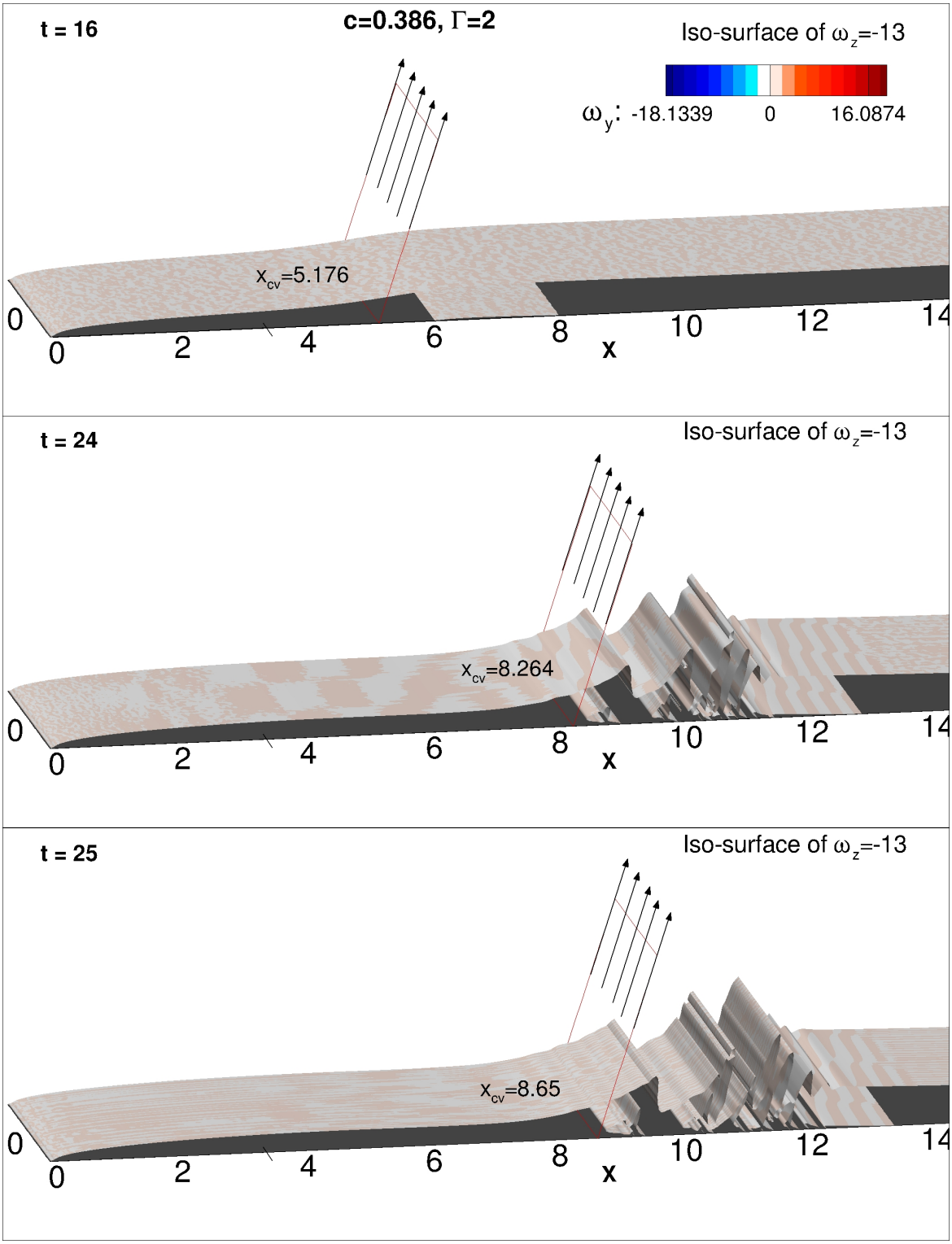

Fig. 6.21 Iso-contours of ω_z at times $t = 16$, 24 and 25, for the test case 3D2. The vortex strength is given by $\Gamma = 2$.

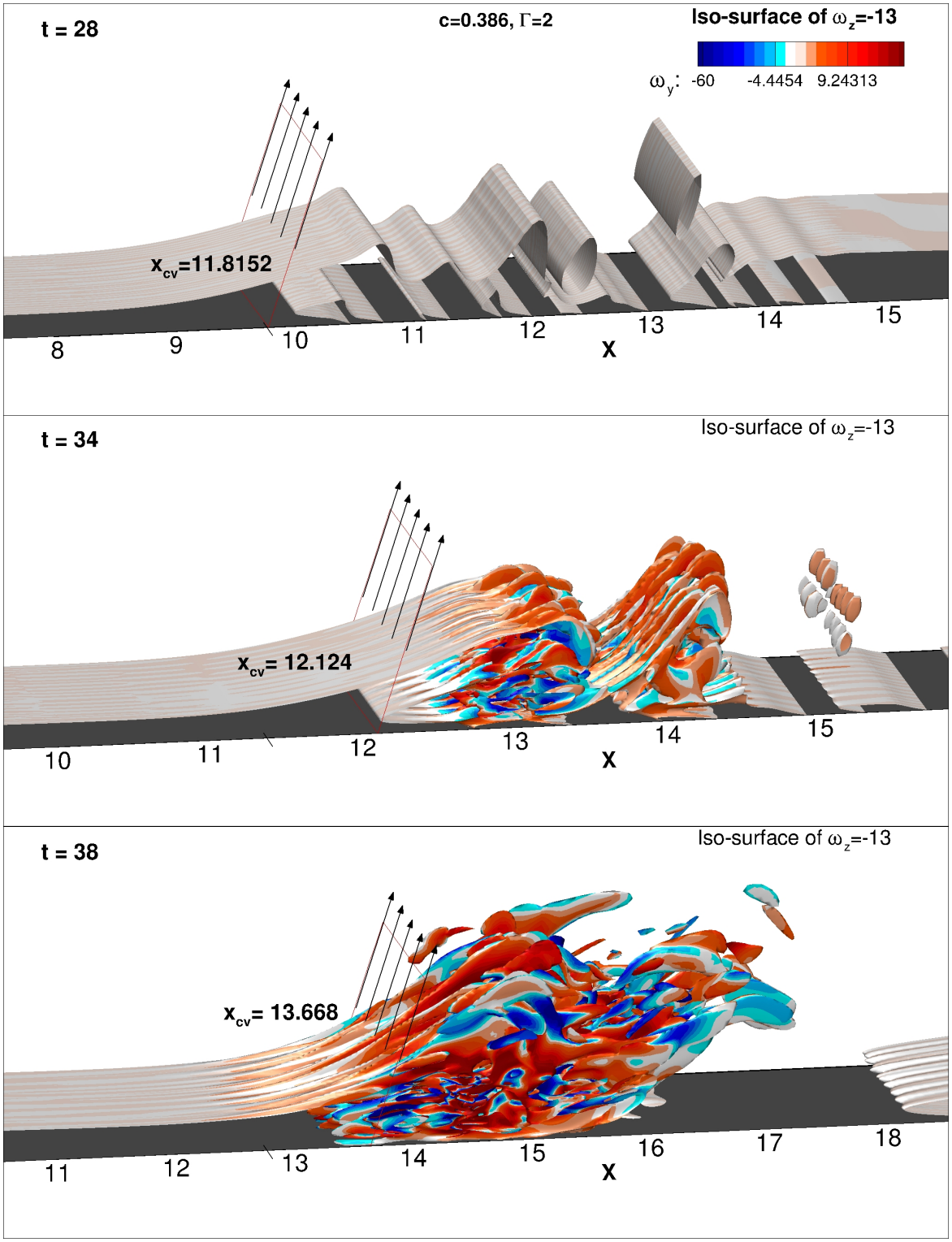

Fig. 6.22 Iso-contours of ω_z at times $t = 28$, 34 and 38, for the test case 3D2. The vortex strength is given by $\Gamma = 2$.

The disturbance field is noted as 2D, without perceptible spanwise variation. In the top frame at $t = 26$ an elongated primary vortex is attached to the wall, while another vorticity sheet originating from the leading edge remains always outside the shear layer. Such an isolation of free-stream vortical sheet from the boundary layer has been termed as shear sheltering (Hunt and Durbin, 1999). While this is always observed experimentally, to capture it computationally, the domain must include the leading edge of plate, as has been emphasized by Bhaumik and Sengupta (2014) and Sengupta et al. (2003) while reporting receptivity computations. The ω_z iso-contour is again coloured with ω_y in the range of -18.1339 to +16.0874, in these time ranges. With further increase in time, the iso-contour of ω_z develops folds via stretching, along with induced separation bubble on the plate. In the bottom frame at $t = 31$, two clean vortical rolls are lifted off the shear layer.

In Fig. 6.24 for the frame at $t = 39$, quasi-2D nature of the flow is still maintained, although the spanwise variation has become very prominent. Spanwise variation is noted in the form of streamwise streaks, along with very coherent ω_z contours which are lifted off from the boundary layer. In the next frame at $t = 42.15$, one can not only see the growth of the two rolls, noted at $t = 31$ and 39 as the leading 3D vortical structures, but also there is a second trailing 3D packet, whose upstream end is seen to extend beyond the location of the free-stream convecting vortex. The evolution of two distinct sites over which vortex-induced instability is formed, is observed at this time, centered at $x = 13$ and $x = 14$. Such primary and secondary instabilities are also noted in experimental visualization of Fig. 6.3 for the test case 3D2. However, distinct turbulent spot-like packets are observed in this lower convection speed case, as compared to the case 3D2 shown in Fig. 6.22, where the vortical packets merge together. The effects of evolving perturbation field can also be seen to move upstream of the location of the free-stream vortex at $t = 43.1$.

In Fig. 6.20, we have noted the evolution of maximum value of the vorticity components with time. This provides a global view about how the nominally 2D equilibrium flow (even though calculated using the 3D NSE) under the influence of 2D free stream excitation becomes 3D. However, one would be interested to know how the other two components, ω_x and ω_y, grow from negligible values to values comparable to ω_z. The flow is treated as periodic, and hence one would expect symmetry or anti-symmetry of the computed flow field in the spanwise direction.

In Fig. 6.25, we show the contour plots of ω_x and ω_y (labelled as ω_1 and ω_2) in the $(z = 0)$-plane at the indicated times for the case of $\Gamma = 2$ and $c = 0.386$. While the streamwise location of the free stream vortex is marked by a vertical arrow, the maximum and minimum values of the plotted quantities are also noted in each frame. We have also checked the contours for $(z = \pm 0.4)$-planes for symmetry or antisymmetry of the flow in the spanwise

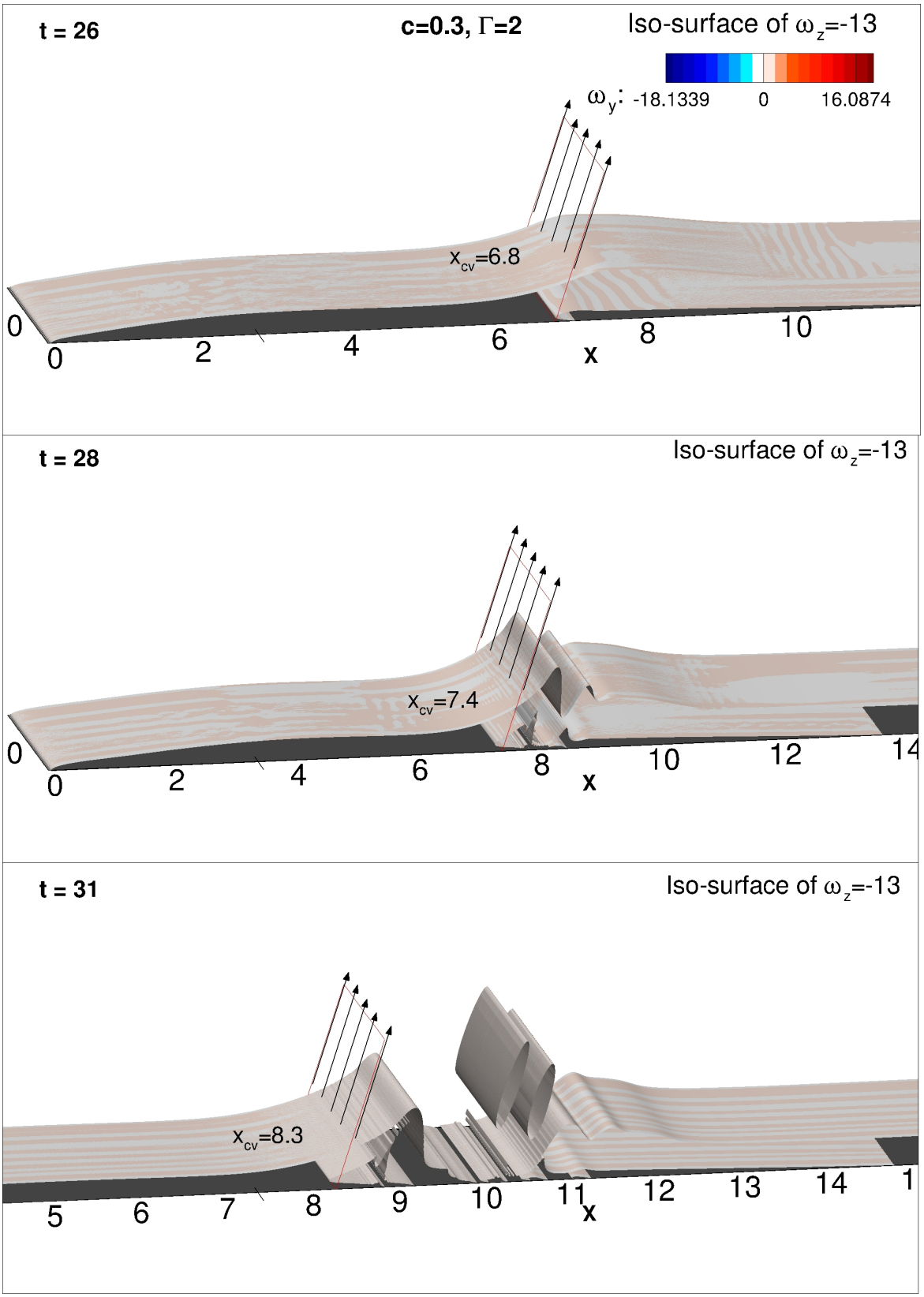

Fig. 6.23 Iso-contours of ω_z at times $t = 26$, 28 and 31, for the test case 3D1. The vortex strength is given by $\Gamma = 2$.

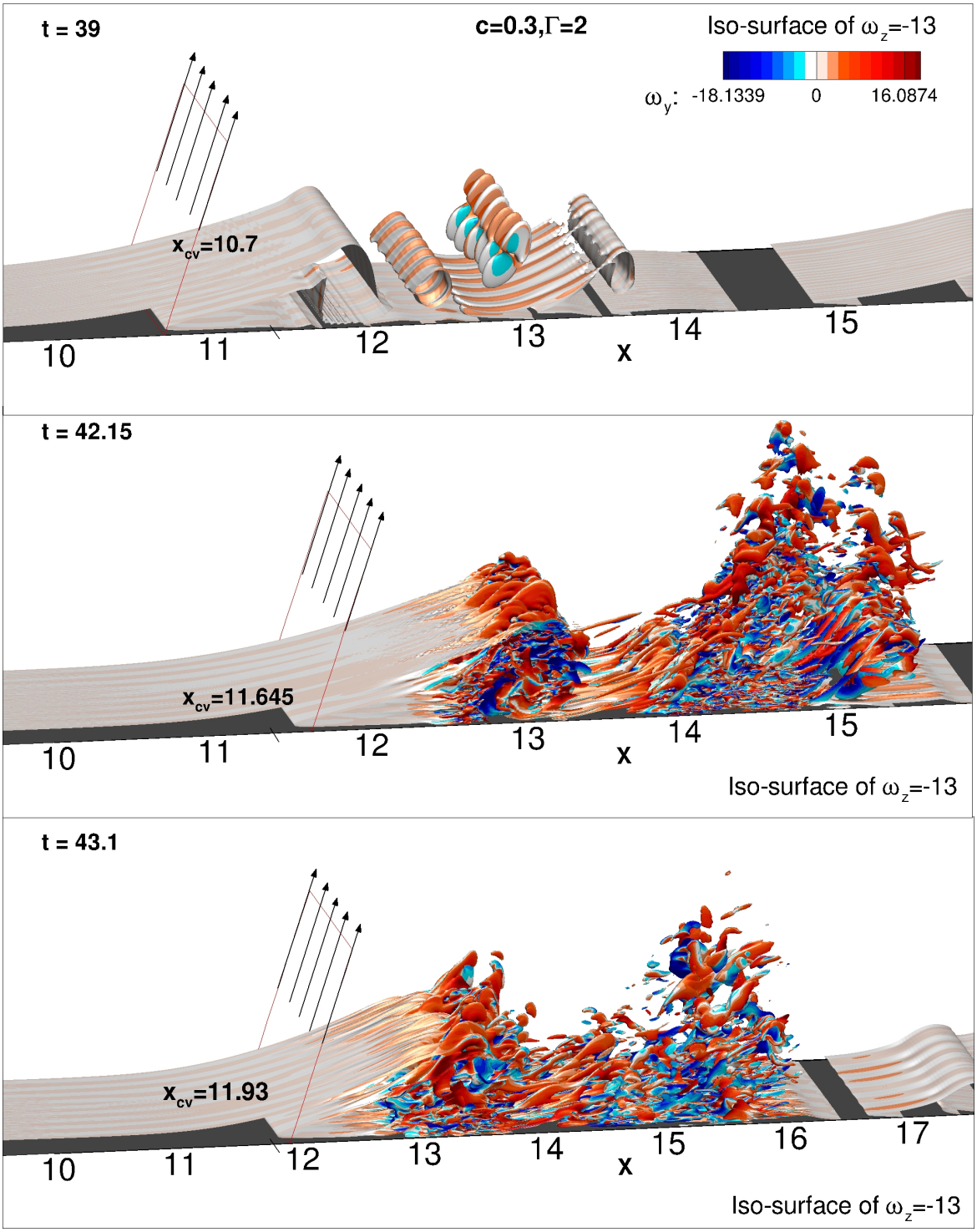

Fig. 6.24 Iso-contours of ω_z at times $t = 41$, 42.15 and 43.1, for the test case 3D1. The vortex strength is given by $\Gamma = 2$.

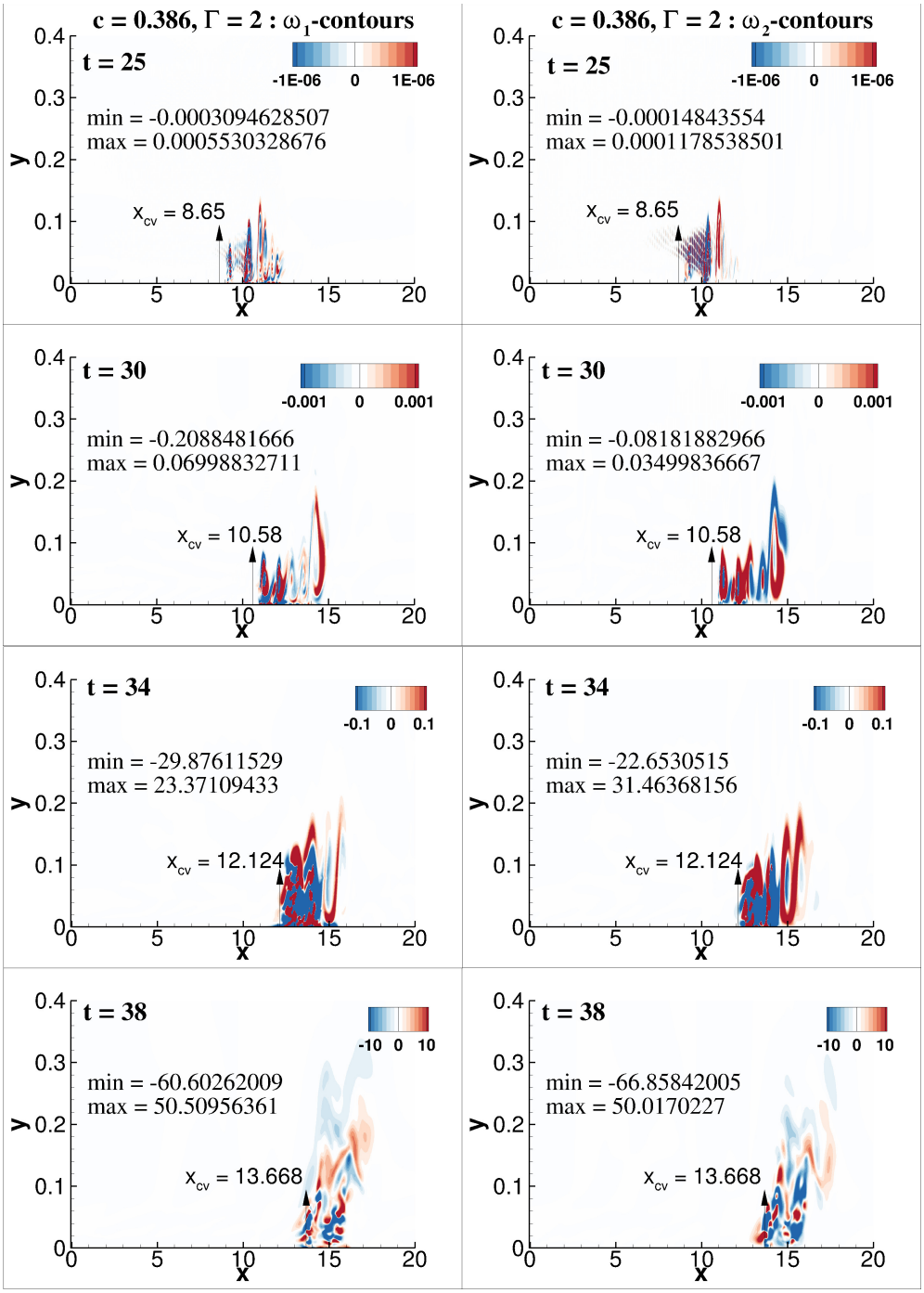

Fig. 6.25 Contours plotted in $z = 0$-plane, for ω_x (left) and ω_y (right) at $t = 25$, 30, 34 and 38, for the case of $\Gamma = 2$ and $c = 0.386$. The free stream vortex x-location is shown by the vertical arrowhead and value given by x_{cv}. Also, indicated are minima and maxima values for each frame for both the components.

direction (not shown here). From Fig. 6.25, the following attributes of 3D nature are noted: (i) The primary instability noted at early times is strictly 2D, that leads to formation of unsteady separations, which accumulates into two rolls, as seen in Figs. 6.21 and 6.22. These two rolls in the advanced stage, appear as the spatio-temporal wave front (STWF) reported in Sengupta et al. (2006a) for wall excitation cases; (ii) There is asymmetry of the flow in the spanwise direction, only in the secondary stage of instabilities shown in Figs. 6.21 and 6.22. With the use of periodic boundary condition in the z-direction, such asymmetry indicates nonlinearity during the secondary instabilities; (iii) In Fig. 6.20, streamwise component of vorticity is seen to be more than the wall-normal component; (iv) The locations where the three-dimensionality is manifested with non-negligible values are seen to be highly localized, which originated in two primary unstable rolls noted above; (v) The unstable regions formed ahead of the free stream vortex, relax back to unperturbed state after the free stream vortex has passed over it; (vi) The two sites which appear as STWF are created due to vortex-induced instability. Despite the vortical eruptions, the locations where ω_x and ω_y are minimum and maximum are always near the wall. For the four time instants shown in Fig. 6.25, the minima and maxima are given in Table 6.2.

In Table 6.2, the streamwise and wall-normal locations, where the minimum and maximum values of ω_x and ω_y occur, are given for different times. One notes that the minima and maxima are usually located very near to the wall. Another point to be noted is that the locations of minimum and maximum at $t = 25$ and 30 are further downstream of instantaneous streamwise vortex location. These are during the primary stage of instability seen in Fig. 6.21. In fact, the vortex roll up seen in Fig. 6.22 at $t = 25$ corresponds to the location of minimum and maximum. However, at later times ($t = 34$ and 38), which fall in the secondary instability stage, one notes that the location of minima/maxima relative to instantaneous streamwise vortex location is not as downstream as seen at earlier times.

Table 6.2 The location of maximum and minimum values of ω_x and ω_y with time

Time		ω_x		ω_y	ω_y	ω_y
		Minimum	Maximum	Minimum	Maximum	
25	x	10.2527	10.2229	10.26600	10.26612	
	y	0.00580	8.822×10^{-5}	0.048688	0.01393	
30	x	12.084	11.996	12.722	12.0614	
	y	2.78×10^{-5}	8.39×10^{-6}	0.0335	0.037762	
34	x	13.05615	12.87140	13.2086	12.841366	
	y	6.4718×10^{-6}	1.2142×10^{-5}	0.03874	0.005945	
38	x	13.8355005	13.77099	13.7302	13.68795	
	y	0.050906363	0.0544398	0.04946	0.02206	

6.6.2 Counter-clockwise Vortex of Strength $\Gamma = 0.5$, Convecting with $c = 0.77$

In Fig. 6.26, the iso-surfaces of $\omega_z = -13$ and -24 coloured with ω_y of very small values compared to those in Figs. 6.21 to 6.24, are shown at $t = 11$, 15, 20, 25 and 27 for the test case 3D6. The chosen time range is such that the last frame corresponds to when the free-stream vortex is very near to the exit-plane of the computational domain. The higher convection speed ($c = 0.77$), induces significantly weaker displacement and circulatory effects on the 2D excitation field, and only the mild undulation of the iso-surface is noted in the frame at $t = 20$, which remains perfectly invariant in the spanwise direction. This implies that the created disturbances are essentially 2D. This is also verified by the noted maximum values of ω_x and ω_y, as compared to the maximum values of the higher receptivity cases 3D1 and 3D2. In the top frame at $t = 11$, the fold in the contour for $\omega_z = -24$ is ahead of the location of the convecting vortex, while the maximum bulge is slightly upstream of the convecting vortex. In the subsequent frames at $t = 25$ and 27, the convecting free-stream vortex outstrips the fold of the $\omega_z = -24$ iso-surface. However, the perturbation imposed via the adverse pressure gradient is insignificant and does not lead to even a visible primary instability. Thus, for this case, there is a weak 2D perturbation field for the weak convecting free-stream vortex.

6.6.3 Clockwise Vortex of Strength $\Gamma = 0.5$, Convecting with $c = 0.19$

With reference to Fig. 6.5(b), we have noted for the case of $c = 0.19$ and $\Gamma = -0.5$, that the vorticity field remains invariant in the spanwise direction up to $t = 104$, when ω_z contours coloured with ω_y are plotted. Hence, for this lower strength convecting vortex case, the flow does not evolve to a 3D field within the computed domain. This is also noted from the experimental snapshots shown in Fig. 6.5(a), where the dye streak is predominantly lifted up in its own plane without spanwise convection or diffusion.

6.7 3D Nature of Vortex-Induced Instability Explained from DETE

Apart from the quantitative description of three-dimensionalization from the computed 3D NSE given in the previous section, another alternative is to study the enstrophy transport equation developed in Sengupta et al. (2018a). This has been attempted for the 3D vortex-induced instability in Sengupta et al. (2019a).

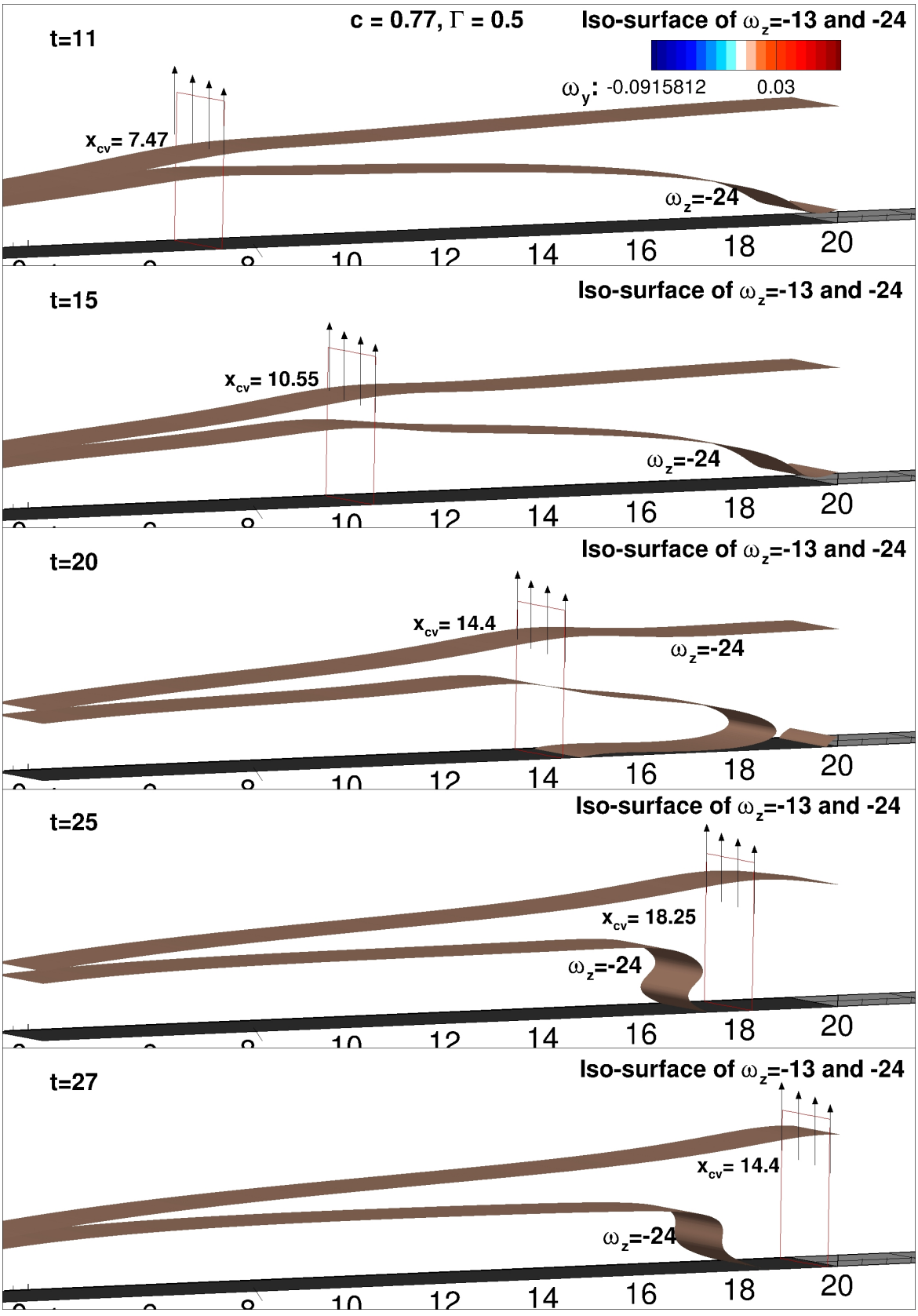

Fig. 6.26 ω_z iso-contours at indicated times for case 3D6 at convecting speed $c = 0.77$ and vortex strength $\Gamma = 0.5$.

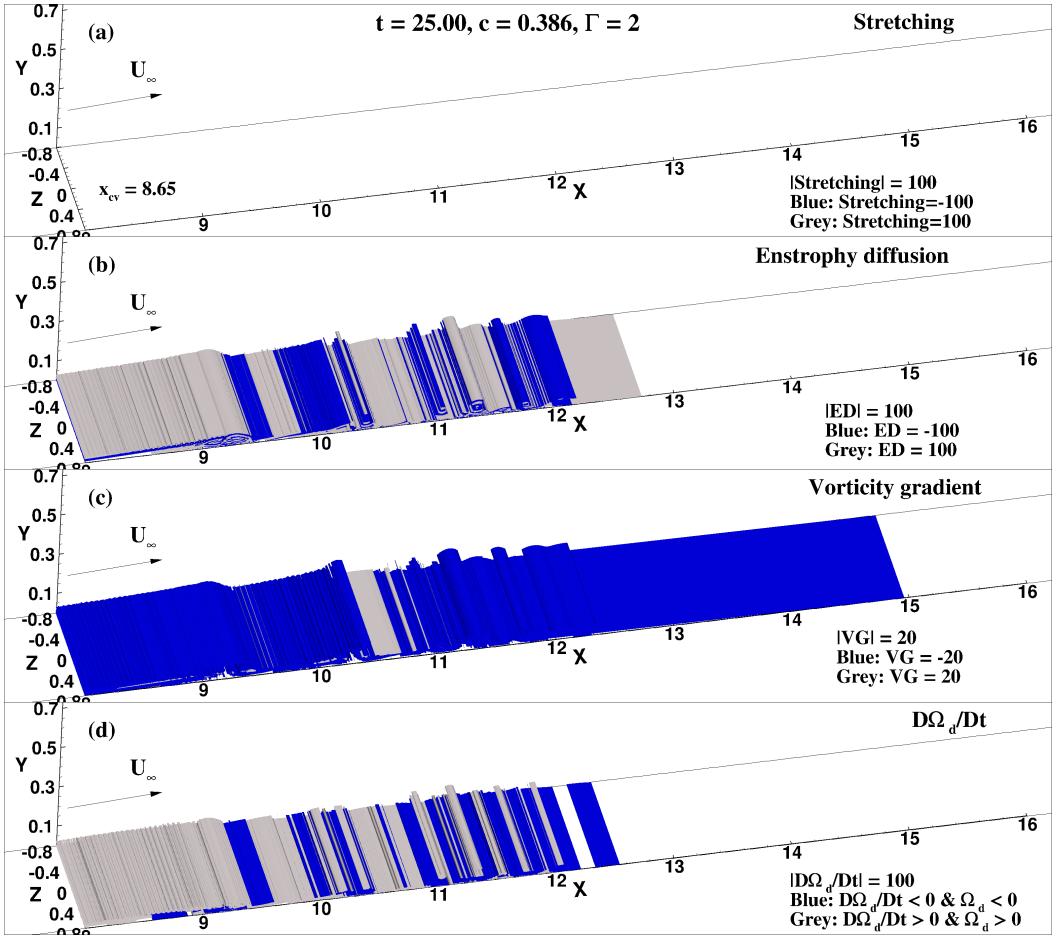

Fig. 6.27 Perspective plots for DETE budget terms at $t = 25$, with the top frame showing contribution from vortex-stretching (Term1); the second frame showing the contribution originating from enstrophy diffusion (Term2) and the third frame showing contribution from dissipation (Term3). In the bottom frame, the dark (blue) regions are where negative Ω_d become more negative and light (gray) regions are where positive Ω_d become more positive for free-stream vortex with $\Gamma = 2$ and $c = 0.386$ located at x_{cv}.

In Fig. 6.27, the DETE budget is shown at $t = 25$, as given by Eq. (2.9), for growth rate of Ω_d. It is readily evident from the bottom frame that the flow is unstable in 2D, with no spanwise variations. The middle two frames (Term2 and Term3 of Eq. (2.9)) taken together indicate the instability to be contributed by viscous diffusion, as the Term1 (due to stretching) is absent. We note that the viscous diffusion term in the NSE contributed by Term2 and the term due to vorticity gradient (Term3), can be either positive or negative, indicating that this can be dissipative or contribute to instability. Thus the primary instability, as indicated by this figure, is essentially due to the 2D mechanism for vortex-induced instability of viscous diffusion.

Figure 6.28 shows the DETE budget at $t = 30$, with the growing instability indicated by increasing magnitude of Ω_d. Due to spanwise periodicity of the flow in the domain, disturbance growth due to vortex stretching originates from the domain boundary in the spanwise direction. However, Term2 and Term3 originating from enstrophy diffusion and dissipation show 2D structures. This 2D mechanism predominantly lifts the disturbances above the plate surface, while the disturbance growth due to stretching at this time is seen to be located primarily near the surface. These two complementary natures of disturbance growth are shown in the bottom frame at $x > 11$.

Figure 6.29 shows the evolution of three-dimensionality with the help of DETE budget at $t = 34$. As compared to the events at $t = 30$, here the vortex stretching term is seen to be clustered around $x = 13$ and 14, which are lifted off the plate surface, whereas the advancing front ($x > 15$) is still attached to the wall, as noted in the top frame. Since the flow has become 3D, corresponding contributions originating from Term2 and Term3 of Eq. (2.9) also exhibit three-dimensionality around these two locations. Noticeably, the spanwise scales at these two sites are finer for these two terms as compared to the stretching contribution. As a consequence, the instability patterns noted in the bottom frame indicates the 3D instability in the trailing part, behind the leading instability which is dominated by 2D mechanism.

Figure 6.30 shows the DETE budget at $t = 38$, where one notes very strong contributions coming from vortex-stretching, which lifts off near the advancing front. This is mirrored in the growth rate of Ω_d shown in the bottom frame, indicating the major role played by vortex-stretching in causing the instability at this time. The spanwise length scales associated with the stretching term are distinctly different near the leading front, as compared to finer scales at upstream locations. A complementary picture is seen for the growth rate of Ω_d shown in the bottom frame. For the contributions originating from Term2 and Term3 in Eq. (2.9), one notes however, finer spanwise length scales.

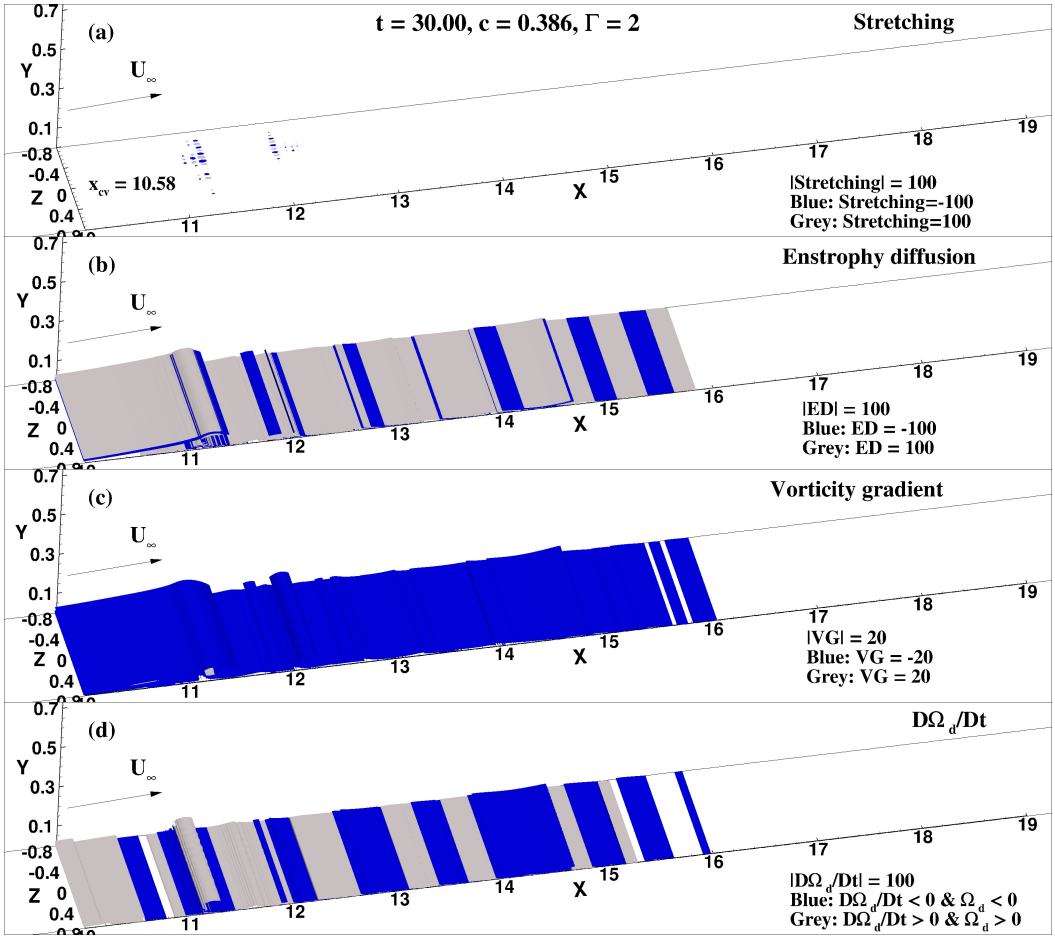

Fig. 6.28 Perspective plots for DETE budget terms at $t = 30$, with the top frame showing contribution from vortex-stretching (Term1); the second frame showing the contribution originating from enstrophy diffusion (Term2) and the third frame showing contribution from dissipation (Term3). In the bottom frame, the dark (blue) regions are where negative Ω_d become more negative and light (gray) regions are where positive Ω_d become more positive for free-stream vortex with $\Gamma = 2$ and $c = 0.386$ located at x_{cv}.

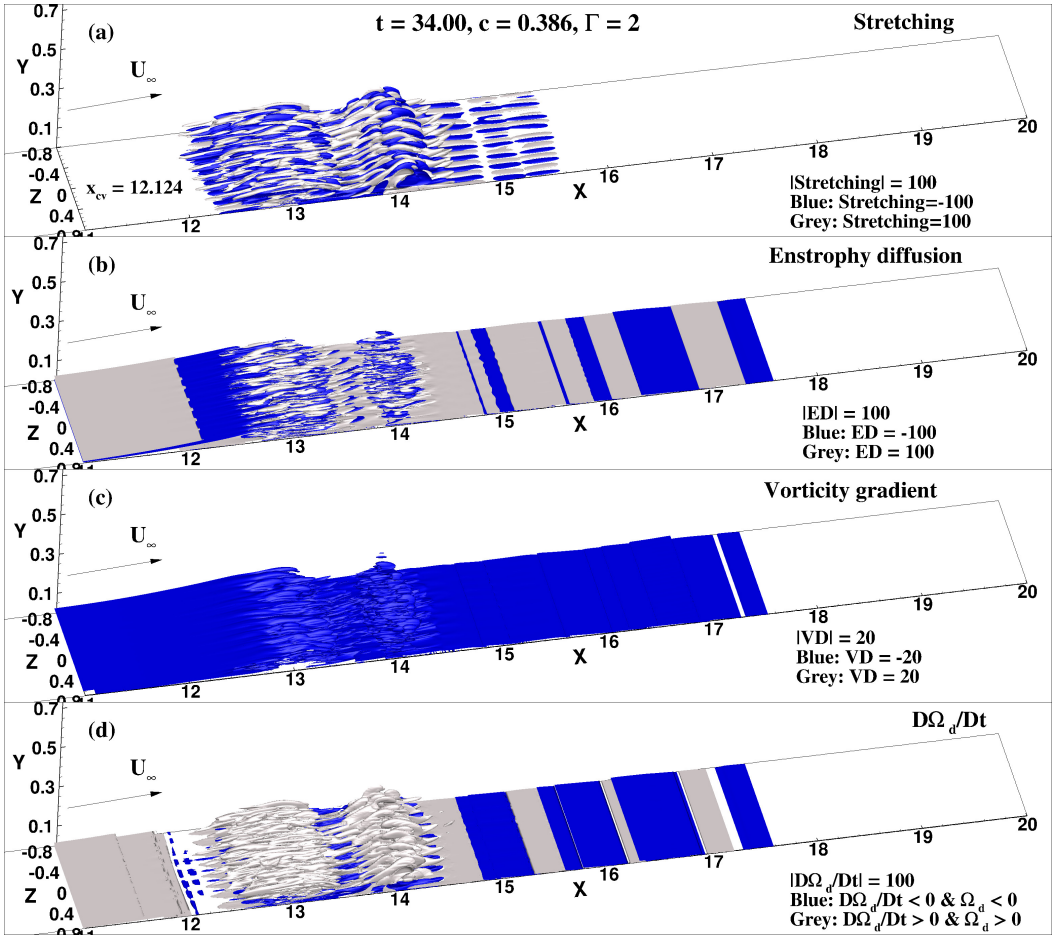

Fig. 6.29 Perspective plots for DETE budget terms at $t = 34$, with the top frame showing contribution from vortex-stretching (Term1); the second frame showing the contribution originating from enstrophy diffusion (Term2) and the third frame showing contribution from dissipation (Term3). In the bottom frame, the dark (blue) regions are where negative Ω_d become more negative and light (gray) regions are where positive Ω_d become more positive for free-stream vortex with $\Gamma = 2$ and $c = 0.386$ located at x_{cv}.

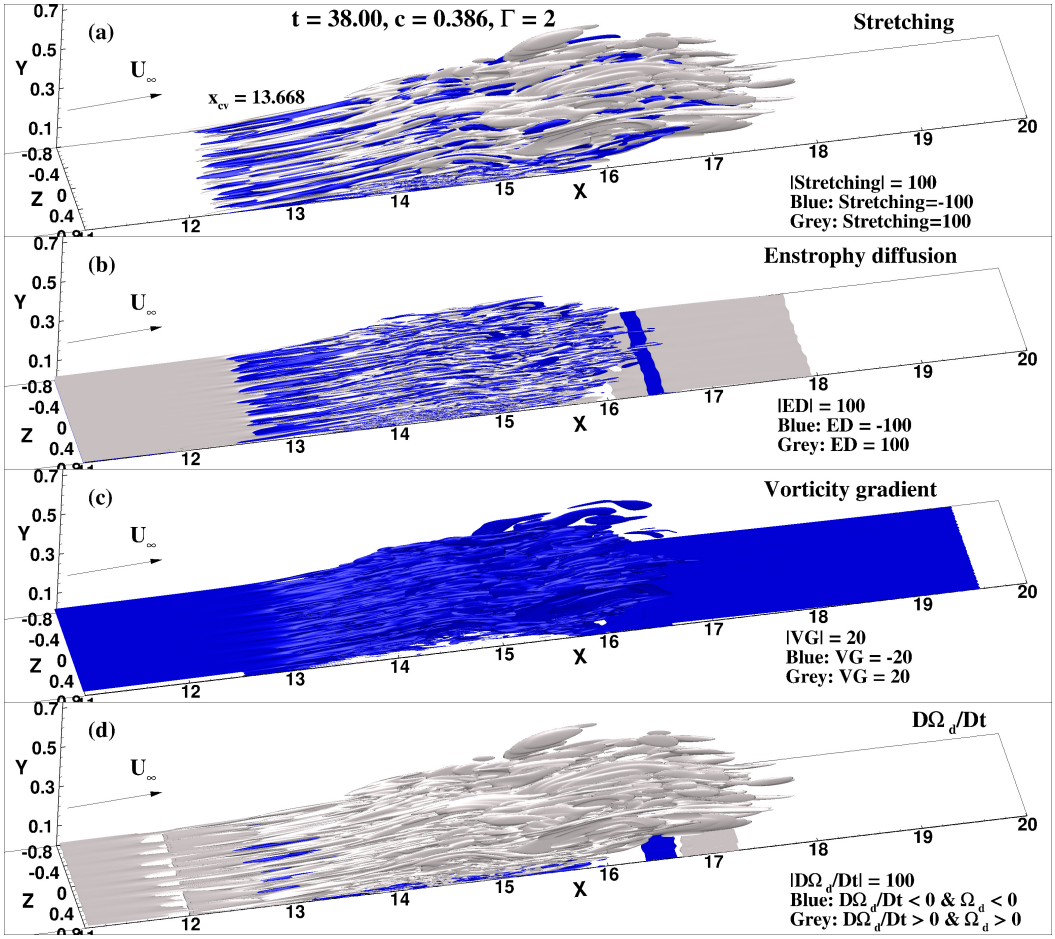

Fig. 6.30 Perspective plots for DETE budget terms at $t = 38$, with the top frame showing contribution from vortex-stretching (Term1); the second frame showing the contribution originating from enstrophy diffusion (Term2) and the third frame showing contribution from dissipation (Term3). In the bottom frame, the dark (blue) regions are where negative Ω_d become more negative and light (gray) regions are where positive Ω_d become more positive for free-stream vortex with $\Gamma = 2$ and $c = 0.386$ located at x_{cv}.

Spanwise scale selection during three-dimensionalization

Here, we report how three-dimensionalization evolves in the flow during vortex-induced instability for the case of $\Gamma = 2$ and $c = 0.386$. The global maxima for the three components of vorticity shown in Fig. 6.20 gives the preliminary idea of when the flow starts becoming 3D. In Fig. 6.25, contours are shown for $(z = 0)$-plane, for ω_x and ω_y at $t = 25$, 30, 34 and 38.

In Fig. 6.31, we show the spanwise variation of the DETE budget, by showing term-wise contributions (top three frames) to the overall variation of $D\Omega_d/Dt$ shown in the bottom frame. The results are presented for a height which is very close to the wall ($y = 0.0035$) for the streamwise locations, $x = 13$ and 15. The perspective plot of this case in Fig. 6.30 shows the distinct contributions from vortex-stretching, enstrophy diffusion and dissipation (or the vorticity gradient) terms at different heights. The spanwise variations of these three contributions clearly show the contributions from Term3 to be mostly negative, and vortex-stretching term to be localized at few z-locations for $x = 15$. Comparatively, vortex-stretching contribution is quite small at $x = 13$. Despite spanwise variations shown by Term2 and Term3, the vortex-stretching contribution is almost an order of magnitude higher. This is clearly reflected in the spanwise variation of $D\Omega_d/Dt$, noted as very localized. In Fig. 6.32, corresponding variations for the constituent terms and for the total quantity, $D\Omega_d/Dt$, are shown for the same case, but at the edge of unperturbed boundary layer. At this height, there is hardly any variation noted for $x = 13$, while the events are less localized for $x = 15$, with variations for $D\Omega_d/Dt$ seen at many off-center planes ($z \neq 0$). This implies 3D nature during vortex-induced instability is mostly contributed by vortex-stretching.

In Fig. 6.33, we show the Fourier transform of the spanwise variation data shown in Figs. 6.31 and 6.32, for the streamwise location of $x = 13$ at the height $y = 0.0035$ and for $x = 15$ at the height $y = 0.1$, in the top and bottom frames, respectively. In discussing about the spanwise variation, we noted that the contribution of vortex-stretching at both the heights is significantly larger in magnitude by almost an order, as compared to the contributions originating from enstrophy diffusion and vorticity gradient terms. This is readily evident in Fig. 6.33 for both the heights. Close to the wall, the spanwise scales are dominated by all the three components shown, and peak spanwise wavenumber is decided by the size of the domain in the spanwise direction. All the other dominant spanwise length scales are completely decided by vortex stretching. This is also the case for $y = 0.1$, where the vortex-stretching actually accounts for the total contribution for the disturbance enstrophy growth for all the peaks, including the smallest wavenumber peak. The DETE budget is quite dissimilar for the two heights shown. This is also true for other heights, due to the nature of vortex-induced instability, by which the disturbances are lifted up from the plate and are

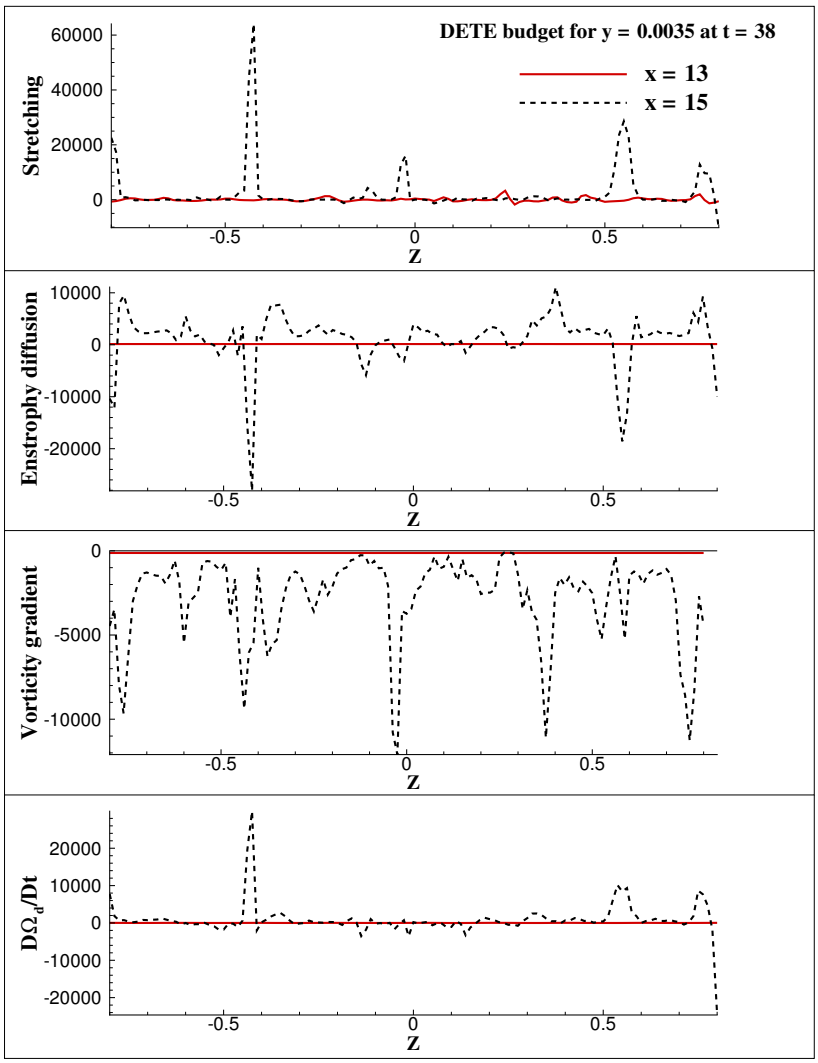

Fig. 6.31 Spanwise distribution of DETE budget terms shown in Fig. 6.30 ($t = 38$). The contribution from the stretching term (top) dominates over the terms originating from enstrophy diffusion and dissipation. The data are for $x = 13$ and 15, and height $y = 0.0035$, for $\Gamma = 2$ and $c = 0.386$ case.

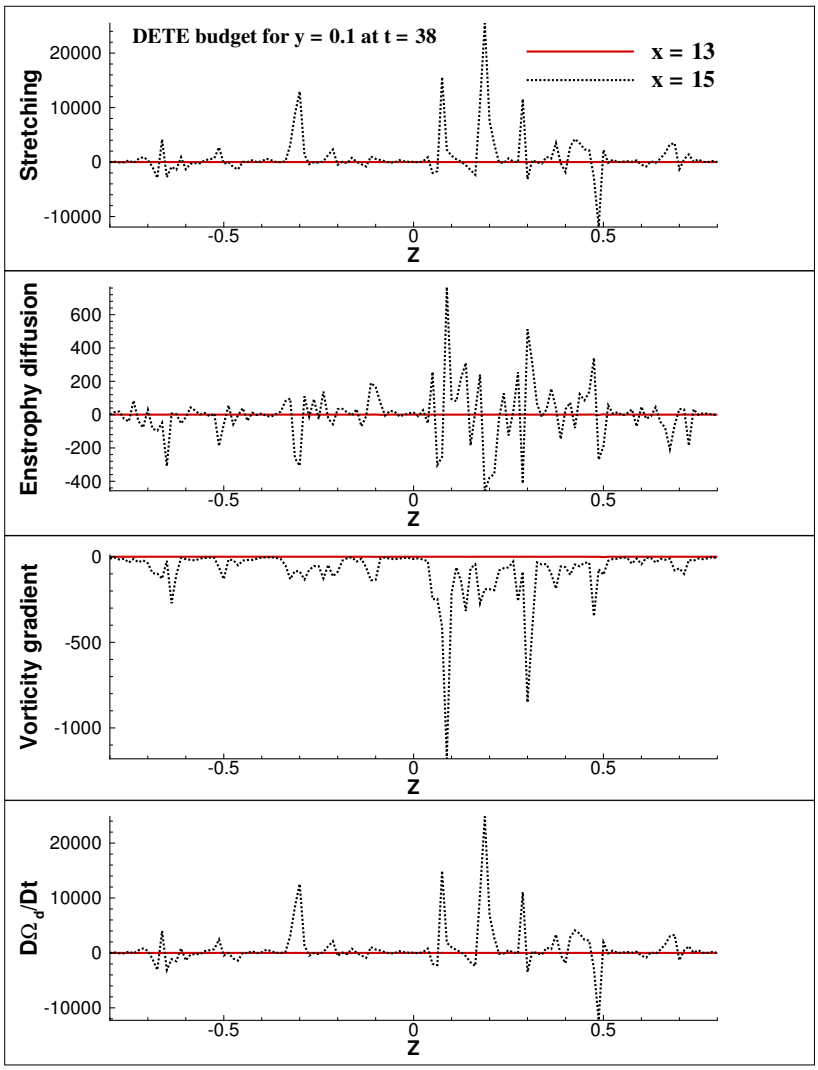

Fig. 6.32 Spanwise distribution of DETE budget terms shown in Fig. 6.30 ($t = 38$). The data are for $x = 13$ and 15, and height $y = 0.1$, for $\Gamma = 2$ and $c = 0.386$ case.

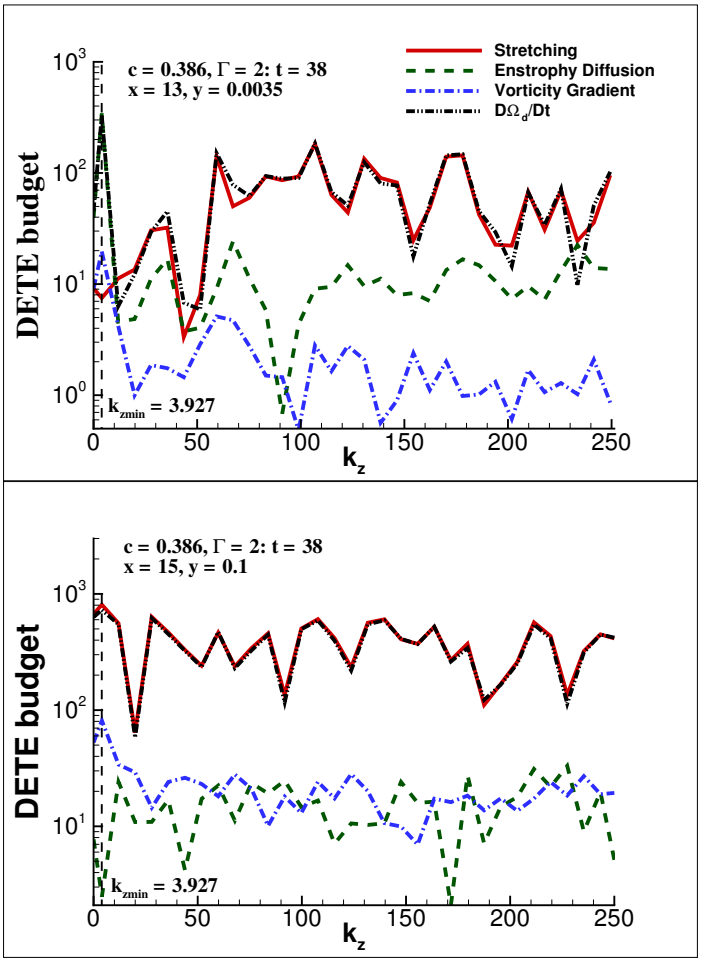

Fig. 6.33 Fourier transform of spanwise distribution of DETE budget terms shown in Figs. 6.31 and 6.32 for $x = 13$ and 15 at $t = 38$, for the indicated heights $y = 0.0035$ and 0.1, for $\Gamma = 2$ and $c = 0.386$ case.

localized in the streamwise direction. Thus, the spanwise variation of the disturbance field is completely determined by the contribution by vortex-stretching.

6.8 Dependence of Vortex-Induced Instability on c and Γ of Vortex

Earlier research on vortex-induced instability focused on the receptivity caused as a consequence of different speeds and signs of rotation of the convecting vortex, experimentally in Lim et al. (2004) and computationally in Sengupta et al. (2018a) and Sengupta et al. (2003). The dynamics of the flow can be influenced by parameters like the height and strength of

the vortex. For example, the effects of Γ is directly visible from Eq. (6.2), in terms of the induced stream function perturbation.

It has been seen in Figs. 6.4 and 6.26 that for $\Gamma = 0.5$, the flow for $c = 0.77$ shows mild receptivity and no discernible instability as seen from experimental results and computational frames, respectively. The experiments of Lim et al. (2004) showed that the counter-clockwise free-stream vortex triggered vortex-induced instability, when the convection speed of the source was chosen as $c = 0.39$, while receptivity was very mild for $c = 0.77$. In this section, the roles played by the strength and convection speed of free-stream vortex are explored.

One of the observations of the previous studies on vortex-induced instability (Lim et al. (2004), Sengupta et al. (2018a) and Sengupta et al. (2003)) was that the action of free-stream vortex with counter-clockwise circulation scours out the boundary layer ahead of it, but the present investigation for test case 3D5 with $c = 0.77$ and $\Gamma = 2$, does not follow this general rule. This can be attributed to variation of longitudinal pressure gradient at different heights during vortex-induced instability for different combinations of Γ and c. Taylor (1936) postulated first that a distant vortex can create a small longitudinal pressure gradient to destabilize the underlying boundary layer, as the dominant effect of free-stream turbulence. Monin and Yaglom (1971) in describing this observation, noted that *"the change in critical Reynolds number by the small longitudinal adverse pressure gradient is due to a sequence of unsteady separation .... the effect is connected with the generation of fluctuations of longitudinal pressure gradient by the disturbances, leading to the random formation of individual spots of unstable S-shaped velocity profiles.*"

In Fig. 6.34, various flow parameters for case 3D6 are shown. In the top frame, velocity profiles are shown for the indicated streamwise stations ($x = 15.6738$, 16.9717 and 17.188), at $t = 24$. The bottom three frames on the left show the stream-traces at the indicated times in the $z = 0$ plane, along with a vertical arrowhead indicating the streamwise location of the vortex at that instant. The presence of the free-stream vortex causes the streamlines to show a depression, as a consequence of which the flow accelerates upstream of the location of the convecting vortex, while there is an adverse pressure gradient downstream of it, due to streamline divergence. Corresponding spanwise component of vorticity (ω_z) is shown at the same times, on the bottom three frames on the right hand side. As the imposed excitation is due to a counter-clockwise vortex, the instability is noted downstream of the convecting vortex location. This is consistent with the findings of Lim et al. (2004) and Sengupta et al. (2003) where it was found that the action of the convecting counter-clockwise vortex is to impose an adverse pressure gradient ahead of the convecting vortex in the free stream, which is also consistent with the imposed disturbance field given by Eq. (6.2). It has also been noted in Sengupta et al. (2018a) from the solution of 3D NSE that the perturbed flow is 2D

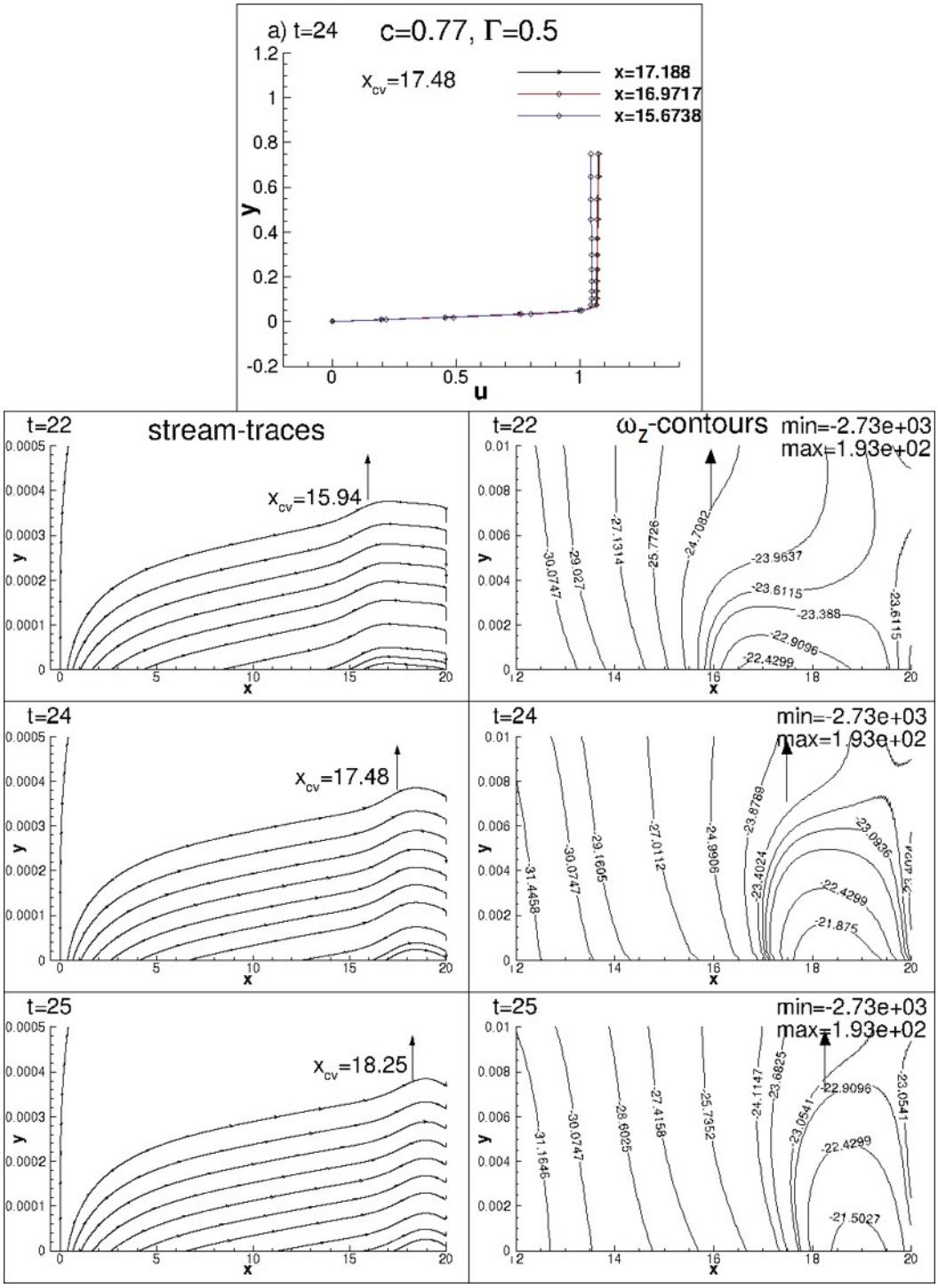

Fig. 6.34 Velocity profiles for $x = 15.6738$, 16.9717 and 17.188 at $t = 24$ with the vortex at $x_{CV} = 17.48$ (top frame); stream-traces at the mid-span ($z = 0$) at $t = 22$, 24 and 25, with $x_{CV} = 15.94$, 17.48 and 18.25, respectively (left frames); spanwise vorticity contours in $z = 0$ plane (right frames) for case 3D6 with $\Gamma = 0.5$ and $c = 0.77$

during the primary stage of instability, with only spanwise vorticity being dominant.

Next, the case 3D5 with $c = 0.77$ and increased vortex strength $\Gamma = 2$ is described in Fig. 6.35. The vortex-induced instability is qualitatively different for the higher Γ case, even though the imposed pressure gradient outside the boundary layer is qualitatively the same. From the stream-trace and vorticity contours in Fig. 6.35, it is observed that the higher Γ value shows instability appearing earlier than at $t = 22$. The instability is created upstream of the instantaneous free-stream vortex location. This suggests that the instability is not only stronger due to increase in Γ, but it is qualitatively different. To investigate the reason, the streamwise velocity profiles are plotted for three streamwise locations at $t = 24$ in the top frame of Fig. 6.35. Unlike the monotonically growing velocity profile for the case 3D6 in Fig. 6.34, case 3D5 shows an overshoot in the velocity profile at $x = 16.9717$, while for the other two streamwise stations, the instantaneous velocity profiles are monotonic. One of the effects of such large overshoot is that it indicates the presence of an inflection point very close to the plate, which has been postulated as S-shaped profile by Monin and Yaglom (1971) due to effects of free-stream turbulence. According to Rayleigh's theorem (Drazin and Reid, 1981), a temporal instability is likely to be present for case 3D5 in Fig. 6.35. This is evident from ω_z contours shown at $t = 22$, 24 and 26 in this figure, which show strong unsteady separations on the wall. For the case 3D6 with $\Gamma = 0.5$, shown in Fig. 6.34, the receptivity of the boundary layer is essentially via a 2D mechanism and the disturbance grows very little, which can be viewed as a mild spatio-temporal growth. In contrast for the case 3D5 with $\Gamma = 2$, stronger induced perturbations induce unsteady separations, leading to very strong spatio-temporal instability. Stronger unsteady separations for $\Gamma = 2$ case can be seen in the stream-traces near the wall in Fig. 6.35.

Another interesting observation can be made regarding the propagation speed of the free-stream vortex and the disturbance field inside the shear layer. For the case 3D6 with $\Gamma = 0.5$, the weak perturbation field has a lower speed than the speed of the free-stream vortex ($c = 0.77$). This is noticed in the ω_z contours in Fig. 6.34, in which the free-stream vortex not only catches up with the wall perturbations at $t = 25$, but overtakes it, leading to attenuation of the disturbance field. In contrast, the perturbation field shown in Fig. 6.35 is seen to be centred around the location of free-stream vortex and the disturbances are seen to move both in upstream and downstream direction. In the top right hand side frame of Fig. 6.35, the velocity profile at $x = 16.9717$ shows the presence of micro-bubbles close to the plate and inflection point(s) during the interval, $t = 23$ to 26. For $t = 24$, two inflection points are observed which are reflected in the ω_z contours at $t = 26$. The rapid spatial fluctuations

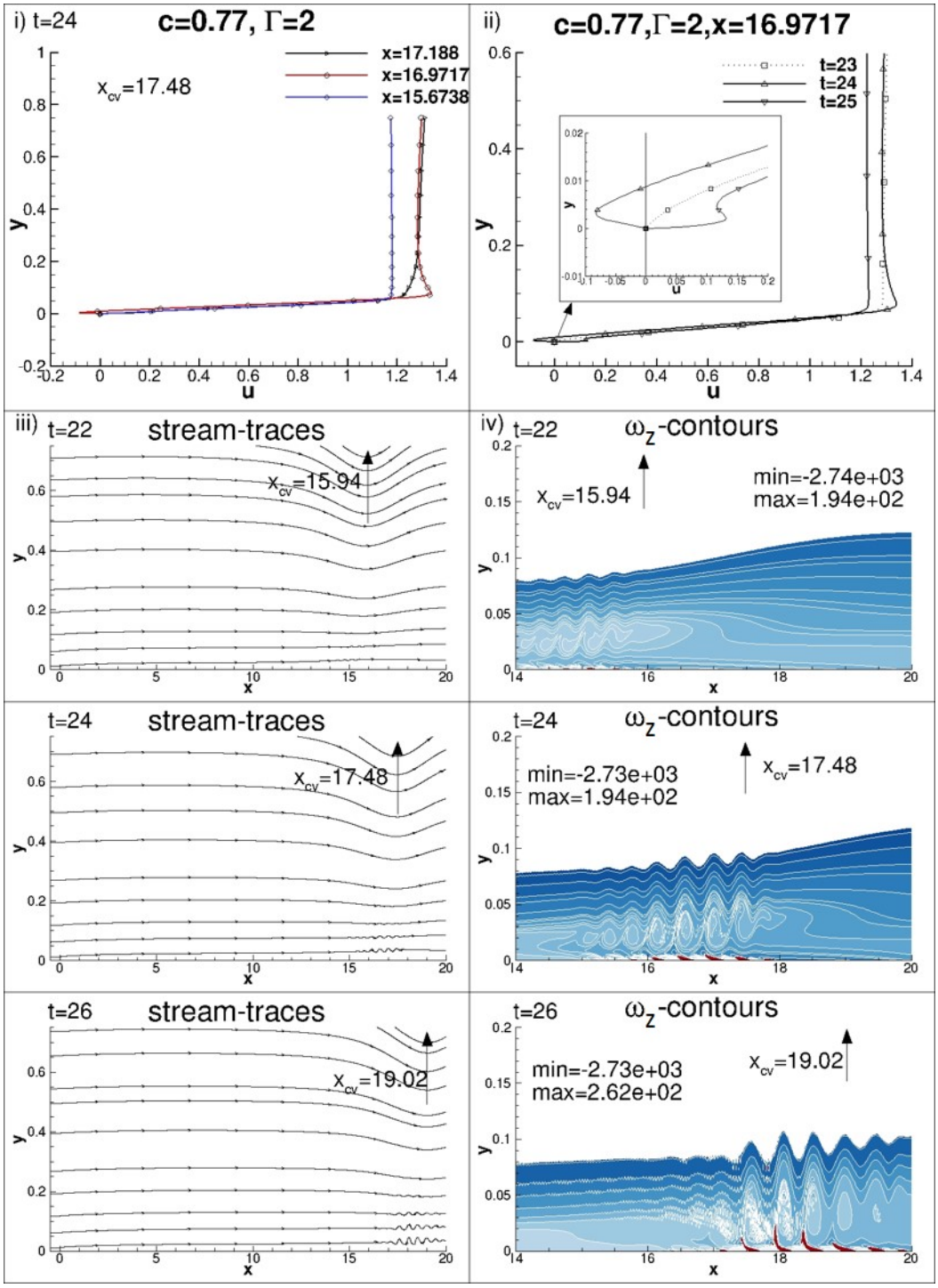

Fig. 6.35 (i)Velocity profiles for $x = 15.6738$, 16.9717 and 17.188 at $t = 24$ with the vortex at $x_{CV} = 17.48$; (ii) Velocity profiles shown at $t = 23$, 24, 25 for $x = 16.9717$; (iii) Stream-traces at the mid-span ($z = 0$) at $t = 22$, 24 and 26, with $x_{CV} = 15.94$, 17.48 and 19.02, respectively; (iv) Spanwise vorticity contours in $z = 0$ plane for case 3D5 with $\Gamma = 2$ and $c = 0.77$.

at heights corresponding to the outer inflection point are caused by a very high frequency temporal instability.

Next, we investigate the case of receptivity for counter-clockwise free-stream vortex destabilizing the boundary layer, in conjunction with discrete roughness element to study the cumulative effects of unit processes due to FST and roughness.

6.9 Vortex-Induced Instability with Discrete Roughness

In Fig. 6.36, the iso-surfaces of $\omega_z = -13$ coloured with wall-normal vorticity, ω_y are shown for convecting speed, $c = 0.3$ for the cases 3D1 (for an isolated vortex) and 3D3 (vortex with bump) are compared. The position of the bump is marked in the top right frame at $x = 1.5$ by an arrow. For the frames at $t = 5$, for case 3D1, a single vortex sheet originating from the leading edge is observed. For the case 3D3, however, the presence of the bump accentuates the effect of the adverse pressure gradient created downstream of the convecting vortex and leads to the formation of streamwise streaks downstream of the location of the roughness element. By $t = 10$, in the left frame for the case 3D1 without any roughness, only the leading edge vortex sheet is observed. In the corresponding right frame of Fig. 6.36, the vortex has convected beyond the streamwise location of roughness, and the cumulative effect of the adverse pressure gradient due to the convecting vortex and the streamwise disturbance packet originating from the earlier transition triggered by the roughness is observed. At $t = 15$, while for the case 3D1 in the left frame, a near wall separation bubble is observed between $x = 3.8$ and 5 along with lift-off of the vortex sheet, for the case 3D3 in the right frame, the streamwise streaks have begun to display three-dimensionality with spanwise waviness of the streaks, filling up the entire domain. The transition initially triggered by the bump, has led to turbulence and the wall excitation in the form of roughness is seen to have a more prominent effect than the free-stream excitation in the form of the convecting vortex. The convecting vortex at $t = 20$ in the left frame for case 3D1, has induced relatively weak streamwise streaks in the flow and the entire vortex sheet beyond $x = 7.2$ has been lifted off from the plate. For the right frame at $t = 20$, for the case 3D3, the flow has become fully developed turbulent, with the streaks no longer retaining their coherence in the streamwise direction. All these observations seem to suggest that the bump has a profound effect directly on the mean flow and leads to early transition to turbulence. There is a synergistic effect of the free-stream vortex and the roughness on the plate surface for the 3D computed cases. Even in the frames for the case 3D3 with roughness, upstream of the roughness element, the streamwise Klebanoff streaks due to the free-stream convecting vortex are clearly visible.

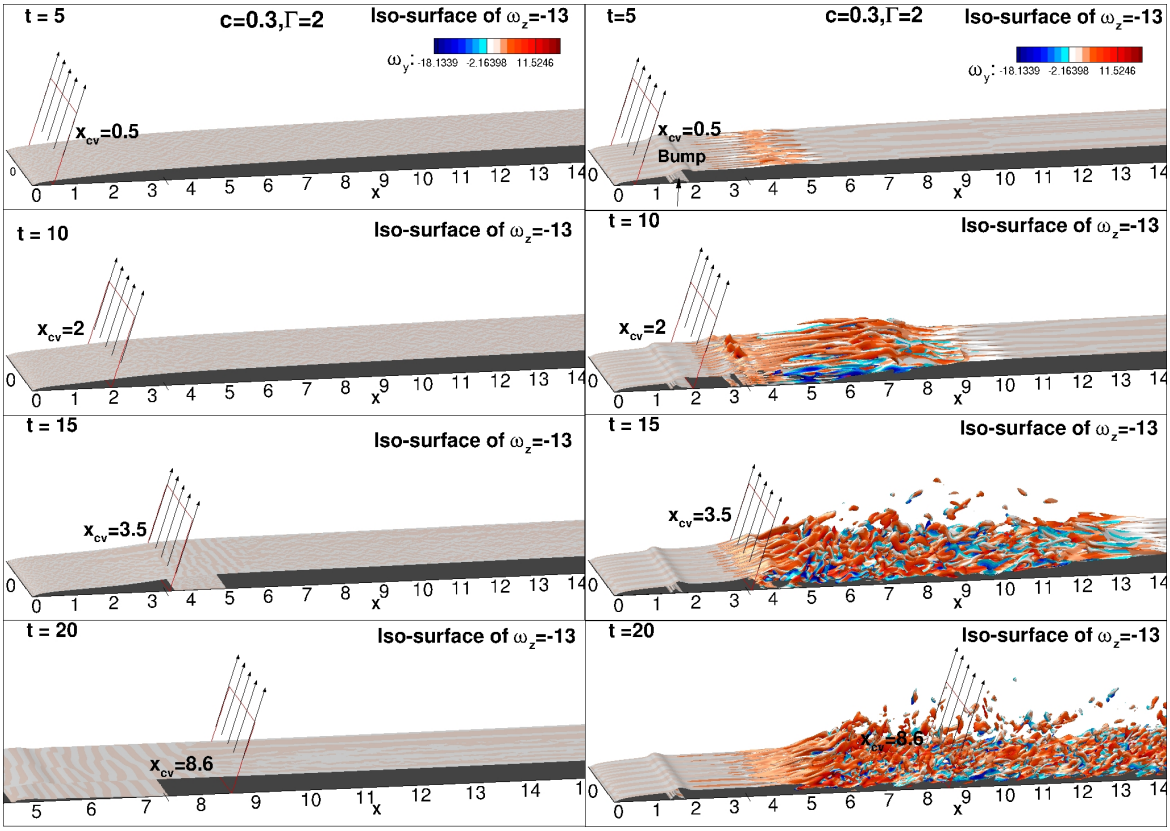

Fig. 6.36 ω_z iso-contours at indicated times for cases 3D1 and 3D3, at convecting speed $c = 0.3$, with and without the bump. Arrowheads show the streamwise location of the convecting vortex.

6.10 Vortex-Induced Instability as Bypass Transition

Experimental and computational results shown so far suggest the existence of a receptivity mechanism inside the shear layer, which induces instability as a consequence of a single vortex traversing in the free-stream, and due to the cumulative effects of free-stream vortex and a discrete roughness element on the plate. Here, the free-stream vortex convects at a uniform speed at a constant height from the plate. This is done to avoid variability of multiple parameters simultaneously. As an example, if the height of the convecting vortex is not fixed, then the Biot-Savart interaction would provide different coupling between vorticity fields and make it more complicated to isolate the causality of the excitation parameters in causing the vortex-induced instability. Once the unit processes are understood, a real flow situation can be deconstructed, where several parameters can change simultaneously.

One way of understanding instability in flows, is to track the sources/sinks of instability via the right hand side of the DME equation in Eq. (2.8), derived in appendix A. It is to be noted here that negative values of the right hand side of the DME equation denote a source of disturbance mechanical energy causing instability. Next, results for DME at some representative times for the test cases 3D2 (with higher receptivity) and 3D3 (to understand the effects of discrete roughness) are described.

In Fig. 6.37, the iso-contours of the right hand side of DME for $\nabla^2 E_d = -5$ and -10 are shown at times $t = 20$, 24, 30 and 38, for the test case 3D2, to track instability from its inception. In the first frame at $t = 20$, the level with value equal to -5 traverses the whole length of the domain. However the higher strength source of DME with value -10 is noted in a narrow region, very close to the wall upstream of the convecting vortex at $x_{cv} = 6.72$. Downstream of the vortex, this strip is lifted off from the plate in a narrow vortex sheet. At $t = 24$, stacks of vortex sheets are piled over each other for level -5. $\nabla^2 E_d = -10$ is noted in a thin layer on the edges of the vortex stacks. By $t = 30$, the region with higher source of DME has grown, but it still outlines the edge of the vortex sheet, which has rolled up and lifted off from the plate. At a later time, at $t = 38$, the source of instability are clearly visible over the spanwise extent of the domain. Strong streamwise streak-like structures are observed upstream of the location of the vortex, in the region of favourable pressure gradient, which are lifted off and break down to three-dimensionality, downstream of the convecting vortex in the region of adverse pressure gradient. These streaks are reminiscent of the Klebanoff streaks noted for boundary layers with FST.

In Fig. 6.38, the iso-contours of the right hand side of DME for $\nabla^2 E_d = -5$ and -10 are shown at times $t = 5$, 10, 15 and 20, for the test case 3D3. The location of the 2D bump centred at $x_b = 1.5$, is indicated in the top frame. At $t = 5$, the lighter iso-contour of

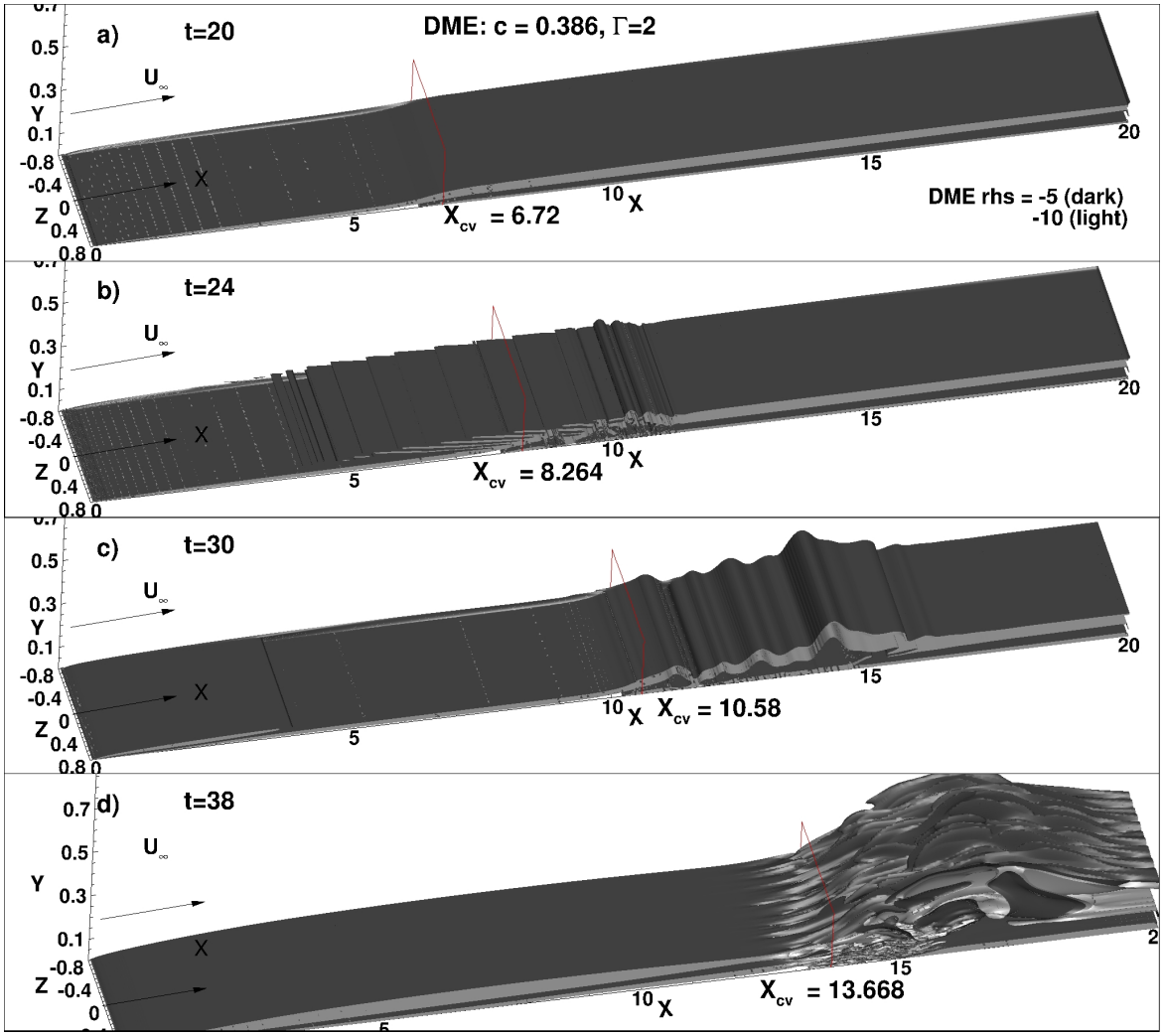

Fig. 6.37 Right hand side of the DME contours at indicated times for test case 3D2 for two iso-contour levels, $\nabla^2 E_d = -5$ and -10, at convecting speed $c = 0.386$.

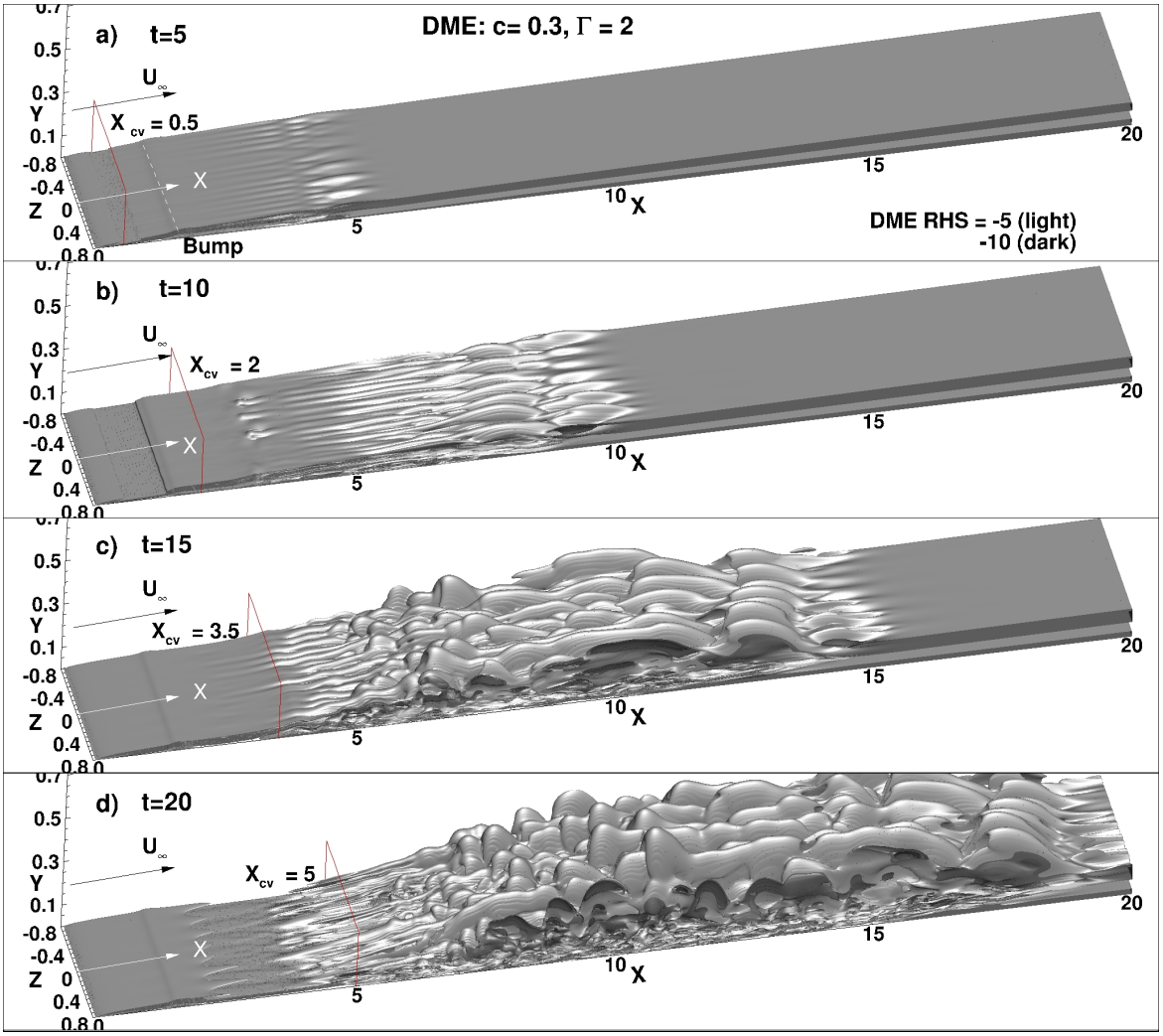

Fig. 6.38 Right hand side of DME contours at indicated times for test case 3D3 for two iso-contour levels, $\nabla^2 E_d = -5$ and -10, at convecting speed $c = 0.3$ with a bump.

$\nabla^2 E_d = -5$, is seen for streamwise streaks created downstream of the bump in the region of weak adverse pressure gradient. These streaks are induced purely by the effect of the roughness element, as the vortex is at $x_{cv} = 0.5$. The darker iso-contour of $\nabla^2 E_d = -10$ is noted at the outer edge of the boundary layer in a thin region lifted off from the plate. This is in contrast with Fig. 6.37 for the test case 3D2, where even by $t = 20$, the boundary layer was largely undisturbed. At $t = 10$, the streamwise streaks due to the 2D bump acquire coherence and by $x = 8$, the streaks are lifted off from the plate in bulge-like structures. Here, once again the darker, higher iso-contour level is noted at the edge of the structures identified for $\nabla^2 E_d = -5$. The adverse pressure gradient downstream of the roughness element is much stronger than in the top frame, due to the location of the free-stream vortex, and thus, the streaks due to roughness element are accentuated in this region. By $t = 15$, strong streamwise streaks are noted immediately downstream of the position of the free-stream vortex at $x_{cv} = 3.5$, which rapidly break down to three-dimensionality and appear as 'bulges' in the free stream. The dark iso-contours are noted at the edges of these bulges. In the last frame at $t = 20$, Λ-shaped vortices are noted in the region of favourable pressure gradient upstream of the vortex location, $x_{cv} = 5$. These show streamwise coherence for a short distance downstream of the convecting vortex, after which the streaks show spanwise waviness which are lifted off from the plate. There is interaction between the light and dark iso-contours at the edges near the plate and away from the plate. The type of transition shown in Fig. 6.38 varies greatly from that is shown in Fig. 6.37. This difference can be explained by the fact that for the test case 3D3, the wall excitation in the form of a discrete roughness element governs the early transition by altering the mean flow directly. But, in the test case 3D2, for the counter-clockwise rotating free-stream vortex, the flow is disturbed by it to induce a local favourable and adverse pressure gradient, upstream and downstream of it, respectively. This does not have as strong an effect on the flow as the wall excitation case does.

Another method for studying the disturbance field is the DETE method, given by Eq. (2.9) and derived in appendix B. The discerning feature in this method is that the disturbance enstrophy gives vital information about the disturbance field, as it is not bound by the classical definition of enstrophy, wherein enstrophy is always a positive quantity. Thus, with DETE, one can quantitatively assess the regions of growth of instability with positive growth rate, or alternatively for instability with negative growth rates.

In Fig. 6.39, the iso-contours for positive and negative DETE, $\frac{D\Omega_d}{Dt} = \pm 0.1$, are provided at times $t = 20$, 24, 30 and 38, for the test case 3D2. At $t = 20$, a sheet of instability with negative Ω_d arising from the leading edge is observed upstream of the convecting vortex at $x_{cv} = 6.72$. Immediately downstream of the vortex, the sheet of instability with positive Ω_d,

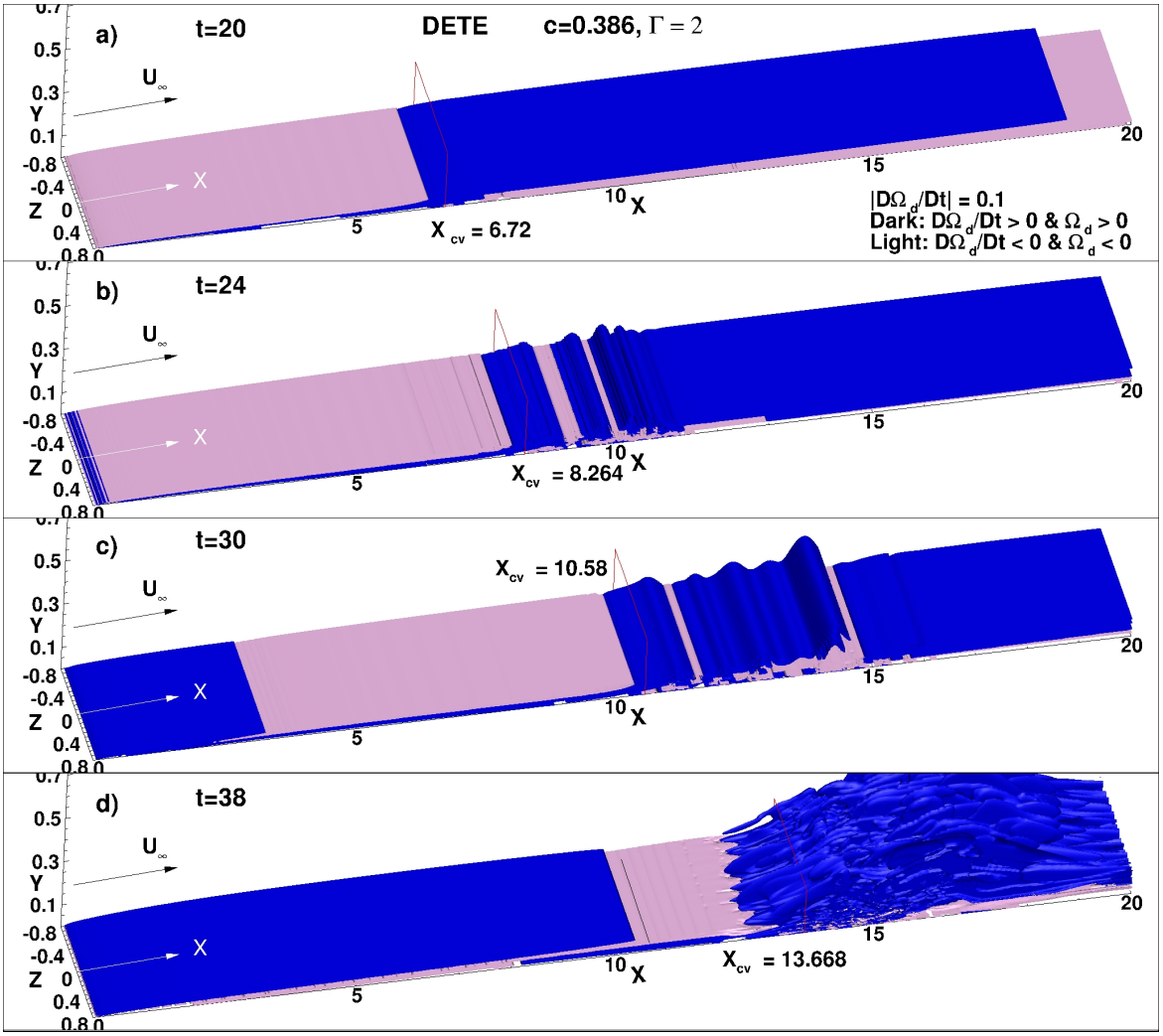

Fig. 6.39 DETE iso-contours at indicated times for test case 3D2 at $c = 0.386$ for $\frac{D\Omega_d}{Dt} = 0.1$ when Ω_d is positive and $\frac{D\Omega_d}{Dt} = -0.1$ when Ω_d is negative.

which was beneath the sheet of negative instability prior to this, lifts up from the surface of the plate, over the sheet of negative Ω_d. At $t = 24$, the sheet of negative Ω_d has shifted with the position of the convecting vortex, but just like the earlier frame, immediately downstream of the vortex at $x_{cv} = 8.264$, the dark positive Ω_d sheet rolls up and is lifted off from the plate in the form of discrete 2D vortex rolls. By $t = 30$, the sheet of negative Ω_d, which was earlier at the leading edge, has convected with the free-stream vortex. The 2D vortex rolls of positive Ω_d are no longer attached to the plate. In the last frame at $t = 30$, the region of negative Ω_d, which is visible upstream of the convecting vortex at $x_{cv} = 13.668$ is in a narrow region before the positive Ω_d structures gain three-dimensionality and cover the spanwise extent of the domain. It is only through DETE analysis that one is able to discern, which structures in the flow are characteristics of positive Ω_d, and which have negative Ω_d. It is also of interest to note that the respective regions of positive and negative growth rates are dynamic, and depend greatly on the position of the free-stream convecting vortex.

In Fig. 6.40, the iso-contours for positive and negative DETE, $\frac{D\Omega_d}{Dt} = \pm 0.1$, are provided at times $t = 5$, 10, 15 and 20, for the test case 3D3. The position of the bump is indicated in the top frame, while the locations of the free-stream convecting vortex are given by x_{cv}. Here, even at $t = 5$, there are streamwise streaks downstream of the bump in the region of adverse pressure gradient. These are attributed to the bump, which has an effect on the thin boundary layer formed over the plate. A region of negative Ω_d is noted immediately downstream of the convecting vortex at $x_{cv} = 0.5$, and ends before the bump. At $t = 10$, the convecting vortex has surpassed the bump, and thus, the streamwise streaks have gained larger streamwise extent due to the stronger adverse pressure gradient. As noted in the previous frame, a region of negative Ω_d is noted in the region of favourable pressure gradient, upstream of the convecting vortex. By $t = 15$, the streaks of positive Ω_d have acquired waviness in the spanwise direction and have lifted off from the surface of the plate. It is to be noted here that the negative Ω_d has interacted with the streamwise streaks due to roughness element in this frame. In the last frame at $t = 20$, much of the streamwise streaks due to the bump in the boundary layer have acquired a negative Ω_d, while the streaks of positive Ω_d are in a layer above the negative near-wall Ω_d. The positive streaks have acquired three-dimensionality in the form of enhanced spanwise waviness of the streaks. Thus, comparing the flow field with a roughness element triggering the transition (as in Fig. 6.40) with the flow field in Fig. 6.39, it can be concluded that a wall-excitation in the form a roughness element is much more direct and effective in triggering early transition, than a free-stream excitation in the form of a convecting vortex, where the mechanism is more subtle. Of course in many flows, as in turbomachineries, actual transition is driven by both wall and free-stream excitations, and it is paramount that one understands the unit processes for each of the contributing factors.

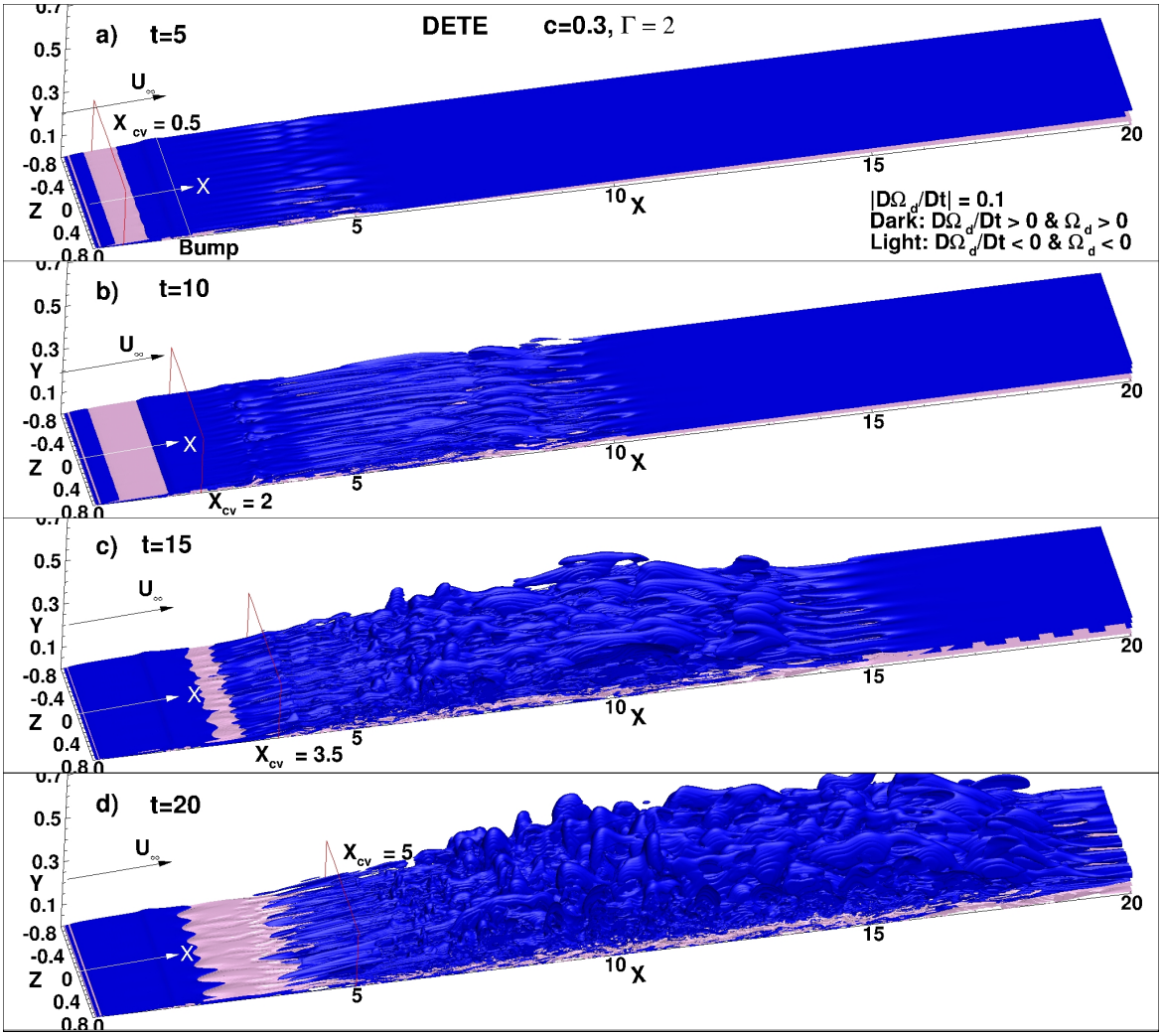

Fig. 6.40 DETE iso-contours at indicated times for test case 3D3 at $c = 0.3$ with bump for $\frac{D\Omega_d}{Dt} = 0.1$ when Ω_d is positive and $\frac{D\Omega_d}{Dt} = -0.1$ when Ω_d is negative.

6.11 Concluding Remarks

A kernel experiment for the bypass transition mechanism of the isolated and cumulative perturbation fields of a convecting vortex and a discrete roughness element has been performed through direct numerical simulations. The free-stream vortex induces a local adverse pressure gradient found on the suction surface of a low pressure turbine blade in the case of counter-clockwise rotation. A flat plate subjected to a convecting vortex has been numerically investigated and calibrated against existing experimental investigations. The equilibrium boundary layer over a semi-infinite flat plate has been computed to provide a baseline flow for all disturbance calculations, with and without the roughness.

The strong dependence of the boundary layer receptivity to the convection speeds, strengths and signs of circulation of the free-stream vortex has been shown through 3D iso-surfaces of vorticity. The routes of transition adopted in the cases with different speeds and strengths of the vortex, have been demarcated, and both the 2D and 3D flow field has been characterized by the unsteady nonlinear receptivity theories based on disturbance enstrophy and disturbance mechanical energy. It has been found that the presence of the roughness element acts as a triggering mechanism for the early onset of transition. Strong streamwise streaks are noted for the cases with roughness even upstream of the instantaneous vortex location. Roughness has a more pronounced effect in triggering early transition and leads to early breakdown to turbulence. A case with significantly different response of the flow field to the same pressure gradients has been studied through the vortex with convecting speed $c = 0.77$ and $\Gamma = 2$, and comparisons are made with a lower strength, $\Gamma = 0.5$. It is found that the higher vortex strength case undergoes transition through the presence of inflection points in the velocity profile, which are absent at the lower vortex strength which is concurrent with the effect of varying amplitude of disturbance in the bypass transition mechanism displayed by the flow field, proposed by Saric et al. (2002). The highest receptivity has been observed for the case with $c = 0.386$, with the case with $c = 0.3$ following close behind. This finding is supported by the experiments of Kendall (1987) for periodic free-stream vortices where maximum receptivity was noted for approximate convection speeds of 0.35 relative to the free-stream velocity. If the free-stream vortex translates at the free-stream velocity, there is no displacement effect in the induced stream-function given by Eq. (6.2). The strength of the vortex giving rise to the circulation effect in Eq. (6.2) is the sole governing parameter for receptivity in such a case. Enhanced receptivity will be observed for higher strengths of the vortex.

The evolution of three-dimensionalization of the flow field, characterized by the dominance of the vortex stretching term of the disturbance enstrophy transport budget, is traced through the forementioned receptivity tracking mechanisms, as has also been shown in

Sengupta et al. (2019a). The breakdown to turbulence is fastest for the case with roughness. In the 2D flow visualizations, although an array of unsteady separation bubbles are observed along the length of the plate, these are fairly two-dimensional. In contrast, for the 3D flow field, although the initial perturbation field is 2D, there is eventual three-dimensionality observed in the flow due to the growth of the streamwise and wall-normal fluctuations. This is consistent with the flow field observed in chapter 5 for a flat plate geometry mimicking the pressure gradient of an 'ultra high-lift' LPT blade, where 2D cylindrical roll-ups eventually acquired spanwise waviness and three-dimensionalization of the flow.

Chapter 7

Aeroelastic Effects on Wake-Induced Instability on Ultra High-Lift Blades

In this chapter, the individual and cumulative effects of imposed aeroelastic blade vibrations and the wake-induced instability, on the transition of the separated shear layer formed on the suction surface of the LPT blade are detailed. A series of DNS are performed on a flat plate geometry subjected to a pressure gradient representative of that observed on a ultra high-lift LPT blade. The problem formulation, boundary conditions and parameters characterizing the test cases are provided. The characteristics of the various disturbance environments in the three test cases considered are investigated through instantaneous and time-averaged quantities: vorticity iso-contours, skin friction, velocity profiles, root mean square velocities etc. The turbulent kinetic energy budget is used to quantify the extent and nature of the separation bubble observed. The evolution of the instabilities observed and the mechanisms of wake-induced transition are described through non-linear instability mechanisms derived directly from the incompressible Navier-Stokes equation.

7.1 Problem Formulation

The computational domain and boundary conditions, considered in the present study on wake-induced instability in the presence of aeroelastic vibration of the blade, are shown in Fig. 7.1. The geometry considered is similar to the one considered in chapter 5, the difference is in the streamwise extent of the domain upstream of the flat plate with finite thickness ($-0.0005 < y < 0.0005$) and a rounded leading edge indicated by LE in Fig. 7.1. The domain has been extended upstream of the leading edge, LE to allow the wake introduced at the inlet to travel some distance in the streamwise direction before impinging

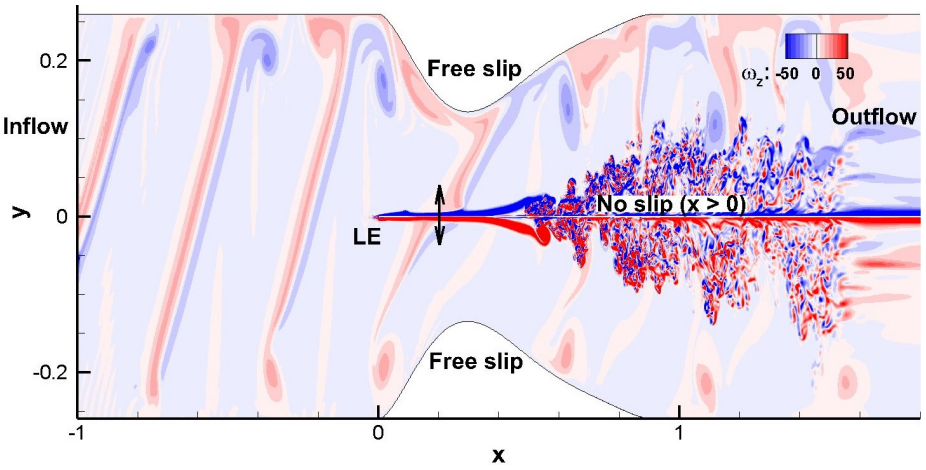

Fig. 7.1 Schematic for wake-induced instability in presence of aeroelastic vibration of LPT blade. The spanwise vorticity has been shown in the figure.

on the blade surface. The flat plate is subjected to a streamwise pressure gradient on the top half, which is representative of the pressure gradient found on the suction surface of a LPT blade. This pressure gradient is imposed due to the upper contoured inviscid wall. The given configuration has been studied experimentally at higher Reynolds numbers by Lou and Hourmouziadis (2000) and numerically at lower Reynolds numbers by Lardeau et al. (2012), Sengupta et al. (2017), Vadlamani et al. (2013) and Wissink and Rodi (2004). Here, the geometry has been mirrored about the $y = 0$ line to remove the need for prescribing a free-slip boundary condition in the symmetry plane upstream of the flat plate ($x < 0$) in the original configuration. This symmetry plane experiences a time varying angle of attack in the test case involving an aeroelastic oscillation of the plate, as a body-force method has been implemented to account for the blade vibration, as discussed previously in chapter 5.

Free-slip boundary conditions are imposed on the contoured walls. This has been done in order to prevent flow separation on these walls and also enable the use of a coarser mesh progressively away from the plate in the wall-normal direction, as has been done previously by Wissink and Rodi (2004). A no-slip condition is imposed on the flat plate downstream of the rounded leading edge ($x > 0$) with the help of an immersed boundary method adopted previously by Yuan and Piomelli (2014). The domain is periodic in the spanwise direction. A spanwise width of 12% of the reference length is used. The size of the span is sufficient to accommodate all dominant modes for the separation-induced transition simulated in this geometry (Lardeau et al. (2012) and Wissink and Rodi (2004)). For the outflow, static pressure at the exit is specified and the velocities are extrapolated. Riemann boundary condition has been imposed at the inflow along with the incoming wake.

For the present computations 57 million points have been used, with 873 points in the streamwise direction resolving $-1 < x < 2$. There is a buffer zone in the streamwise direction beyond $x > 2$ to avoid reflections from the outflow, where a much coarser resolution has been employed. Additionally, hyperbolic tangent stretching has been used in the streamwise and wall-normal directions with higher resolution employed in regions of separation and reattachment in the streamwise extent and closer to the plate in the wall-normal direction. In the wall-normal direction, there are 513 points resolving $-0.26 < y < 0.26$, while the spanwise length, $0 < z < 0.12$ is resolved with 128 points. The resolution implemented for this geometry is the same as in chapter 5, the details of the streamwise variation for near wall spacing in terms of wall units x^+, y^+, z^+ have already been shown in Fig. 5.2. In the extended streamwise extent $-1 < x < -0.5$ for this geometry, compared to the one adopted in chapter 5, the same resolution found at $x = -0.5$ has been extended upstream.

Computations are carried out at a Reynolds number of 60000, based on the reference inlet velocity and reference length. The flow operates at a Mach number (Ma) of 0.1. Due to this low Mach number, one can safely operate in the incompressible limit, as has been adopted in DNS of Wissink and Rodi (2004) for ultra high-lift blades. The unsteady wake is imposed at the inlet using the Gaussian expression provided by Eq. (3.47) in chapter 3. The time period and amplitude of the wake passing has been callibrated using a series of 2D computations against available data for a LPT wake (Karaca and Gungor (2016) and Stieger (2002)).

7.1.1 Test Cases

Three test cases have been used to demonstrate the differences in the separation-induced transition seen on suction surface of LPT blade with different levels of disturbance. A baseline case without any imposed external disturbance is calculated in test case LI, which has a laminar inflow. Test case WK invokes an unsteady Gaussian wake at the inlet provided by Eq. (3.47), where the time period of wake passing is given as $t_w = 0.35$, amplitude associated with the wake is $a_w = 0.8$, and exponential constant of the Gaussian is $\alpha = 19$. The parameters have been selected to mimic the distance between wakes considered by Karaca and Gungor (2016), while staying within the limits of permissible non-dimensional Strouhal number for upstream blade induced wakes. In test case, WO, with the wake at the inlet, there is an additional source of disturbance given in the form of oscillation of the plate. The oscillation is defined by reduced frequency, $k_{osc} = 0.1$ in Eq. (2.1), amplitude, $a = 0.031$ and time period of oscillation given by $t_o = 0.0775$ in Eq. (3.46). As mentioned in chapter 5, the reduced frequency has been chosen to match values seen for turbomachines (Vogt, 2005). The non-dimensional Strouhal number associated with the wake imposed is $St = 0.34033$,

while the typical value observed for a wake from upstream blades is ≈ 0.3 (Tucker, 2014). The details of the three different test cases simulated are provided in Table 7.1.

Table 7.1 Parameters used and description for test cases reported. Here, t_w and a_w are the time period and amplitude of the imposed wake. t_o and a are the time period and amplitude of imposed blade oscillation.

Case	t_w	a_w	t_o	a	Description
LI	-	-	-	-	Laminar inflow
WK	0.35	0.8	-	-	Wakes at inlet
WO	0.35	0.8	0.0775	0.031	Wakes at inlet and forced oscillation of blade

7.2 Initializing the Flow

The laminar case, LI is computed as the equilibrium solution for the other two test cases WK and WO, for the fluctuation calculations in applying the tools of DME and DETE. In all test cases, the transients are flushed after 5 through-flows of the computation and the flow is allowed to settle, after which quantities are recorded for time averaging. Time averaging takes place over another 6 through-flows of computation. For the test case WO with oscillation, the flow is initiated with oscillation at t = 0, by including the body force term as mentioned in chapter 3. The wake is initiated at the inflow from t = 0, by adding the unsteady Gaussian wake term, explained in chapter 3, at every successive iteration for the test cases WK and WO, of Table 7.1.

7.3 Instantaneous Flow Features

The instantaneous flow field for the suction surface of a LPT blade is governed by the pressure gradient arising on the blade due to the contoured upper wall. The plate experiences a favourable pressure gradient in the region of convergence of the blade passage, followed by a region of adverse pressure gradient beyond $x = 0.3$ in the diverging blade passage, as can be seen in Fig. 7.1. It is this adverse pressure gradient which leads to flow separation. In the present study, imposed perturbations in the form of wakes at inflow and plate oscillations will alter the flow topology of the separation-induced transition for the baseline LI case. In this section, this will be highlighted through iso-contours of the instantaneous flow field,

vorticity contours and Q-criterion plots for the cases WO and WK of Table 7.1.

In Fig. 7.2, the iso-contours of spanwise vorticity ($\omega_z = -80$) coloured with wall-normal vorticity ($-20 > \omega_y > 20$) are shown at indicated times to highlight the primary stage of instability growth for the test case WK. In the top frame at $t = 1.05$, the disturbance field is 2D without any spanwise variation seen for the vortex rolls at $x = 0.6$ and 0.8. At $t = 1.18125$, there is a lift off of the spanwise roll originating at $x = 0.6$ in the previous frame. Another roll is seen to commence from $x = 1$, however, there is still no spanwise variation at this stage. By $t = 1.3125$, mild spanwise variation originating from the periodic spanwise boundaries is observed. The roll that had been initiated in the previous frame has become a coherent vortex roll and is lifted off from the plate. In the last frame of Fig. 7.2, at $t = 1.4$, discernible spanwise variation is observed in the form of faint streamwise streaks, along with coherent spanwise rolls lifted off from the boundary layer.

In Fig. 7.3, the iso-contours of spanwise vorticity ($\omega_z = -80$) coloured with wall-normal vorticity ($-20 > \omega_y > 20$) are shown at indicated times to highlight the secondary stage of instability growth for test case WK. In the top frame at $t = 1.4875$, significant spanwise variation is observed in the vortex rolls initially observed in the bottom frame of Fig. 7.2. There is a slow amalgamation of disparate rolls to a single, longer perturbed region in $0.62 < x < 1$. In the frame at $t = 1.575$, the vortex roll previously located at $x = 0.45$ has gained spanwise waviness and is the leading front of the lifted off boundary layer. One also observes that the spanwise 2D roll at $x = 1.2$, has spanwise undulations. The singular perturbed region has broken down and small scale structures are observed at some distance from the wall. By $t = 1.6625$, the coherent vortex rolls can no longer be observed. Increased small-scale structures are visible throughout the flow. Similar evolution of flow was shown for the canonical problem of vortex-induced instability for convection speeds of 0.3 and 0.386 in chapter 6. At this stage, there is still a demarcation between the three locations of instability: (i) due to the spanwise roll lifted off from the boundary layer at $x = 0.5$, (ii) the amalgamated perturbed region in $0.6 < x < 1.2$, (iii) due to the spanwise roll at $x = 1.2$. While locations (i) and (iii) are near-wall instability regions, location (ii) has structures which are lifted off from the boundary layer, in the free-stream. This localization of disturbance field across the boundary layer are reminiscent of the wall and free-stream modes for the solution of Orr-Sommerfeld equation for the study of linear instability (Sengupta, 2012). In the last frame at $t = 1.8375$, the three demarcated regions of instability growth are clustered to a single stronger and longer perturbed region. In all the frames in Fig. 7.3, undulations in the separated shear layer are noted upstream of the separated structures, which can be

attributed to the travelling wake in test case WK.

In Fig. 7.4, the iso-contours of spanwise vorticity ($\omega_z = -80$) coloured with wall-normal vorticity ($-20 > \omega_y > 20$) are shown at indicated times to highlight the primary stage of instability growth for test case WO. The primary stages for WK and WO cases, shown in Figs. 7.2 and 7.4, respectively, are similar in the frames shown at times $t = 1.05$ and $t = 1.18125$. In the frame at $t = 1.3125$ for case WO in Fig. 7.4, the vortex rolls are thinner compared to their counterparts noted for case WK in Fig. 7.2. This can be attributed to the delayed separation expected in case WO with added perturbation of blade oscillations, which will be explained in Figs. 7.8 and 7.10 for time-averaged streamwise velocity and skin friction, respectively. A similar observation can be made in the bottom frame at $t = 1.4$ for WO in Fig. 7.4, compared to the corresponding WK frame in Fig. 7.2. The vortex rolls have gained more spanwise undulations for case WK compared to case WO. Also, the rolls have more coherency as independent structures for case WO seen in Fig. 7.4, as compared to those seen in Fig. 7.2 for case WK.

In Fig. 7.5, the iso-contours of spanwise vorticity ($\omega_z = -80$) coloured with wall-normal vorticity ($-20 > \omega_y > 20$) are shown at indicated times to highlight the secondary stage of instability growth for test case WO. In the top frame at $t = 1.4875$, more spanwise waviness is seen for the first vortex roll at $x = 0.55$ for test case WO in Fig. 7.5 as compared to the corresponding frame of Fig. 7.3 for case WK. But, overall the iso-contours at this time are pretty similar for cases WO and WK at this time. In the second frame at $t = 1.575$, for case WO the flow has progressed further towards three-dimensionality than the corresponding frame for case WK in Fig. 7.3, where three disparate locations for instability can be identified. In WO case, there is a long, perturbed region where only the spanwise roll at $x = 1.2$ retains its identity. The higher perturbation levels in WO case trigger earlier transition to turbulence compared to WK case. In the third frame at $t = 1.6625$, for case WO, one single perturbed region in $0.4 < x < 1.2$ and a spanwise roll at $x = 1.3$ is seen whereas for corresponding time frame for case WK, in Fig. 7.3, three distinct instability regions are noted: (i) between $x = 0.4$ and 0.62, (ii) one strong perturbed region in $0.65 < x < 1.2$ and (iii) a spanwise roll at $x = 1.3$. In case WO, locations (i) and (ii) have amalgamated to a single stronger perturbed length. In the last frame at $t = 1.8375$, for case WO, breakdown of 2D instability to small scale 3D disturbances has taken place and the vortex rolls observed in the primary stage no longer are discernible in the flow. The corresponding frame for case WK in Fig. 7.3 also shows three-dimensionality, however, although the three locations of instability no longer retain their coherence, yet one can still observe three major clusters along which insta-

bility has grown, and at a later time these will merge to a single structure as seen for case WO.

In Fig. 7.6, the iso-surfaces of second invariant of the velocity gradient tensor Q contoured with streamwise velocity are shown for test cases LI, WK and WO at $t = 4.24375$. This visualization parameter is found to be an efficient tool in highlighting the major vortical events occurring in the separated shear layer. For the LI case, shown in the top frame, 2D spanwise vortices ($x = 0.52$ and 0.60) are shed by the separated shear layer via Kelvin-Helmholtz instability. The interaction of this vortex with the hairpin vortices lying underneath gradually amplify the spanwise waviness of the vortex until it breaks down to small three-dimensional flow structures, which is consistent with the findings of Brinkerhoff and Yaras (2011). The turbulent breakdown is followed by reattachment of the flow enclosing a separation bubble. The transition mechanism in the presence of unsteady wakes and blade oscillation deviates significantly from that for a laminar inflow. For test cases WK and WO, shown in the middle and bottom frames of Fig. 7.6, the vortex shed by the separated shear layer has enhanced spanwise waviness and has moved much closer to the wall compared to the LI case. With the increased undulations in the spanwise direction and the influence of the wall, the vortex is more susceptible to transition and undergoes breakdown to turbulence. A reduction in the intensity and extent of the reversed flow and a decrease in the free-stream velocity for test cases WK and WO are observed, when compared with case LI. The unsteady Gaussian wake in test cases WK and WO interacts with the hairpin vortices and one such event has been captured in WK case ($x = 0.54$). This interaction is effective in suppressing the separation bubble. The added disturbance in the form of blade oscillation in test case WO, further accentuates the increased spanwise waviness of the shed vortices when compared to test case WK.

In Fig. 7.7, contours of absolute wall-normal vorticity, $|\omega_y|$, are shown at the indicated times for test case WK at (x,z)-planes within the boundary layer at $y = 0.0022$ for eight different phases of the wake passing cycle. The undulations noted in the separated shear layer upstream of the separated structures for Figs. 7.2 to 7.5, indicative of the location of the travelling wake are explored through the contours of $0.01 < |\omega_y| < 100$. At $t = 1.44375$, a train of vortices are noted, indicating the response of the instantaneous location of the vortex on the boundary layer. Tracking the same train of vortices in the next frame at $t = 1.4875$, indicates that the wake has traversed a distance from $x = 0.26$ to $x = 0.29$ in a time interval $\Delta t = 0.04375$. This observation suggests that while the wake convects at local free-stream velocity, its impression in the boundary layer convects much slower, between 50% and 70% of the local free-stream velocity. The effect of wake is evident only after the rear of the wake

crosses the separation bubble, which is consistent with the observations of Vadlamani (2015) and Coull and Hodson (2011). The effect of the unsteady wakes is to promote early transition as these convect downstream. The location of breakdown to turbulence moved upstream to $x = 0.4$ from $x = 0.45$, as noticed in frames at $t = 1.75$ and $t = 1.44375$, respectively. This was also observed in the instantaneous flow field computed by Vadlamani (2015).

7.4 Time-Averaged Features

In the previous section, the instantaneous flow field was visualized and the primary and secondary stages of instability growth were demarcated for the test cases WK and WO, with earlier breakdown to turbulence observed for the test case, WO with higher level of disturbance in the form of a wall excitation (blade oscillation). In this section, the test cases WK and WO are compared for time-averaged and spanwise-averaged quantities to quantify the time-averaged separation bubble observed in the flow by time and spanwise averaging. As noted in chapter 2, there is a qualitative difference between steady and unsteady separation. For the steady separation, zero skin friction given by Prandtl's criterion is adopted while the Moore-Rott-Sears criterion can be used to characterize unsteady separation in the Eulerian formulation. According to the Moore-Rott-Sears principle, vanishing wall shear is not sufficient in determining separation for an unsteady flow. Unsteady separation takes place at a point off the boundary where the wall-component of the shear vanishes and the local streamwise velocity equals the velocity of the moving separation structure (Haller, 2004). However, in the time-averaged sense, zero crossing for the skin friction is a qualitative description of unsteady separation also. This convention has been adopted in the following results.

In Fig. 7.8, the time-averaged separation bubble is shown for the three test cases LI, WK and WO through the streamlines (shown by the lines) embedded on the streamwise velocity contours on a spanwise-averaged plane. The blue coloured contours indicate regions of reversed flow preceded by separation of the flow. For the baseline unperturbed case, LI, the wall-normal extent of the bubble is the maximum with $y \approx 0.06$. Additionally the streamwise extent of the bubble, i.e. the separation region, is also the largest among the three test cases ($0.37 < x < 1.1$). With additional disturbances in the flow, such as wakes at the inflow in the test case, WK, both the wall-normal ($y \approx 0.02$) and streamwise ($0.4 < x < 0.61$) extents of the bubble have significantly diminished. Thus, with added perturbation the separation region has been suppressed. A similar observation is made for the test case WO, with both wakes convected at inflow and the blade oscillating. A further suppression of the size of the

separation bubble occurs, which seems to indicate that the effects of wakes and oscillations in conjunction have a net cumulative beneficial effect on the flow. This observation is further highlighted in Fig. 7.10, where the time-averaged skin friction is compared for the test cases on the surface of the blade. Another aspect to be noted in Fig. 7.8 is the formation of time-averaged secondary separation bubbles for the test cases, LI and WK, which was also noted by Wissink and Rodi (2004) and Lardeau et al. (2012) in their DNS and LES studies, respectively. Secondary separation bubbles are formed due to the recirculation and separation of reversed flow inside the 'dead-air' region. The primary bubble represents a vortex above the plate, and depending on its strength and interaction with its image system, a secondary bubble is formed (Brinckman and Walker, 2001). In the test case, LI, a large secondary bubble is observed in the region: $0.52 < x < 0.59,\ y < 0.01$; whereas, it is suppressed for the case WK, and is observed for $0.47 < x < 0.49,\ y < 0.002$. For the test case WO, this secondary bubble has been suppressed further and is not discernible in the streamlines, implying weakening of the primary bubble.

Figure 7.9 compares the time-averaged streamwise velocity profiles for the test cases LI, WK and WO along the separated shear layer at the indicated streamwise stations, on a spanwise-averaged plane. In all the frames, a common feature is noted by a shift in the inflection point of the velocity profile towards the wall, as the level of perturbation keeps increasing from LI to WK to WO cases. This shift in the inflection point is observed due to the enhanced v', which also shifts the point of separation downstream. Reversed flow is observed for all the three test cases. At $x = 0.50$, the magnitude of reversed flow experienced by the test cases WK and WO is larger than that is observed for the case LI. This can be explained by the early transition triggered for the cases WK and WO, due to the enhanced perturbations. By $x = 0.55$, the magnitude for reversed flow is higher for the case WK than that is observed for the case WO, which can be explained by the effectiveness of the wall excitation via vibration in suppressing the separation bubble. For the case LI, it has been observed in Fig. 7.8 that this streamwise station lies within the region of secondary separation bubble. This is also observed here, by the local reversal of the reversed flow noted for case LI below $y = 0.01$. At $x = 0.60$, the magnitude of the reversed flow is maximum for test case LI, whereas for cases WK and WO this is approximately where the flow reattaches and thus, the reversed flow is of lower magnitude. Case WK has higher magnitude of reversed flow than test case WO, which can be again explained by the more effective suppression of separation bubble by added blade oscillation.

In Fig. 7.10, the time-averaged skin friction (evaluated using Eq. (5.1)) lines are compared for the test cases LI, WK and WO. For steady separation, the zero crossings of the skin friction line provide the locations of separation and reattachment, whereas the global minima is representative of the transition location. This definition of separation, transition and reattachment through skin friction has been used previously in the literature (Vadlamani, 2015). Although the instantaneous flow field is unsteady, for the time-averaged flow field the skin friction criteria of separation can be used to compare quantitatively between the three test cases. For the test case LI, the point of separation is noted to be at $x = 0.37$ indicated by the zero crossing of skin friction line. A secondary separation bubble, denoted by SSB in the figure, is observed at $0.52 < x < 0.60$, as has been shown in Figs. 7.8 and 7.9. The transition location is at $x = 0.86$, while the reattachment location is at $x = 1.18$. For the test cases WK and WO, a delayed separation is observed at $x = 0.39$, with a slightly more delayed location noted for the case WO. The reattachment location is advanced upstream to $x = 0.62$ for the case WK, and to $x = 0.61$ for the case WO. An effective reduction in the separation region is observed for both the test cases with wake at inflow, with a more pronounced effect observed for the test case WO, with added blade oscillations. The secondary separation bubble observed in Fig. 7.8, and characterized by positive skin friction and denoted by SSB in Fig. 7.10, has been shown here for the test case WK. For the test case WO, as seen in Fig. 7.8, the secondary separation bubble has been suppressed completely and is not seen here in Fig. 7.10 in the time-averaged skin friction plot.

In Fig. 7.11, the rms u-velocity fluctuation contours are shown for the test cases LI, WK and WO. For the test case LI, the wall-normal location of the peak u-rms fluctuation is at $y_{max} = 0.053$. It is seen that with the test cases WK and WO, which promote enhanced near wall mixing the peak wall-normal location shifts towards the wall, and is at $y_{max} = 0.018$ for the test case WK and at $y_{max} = 0.014$ for the test case WO. The shift in the wall-normal location is most prominent for the case WO. The Gaussian wake imposed at the inflow induces a fluctuating component which traverses the flow field, and this in turn has a direct effect on the velocity fluctuations. Another observation to be made here is the upstream shift in the streamwise peak location from $x_{max} = 0.6846$ for case LI to $x_{max} = 0.5748$ for the case WK to $x_{max} = 0.5697$ for the case WO. It must be noted here that although blade oscillation has a net cumulative effect on suppressing the separation region, the small amplitude oscillation in the current simulations do not alter the flow topography significantly in the time-averaged sense.

Turbulent kinetic energy (TKE) budget given by Eq. (5.2), is also a good measure of the disturbance flow field. It also provides essential information to the turbulence modelling community. Here, only the TKE production term, given by P in Eq. (5.2), is evaluated for the three test cases LI, WK and WO in Fig. 7.12. As has been noted in Fig. 7.11, there is a wall-normal shift towards the wall for the test cases WK and WO, as compared to the baseline LI case. This can be explained by the constituent product terms involved in the TKE production term: (i) the product of fluctuating velocity components brought about by the wake imposed at the inflow, (ii) the mean velocity gradient, which is directly affected by the wall excitation in the form of blade oscillation. An interesting occurence is in the form of a small patch of TKE production formed at $x = 0.50$ for the test cases WK and WO. This near-wall patch of production can be attributed to the near-wall turbulence brought about by enhanced mixing in the cases WK and WO. The flow at the streamwise locations inclusive of this patch, will have a peak in the free shear layer and one peak corresponding to the newly formed turbulent boundary layer. A similar observation was made by Alam and Sandham (2000) in their DNS studies on a laminar separation bubble. This near-wall peak will be seen in detail for the cases WK and WO in Fig. 7.13, where TKE production profiles are shown at locations within the separated shear layer.

In Fig. 7.13, the TKE production profiles are extracted at indicated streamwise locations for the test cases LI, WK and WO. In the frame at $x = 0.45$, a shift in the wall-normal location of the peak TKE production is observed successively towards the wall from the case LI to WK to WO. The highest peak is observed in the test case WO, with highest level of perturbation. Compared to the cases WK and WO, the peak for the LI case for TKE production is much lower in magnitude. At $x = 0.50$, it is seen that there is a larger difference in production peaks for the cases WK and WO. This can be explained by the earlier transition triggered by the additional wall excitation for the case WO. As seen in the production contours, an additional near-wall TKE production peak is observed for the cases WO and WK. By $x = 0.55$, the baseline case LI has a discernible production peak, but the magnitude is still 4-5 times lower than the highest peak observed for the case WK. As seen previously in the u-velocity profiles in Fig. 7.9 at $x = 0.55$, the case WK dominates the case WO in terms of the peak production value. This can be attributed to the earlier reattachment noted for the case WO compared to the case WK, as seen in Fig. 7.10. In the frame at $x = 0.60$, the peak associated with the case LI has the highest magnitude, which can be observed from the early reattachment of flow in the cases WK and WO.

7.5 Disturbance Field Mechanics

The process of transition to turbulence often is characterized with the formation of coherent structures and vortices in the flow, which propagate in the underlying fluctuation field. Some of the popular vortex visualization methods such as Q- and λ_2-criteria have been used in this chapter also, as in previous chapters, to highlight the important vortical events occurring in the instantaneous flow field undergoing transition to turbulence. These methods are primarily used for identifying vortical coherence, thus detecting the near-wall structures is not possible with these methods.

With this in mind, two methods for studying instability mechanisms derived in appendix A for the DME method and in appendix B for the DETE method are used to provide additional information about the nature of the transition routes adopted in the various test cases, apart from information already acquired through the instantaneous and time-averaged results.

The DME method is a tool to characterize instabilities which arises due to the interaction of the velocity and vorticity fields through convective acceleration term. The governing equation for instantaneous distribution of DME is given by Eq. (2.8), which is a Poisson equation. A source of instability appears as a negative right hand side of the equation, whereas a positive right hand side is a sink of instability. In the following figures we show results at the selected time $t = 4.24375$ or $t = 97t_w/8$. This time frame has been chosen as we can see significant turbulent activity at this time, and also to compare with the structures detected by the Q-criterion.

In Fig. 7.14, the iso-surfaces of the right hand side of DME for the test cases WK and WO are contoured with the streamwise velocity at $t = 4.24375$. The iso-surface value of DME has been chosen by taking the iso-surface of spanwise vorticity, $\omega_z = -80$ as the reference for test cases WK and WO at the same time. The equilibrium flow, to define disturbance flow for cases WK and WO, is given by test case LI. The right hand side of DME is related to the Q-criterion through the expression, $\nabla^2 E_d = 2Q + \nabla^2[\frac{1}{2}(V^2 - V_m^2)]$, and thus comprises of not only the Q-criterion, but also the fluctuating kinetic energy. The coherent structures observed by DME differ from those observed by Q-criterion in Fig. 7.6. At streamwise locations downstream of $x = 0.7$, the field is dominated by arrays of lifted off hairpin vortices for both test cases WK and WO, which is a similar feature noted in the Q-criterion iso-contours of Fig. 7.6. Beyond the edge of the separated region, $0.4 < x < 0.6$, the structures observed by DME in Fig. 7.14 for test cases WK and WO, have a stacked hairpin-shaped appearance contrary to the corresponding structures shown by Q-criterion in Fig. 7.6, wherein stacks

were not present. The process by which structures due to the unsteady wake have evolved in the upstream part of frames WK and WO are observed, which was not seen for Q-criterion in Fig. 7.6. DME emphasizes stronger three-dimensionality as compared to Q-criterion. For test case WO, shown in the bottom frame, the additional wall excitation of blade vibration promotes a reversed flow with higher intensity, seen by the dark (blue) contours, as compared to test case WK. The spanwise undulations of the shed vortex are maximum for the test case WO. Blade oscillation, thus has a cumulative effect in suppressing the separation region and promoting early transition, when compared to test case WK, which has the effect of the unsteady wake alone.

The second method is based on disturbance enstrophy and helps explain the creation and growth of rotationality in the flow. A discerning feature of this method is that it retains the unsteady and viscous terms of the incompressible NSE, and thus serves as an apt tool in tracking instabilities and picking up small scale near-wall structures. The derivation of DETE is given in appendix B and the governing equation has been provided by Eq. (2.9), with the condition for an instability dictated by Eq. (2.10). The first, second and third set of terms in Eq. (2.9) are the respective contributions from the vortex stretching, diffusion and dissipation terms of the enstrophy transport equation (Sengupta et al., 2013). The vortex stretching term is absent for 2D flows and plays a major role in 3D flows. Here, an attempt to understand the contributions arising from the various constituent terms of DETE are provided for the test case WK in Figs. 7.16 and 7.18 and for the test case WO in Figs. 7.17 and 7.19 for Ω_d taking positive and negative values respectively.

In Fig. 7.15, iso-surfaces of growth rate of disturbance enstrophy $|\frac{D\Omega_d}{Dt}|$ are shown for the test cases WK and WO at $t = 4.24375$, with the equilibrium solution taken as the test case LI. The iso-surface value has been chosen by taking the iso-surface of spanwise vorticity, $\omega_z = -80$ as the reference at the same time, for test cases WK and WO. The structures identified by DETE vary from those identified by DME in Fig. 7.14, which can be attributed to the absence of unsteady and viscous terms in the equation for DME. The dominance of the red contours suggests that the instabilities in the flow are governed by a positive disturbance enstrophy and positive growth rate. The near-wall small scale viscous structures, on the other hand, illustrate a stronger effect of instabilities arising with negative growth rates. This occurrence of the positive and negative growth rate bounded instabilities has also been seen for aeroelastic blade vibration calculations in chapter 5 and for the vortex-induced instability in chapters 4 and 6. For the test case WK, a vortex roll with substantial spanwise waviness is observed. This vortex roll loses its identity in the frame for test case WO with higher

disturbance level, showing higher spanwise perturbations. This feature is more pronounced for the structures identified by DETE, as compared to the corresponding structures seen by DME in Fig. 7.14. The near-wall sheet immediately upstream of the separated shear layer is seen to have a negative growth rate for test case WO as compared to test case WK. This can be attributed to the wall excitation in the form of the imposed blade oscillation in this case.

In Figs. 7.16 and 7.17, the iso-surfaces of constituent terms of DETE and the growth rate of the disturbance enstrophy are shown for instabilities with positive Ω_d and positive growth rates for test cases WK and WO, respectively at $t = 4.24375$. Three iso-surface levels indicated by the colour bar are shown for all the frames. The contribution from dissipation is insignificant in comparison to the effects of the vortex stretching term and diffusion. The most significant contributions from the vortex stretching term and diffusion terms indicated by the light blue contours arise and propagate near the wall. The order of magnitude of each term, when compared with its counterpart for negative Ω_d, shows it to be higher. This information is provided only by the DETE, wherein classification of instabilities into arising due to positive/negative Ω_d can be carried out. It is also pertinent to understand which sign of Ω_d originates from the inviscid/viscous and separated/unseparated part of the flow. For test case WK, in Fig. 7.16, two vortex rolls with spanwise undulations are observed, but for test case WO shown in Fig. 7.17, these two rolls have amalgamated into a single perturbed region. This shows the higher receptivity of test case WO due to higher level of imposed disturbance.

In Figs. 7.18 and 7.19, the iso-surfaces of constituent terms of DETE and the growth rate of the disturbance enstrophy are shown for instabilities with negative Ω_d and negative growth rates for test cases WK and WO, respectively at $t = 4.24375$. Three iso-surface levels indicated by the colour bar have been shown for all the frames. For diffusion, dissipation and growth rate of Ω_d, there is a small, but net contribution from the upstream part of the flow before separation. This is indicated by the near-wall strip ($x < 0.4$) and is more discernible for case WK. The contributions to the growth rate of Ω_d from the vortex stretching and dissipation terms is more, while the contribution from diffusion term is scant for both test cases WK and WO. It is worth noting that the vortex stretching term only becomes important after the flow has already separated. This observation is consistent with the DETE budget results of aeroelastic oscillation with FST in chapter 5 and the vortex-induced instability in chapter 6. The most significant contributions from vortex stretching term (red contours) are found in a thin strip near the wall for both test cases WK and WO. For the test cases WK and WO, the contributions from positive Ω_d is significantly higher than for negative Ω_d. Overall,

the instability creates more positive Ω_d than negative Ω_d. The instability is driven mostly by stretching and diffusion term for positive Ω_d, while the dissipation term is important for negative Ω_d. This is also seen for the DETE budget results in chapters 5 and 6. As seen before for Figs. 7.16 and 7.17 showing positive growth rates of Ω_d, here too, the test case WK shows a more pronounced vortex roll with spanwise undulations, whereas for test case WO, there is a single perturbed region with enhanced spanwise perturbations.

In general, the structures governed by positive growth rates are found in a deck lifted off from the boundary layer, whereas the structures governed by negative growth rates of disturbance enstrophy are found near the wall. This has been seen previously for the 2D computations of linearized growth rates of disturbance enstrophy shown in Figs. 6.13 to 6.16 for vortex-induced instability in chapter 6 and for the budget results for aeroelastic oscillations in chapter 5. Another aspect of the DETE budget is that the diffusion term is more prominent for structures indicated by positive growth rates, while the dissipation term is more prominent when accounting for structures governed by negative growth rates.

7.6 Conclusions

The individual and coupled effects of incoming unsteady, periodic wakes and aeroelastic blade oscillations on the separation of the suction surface boundary layer over a flat plate is numerically investigated. Two different direct numerical simulations have been performed for distinguishing between the individual and cumulative effects of the imposed disturbance fields. The upper wall of the test section is specifically contoured to simulate the pressure distribution on the suction surface of a 'ultra high-lift' low pressure turbine (LPT) blade. The wake at the inlet is imposed by a periodic Gaussian function and parameters have been chosen to simulate the effect of upstream blade rows on the LPT blade. The oscillation on the blade surface is imposed by a sinusoidal wall-normal perturbation and parameters have been chosen to simulate blade flutter in real LPT blades.

The results showed the evidence of enhanced spanwise undulations in the separated shear layer in the presence of unsteady wakes and blade oscillation causing early destabilization. While the wake convects at local free-stream velocity, its impression in the boundary layer convects much slower, between 50% and 70% of the local free-stream velocity. The lag between the wake passing and the transition is demonstrated using sequence of y-vorticity plots at a wall-normal plane in Fig. 7.7. Both unsteady wakes and blade oscillation promoted near-wall mixing. This resulted in the upstream shift of the transition point and a significant reduction in the size of the separation bubble. The combined effect of unsteady wakes and

blade oscillations further reduced the size of separation bubble. The secondary separation bubble observed in the unperturbed flow was reduced with the presence of wakes and was completely suppressed with the addition of the blade oscillation. The net effect of mixing was to shift the inflection point of the velocity profile towards the wall. The budgets of turbulent kinetic energy showed that the production largely dominates with higher level of disturbance in the separated shear layer. The structures identified by various instability mechanisms are compared and the source of the instability is traced back. Smoother structures are noted for Q-criterion and disturbance mechanical energy, whereas the structures observed through the disturbance enstrophy transport equation capture those arising due to unsteady and viscous terms of the Navier-Stokes equation. The structures indicate a smaller extent of reversed flow with added disturbance, with the least seen with the cumulative effect of unsteady wakes and blade oscillations. Structures governed by positive growth rate of disturbance enstrophy are found in the free stream whereas those due to negative growth rates of enstrophy are observed in the near-wall region.

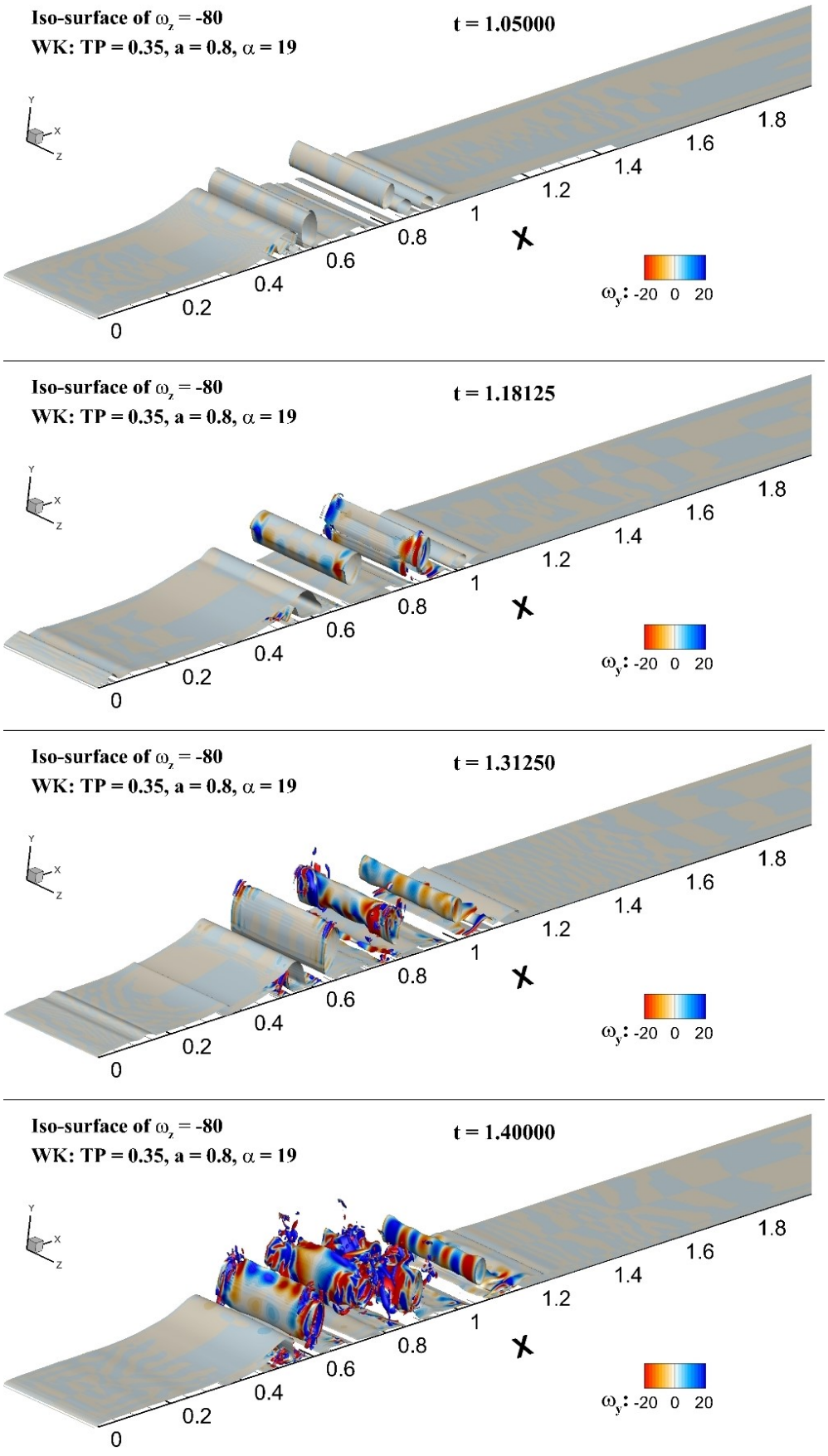

Fig. 7.2 Primary stage of wake-induced instability for test case WK shown through the iso-surface of spanwise vorticity $\omega_z = -80$ coloured with wall-normal vorticity $-20 > \omega_y > 20$.

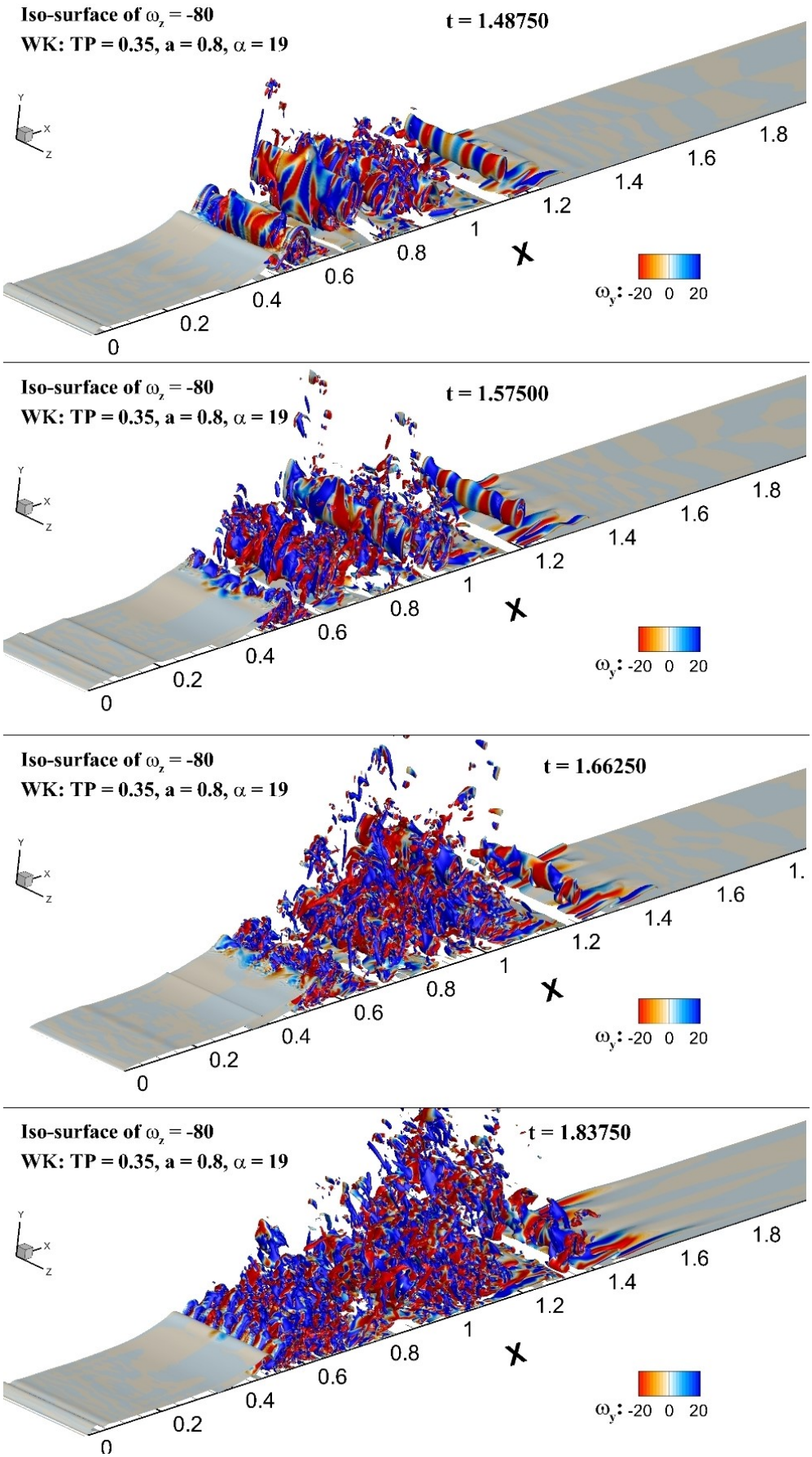

Fig. 7.3 Secondary stage of wake-induced instability for test case WK shown through the iso-surface of spanwise vorticity $\omega_z = -80$ coloured with wall-normal vorticity $-20 > \omega_y > 20$.

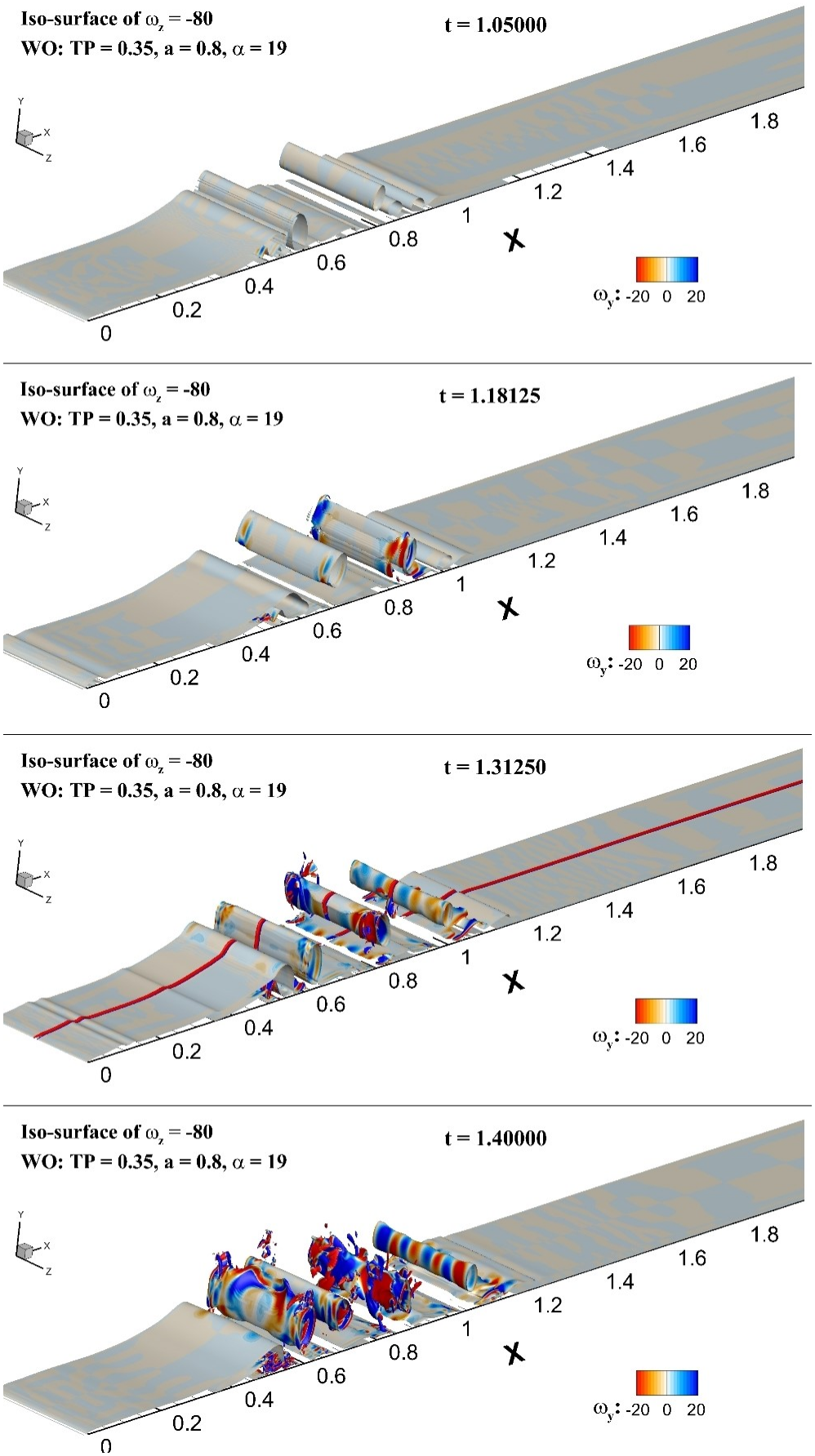

Fig. 7.4 Primary stage of wake-induced instability in the presence of aeroelastic vibration for test case WO shown through the iso-surface of spanwise vorticity $\omega_z = -80$ coloured with wall-normal vorticity $-20 > \omega_y > 20$.

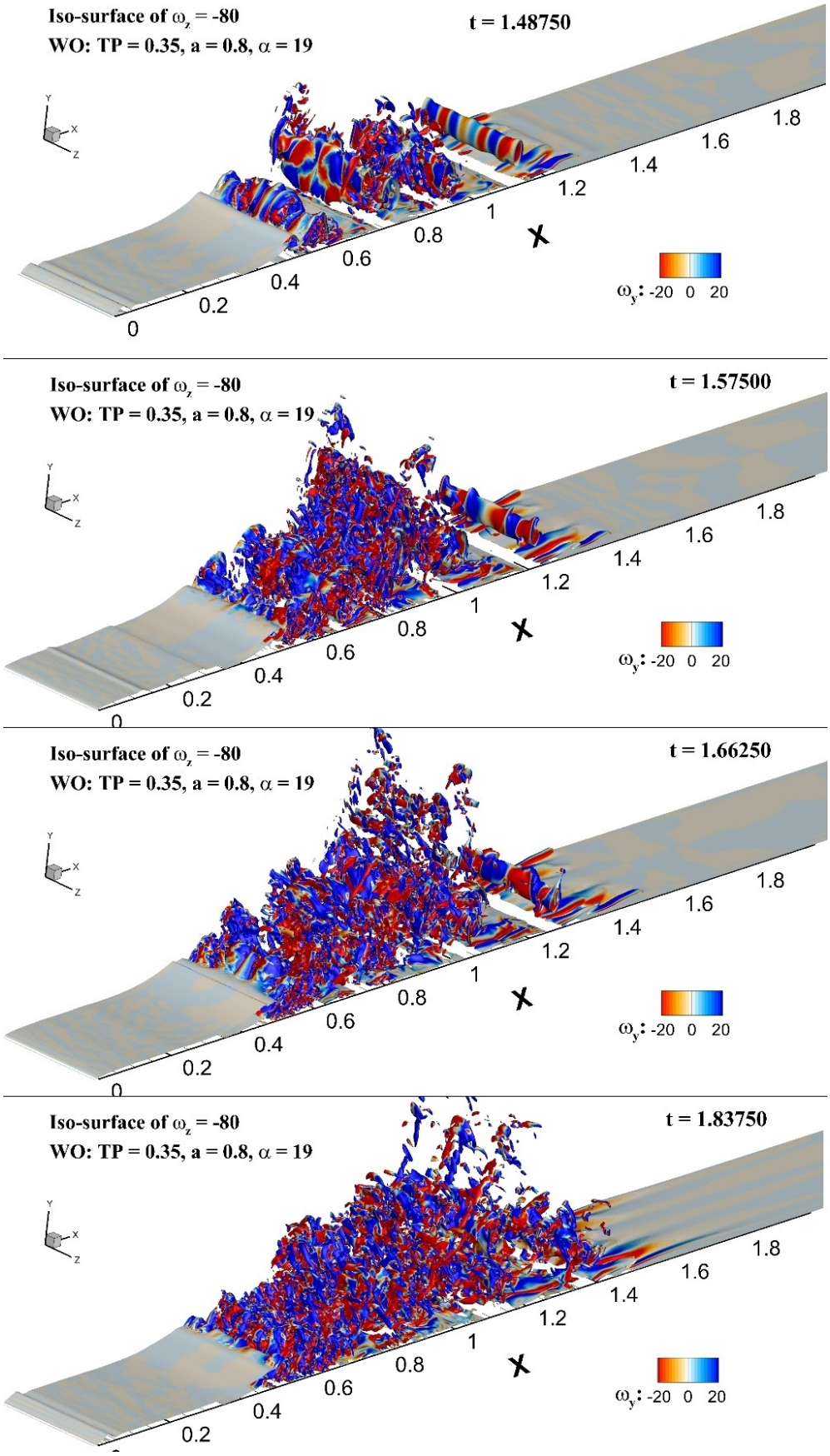

Fig. 7.5 Secondary stage of wake-induced instability in the presence of aeroelastic vibration for test case WO shown through the iso-surface of spanwise vorticity $\omega_z = -80$ coloured with wall-normal vorticity $-20 > \omega_y > 20$.

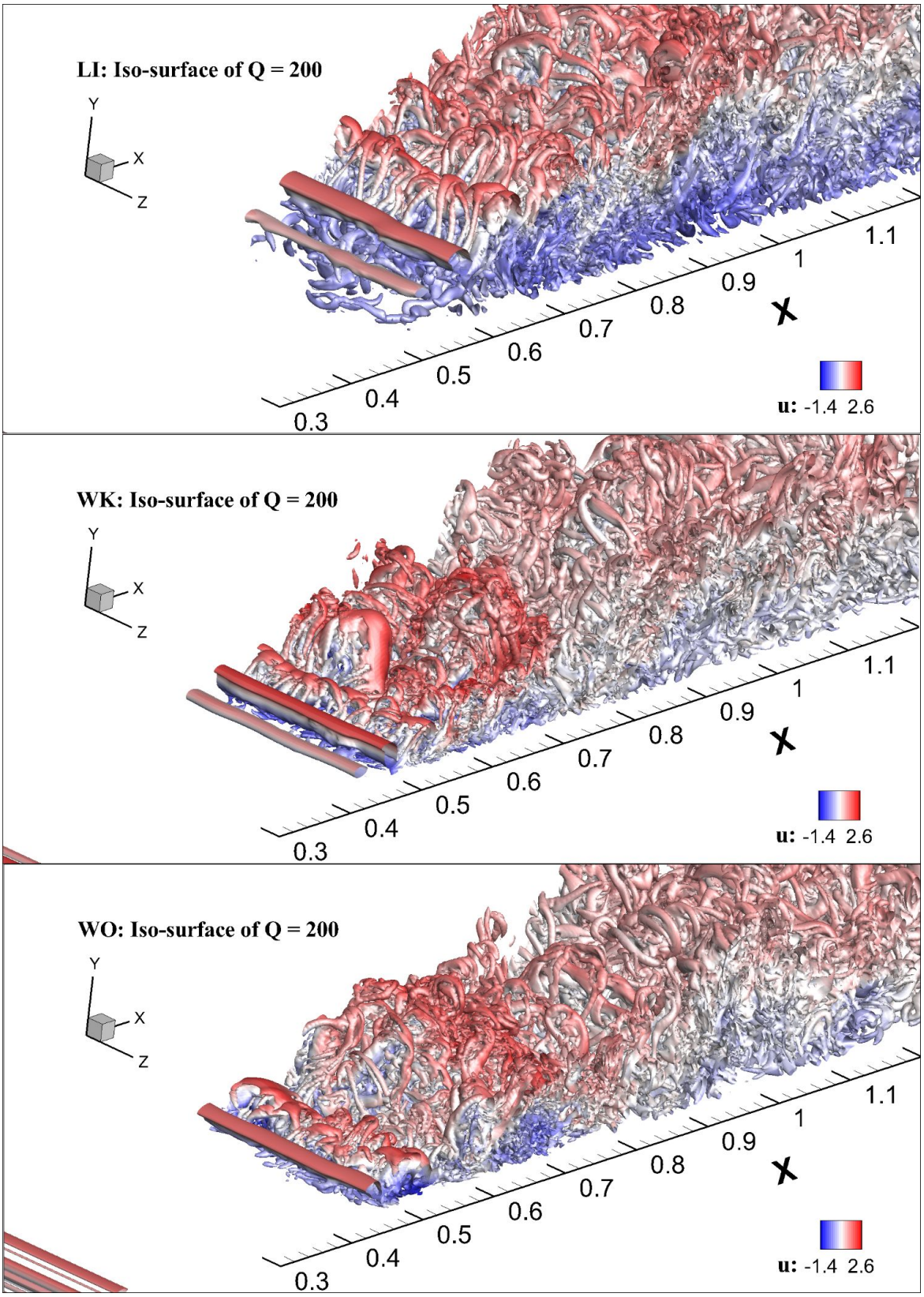

Fig. 7.6 Iso-surfaces of Q-criterion ($Q = 200$) coloured with streamwise velocity ($-1.4 < u < 2.6$) for test cases LI, WK and WO. Reversed flow is indicated by the blue contours.

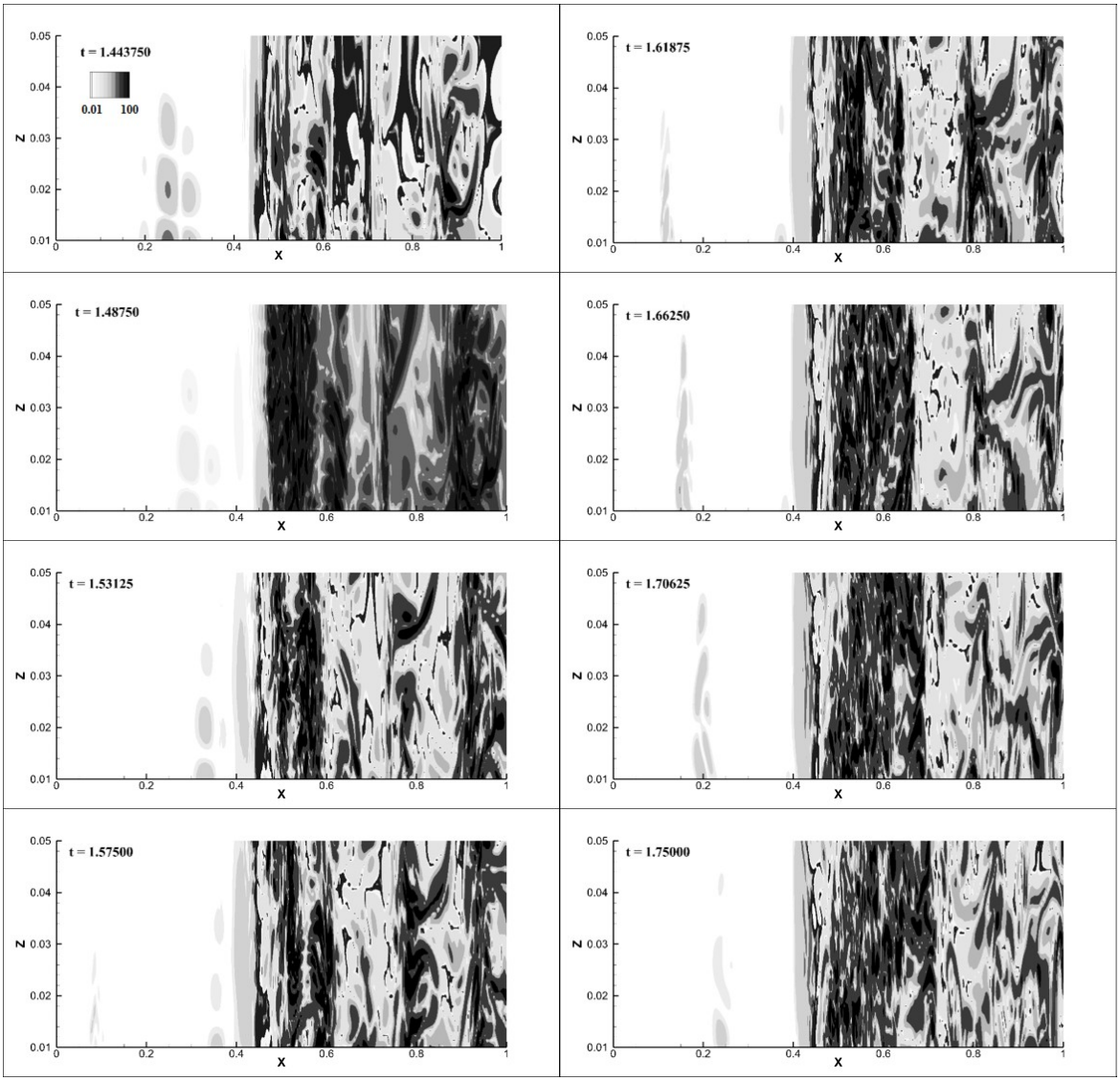

Fig. 7.7 Contours of the absolute wall-normal vorticity, $|\omega_y|$ extracted at a plane within the boundary layer at $y = 0.0022$ for test case WK, at the indicated times.

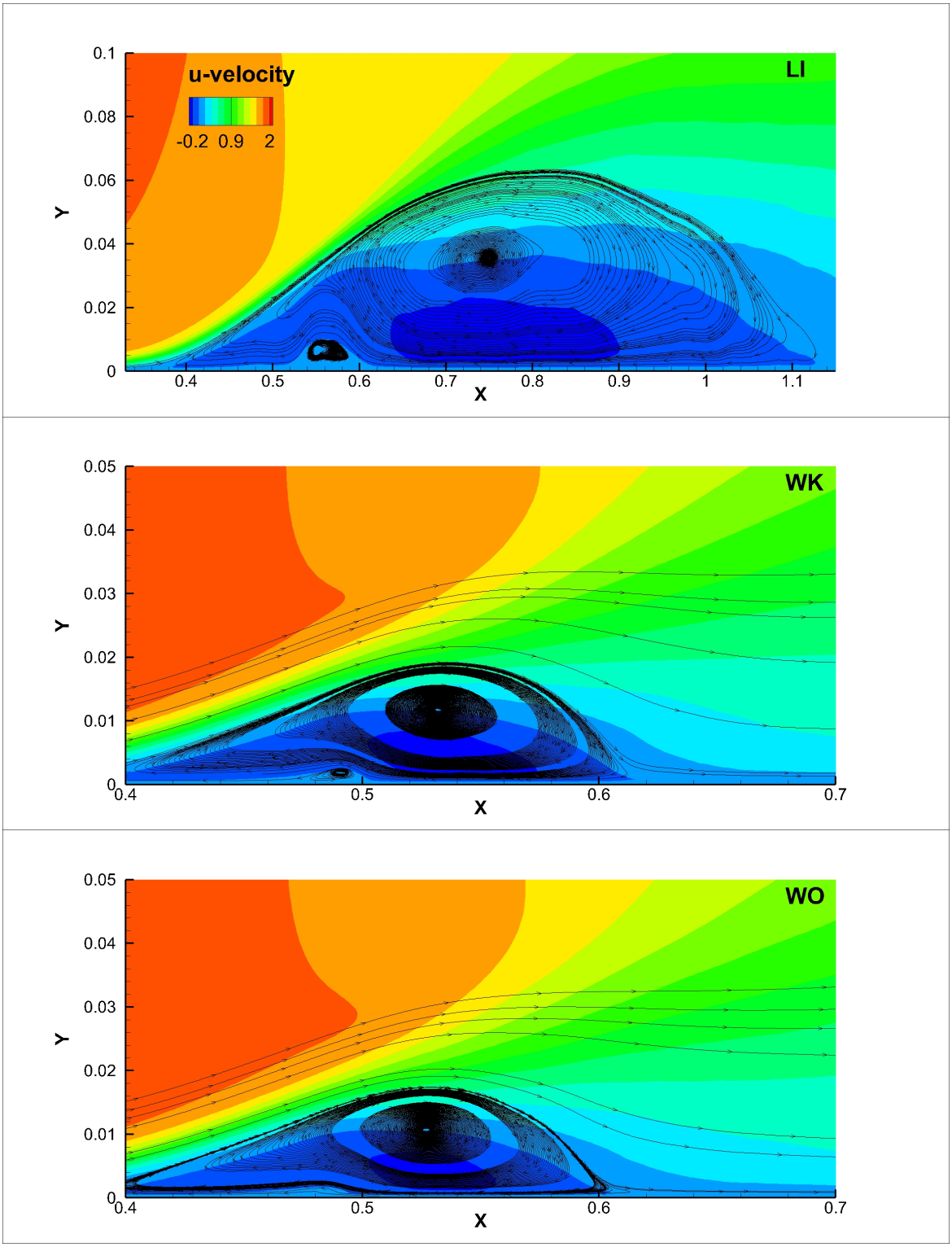

Fig. 7.8 Laminar separation bubble shown by streamlines in u-velocity contours for test cases LI, WK and WO.

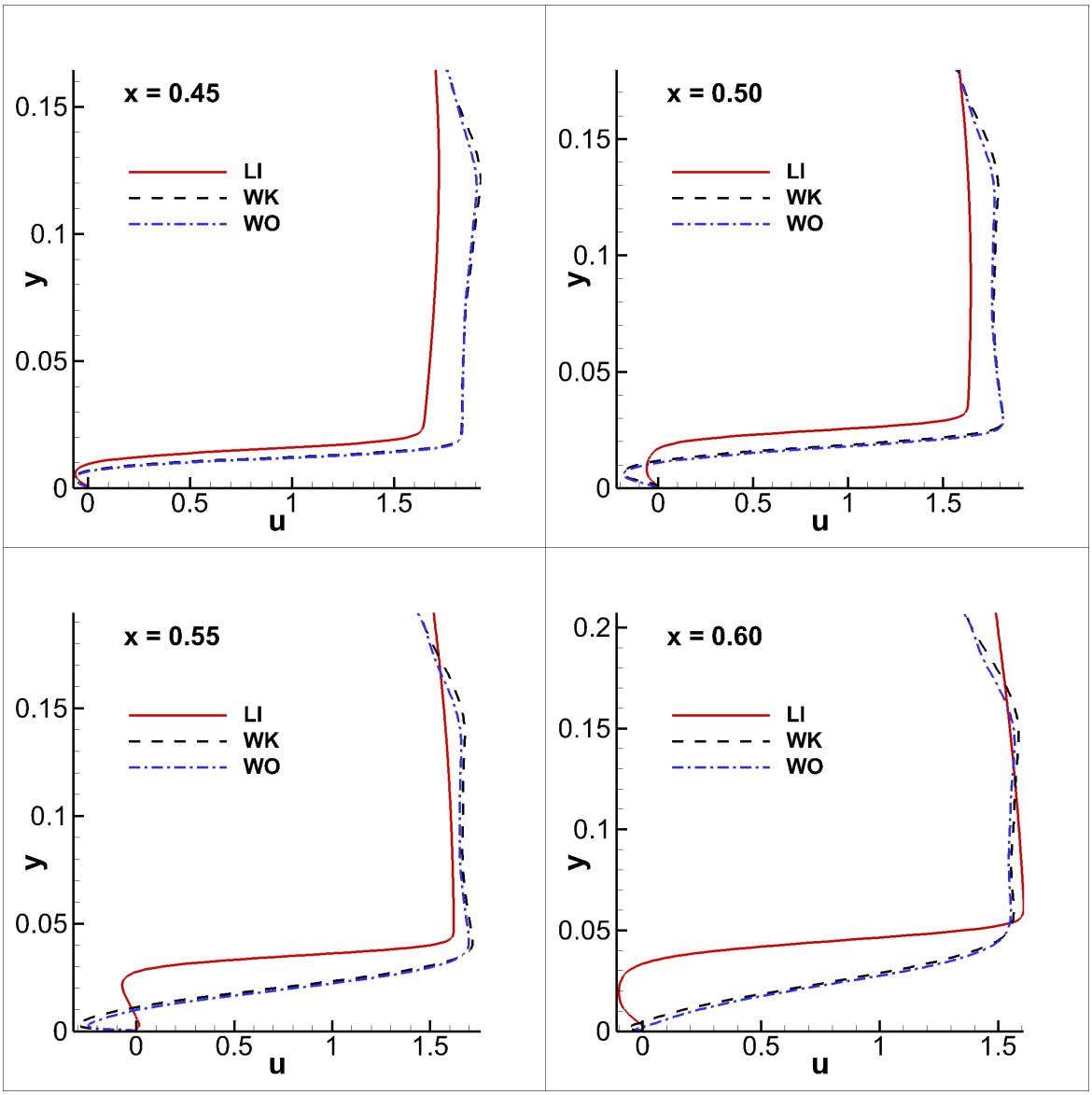

Fig. 7.9 Streamwise velocity (u) extracted at various locations in the separated shear layer at $x = 0.45,\ 0.50,\ 0.55$ and 0.60 for test cases LI, WK and WO.

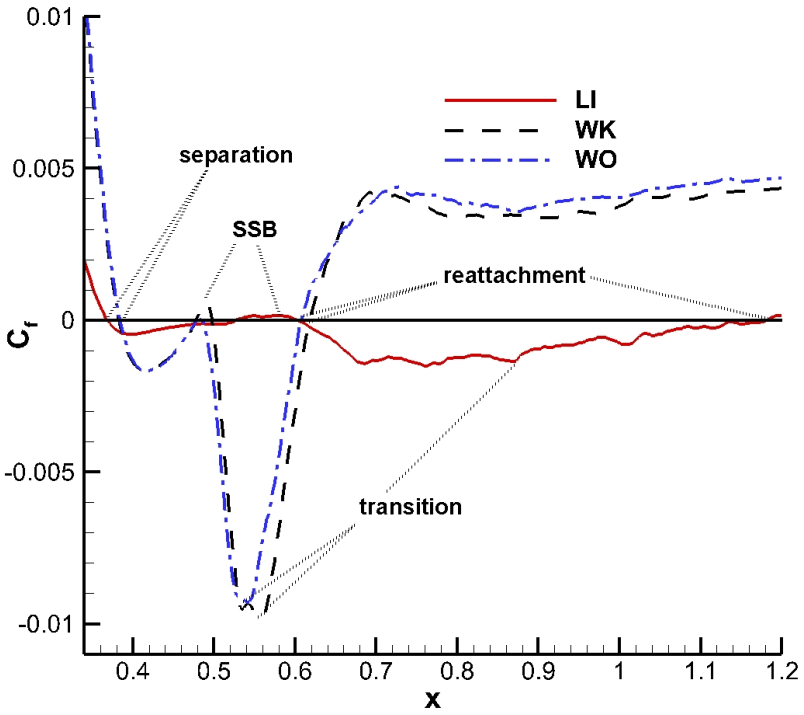

Fig. 7.10 Skin friction lines for the test cases LI, WK and WO showing the separation, transition and reattachment points in the flow. The secondary separation bubble for cases LI and WK has been denoted by SSB in the figure.

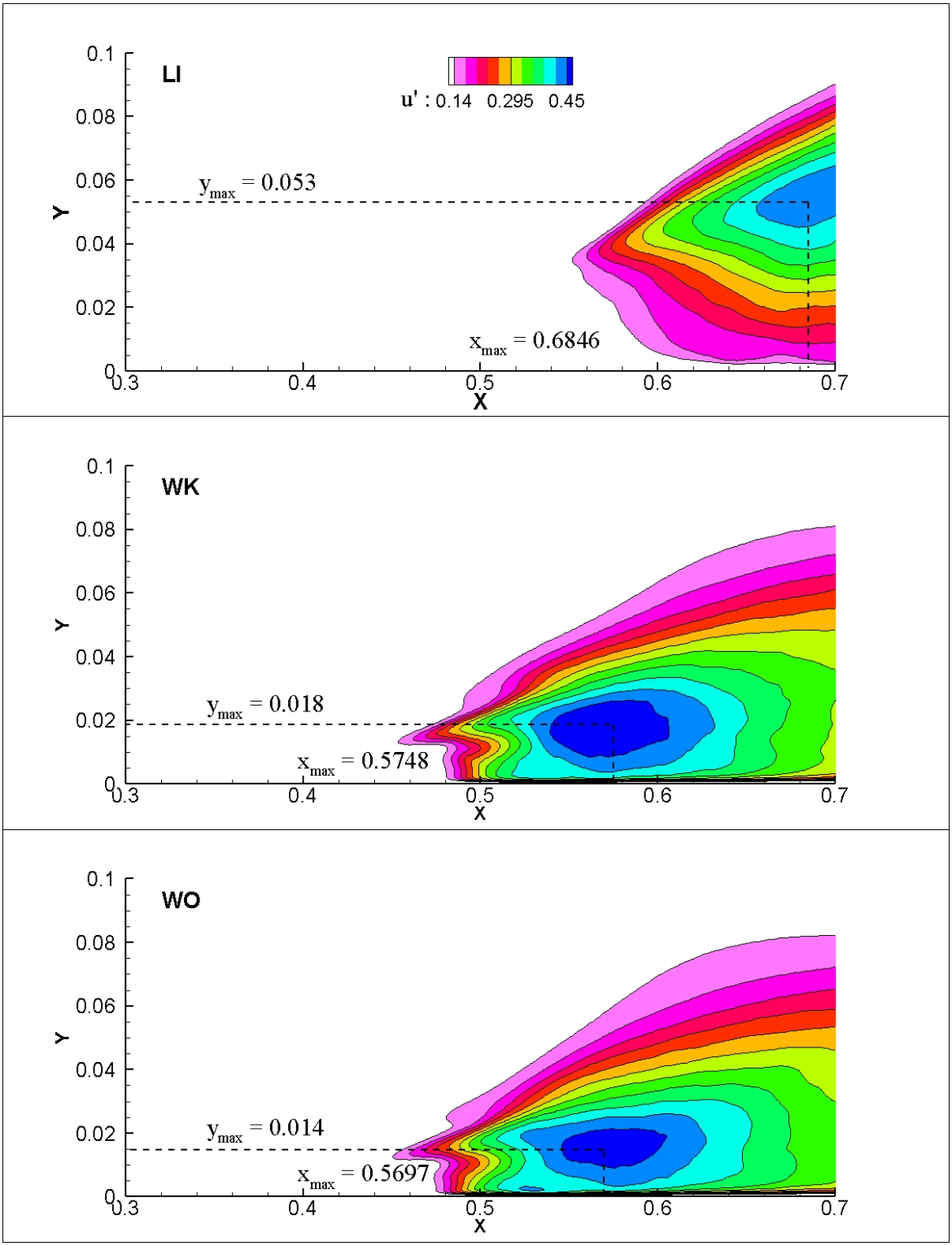

Fig. 7.11 Root mean square u-velocity fluctuation contours for test cases LI, WK and WO showing the wall normal and streamwise location of the peak value.

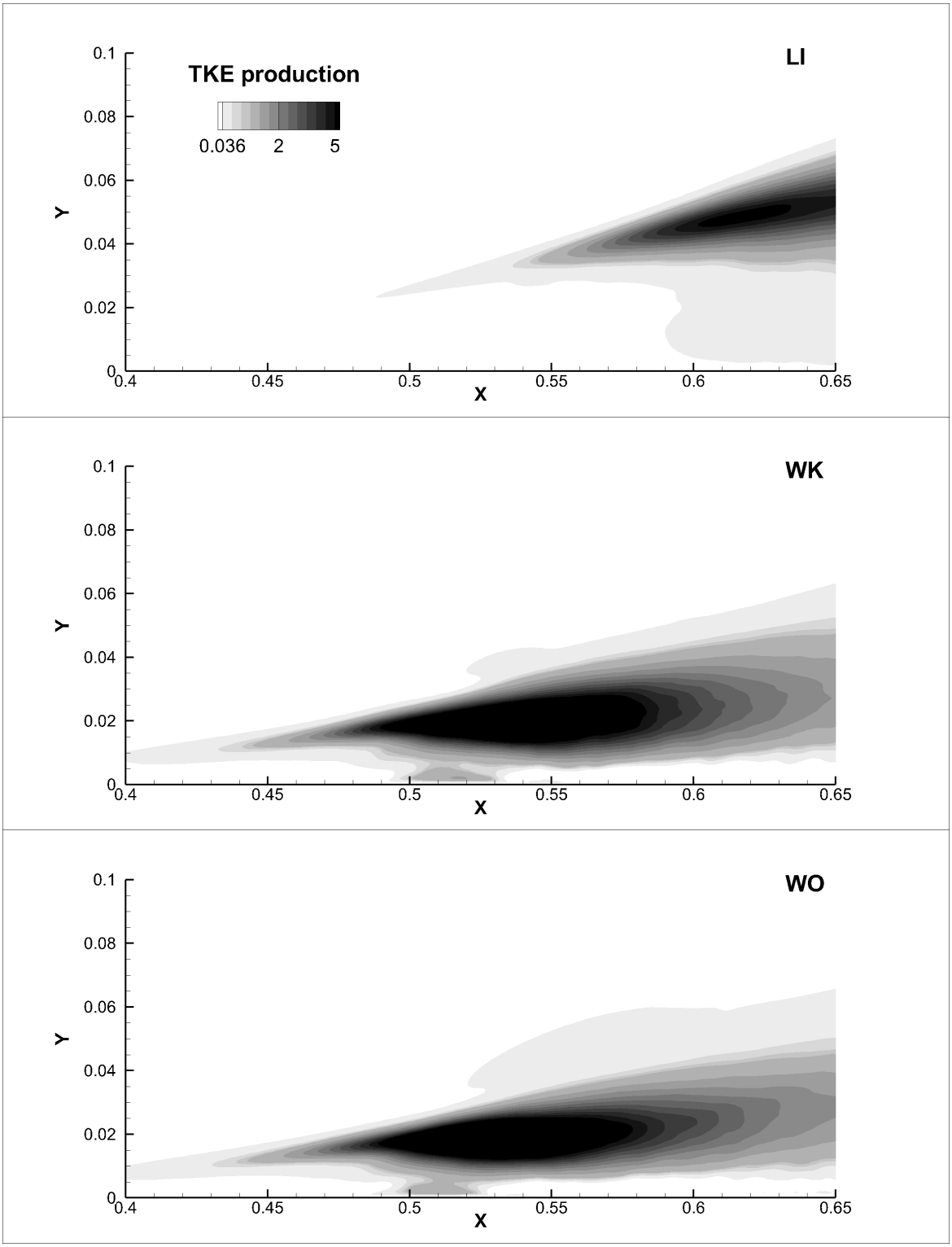

Fig. 7.12 TKE production contours for test cases LI, WK and WO.

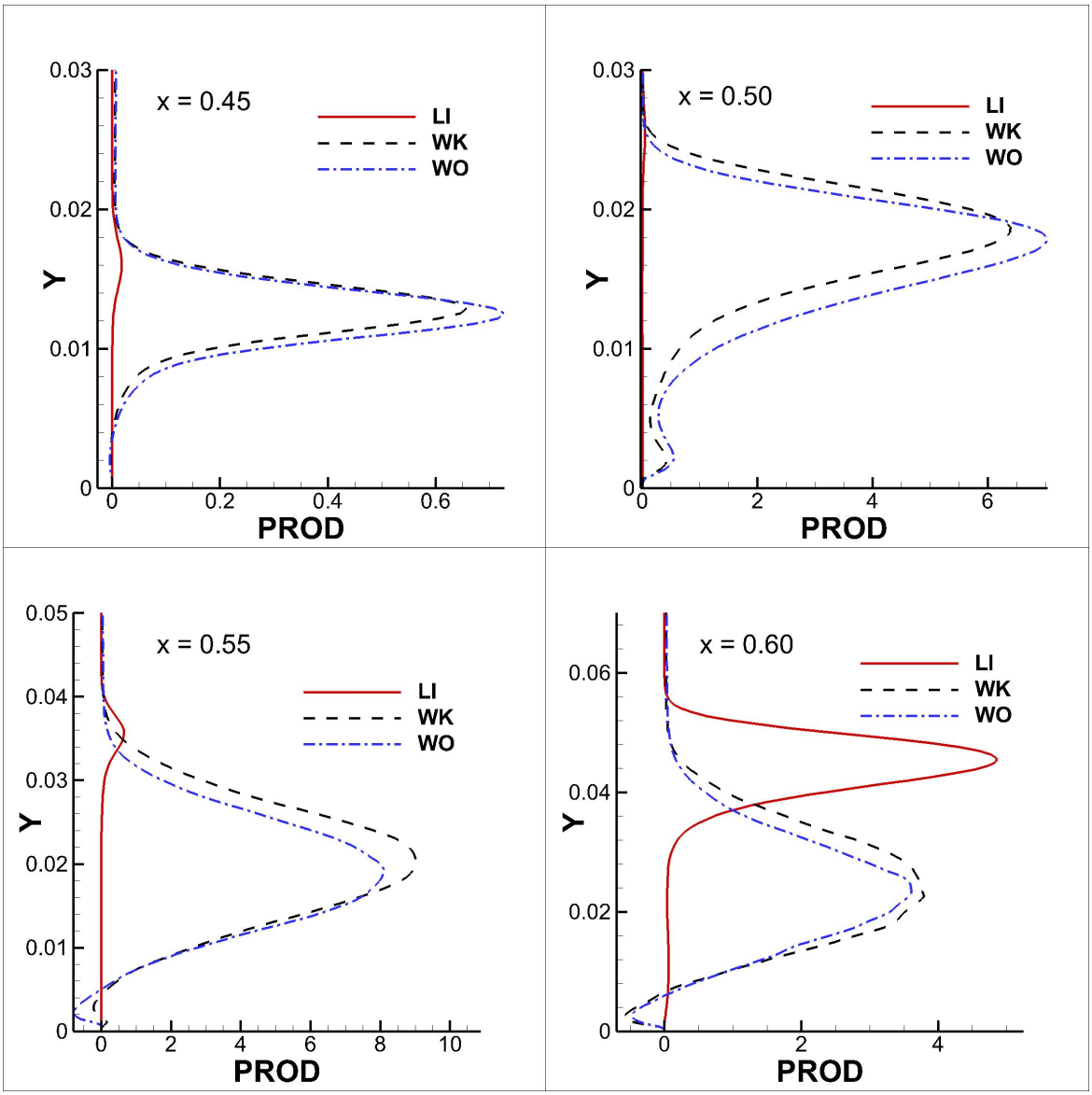

Fig. 7.13 TKE production extracted at various locations in the separated shear layer at $x = 0.45$, 0.50, 0.55 and 0.60 for test cases LI, WK and WO.

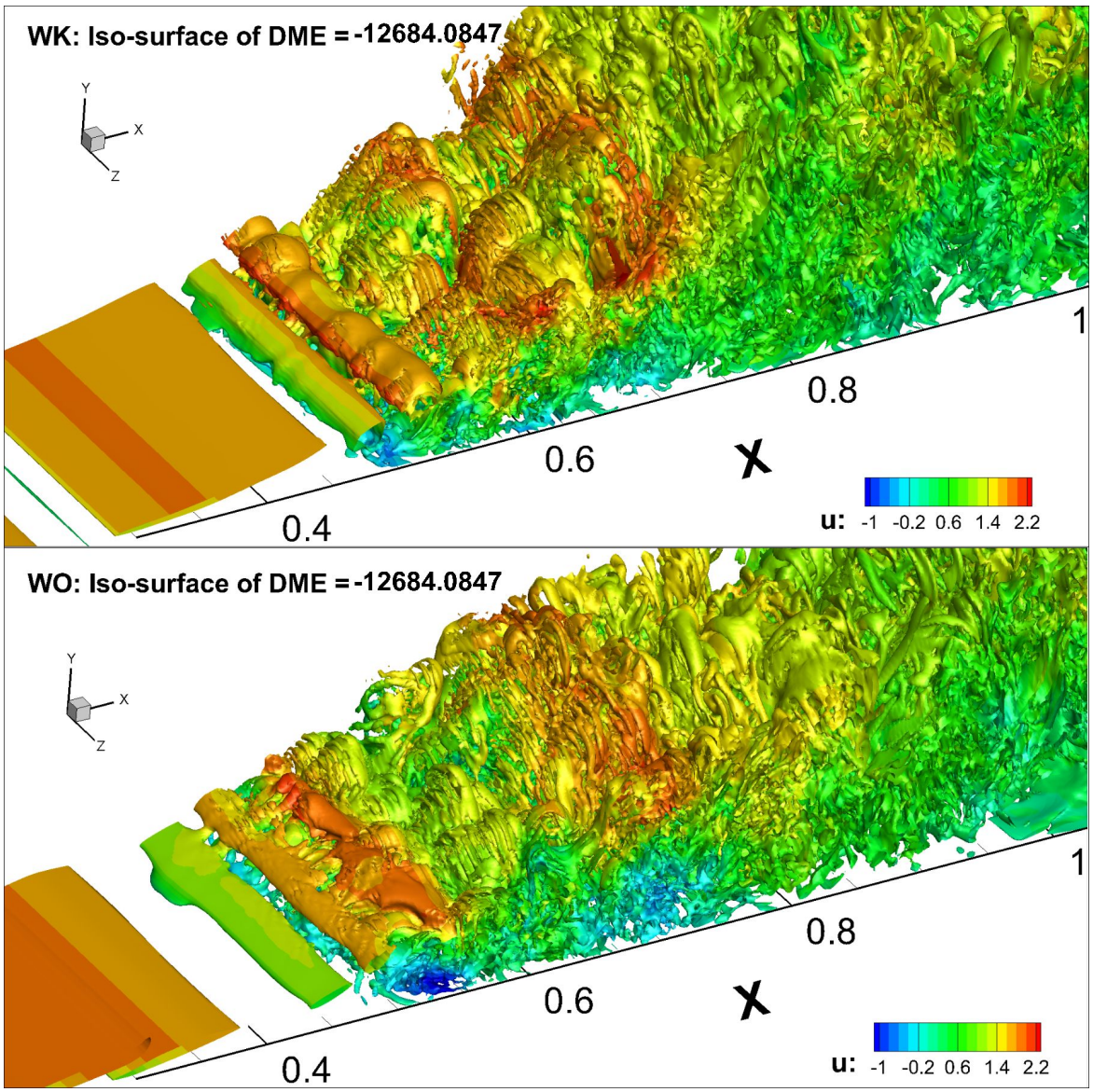

Fig. 7.14 Iso-surfaces of the right hand side of DME ($\nabla^2 E_d$ = -12684.0847) coloured with streamwise velocity for test cases WK and WO at $t = 4.24375$.

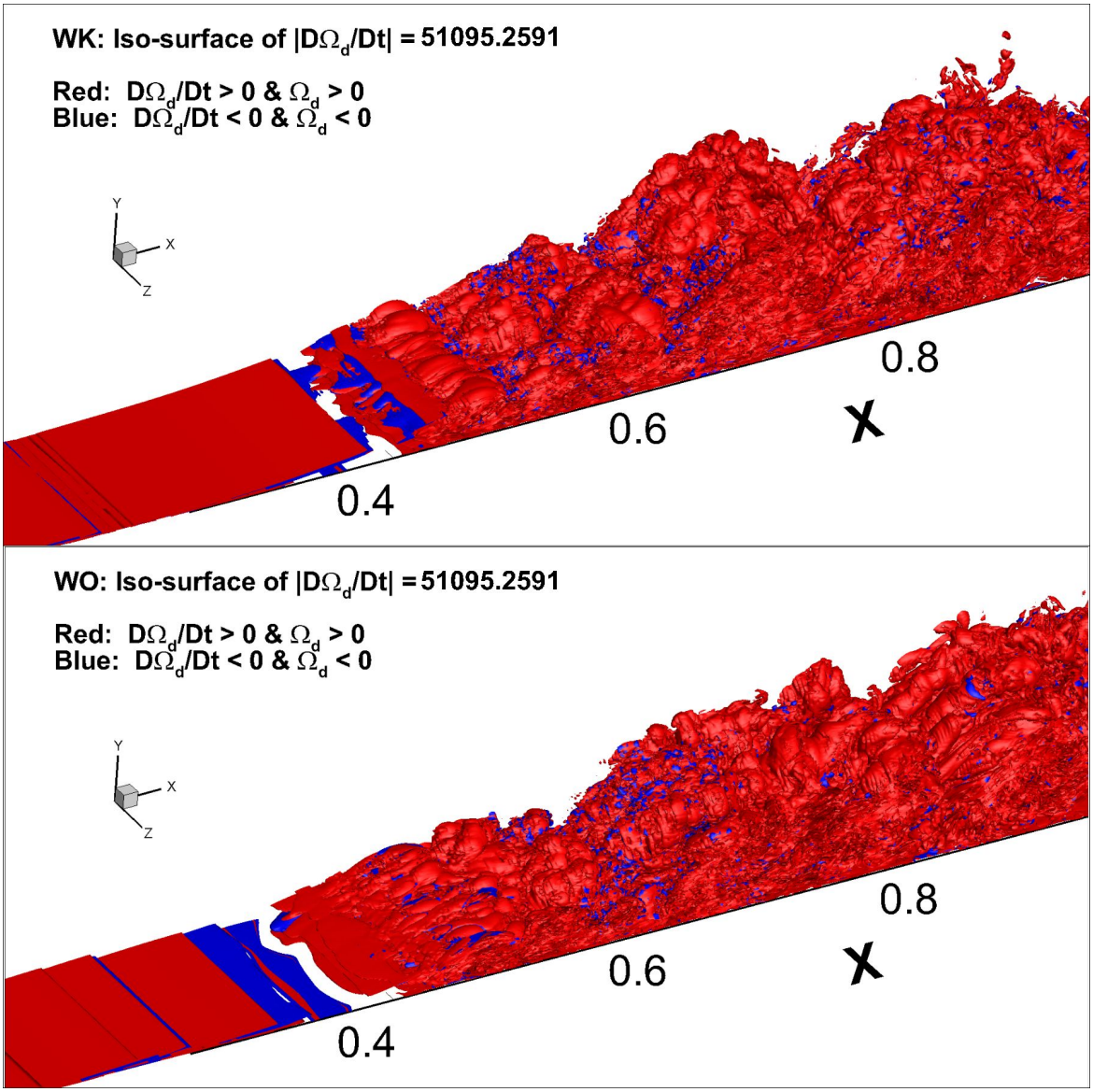

Fig. 7.15 Iso-surfaces of $\frac{D\Omega_d}{Dt}$ ($|\frac{D\Omega_d}{Dt}| = 51095.2591$) for test cases WK and WO at $t = 4.24375$. The lighter (red) contours are for positive growth rate and for positive disturbance enstrophy, whereas the darker (blue) contours indicate negative growth rate for negative disturbance enstrophy.

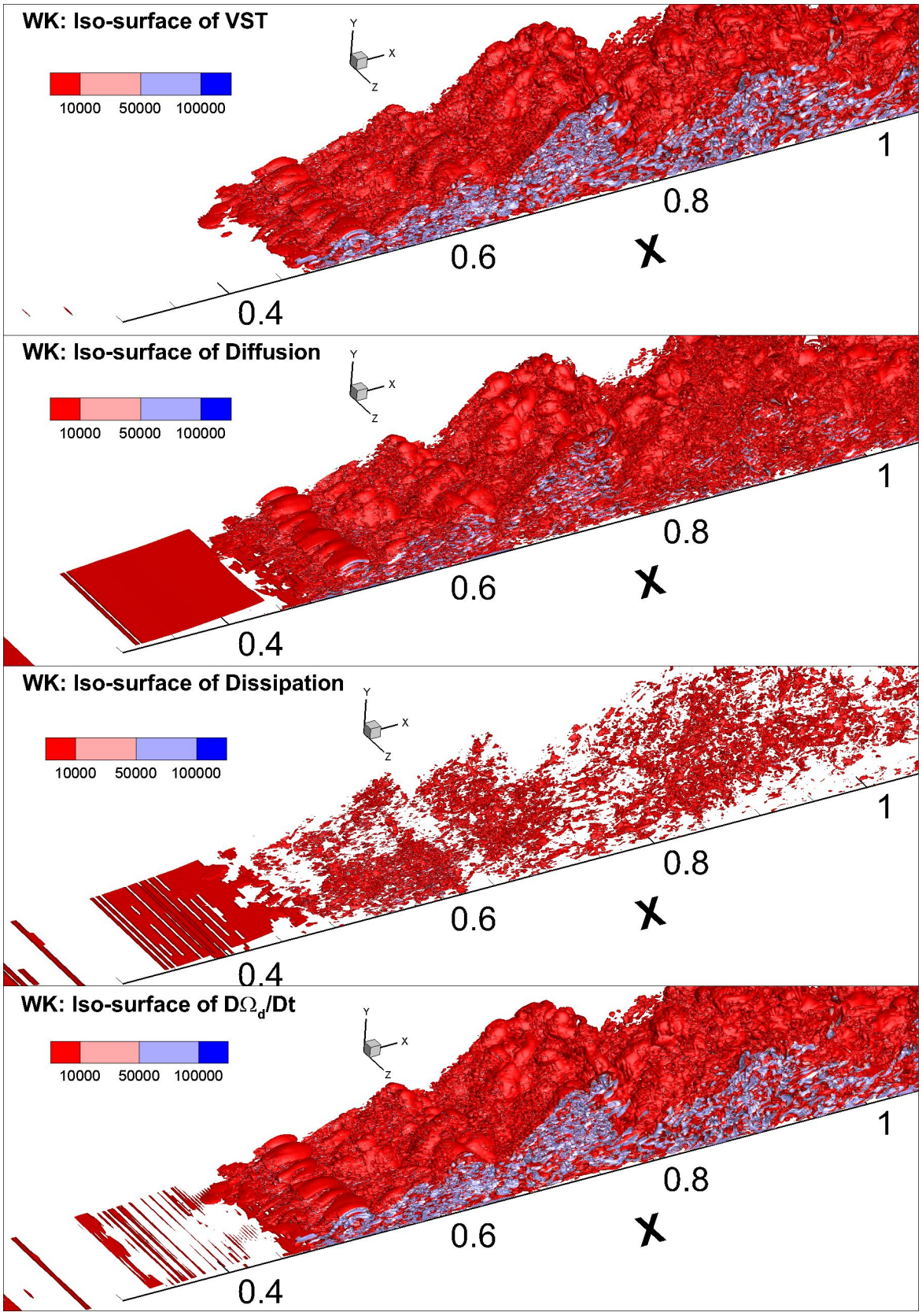

Fig. 7.16 Iso-surfaces of constituent terms of DETE shown for test case WK, when $\frac{D\Omega_d}{Dt} > 0$ and $\Omega_d > 0$ at $t = 4.24375$.

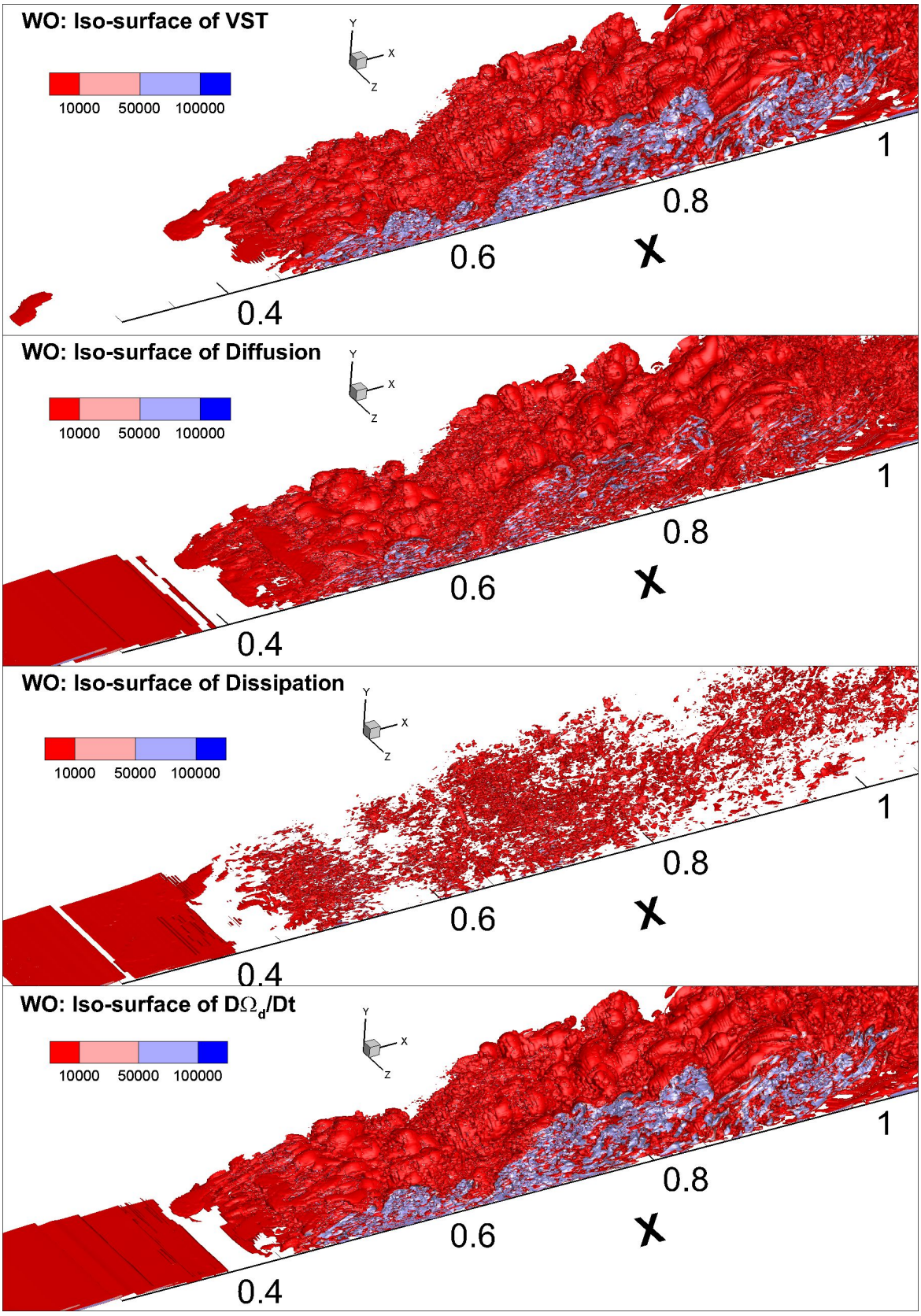

Fig. 7.17 Iso-surfaces of constituent terms of DETE shown for test case WO, when $\frac{D\Omega_d}{Dt} > 0$ and $\Omega_d > 0$ at $t = 4.24375$.

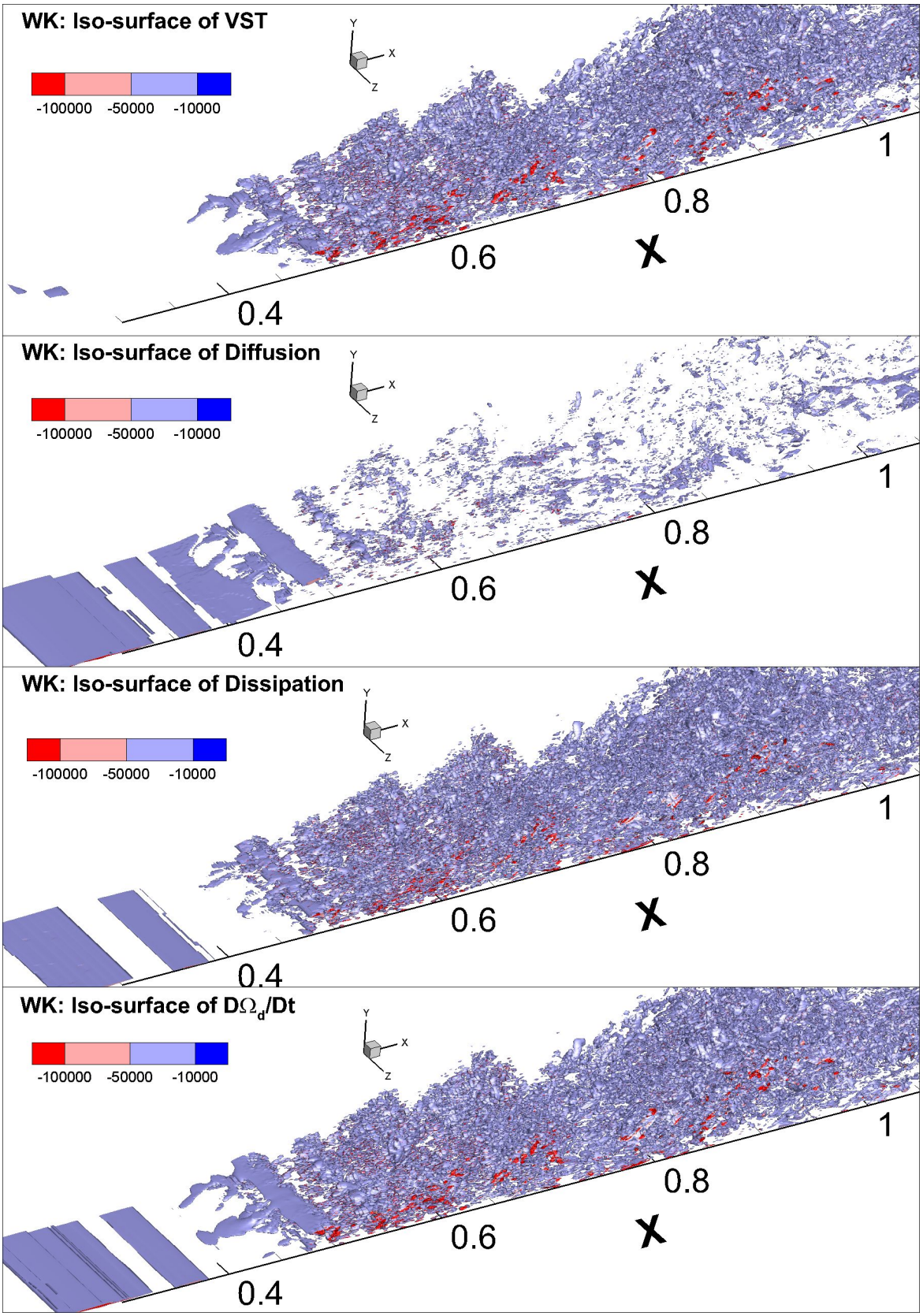

Fig. 7.18 Iso-surfaces of constituent terms of DETE shown for test case WK, when $\frac{D\Omega_d}{Dt} < 0$ and $\Omega_d < 0$ at $t = 4.24375$.

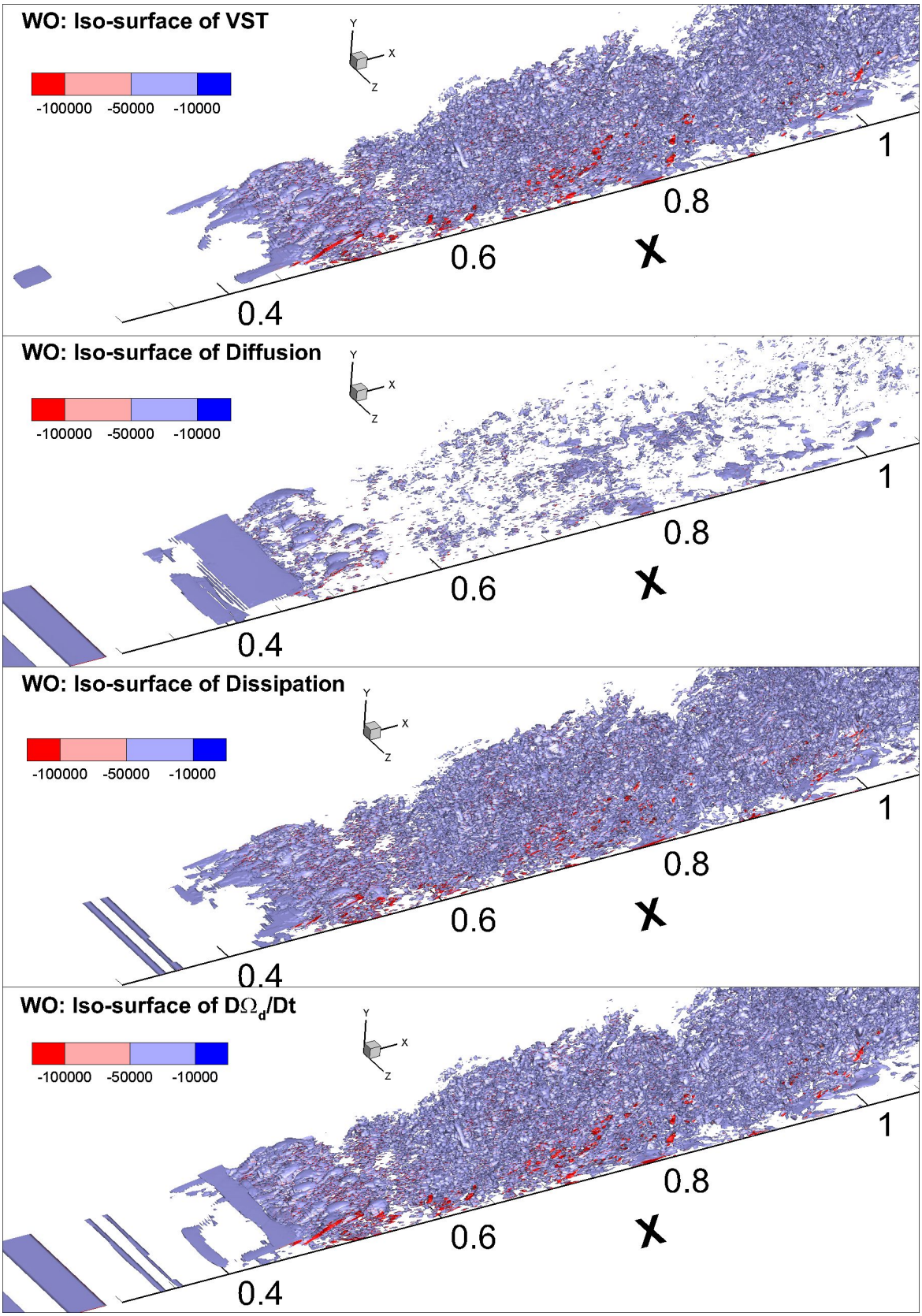

Fig. 7.19 Iso-surfaces of constituent terms of DETE shown for test case WO, when $\frac{D\Omega_d}{Dt} < 0$ and $\Omega_d < 0$ at $t = 4.24375$.

Chapter 8

Nonlinear and Linear Receptivity Analysis of Disturbance Fields

8.1 Correlating DETE and DME with Orr-Sommerfeld Equation

First, we will correlate the methods of DETE and DME with the linear viscous receptivity method of solving the Orr-Sommerfeld equation (OSE). Next, we will demonstrate the scope of using these methods for receptivity study by comparing with the solution of OSE via a case where the ZPG boundary layer is excited from inside the shear layer.

8.1.1 The Disturbance Enstrophy Transport Equation (DETE) related to the Orr-Sommerfeld equation (OSE):

The linearized disturbance enstrophy transport equation (DETE), as shown in Sengupta et al. (2018a) and Appendix B, is obtained by retaining only $O(\varepsilon)$ terms of the full nonlinear DETE as,

$$\frac{D\Omega_d}{D\tilde{t}} = \omega_{im}\omega_{jm}\frac{\partial u_{id}}{\partial \tilde{x}_j} + \omega_{im}\omega_{jd}\frac{\partial u_{im}}{\partial \tilde{x}_j} + \omega_{id}\omega_{jm}\frac{\partial u_{im}}{\partial \tilde{x}_j} + \frac{1}{Re}\frac{\partial^2\Omega_d}{\partial \tilde{x}_j\partial \tilde{x}_j} - \frac{2}{Re}\left(\frac{\partial \omega_{im}}{\partial \tilde{x}_j}\right)\left(\frac{\partial \omega_{id}}{\partial \tilde{x}_j}\right) \tag{8.1}$$

Expanding each term on the left and right hand side of DETE,

$$\frac{D\Omega_d}{D\tilde{t}} = \frac{\partial \Omega_d}{\partial \tilde{t}} + u_{1m}\frac{\partial \Omega_{1d}}{\partial \tilde{x}_1} + u_{2m}\frac{\partial \Omega_{2d}}{\partial \tilde{x}_2} + u_{3m}\frac{\partial \Omega_{3d}}{\partial \tilde{x}_3} + u_{1d}\frac{\partial \Omega_{1m}}{\partial \tilde{x}_1} + u_{2d}\frac{\partial \Omega_{2m}}{\partial \tilde{x}_2} + u_{3d}\frac{\partial \Omega_{3m}}{\partial \tilde{x}_3} \tag{8.2}$$

$$\omega_{im}\omega_{jm}\frac{\partial u_{id}}{\partial \tilde{x}_j} = \omega_{1m}\omega_{1m}\frac{\partial u_{1d}}{\partial \tilde{x}_1} + \omega_{1m}\omega_{2m}\frac{\partial u_{1d}}{\partial \tilde{x}_2} + \omega_{1m}\omega_{3m}\frac{\partial u_{1d}}{\partial \tilde{x}_3} + \omega_{2m}\omega_{1m}\frac{\partial u_{2d}}{\partial \tilde{x}_1} + \omega_{2m}\omega_{2m}\frac{\partial u_{2d}}{\partial \tilde{x}_2} + \omega_{2m}\omega_{3m}\frac{\partial u_{2d}}{\partial \tilde{x}_3} + \omega_{3m}\omega_{1m}\frac{\partial u_{3d}}{\partial \tilde{x}_1} + \omega_{3m}\omega_{2m}\frac{\partial u_{3d}}{\partial \tilde{x}_2} + \omega_{3m}\omega_{3m}\frac{\partial u_{3d}}{\partial \tilde{x}_3} \tag{8.3}$$

$$\omega_{im}\omega_{jd}\frac{\partial u_{im}}{\partial \tilde{x}_j} = \omega_{1m}\omega_{1d}\frac{\partial u_{1m}}{\partial \tilde{x}_1} + \omega_{1m}\omega_{2d}\frac{\partial u_{1m}}{\partial \tilde{x}_2} + \omega_{1m}\omega_{3d}\frac{\partial u_{1m}}{\partial \tilde{x}_3} + \omega_{2m}\omega_{1d}\frac{\partial u_{2m}}{\partial \tilde{x}_1} + \omega_{2m}\omega_{2d}\frac{\partial u_{2m}}{\partial \tilde{x}_2} + \omega_{2m}\omega_{3d}\frac{\partial u_{2m}}{\partial \tilde{x}_3} + \omega_{3m}\omega_{1d}\frac{\partial u_{3m}}{\partial \tilde{x}_1} + \omega_{3m}\omega_{2d}\frac{\partial u_{3m}}{\partial \tilde{x}_2} + \omega_{3m}\omega_{3d}\frac{\partial u_{3m}}{\partial \tilde{x}_3} \tag{8.4}$$

$$\omega_{id}\omega_{jm}\frac{\partial u_{im}}{\partial \tilde{x}_j} = \omega_{1d}\omega_{1m}\frac{\partial u_{1m}}{\partial \tilde{x}_1} + \omega_{1d}\omega_{2m}\frac{\partial u_{1m}}{\partial \tilde{x}_2} + \omega_{1d}\omega_{3m}\frac{\partial u_{1m}}{\partial \tilde{x}_3} + \omega_{2d}\omega_{1m}\frac{\partial u_{2m}}{\partial \tilde{x}_1} + \omega_{2d}\omega_{2m}\frac{\partial u_{2m}}{\partial \tilde{x}_2} + \omega_{2d}\omega_{3m}\frac{\partial u_{2m}}{\partial \tilde{x}_3} + \omega_{3d}\omega_{1m}\frac{\partial u_{3m}}{\partial \tilde{x}_1} + \omega_{3d}\omega_{2m}\frac{\partial u_{3m}}{\partial \tilde{x}_2} + \omega_{3d}\omega_{3m}\frac{\partial u_{3m}}{\partial \tilde{x}_3} \tag{8.5}$$

$$\frac{1}{Re}\frac{\partial^2 \Omega_d}{\partial \tilde{x}_j \partial \tilde{x}_j} = \frac{1}{Re}\left(\frac{\partial^2 \Omega_d}{\partial \tilde{x}_1^2} + \frac{\partial^2 \Omega_d}{\partial \tilde{x}_2^2} + \frac{\partial^2 \Omega_d}{\partial \tilde{x}_3^2}\right) \tag{8.6}$$

$$\frac{2}{Re}\frac{\partial \omega_{im}}{\partial \tilde{x}_j}\frac{\partial \omega_{id}}{\partial \tilde{x}_j} = \frac{2}{Re}\left(\frac{\partial \omega_{1m}}{\partial \tilde{x}_1}\frac{\partial \omega_{1d}}{\partial \tilde{x}_1} + \frac{\partial \omega_{1m}}{\partial \tilde{x}_2}\frac{\partial \omega_{1d}}{\partial \tilde{x}_2} + \frac{\partial \omega_{1m}}{\partial \tilde{x}_3}\frac{\partial \omega_{1d}}{\partial \tilde{x}_3}\right) + \frac{2}{Re}\left(\frac{\partial \omega_{2m}}{\partial \tilde{x}_1}\frac{\partial \omega_{2d}}{\partial \tilde{x}_1} + \frac{\partial \omega_{2m}}{\partial \tilde{x}_2}\frac{\partial \omega_{2d}}{\partial \tilde{x}_2} + \frac{\partial \omega_{2m}}{\partial \tilde{x}_3}\frac{\partial \omega_{2d}}{\partial \tilde{x}_3}\right) + \tag{8.7}$$

$$\frac{2}{Re}\left(\frac{\partial \omega_{3m}}{\partial \tilde{x}_1}\frac{\partial \omega_{3d}}{\partial \tilde{x}_1} + \frac{\partial \omega_{3m}}{\partial \tilde{x}_2}\frac{\partial \omega_{3d}}{\partial \tilde{x}_2} + \frac{\partial \omega_{3m}}{\partial \tilde{x}_3}\frac{\partial \omega_{3d}}{\partial \tilde{x}_3}\right) \tag{8.8}$$

Application in a 2D flow:

For a 2D flow, the spanwise components of mean and disturbance velocities are zero, i.e. $u_3 = u_{3m} = u_{3d} = 0$ and the corresponding spanwise derivatives are also zero, i.e. $\frac{\partial(.)}{\partial \tilde{x}_3} = 0$. From the expression of vorticity, it follows that $\omega_1 = \omega_2 = \omega_{1m} = \omega_{2m} = \omega_{1d} = \omega_{2d} = 0$.

For a fully developed 2D parallel flow (which is the equilibrium flow for the OSE), $u_{2m} = \frac{\partial(.)}{\partial \tilde{x}_1} = 0$ and $u_{1m} = U(\tilde{x}_2) = U(\tilde{y})$; $\omega_3 = \omega$; $\omega_m = -U^{'}$; $\Omega_d = 2\omega \cdot \omega_d$ and the DETE given in Eq. (8.1) reduces to the form given below,

$$\frac{D\Omega_d}{D\tilde{t}} = \frac{1}{Re}\left(\frac{\partial^2 \Omega_d}{\partial \tilde{x}^2} + \frac{\partial^2 \Omega_d}{\partial \tilde{y}^2}\right) - \frac{2}{Re}\left(\frac{\partial \omega_m}{\partial \tilde{y}}\frac{\partial \omega_d}{\partial \tilde{y}}\right) \tag{8.9}$$

which can also be written as

$$\frac{\partial \Omega_d}{\partial \tilde{t}} + U\frac{\partial \Omega_d}{\partial \tilde{x}} = \frac{1}{Re}\left(\frac{\partial^2 \Omega_d}{\partial \tilde{x}^2} + \frac{\partial^2 \Omega_d}{\partial \tilde{y}^2}\right) + \frac{2}{Re}\frac{d^2U}{d\tilde{y}^2}\left(\frac{\partial^2 v_d}{\partial \tilde{x}\partial \tilde{y}} - \frac{\partial^2 u_d}{\partial \tilde{y}^2}\right) \tag{8.10}$$

As stated in Chapter 2, on the basis of Abel's and Tauber's theorems, we can represent any arbitrary unknown by using the Fourier-Laplace transform. Using it for the disturbance stream function one obtains,

$$\psi_d(\tilde{x}, \tilde{y}, \tilde{t}) = \int_{Br}\int_{Br} \phi(\alpha, \omega_o, \tilde{y}) e^{i(\alpha\tilde{x} - \omega_o\tilde{t})} d\alpha \, d\omega_o \tag{8.11}$$

where we integrate along the Bromwich contours in α- and ω_o-planes. The expressions for streamwise and wall-normal disturbance velocities are then obtained as,

$$u_d = \frac{\partial \psi_d}{\partial \tilde{y}} = \int_{Br}\int_{Br} \phi^{'} e^{i(\alpha\tilde{x} - \omega_o\tilde{t})} d\alpha \, d\omega_o \tag{8.12}$$

$$v_d = -\frac{\partial \psi_d}{\partial \tilde{x}} = \int_{Br}\int_{Br} -i\alpha\phi e^{i(\alpha\tilde{x} - \omega_o\tilde{t})} d\alpha \, d\omega_o \tag{8.13}$$

where prime indicates differentiation with respect to $\tilde{y}$. The other disturbance quantities are also obtained as,

$$\omega_d = -\nabla^2 \psi_d = \int_{Br}\int_{Br} -(\phi^{''} - \alpha^2\phi) e^{i(\alpha\tilde{x} - \omega_o\tilde{t})} d\alpha \, d\omega_o \tag{8.14}$$

$$\Omega_d = -2U^{'}\omega_d = \int_{Br}\int_{Br} 2U^{'}(\phi^{''} - \alpha^2\phi) e^{i(\alpha\tilde{x} - \omega_o\tilde{t})} d\alpha \, d\omega_o \tag{8.15}$$

Evaluating the terms on the left hand side of Eq. (8.10), we obtain,

$$\frac{\partial \Omega_d}{\partial \tilde{t}} = \int_{Br}\int_{Br} -2i\omega_o U^{'}(\phi^{''} - \alpha^2\phi) e^{i(\alpha\tilde{x} - \omega_o\tilde{t})} d\alpha \, d\omega_o \tag{8.16}$$

$$U\frac{\partial \Omega_d}{\partial \tilde{x}} = \int_{Br}\int_{Br} 2i\alpha U U^{'}(\phi^{''} - \alpha^2\phi)e^{i(\alpha\tilde{x}-\omega_o\tilde{t})}d\alpha\, d\omega_o \tag{8.17}$$

Therefore, the total derivative is evaluated from the following expression,

$$\frac{D\Omega_d}{D\tilde{t}} = \int_{Br}\int_{Br} 2i\alpha U^{'}\left(U - \frac{\omega_o}{\alpha}\right)(\phi^{''} - \alpha^2\phi)e^{i(\alpha\tilde{x}-\omega_o\tilde{t})}d\alpha\, d\omega_o \tag{8.18}$$

We have already derived the OSE where the disturbance and mean fields are 2D (given in Eq. (2.23) of Chapter 2), which is given as:

$$\phi^{iv} - 2\alpha^2\phi'' + \alpha^4\phi = iRe[(\alpha U - \omega_o)[\phi'' - \alpha^2\phi] - \alpha U''\phi] \tag{8.19}$$

Rearranging the above equation, we obtain,

$$\left(U - \frac{\omega_o}{\alpha}\right)(\phi'' - \alpha^2\phi) = \frac{\phi^{iv} - 2\alpha^2\phi'' + \alpha^4\phi}{i\alpha Re} + U^{''}\phi$$

Therefore, the substantive derivative of disturbance enstrophy in Eq. (8.18) is given by,

$$\frac{D\Omega_d}{D\tilde{t}} = \int_{Br}\int_{Br} 2i\alpha U^{'}\left(\frac{\phi^{iv} - 2\alpha^2\phi'' + \alpha^4\phi}{i\alpha Re} + U^{''}\phi\right)e^{i(\alpha\tilde{x}-\omega_o\tilde{t})}d\alpha\, d\omega_o \tag{8.20}$$

This can be rewritten in the form where viscous and inviscid terms are separated as,

$$\frac{D\Omega_d}{D\tilde{t}} = \int_{Br}\int_{Br} \frac{2U^{'}}{Re}(\phi^{iv} - 2\alpha^2\phi^{''} + \alpha^4\phi)e^{i(\alpha\tilde{x}-\omega_o\tilde{t})}d\alpha d\omega_o +$$

$$\int_{Br}\int_{Br} 2i\alpha U^{'}U^{''}\phi e^{i(\alpha\tilde{x}-\omega_o\tilde{t})}d\alpha\, d\omega_o \tag{8.21}$$

Comparing Eq. (8.21) with the expressions for v_d and ω_d given by Eqs. (8.13) and (8.14), we get an alternate expression for the growth rate of disturbance enstrophy as

$$\frac{D\Omega_d}{D\tilde{t}} = 2U^{'}\left(\frac{\nabla^2\omega_d}{Re} - U^{''}v_d\right) \tag{8.22}$$

The inviscid term (second term on the right hand side of Eq. (8.22)) is proportional to the perturbation wall-normal velocity, while the viscous term is due to diffusion of disturbance vorticity and will be a smaller contribution due to division by Re.

8.1.2 Disturbance Mechanical Energy (DME) Equation Related to the Orr-Sommerfeld equation (OSE):

The equivalence of disturbance growth in a ZPG boundary layer obtained by the DME equation and the OSE has been provided in Sengupta et al. (2006a) by showing the Tollmien-Schlichting wave structure shown in terms of DME for a spatially unstable case. Here, we will instead show a case where the corresponding Tollmien-Schlichting waves are all damped, so that one can distinguish between modal and non-modal growth. The linearized equation for the DME (obtained by retaining only O(ε) terms) is given by

$$\nabla^2 E_d = 2\omega_m \cdot \omega_d - V_m \cdot (\nabla \times \omega_d) - V_d \cdot (\nabla \times \omega_m) \tag{8.23}$$

Once again substituting for the 2D mean and disturbance flow fields, we get $V_m = U(\tilde{y})\hat{i}$ and $V_d = u_d\hat{i} + v_d\hat{j}$. The corresponding vorticity fields are then computed as $\omega_m = -U^{'}\hat{k}$ and $\omega_d = \left(\frac{\partial v_d}{\partial \tilde{x}} - \frac{\partial u_d}{\partial \tilde{y}}\right)\hat{k}$. The constituent terms of the DME equation are evaluated by substituting for the values of mean and disturbance components of velocity and vorticity as

$$2\omega_m \cdot \omega_d = -2U^{'}\omega_d \tag{8.24}$$

Since,

$$\nabla \times \omega_d = \left(\frac{\partial^2 v_d}{\partial \tilde{x}\partial \tilde{y}} - \frac{\partial^2 u_d}{\partial \tilde{y}^2}\right)\hat{i} - \left(\frac{\partial^2 v_d}{\partial \tilde{x}^2} - \frac{\partial^2 u_d}{\partial \tilde{x}\partial \tilde{y}}\right)\hat{j}$$

Thus,

$$V_m \cdot (\nabla \times \omega_d) = U\left[\frac{\partial}{\partial \tilde{x}}\left(-\frac{\partial u_d}{\partial \tilde{x}}\right) - \frac{\partial^2 u_d}{\partial \tilde{y}^2}\right] = -U\nabla^2 u_d \tag{8.25}$$

Similarly

$$\nabla \times \omega_m = -U^{''}\hat{i}$$

therefore,

$$V_d \cdot (\nabla \times \omega_m) = -u_d U^{''} \tag{8.26}$$

The expressions in Eqs. (8.24) to (8.26) are substituted back in Eq. (8.23) to get an alternative expression for the DME equation with a parallel mean flow as,

$$\nabla^2 E_d = -2U^{'}\omega_d + U\nabla^2 u_d + u_d U^{''} \tag{8.27}$$

Next, the disturbance mechanical energy, E_d, is expressed by its Fourier-Laplace Transform as

$$E_d = \int_{Br}\int_{Br} \hat{E}_d(\tilde{y}) e^{i(\alpha\tilde{x}-\omega_o\tilde{t})} d\alpha d\omega_o \tag{8.28}$$

Then the left hand side of Eq. (8.27) is evaluated as

$$\nabla^2 E_d = \int_{Br}\int_{Br} (\hat{E}_d^{''} - \alpha^2\hat{E}_d) e^{i(\alpha\tilde{x}-\omega_o\tilde{t})} d\alpha d\omega_o \tag{8.29}$$

The expressions for ω_d and u_d have been provided during the derivation of the linearized DETE operator in Eqs. (8.13) and (8.12), respectively. It follows from Eq. (8.12) that

$$\nabla^2 u_d = \int_{Br}\int_{Br} (-\alpha^2\phi^{'} + \phi^{'''}) e^{i(\alpha\tilde{x}-\omega_o\tilde{t})} d\alpha d\omega_o \tag{8.30}$$

Substituting the values from Eqs. (8.12), (8.13), (8.29) and (8.30) into the expression in Eq. (8.27), we obtain an equation for the bilateral Laplace amplitude $\hat{E}_d$, as

$$\hat{E}_d^{''} - \alpha^2\hat{E}_d = 2U^{'}(\phi^{''} - \alpha^2\phi) + U(\phi^{'''} - \alpha^2\phi^{'}) + U^{''}\phi^{'}$$

or

$$\hat{E}_d^{''} - \alpha^2\hat{E}_d = \phi^{'''}U + 2\phi^{''}U^{'} + \phi^{'}(U^{''} - \alpha^2 U) - 2\alpha^2 U^{'}\phi^{'} \tag{8.31}$$

As the right hand side of the above equation can be obtained from the OSE, the above inhomogeneous equation can be solved as a function of wall-normal height for $\hat{E}_d$, and from Eq. (8.28) one can obtain DME as a function of $(\tilde{x},\tilde{y},\tilde{t})$. This was plotted for a case of growing Tollmien-Schlichting wave in Sengupta et al. (2006a), without distinguishing between modal and non-modal growth. Here, an appropriate choice of Reynolds number and circular frequency will enable to distinguish between the modal and non-modal contributions, where the modal part will be decaying function of space, while the non-modal part will grow in space and time. Utility of DETE and DME is shown next by solving Eqs. (8.22) and (8.31), and performing double inverse transform to obtain E_d and Ω_d to study receptivity for excitation to a perturbation at the wall.

8.2 Receptivity to Wall Excitation Using OSE: Scope of DETE and DME

The physical problem being studied here is shown in Fig. 8.1, where the 2D incompressible boundary layer developing over a flat plate is excited by a localized impulsively started harmonic source located at the origin of the coordinate system, which is determined by the location of the exciter, for the ease of representation using Fourier-Laplace transform. In this spatio-temporal linear receptivity method to be employed, an equivalent parallel shear layer is considered with the same thickness at the position of the exciter, shown by the dashed line. In the results presented here, all the lengths are nondimensionalized by displacement thickness δ^*, all the velocities with free-stream velocity U_∞ and time by $\tilde{t} = \delta^*/U_\infty$. The Reynolds number is then defined as $Re_{\delta^*} = \delta^* U_\infty/\nu$.

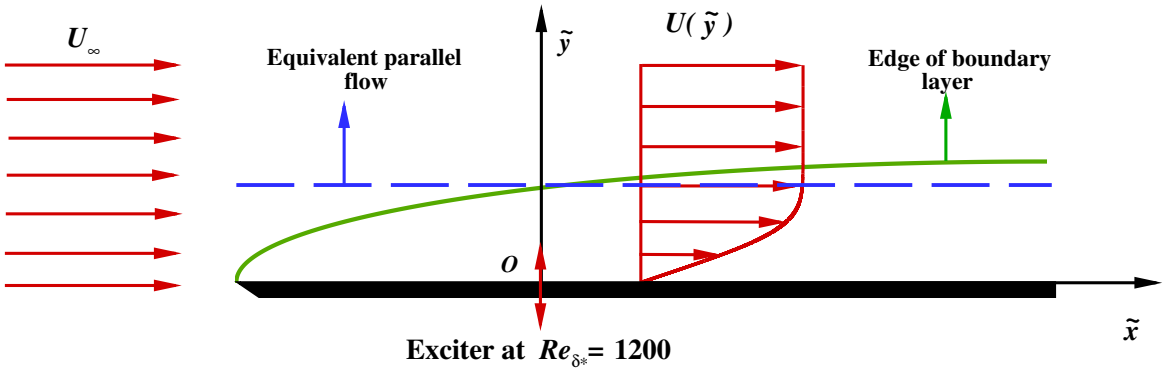

Fig. 8.1 Wall-excitation receptivity problem in the physical plane.

For the purpose of demonstration, a case is considered here for which, $Re_{\delta^*} = 1200$ and the frequency of exciter is chosen as, $\overline{\omega}_o = 0.13$, so that all the spatial modes are damped. The purpose here is to show by the adopted linear spatio-temporal analysis, that there is a non-modal growth, despite the fact that all the Orr-Sommerfeld modes are known to be stable.

If the disturbance created by this excitation has an excitation frequency of $\overline{\omega}_o$, then the disturbance stream function is given by

$$\psi_d(\tilde{x},\tilde{y},\tilde{t}) = \frac{1}{(2\pi)^2}\int\int_{Br}\phi(\tilde{y},\alpha,\omega_o)e^{i(\alpha\tilde{x}-\omega_o\tilde{t})}d\alpha d\omega_o \tag{8.32}$$

where Br represents the Bromwich contours followed in evaluating the above integral in the complex α- and ω_o-planes. As, we have discussed in Chapter 2, the mathematical basis of choosing the Bromwich contour is to identify appropriate strips of convergence in the α- and

ω_o- planes, so that the integral given in Eq. (8.32) does not diverge. Identifying and using the appropriate Bromwich contours for the spatio-temporal problem of viscous receptivity is of paramount importance, and the values of the Bromwich contour used here are provided in Fig. 8.2. The mathematical approach behind the strip of convergence and the Bromwich contour are detailed in Papoulis (1962); van der Pol and Bremmer (1959). The receptivity problem solved here using the OSE is an example of the application of the Bromwich contour. In Fig. 8.2, the path A is so chosen that all the downstream propagating modes lie above this path, while the upstream propagating modes lie below the path A. After finding all the modes by the adopted compound matrix method (CMM) detailed in Chapter 3, one calculates the group velocity of individual modes to ascertain their directions of propagation. The CMM has been used to compute the eigenvalues at $Re_{\delta^*} = 800$ and $\alpha = 1$ using temporal theory in Section 8.2.3, to validate the eigenvalues obtained from CMM with existing eigenvalue data (Schmid and Henningson, 2001) for the chosen parameter values. Here for $Re_{\delta^*} = 1200$ and $\overline{\omega}_o = 0.13$, the three spatial modes (as shown in Fig. 8.3) are downstream propagating and the choice of path A along $\alpha_i = -0.008$ satisfies the criterion of direction of propagation. In the circular frequency plane, the path B is chosen to satisfy causality, i.e. any mode will be below the path B. This search for Bromwich contours in circular frequency plane is performed by manual search so that causality is not violated, after performing a grid search using CMM for the spatial problem. It is very easy to check for the violation of causality.

The bilateral Laplace transform in Eq. (8.32) is governed by the OSE which has been provided in Eq. (8.19). For the excitation shown in Fig. 8.1, the boundary conditions at the wall ($\tilde{y} = 0$) are:

$$u_d = 0 \tag{8.33}$$

$$\psi_d(\tilde{x}, 0, \tilde{t}) = U_1(\tilde{t})\delta(\tilde{x})e^{-i\overline{\omega}_o\tilde{t}} \tag{8.34}$$

The effect of periodic suction and blowing at the origin at the prescribed frequency $\overline{\omega}_o$ is given in Eq. (8.34). The Dirac delta function $\delta(\tilde{x})$ indicates the localized nature of the excitation and $U_1(\tilde{t})$ is the Heaviside function, which indicates the onset of the periodic excitation impulsively at $\tilde{t} = 0$. The free stream boundary ($\tilde{y} \to \infty$) conditions are provided as: u_d, $v_d \to 0$. The corresponding spectral plane boundary conditions are then given as

$$\phi^{'}(\alpha, 0, \omega_o) = 0 \tag{8.35}$$

$$\phi(\alpha, 0, \omega_o) = WBC \tag{8.36}$$

$$\phi(\alpha, \tilde{y} \to \infty, \omega_o) \to 0 \tag{8.37}$$

$$\phi^{'}(\alpha, \tilde{y} \to \infty, \omega_o) \to 0 \tag{8.38}$$

where $WBC = [i(\overline{\omega}_o - \omega_o)]^{-1} + \pi\delta(\omega_o - \overline{\omega}_o)$ is the wall boundary condition corresponding to Eq. (8.34). The second part of WBC will contribute to the formation of Tollmien-Schlichting wave, while the first part is the source of disturbance field contributed by all other frequencies, due to the Heaviside function. This first part produces the spatio-temporal wave front (STWF) which is due to non-modal growth and is shown next. When the free stream boundary conditions in Eqs. (8.37) to (8.38) are accounted for, the solution of the OSE is given by the following expression

$$\psi_d(\tilde{x}, \tilde{y}, \tilde{t}) = \frac{1}{(2\pi)^2} \int \int_{Br} \frac{\phi_1(\alpha, \tilde{y}, \omega_o)\phi_{30}^{'} - \phi_3(\alpha, \tilde{y}, \omega_o)\phi_{10}^{'}}{\phi_{10}\phi_{30}^{'} - \phi_{30}\phi_{10}^{'}} WBC e^{i(\alpha\tilde{x} - \omega_o\tilde{t})} d\alpha \, d\omega_o \tag{8.39}$$

where ϕ_1 and ϕ_3 are the decaying inviscid and viscous modes, respectively (also referred to as the wall modes of the OSE). The details of the derivation of Eq. (8.39) are provided in Chapter 2. It is to be noted that the denominator of Eq. (8.39) is the dispersion relation of the eigenvalue problem, which identifies the eigenvalues of the corresponding signal problem. Thus, this expression connects the eigenvalue and receptivity approach, where for the latter the asymptotic solutions (Tollmien-Schlichting waves) are given by the poles of the integrand in Eq. (8.39). The set of terms $\frac{\phi_1(\alpha,\tilde{y},\omega_o)\phi_{30}^{'} - \phi_3(\alpha,\tilde{y},\omega_o)\phi_{10}^{'}}{\phi_{10}\phi_{30}^{'} - \phi_{30}\phi_{10}^{'}}$ on the right hand side of Eq. (8.39) and WBC together comprise the complex amplitude function of the wall-normal velocity (ϕ), which is computed by the first of the four differential equations obtained from the CMM, the detailed description of which has been shown in Chapter 3.

To discuss the receptivity of the boundary layer, we consider a case for which $Re = 1200$ and $\overline{\omega}_o = 0.13$. Here, we have taken 2^{14} points from -8π to 8π in the α-plane along path A of Fig. 8.2, such that $\Delta\alpha_r = 3.068 \times 10^{-3}$. Similarly, in the ω_{or}-plane, we have taken 2^{11} points from $-\pi/2$ to $\pi/2$ along path B, such that $\Delta\omega_{or} = 1.534 \times 10^{-3}$. There are four times as many points taken in the α-plane and two times as many points taken in the ω_o-plane, as compared to the calculations performed in Sengupta et al. (2006a). These are very refined calculations, as we have taken 2^{14} points from $\tilde{x} = -1024$ to 1024, while we have taken 2^{11} points for $\tilde{t} = 0$ to 2048. Over and above, we also emphasize that the boundary layer co-ordinates used in the Bromwich contour integral method stretches the space and time by the ratio of the convection length scale with the boundary layer thickness. Quite often, this is

a stretching factor which is two orders of magnitudes between the two, i.e. the solution of Navier-Stokes equation using convection scale of the order of tens will be in the orders of thousands in the solution obtained by Bromwich contour integral method. This shows that the Bromwich contour integral method provides nonmodal growth with significantly higher degree of precision. The OSE itself is solved for $0 \leq \tilde{y} \leq 6.7$ (in displacement thickness units) with 3000 points.

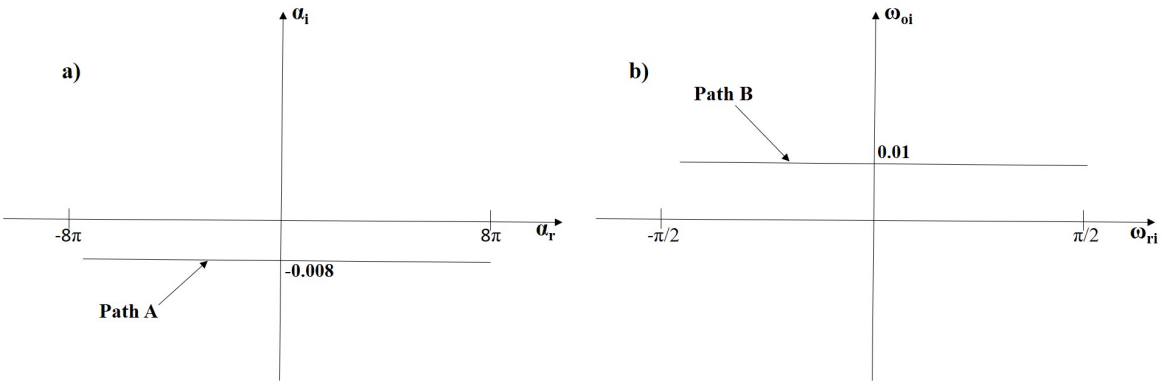

Fig. 8.2 Locations of the Bromwich contours in the (a) α- and (b) ω_o-planes.

As mentioned in Chapter 3, the stiffness of the OSE is removed by the CMM, wherein a new set of six variables (q_1 to q_6) are defined, which are linear combinations of the wall modes, ϕ_1 and ϕ_3 and their derivatives. The eigenvalues of the OSE are obtained through a grid search method, where the real and imaginary parts of the new variable q_1 at the wall are zero simultaneously. This is equivalent to enforcing the dispersion relation of the eigenvalues, found from the grid search method with further refinement by Newton-Rhapson method for the variable q_1 ($\tilde{y} = 0$), are provided in Fig. 8.3. The red lines represent contours along which the real part of the wall component (at $\tilde{y} = 0$) of q_1 are zero. The black dotted lines are the corresponding zero contour lines for the imaginary part of q_1. The locations where these red and dotted black lines intersect are the approximate locations of eigenvalues. Such approximate eigenvalues can be polished to desired precision by Newton-Raphson search method. From Fig. 8.3, we can see that for the designed receptivity problem, there are only three discrete eigenvalues for the spatial problem. The choice of the Bromwich contour depends on the eigenvalues obtained, particularly the constant α_i values, along which the contour is fixed. We also highlight the fact that the Bromwich contour can be any line in the strip of convergence. Here, the straight lines are chosen for the ease and accuracy with which discrete fast Fourier transform can be obtained. The value of α_i for the Bromwich contour, parallel to the α_r-plane, has been chosen as $\alpha_i = -0.008$, along the path A shown in Fig. 8.2, which is below all the eigenvalues in Fig. 8.3.

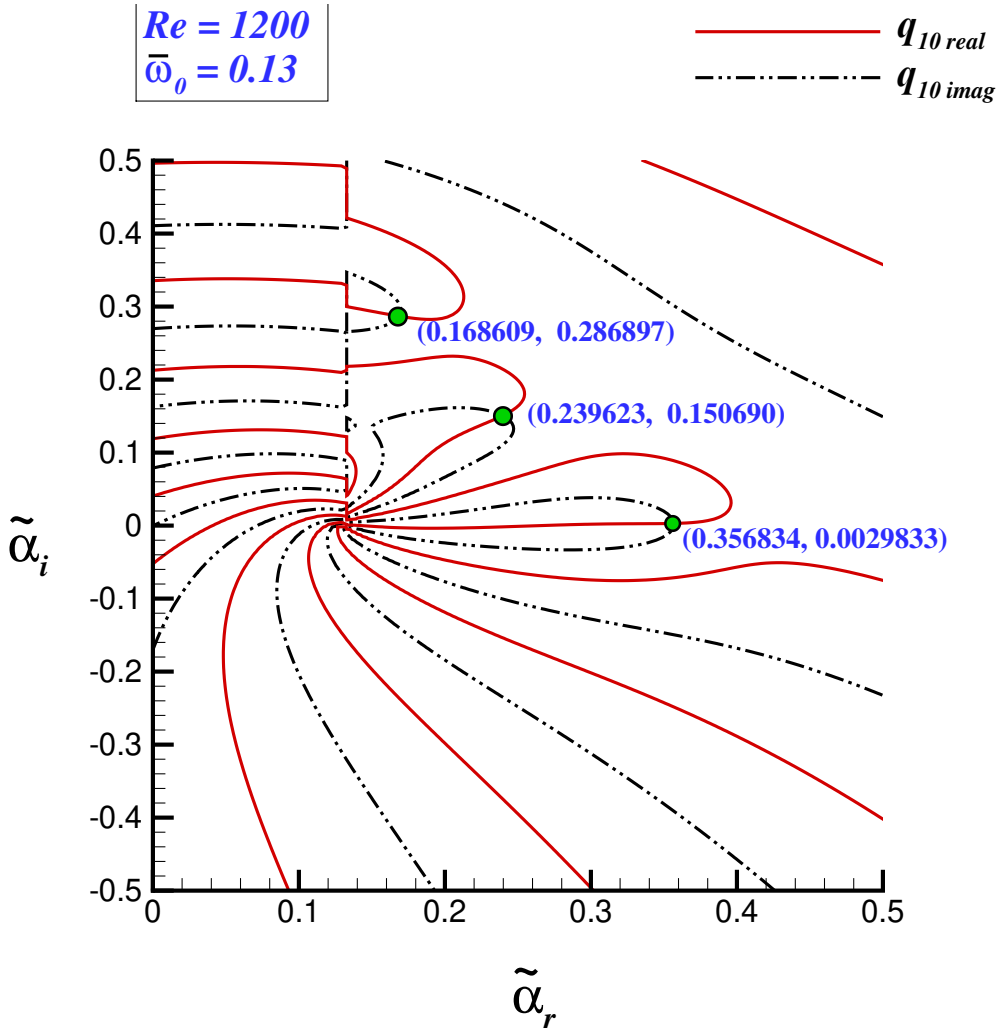

Fig. 8.3 Eigenvalues obtained from the zero crossings of the real and imaginary parts of q_1 at the wall for the receptivity problem at $Re = 1200$ and $\overline{\omega}_o = 0.13$.

The computed streamwise disturbance velocity component (u_d) at the indicated times is shown in Fig. 8.4, as a function of $\tilde{x}$ at a wall-normal location, $\tilde{y} = 0.278$. Here, $\tilde{x} = 0$ represents the location of the exciter. During the evolution of disturbances, we note three distinct components in Fig. 8.4: (i) a local solution in the immediate neighbourhood of the exciter, (ii) an asymptotic solution away from the exciter and (iii) a wave-packet like structure referred to as the spatio-temporal wave-front (STWF) that displays non-modal growth, which grows both in space and time. In the linear theory, this is the constantly growing wave-front in space and time. This case has been chosen specifically, as the Tollmien-Schlichting waves are all damped for the three modes shown in Fig. 8.3. We note that for these cases, $\tilde{t}$ represents the viscous time scale which is related to the convective time scale by $\tilde{t} = 83.33t$,

if the convection length scale (L) is chosen such that the Reynolds number based on L is $Re_L = 10^5$. Thus, the top frame corresponds to a solution at $t = 7.8$, which is essentially an early time solution and the corresponding growth can be identified as transient. In the middle frame of Fig. 8.4, we observe the fully developed STWF for which the maximum amplitude of $u_d \sim 0.05$ at $t = 13.8$. The bottom frame represents the solution at $t = 19.8$, where the maximum amplitude of $u_d \sim 0.35$. Thus, we note an amplification of the STWF by a factor of 7, when t changes from 13.8 to 19.8. Therefore, the STWF shows a definite early time growth for the wall excitation problem. From the eigenvalue solution in Fig. 8.3, we note that all the modes are damped due to positive values of α_i, while the response field in Fig. 8.4 is due to the constructive interference of the spectrum (shown next) which can be identified as the non-modal growth.

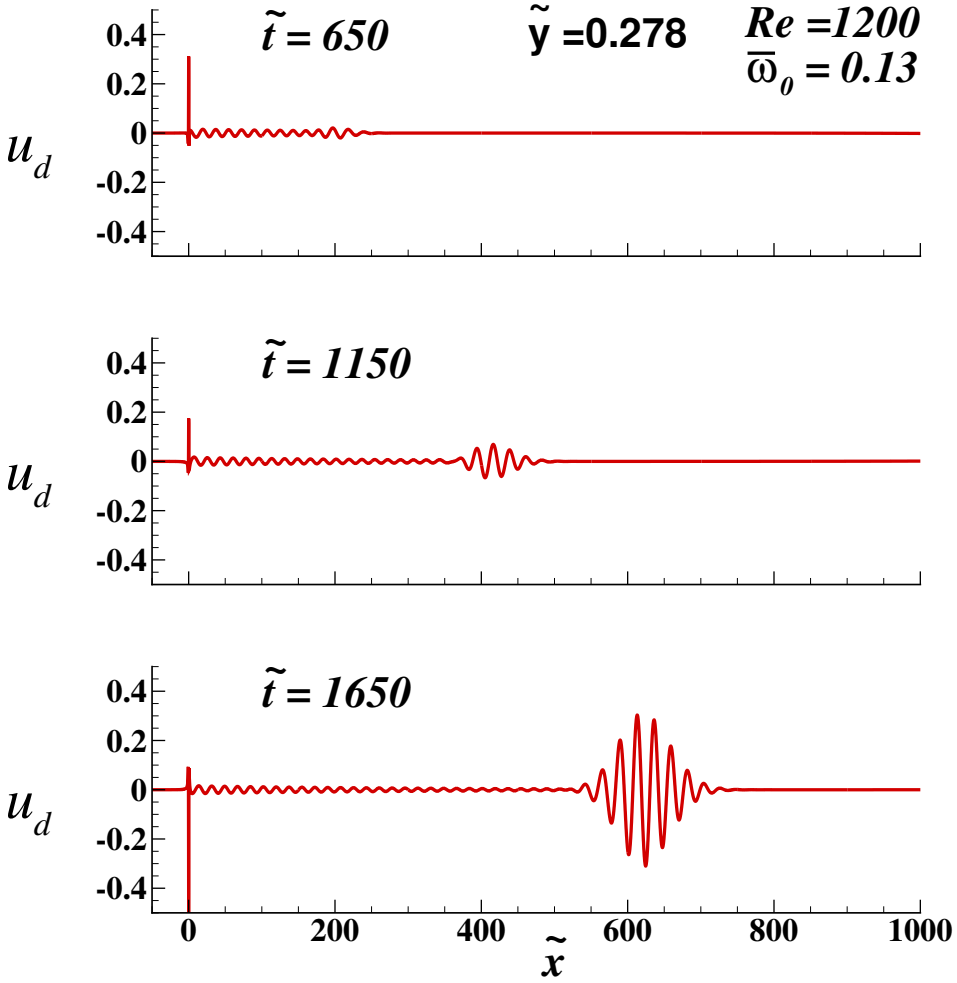

Fig. 8.4 Streamwise disturbance velocity plotted as a function of $\tilde{x}$ at indicated times for $Re = 1200$, $\bar{\omega}_o = 0.13$ at $\tilde{y} = 0.278$.

In Fig. 8.5, the complex amplitude function for velocity in wall-normal direction $\phi(\alpha,\tilde{t})$, obtained by taking a Fourier transform is plotted as a function of α_r, at the indicated times, for the considered receptivity problem at $\tilde{y} = 0.278$. The peak corresponding to least stable Tollmien-Schlichting wave is seen for all time frames at the same α_r location ($\alpha_r = 0.3589$) and remains relatively unaltered in amplitude, but the peak of the Tollmien-Schlichting wave becomes more localized with time. At $\tilde{t} = 650$, the waves associated with non-modal contributions for the STWF are distinct and have lower amplitude, as compared to the peak for the Tollmien-Schlichting wave. In the middle frame at $\tilde{t} = 1150$, the constituent waves within the STWF undergo constructive interference and lead to a nonmodal growth of the STWF. By $\tilde{t} = 1650$, the hump associated with STWF has overtaken the Tollmien-Schlichting wave in terms of amplitude, which was also noted in Fig. 8.4 in the physical plane. The STWF for all the frames is centred around $\alpha_r = 0.2698$. This once again reinforces the importance of linear nonmodal growth to account for the appearance of STWF, and the constituents are in the form of a continuum centred around the identified peak noted above. These are also parts of the solution of the OSE but are not given by discrete eigenvalues. The choice afforded by CMM in densely packing the number of points in the streamwise wavenumber direction allows one to identify the STWF which is the spatio-temporally growing structure.

8.2.1 DME Based Receptivity Analysis

Having obtained the disturbance velocity components, we solve Eq. (8.31) for the disturbance mechanical energy as a function of $\tilde{y}$ for any choice of α and ω_o along the Bromwich contours. From the solution, we can reconstruct E_d as a function of $\tilde{x}$, $\tilde{y}$ and $\tilde{t}$ by performing double inverse transforms successively in Eq. (8.28). In Fig. 8.6, variation of the source term for $\nabla^2 E_d$ (left frames) and E_d (right frames) as a function of $\tilde{x}$ at discrete times are shown for $\tilde{y} = 0.278$. The most prominent feature one notes, when comparing E_d plots with the u_d plots in Fig. 8.4, is that the variation of E_d across the exciter is smoother. Additionally, one picks up oscillations due to the pressure term at higher wavenumbers for E_d, as compared to the corresponding frames of u_d. The wavelength and the growth rate of the STWF in the E_d as well as its Laplacian (left frames of Fig. 8.6) plots match very well with the corresponding values in the u_d plots. This figure provides a demonstration of the efficacy of the DME method in characterizing the instability and how it relates well with the linear OSE calculations. In this case, the modal solution corresponding to discrete eigenvalues is shown to be a decaying function of $\tilde{x}$, while the non-modal part grows with space and time, as has been discussed.

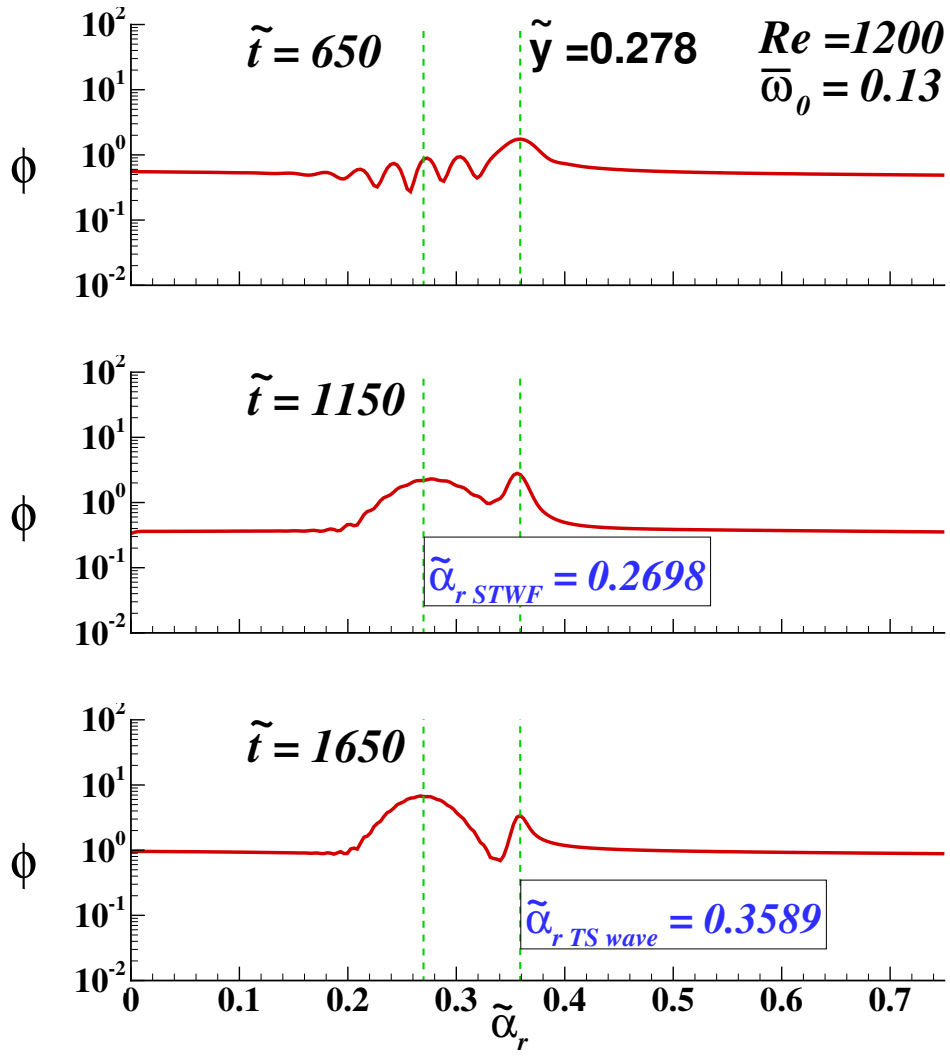

Fig. 8.5 Amplitude of wall-normal Fourier Laplace transform plotted as a function of α_r at indicated times for $Re = 1200$, $\overline{\omega}_o = 0.13$ at $\tilde{y} = 0.278$.

8.2.2 Disturbance Enstrophy Based Receptivity Analysis

Using the expression in Eq. (8.22), which correlates the growth rate of disturbance enstrophy with the Orr-Sommerfeld disturbance operators, we obtain the plots shown in Fig. 8.7. In this figure, the growth rate of disturbance enstrophy ($D\Omega_d/Dt$) (left frames) and the disturbance enstrophy (Ω_d) (right frames), are plotted as a function of $\tilde{x}$ at the indicated time instants for $\tilde{y} = 0.278$ to facilitate comparisons with the u_d plots in Fig. 8.4. Similar to E_d, one notes that both $D\Omega_d/Dt$ and Ω_d show a good match with the plots of u_d, particularly with respect to the STWF, which grows in space and time. The maximum amplitudes of $D\Omega_d/Dt$ and Ω_d at $\tilde{t} = 1150$ are 0.002 and 0.006, respectively, while the corresponding values at the later time of $\tilde{t} = 1650$, are 0.014 and 0.35, respectively, indicating an amplification by approximately

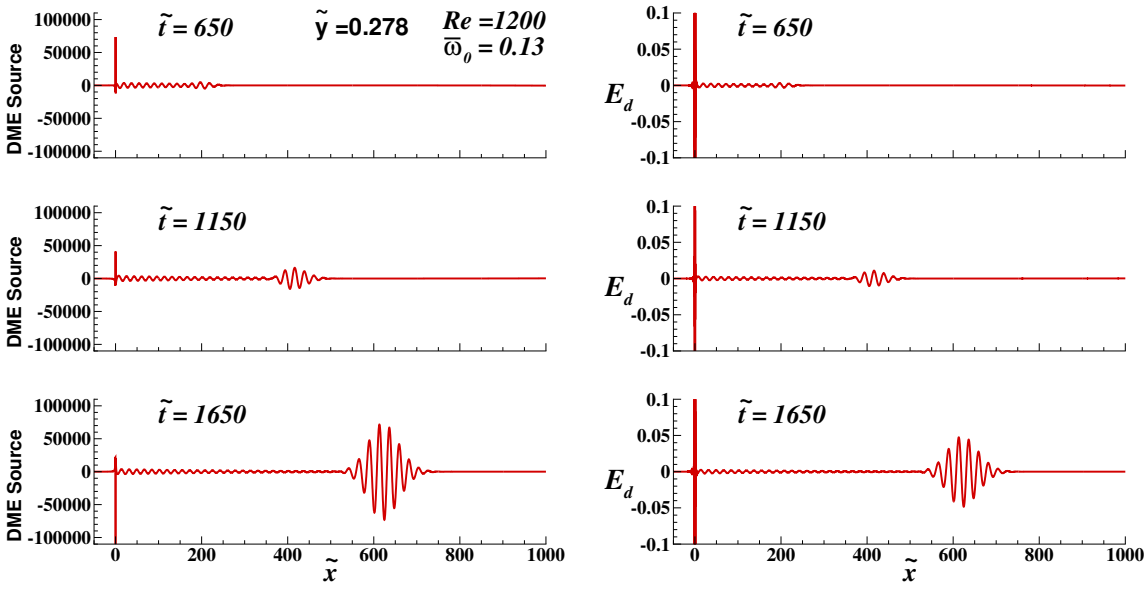

Fig. 8.6 Source of disturbance mechanical energy ($\nabla^2 E_d$) (left) and disturbance mechanical energy E_d (right) plotted as a function of $\tilde{x}$ at indicated times for $Re = 1200$, $\overline{\omega}_o = 0.13$ at $\tilde{y} = 0.278$.

a factor of 7. This was also observed in Fig. 8.4 for the u_d plots. Overall, both DME and DETE methods show a good agreement in terms of nonmodal growth of disturbance mechanical energy and disturbance enstrophy, with the disturbance quantities computed from the solution of the OSE, thus providing a justification for the use of these methods in providing an estimate for receptivity. Additionally, one can use information obtained from the NSE in these tools for tracing nonlinear growth. This will be shown while presenting the results of global linear and nonlinear receptivity analyses based on the vortex-induced instability in section 8.7.

8.2.3 Numerical Validation of Compound Matrix Method

Here, we validate the CMM with the spectral collocation method used in Schmid and Henningson (2001) for a particular case of eigenspectrum of Blasius boundary layer for $Re_{\delta^*} = 800$, derived by temporal approach.

As mentioned in the discussion of Fig. 8.3, the intersection of zero contour lines of real and imaginary parts of the second compound (new variable q_1) at the wall are the eigenvalues. Since, temporal theory has been followed here for the grid search method, the contours shown in Fig. 8.8 are plotted in the (ω_{or},ω_{oi}) plane. Here, the grid search has been performed over 12,000 points along the real axis and 6000 points along the imaginary axis. The black solid lines represent the zero contour lines for the real part of q_1, while the red dotted lines

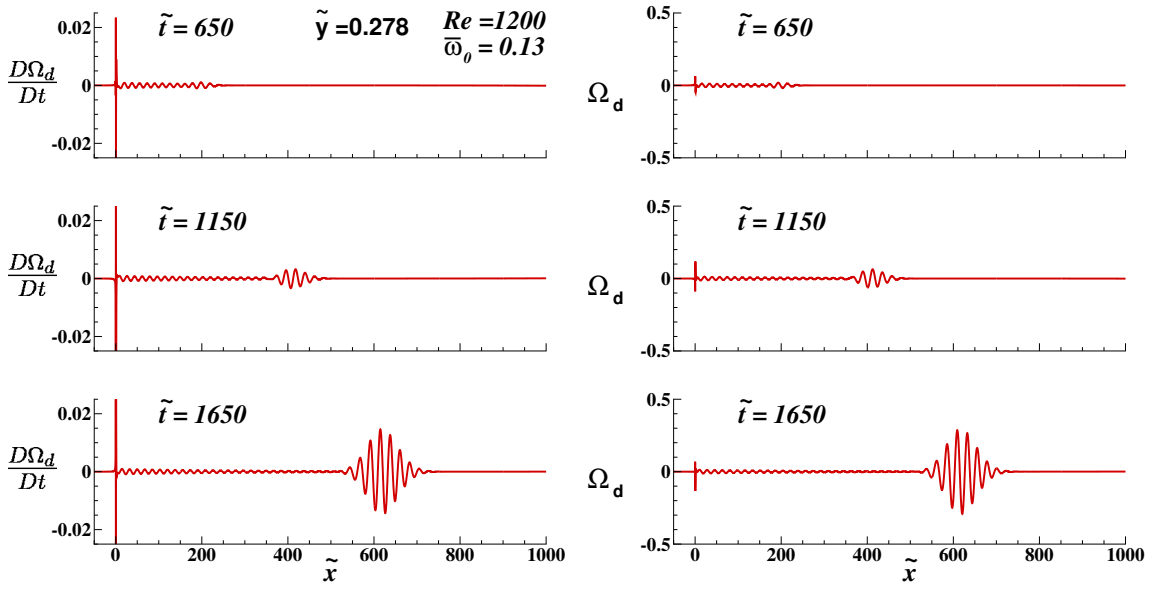

Fig. 8.7 Growth rate of disturbance enstrophy ($D\Omega_d/Dt$) (left) and disturbance enstrophy (Ω_d) (right) plotted as a function of $\tilde{x}$ at indicated times for $Re = 1200$, $\overline{\omega}_o = 0.13$ at $\tilde{y} = 0.278$.

are the corresponding contour lines for the imaginary part of q_1. We can observe clearly from the figure that there are nine intersections of the real and imaginary lines for the Blasius boundary layer at $Re_{\delta^*} = 800$ and $\alpha = 1$. The eigenvalues obtained from the CMM are listed in Table 8.1, which match very well with those given in the appendix of Schmid and Henningson (2001).

Table 8.1 Eigenvalues obtained for the Blasius boundary layer with $Re_{\delta^*} = 800$ and $\alpha = 1$.

ω_{or}	ω_{oi}
0.29440241	-0.08240950
0.46408909	-0.16979272
0.58341129	-0.21355653
0.23752687	-0.21441674
0.67030454	-0.28694562
0.42182039	-0.29556203
0.78472729	-0.35432638
0.57920607	-0.35865002
0.72486190	-0.40824005

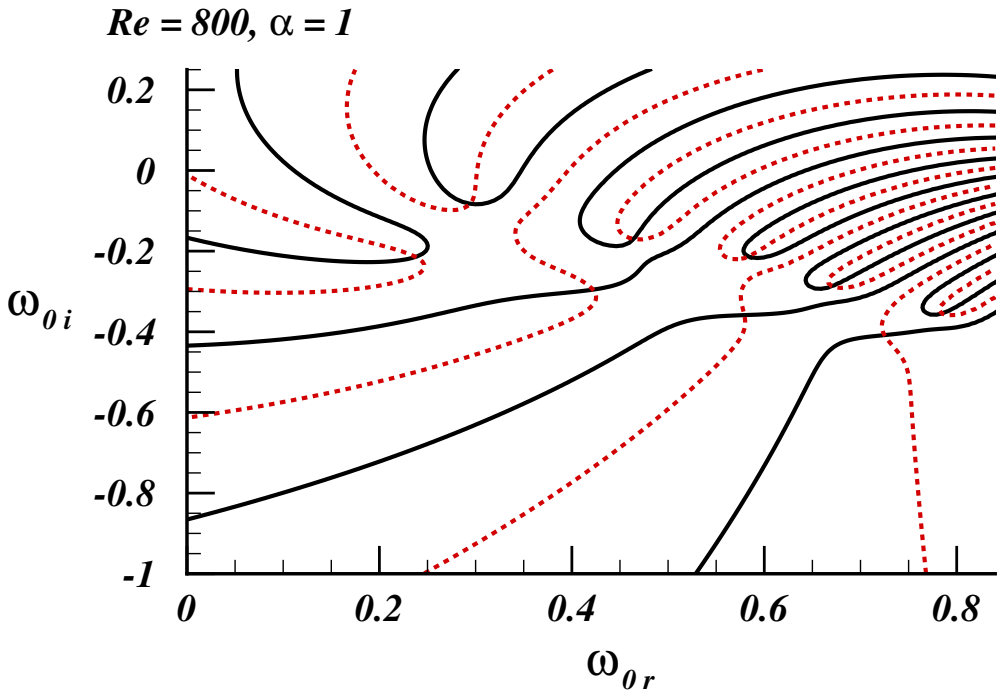

Fig. 8.8 Eigenvalues obtained from the zero crossings of the real and imaginary parts of q_1 at the wall for the Blasius boundary layer at $Re = 800$ and $\alpha = 1$.

8.3 Receptivity Analysis of Pressure Gradient Dominated Flows

Here, we analyse the time-averaged and spanwise-averaged velocity profiles for the case LI (unperturbed flow over a flat plate geometry over which a pressure gradient is imposed via a contoured upper wall) by performing a localized linear spatio-temporal viscous stability analysis for the evolving transitional flow field. The corresponding DNS results of this case are provided in Chapters 5 and 7.

The computational domain considered is shown in Fig. 5.1, which consists of a flat plate of finite thickness subjected to a streamwise pressure gradient, indicative of the pressure distribution on the suction surface of an ultra-high-lift low pressure turbine blade. The flow parameters are listed below in Table 8.2.

The flow field computed with the input parameters, shown in Table 8.2, is time-averaged over six through-flows (after flushing off transients for five through-flows) and the resulting flow field is spanwise averaged to obtain the mean statistics. Here, the effect of pressure gradient is studied by considering streamwise velocity profiles of the spanwise and time-averaged flow field extracted for (i) an attached flow location ($x = 0.32$) (ii) location on the verge of separation ($x = 0.34$) and (iii) a location where flow has separated ($x = 0.40$).

Table 8.2 Flow parameters and numerical details for the test case LI.

Length scale (L) = 0.0257m
Velocity scale (U_∞) = 34.56 m/s
Reynolds number based on length (Re_L)=60000
Span = 0.12L
Peak suction: 0.3L from leading edge

The time-averaged, spanwise-averaged velocity profile extracted at $x = 0.32$ is shown in Fig. 8.9, along with its first derivatives with respect to wall-normal coordinate, $U^{'}$ and the second derivative, $U^{''}$. This profile has been chosen on purpose, as the flow is still attached at this location despite being in a region of adverse pressure gradient ($x > 0.3$). To estimate the adverse pressure gradient existing at this streamwise station, we calculate the Falkner-Skan parameter ($m = \frac{x}{U_e}\frac{dU_e}{dx}$, where U_e is the velocity at the edge of the boundary layer). We trace the edge of the boundary layer by using the minimum vorticity threshold for the spanwise-averaged contour plot. We calculate all the necessary numerical parameters required for the solution of the OSE and tabulate those in Table 8.3 for the three streamwise stations considered here.

Table 8.3 Parameters obtained for velocity profiles used in spatio-temporal linear receptivity analysis for case LI.

x-station	m	δ^*/L	U_e/U_∞	Re_{δ^*}	$\overline{\omega}_o$
$x = 0.32$	-0.13422	0.0028	1.76528	290.217	9.8635×10^{-5}
$x = 0.34$	-0.26334	0.0036	1.74545	370.125	*NA*
$x = 0.40$	-1.21199	0.0078	1.66148	770.934	2.4267×10^{-4}

where, $Re_{\delta^*} = (U_e\delta^*)/\nu$ is the Reynolds number based on displacement thickness and $\overline{\omega}_o$ is the dimensionless circular frequency of the imposed excitation required for receptivity studies and the values have been chosen to compare with corresponding profiles of case WS, provided in Table 8.5. For the station at $x = 0.34$, we have used an impulsive wall excitation (which excites all frequencies and wavenumbers at the same time) for receptivity study, thus no frequency of excitation is required. The station at $x = 0.32$ has a strong adverse pressure gradient, close to the m value noted for incipient separation of a Falkner-Skan boundary layer, i.e. $m = -0.1988$. The Re_{δ^*} at this location, however, is of small magnitude, such that for a Blasius profile, this station would certainly be outside the unstable region. All lengths are nondimensionalized by displacement thickness δ^* and all velocities by U_e.

The streamwise velocity profile in Fig. 8.9 shows that the flow has not separated yet, due to absence of any reversed flow. The mean velocity profiles and the derivatives with

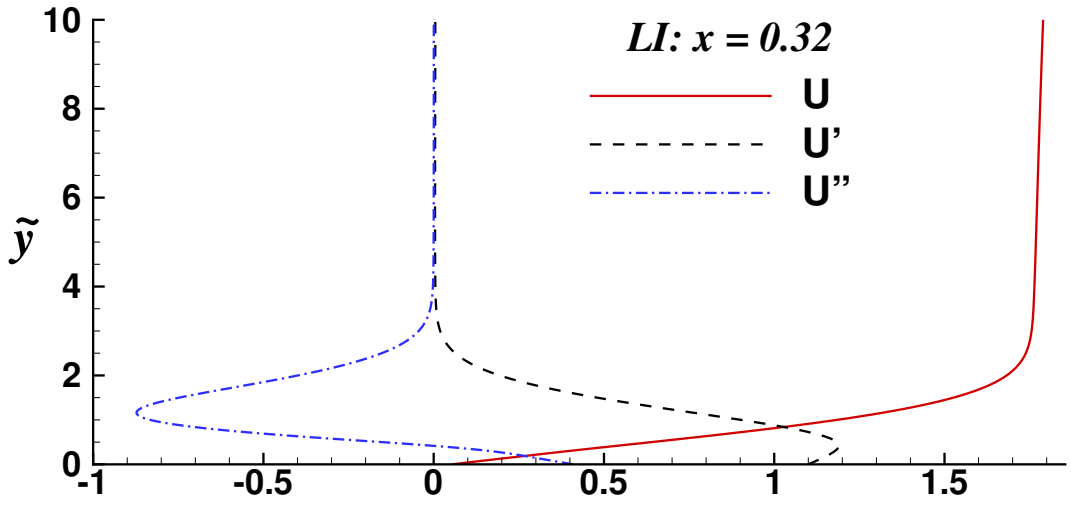

Fig. 8.9 Time-averaged and spanwise-averaged streamwise velocity profile (solid line), first derivative with respect to y (dashed line) and second derivative with respect to y (dash-dotted line) extracted at $x = 0.32$ for case LI.

respect to y are required while computing the OSE given by Eq. (8.19). After obtaining ϕ, one can obtain the streamwise disturbance velocity from Eq. (8.12). The importance of chosing Bromwich contours, along which the integrals are computed in the complex α- and ω_o-planes so that one operates within the strip of convergence, has been discussed in Chapter 2, for receptivity studies via solution of the OSE. In Eq. (8.12), we note the viscous length ($\tilde{x}$) and time ($\tilde{t}$) scales which involve nondimensionalizing with the displacement thickness and the boundary layer edge velocity, as shown in Table 8.3. The receptivity of the extracted mean velocity profiles to an infinitesimal wall-normal perturbation at the wall given by Eq. (8.34) is studied. This is the same Heaviside perturbation used in the previous section for the wall excitation case. The Dirac delta function $\delta(\tilde{x})$ indicates the localized nature of the excitation at the origin and $U_1(\tilde{t})$ is the Heaviside function, which indicates the onset of the periodic excitation impulsively at $\tilde{t} = 0$. The value of $\overline{\omega}_o$ is fixed from Table 8.3. As in the receptivity to wall excitation in the previous section, we have considered a domain such that: $-1024 < \tilde{x} < 1024$, $0 < \tilde{t} < 2048$ for $-8\pi < \alpha_r < 8\pi$,$-\pi/2 < \omega_{or} < \pi/2$ and there are 2^{14} points in $\tilde{x}$- and 2^{11} points in $\tilde{t}$-plane.

8.3.1 Response for profile at x = 0.32

The plots of streamwise disturbance velocity (u_d) versus $\tilde{x}$ are shown in Fig. 8.10 for the time- and spanwise-averaged profile shown in Fig. 8.9. The plots are shown for a wall-normal

location $\tilde{y} = 0.1$. The Bromwich contours for this profile are located along: $\alpha_i = -0.01$ and $\omega_{oi} = 0.02$. The local solution associated with the exciter at $\tilde{x} = 0$, and with an initial amplitude of 10^{-1} is represented by the vertical line in all the frames of Fig. 8.10. For the frame at $\tilde{t} = 200$, we note the inception of a wave-like structure identified as the STWF. However, due to the low Re_{δ^*} at this station, we are operating outside the unstable region. Therefore, as time progresses, we note damping of the STWF. At $\tilde{t} = 700$, the amplitude of the STWF has reduced by several orders of magnitude. It should be noted here that the viscous time scale is related to the convective time scale by the relationship between Re_L and Re_{δ^*} as $t = 2.74004 \times 10^{-4}\tilde{t}$. Thus, the first frame corresponds to $t = 0.0548$, while the last frame corresponds to $t = 0.1918$. The total time over which the STWF dampens is only $\Delta t = 0.137$. We note that the frequency of excitation given in Table 8.3, is so low that there are no Tollmien-Schlichting waves excited here. Thus, for this station, the disturbance displays very weak receptivity as the STWF is unable to dominate the local solution imposed by the Heaviside function.

8.3.2 Response for profile at x = 0.34

In Fig. 8.11, the time- and spanwise-averaged streamwise velocity profile and its first and second derivatives, extracted at $x = 0.34$ are shown. The Falkner-Skan parameter for this streamwise location is -0.2633, as shown in Table 8.3. The Re_{δ^*} is 370.125, which is large enough to be in an unstable region for an adverse pressure gradient flow, as the Re_{cr} shifts towards a lower value for a flow with a higher adverse pressure gradient. For the case under consideration, from the velocity profile in Fig. 8.11, we note that there is no inflection point near the wall, and thus, the flow has not yet separated at this location. The velocity profile and its derivatives are fed into the OSE in Eq. (8.19) and receptivity of the flow to a periodic suction-blowing excitation at the wall, given by Eq. (8.34), is studied.

The plots of u_d as a function of $\tilde{x}$ are shown in Fig. 8.12 for the time- and spanwise-averaged streamwise velocity profile extracted for the case LI at $x = 0.34$. The plots are shown for $\tilde{y} = 0.1$. The Bromwich contours identified for this velocity are located along: $\alpha_i = -0.01$ and $\omega_{oi} = 0.03$. The change in the Bromwich contour in the ω_o-plane can be explained by the fact that the velocity profile at $x = 0.34$, is on the verge of separation and is more receptive to any infinitesimal perturbation (even due to round-off error), as compared to the profile at $x = 0.32$ in the circular frequency range given by $\omega_{oi} = 0.02$ and $\omega_{oi} = 0.03$ lines in the complex ω_o-plane. These are additional high growth rate temporal modes, which are automatically accounted for in the solution of the OSE by Bromwich contour integral method. The local solution associated with the impulse start at $\tilde{x} = 0$, $\tilde{t} = 0$ has an initial amplitude of 10^{-3}. For this case, we have used an impulsive excitation (which excites all

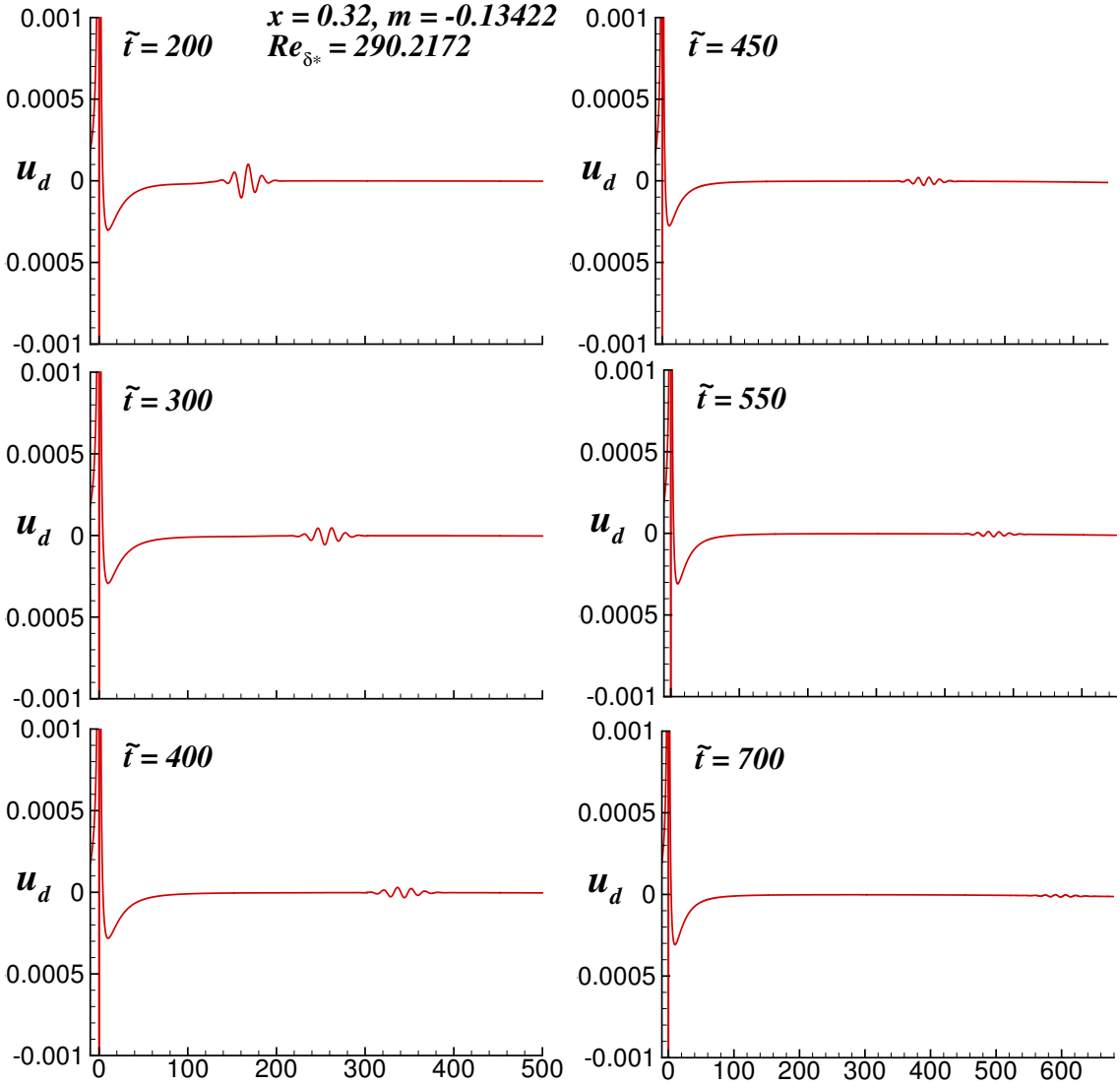

Fig. 8.10 Streamwise disturbance velocity plotted as function of $\tilde{x}$ shown at $\tilde{y} = 0.1$ for profile extracted at $x = 0.32$ for case LI.

wavenumbers and frequencies simultaneously) for receptivity studies, as case LI does not have any imposed frequency in terms of wakes or blade oscillations. This velocity profile is much more receptive to the imposed wall excitation compared to the profile at $x = 0.32$. At $\tilde{t} = 200$ a STWF is observed which grows spatio-temporally, but with the temporal growth dominating. The amplitude of the STWF increases from ~ 0.0025 at $\tilde{t} = 200$ to ~ 2.2 at $\tilde{t} = 400$, thus a massive amplification of the STWF by a factor 880 is noted for $\Delta\tilde{t} = 200$ which corresponds to convection time interval of $\Delta t = 0.74503$.

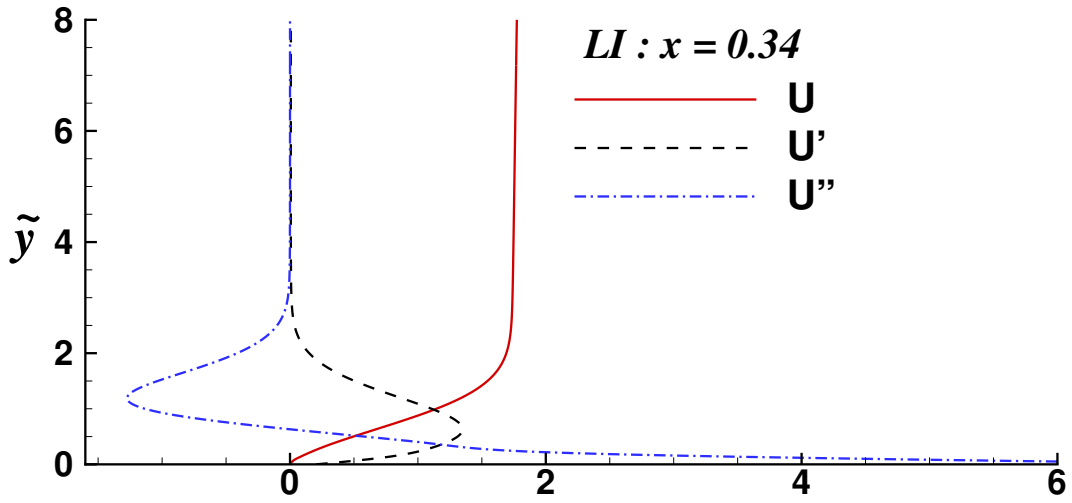

Fig. 8.11 Time-averaged and spanwise-averaged streamwise velocity profile (solid line), first derivative with respect to y (dashed line) and second derivative with respect to y (dash-dotted line) extracted at $x = 0.34$ for case LI.

In Fig. 8.13, the evolution of the maximum streamwise disturbance velocity (top) and the streamwise station of the maximum disturbance velocity (bottom) are traced for the velocity profile extracted at $x = 0.34$. We note that the impulsive start excites the solution initially till the STWF takes over and becomes prominent. This does not happen for the velocity profile extracted at $x = 0.32$, wherein the STWF is not able to overtake the local solution and it eventually dampens out due to low receptivity and operation in the stable region outside neutral curve. Another feature to be highlighted here is that the maximum amplitude noted at $\tilde{t} = 1020$, when the STWF is close to exiting the domain is of the order 10^9 compared to the corresponding plot for $x = 0.32$, where the STWF dampened and only the local solution remains. This once again shows that the velocity profile at $x = 0.34$ is highly receptive to any excitation (even if it is in the background due to round-off error) as the flow is about to separate, in contrast with the attached profile at $x = 0.32$ with lower receptivity. The streamwise station of maximum streamwise disturbance velocity is initially due to the impulsive start but soon thereafter is due to the STWF, seen by the step-like appearance in the bottom frame of Fig. 8.13. The group velocity of the STWF can be calculated and is found to be $V_g = 0.815157$.

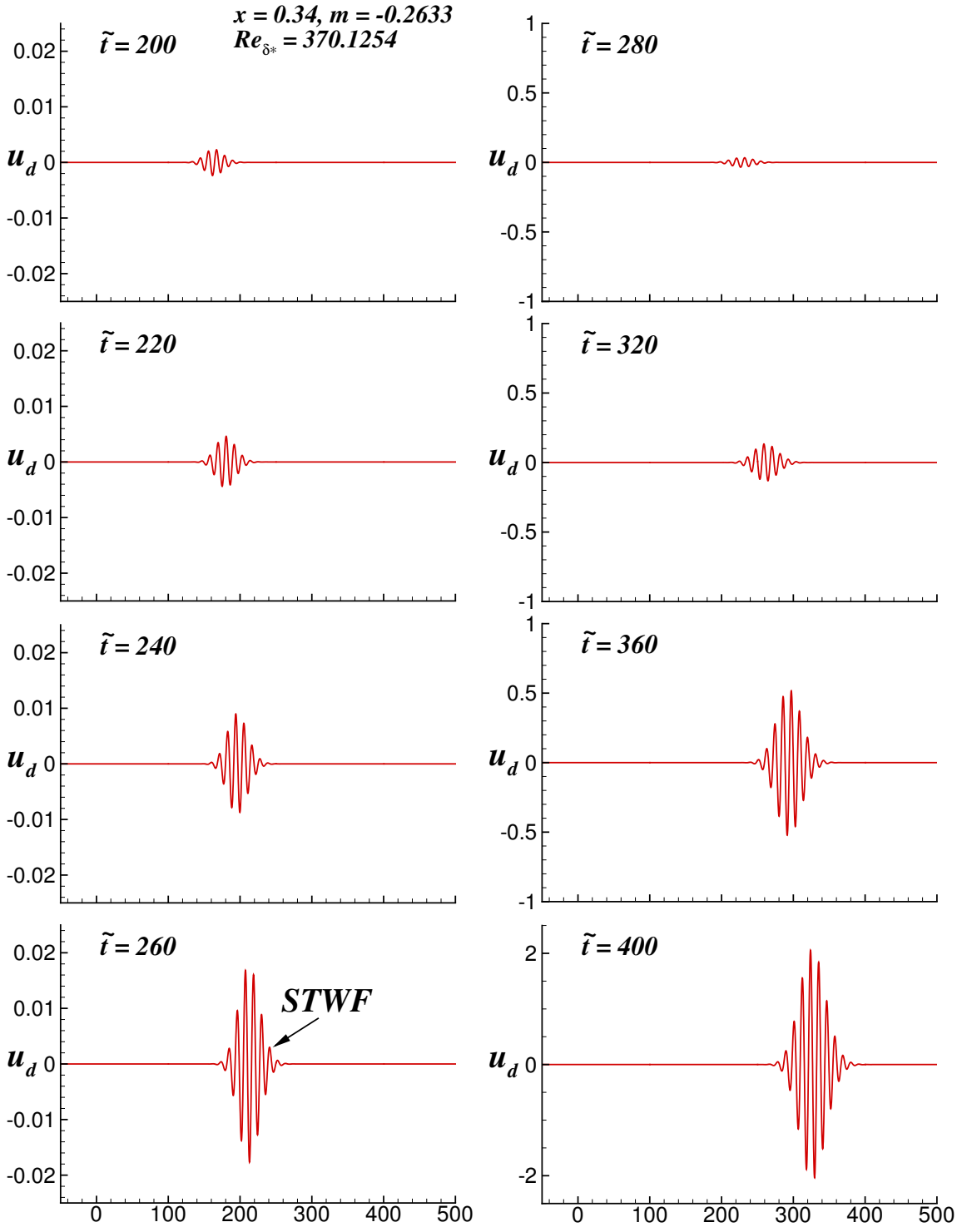

Fig. 8.12 Streamwise disturbance velocity plotted as function of $\tilde{x}$ shown at $\tilde{y} = 0.1$ for profile extracted at $x = 0.34$ for case LI.

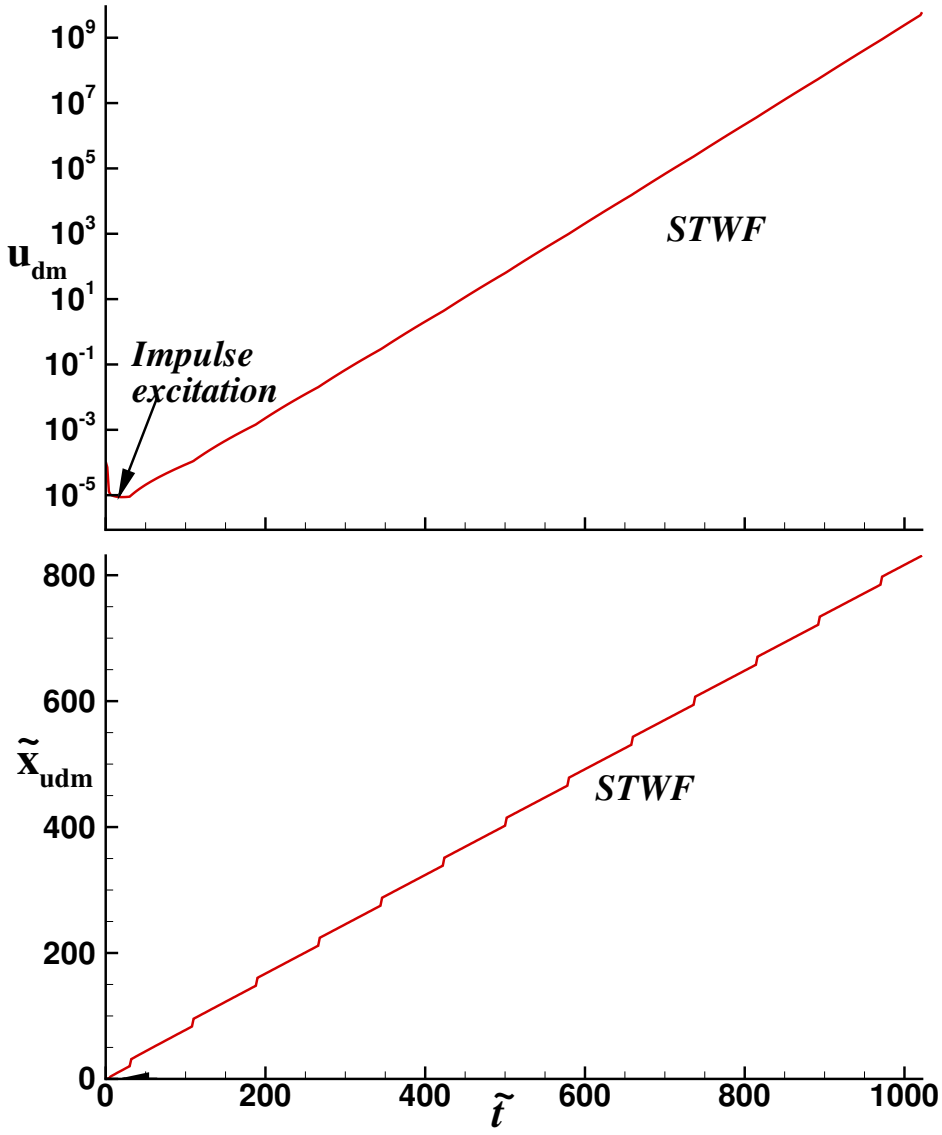

Fig. 8.13 Evolution of maximum streamwise disturbance velocity and streamwise station where maximum is located, showing the local solution and STWF for profile extracted at $x = 0.34$ for case LI.

8.3.3 Response for profile at x = 0.40

The time- and spanwise-averaged velocity profile extracted at $x = 0.40$ is shown in Fig. 8.14. We note a near-wall region, which has reversed velocity, indicating that the profile has been extracted from within the separated flow region. This is also seen in the Falkner-Skan parameter of -1.2119 in Table 8.3, for this case. This is a region of severe adverse pressure gradient. The Reynolds number associated with this profile ($Re_{\delta^*} = 770.934$) is almost twice

the value we had observed for the velocity profiles at $x = 0.34$. There is also an inflection point associated with this velocity profile as can be seen from the plot of the second derivative in Fig. 8.14. The response of such a severe adverse pressure gradient to an infinitesimal wall-excitation in the form of a Heaviside function is studied, even though the parallel flow approximation for such a separated profile is not strictly true. Still this procedure will yield a qualitative view of the flow properties and the underlying spatio-temporal instability.

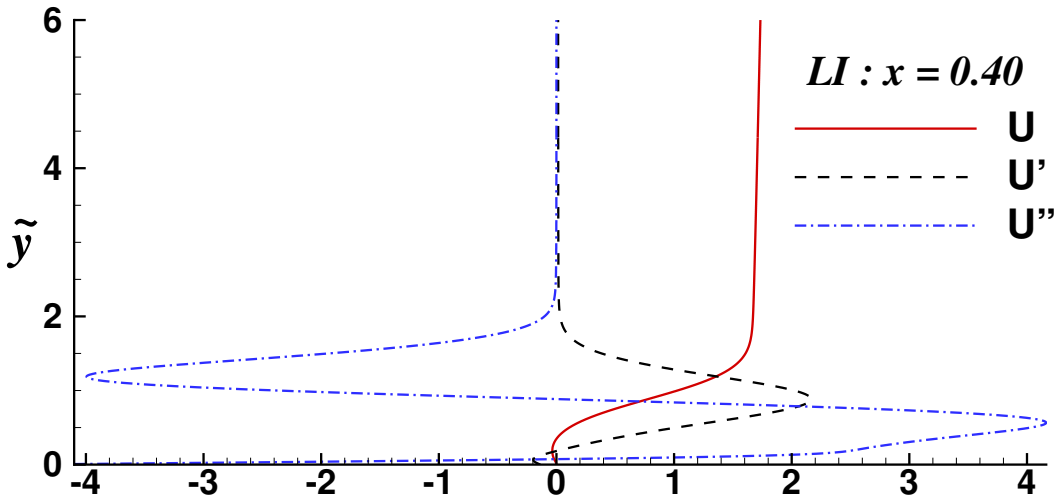

Fig. 8.14 Time-averaged and spanwise-averaged streamwise velocity profile (solid line), first derivative with respect to y (dashed line) and second derivative with respect to y (dash-dotted line) extracted at $x = 0.40$ for case LI.

The plots of u_d as a function of $\tilde{x}$ are shown in Fig. 8.15 for a time- and spanwise-averaged streamwise velocity profile extracted at $x = 0.40$. The plots are shown for a wall-normal location $\tilde{y} = 0.1$. The Bromwich contours identified for this velocity are located along: $\alpha_i = -0.05$, $\omega_{oi} = 0.3$. The choice of the Bromwich contours both in α- and ω_o-planes have been altered significantly, as compared to the values chosen for profiles at $x = 0.32$ and $x = 0.34$. Here, the amplitude of the wall-excitation imposed has been reduced by one order of magnitude to 10^{-4} while the corresponding small frequency of oscillation is equal to $\overline{\omega}_o = 2.4267 \times 10^{-4}$. We had to lower the excitation amplitude to curb the uncontrollable amplification of the STWF for this velocity profile with separated flow. Even for an early time $\tilde{t} = 56$, we can identify the STWF which has significantly overtaken the local solution amplitude. A short time later, at $\tilde{t} = 60$, the amplitude of the STWF has risen to 11 as compared to its amplitude at $\tilde{t} = 56$, which is 4. Thus, an amplification of the STWF by a

factor of 2.75 is noted for a very short time period, $\Delta\tilde{t} = 4$ which corresponds to a convective time interval of $\Delta t = 0.0186$.

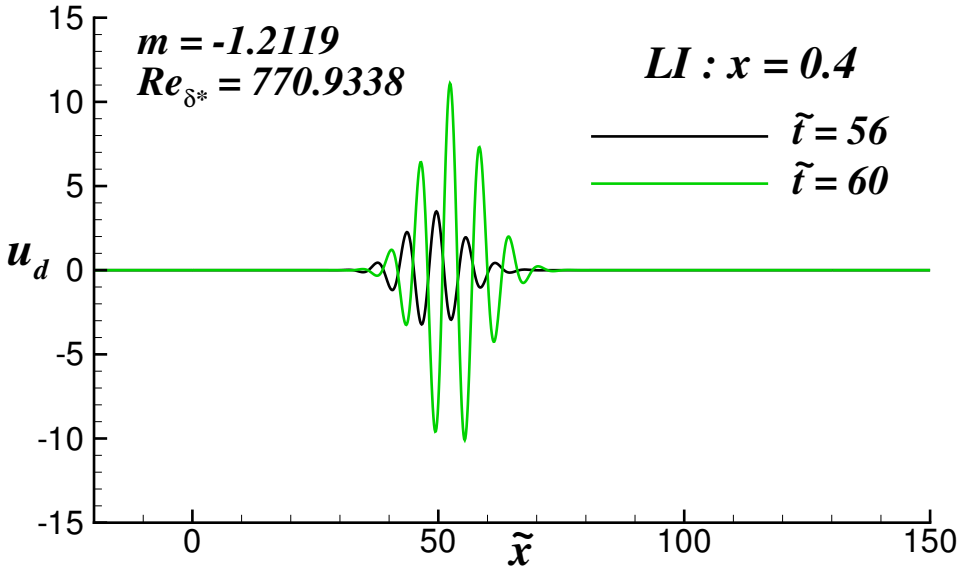

Fig. 8.15 Streamwise disturbance velocity plotted as function of $\tilde{x}$ shown at $\tilde{y} = 0.1$ for profile extracted at $x = 0.40$ for case LI.

In fact, the growth observed for the STWF is such that at the end of the domain at $\tilde{t} = 1020$, amplifications of the order of 10^{50} are observed even after the input wall-excitation has been brought down by an order of magnitude. While for $x = 0.34$, at a location where flow has not yet separated, the amplification at $\tilde{t} = 1020$ is found to be of the order 10^9. This kind of a violent temporal instability can be noted only when the flow has separated in regions of severe adverse pressure gradients and is an indication of a Kelvin-Helmholtz type instability at play, which we have termed more generically as the STWF. Thus, through these localized receptivity studies for the extracted velocity profiles for the unperturbed flow in case LI, we note that the STWF is the spatially and temporally growing wave-front which needs to be traced. The STWF is in fact created due to the constructive interference between constituent wavelets (Sengupta et al., 2006a) and the growth is associated with the nonmodal component of the response.

8.4 Receptivity Analysis of Pressure Gradient Dominated Flows with Forced Frequency Oscillations

Here, we analyse the time-averaged and spanwise-averaged velocity profiles for the case WS (i.e. blade oscillating at a reduced frequency of 0.1) by performing a localized linear spatio-temporal viscous stability analysis for different stages of the evolving transitional flow field. The corresponding DNS results of this case are provided in Chapter 5. This has been done with the aim of explaining the mechanisms underlying the flow instability and trying to correlate the structures observed with classical instabilities. We will first provide a brief summary of the parameters governing the computed flow.

The same computational domain for the pressure gradient effects is considered here. A sinusoidal wall-normal velocity is induced on the flat plate to mimic the heaving oscillation that a low pressure turbine blade may incur due to a combination of inflow conditions. The equation for the blade oscillations is given by Eq. (3.46) in Chapter 3. The additional flow parameters for imposed blade oscillation are listed below in Table 8.4.

Table 8.4 Flow parameters and numerical details for the test case WS.

Amplitude of blade oscillation (a) = 0.031 (blade pitch/30)
Frequency of oscillation (f) = 12.9 Hz
Reduced frequency ($k_{osc} = 2(2L)/U_\infty$) = 0.1

The flow field computed with the input parameters, as shown in Table 8.4, is averaged over 77 cycles of imposed oscillation (after flushing off transients for 65 cycles of imposed oscillation) and the resulting flow field is subsequently spanwise-averaged to obtain the mean statistics. Here, we will only focus on the streamwise velocity profiles of the spanwise and time-averaged flow field for the case WS extracted for (i) an attached flow location ($x = 0.32$) (ii) location on the verge of separation ($x = 0.34$) and (iii) a location where flow has separated ($x = 0.40$).

The time-averaged, spanwise-averaged velocity profile extracted at $x = 0.32$ is shown in Fig. 8.16(a). The profile is chosen as the flow is still attached at this location despite being in a region of adverse pressure gradient ($x > 0.3$). To estimate the adverse pressure gradient existing at this streamwise station, we calculate m. For $x = 0.32$ the values obtained are as follows: $U_e/U_\infty = 1.80508$ and $m = -0.16716$.

This indicates that the location has a strong adverse pressure gradient. We calculate all the necessary numerical parameters required for the solution of the OSE and tabulate those in Table 8.5 for the three streamwise stations considered here.

Table 8.5 Parameters obtained for extracted velocity profiles required for spatio-temporal linear receptivity analysis for test case WS.

x-station	m	δ^*/L	U_e/U_∞	Re_{δ^*}	$\overline{\omega}_o$
$x = 0.32$	-0.16716	0.0029	1.80508	309.963	9.8635×10^{-5}
$x = 0.34$	-0.18130	0.0034	1.78794	359.954	1.1462×10^{-4}
$x = 0.40$	-0.79470	0.0069	1.71374	701.441	2.4267×10^{-4}

where, Re_{δ^*} is the Reynolds number based on displacement thickness and $\overline{\omega}_o = 2\pi f \delta^*/U_e$ is the dimensionless circular frequency based on the imposed blade oscillation frequency.

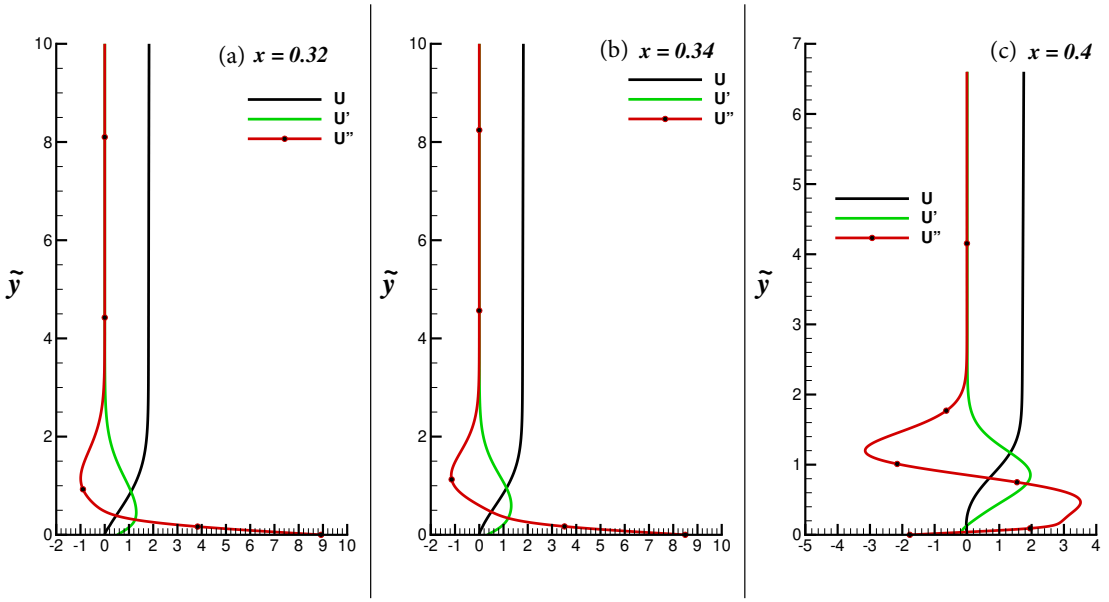

Fig. 8.16 Time-averaged and spanwise-averaged streamwise velocity profile (black line), first derivative with respect to y (green line) and second derivative with respect to y (red line with symbols) extracted at (a) $x = 0.32$, (b) $x = 0.34$ and (c) $x = 0.4$ for case WS.

The streamwise velocity profile in Fig. 8.16(a) shows that the flow has not separated yet with notable absence of any reversed flow regions. The receptivity of the extracted velocity profiles to an infinitesimal wall-normal perturbation at the wall given by Eq. (8.34) is studied where the value of $\overline{\omega}_o$ is fixed from Table 8.5. We have used the same domain considered in the previous section.

8.4.1 Response for the profile at x = 0.32

The plots of streamwise disturbance velocity (u_d) as a function of $\tilde{x}$ are shown in Fig. 8.17(a) for a time- and spanwise averaged streamwise velocity profile extracted for case WS at a

streamwise station ($x = 0.32$) as shown in Fig. 8.16(a). The plots are shown for a wall-normal location $\tilde{y} = 0.1$. The Bromwich contours identified for this velocity are located along: $\alpha_i = -0.01$ and $\omega_{oi} = 0.02$. The local solution associated with the exciter at $\tilde{x} = 0$, and with an initial amplitude of 10^{-3} is represented by the vertical line in the frames at $\tilde{t} = 350$ to 650 of Fig. 8.17(a). For the frame at $\tilde{t} = 350$, we note the inception of a wave-like structure identified as the STWF, the fully developed version of which is seen in the frame at $\tilde{t} = 650$. The ordinates in the frames, for $\tilde{t} = 750$ to 1020, have been adjusted to follow the evolution of the STWF, which grows both in space and time. By the time the STWF is near the end of the domain (noted in the frame at $\tilde{t} = 1020$), we evaluate the amplification associated with the STWF is ~ 120 times the value seen at $\tilde{t} = 350$. It should be noted here that the viscous time scale is related to the convective time scale by the relationship between Re_L and Re_{δ^*} as $t = 1.60657 \times 10^{-3}\tilde{t}$. Thus, the first frame corresponds to $t = 0.5622$, while the last frame corresponds to $t = 1.6387$. The total time over which such a large amplification is noted is only $\Delta t = 1.0765$. Thus, a nonmodal transient growth of the disturbance field is observed through the growing unstable solution of the OSE in the form of the STWF. We note that the frequency of excitation, given in Table 8.5, is so low that there are no Tollmien-Schlichting waves excited here.

This corresponds to the explanation given in Sengupta (2012) following the observation from Gaster et al. (1994) that *"a proper mathematical account of these disturbances has not yet appeared"*, with no 2D Tollmien-Schlichting modes observed for such low frequency excitations. Presented results here are consistent with these observations. In such cases, one would observe only the local solution and the STWF.

In Fig. 8.18(a), the evolution of the maximum disturbance streamwise velocity component (top) and streamwise location of the maximum value (bottom) are shown for the velocity profile extracted at $x = 0.32$. This figure provides us with an estimate of time when the STWF becomes important and overtakes the local solution created by the exciter. Till $\tilde{t} = 450$ or so, it is the local solution which dominates the disturbance field, and this can also be seen with respect to the streamwise location of the maximum in the bottom frame (i.e. at $\tilde{x} = 0$). It is only after this time that the STWF begins to dominate in the maximum disturbance velocity plot, these demarcations have been marked in Fig. 8.18. This feature is also seen in the plots of u_d in Fig. 8.17(a). We note here, that since the STWF propagates both in space and time, the streamwise location of the maximum disturbance velocity also keeps changing with time.

8.4.2 Response for profile at x = 0.34

In Fig. 8.16(b), the time-averaged and spanwise averaged streamwise velocity profile and its first and second derivatives, extracted at $x = 0.34$ are shown. The Falkner-Skan parameter

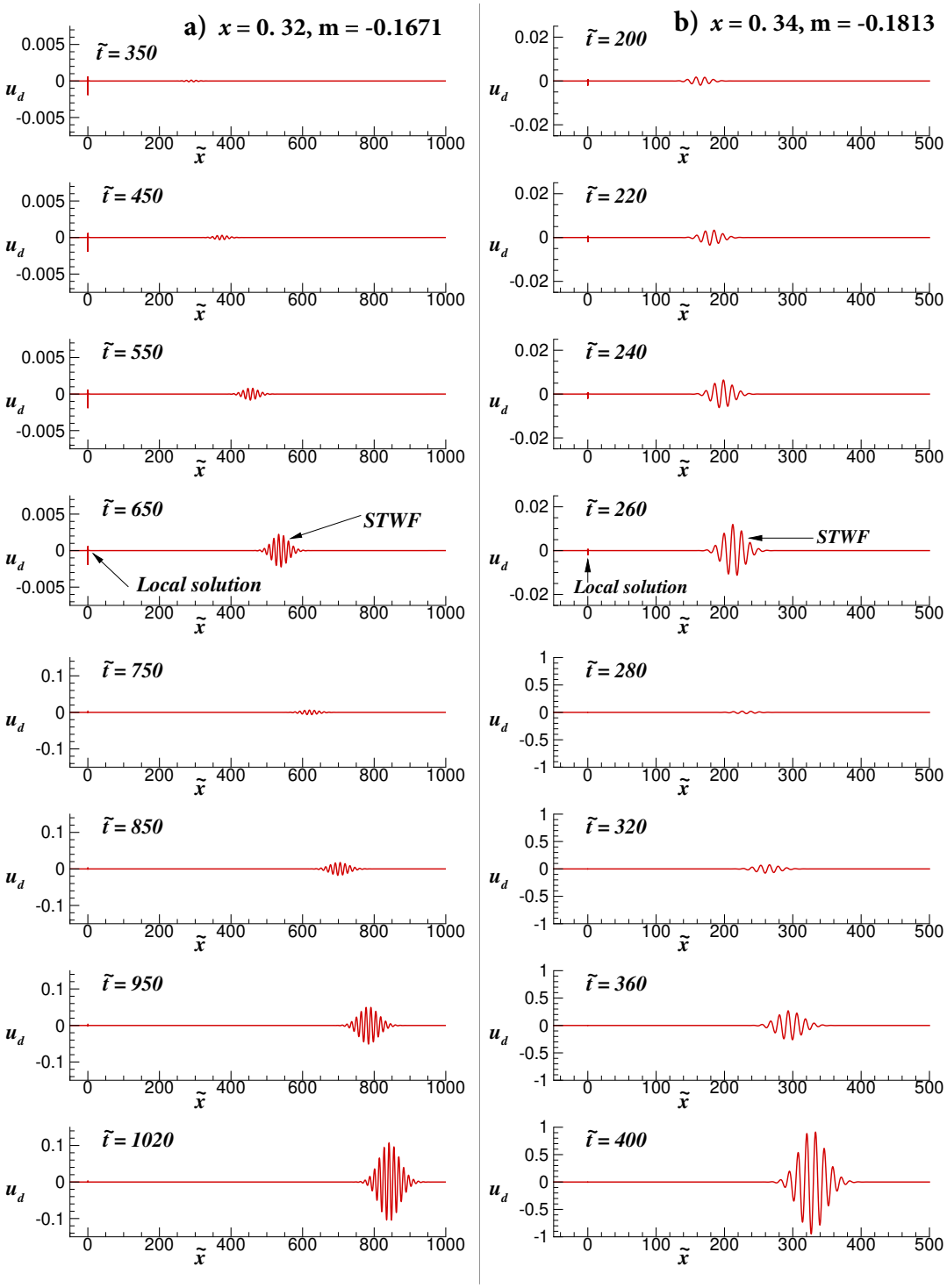

Fig. 8.17 Streamwise disturbance velocity plotted as function of $\tilde{x}$ shown at $\tilde{y} = 0.1$ for profile extracted at (a) $x = 0.32$ and (b) $x = 0.34$ for case WS.

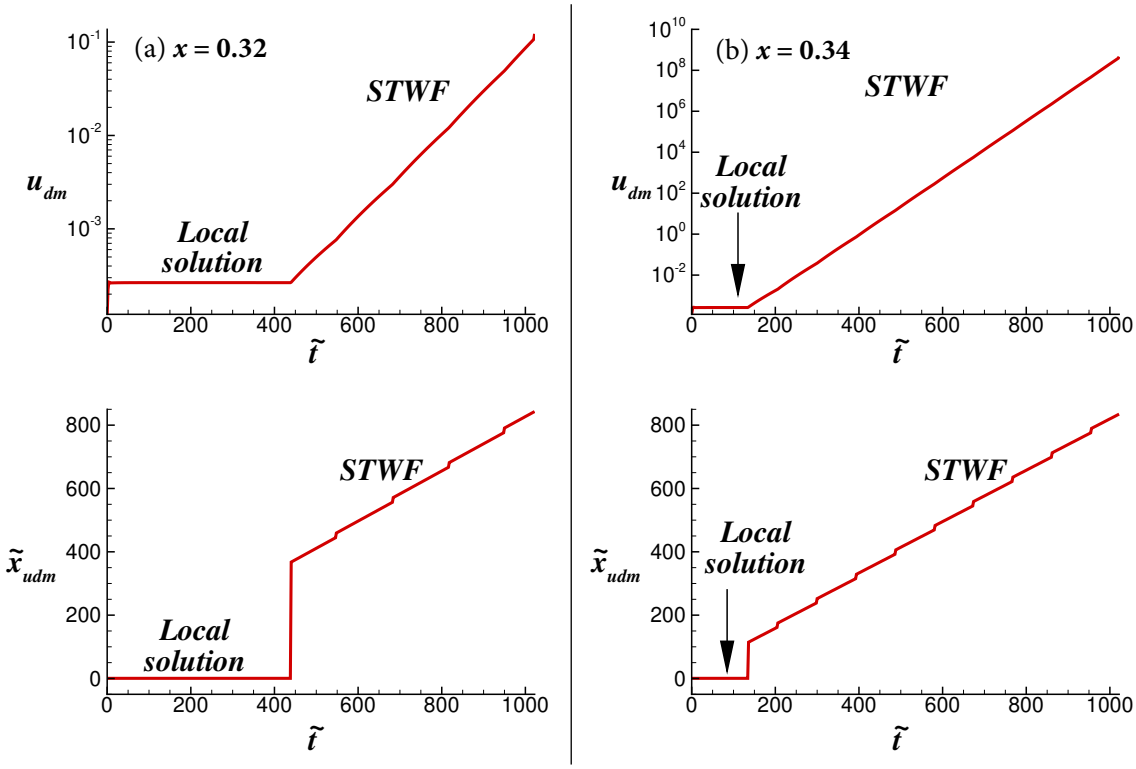

Fig. 8.18 Evolution of maximum streamwise disturbance component and streamwise station where maximum is located, showing the local solution and STWF for profile extracted at (a) $x = 0.32$ and (b) $x = 0.34$ for case WS.

for this streamwise location is -0.1813, as shown in Table 8.5, which for the Falkner-Skan boundary layer profile is on the verge of separation. For the case under consideration, from the velocity profile in Fig. 8.16(b), we note that there is no reversed flow, and thus, the flow has not yet separated for this location. The velocity profile and its derivatives are fed into the OSE in Eq. (8.19) and receptivity of the flow to a periodic suction-blowing excitation at the wall given by Eq. (8.34) is studied.

The plots of streamwise disturbance components (u_d) as a function of $\tilde{x}$ are shown in Fig. 8.17(b) for the time- and spanwise-averaged streamwise velocity profile extracted for the case WS at $x = 0.34$. The plots are shown for $\tilde{y} = 0.1$. The Bromwich contours identified for this velocity are located along: $\alpha_i = -0.01$ and $\omega_{oi} = 0.03$. The change in the Bromwich contour in the ω_o-plane can be explained by the fact that the velocity profile at $x = 0.34$, is on the verge of separation and thus, is more receptive to any infinitesimal perturbation (even due to round-off error), as compared to the profile at $x = 0.32$ in the circular frequency range given by $\omega_{oi} = 0.02$ and $\omega_{oi} = 0.03$ lines in the complex ω_o-plane. These are additional high growth rate temporal modes, which are automatically accounted for in the solution of

the OSE by Bromwich contour integral method for this velocity profile. The local solution associated with the exciter at $\tilde{x} = 0$, and with an initial amplitude of 10^{-3} is represented by the vertical lines till $\tilde{t} = 260$ in Fig. 8.17(b). We can already note that this velocity profile is far more receptive to the imposed wall excitation, by the ordinates of the frame at $\tilde{t} = 400$. For the velocity profile extracted at $x = 0.32$, the inception of the STWF began by $\tilde{t} = 350$, however in this case, by $\tilde{t} = 200$ we note a more pronounced STWF with higher amplitude. The amplitude of the STWF increases from ~ 0.025 at $\tilde{t} = 200$ to ~ 1 at $\tilde{t} = 400$, thus an amplification of the STWF by a factor 400 is noted for $\Delta\tilde{t} = 200$ which corresponds to convection time interval of $\Delta t = 0.3803$.

In Fig. 8.18(b), the evolution of the maximum streamwise disturbance velocity (top) and the streamwise station of the maximum disturbance velocity (bottom) are traced for the velocity profile extracted at $x = 0.34$. We note that the local solution dominates the solution till $\tilde{t} = 180$, after which the STWF becomes prominent. This happened at $\tilde{t} = 450$ for the velocity profile extracted at $x = 0.32$. Another feature to be highlighted here is that the maximum amplitude at $\tilde{t} = 1020$, when the STWF is close to exiting the domain is of the order 10^{10} compared to the corresponding plot for $x = 0.32$, where the maximum amplitude was only of the order of 10^{-1} (not shown). This once again shows that the velocity profile at $x = 0.34$ is highly receptive to any excitation (even if it is in the background due to round-off error) as the flow is about to become separated, which is in contrast with the attached profile at $x = 0.32$ with lower receptivity. The streamwise stations at which maximum streamwise disturbance velocity are located are first attributed to the local solution till $\tilde{t} = 180$, and thereafter to the STWF which is seen by the step-like appearance of the streamwise location of the maximum disturbance velocity in the bottom frame of Fig. 8.18(b). The group velocity of the STWF is calculated and is found to be $V_g = 0.818707$.

8.4.3 Response for profile at x = 0.40

The time- and spanwise-averaged velocity profile extracted at $x = 0.40$ is shown in Fig. 8.16(c). We note a near-wall region which has reversed velocity, indicating that the profile has been extracted from within the separated flow region. This is also seen in the Falkner-Skan parameter of -0.7947 in Table 8.5, for this case. This is a region of severe adverse pressure gradient. The Reynolds number associated with this profile ($Re_{\delta^*} = 701.441$) is almost twice the value we had observed for the velocity profile at $x = 0.34$. There is also an inflection point associated with this velocity profile as can be seen from the plot of the second derivative in Fig. 8.16(c). It is interesting to note how such a severe adverse pressure gradient responds to an infinitesimal wall-excitation, even though the parallel flow approximation for

such a separated profile is not very rigorous. Still it will yield a qualitative view of the flow properties, as noted by time- and spanwise-averaging.

The plots of streamwise disturbance components (u_d) as a function of $\tilde{x}$ are shown in Fig. 8.19 for a time- and spanwise-averaged streamwise velocity profile extracted at $x = 0.40$. The plots are shown for a wall-normal location $\tilde{y} = 0.1$. The Bromwich contours identified for this velocity are located along: $\alpha_i = -0.065$, $\omega_{oi} = 0.18$. The choice of the Bromwich contours, both in α- and ω_o-planes, have been altered significantly, as compared to the values chosen for profiles at $x = 0.32$ and $x = 0.34$. Here, the amplitude of the wall-excitation imposed has been reduced by one order of magnitude to 10^{-4} while the corresponding small frequency of oscillation is equal to $\overline{\omega}_o = 2.24267 \times 10^{-4}$. We had to lower the excitation amplitude to curb the uncontrollable amplification of the STWF for this velocity profile with reverse flow. Even for an early time $\tilde{t} = 56$, we can identify the STWF which has already overtaken the local solution amplitude. A short time later, at $\tilde{t} = 64$, the amplitude of the STWF has risen to 1.4 as compared to its amplitude at $\tilde{t} = 56$ which is 0.2. Thus, an amplification of the STWF by a factor of 7 is noted for a very short time period, $\Delta\tilde{t} = 8$ which corresponds to a convective time interval of $\Delta t = 0.0322$.

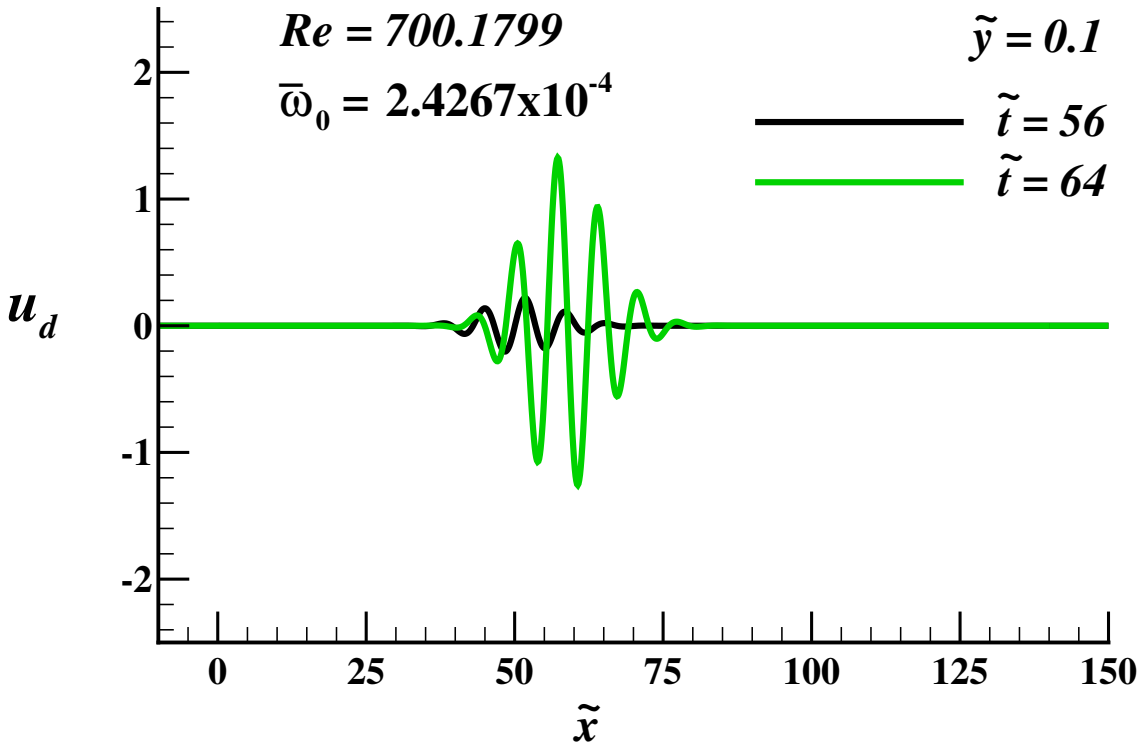

Fig. 8.19 Streamwise disturbance component plotted as function of $\tilde{x}$ shown at $\tilde{y} = 0.1$ for profile extracted at $x = 0.4$ for case WS.

In fact, the growth observed for the STWF is such that at the end of the domain, amplifications of the order of 10^{36} are observed even after the input wall-excitation has been brought down by an order of magnitude. This kind of a violent instability can be noted only when the flow has separated in regions of severe adverse pressure gradients. Thus, through these localized receptivity studies for the extracted velocity profiles for the case WS, we note that the STWF is the spatially and temporally growing wave-front which needs to be traced. The effect of added blade oscillations has led to a delayed separation compared to test case LI. This can be viewed through the lower m values noted beyond $x = 0.32$ for case WS compared to those for case LI. Thus, blade oscillations alter the flow by allowing it to overcome the adverse pressure gradient even though the underlying spatio-temporal instability and its mechanism (the STWF) is the same.

As we have noted in the response fields to the three extracted velocity profiles, the first two profiles are in the unseparated part of the flow field, and hence do not have an inflection point. For the profile at $x = 0.4$, however, an inflection point is found to lead the flow to amplifications of the order of 10^{36}. The effect of the presence/absence of the inflection point on the amplification is shown next by considering the maximum u_d as a function of $\tilde{y}$ for the three streamwise stations.

In Fig. 8.20, the maximum u_d, mean velocity, U and its double derivative are shown as a function of $\tilde{y}$. There is no inflection point in U for this station and u_{dmax} attains a maximum for $\tilde{y} = 0.25$ with a value 0.135.

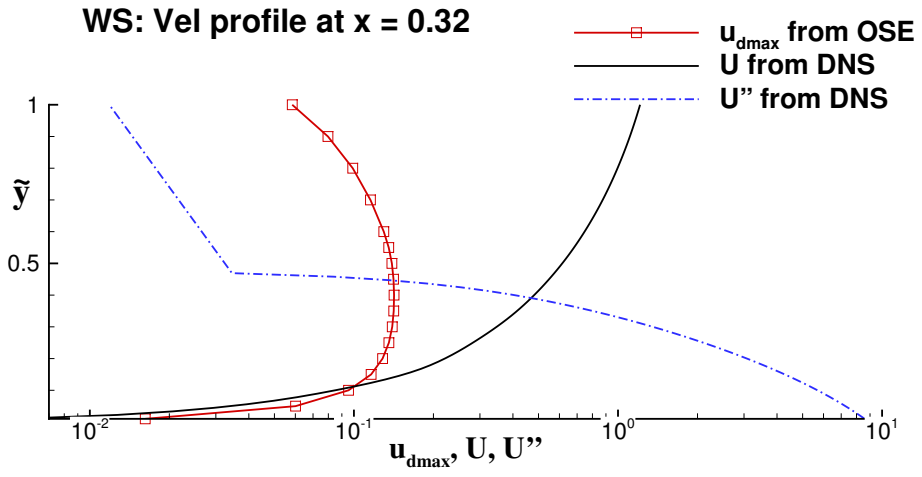

Fig. 8.20 Maximum streamwise disturbance velocity plotted as function of $\tilde{y}$ for profile extracted at $x = 0.32$ for case WS.

In contrast, at a downstream streamwise station of $x = 0.34$ shown in Fig. 8.21, the maximum amplification in u_d is observed at the same wall-normal location of $\tilde{y} = 0.25$, but with a much larger value of 1.05. This profile also does not have an inflection point, but

as the location is close to the separation point, it is far more receptive to disturbances than $x = 0.32$.

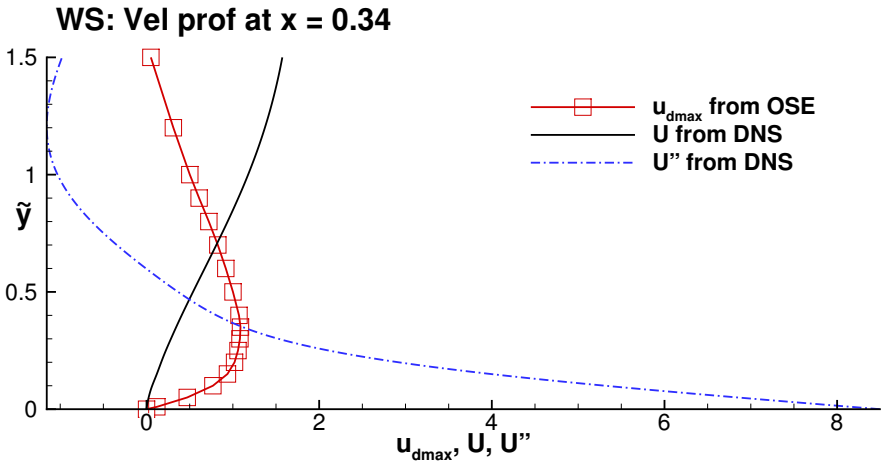

Fig. 8.21 Maximum streamwise disturbance velocity plotted as function of $\tilde{y}$ for profile extracted at $x = 0.34$ for case WS.

For the station at $x = 0.4$ shown in Fig. 8.22, there is an inflection point observed very close to the wall at $\tilde{y} = 0.05$. This indicates that the flow has separated at this location. In fact, the recirculating separated flow leads to enhanced mixing, resulting in the maximum of u_d being attained at a location which is much closer to the wall, at $\tilde{y} = 0.12$, as compared to the profiles at $x = 0.32$ and 0.34. The maximum u_d has a value of 1.25, showing that the presence of the inflection point leads to greater amplification in the disturbance field.

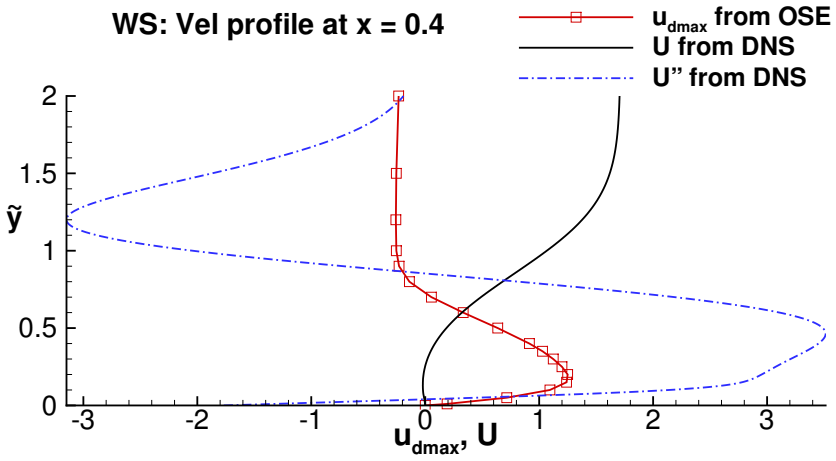

Fig. 8.22 Maximum streamwise disturbance velocity plotted as function of $\tilde{y}$ for profile extracted at $x = 0.40$ for case WS.

The presence of an inflection point suggests a Kelvin-Helmholtz type instability at play for the domain considered in Chapters 5 and 7, and this is in corroboration with prior studies on this geometry (Alam and Sandham, 2000; Vadlamani et al., 2013; Wissink and Rodi, 2004). In the present results, this spatio-temporal wave-packet has been termed as the STWF, supported by studies on ZPG flows excited at the wall (Bhaumik and Sengupta, 2017; Kang, 2015; Kang and Yeo, 2017, 2020; Sengupta et al., 2006a; Sundaram et al., 2018; Yeo et al., 2010), and over compliant surfaces (Wang, 2003; Wang et al., 2005; Zhao, 2007). Recently, this has also been shown for free-stream excitation in a 3D numerical investigation (Sengupta et al., 2019a).

8.5 Receptivity Analysis of Pressure Gradient Dominated Flows with Unsteady Wakes at Inflow

Here, we perform local linear viscous spatio-temporal receptivity analysis, on time- and spanwise-averaged velocity profiles extracted for the case WK (DNS results of this case have been shown in Chapter 7), wherein unsteady wakes are imposed at the inflow. The profiles are chosen to represent different stages of the evolving flow field to explain the underlying spatio-temporal instability and its mechanisms. The structures observed are linked to spatio-temporal growth of the disturbance field.

Time- and spanwise-averaged velocity profiles are extracted from the computational domain in Fig. 7.1, subjected to a Gaussian wake at the inflow which mimics the wakes shed by an upstream row of stator blades. The equation for the Gaussian wake to be added to the streamwise component of velocity at the inflow is given in Eq. (3.47) in Chapter 3. The flow parameters for the test case WK considered here, are listed in Table 8.6, for the sake of completeness.

Table 8.6 Flow parameters and numerical details for test case WK

Flow parameters and numerical details:
Length scale (L) = 0.0257m
Velocity scale (U_∞) = 34.56 m/s
Reynolds number based on length (Re) = 60000
Peak suction: 0.3L from leading edge
Amplitude of wake (a_w) = 0.80
Frequency of wake passing ($f_w = 1/t_w$) = 2.8571 Hz
Exponential constant of the Gaussian (α_w) = 19

The flow field is averaged over 18 cycles of wake passing (after flushing off transients for 15 cycles of wake passing) and the resulting flow field is subsequently spanwise-averaged to obtain the mean statistics. To provide an estimate of the flow physics governing the flow, we choose three streamwise locations, where the time- and spanwise-averaged flow fields for the case WK are such that where either (i) the flow is attached ($x = 0.32$) or (ii) the flow is on the verge of separation, as at $x = 0.33$ and $x = 0.34$.

The time- and spanwise-averaged velocity profile extracted at $x = 0.32$ is shown in Fig. 8.23(a), along with its first derivative with respect to wall-normal coordinate, U' and the second derivative, U''. This profile has been chosen on purpose, as the flow is still attached at this location despite being in a region of adverse pressure gradient ($x > 0.3$). A parameter providing an estimate of the nature of the pressure gradient at the streamwise station, is the Falkner-Skan parameter ($m = \frac{x}{U_e}\frac{dU_e}{dx}$), where U_e is the velocity at the edge of the boundary layer. This edge velocity has been calculated by tracing the edge of the boundary layer using a minimum vorticity threshold for the spanwise-averaged contour plot. For $x = 0.32$ the values obtained are as follows: $U_e/U_\infty = 1.96383$ and $m = -0.1166$.

This value of Falkner-Skan parameter indicates that the location $x = 0.32$ has an adverse pressure gradient which is not negligibly small, as compared to the value of m noted for incipient separation of a Falkner-Skan boundary layer for $m = -0.1988$. For calculating the disturbance quantities via the OSE, we require that all lengths are nondimensionalized by displacement thickness δ^* and all velocities by U_e. We calculate all the necessary numerical parameters required for the solution of the OSE and tabulate those in Table 8.7, for the three streamwise stations considered here.

Table 8.7 Parameters obtained for extracted velocity profiles required for spatio-temporal linear receptivity analysis for test case WK.

x-station	m	δ^*/L	U_e/U_∞	Re_{δ^*}	$\overline{\omega}_o$
$x = 0.32$	-0.11660	0.0025	1.96383	290.4398	1.6994×10^{-5}
$x = 0.33$	-0.15316	0.0027	1.95448	312.3208	1.8441×10^{-5}
$x = 0.34$	-0.21247	0.0030	1.94293	340.1296	2.0612×10^{-5}

where, Re_{δ^*} is the Reynolds number based on displacement thickness and $\overline{\omega}_o$ is the dimensionless circular frequency based on the wake-passing frequency. The governing OSE for the linearized disturbance field is given by Eq. (8.19). The mean velocity U and its second derivative in the wall-normal direction U'', used in the OSE are obtained from the time- and spanwise-averaged velocity profiles in Fig. 8.23.

The receptivity of the extracted velocity profiles to a periodic suction-blowing excitation at the wall is studied here. The disturbance source at the wall has an excitation frequency

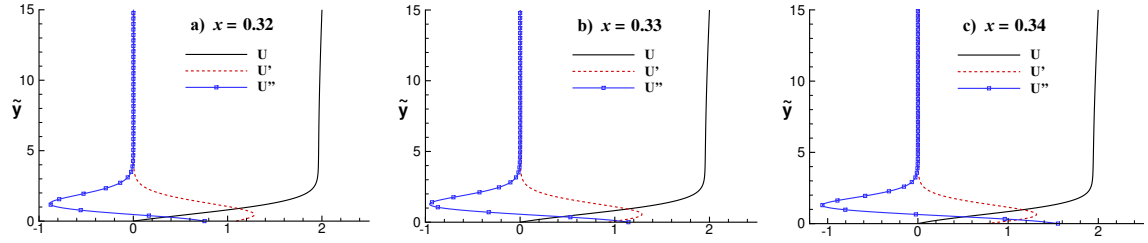

Fig. 8.23 Time-averaged and spanwise-averaged streamwise velocity profile (black line), first derivative with respect to y (green line) and second derivative with respect to y (red line with symbols) extracted at (a) $x = 0.32$, (b) $x = 0.33$ and (c) $x = 0.34$ for case WK.

of $\overline{\omega}_o$, which has been calculated on the basis of wake-passing frequency in Table 8.7. The disturbance stream function of this wall excitation is given by Eq. (8.34). The viscous length and time scales in the expression, i.e. $\tilde{x}$ and $\tilde{t}$, are obtained by nondimensionalizing all length scales with δ^* and all velocity scales with U_e. Expressions relating the viscous and convective time scales for the streamwise stations considered follow, which are given as

$$x = 0.32 : t/\tilde{t} = 1.27302 \times 10^{-3} \tag{8.40}$$

$$x = 0.33 : t/\tilde{t} = 1.38145 \times 10^{-3} \tag{8.41}$$

$$x = 0.34 : t/\tilde{t} = 1.544068 \times 10^{-3} \tag{8.42}$$

For the OSE calculations, we have considered a domain such that: $-1024 < \tilde{x} < 1024$, $0 < \tilde{t} < 2048$ with a choice of Bromwich contour for $-8\pi < \alpha_r < 8\pi$ and $-\frac{\pi}{2} < \omega_{or} < \frac{\pi}{2}$. There are 2^{14} points in $\tilde{x}$- and 2^{11} points in $\tilde{t}$-plane. Once we have solved for the disturbance stream function in the domain, after choosing the appropriate Bromwich contours in space and time, we can solve for the streamwise disturbance velocity u_d using Eq. (8.12).

8.5.1 Response for profile at $x = 0.32$:

From the velocity profile in Fig. 8.23(a), it is clear that the flow has not yet separated at this streamwise station (due to the absence of any reversed flow region), even though beyond $x > 0.3$ there is a region of adverse pressure gradient.

The plots of streamwise disturbance velocity (u_d) as a function of $\tilde{x}$ are shown at the indicated times in Fig. 8.24 for the time- and spanwise-averaged velocity profile extracted at $x = 0.32$. The plots are shown for a wall-normal location $\tilde{y} = 0.1$. The Bromwich contours identified for this velocity are located along $\alpha_i = -0.009$ and $\omega_{oi} = 0.02$. The local solution associated with the exciter at $\tilde{x} = 0$, with an initial amplitude of 10^{-1}, is represented by the vertical line in all the frames of Fig. 8.24. Although we observe an incipient spatially

and temporally evolving wave front, as early in the frame at $\tilde{t} = 350$, its amplitude remains orders of magnitude lower than the local solution in the last frame at $\tilde{t} = 950$, implying sluggish growth of the nonmodal structure i.e. the STWF. This comprises of non-normal spectral neighbours undergoing constructive interference with one another. The STWF for the velocity profile at $x = 0.32$ is unable to overtake the local solution of the exciter, which shows weak receptivity at this station. The frequencies of excitation for the streamwise stations, shown in Table 8.7 are so low that there are no Tollmien-Schlichting waves excited here.

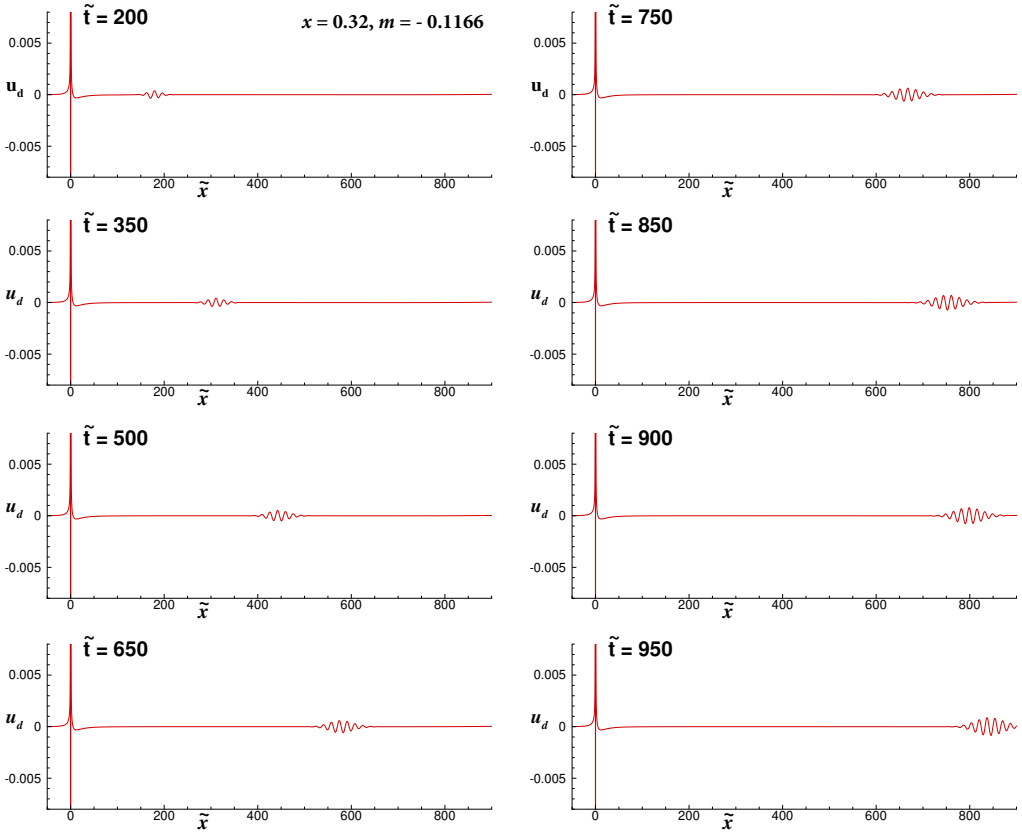

Fig. 8.24 Streamwise disturbance component plotted as function of $\tilde{x}$ shown at $\tilde{y} = 0.1$ for profile extracted at $x = 0.32$ for case WK.

In the presence of wakes, the flow is capable of sustaining the adverse pressure gradient imposed by the liner due to higher local velocity, as we have seen by the value of U_e at this x-location in Table 8.7. This feature is also observed through the local Falkner-Skan parameter (m) values. Despite being in a region with strong adverse pressure gradient, the flow does not separate, as the STWF is not receptive at $x = 0.32$. This corroborates with the time-averaged flow statistics wherein a delayed separation is observed in the presence of

wakes (case WK) in the skin friction and turbulent kinetic energy plots, as compared to the unperturbed flow (case LI) in Chapter 7.

The evolution of the maximum u_d and streamwise location of the maximum (x_{dm}) for the velocity profile extracted at $x = 0.32$, shows that the STWF is orders of magnitude smaller in amplitude than the local solution (not shown here).

8.5.2 Response for profile at $x = 0.33$:

In Fig. 8.23(b), the time- and spanwise-averaged streamwise velocity profile and its first derivative, U' and second derivative, U'' extracted at $x = 0.33$ are shown. The Falkner-Skan parameter for this streamwise location is -0.15316, which for the Falkner-Skan boundary layer profile is close to separation. For the case under consideration, from the velocity profile in Fig. 8.23(b), there is no reversed flow. The velocity profile and its derivatives are substituted in the OSE given in Eq. (8.19) and receptivity to a periodic suction-blowing excitation at the wall, given by Eq. (8.34) is studied. At a glance, it would appear the velocity profile extracted at $x = 0.32$ and $x = 0.33$ in Fig. 8.23(a) and 8.23(b) are similar, but the receptivity to the imposed wall excitation in the latter case is significantly altered, as demonstrated next.

In Fig. 8.25(a), the plots of u_d as a function of $\tilde{x}$ are shown for the time- and spanwise-averaged velocity profile at $x = 0.33$ for the case WK, for a wall-normal location $\tilde{y} = 0.1$. The Bromwich contours used for this case are located along: $\alpha_i = -0.01$ and $\omega_{oi} = 0.02$. The local solution associated with the exciter at $\tilde{x} = 0$ with an input amplitude of 10^{-3} is shown by vertical lines in the frames at $\tilde{t} = 350$ to 650 of Fig. 8.25(a). Here, the STWF noted in its primary stage at $\tilde{t} = 350$ grows in space and time as noted in the subsequent frames. By $\tilde{t} = 550$, the amplitude of the STWF has overtaken the local solution of the exciter. In general, compared to the velocity profile for $x = 0.32$, the velocity profile at $x = 0.33$ is much more receptive to the nonmodal growth exhibited by the STWF. This is also noted in the ordinate change in the frames at $\tilde{t} = 750$ to 1020 of Fig. 8.25(a). The amplitude of the STWF increases from 0.0008 at $\tilde{t} = 350$ to 1.5 at $\tilde{t} = 1020$, thus an amplification of the STWF by a factor 1875 is noted for $\Delta\tilde{t} = 670$. This viscous time is converted to the convective time by the expression in Eq. (8.41) as $\Delta t = 0.9255$. The flow for this velocity profile at $x = 0.33$ can be demarcated into two parts: one which is driven by the input amplitude of the exciter at the wall, and the second which is dominated by the transient growth of the STWF in the later stages of the disturbance growth. It is this latter part which is the stronger mechanism of the instability and precursor for transition to turbulence.

In Fig. 8.26(a), the evolution of the maximum streamwise disturbance velocity u_{dm} and the streamwise station of the maximum disturbance velocity x_{dm} are traced for the velocity

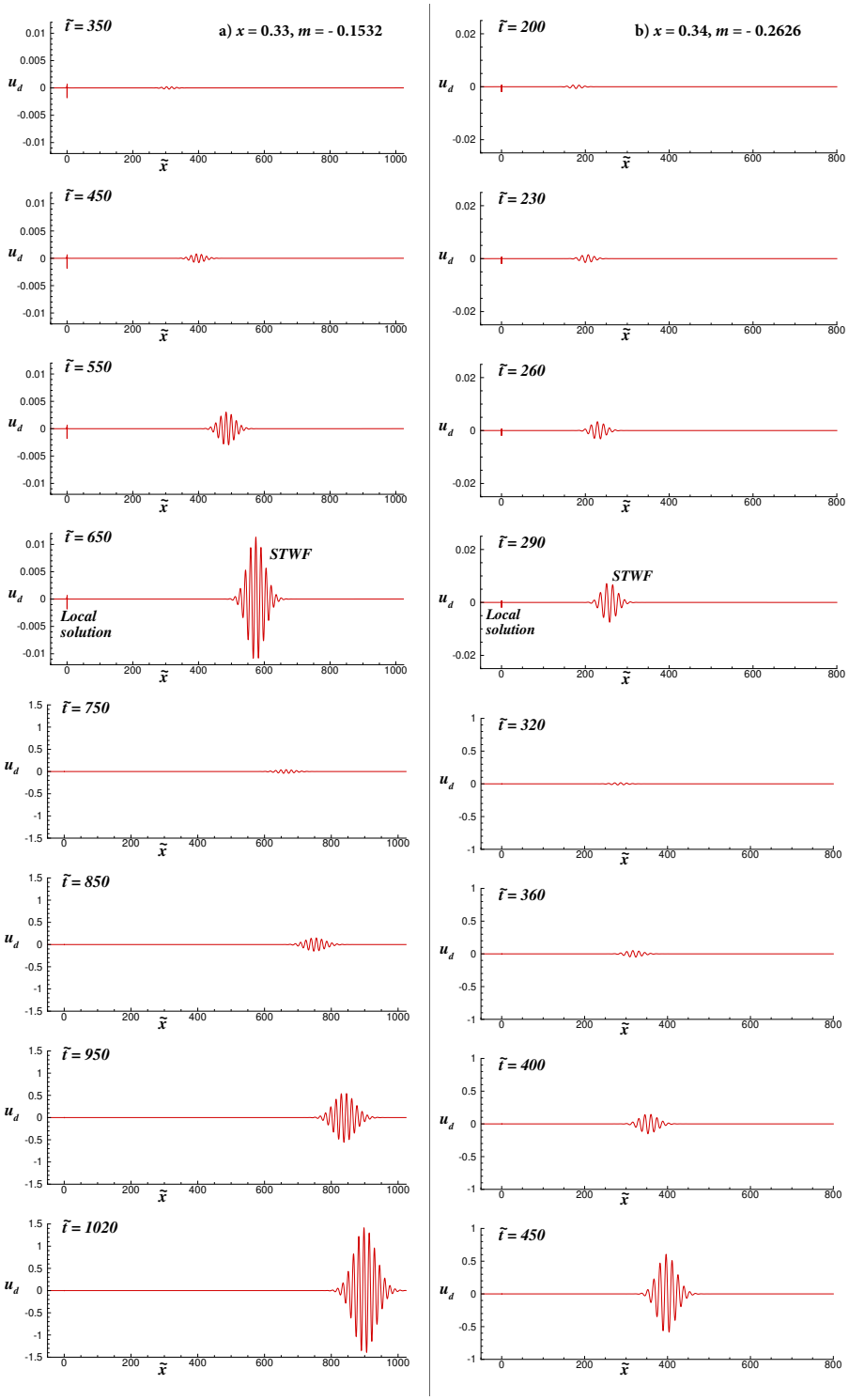

Fig. 8.25 Streamwise disturbance component plotted as function of $\tilde{x}$ shown at $\tilde{y} = 0.1$ for profile extracted at (a) $x = 0.33$ and (b) $x = 0.34$ for case WK.

profile extracted at $x = 0.33$. We note that the local solution dominates the solution till $\tilde{t} = 350$, after which the STWF becomes prominent. This did not happen for the velocity profile extracted at $x = 0.32$. Another feature to be highlighted here is that the maximum amplitude noted at $\tilde{t} = 1020$, when the STWF is close to exiting the domain is of the order 10^0 compared to the input amplitude of the order of 10^{-3}, indicating an amplification of three orders of magnitude. Thus the wake-induced velocity profile at $x = 0.33$ is much more receptive to wall excitation, as the flow is close to separation, which is in contrast with the attached profile at $x = 0.32$. The streamwise stations at which maximum streamwise disturbance velocity are located are first attributed to the local solution till $\tilde{t} = 350$, and thereafter to the STWF which is seen by the step-like appearance of the streamwise location of the maximum disturbance velocity in the bottom frame of Fig. 8.26(a).

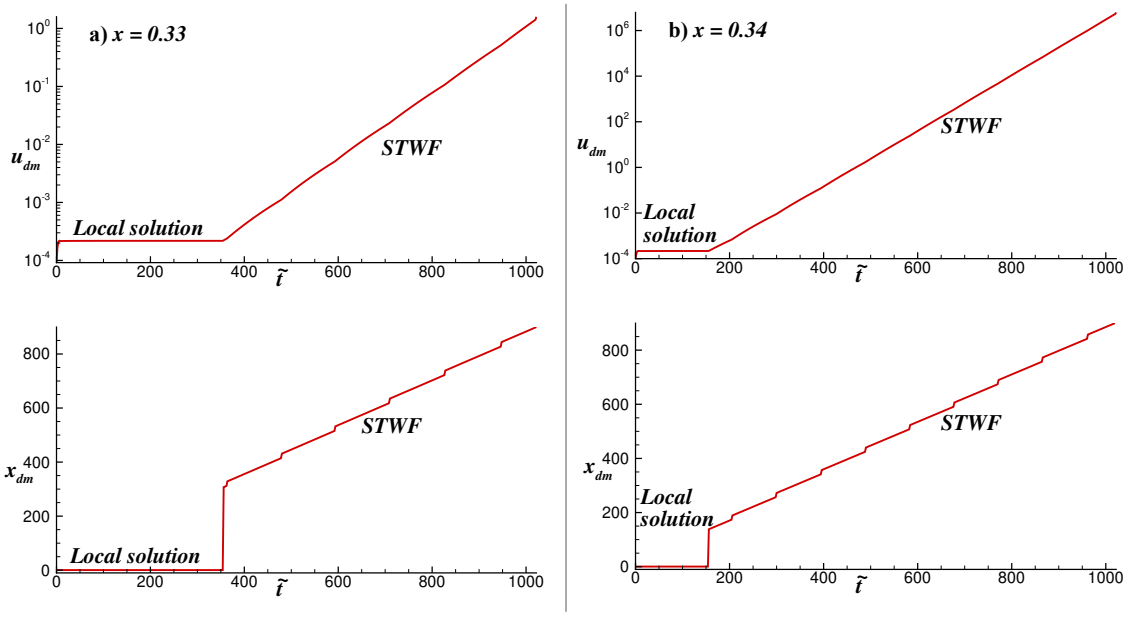

Fig. 8.26 Evolution of maximum streamwise disturbance component and streamwise station where maximum is located, showing the local solution and STWF for profile extracted at (a) $x = 0.33$ and (b) $x = 0.34$ for case WK.

8.5.3 Response for profile at $x = 0.34$:

The time- and spanwise-averaged velocity profile extracted at $x = 0.34$ is shown in Fig. 8.23(c), along with its first and second derivatives. Here, in the velocity profile, we do not observe any indication of a separated flow (i.e. reversed flow in the near-wall region). However, the Falkner-Skan parameter for this streamwise station has a value -0.26265 as shown in Table 8.7, which is beyond the value of separation noted for a Falkner-Skan profile

($m = -0.1988$) and yet the flow has not separated. This can be explained by the high local edge velocity at this station ($U_e/U_\infty = 1.9429$) shown in Table 8.7 which has enough momentum to overcome the adverse pressure gradient. This is due to the passing wakes in the free stream which counteracts the strong adverse pressure gradient induced by the upper contoured wall, thereby allowing the flow to remain attached at this streamwise location. It will be interesting to note how the flow in the presence of such a strong adverse pressure gradient responds to an infinitesimal wall-excitation, when the local flow profile remains attached.

The plots of u_d as a function of $\tilde{x}$ are shown in Fig. 8.25(b) for the time- and spanwise-averaged streamwise velocity profile extracted at $x = 0.34$ for case WK. The wall-normal location of extraction is $\tilde{y} = 0.1$. The Bromwich contours identified for this velocity are located along: $\alpha_i = -0.01$ and $\omega_{oi} = 0.03$. The change in the Bromwich contour in the ω_o-plane, as compared to the case of velocity profile for $x = 0.33$, can be explained by the fact that the velocity profile at $x = 0.34$ is nearer to the separation location. Thus, it is more receptive to an infinitesimal perturbation (even due to round-off error), as compared to the profile at $x = 0.33$, which is reflected on the location of the Bromwich contour located along $\omega_{oi} = 0.02$ for $x = 0.33$ as compared to $\omega_{oi} = 0.03$ for $x = 0.34$. There are additional high growth rate temporal modes, which are automatically accounted for in the solution of the OSE by Bromwich contour integral method for this velocity profile at $x = 0.34$, for the higher location of the Bromwich contour. The local solution associated with the exciter at $\tilde{x} = 0$ with an input amplitude of 10^{-3}, is noted as a vertical line in frames at $\tilde{t} = 200$ to 290 in Fig. 8.25(b). This velocity profile is far more receptive to the imposed wall excitation, as noted by the change in the ordinates of the frames at $\tilde{t} = 320$ to 450. For the velocity profile extracted at $x = 0.33$, the inception of the STWF shown in Fig. 8.25(a), is at $\tilde{t} = 350$. For $x = 0.34$, by $\tilde{t} = 200$ we note a STWF with higher amplitude. The amplitude of the STWF increases from 0.001 at $\tilde{t} = 200$ to 0.7 at $\tilde{t} = 450$, thus an amplification of the STWF by a factor 700 is noted for $\Delta\tilde{t} = 250$. The conversion of this viscous time scale to a convective one involves the use of the expression in Eq. (8.42) such that $\Delta t = 0.3861$. Thus, for such a short time period, we note an amplification of the STWF by a factor of 700, which can be considered as a demonstration of the dominant nonmodal nature of the STWF.

In Fig. 8.26(b), the evolution of the maximum streamwise disturbance velocity u_{dm} and the streamwise station of the maximum disturbance velocity x_{dm} are traced for the velocity profile at $x = 0.34$. We note that the local solution dominates the solution till $\tilde{t} = 150$, after which the STWF becomes prominent. This happened at $\tilde{t} = 350$ for the velocity profile at $x = 0.33$. Another feature to highlight is the maximum amplitude at $\tilde{t} = 1020$, when the STWF is about to exit the domain, has amplitude of the order of 10^6 as compared to the

corresponding value for $x = 0.33$ with the maximum amplitude only of the order of 10^0. This emphasizes the higher receptivity of the profile at $x = 0.34$ to excitation inside the boundary layer (even if it is due to round-off error) when the flow is about to separate, in contrast to the attached profiles at $x = 0.32$ and $x = 0.33$ showing lower receptivity. The streamwise station for maximum u_d is determined by the local solution till $\tilde{t} = 150$, and thereafter by the STWF. The group velocity of the STWF is calculated and is found to be $V_g = 0.88354$. This higher group velocity can be explained by the alteration of the mean velocity by the imposed wake in the free-stream.

Thus, in the extracted profiles for case WK, we are able to identify the STWF to have the dominant mechanism required to take the perturbation from its onset to a fully developed stage. The deterministic route followed by the bypass transition process to turbulence has been shown through the propagation of the STWF for the flow field excited by unsteady wakes at inflow.

8.6 Comparison of DNS Results with Solution from OSE

The streamtraces from the instantaneous flow field of test case LI are shown in Fig. 8.27. The spacing between two successive Kelvin-Helmholtz roll-up vortices, λ is $\sim 0.045L$. Distinct travelling waves in streamwise direction are evident for $x > 0.45$. These can be associated with the vortex shedding from the separated shear layer (Vadlamani, 2015). The number of waves travelling per second are around 15 for test case LI. From the linear viscous receptivity analysis of the test cases LI, WS and WK, the wavelength and frequency associated with the STWF are calculated and the values are given in Table 8.8.

Table 8.8 Wavelengths and frequencies associated with the STWF obtained from spatio-temporal linear receptivity analysis of test cases LI, WS and WK.

Case	Λ	*Frequency*
LI	0.046L	15.67Hz ($St = 0.00926$)
WS	0.047L	13.65Hz ($St = 0.00908$)
WK	0.043L	19.29Hz ($St = 0.00988$)

The wavelengths are in good agreement with the distance observed in the DNS between two successive Kelvin-Helmholtz roll-ups. The peak disturbance growth rate for case LI occurs at a frequency of 15.67Hz or $St = 0.00926$ where St is the Strouhal number based on separation conditions ($St = f\theta_{sep}/U_{sep}$ where θ_{sep} is the momentum thickness and U_{sep} is the free-stream velocity at separation). McAuliffe and Yaras (2010) have shown that

for separated shear layers, the frequency associated with maximum amplification of the instability is generally in close agreement to that of planar free shear layers. The *St* obtained by various researchers was consolidated and identified to lie between 0.005-0.016. The *St* from the current simulations is well within this range for all the test cases.

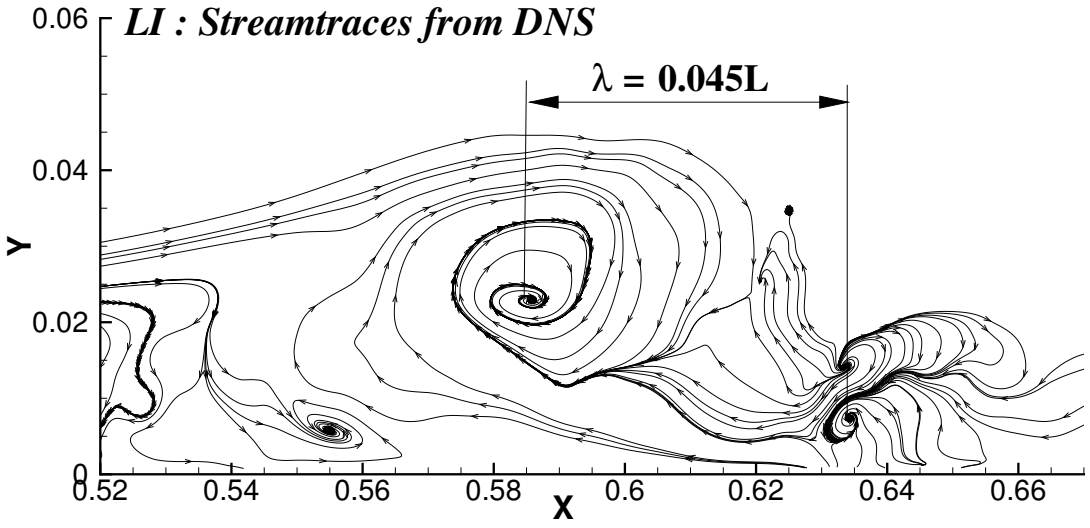

Fig. 8.27 Streamtraces of the DNS results for case LI showing the distance between successive Kelvin-Helmholtz roll ups.

8.7 Global Linear and Nonlinear Receptivity of Vortex-Induced Instability

Here, we provide an explanation of the mechanisms of vortex-induced instability in greater details, results of which have been shown in Chapter 6. We perform a global stability analysis in 2D by solving the linearized and the full nonlinear Navier-Stokes equation. We also show the utility of the DME and DETE methods as diagnostic tools. The vortex-induced instability in Chapter 6 is for a canonical flow for which we need to provide physical mechanisms without empiricism. Keeping this in mind, we have focused on linear and nonlinear analysis of the Navier-Stokes equation.

A review of global linear instability in nonparallel 2D and 3D flows is provided in Theofilis (2011). The global linear stability involves tracing the development in space and time of small amplitude perturbations superposed on an equilibrium flow through the solution of linearized NSE and continuity equations. This is similar to the linear receptivity analysis

detailed in Chapter 2, except that for global linear stability, a parallel flow assumption is not necessary. Here, we trace the disturbance induced by a free-stream convecting vortex globally in a spatio-temporal framework using both the linearized 2D Navier-Stokes equation, as well as the full set of 2D Navier-Stokes equation. Theofilis (2011) proposed the terms BiGlobal and TriGlobal instability analysis to describe modal or nonmodal analyses of 2D and 3D equilibrium flows, respectively. According to the author, *"In contrast with the local analysis, eigenfunctions resulting from a global linear stability theory depend in an inhomogeneous manner on two or three spatial directions, reflecting the inhomogeneity of the respective underlying basic states."* This forms the basis of why a global receptivity analysis is important particularly for a time-varying inhomogeneous base state.

The 2D Navier-Stokes equation allows us to use streamfunction-vorticity formulation, which helps in avoiding numerical problems associated with divergence free condition of the velocity field. However, in Chapter 6, 2D and 3D problems are solved, which require the use of velocity-vorticity formulation. Additionally, we will conclude with a discussion on global stability studies reported in the literature and correlate the present results with the previous works.

8.7.1 Computational domain and boundary conditions

We start with a description of the vortex-induced instability problem considered here. We have used a (ψ, ω)-formulation of the NSE for the 2D flow field shown in Fig. 8.28, to study the receptivity of ZPG boundary layer to a convected vortex in the free stream. The time-dependent boundary forcing by the convecting vortex excites the inherent physical instability in the flow. The equilibrium flow is also calculated by solving the NSE in the same numerical framework, without the external forcing. This numerical framework has been used in a prior study of the 2D vortex-induced instability via the application of DME in Sengupta et al. (2003), and recently by Sengupta et al. (2020).

The origin of the coordinate system is placed at the leading edge of the plate, whereas the computational domain starts ahead of it. A vortex with counterclockwise circulation (Γ) translates from left to right with a constant speed (c), at a constant height (H_1) above the plate. This free stream vortex convecting far outside the shear layer requires an image vortex below the plate to ensure zero wall-normal velocity condition. In solving this problem, we define a length scale (L) based on which the Reynolds number (Re_L) is 10^5. For the present 2D simulations, we have used: $x_{in} = -0.05$, $x_{out} = 120$ and $y_{max} = 1.5$. The study of receptivity requires as small an excitation as possible, thus, for the present simulations we have used $\Gamma = 0.1$. Once the equilibrium solution is obtained, the free stream vortex is initiated at $x = -1, y = 2$. We study the effect of the free stream vortex convecting at two

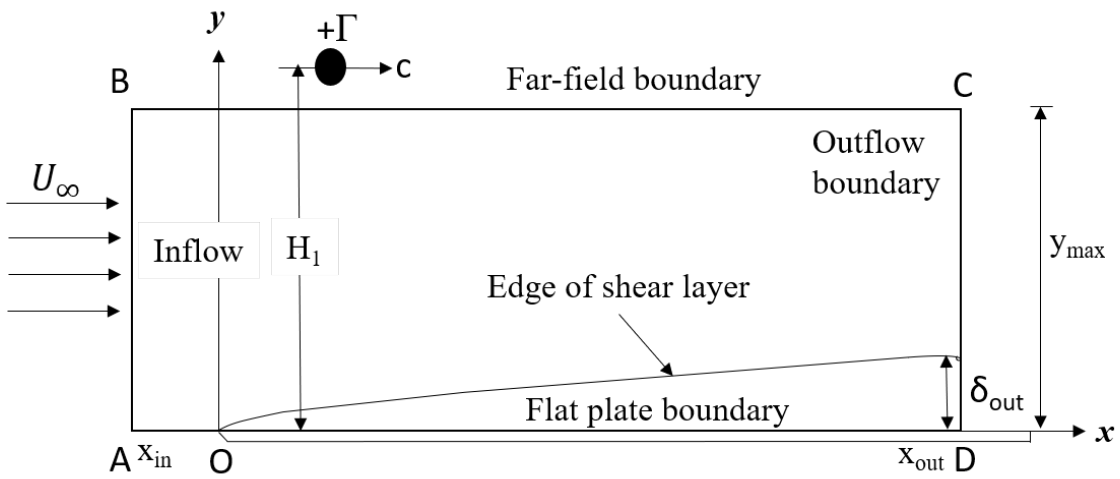

Fig. 8.28 Computational domain for studying vortex-induced instability by an isolated convecting (at speed c) vortex (of strength Γ) in the free stream over a ZPG boundary layer flat plate.

speeds: $c = 0.3$ and 0.386. The time-step for the 2D simulations is $\Delta t = 2.5 \times 10^{-5}$ on a grid with 12000 points in the streamwise direction and 400 points in the wall-normal direction.

This receptivity problem has been attempted previously in an experimental framework by Lim et al. (2004) and computationally by Sengupta et al. (2019a, 2018a, 2003) wherein the flow features were captured through growth of DME and disturbance enstrophy, respectively. Recently, global receptivity study of the convecting vortex problem has been performed by Sengupta et al. (2020), highlighting the role of nonlinearity and that of the STWF. The experiments and the computations have been performed considering this as one of the processes involved in free-stream vortical excitation. As such vortices in the free stream moves with the local speed, the convection speed is not known apriori because the local speed for Γ is determined by many Biot-Savart interactions due to the primary vortex, its image system and the vorticity in the boundary layer over the plate. Hence, these experiments and computations are attempts in finding the optimal convection speed for which the underlying boundary layer shows maximum receptivity.

Next, we provide a brief overview of the linearized and nonlinear versions of NSE in the (ψ, ω)-formulation, adopted here. As noted in Chapter 6, vortex-induced instability is not due to Tollmien-Schlichting wave, instead, the onset and progression of the instability is associated with unsteady separation. Here, we propose that the vortex-induced instability is also a manifestation of nonmodal growth via STWF, which we have demonstrated in the previous sections for the DNS results of Chapters 5 and 7. While linear analysis has shown the creation and growth of STWF for wall excitation, by local analysis of solving

OSE (requiring parallel flow assumption), it is necessary to show the STWF directly from the solution of linear and nonlinear NSE.

8.7.2 Solution of the linearized Navier-Stokes equation (LNSE)

A direct simulation of the flow field shown in Fig. 8.28 has been performed here using the linearized version of the NSE using the stream function-vorticity formulation, given as,

$$\frac{\partial^2 \psi_l}{\partial x^2} + \frac{\partial^2 \psi_l}{\partial y^2} = -\omega_l \tag{8.43}$$

$$\frac{\partial \omega_l}{\partial t} + \frac{\partial}{\partial x}(u_l\omega_l + u_{bl}\omega_l + u_l\omega_{bl}) + \frac{\partial}{\partial y}(v_l\omega_l + v_{bl}\omega_l + v_l\omega_{bl}) = \frac{1}{Re_L}\left[\frac{\partial^2 \omega_l}{\partial x^2} + \frac{\partial^2 \omega_l}{\partial y^2}\right] \tag{8.44}$$

where u_{bl}, v_{bl} and ω_{bl} are the unperturbed base flow quantities for the flat plate boundary layer flow computed in the absence of the convecting vortex. The boundary conditions at the inflow and the top of the computational domain are obtained from Eq. (6.2), which prescribes the disturbance stream function, used for ψ and ω. On the flat plate, no-slip boundary condition simultaneously provides a Dirichlet boundary condition for the stream function and the wall vorticity, at every instant of time. At the outflow of the domain, extrapolation based on $\frac{\partial^2 \psi}{\partial x^2} = \frac{\partial^2 \omega}{\partial x^2} = 0$ has been applied for the stream function and vorticity transport equations.

In Fig. 8.29, disturbance vorticity plots at the indicated times are obtained through the solution of the LNSE for $c = 0.3$ (left) and 0.386 (right). The vortex strength for both the cases is $\Gamma = 0.1$. The plots are for $y = 0.0058$. We observe that for the case with $c = 0.3$ a disturbance packet which grows in space and time, is seen at $t = 125$. In contrast, for $c = 0.386$, the disturbance packet grows from $t = 200$ onwards. This is the STWF showing nonmodal growth by two orders for $c = 0.3$ between $t = 125$ and 175. The STWF is always seen downstream of the location of the free-stream vortex shown by a vertical arrow for $c = 0.3$ case, while it is located upstream of the location of the free-stream vortex for $c = 0.386$, which is consistent with the 3D results of spanwise vorticity contours shown in Figs. 6.21 to 6.24 in Chapter 6. This indicates that the STWF propagates with a speed between 0.3 and 0.386. It is worth noting here that $c = 0.3$ case is more receptive at this wall-normal location. This figure shows the creation of STWF by LNSE, but at different times depending on c.

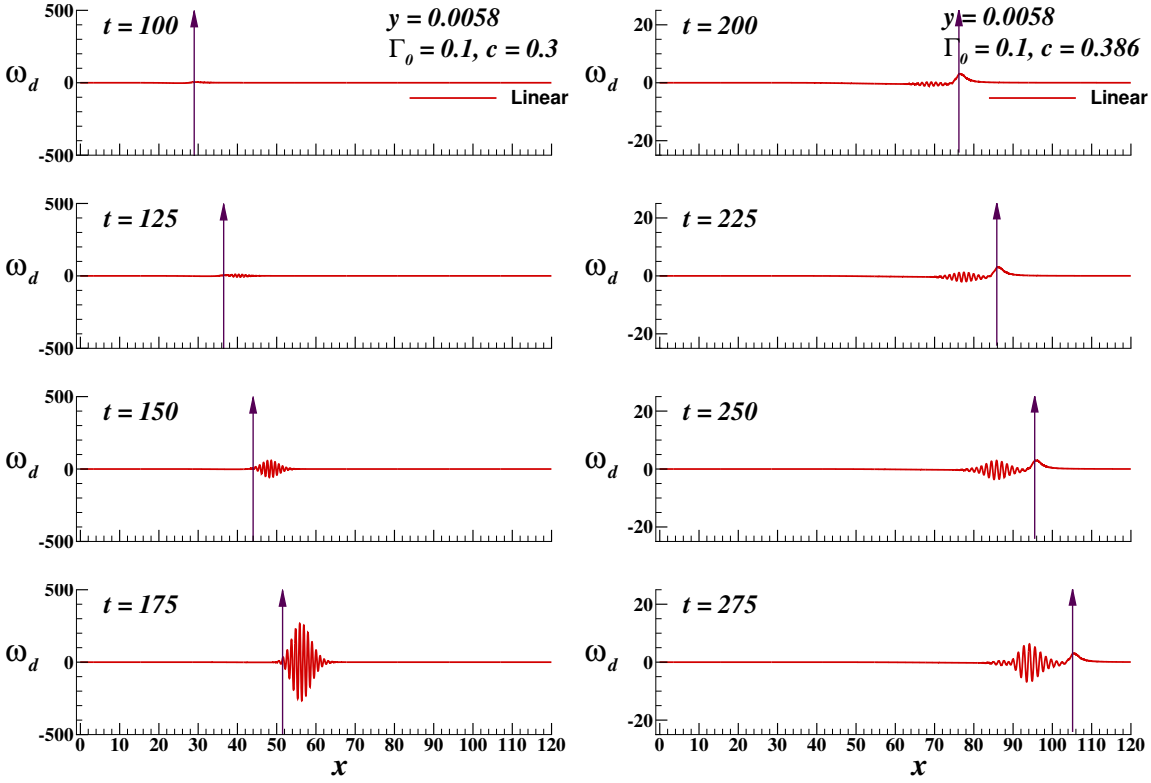

Fig. 8.29 Disturbance vorticity plotted as a function of x at the indicated times, solved by LNSE for a convecting free-stream vortex with $c = 0.3$ (left) and 0.386 (right) at $y = 0.0058$.

8.7.3 Solution of the nonlinear Navier-Stokes equation (NNSE)

The governing 2D NNSE is solved for the flow field in Fig. 8.28, by the following equations

$$\frac{\partial^2 \psi_n}{\partial x^2} + \frac{\partial^2 \psi_n}{\partial y^2} = -\omega_n \tag{8.45}$$

$$\frac{\partial \omega_n}{\partial t} + u_n \frac{\partial \omega_n}{\partial x} + v_n \frac{\partial \omega_n}{\partial y} = \frac{1}{Re_L}\left[\frac{\partial^2 \omega_n}{\partial x^2} + \frac{\partial^2 \omega_n}{\partial y^2}\right] \tag{8.46}$$

Next, we provide a comparison between the LNSE and NNSE and show that the mechanism of transition during vortex-induced instability requires nonlinearity, as the solution of LNSE does not show saturated fully developed turbulence. This is one of the major results established here that nonlinearity is essential for the eventual transition to turbulence.

In Fig. 8.30, the disturbance vorticity is compared at $y = 0.0058$ at the indicated times as a function of x, obtained by LNSE and NNSE for $c = 0.3$ and 0.386 cases. While the solution from LNSE does not show STWF at these early times, the solutions from NNSE show onset of STWF at $t = 55$ and 80, respectively, for the two c cases. The nonlinear STWF is similar

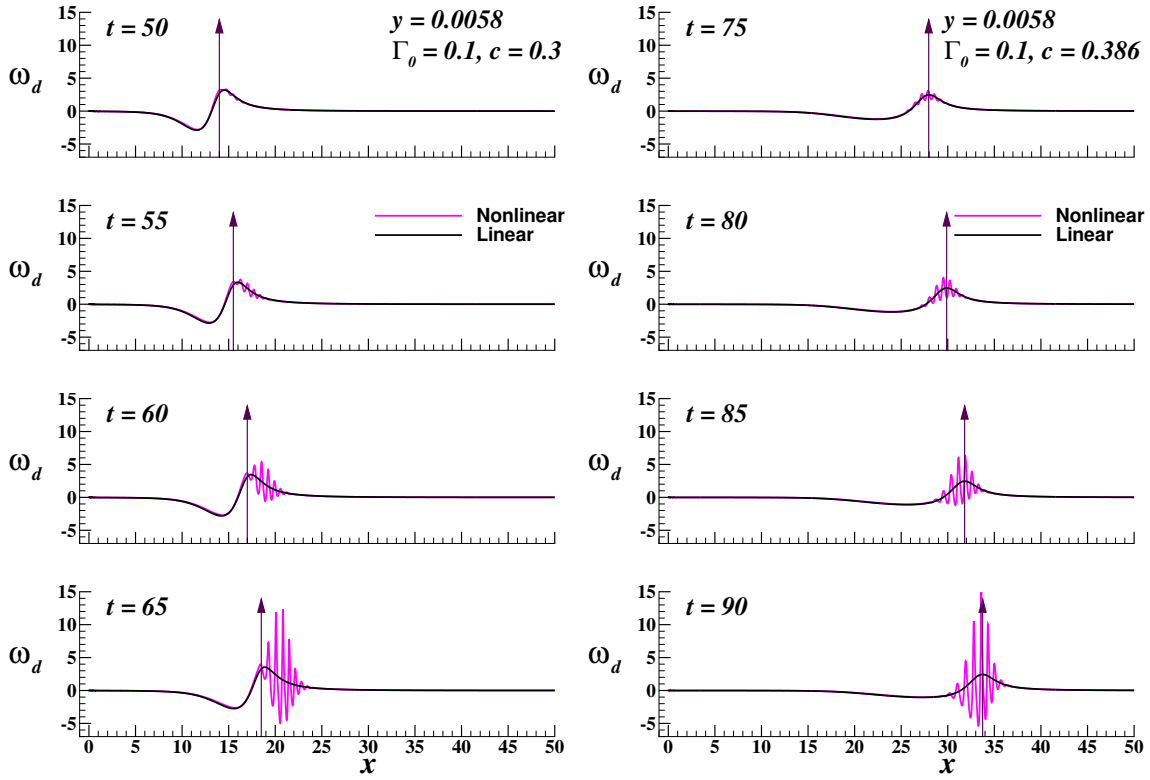

Fig. 8.30 Comparison of ω_d plotted as a function of x at the indicated times, solved by LNSE and NNSE for a convecting free-stream vortex with speed $c = 0.3$ (left) and 0.386 (right) at $y = 0.0058$.

to linear case shown in Fig. 8.29, and this is observed downstream of the vortex location for $c = 0.3$ and upstream for $c = 0.386$. Another feature is the asymmetry of nonlinear STWF, with respect to $\omega_d = 0$, as compared to the LNSE case. For $c = 0.386$, the growth rate of the nonlinear STWF is higher, than for $c = 0.3$ for the same time interval. From $t = 60$ to 65, the STWF grows by a factor of 2.083 for $c = 0.3$, whereas from $t = 85$ to 90, it grows by a factor of 2.5 for $c = 0.386$. Thus, at a later time, the nonlinear STWF for $c = 0.386$ will have higher amplitude, as compared to the case of $c = 0.3$. The information contained in Fig. 8.30 is for early stages of disturbance growth. However, we note that the convection time scale is significantly higher as compared to the viscous time scale used for the OSE.

The onset and propagation of the STWF are noted from the solutions of LNSE and NNSE in Figs. 8.31(a) and 8.31(b), respectively for $c = 0.3$. For the LNSE, the early indication of STWF is noted at $t = 100$, that emerge out of the local solution, which is always below the translating vortex. Subsequently, the STWF grows exponentially in space and time, as given by the linear theory. For LNSE, by $t = 140$, the peak-to-peak amplitude of the STWF overtakes the amplitude of the local solution. The local solution for LNSE remains

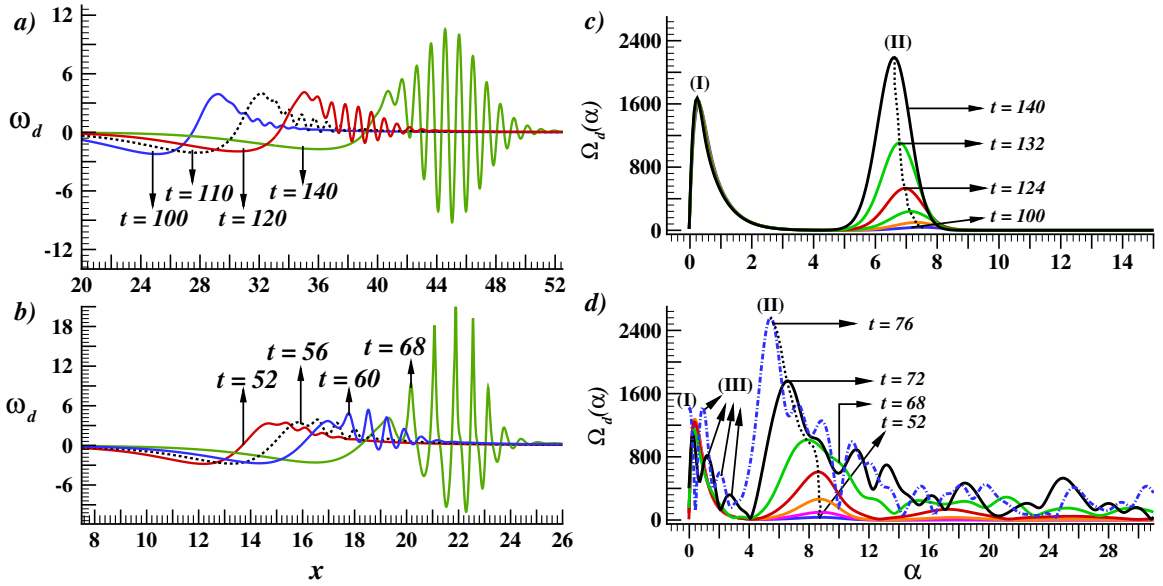

Fig. 8.31 Disturbance vorticity (ω_d) and its spectrum at indicated times for $y = 0.0058$, evaluated from (a,c) LNSE and (b,d) NNSE. While the LNSE indicates later onset of STWF, the NNSE displays strong effects of nonlinearity in shorter span of time, as noted at $t = 68$. In frame (d), the spectrum shows the interaction between local solution and the STWF.

invariant. Comparatively in Fig. 8.31(b) for NNSE, the onset of the STWF is earlier at $t = 52$. Furthermore, the local solution Fourier-amplitude decreases with time for NNSE, and by $t = 68$, additional peaks appear in its vicinity due to interactions with the STWF. While the growth of the STWF given by NNSE indicates identical onset mechanism, but the nonlinear effects are significant. The formation of STWF is by the same mechanism, as in wall-excitation case Bhaumik and Sengupta (2014, 2017); Sengupta and Bhaumik (2011); Sengupta et al. (2006b). In Fig. 8.31(b), at $t = 68$, nonlinear growth of the STWF is observed. Along with earlier onset, saturation of amplitude for the STWF is also rapid for NNSE, while LNSE shows later onset and no saturation. The nonlinear saturation for NNSE indicates multiple length scales in Fig. 8.31(d), while the LNSE shows the same length scale, as noted in Fig. 8.31(c). Thus, to correctly understand the dynamics during transition for free-stream excitation, one must use the NNSE.

The local solution is indicated by (I) in Figs. 8.31(c) and 8.31(d), and the STWF is identified by (II). The STWF is due to constructive interference of nonmodal part of the spectrum. The maximum wavenumber of the peak is traced by a dotted line, which identifies the STWF. In Fig. 8.31(d) at $t = 60$, in addition to the peak for the central wavenumber, secondary peaks are noted for higher α. These additional peaks attain significant amplitude with time. The bandwidth of the spectra for NNSE is larger. From $t = 72$ onwards, there are additional peaks in the spectrum near the local solution component due to interaction with the

STWF, marked as (III) in Fig. 8.31(d). This is in accordance with the Abel's theorem (van der Pol and Bremmer, 1959), which states that the far-field in the physical plane corresponds to spectrum in the vicinity of the origin of the spectral plane.

8.7.4 Later stage of vortex-induced instability

The disturbance growth is compared in Fig. 8.32 at the same height, $y = 0.0058$, with the solution of LNSE and NNSE for the disturbance vorticity, for the two convection speeds considered. The receptivity is more for $c = 0.3$ both in the linearized, as well as nonlinear frameworks, as seen in Figs. 8.29 and 8.30. A turbulent spot-like structure is observed at $t = 105$ and 125, for the solution of the NNSE for $c = 0.3$. The spikes observed at the earlier time frame spreads over longer streamwise stretch, as can be seen by comparing the frames at $t = 105$ and 125, for $c = 0.3$ case. A similar structure is observed for $c = 0.386$ at $t = 125$, spread over a shorter streamwise stretch.

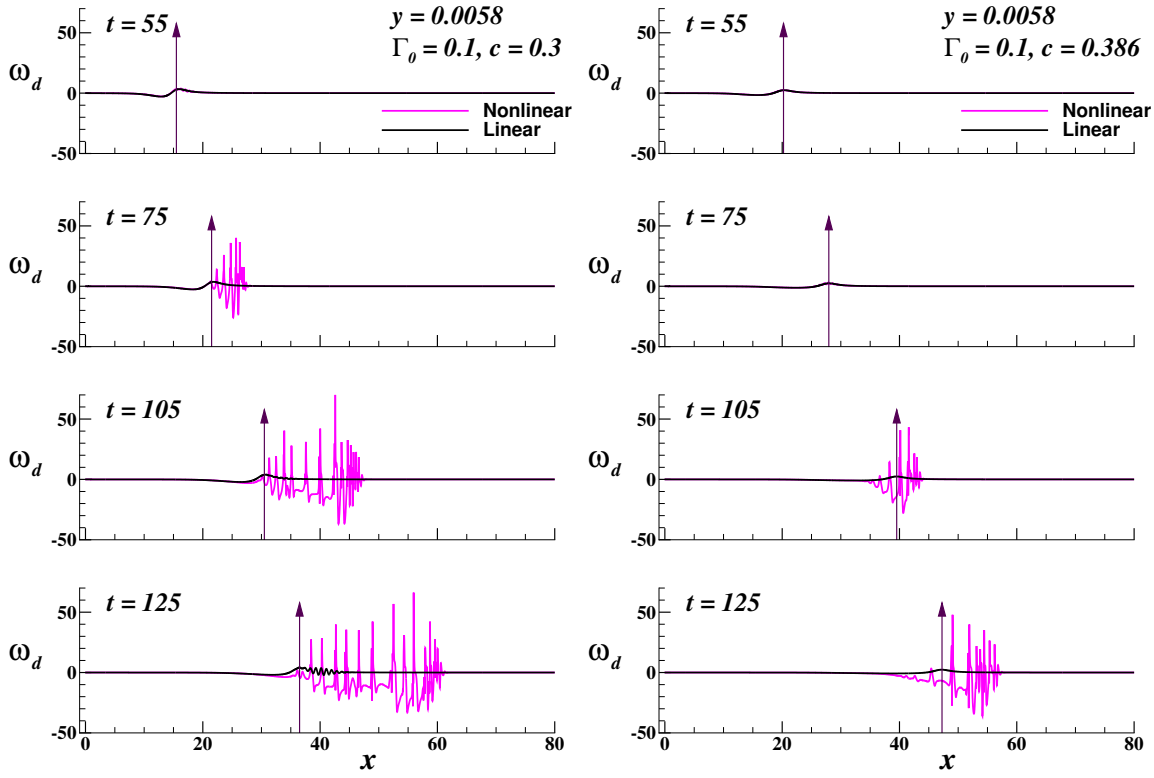

Fig. 8.32 Comparison of ω_d plotted as a function of x at the indicated times, solved by LNSE and NNSE for a convecting free-stream vortex with speed $c = 0.3$ (left) and 0.386 (right) at $y = 0.0058$ showing later stages of disturbance growth.

The comparison between LNSE and NNSE results show the need to consider the latter to trace the perturbation field. For the study of vortex-induced instability, the performed

global receptivity study clearly identifies the need to include the nonlinear growth stage to capture the correct transition sequence. The linearized Navier-Stokes equation captures the creation of the nonmodal growth, even though it is delayed in time, and the onset location is completely different.

8.7.5 The Roles of DME and DETE in Explaining Vortex-Induced Instability

In the present cases, with the 2D flow field evaluated by the LNSE and NNSE, we can show the effects of linear and nonlinear global stability analysis for Ω_d and E_d. As we have 2D mean and disturbance fields, corresponding vorticities are in the same plane (z-plane). This has been purposely done to remove complications arising out of the angle between the two vorticity fields in interpreting Ω_d. The expressions correlating DETE and the DME equation with the mean and disturbance flow quantities, for the full nonlinear system are given in Eq. (2.9) and (2.8), where the disturbance enstrophy is, $\Omega_d = 2\omega_m \cdot \omega_d + \varepsilon\omega_d \cdot \omega_d$. These expressions have been derived in the appendices A and B for a nonlinear 3D system. For the DETE expression, since we are looking at the 2D equation, the vortex stretching term is not present. The corresponding linear values of these physical quantities are obtained by dropping the terms multiplied with ε, as these are the nonlinear contributions.

In Fig. 8.33, the plots of Ω_d as a function of x, are shown at $y = 0.0058$ for the indicated times, using the LNSE and the NNSE results for the $c = 0.3$ and 0.386 cases. One notices the structures for Ω_d also appear as the STWF, when obtained using NNSE for the displayed early times. The disturbance enstrophy, Ω_d is nothing but twice the product of equilibrium and disturbances vorticity for the linearized solution, whereas for the nonlinear solution the higher order terms of square of disturbance vorticity is added, which is readily noted from the figure, wherein the NNSE solution initially falls on the LNSE solution. After ω_d becomes significant, the NNSE solution deviates from the LNSE. The STWF noted in Figs. 8.29 to 8.32 is also noted here with a change in sign for early times when ω_d is insignificant, as ω_m is negative for the ZPG boundary layer. The STWF noted for the frames with $c = 0.3$ are located downstream of the location of the vortex indicated by the vertical line, whereas the corresponding STWF for frames with $c = 0.386$ are located upstream of the vortex location, at later time.

In Fig. 8.34, the plots of $D\Omega_d/Dt$ are shown using solution of the LNSE and the NNSE for $c = 0.3$ and 0.386 at $y = 0.0058$. As we have seen for Ω_d in Fig. 8.33, the LNSE does not show any STWF for the selected time frames, identifying similar features here for $D\Omega_d/Dt$. The plots of $D\Omega_d/Dt$ display an STWF from $t = 50$ onwards for $c = 0.3$ and from $t = 75$

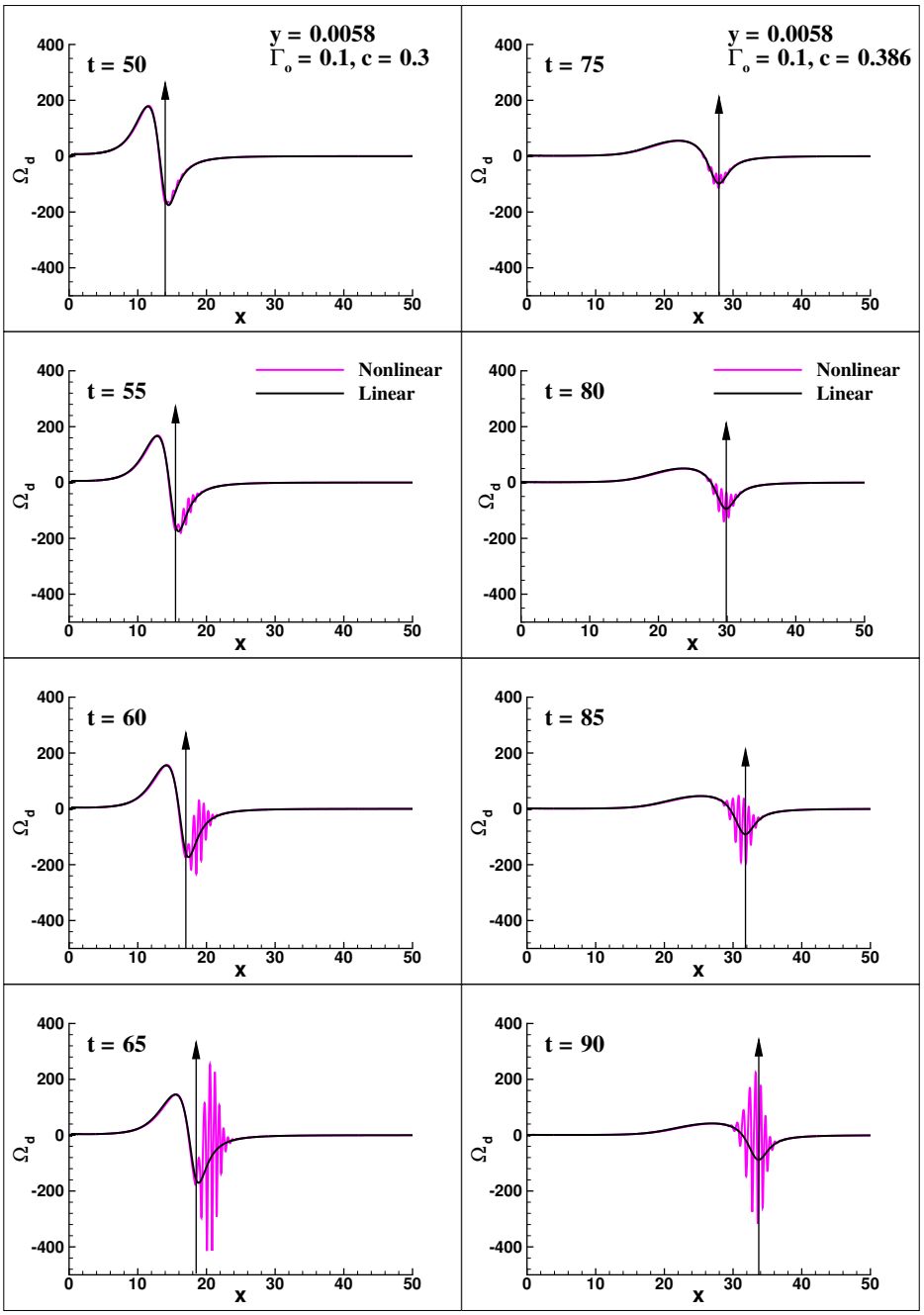

Fig. 8.33 Comparison of Ω_d plotted as a function of x at the indicated times, solved by LNSE and NNSE for a convecting free-stream vortex with speed $c = 0.3$ (left) and 0.386 (right) at $y = 0.0058$.

onwards for $c = 0.386$ for the NNSE solution. The $D\Omega_d/Dt$ of STWF obtained from NNSE, observed at a time interval of 5 in the last two frames of each convection speed, increases by a factor of three. The trend shown by the $D\Omega_d/Dt$ plots is identical to that observed for ω_d in

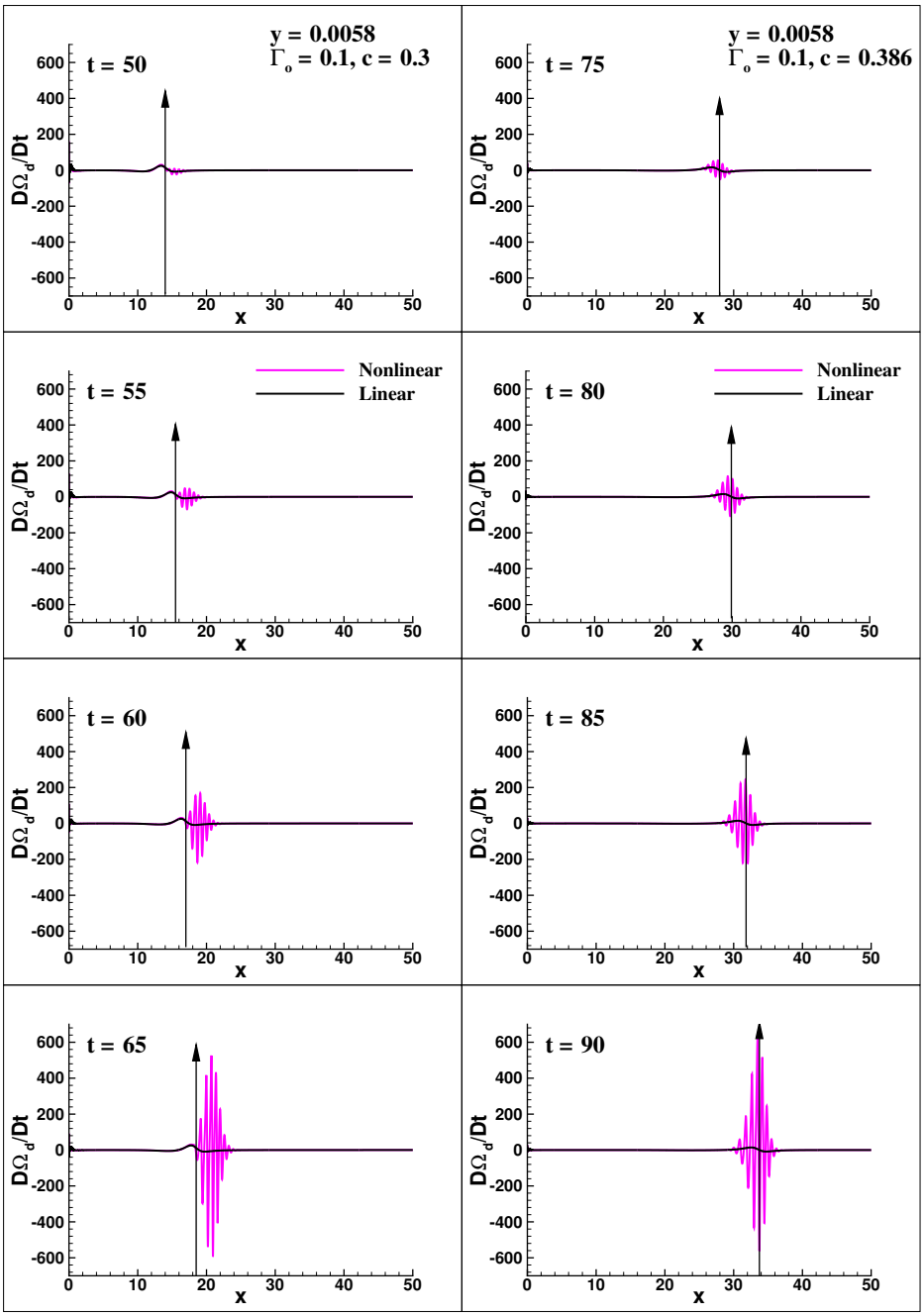

Fig. 8.34 Comparison of $D\Omega_d/Dt$ plotted as a function of x at the indicated times, solved by LNSE and NNSE for a convecting free-stream vortex with speed $c = 0.3$ (left) and 0.386 (right) at $y = 0.0058$.

Figs. 8.29 and 8.30, which indicates that DETE is a good tool to characterize the receptivity of the evolving disturbance flow field.

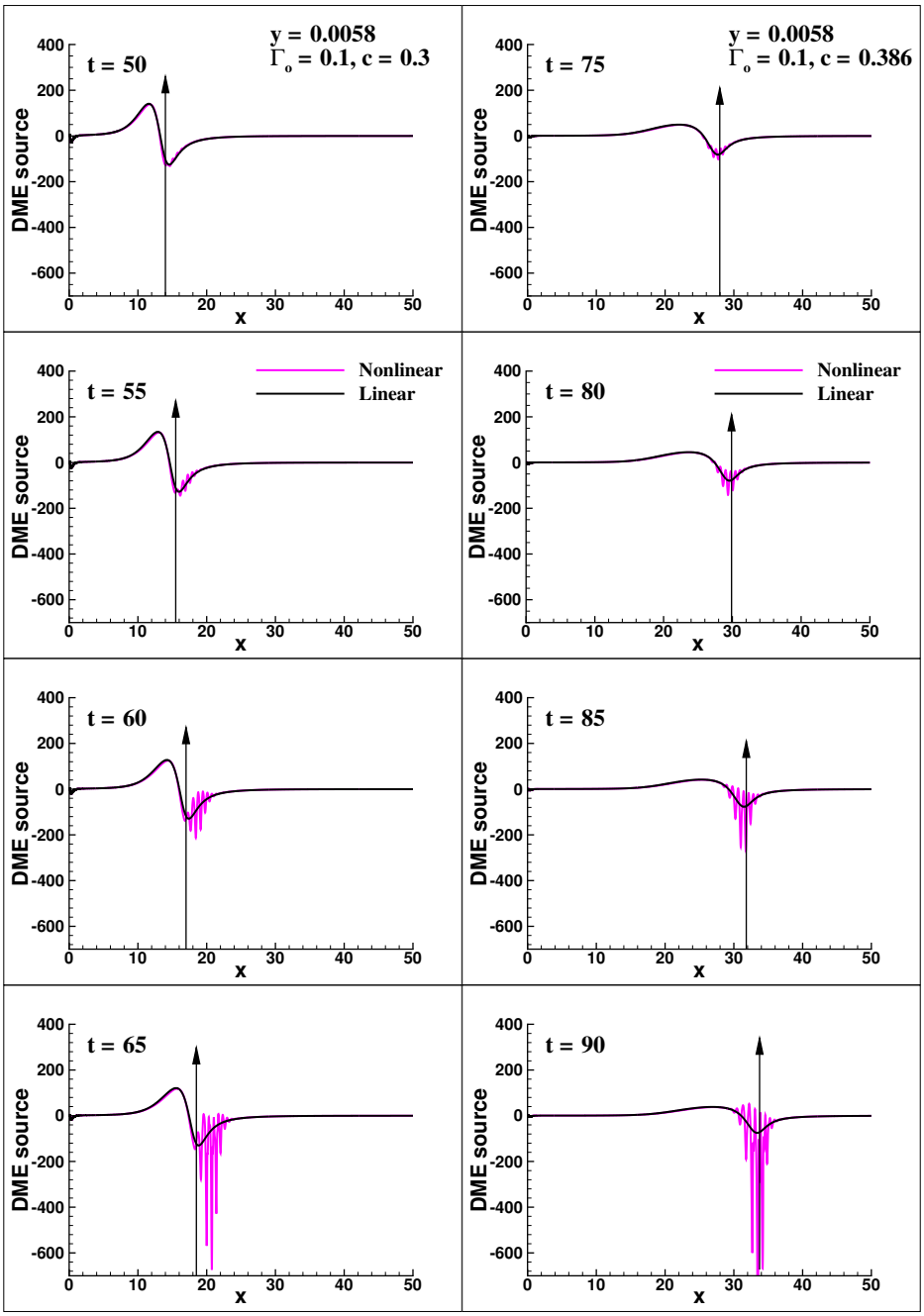

Fig. 8.35 Comparison of $\nabla^2 E_d$ plotted as a function of x at the indicated times, solved by LNSE and NNSE for a convecting free-stream vortex with speed $c = 0.3$ (left) and 0.386 (right) at $y = 0.0058$.

In Fig. 8.35, the source of DME ($\nabla^2 E_d$), given by Eq. (8.23), is shown by using the LNSE and the NNSE solutions for $c = 0.3$ and 0.386 at $y = 0.0058$. As we have seen for the plots of Ω_d, the source terms created by LNSE do not show any STWF, for the shown

time frames. The onset of STWF in the DME plots is from $t = 50$ onwards for $c = 0.3$ and from $t = 75$ onwards for $c = 0.386$, as we have noted for DETE also in the previous figure. However, the STWF observed in the DME plots is aligned towards the negative $\nabla^2 E_d$, which indicates a source of DME (Sommerfeld, 1949). The amplification of the nonlinear STWF, observed for a time interval of 5 in the last two frames of each convection speed, is significantly higher than in other frames with the same interval. This is due to the higher order nonlinear terms being accounted for in NNSE solution. The trend shown by the $\nabla^2 E_d$ plots is identical to the one observed for ω_d in Figs. 8.29 and 8.30, which also indicates that DME can be used to trace nonmodal growth of the disturbance field.

Late stages of disturbance growth for vortex-induced instability using DETE:

It is of interest to trace the disturbance field at later stages when the nonlinearity becomes important in creating 2D turbulent spot-like structures, as we have noted in Fig. 8.32. With this in mind, we plot Ω_d for later time frames and show its Fourier transform (FFT) as a function of wavenumber (k) to determine structures in the physical plane with corresponding peaks in the spectral plane. A distinction between the solutions obtained from the LNSE and the NNSE can also be obtained by determining the k for different excitation levels.

In Fig. 8.36, the plots of Ω_d are shown as a function of x for the indicated time frames for $c = 0.3$ and 0.386 at $y = 0.0058$, to highlight the later stages of STWF development. For the frames with $c = 0.3$, the LNSE solution shows an incipient STWF downstream of the vortex location at $t = 115$. This STWF grows both in space and time in a symmetric manner but does not spread out in the streamwise direction, unlike the NNSE solution. For the NNSE solution, the peaks of Ω_d observed at $t = 145$ disperses and spread over a larger streamwise extent in the subsequent time frame. For the case with $c = 0.386$, the LNSE solution does not show any indication of a nonmodal STWF for the times shown. However, the NNSE solution shows a STWF, the peaks of which spread out in the streamwise direction. The behaviour of Ω_d shows identical variation of features, as noted for disturbance vorticity in Fig. 8.32. An important observation for the NNSE solution for both values of c is that as time progresses, Ω_d is primarily a positive quantity, which can be explained by the dominance of the ω_d which acts as a positive definite contribution to Ω_d. This is not necessarily the case for a location further away from the wall with a lower ω_d.

8.7.6 Disturbance Enstrophy Spectrum at Late Stages

For case with $c = 0.3$: In Fig. 8.37, the FFT of the linearized (left) and nonlinear (right) plots of Ω_d are shown at discrete times, as a function of streamwise wavenumber k, for the

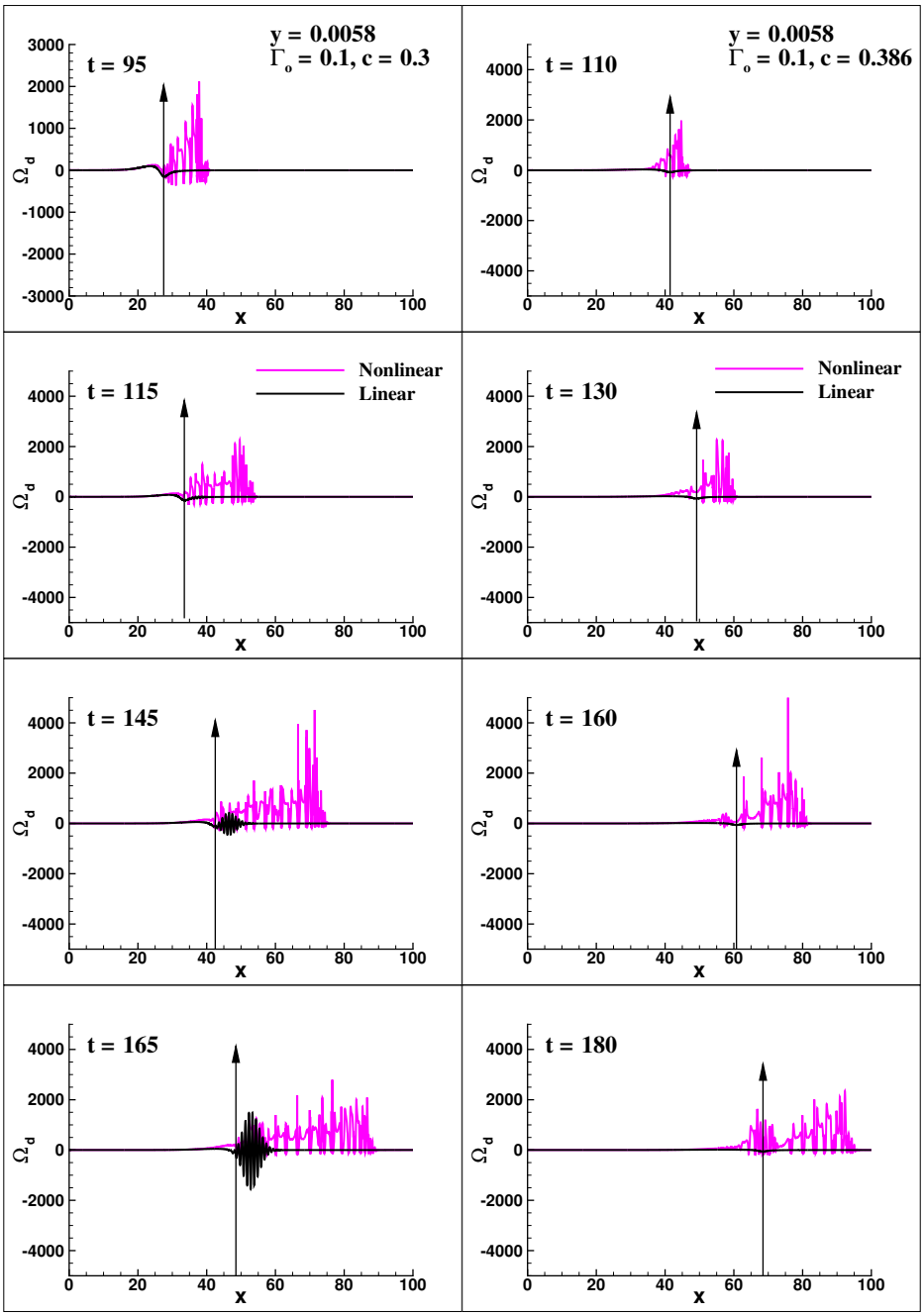

Fig. 8.36 Comparison of Ω_d plotted as a function of x at the indicated times, solved by LNSE and NNSE for a convecting free-stream vortex with speed $c = 0.3$ (left) and 0.386 (right) at $y = 0.0058$ showing later stages of disturbance growth.

case of $c = 0.3$. In all the time frames for the FFT of Ω_d obtained using LNSE, we observe a central lobe, flanked by two lobes on either side. In this figure, the ordinate axis is an exponent of 10. For $t = 95$, the peak central lobe corresponds to a value $10^{0.7791}$, whereas

the peaks of the side lobes are much lower at $\Omega_d(k) = 10^{-1.1607}$. Thus, at this time the central peak is prominent and correlated with the single wavelet structure in the physical plane in Fig. 8.36. By $t = 115$, the central lobe has a peak value of $\Omega_d(k) = 10^{0.7507}$ whereas the side lobes have $\Omega_d(k) = 10^{-0.1796}$ which signifies a growth by a factor of ten for the side lobes. This can be explained by the onset of the STWF in the LNSE solution in Fig. 8.36, which corresponds to the side lobes in the spectral plane. The reduction in the peak value of the central lobe suggests that the single wavelet in the physical plane spawns the STWF at later times. At $t = 145$, the side lobes dominate over the central lobe, which is $\Omega_d(k) = 10^{0.7069}$, as compared to the side lobe peaks with $\Omega_d(k) = 10^{0.9591}$. This is also seen in the Ω_d plots, where the STWF dominates over the wavelet in Fig. 8.36. By $t = 165$, the STWF has completely taken over in the physical plane, which is also observed in the spectral plane by the dominance of the side lobe peaks with $\Omega_d(k) = 10^{1.5525}$, as compared to the central lobe with a value of $\Omega_d(k) = 10^{0.6797}$.

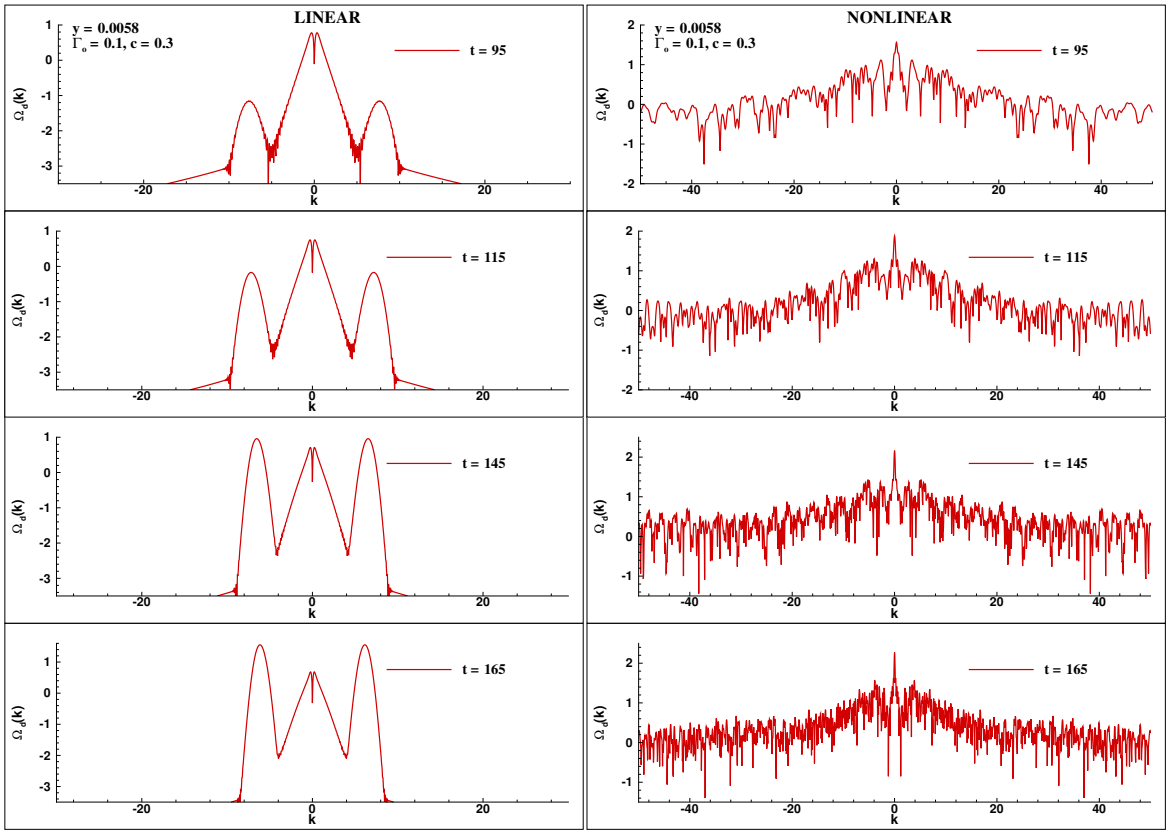

Fig. 8.37 FFT of linear (left) and nonlinear (right) Ω_d as a function of k at indicated times for a vortex with $c = 0.3$ at $y = 0.0058$. The ordinate scale indicates the exponent of 10.

For the corresponding FFT of Ω_d obtained from NNSE, we observe that a much wider range of wavenumbers are excited, as compared to the linear case. The peak associated

with the NNSE solution at $t = 95$ corresponds to $\Omega_d(k) = 10^{1.5611}$, while the edges of the spectrum have a $\Omega_d(k) = 10^{-0.4774}$. This peak value grows in the next time frame to $\Omega_d(k) = 10^{1.8781}$, while the edges have a reduced value of $\Omega_d(k) = 10^{-0.7356}$. The reduction in the edge spectrum can be attributed to the observation in the physical plane, where the peaks associated with the nonlinear solution reduce in intensity due to dispersion, causing even more streamwise spreading of the STWF in the subsequent time frame. We observe the same phenomenon between $t = 145$ and 165. The maximum peak at $t = 165$ is at $\Omega_d(k) = 10^{2.2696}$, where a turbulent structure is noted in the physical plane. As time progresses the peak becomes more pronounced.

For case with $c = 0.386$: In Fig. 8.38, the FFT of the linearized (left) and nonlinear (right) Ω_d plots are shown at discrete times as a function of k for the case of $c = 0.386$. For the frames with the linearized results, as seen previously for $c = 0.3$ case, there are two primary spectra: (i) a central lobe associated with the wavelet in the physical plane and (ii) the side lobes which become prominent after the STWF begins to dominate in the physical plane. From Fig. 8.36 for $c = 0.386$, we note that there is no discernible STWF structure in the LNSE solution for the chosen time frames, and this feature is also reflected in the corresponding FFT plots. The peak associated with the central lobe reduces from $\Omega_d(k) = 10^{0.5743}$ for $t = 110$ to $\Omega_d(k) = 10^{0.4286}$ for $t = 180$. The peak of the side lobes, on the other hand, increase from $\Omega_d(k) = 10^{-2.7241}$ for $t = 110$ to $\Omega_d(k) = 10^{-1.1643}$ for $t = 180$, but these are not able to overcome the peak spectrum of the central lobe for the chosen time frames. The STWF would only become prominent in the physical plane, when the peaks of the side lobes overtake the peak of the central lobe, as we had seen in the previous case for $c = 0.3$.

The FFT of Ω_d obtained using NNSE shows qualitatively similar features for $c = 0.386$, as we have seen in Fig. 8.37 for $c = 0.3$. The peak of the spectrum is $\Omega_d(k) = 10^{1.4848}$ at $t = 110$ and $\Omega_d(k) = 10^{2.1314}$ for $t = 180$. The nonlinear solution in physical space spreads over larger streamwise extent for $c = 0.386$, as compared to the case for $c = 0.3$, but the peaks associated with the STWF are higher for $c = 0.3$, which is corroborated by the FFT, as well as in physical plane plots of Ω_d.

We have repeated the exercise performed in Figs. 8.37 and 8.38 for a higher wall-normal location of $y = 0.0089$, and the results show a similar qualitative trend as noted for $y = 0.0058$, the only difference being in the amplitudes in the physical and spectral planes. At the higher $y = 0.0089$, a lower amplitude of Ω_d and its FFT are observed. We have not included these results here.

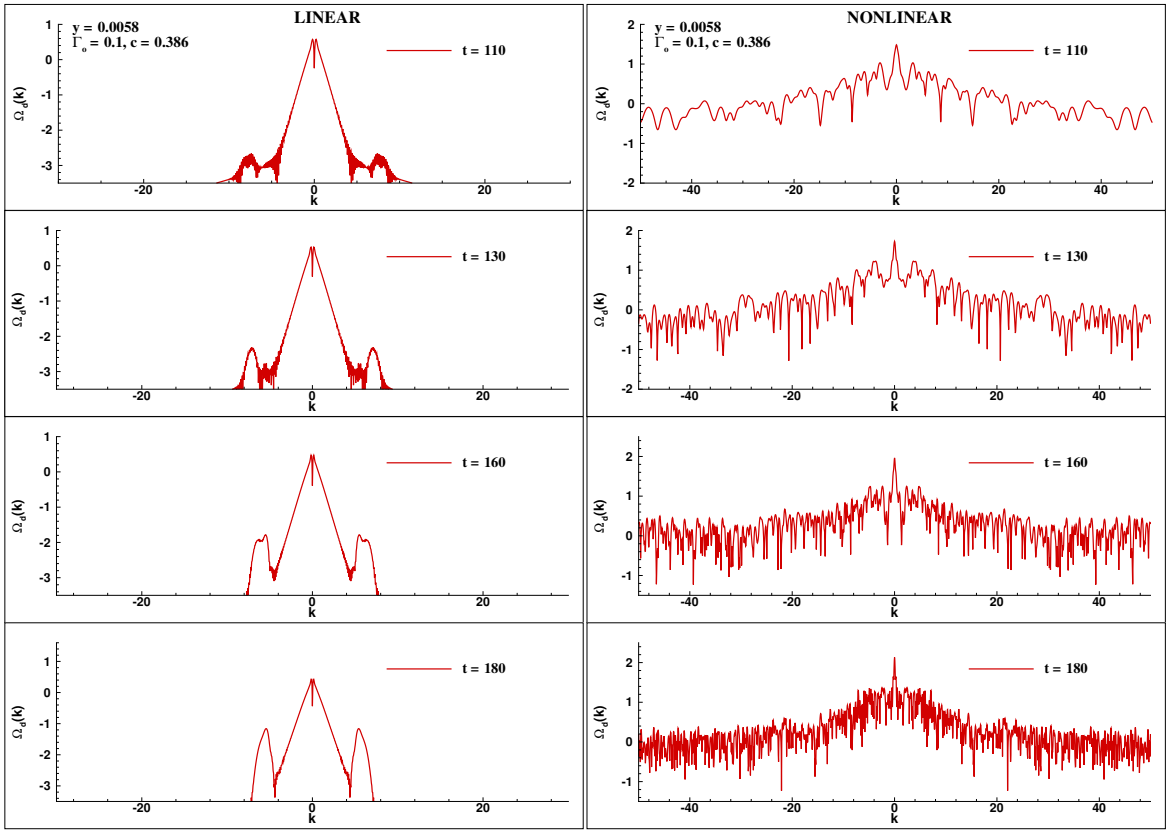

Fig. 8.38 FFT of linear (left) and nonlinear (right) Ω_d as a function of k at indicated times for a vortex with $c = 0.386$ at $y = 0.0058$. The ordinate scale indicates the exponent of 10.

8.7.7 Temporal evolution of Ω_d

In Fig. 8.39, the evolution of the maximum Ω_d obtained via solution of the LNSE is shown for the indicated wall-normal heights for the case of $c = 0.3$. As we have noted previously the wall-normal locations closer to the wall have higher mean and disturbance vorticities caused by the imposed free-stream excitation. For the wall-normal locations inside the boundary layer ($y = 0.0010$, 0.0058 and 0.0089) in the early stages, there is transient growth, followed by a fall in the maximum Ω_d. For the wall-normal stations outside the boundary layer ($y = 0.05$ and 0.1), there is a steady growth for Ω_{dmax}. It is noted that for these wall-normal locations, Ω_d starts from a value which is 7 to 9 orders of magnitude lower than that is observed for $y = 0.0010$. There is a general trend for the wall-normal stations inside the boundary layer, which can be demarcated into the following segments: (i) transient growth stage till $t = 7$, (ii) a fall in the maximum Ω_d when the linear solution is dominated by the wavelet structure, as seen in Figs. 8.30 to 8.36; (iii) a plateau when the disturbance field is transitioning to a state, which is dominated by the STWF and (iv) a sharp log-linear rise in

Ω_d, after the STWF overtakes the initial wavelet of the linear solution. For the wall-normal stations, which are outside the boundary layer, there are two demarcations: (i) a curvilinear rise in Ω_d, when the linearized disturbance field is dominated by the wavelet structure; (ii) a sharp log-linear rise in Ω_d, when the STWF dominates the disturbance field. This evolution pattern provides a picture of the disturbance field, as a function of wall-normal location. Next, we trace the disturbance field solved using the NNSE.

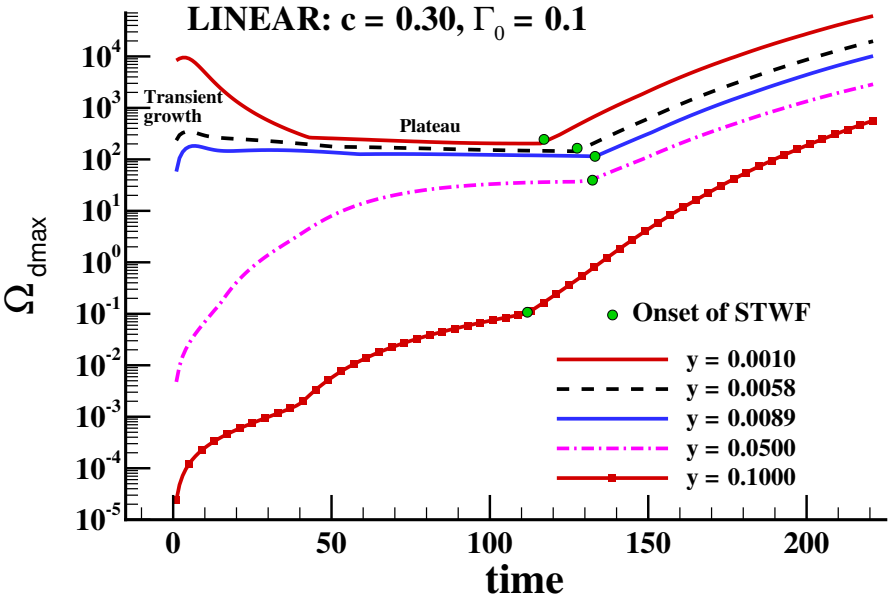

Fig. 8.39 Evolution of maximum Ω_d at indicated wall-normal heights obtained from solution of LNSE for a convecting free-stream vortex with $c = 0.3$.

In Fig. 8.40, the evolution of the maximum Ω_d is shown for the indicated wall-normal heights evaluated from the solution of the NNSE for $c = 0.3$. As we have noted in Fig. 8.39, the maximum Ω_d is higher due to higher values of ω_m and ω_d near the wall. By comparing the magnitudes alone, the nonlinear solution provides a higher value of Ω_{dmax} than the corresponding Ω_{dmax} calculated from LNSE. For the stations within the boundary layer, there is a short time interval at the beginning, when an amplification of Ω_d is followed by a fall in the maximum Ω_d. This short time growth is considered as a transient growth region. As before for LNSE solution, for the stations inside the boundary layer the disturbance field is characterized by four types of time variations: (i) transient growth stage marked by an amplification of the maximum Ω_d; (ii) a fall in the maximum Ω_d, where the nonlinear peaks of Figs. 8.37 and 8.38 are gaining in amplitude; (iii) the dominance of the asymmetric STWF indicated by an abrupt rise in the maximum Ω_d and (iv) a plateau which oscillates about a mean Ω_d value for which the peaks of the STWF are spread over streamwise extent of the

domain. It is noted that these nonlinear fluctuations, which are observed in the last stage are not seen for LNSE solution. For the stations outside the boundary layer, there are three primary regions of interest: (i) a slow rise in the maximum Ω_d for which the nonlinear solution follows the wavelet observed in the linear solution, (ii) an abrupt amplification of maximum Ω_d, when the STWF dominates the perturbation field and (iii) a plateau, fluctuating around a mean Ω_{dmax}, when there is streamwise spreading of the turbulent spot. Moreover, in general the nonlinear solution propagates much faster, than its linear counterpart, and the STWF shows the solution reaching a fully developed turbulent stage for the displayed time frame, which does not happen for the LNSE solution. This shows that for the vortex-induced instability under consideration, even in a 2D framework, it is essential to account for the full NSE while studying transition.

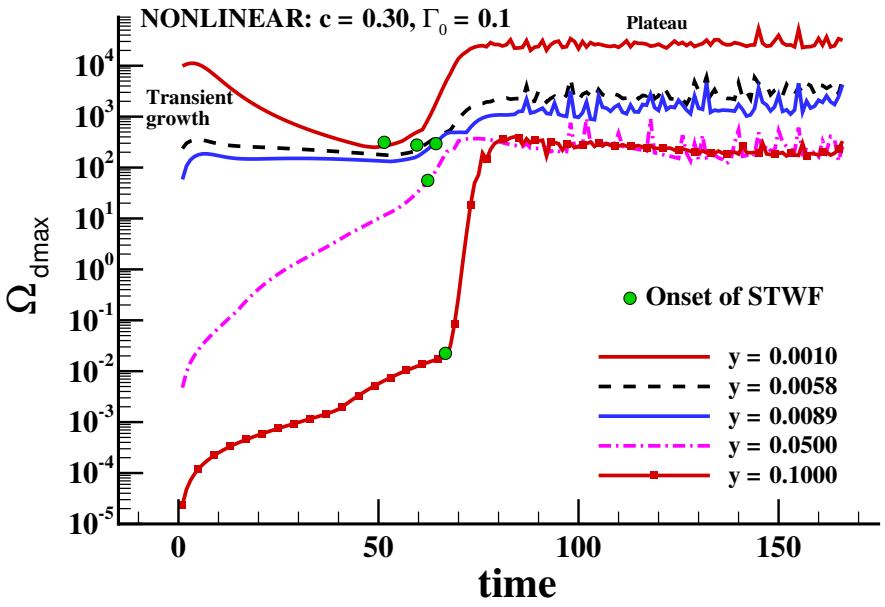

Fig. 8.40 Evolution of maximum Ω_d at indicated wall-normal heights obtained from solution of NNSE for a convecting free-stream vortex with $c = 0.3$.

8.7.8 Effect of Wall-Normal Location on Receptivity

In Fig. 8.39, for the evolution of Ω_d obtained using LNSE, we identify the time after which there is a distinct discontinuous rise of Ω_d as the predominance of the STWF. The trend for this is not immediately clear. The points inside the boundary layer show this onset to occur at later times as we move away from the wall. However, for the y-stations located outside the boundary layer, this trend does not hold. To explain this anomalous behaviour of the outer

points, we compare between the Ω_d plots for two points, one in the interior and the other in the exterior, in Fig. 8.41.

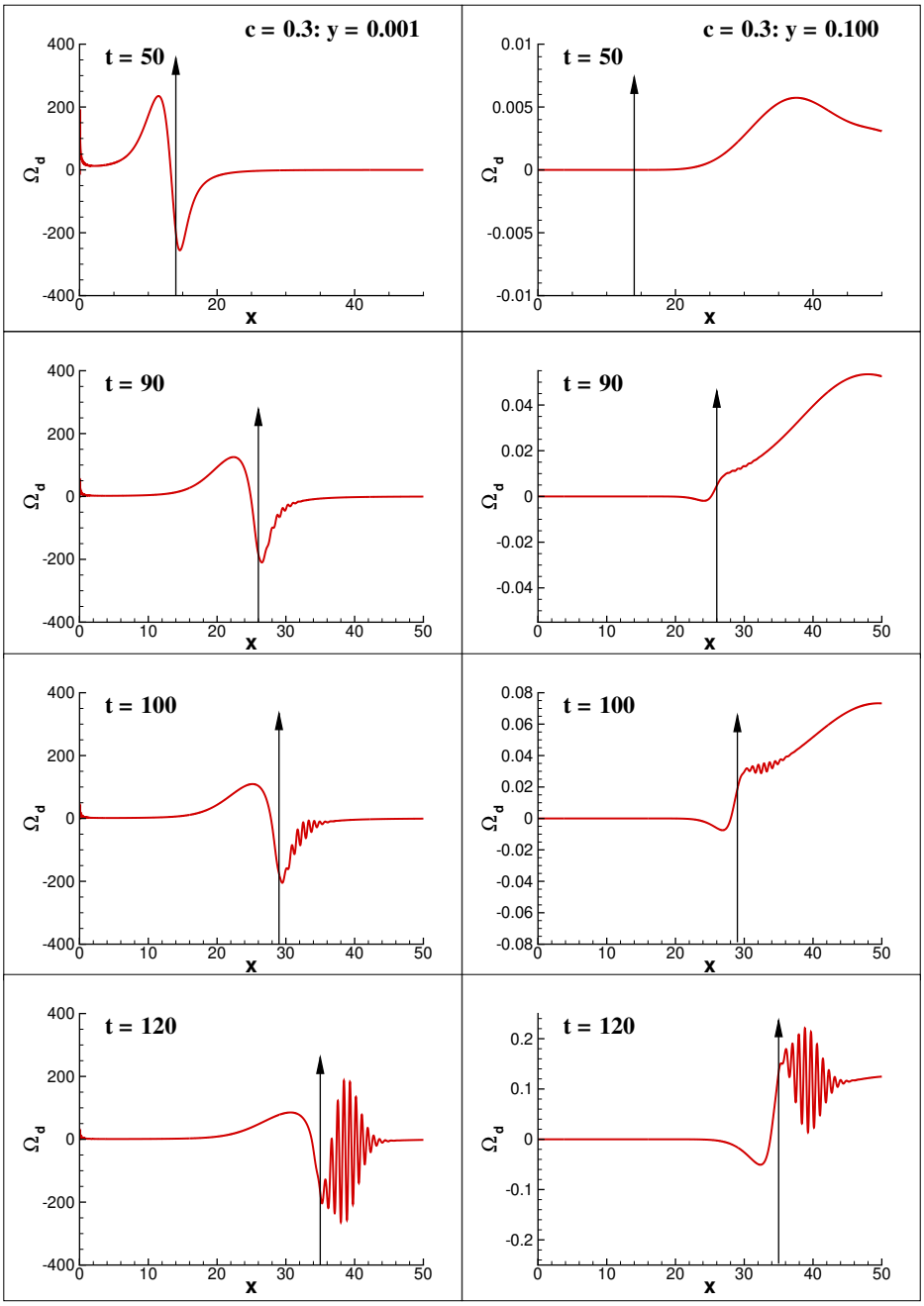

Fig. 8.41 Plot of Ω_d at indicated times obtained from solution of LNSE for a convecting free-stream vortex with c = 0.3 at $y = 0.001$ (left) and $y = 0.1$ (right).

In Fig. 8.41, we show Ω_d as a function of x for the critical times of onset and propagation of the STWF for $y = 0.001$ (left) and 0.1 (right). The strength of the vortex and the convection

speed are $\Gamma = 0.1$ and $c = 0.3$ for all frames. We observe that at $t = 50$, the STWF cannot be seen, only a single wavelet structure is visible, however the magnitudes of Ω_d differ by five orders as we had seen for the evolution plot in Fig. 8.39. The onset of STWF is noted for both heights at $t = 90$, but the magnitudes differ by four orders. At $t = 100$, the STWF grows from its incipient stage for both heights. For $y = 0.001$ and 0.1, the time at which the STWF dominates in the disturbance field is similar, even when the magnitudes differ by several orders. This can be explained by the observation that for $y = 0.001$, we are inside the boundary layer and the response field shows the receptivity/instability to the imposed free-stream excitation creating adverse pressure gradient and the disturbance field draws its energy from the shear in the mean flow. This explains why the interior points show a delayed onset of STWF as the height is increased. In contrast, for $y = 0.1$ (which is outside the boundary layer), there is a direct influence of forcing by the convecting vortex. This induced effect outside the boundary layer, is not fed by the local shear. The weaker amplitude is due to the direct effect of the forcing. This explains why we can see the STWF at an earlier time for $y = 0.1$ compared to $y = 0.05$.

To demonstrate that the NNSE solution takes the flow to a fully developed 2D turbulent stage at later times, the spectrum of the energy of the disturbance field is shown for $c = 0.3$ in Fig. 8.42. Usually, 2D turbulence is characterized by the direct cascade (dictated by enstrophy) for which $E(\alpha) \sim \alpha^{-3}$ and an inverse cascade (dictated by energy) for which $E(\alpha) \sim \alpha^{-5/3}$ (show in Fig. 3.8 of Doering and Gibbon (1995)), which is also the case in Fig. 8.42. The FFT of the turbulent spot visualized at $t = 165$ in Fig. 8.36 is investigated and the corresponding spectrum is a typical feature of 2D turbulence, as shown by Batchelor (1969); Kraichnan and Montgomery (1980). This highlights the need of working within a nonlinear, spatio-temporal framework to account for all stages of the receptivity problem.

8.7.9 Role of nonlinearity and nonlinear phase effects

In this section, the role of the additional nonlinear terms in the NNSE in taking a system to fully developed turbulence is demonstrated by considering results obtained from solutions of the NNSE and LNSE with $c = 0.3$. Specifically, we comment on the dispersion demonstrated by the STWF in the nonlinear solution, a clear demarcation from the exponential amplification of the STWF in the linear solution.

The nonlinear saturated state of the STWF and its spectrum are shown in Fig. 8.43. Such wideband spectrum of the signal shown in Figs. 8.43(a) to (c), have also been noted in receptivity of ZPG boundary layer to a wall-excitation (Sengupta and Bhaumik, 2011). The discrete times in Fig. 8.43, have been specifically chosen to show the formation of intermittent spike-like structures in the physical plane with the formation of a vortex-doublet,

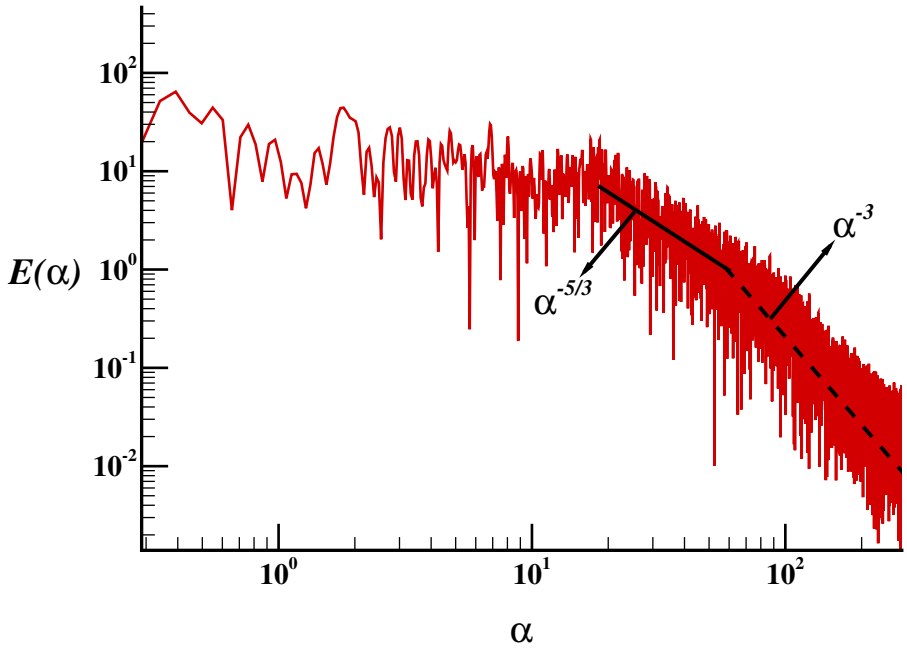

Fig. 8.42 Spectrum of kinetic energy of disturbance field, evaluated from the NNSE, plotted as a function of wavenumber α for $c = 0.3$ at $t = 165$ showing -5/3 and -3 type variation typical of 2D turbulence.

as shown in Fig. 8.43(b) at $x_o = 38.75$. This is akin to a singularity added at that time, which is localized in space and causes the spectrum in Fig. 8.43(e) with a qualitative difference. By $t = 99$, the vortex-doublet disappears, and the spectrum in frame (f) reverts to that observed in frame (d). The sudden appearance of a spike adds a band-limited component in the form of $e^{i\alpha x_o}$ at all wavenumbers (which can be related by an equivalent *time shift* property of Fourier-Laplace transform (Papoulis, 1962)). Such nonlinear events altering the wideband signal is a very special effect of nonlinearity for a fluid dynamical system, seen clearly at high wavenumber ranges of the spectrum in frame (e). Such events repeatedly occur, whenever secondary separation bubbles form on the wall. This has been identified here and termed as *twinkling* of the spectrum (Sengupta et al., 2020). The attributes of the nonlinearity are explained further in Fig. 8.44, with the spectra shown in the wavenumber-frequency plane for indicated time ranges.

The spectrum of ω_d obtained from the LNSE and NNSE are shown in Fig. 8.44. The group velocity of the STWF in the early stage can be calculated from the spectra in frames (a) to (d) from $d\omega_o/d\alpha$ at the peak amplitude, marked as STWF. For the spectrum in Fig. 8.44(a), the local solution dominates over the STWF. In Fig. 8.44(b), the spectrum shows that the local solution and the STWF retain distinct identities, with the local solution retaining its amplitude with time, while the STWF grows exponentially for the LNSE. The wavenumber

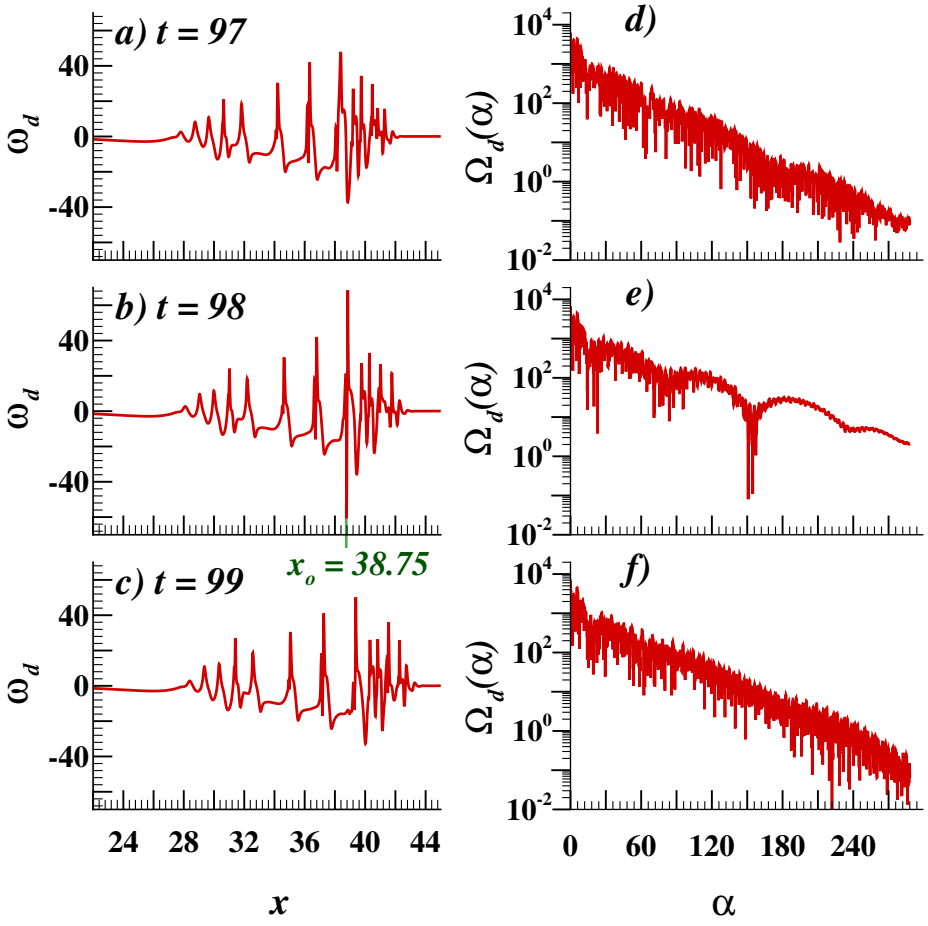

Fig. 8.43 (a-c) Disturbance vorticity as a function of x at indicated times and (d-f) the corresponding Fourier transforms ($\Omega_d(\alpha)$), evaluated from NNSE for $y = 0.0058$. Wideband shift in spectrum in (e) is observed due to intermittent formation of spikes in the STWF in (b) at $x_o = 38.75$.

and frequency of the STWF change with time slowly for the LNSE. For the NNSE in Fig. 8.44(c), one notes the onset of STWF with the effects of nonlinearity accelerating the growth significantly. For the spectrum in Figs. 8.44(d) and 8.44(e), the effects of nonlinearity cause significant dispersion over a wide range of wavenumbers and frequencies. The spectrum of the local solution is also affected by the appearance of higher amplitude and additional peaks induced by the nonlinear interaction.

8.7.10 Concluding remarks

One application of the global nonmodal analysis of leading edge flows is provided by Obrist and Schmid (2003) which demonstrated the role of the continuous spectrum in

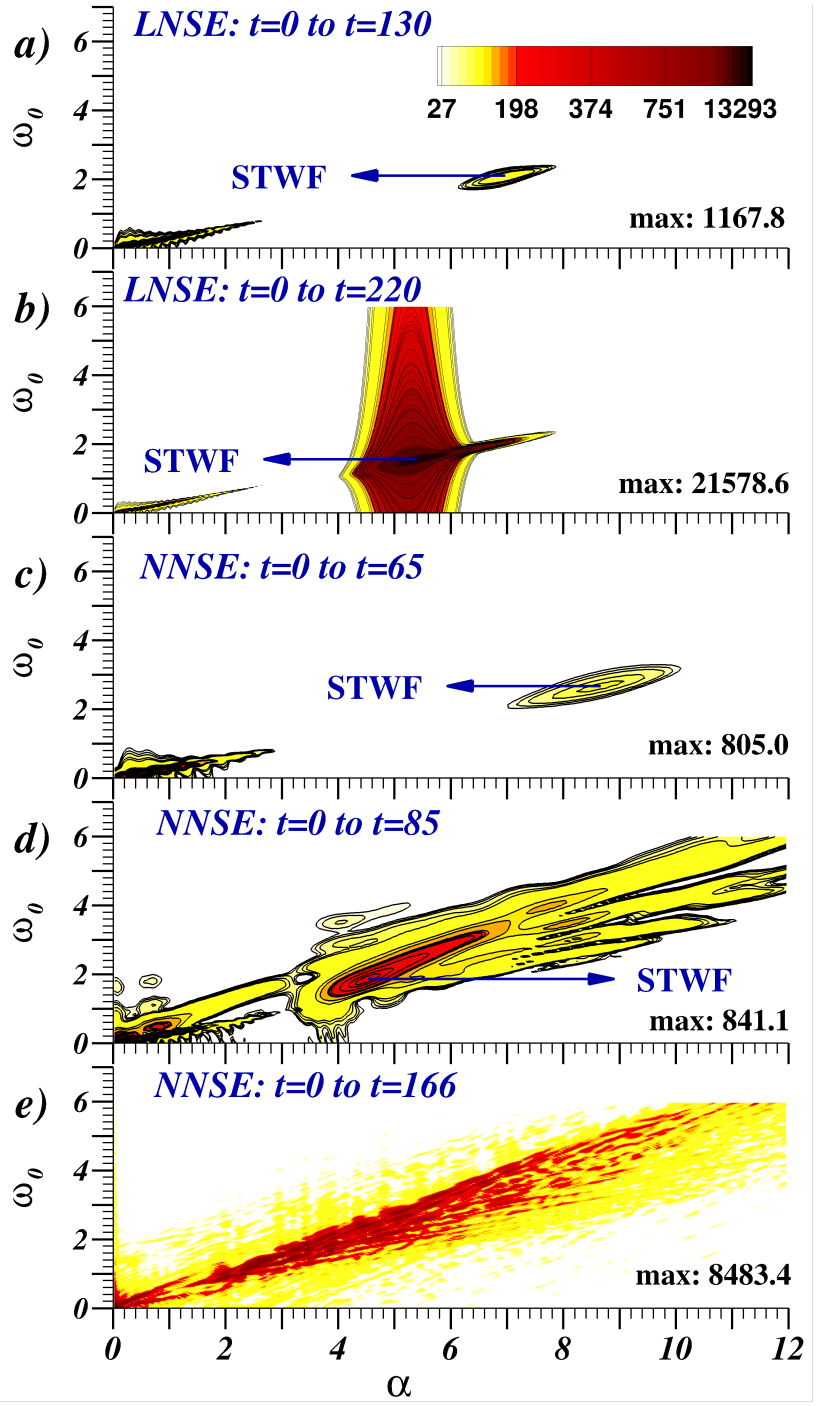

Fig. 8.44 Fourier-Laplace transform of ω_d for $y = 0.0058$ in (α, ω_o)-plane showing the local solution (near the origin of the spectral plane) and the STWF from (a,b) LNSE and (c-e) NNSE for the indicated time ranges. The evolution of STWF for NNSE transforms the single peak in (c) to a dispersed nonmodal spectrum in (d) and (e).

increasing transient growth by solving adjoint BiGlobal equations. In describing the linear nonmodal theory, Schmid (2007) considered 3D linearized perturbation field, in terms of Orr-Sommerfeld and Squire equations. The transient growth is for an initial energy perturbation, and is noted for very early time only, beyond which the energy functional decays. Despite the fact that the present analysis is for 2D flows, we also have noted the existence of transient growth in Fig. 8.39 and 8.40 for LNSE and NNSE, respectively. Also, in the present analysis the DME accounts for the mechanical energy and its growth, which is followed in Fig. 8.35, showing more instability for NNSE, and marginal variation of disturbance energy using LNSE.

For laminar separation bubbles, the absolute/convective theory of Hammond (1998) and the solution of the BiGlobal equations by Theofilis et al. (2000) demonstrated the self-sustaining nature of perturbations in the flow, besides the amplification of incoming 2D and 3D disturbances. Present 2D analysis, show growth via linear mechanism through the nonmodal STWF in Fig. 8.29, which keeps growing continually without any saturation. In contrast, NNSE shows not only the nonmodal growth of vorticity, disturbance enstrophy in Figs. 8.32 and 8.36 at the early time, but also eventually shows transition to 2D turbulent spot stage.

For four different laminar separated flow configurations (Barkley et al., 2008; Blackburn et al., 2008; Ehrenstein and Gallaire, 2008; Marquet et al., 2008), there exists a consistently strong transient growth of linear, nonmodal perturbations with regard to BiGlobal nonmodal instability analysis. All these flows suffer instability due to creation of unsteady separation, as is the present case of ZPG boundary layer perturbed by free stream convecting vortex, which has been conjectured by Taylor (1936) and referred to in Monin and Yaglom (1971).

Kitsios et al. (2009) analysed flow around a NACA-0015 airfoil identified a travelling wake mode and a stationary 3D global mode of instability. Abdessemed et al. (2009) performed an instability analysis of a periodic cascade of low pressure turbine blades, where they found the same two branches of instability, whereas a full transient growth analysis of the same cascade was carried out by Sharma et al. (2011). It was found that the transient growth mechanism was the strongest of the three instability scenarios in the cascade.

Here, we have studied the receptivity of the ZPG boundary layer excited by a convecting vortex in the free stream, using both linear and nonlinear formulations with identical numerical setups. In the presented results, we have noted an early transient growth in both the linear and nonlinear frameworks. Additionally, an amplification of the disturbance field is carried out via a spatially and temporally evolving wave-front, i.e. the STWF, which displays nonmodal growth of the disturbance field induced by the convecting vortex in the free-stream. The onset of the STWF is captured by solving both the linearized and nonlinear Navier-

Stokes equation, with the rate of growth being higher for the nonlinear case. The evolution of STWF is completely different following these two formulations and only the nonlinear formulation captures the transition to turbulence. We have explored the long term nonlinear dynamics of STWF, and shown that the transition occurs due to its growth. The later stages of transition are dictated by the secondary, nonlinear effects on the STWF, which lead to unsteady separation, resulting in the broadband spectrum. The initial STWF transforms into a turbulent spot creating additional STWFs, which merge downstream to create the turbulent flow. Here, we have shown a definitive, deterministic route to 2D turbulence by NNSE, even though the onset may appear similar to linear mechanism (Sengupta et al., 2006b). Thus, a global nonlinear receptivity study is pertinent for the study of the vortex-induced instability to trace the later stages of transition to turbulence, as has been shown in Sengupta et al. (2020). The route for 3D vortex-induced instability and the STWF has been investigated in Sengupta et al. (2019a) by solving the NNSE, results of which have been presented in Chapter 6, showing the central role of the STWF in the transition process.

Chapter 9

Conclusions and Recommendations for Future Work

9.1 Conclusions

The aim of this thesis is to explore the various disturbance environments that exist for a low pressure turbine and to study the transitional flows under the influence of these disturbances. After incorporating the necessary enhancements to the solvers, the individual and combined effects of aeroelastic blade vibrations, free-stream turbulence, unsteady wakes and roughness on the transition of a separated shear layer have been investigated using a range of numerical simulations. Two configurations have been considered: (i) a flat plate subjected to streamwise pressure gradient, representative of the suction surface of an ultra high-lift LPT blade (ii) a flat plate placed downstream of a convecting vortex at a fixed height in the free-stream, inducing an adverse pressure gradient similar to that observed on the suction surface of an ultra high-lift blade. It has been proposed that the vortex represents a unit process of free-stream turbulence. Wherever possible, validation has been provided against either the numerical or the experimental data available for these configurations. It has been demonstrated using the velocity profiles, spectra of streamwise velocity fluctuations and flow structures, that the numerical framework has captured much of the phenomena to a reasonable level of accuracy. Further investigations have been carried out to explore the transition mechanisms and their implications on loss on the suction surface.

At low disturbance levels, the transition to turbulence is primarily due to the breakdown of 'Kelvin-Helmholtz' roll up vortices. In the presence of aeroelastic blade oscillations, unsteady wakes, free-stream turbulence and roughness, the bypass transition route was adopted

and the results show an evidence of streamwise streaks. These streaks impart spanwise waviness to the separated shear layer and cause early destabilisation. The losses on the suction surface of the low pressure turbine blade are dominated by the separation bubble at low Reynolds numbers, and thereby suppression of the separation region by the presence of disturbances is effective in bringing down blade profile losses. It is observed that the blade oscillation has an effect in reducing profile loss, which is further accentuated in the presence of free-stream turbulence. A blade fluctuating at higher reduced frequency is found to be more effective in shrinking the separation region. Blade vibration is found to increase the level of pre-transitional fluctuations, without having a significant influence on the growth beyond separation. As a consequence, it shifts the inflection point of the mean velocity profile towards the wall by enhanced mixing. Free-stream turbulence, on the other hand, has a direct influence on the turbulent fluctuations. Klebanoff streaks are observed in the presence of free-stream turbulence, which induce local perturbations in the flow relative to the mean flow. There is a cumulative effect in suppressing the separation region when blade oscillation and free-stream turbulence are studied in conjunction, although the additional effect of free-stream turbulence is marginal. The flow shows a linear response to the frequency of the blade vibration, visible through the time-series and phase-averaged results. An increase in turbulent kinetic energy production is observed with the blade oscillation which is enhanced by the introduction of free-stream disturbance.

The effect of a unit process of free-stream turbulence on the suction surface of a LPT blade, in the presence of a discrete roughness element (similar in functionality to a trip wire) is studied. The roughness element is found to trigger early transition by destabilizing the mean flow. Streaks are observed in the presence of the convecting and rotating cylinder, generating a vortex of fixed strength, and are enhanced by the presence of roughness in the pre-transitional zone. Enhanced spanwise waviness is noted with the roughness. The route of transition and the origin of three-dimensionality marked by the prominence of the vortex stretching is shown. Earlier breakdown to turbulence is noted in the presence of roughness. An optimum range of convection speeds of the convecting vortex is observed and the maximum receptivity is noted at a speed of 0.386, which concurs with prior experiments on a periodic convecting vortex. Although this convection speed of the vortex may not be an accurate representation of free-stream turbulence occurring in turbomachines, it is of interest to know the conditions required for maximum receptivity in a controlled experiment studying bypass transition mechanisms. The wall excitation in the form of roughness is more effective in triggering early transition.

The unsteady wake is found to have a direct effect on the velocity profile. A lag is noted between the wake passing and transition. While the wake convects at local free-stream velocity, its impression in the boundary layer convects much slower, between 50% and 70% of the local free-stream velocity. Both unsteady wakes and blade oscillation promote near-wall mixing. This results in the upstream shift of the transition point and a significant reduction in the size of the separation bubble. The unsteady wakes and blade oscillations have a conjunctive effect on reducing the size of separation bubble. The secondary separation bubble observed in the unperturbed flow is reduced with the presence of wakes and is completely suppressed with the addition of the blade oscillation. Turbulent production is increased with the increasing perturbation levels, with the maximum effect seen for the combination of wakes and oscillation. Wakes have a more pronounced effect than free-stream turbulence on lowering profile loss by separation region suppression.

A method for nonlinear receptivity is proposed, based on disturbance enstrophy transport equation (DETE). It is effective in segmenting regions of flow instabilities into those dictated by positive growth rates of disturbance enstrophy, and those due to its negative counterpart. It is found that the positive growth rates are associated with large scale coherence in the free-stream whereas the negative growth rates are found to be arising in near-wall viscous structures (Sengupta et al., 2019a,b). The enstrophy budget terms provide essential characterization of the disturbance field. As an example, for the vortex-induced instability how three-dimensionality manifests itself despite the 2D mean flow being excited by a 2D disturbance field is demonstrated by the prominence of vortex stretching as the flow becomes three-dimensional. The extension of this method to a structure detection criterion and comparison against existing coherence identification methods, indicates the ability of the DETE method to capture small scale structures induced by the viscous term of the Navier-Stokes equation. The DETE method accounts for the unsteady and viscous terms, when compared to λ_2-criterion and a method based on disturbance mechanical energy (DME), thus enabling its application in tracking a coherent structure from its nascent stage to a fully developed turbulent stage with reasonable accuracy. In this thesis, DETE has been used for the two configurations operating under varying perturbation levels and valuable information pertaining to the flow dynamics has been attained.

The role of the spatio-temporal wave front as the forerunner for transition has been demonstrated for the first time for flows dictated by pressure gradient, wall oscillations, wakes and free-stream excitation, despite its role already being well-established for flows with excitation at the wall. The nonlinear dispersion effects have been captured in the presence

of free-stream excitation. It is shown that while both the linear and nonlinear frameworks produce a spatio-temporal wavepacket, the nonlinear saturation stage to fully developed turbulence is only captured by operating within the nonlinear regime. It is thus essential to perform a global nonlinear receptivity analysis, even though linear analyses provide essential information about the early stages of the disturbance. This distinction between linear and nonlinear analyses becomes much more prominent for free-stream excitation (Sengupta et al., 2020).

9.2 Challenges and Future Scope

In the present simulations a discrete roughness distribution element has been computed via an immersed boundary method. It will be interesting to study real roughness profiles found on blade surfaces or spanwise-periodic discrete roughness elements such as along the swept wing model of Saric et al. (2019). Additionally, it will be interesting to calibrate the immersed boundary method adopted by the use of an orthogonal grid simulation, over the same geometry.

The benefits to the profile loss brought by the introduction of blade oscillation and roughness are observed at low Reynolds numbers (observed in cruising conditions), where the loss is dictated by the occurrence of the separation bubble. Blade oscillation and surface roughness were found to be beneficial as they suppressed the separation zone. This may not be strictly true at higher Reynolds numbers, which are encountered during take-off. The separation bubble does not play such a major role at such higher Reynolds numbers (Gaster, 1967). At high Reynolds numbers, the boundary layer rapidly is turbulent and is able to accommodate the adverse pressure gradient with minimum disturbance. Although the roughness considered in the present study was very much within the boundary layer, in certain cases, the roughness could act as a hydraulically rough surface in thinner boundary layers. The benefit gained due to the suppression of the separation bubble by roughness in the pre-transitional region may not be sufficient when compared with the loss incurred by the enhanced form drag and increased turbulent wetted area due to roughness in the turbulent region. Experiments and numerical simulations to explore the possibility of any penalty due to the roughness at high Reynolds numbers will be helpful. The long term blade oscillation at high Reynolds numbers may lead to blade fatigue and catastrophic failure of the blade and thus its benefit in the suppression of the separation bubble and thereby bringing down suction surface losses may not be worth the detrimental effects on the engine. Most aeroelastic studies consider the aerodynamic forces during blade vibration and approach the situation by analyzing the effect on the structure of the blade. Conducting experiments and

simulations on the transitional aspects of the flow under the influence of blade oscillations is of paramount importance in understanding the penalty incurred by oscillation, particularly at higher Reynolds numbers.

The proposed DETE method has been used for various transitional flows in this thesis. It will be interesting to see how it will operate for fully developed turbulent flows such as channel flows. It will also be pertinent to determine whether the computational costs and data storage requirements associated with time-resolved unsteady calculations for disturbance tracking are outweighed by the new flow features it may capture. Standardization of the method and establishing thresholds of its application will be worth exploring. An extension to compressible flows is essential for providing a more complete picture of realistic turbomachine flow scenarios.

It will be worthwhile to extend the global linear and nonlinear receptivity analysis to three-dimensional framework, while also highlighting the role of perturbations from within the boundary layer or from the free stream.

Appendix A

Deriving the Disturbance Mechanical Energy (DME) Equation

To understand instabilities in flows, simply accounting for the disturbance kinetic energy may not be an adequate representation of the transitional and turbulent flows. Landahl and Mollo-Christensen (1992) emphasize the importance of studying the growth of the total mechanical energy, without deriving any equation for the same. This has been reported here and a brief derivation of the governing equation follows here. The total mechanical energy can be decomposed into its mean and disturbance components for transitional and turbulent flows. The first step in deriving the disturbance mechanical energy equation is to start from the incompressible Navier-Stokes equation given by the primitive variables as,

$$\frac{\partial \vec{V}}{\partial t} + (\vec{V} \cdot \nabla)\vec{V} = -\frac{\nabla p}{\rho} + \nu \nabla^2 \vec{V} \tag{A.1}$$

This is solved subject to the continuity equation, which for incompressible flow is nothing but the solenoidality of the velocity field given by,

$$\nabla \cdot \vec{V} = 0$$

Equation (A.1) is first converted to the rotational form of Navier-Stokes equation.
We use the vector identity for the convective acceleration term given by,

$$(\vec{V}\cdot)\vec{V} = \frac{1}{2}\nabla(|\vec{V}|^2) - \vec{V} \times (\nabla \times \vec{V})$$

which yields the Navier-Stokes equation as,

$$\frac{\partial \vec{V}}{\partial t} + \frac{1}{2}\nabla(|\vec{V}|^2) - \vec{V} \times \vec{\omega} = -\frac{\nabla p}{\rho} + \nu \nabla^2 \vec{V}$$

where ω is vorticity vector. Thus, we get the rotational form of the Navier-Stokes equation as,

$$\frac{\partial \vec{V}}{\partial t} - \vec{V} \times \vec{\omega} = -\nabla\left(\frac{p}{\rho} + \frac{1}{2}\nabla(|\vec{V}|^2)\right) + \nu \nabla^2 \vec{V} \tag{A.2}$$

Defining the total mechanical energy as,

$$E = \frac{p}{\rho} + \frac{|\vec{V}|^2}{2}$$

The Navier-Stokes equation is written with E as,

$$\frac{\partial \vec{V}}{\partial t} - \vec{V} \times \vec{\omega} = -\nabla E + \nu \nabla^2 \vec{V} \tag{A.3}$$

By taking divergence of the above equation and using the divergence free condition for the velocity field, one notices that the unsteady and viscous terms drop out automatically, to give the Poisson equation for E as,

$$\nabla^2 E = \nabla \cdot (\vec{V} \times \vec{\omega}) \tag{A.4}$$

The expression in the brackets on the right hand side of the above equation can be simplified using the vector cross product identity,

$$\nabla \cdot (\vec{V} \times \vec{\omega}) = \vec{\omega} \cdot (\nabla \times \vec{V}) - \vec{V} \cdot (\nabla \times \vec{\omega})$$

one obtains the following expression,

$$\nabla^2 E = \vec{\omega} \cdot \vec{\omega} - \vec{V} \cdot (\nabla \times \vec{\omega}) \tag{A.5}$$

The above equation represents a Poisson equation for the distribution of the total mechanical energy and the sign of the right hand side of the equation gives valuable information about the nature of the instabilities present in the flow. A negative right hand side indicates a source of energy while a positive quantity represents a sink. If one divides E into a mean and disturbance part via

$$E = E_m + \varepsilon_1 E_d \tag{A.6}$$

and substitutes the given expression in Eq. (A.5) one obtains an expression for the distribution of disturbance mechanical energy, E_d, as,

$$\varepsilon_1 \nabla^2 E_d = \nabla^2 E - \nabla^2 E_m = \vec{\omega} \cdot \vec{\omega} - \vec{V} \cdot (\nabla \times \vec{\omega}) - \vec{\omega_m} \cdot \vec{\omega_m} + \vec{V_m} \cdot (\nabla \times \vec{\omega_m})$$

Dividing the velocity and vorticity fields into their mean and disturbance components and substituting in the above expression yields an equation for the E_d.

$$\varepsilon_1 \nabla^2 E_d = (\vec{\omega_m} + \varepsilon_1 \vec{\omega_d})(\vec{\omega_m} + \varepsilon_1 \vec{\omega_d}) - (\vec{V_m} + \varepsilon_1 \vec{V_d})[\nabla \times (\vec{\omega_m} + \varepsilon_1 \vec{\omega_d})] - \vec{\omega_m} \cdot \vec{\omega_m} + \vec{V_m}(\nabla \times \vec{\omega_m})$$

$$= 2\varepsilon_1 \vec{\omega_m} \cdot \vec{\omega_d} + {\varepsilon_1}^2 \vec{\omega_d} \cdot \vec{\omega_d} - \varepsilon_1 \vec{V_m} \cdot (\nabla \times \vec{\omega_d}) - \varepsilon_1 \vec{V_d} \cdot (\nabla \times \vec{\omega_m}) - {\varepsilon_1}^2 \vec{V_d} \cdot (\nabla \times \vec{\omega_d})$$

Retaining the $O(\varepsilon_1)$ and higher order terms of the above yields the equation for the disturbance mechanical energy as,

$$\nabla^2 E_d = 2\vec{\omega_m} \cdot \vec{\omega_d} + \varepsilon_1 \vec{\omega_d} \cdot \vec{\omega_d} - \vec{V_m} \cdot (\nabla \times \vec{\omega_d}) - \vec{V_d} \cdot (\nabla \times \vec{\omega_m}) - \varepsilon_1 \vec{V_d} \cdot (\nabla \times \vec{\omega_d}) \qquad \text{(A.7)}$$

Note that the second and the last term on the right hand side of the above equation are due to the nonlinear contributions. This equation can be used to describe the onset of instability when a suitable mean or equilibrium flow is defined, and has been applied by Sengupta et al. (2003) on vortex-induced instability in wall-bounded incompressible flows.

Appendix B

Deriving the Disturbance Enstrophy Transport Equation (DETE)

The first step involved in the derivation of the disturbance energy transport equation (DETE) is to start off from the standard form of the Navier-Stokes equation as the vorticity transport equation for incompressible flows.
The non-dimensional vorticity transport equation is given in tensor notation as,

$$\frac{\partial \omega_i}{\partial t} + u_j \frac{\partial \omega_i}{\partial x_j} = \omega_j \frac{\partial u_i}{\partial x_j} + \frac{1}{Re} \frac{\partial^2 \omega_i}{\partial x_j \partial x_j} \tag{B.1}$$

where subscripts $i, j = 1, 2$ and 3, represent the Cartesian axes and repeated indices imply summation. Taking a dot product of Eq. (B.1) with ω_i, one obtains,

$$\omega_i \frac{\partial \omega_i}{\partial t} + u_j \omega_i \frac{\partial \omega_i}{\partial x_j} = \omega_i \omega_j \frac{\partial u_i}{\partial x_j} + \frac{1}{Re} \omega_i \frac{\partial^2 \omega_i}{\partial x_j \partial x_j} \tag{B.2}$$

Next, each term in the above equation is modified. The first term on the left hand side is identified as term A, the second term is called term B; first term on the right hand side is called term C and the second term is called term D. The simplifications of the terms are provided below.

Term A:

$$\omega_i \frac{\partial \omega_i}{\partial t} = \frac{\partial}{\partial t}\left(\frac{{\omega_i}^2}{2}\right) = \frac{1}{2}\frac{\partial}{\partial t}({\omega_i}^2)$$

Term B:

$$u_j \omega_i \frac{\partial \omega_i}{\partial x_j} = u_j \frac{\partial}{\partial x_j}\left(\frac{{\omega_i}^2}{2}\right) = \frac{u_j}{2}\frac{\partial}{\partial x_j}({\omega_i}^2)$$

Term C cannot be simplified further.

Term D:

$$\frac{1}{Re}\omega_i\frac{\partial^2\omega_i}{\partial x_j\partial x_j} = \frac{1}{Re}\omega_i\frac{\partial}{\partial x_j}\left(\frac{\partial\omega_i}{\partial x_j}\right)$$

$$= \frac{1}{Re}\frac{\partial}{\partial x_j}\left(\omega_i\frac{\partial\omega_i}{\partial x_j}\right) - \frac{1}{Re}\left(\frac{\partial\omega_i}{\partial x_j}\right)\left(\frac{\partial\omega_i}{\partial x_j}\right)$$

$$= \frac{1}{2Re}\frac{\partial^2{\omega_i}^2}{\partial x_j\partial x_j} - \frac{1}{Re}\left(\frac{\partial\omega_i}{\partial x_j}\right)\left(\frac{\partial\omega_i}{\partial x_j}\right)$$

In the above expressions, the substitution $\Omega_1 = \omega_i\omega_i = {\omega_i}^2$, with Ω_1 as the local enstrophy has been used. Using all the simplifications deduced above, Eq. (B.2) can be rewritten as a transport equation for enstrophy as,

$$\frac{\partial\Omega_1}{\partial t} + u_j\frac{\partial\Omega_1}{\partial x_j} - 2\omega_i\omega_j\frac{\partial u_i}{\partial x_j} = \frac{1}{Re}\frac{\partial^2\Omega_1}{\partial x_j\partial x_j} - \frac{2}{Re}\left(\frac{\partial\omega_i}{\partial x_j}\right)\left(\frac{\partial\omega_i}{\partial x_j}\right) \tag{B.3}$$

This equation is referred to as the enstrophy transport equation and has been developed by Sengupta et al. (2013) and applied for a rectangular lid driven cavity flow. The third term on the left hand side of Eq. (B.3) is due to vortex stretching, which is absent for 2D flows. The diffusion of ω_i gives rise to the terms on the right hand side of Eq. (B.3). The first term on the right hand side is due to diffusion of Ω_1 and the second term on the right hand side represents strictly a loss or dissipation term for the transport of Ω_1.

Enstrophy can also be expressed in terms of its mean and disturbance components, as

$$\Omega_1 = \Omega_m + \varepsilon_1\Omega_d \tag{B.4}$$

The equation for the transport of mean component of enstrophy can be obtained from Eq. (B.3) as,

$$\frac{D\Omega_m}{Dt} = 2\omega_{mi}\omega_{mj}\frac{\partial u_{mi}}{\partial x_j} + \frac{1}{Re}\frac{\partial^2\Omega_m}{\partial x_j\partial x_j} - \frac{2}{Re}\left(\frac{\partial\omega_{mi}}{\partial x_j}\right)\left(\frac{\partial\omega_{mi}}{\partial x_j}\right) \tag{B.5}$$

The non-linear version of the disturbance enstrophy transport equation (DETE) is obtained by subtraction of Eq. (B.5) from Eq. (B.3) and has already been introduced in chapter 2. This equation accounts for all the nonlinear terms of the transport equation and is given as,

$$\frac{D\Omega_d}{Dt} = \overbrace{\left(2\omega_i\omega_j\frac{\partial u_i}{\partial x_j} - 2\omega_{mi}\omega_{mj}\frac{\partial u_{mi}}{\partial x_j}\right)}^{\textbf{Term1}} + \overbrace{\left(\frac{1}{Re}\frac{\partial^2\Omega_1}{\partial x_j\partial x_j} - \frac{1}{Re}\frac{\partial^2\Omega_m}{\partial x_j\partial x_j}\right)}^{\textbf{Term2}} + \overbrace{\left(-\frac{2}{Re}\frac{\partial\omega_i}{\partial x_j}\frac{\partial\omega_i}{\partial x_j} + \frac{2}{Re}\frac{\partial\omega_{mi}}{\partial x_j}\frac{\partial\omega_{mi}}{\partial x_j}\right)}^{\textbf{Term3}} \tag{B.6}$$

The linearized version of the transport equation for disturbance enstrophy is obtained by only retaining the order $O(\varepsilon)$ terms from Eqs. (B.3) and (B.5). Similar to enstrophy decomposition in Eq. (B.4), vorticity is also demarcated into its mean and disturbance components, given by,

$$\omega = \omega_m + \varepsilon_2\omega_d \tag{B.7}$$

Squaring Eq. (B.7) and comparing with Eq. (B.4) one obtains,

$$\omega^2 = {\omega_m}^2 + {\varepsilon_2}^2{\omega_d}^2 + 2\varepsilon_2\omega_m\omega_d\Omega_1 = \omega^2 = \Omega_m + 2\varepsilon_2\omega_m\omega_d + {\varepsilon_2}^2{\omega_d}^2 = \Omega_m + \varepsilon_1\Omega_d$$

Retaining the order $O(\varepsilon)$ terms, an approximation is found for Ω_d as,

$$\Omega_d \approx \omega_m \cdot \omega_d;\ \varepsilon_1 \approx 2\varepsilon_2 \tag{B.8}$$

The linearized disturbance enstrophy transport equation is obtained by equating order $O(\varepsilon)$ terms on the left hand side and right hand sides of Eq. (B.6). Taking the total derivative of Eq. (B.4) and rearranging, one obtains,

$$\varepsilon_1\frac{D\Omega_d}{Dt} = \frac{D\Omega_1}{Dt} - \frac{D\Omega_m}{Dt} \tag{B.9}$$

The right hand side of the above equation is the same as that of Eq. (B.6) and the three terms are simplified by substituting with Eqs. (B.4), (B.7), (B.8) and $u = u_m + \varepsilon_2 u_d$, as follows,

Term 1:

$$2\omega_i\omega_j\frac{\partial u_i}{\partial x_j} - 2\omega_{mi}\omega_{mj}\frac{\partial u_{mi}}{\partial x_j} = 2\left(\omega_{mi} + \frac{\varepsilon_1}{2}\omega_{di}\right)\left(\omega_{mj} + \frac{\varepsilon_1}{2}\omega_{dj}\right)\frac{\partial u_i}{\partial x_j} - 2\omega_{mi}\omega_{mj}\frac{\partial u_{mi}}{\partial x_j}$$

$$= \left(2\omega_{mi}\omega_{mj} + \varepsilon_1\omega_{mi}\omega_{dj} + \varepsilon_1\omega_{di}\omega_{mj} + \frac{{\varepsilon_1}^2}{2}\omega_{di}\omega_{dj}\right)\frac{\partial u_i}{\partial x_j} - 2\omega_{mi}\omega_{mj}\frac{\partial u_{mi}}{\partial x_j}$$

$$= \left(2\omega_{mi}\omega_{mj} + \varepsilon_1\omega_{mi}\omega_{dj} + \varepsilon_1\omega_{di}\omega_{mj} + \frac{{\varepsilon_1}^2}{2}\omega_{di}\omega_{dj} - 2\omega_{mi}\omega_{mj}\right)\frac{\partial u_{mi}}{\partial x_j} +$$

$$\left(\varepsilon_1\omega_{mi}\omega_{mj} + \frac{{\varepsilon_1}^2}{2}\omega_{mi}\omega_{dj} + \frac{{\varepsilon_1}^2}{2}\omega_{di}\omega_{mj} + \frac{{\varepsilon_1}^3}{4}\omega_{di}\omega_{dj}\right)\frac{\partial u_{di}}{\partial x_j}$$

The higher powers of ε are dropped from the above expression, and term 1 is simplified as,

$$= \varepsilon_1\left(\omega_{mi}\omega_{mj}\frac{\partial u_{di}}{\partial x_j} + \omega_{mi}\omega_{dj}\frac{\partial u_{mi}}{\partial x_j} + \omega_{di}\omega_{mj}\frac{\partial u_{mi}}{\partial x_j}\right)$$

Term 2:

$$\frac{1}{Re}\frac{\partial^2\Omega_1}{\partial x_j\partial x_j} - \frac{1}{Re}\frac{\partial^2\Omega_m}{\partial x_j\partial x_j} = \frac{1}{Re}\frac{\partial^2(\Omega_m + \varepsilon_1\Omega_d)}{\partial x_j\partial x_j} - \frac{1}{Re}\frac{\partial^2\Omega_m}{\partial x_j\partial x_j}$$

$$= \frac{1}{Re}\frac{\partial^2\Omega_m}{\partial x_j\partial x_j} + \frac{\varepsilon_1}{Re}\frac{\partial^2\Omega_d}{\partial x_j\partial x_j} - \frac{1}{Re}\frac{\partial^2\Omega_m}{\partial x_j\partial x_j}$$

Term 3:

$$-\frac{2}{Re}\left(\frac{\partial\omega_i}{\partial x_j}\right)\left(\frac{\partial\omega_i}{\partial x_j}\right) + \frac{2}{Re}\left(\frac{\partial\omega_{mi}}{\partial x_j}\right)\left(\frac{\partial\omega_{mi}}{\partial x_j}\right)$$

$$= -\frac{2}{Re}\left[\frac{\partial}{\partial x_j}\left(\omega_{mi} + \frac{\varepsilon_1}{2}\omega_{di}\right)\right]\left[\frac{\partial}{\partial x_j}\left(\omega_{mi} + \frac{\varepsilon_1}{2}\omega_{di}\right)\right] + \frac{2}{Re}\left(\frac{\partial\omega_{mi}}{\partial x_j}\right)\left(\frac{\partial\omega_{mi}}{\partial x_j}\right)$$

$$= -\frac{2}{Re}\left[\left(\frac{\partial\omega_{mi}}{\partial x_j}\right)\left(\frac{\partial\omega_{mi}}{\partial x_j}\right) + \frac{\varepsilon_1}{2}\left(\frac{\partial\omega_{mi}}{\partial x_j}\right)\left(\frac{\partial\omega_{di}}{\partial x_j}\right) + \frac{\varepsilon_1}{2}\left(\frac{\partial\omega_{di}}{\partial x_j}\right)\left(\frac{\partial\omega_{mi}}{\partial x_j}\right)\right]$$

$$-\frac{2}{Re}\left[\frac{{\varepsilon_1}^2}{4}\left(\frac{\partial \omega_{di}}{\partial x_j}\right)\left(\frac{\partial \omega_{di}}{\partial x_j}\right)\right]+\frac{2}{Re}\left(\frac{\partial \omega_{mi}}{\partial x_j}\right)\left(\frac{\partial \omega_{mi}}{\partial x_j}\right)$$

$$=-\frac{1}{Re}\left[\varepsilon_1\left(\frac{\partial \omega_{mi}}{\partial x_j}\right)\left(\frac{\partial \omega_{di}}{\partial x_j}\right)+\varepsilon_1\left(\frac{\partial \omega_{di}}{\partial x_j}\right)\left(\frac{\partial \omega_{mi}}{\partial x_j}\right)+\frac{{\varepsilon_1}^2}{2}\left(\frac{\partial \omega_{di}}{\partial x_j}\right)\left(\frac{\partial \omega_{di}}{\partial x_j}\right)\right]$$

The higher powers of ε are dropped from the above expression, and term 3 is simplified as,

$$=-\frac{2\varepsilon_1}{Re}\left(\frac{\partial \omega_{mi}}{\partial x_j}\right)\left(\frac{\partial \omega_{di}}{\partial x_j}\right)$$

The order $O(\varepsilon)$ terms from simplified expressions of terms 1-3 and the left hand side of Eq. (B.9) are equated to obtain the linearized disturbance enstrophy transport equation as,

$$\frac{D\Omega_d}{Dt}=\omega_{mi}\omega_{mj}\frac{\partial u_{di}}{\partial x_j}+\omega_{mi}\omega_{dj}\frac{\partial u_{mi}}{\partial x_j}+\omega_{di}\omega_{mj}\frac{\partial u_{mi}}{\partial x_j}+\frac{1}{Re}\frac{\partial^2\Omega_d}{\partial x_j\partial x_j}$$
$$-\frac{2}{Re}\left(\frac{\partial \omega_{mi}}{\partial x_j}\right)\left(\frac{\partial \omega_{di}}{\partial x_j}\right) \tag{B.10}$$

References

Abderrahaman-Elena, N., Fairhall, C. T., and Garciá-Mayoral, R. (2019). Modulation of near-wall turbulence in the transitionally rough regime. *Journal of Fluid Mechanics*, 865:1042–1071.

Abdessemed, N., Sherwin, S. J., and Theofilis, V. (2009). Linear instability analysis of low pressure turbine flows. *Journal of Fluid Mechanics*, 628:57–83.

Alam, M. and Sandham, N. D. (2000). Direct numerical simulation of 'short' laminar separation bubbles with turbulent reattachment. *Journal of Fluid Mechanics*, 410:1–28.

Allen, L. and Bridges, T. J. (2002). Numerical exterior algebra and the compound matrix method. *Numer. Math.*, 92:197–232.

Ashpis, D. E. and Reshotko, E. (1990). Vibrating problem revisited. *Journal of Fluid Mechanics*, 213:531–547.

Balzer, W. and Fasel, H. F. (2016). Numerical investigation of the role of free-stream turbulence in boundary-layer separation. *Journal of Fluid Mechanics*, 801:289–321.

Banieghbal, M. R., Curtis, E. M., Denton, J. P., Hodson, H. P., Huntsman, I., Schulte, V., Harvey, N. W., and Steele, A. (1996). Wake passing in LP turbine blades. *AGARD-CP*, 571.

Barbarossa, F., Parry, A., Green, J., and Di Mare, L. (2016). An Aerodynamic Parameter for Low-Pressure Turbine Flutter. *Journal of Turbomachinery*, 138:051001.

Barkley, D., Blackburn, H. M., and Sherwin, S. J. (2008). Direct optimal growth analysis for timesteppers. *International Journal of Numerical Methods in Fluids*, 57:1435–1458.

Batchelor, G. K. (1969). Computation of the energy spectrum in homogeneous two-dimensional decaying turbulence. *Phys. Fluids*, 12:233–239.

Batchelor, G. K. (1988). *An Introduction to Fluid Dynamics*. Cambridge University Press, UK.

Bendiksen, O. and Friedmann, P. (1980). Coupled Bending-Torsion Flutter in Cascades. *AIAA Journal*, 18:194–201.

Bentley, J. L. (1975). Multidimensional Binary Search Trees Used for Associative Searching. *Communications ACM*, 18:509–517.

Betchov, R. and Criminale Jr., W. O. (1967). *Stability of Parallel Flows*. Academic Press, New York, USA.

Bhaganagar, K., Kim, J., and Coleman, G. (2004). Effect of Roughness on Wall-Bounded Turbulence. *Flow, Turbulence and Combustion*, 72:463–492.

Bhaumik, S. and Sengupta, T. K. (2014). Precursor of transition to turbulence: Spatiotemporal wave front. *Physical Review E.*, 89(4):043018.

Bhaumik, S. and Sengupta, T. K. (2015). A new velocity-vorticity formulation for direct numerical simulation of 3D transitional and turbulent flows. *Journal of Computational Physics*, 284:230–260.

Bhaumik, S. and Sengupta, T. K. (2017). Impulse response and spatio-temporal wave-packets: The common feature of rogue waves, tsunami and transition to turbulence. *Physics of Fluids*, 29:124103.

Biau, D. and Bottaro, A. (2008). An optimal path to transition in a duct. *Philosophical Transactions of the Royal Society A: Mathematical, Physical and Engineering Sciences*, 367.

Bisset, D. K., Antonia, R. A., and Browne, L. W. B. (1990). Spatial organization of large structures in the turbulent far wake of a cylinder. *Journal of Fluid Mechanics*, 218:439–461.

Blackburn, H. M., Barkley, D., and Sherwin, S. J. (2008). Convective instability and transient growth in flow over a backward-facing step. *Journal of Fluid Mechanics*, 603:271–304.

Boberg, L. and Brosa, U. (1988). Onset of turbulence in a pipe. *Z. Naturforsch. A*, 43:697–726.

Bons, J. (2010). A review of surface roughness effects in gas turbines. *Journal of Turbomachinery*, 132:021004.

Bottaro, A., Corbett, P., and Luchini, P. (2003). The effect of base flow variation on flow stability. *Journal of Fluid Mechanics*, 476:293–302.

Brandt, L., Cossu, C., Chomaz, J. M., Huerre, P., and Henningson, D. (2003). On the convectively unstable nature of optimal streaks in boundary layers. *Journal of Fluid Mechanics*, 485:221–242.

Brandt, L. and de Lange, H. C. (2008). Streak interactions and breakdown in boundary layer flows. *Physics of Fluids*, 20:024107.

Brandt, L., Schlatter, P., and Henningson, D. (2004). Transition in boundary layers subject to free-stream turbulence. *Journal of Fluid Mechanics*, 517:167–198.

Brandt, L., Sipp, D., Pralits, J. O., and Marquet, O. (2011). Effect of base-flow variation in noise amplifiers: the flat-plate boundary layer. *Journal of Fluid Mechanics*, 687:503–528.

Bridges, T. J. and Morris, P. (1984). Differential eigenvalue problems in which the parameters appear nonlinearly. *Journal of Computational Physics*, 55:437–460.

Brillouin, L. (1960). *Wave Propagation and Group Velocity*. Academic Press, New York, UK.

Brinckman, K. W. and Walker, J. D. A. (2001). Instability in a viscous flow driven by streamwise vortices. *Journal of Fluid Mechanics*, 432:127–166.

Brinkerhoff, J. and Yaras, M. (2011). Interaction of viscous and inviscid instability modes in separation-bubble transition. *Physics of Fluids*, 23:124102.

Briscolini, M. and Santangelo, P. (1989). Development of the mask method for incompressible unsteady flows. *Journal of Computational Physics*, 84:57–75.

Brown, G. L. and Roshko, A. (1974). On density effects and large structures in turbulent mixing layers. *Journal of Fluid Mechanics*, 64(4):774–816.

Bucci, M. A., Puckert, D. K., Andriano, C., Loiseau, J. C., Cherubini, S., and Rist, U. (2018). Roughness-induced transition by quasi-resonance of a varicose global mode. *Journal of Fluid Mechanics*, 836:167–191.

Buffum, D. H., Capece, V. R., King, A. J., and El-Aini, Y. M. (1998). Oscillating Cascade Aerodynamics at Large Mean Incidence. *ASME Journal*, 120:122–130.

Busse, A., Lützner, M., and Sandham, N. D. (2015). Direct numerical simulation of turbulent flow over a rough surface based on a surface scan. *Computers and Fluids*, 116:129–147.

Buter, T. A. and Reed, H. L. (1993). Numerical investigation of receptivity to freestream vorticity. *AIAA Journal*, pages AIAA–93–0073.

Butler, K. M. and Farrell, B. F. (1992). Three-dimensional optimal perturbations in viscous shear flow. *Physics of Fluids*, 4:1637–1650.

Chakraborty, P., Balachandar, S., and Adrian, J. (2005). On the relationships between local vortex identification schemes. *Journal of Fluid Mechanics*, 535:189–214.

Chaudhari, M. (1996). Boundary layer receptivity to three-dimensional unsteady vortical disturbances in free stream. *AIAA Journal*, pages AIAA–96–0181.

Cherubini, S., De Palma, P., Robinet, J. C., and Bottaro, A. (2011). The minimal seed of turbulent transition in the boundary layer. *Journal of Fluid Mechanics*, 689:221–253.

Cherubini, S., De Palma, P., Robinet, J. C., and Bottaro, A. (2012). A purely nonlinear route to transition approaching the edge of chaos in a boundary layer. *Fluid Dynamics Research*, 44:031404.

Cherubini, S., Robinet, J. C., Bottaro, A., and De Palma, P. (2010). Optimal wave packets in a boundary layer and initial phases of a turbulent spot. *Journal of Fluid Mechanics*, 656:231–259.

Chong, M. S., Perry, A. E., and Cantwell, B. J. (1990). A general classification of three-dimensional flow fields. *Physics of Fluids*, 2(5):765–777.

Collis, S. S. and Lele, S. K. (1996). A computational approach to swept leading-edge receptivity. *AIAA Journal*, pages AIAA–96–0180.

Corral, R. and Vega, A. (2015). The Low Reduced Frequency Limit of Vibrating Airfoils. Part I: Theoretical Analysis. *Journal of Turbomachinery*, 138(2):021004.

Coull, J. and Hodson, H. (2011). Unsteady boundary-layer transition in low-pressure turbines. *Journal of Fluid Mechanics*, 681:370–410.

Crouch, J. D. (1992). Non-localized receptivity of boundary layers. *Journal of Fluid Mechanics*, 244:567–581.

Culler, E. C., Fagley, C., Seidel, J., McLaughlin, T. E., and Farnsworth, J. A. (2017). Developing a reduced order model from structural kinematic measurements of a flexible finite span wing in stall flutter. *Journal of Fluids and Structures*, 71:56–69.

Daviaud, F., Bonetti, M., and Dubois, M. (1990). Transition to turbulence via spatiotemporal intermittency in one-dimensional rayleigh-benard convection. *Phys. Rev. A*, 42:3388.

Davide, L., Simoni, D., Ubaldi, M., Zunino, P., and Bertini, F. (2017). Coherent structures formation during wake-boundary layer interaction on a lp turbine blade. *Flow, Turbulence and Combustion*, 98:57–81.

Davies, S. J. and White, C. M. (1928). An experimental study of the flow of water in pipes of rectangular section. *Proc. Roy. Soc. Lond. A*, 119:92–107.

Degani, A. T., Walker, J. D. A., and Smith, F. T. (1998). Unsteady separation past moving surfaces. *Journal of Fluid Mechanics*, 375:1–38.

del Álamo, J. C., Jiménez, J., Zandonade, P., and Moser, R. D. (2006). Self-similar vortex clusters in the turbulent logarithmic region. *Journal of Fluid Mechanics*, 561:329–358.

Dietz, A. J. (1999). Local boundary layer receptivity to a convected free stream disturbance. *Journal of Fluid Mechanics*, 378:291–317.

Diwan, S. and Ramesh, O. (2009). On the origin of the inflectional instability of a laminar separation bubble. *Journal of Fluid Mechanics*, 629:263–298.

Doering, C. R. and Gibbon, J. D. (1995). *Applied Analysis of the Navier-Stokes Equations*. Cambridge University Press, UK.

Doligalski, T. L., Smith, C. R., and Walker, J. D. A. (1994). Vortex interaction with wall. *Annual Review of Fluid Mechanics*, 26:573–616.

Dovgal, A., Kozlov, V., and Michalke, A. (1994). Laminar boundary layer separation: instability and associated phenomena. *Progress in Aerospace Sciences*, 30(1):61–94.

Dowell, E. H., Peters, D. A., Clark, R., Scanlan, R., Cox, D., Simiu, E., Curtiss Jr., H. C., Sisto, F., Edwards, J. W., Hall, K. C., and Strganac, T. W. (2004). *A Modern Course in Aeroelasticity*. Kluwer Academic Publishers, USA.

Drazin, P. G. and Reid, W. H. (1981). *Hydrodynamic Stability*. Cambridge University Press, UK.

Durbin, P., Zaki, T., and Liu, Y. (2009). Interaction of discrete and continuous boundary layer modes to cause transition. *International Journal of Heat and Fluid Flow*, 30:403–410.

Eckhardt, B., Schneider, T. M., Hof, B., and Westerweel, J. (2007). Turbulence transition in pipe flow. *Annual Review of Fluid Mechanics*, 39:447–468.

Ehrenstein, U. and Gallaire, F. (2008). Two-dimensional global low-frequency oscillations in a separating boundary layer flow. *Journal of Fluid Mechanics*, 614:315–327.

EIA, U. (2013). Annual energy outlook. *US Energy Information Administration, Washington, DC*, pages 60–62.

Farrell, B. F. (1988). Optimal excitation of perturbations in viscous shear flow. *Physics of Fluids*, 31:2093–2101.

Fjørtoft, R. (1950). Application of integral theorems in deriving criteria of stability for laminar flows and for baroclinic circular vortex. *Geofys. Publ. Oslo*, 17(6):1–51.

Gaitonde, D. V. and Visbal, M. R. (1998). High-order Schemes for Navier-Stokes equations: Algorithm and implementation into FDL3DI. *Technical Report*, pages AFRL–VA–WP–TR–1998–3060.

Garai, A., Diosady, L. T., Murman, S. M., and Madavan, N. K. (2018). Scale-resolving simulations of bypass transition in a high-pressure turbine cascade using a spectral element discontinuous galerkin method. *Journal of Turbomachinery*, 140:031004.

Gaster, M. (1965). On the generation of spatially growing waves in a boundary layer. *Journal of Fluid Mechanics*, 22:433.

Gaster, M. (1967). The structure and behaviour of separation bubbles. *Aeronautical Research Council, Reports and Memoranda*, 3595:1–31.

Gaster, M. and Grant, I. (1975). An experimental investigation of the formation and development of a wave packet in a laminar boundary layer. *Proceedings of the Royal Society of London Series A*, 347:253–269.

Gaster, M., Grosch, C. E., and Jackson, T. L. (1994). The velocity created by a shallow bump in a boundary layer. *Phys. Fluids*, 6(9):3079–3085.

Goldstein, D., Handler, R., and Sirovich, L. (1993). Modeling no-slip flow boundary with an external force field. *Journal of Computational Physics*, 105:354–366.

Goldstein, M. E. (1985). Scattering of acoustic waves into Tollmien-Schlichting waves by small streamwise variation in surface geometry. *Journal of Fluid Mechanics*, 154:509–529.

Goldstein, M. E. and Hultgren, L. S. (1989). Boundary layer receptivity to long-wave free-stream disturbances. *Annual Review of Fluid Mechanics*, 21:137–166.

Gungor, A. G., Simens, M. P., and Jiménez, J. (2012). Direct numerical simulations of wake-perturbed separated boundary layers. *Journal of Turbomachinery*, 134:061024.

Gustavsson, L. H. (1991). Energy growth of three-dimensional disturbances in plane poiseulle flow. *Journal of Fluid Mechanics*, 224:241–260.

Hack, M. J. P. (2014). *Localized Instabilities of Klebanoff Streaks and the Influence of Time-Harmonic Wall Forcing on Bypass Transition*. PhD Thesis, Imperial College London, UK.

Häggmark, C. (2000). *Investigations of Disturbances Developing in a Laminar Separation Bubble Flow*. PhD thesis, KTH, Stockholm.

Haller, G. (2004). Exact theory of unsteady separation for two-dimensional flows. *Journal of Fluid Mechanics*, 512:257–311.

Haller, G. (2005). An objective definition of a vortex. *Journal of Fluid Mechanics*, 525:1–26.

Haller, G. (2015). Lagrangian coherent structures. *Annual Review in Fluid Mechanics*, 47:137–162.

Halstead, D., Wisler, D., Okiishi, T., Walker, G., Hodson, H., and Shin, H. (1997). Boundary layer development in axial compressors and turbines: Part 1 of 4 - composite picture. *Journal of Turbomachinery*, 119(1):114–127.

Hammond, D. A. abd Redekopp, L. G. (1998). Local and global instability properties of separation bubbles. *European Journal of Fluid Mechanics B*, 17:145–164.

He, L. (1996). Unsteady flow in oscillating turbine cascade Part 1. Linear cascade experiment. *ASME Journal*, pages 96–GT–374.

Heisenberg, W. (1924). Über stabilität und turbulenz von flüssigkeitsströmen. *Ann. Phys. Lpz.*, 379:577–627.

Herbert, T. (1998). Secondary instability of boundary layers. *Annual Review of Fluid Mechanics*, 20:487–526.

Himmel, C. G. (2010). *Ultra-High Lift Blades for Low Pressure Turbines*. PhD thesis, University of Cambridge, UK.

Hoffman, K. A. and Chiang, S. T. (1993). *Computational Fluid Dynamics for Engineers, Vol I*. Engineering Education System, Kansas.

Holmén, V. (2012). *Methods for Vortex Identification*. Masters thesis, Lund University, Sweden.

Horton, H. P. (1968). *Laminar Separation in Two- and Three-Dimensional Incompressible Flow*. PhD thesis, University of London, UK.

Hougne, P., Lemoult, F., Fink, M., and Lerosey, G. (2016). Spatiotemporal wave front shaping in a microwave cavity. *Physical Review Letters*, 117:134302.

Huerre, P. and Monkewitz, P. A. (1985). Absolute and convective instabilities in free shear layers. *Journal of Fluid Mechanics*, 159:151.

Hultgren, L. S. and Gustavsson, L. H. (1981). Algebraic growth of disturbances in a laminar boundary layer. *Physics of Fluids*, 24:1000–1004.

Hunt, J. C. R. and Durbin, P. A. (1999). Perturbed vortical layers and shear sheltering. *Fluid Dynamics Research*, 24:375–404.

Hunt, J. C. R., Wray, A. A., and Moin, P. (1988). Eddies, stream, and convergence zones in turbulent flows. *Center for Turbulence Research Report CTR-S88, Stanford University USA*, pages 193–208.

Hussain, F. (1983). Coherent structures - reality and myth. *Physics of Fluids*, 26(10):2816.

Hussain, F. (1986). Coherent structures and turbulence. *Journal of Fluid Mechanics*, 173:303–356.

Hussain, F. and Hayakawa, M. (1987). Eduction of large-scale organized structures in a turbulent plane wake. *Journal of Fluid Mechanics*, 180:193–229.

Iaccarino, G. and Verzicco, R. (2003). Immersed boundary technique for turbulent flow simulations. *Applied Mechanical Review*, 56(3):331–347.

Jacobs, R. G. and Durbin, P. A. (1998). Shear sheltering and the continuous spectrum of the Orr-Sommerfeld equation. *Physics of Fluids*, 10(8):2006–2011.

Jacobs, R. G. and Durbin, P. A. (2001). Simulations of bypass transition. *Journal of Fluid Mechanics*, 428:185–212.

Jahanmiri, M. (2011). Boundary layer transitional flow in gas turbines. *Research Report 2011:01*, pages ISSN 1652–8549. Division of Fluid Dynamics, Chalmers University of Technology, Sweden.

Jeong, J. and Hussain, F. (1995). On the identification of a vortex. *Journal of Fluid Mechanics*, 285:69–94.

Jeong, J., Hussain, F., Schoppa, W., and Kim, J. (1997). Coherent structures near the wall in a turbulent channel flow. *Journal of Fluid Mechanics*, 332:185–214.

Jiménez, J. (2018). Coherent structures in wall-bounded turbulence. *Journal of Fluid Mechanics*, 842:1–100.

Juniper, M. P. and Sujith, R. I. (2018). Sensitivity and nonlinearity of thermoacoustic oscillations. *Annual Review of Fluid Mechanics*, 50:661–689.

Kang, K. L. (2015). *Laminar-Turbulent transition spectral analysis and coherent structures of DNS wavepackets*. PhD thesis, National University of Singapore, Singapore.

Kang, K. L. and Yeo, K. S. (2013). The effect of wavepacket frequency bandwidth on the laminar-turbulent transition process in a blasius boundary layer. *AIAA Journal*, page 2615.

Kang, K. L. and Yeo, K. S. (2017). Hybrid pod-fft analysis of nonlinear evolving coherent structures of dns wavepacket in laminar-turbulent transition. *Phys. Fluids*, 29:084105.

Kang, K. L. and Yeo, K. S. (2020). Combined effects of amplitude, frequency and bandwidth on wavepackets in laminar turbulent transition. *Comput. Fluids*, 197:104358.

Karaca, S. and Gungor, A. G. (2003). Dns of fully turbulent flow in a LPT passage. *International Journal of Heat and Fluid Flow*, 24:636–644.

Karaca, S. and Gungor, A. G. (2016). Dns of unsteady effects on the control of laminar separated boundary layers. *European Journal of Mechanics B*, 56:71–81.

Karman, T. V. (1921). Über laminare und turbulente reibung. *ZAMM J. Appl. Math. and Mech./Zeitschrift für Angewandte Mathematik und Mechanik*, 1(4):233–252.

Kawahara, G., Uhlmann, M., and van Veen, L. (2012). The significance of simple invariant solutions in turbulent flows. *Annual Review of Fluid Mechanics*, 44:203–225.

Kendall, J. M. (1987). Experimental study of laminar boundary layer receptivity to a traveling pressure field. *AIAA Conference paper*, pages AIAA–87–1257.

Kerswell, R. R. (2005). Recent progress in understanding the transition to turbulence in a pipe. *Nonlinearity*, 18:17–44.

Kerswell, R. R. (2018). Nonlinear nonmodal stability theory. *Annual Review of Fluid Mechanics*, 50:319–345.

Kirschner, A., Pelet, C., and Gyamarthy, G. (1976). Investigation of blade flutter in a fubsonic turbine. *Revue Francaise de M ècanique, numèro spècial*, pages 97–104.

Kitsios, V., Rodriguez, D., Theofilis, V., Ooi, A., and Soria, J. (2009). Biglobal stability analysis in curvilinear coordinates of massively separated lifting bodies. *Journal of Computational Physics*, 228:7181–7196.

Klebanoff, P. S., Cleveland, W. G., and Tidstrom, K. D. (1992). On the evolution of a turbulent boundary layer induced by a three-dimensional roughness element. *Journal of Fluid Mechanics*, 237:101–187.

Klebanoff, P. S. and Tidstrom, K. D. (1972). Mechanism by which a two-dimensional roughness element induces boundary-layer transition. *Physics of Fluids*, 15(7):1173–1188.

Klebanoff, P. S., Tidstrom, K. D., and Sargent, L. M. (1962). The three-dimensional nature of boundary-layer instability. *Journal of Fluid Mechanics*, 12:1–34.

Kline, S. J., Reynolds, W. C., Schraub, F. A., and Runstadler, P. W. (1967). The structure of turbulent boundary layers. *Journal of Fluid Mechanics*, 30(4):741–771.

Kolár, V. (2007). Vortex identification: New requirements and limitations. *International Journal of Heat and Fluid Flow*, 30(4):638–652.

Kondacki, H. and Abouraddy, A. (2019). Optical space-time wave packets having arbitrary group velocities in free space. *Nature Communications*, 10:929.

Kraichnan, R. H. and Montgomery, D. (1980). Two-dimensional turbulence. *Repts. Prog. Phys.*, 43:547–619.

Kreilos, T., Khapko, T., Schlatter, P., Duguet, Y., Henningson, D., and Eckhardt, B. (2016). Bypass transition and spot nucleation in boundary layers. *Physical Review Fluids*, 1:043602.

Landahl, M. T. (1980). A note on an algebraic instability of inviscid parallel shear flows. *Journal of Fluid Mechanics*, 98:243–251.

Landahl, M. T. and Mollo-Christensen, E. (1992). *Turbulence and Random Processes in Fluid Mechanics*. Cambridge University Press, Cambridge, UK.

Landau, L. D. and Lifshitz, E. M. (1959). *Fluid Mechanics, VI*. Addison-Wesley, Pergamon Press, London, UK.

Lardeau, S., Leschinzer, M., and Zaki, T. (2012). Large eddy simulation of transitional separated flow over a flat plate and a compressor blade. *Flow, turbulence and combustion*, 88:19–44.

Leib, S. J., Wundrow, D. W., and Goldstein, M. E. (1999). Generation and growth of boundary layer disturbances due to free-stream turbulence. *AIAA Conference paper*, pages AIAA–99–0408.

Leonardi, S., Tessicini, F., Orlandi, P., and Antonia, R. (2006). Direct numerical and Large-Eddy simulations of turbulent flows over rough surfaces. *AIAA Journal*, 44(11):2482–2487.

Licari, A. and Christensen, K. (2011). Modeling cumulative surface damage and assessing its impact on wall turbulence. *AIAA Journal*, 49:2305–2320.

Lim, T. T., Sengupta, T. K., and Chattopadhyay, M. (2004). A visual study of vortex-induced subcritical instability on a flat plate laminar boundary layer. *Experiments in Fluids*, 37:47–55.

Lin, N., Stuckert, G. K., and Herbert, T. (1995). Boundary layer receptivity to free-stream vortical disturbances. *AIAA Journal*, pages AIAA–95–0772.

Liu, X. and Rodi, W. (1991). Experiments on transitional boundary layers with wake induced unsteadiness. *Journal of Fluid Mechanics*, 231:229–256.

Liu, Y., Zaki, T. A., and Durbin, P. A. (2008). Boundary-layer transition by interaction of discrete and continuous modes. *Journal of Fluid Mechanics*, 604:199–233.

Logan, E. J. and Roy, R. (2003). *Handbook of Turbomachinery*. Marcell Decker Inc., New York.

Lou, W. and Hourmouziadis, J. (2000). Separation bubbles under steady and periodic unsteady main flow conditions. *Journal of Turbomachinery*, 122:634–643.

Luchini, P. and Bottaro, A. (2014). Adjoint equations in stability analysis. *Annual Review of Fluid Mechanics*, 46:493–517.

Lugt, H. J. (1979). The dilemma of defining a vortex. *In Recent Developments in Theoretical and Experimental Fluid Mechanics, eds. U. Müller, K. G. Roesner and B. Schmidt*, pages 309–321.

Mack, L. M. (1984). Boundary layer stability theory. special course on. *Stability and Transition of Laminar Flow*, page AGARD Report No. 709.

Mao, X., Zaki, T. A., Sherwin, S. J., and Blackburn, H. M. (2017). Transition induced by linear and nonlinear perturbation growth in flow past a compressor blade. *Journal of Fluid Mechanics*, 820:604–632.

Marquet, O., Sipp, D., Chomaz, J. M., and Jacquin, L. (2008). Amplifier and resonator dynamics of a low reynolds number recirculation bubble in a global framework. *Journal of Fluid Mechanics*, 605:429–443.

Matsubara, M. and Alfredsson, P. H. (2001). Disturbance growth in boundary layers subjected to free-stream turbulence. *Journal of Fluid Mechanics*, 430:149–168.

McAuliffe, B. and Yaras, M. (2010). Transition mechanisms in separation bubbles under low and elevated freestream turbulences. *Journal of Turbomachinery*, 132:011004.

McWilliams, J. C. (1984). The emergence of isolated coherent vortices in turbulent flow. *Journal of Fluid Mechanics*, 146:21–43.

Michelassi, V., Wissink, J., Fröhlich, J., and Rodi, W. (2003). Large-eddy simulation of flow around low-pressure turbine blade with incoming wakes. *AIAA Journal*, 41:2143–2156.

Mittal, R. and Iaccarino, G. (2005). Immersed Boundary Methods. *Annual Review of Fluid Mechanics*, 37:239–261.

Monin, A. S. and Yaglom, A. M. (1971). *Statistical Fluid Mechanics: Mechanics of Turbulence*. The MIT Press, Cambridge, MA.

Monokrousos, A., Bottaro, A., Brandt, L., Di Vita, A., and Henningson, D. S. (2011). Nonequilibrium thermodynamics and the optimal path to turbulence in shear flows. *Physical Review Letters*, 106:134502.

Monokrousos, A., Brandt, L., Schlatter, P., and Henningson, D. S. (2008). Dns and les of estimation and control of transition in boundary layers subject to free-stream turbulence. *International Journal of Heat and Fluid Flow*, 29:841–855.

Montomoli, F., Hodson, H., and Haselbach, F. (2010). Effect of roughness and unsteadiness on the performance of a new LPT blade at low Reynolds numbers. *Journal of Turbomachinery*, 132:03108.

Morkovin, M. V. (1969). On the many faces of transition. In *Viscous Drag Reduction*, pages 1–31. Springer US.

Morkovin, M. V. (1991). Panoramic view of changes in vorticity distribution in transition, instabilities and turbulence. *Transition to Turbulence (Eds. D. C. Reda, H. L. Reed and R. Kobyashi), ASME FED Publication*, 114:1–12.

Morkovin, M. V. (1993). *Bypass-Transition Research: Issues and Philosophy*, pages 3–30. Springer Netherlands, Dordrecht.

Mu, M., Sun, L., and Dijistra, H. A. (2004). The sensitivity and stability of the ocean's thermohaline circulation to finite-amplitude perturbations. *J. Phys. Oceanogr.*, 34:2305–2315.

Nagarajan, S., Lele, S. K., and Ferziger, J. H. (2003). A robust high-order compact method for large eddy simulation. *Journal of Computational Physics*, 191:392–419.

Ng, B. S. and Reid, W. H. (1980). On the numerical solution of the orr-sommerfeld problem: Asymptotic initial conditions for shooting method. *Journal of Computational Physics*, 38:275–293.

Ng, B. S. and Reid, W. H. (1985). The compound matrix method for ordinary differential systems. *Journal of Computational Physics*, 58:209–228.

Nowinski, M. and Panovsky, J. (2000). Flutter Mechanisms in Low Pressure Turbine Blades. *ASME Journal of Engineering for Gas Turbines and Power*, 122:82–87.

Obrist, D. and Schmid, P. J. (2003). On the linear stability of swept attachment-line boundary layer flow. part 2. non-modal effects and receptivity. *J. Fluid Mech.*, 493:31–58.

Olvera, D. and Kerswell, R. R. (2017). Optimising energy growth as a tool for finding exact coherent structures. *Phys. Rev. Fluids*, 2:083902.

Onoue, K. and Breuer, K. S. (2016). Vortex formation and shedding from a cyber-physical pitching plate. *Journal of Fluid Mechanics*, 793:229–247.

Opoka, M. M. and Hodson, H. P. (2008). Experimental investigation of unsteady transition processes on high-lift T106A turbine blades. *Journal of Propulsion and Power*, 24(3):424–432.

Orr, W. M. (1907). The stability or instability of the steady motions of a perfect liquid and of a viscous liquid. part I: A perfect liquid. part II: A viscous liquid. *Proc. Roy. Irish Acad. A*, 27:9–68.

Panovsky, J. and Kielb, R. E. (2000). A Design Method to Prevent Low Pressure Turbine Blade Flutter. *ASME Journal of Engineering for Gas Turbines and Power*, 122(1):89–98.

Papoulis, A. (1962). *Fourier Integral and its Application*. McGraw Hill, New York, USA.

Peng, C. and Vahdati, M. (2002). The Effects of Fundamental Mode Shapes on Flutter Stability of an Aero Engine Compressor Blade: Introduction of a Modified Reduced Frequency Parameter. *Proceedings of the 7th National Turbine Engine High Cycle Fatigue Conference*.

Perry, A. E. and Chong, M. S. (1987). A description of eddying motions and flow patterns using critical-point concepts. *Annual Review of Fluid Mechanics*, 19:125–155.

Peskin, C. (1977). Numerical analysis of blood flow in the heart. *Journal of Computational Physics*, 25(3):220 – 252.

Pope, S. B. (2000). *Turbulent Flows*. Cambridge University Press, UK.

Pringle, C. C. T. and Kerswell, R. R. (2010). Using nonlinear transient growth to construc the minimal seed for shear flow turbulence. *Physical Review Letter*, 105:154502.

Rajpoot, M., Sengupta, T. K., and Dutt, P. K. (2010). Optimal time advancing dispersion relation preserving schemes. *Journal of Computational Physics*, 229:3623–3651.

Raudkivi, A. J. and Callander, R. A. (1975). *Advanced Fluid Mechanics: An Introduction*. Edward Arnold, USA.

Rayleigh, L. (1880). On the stability, or instability, of certain fluid motions. *Proc. Lond. Math. Soc.*, 11:57–70.

Rayleigh, L. (1889). *Scientific Papers I*. Cambridge Univ. Press, UK.

Rayleigh, L. (1890). *Scientific Papers II*. Cambridge Univ. Press, UK.

Reddy, S. C. and Henningson, D. S. (1993). Energy growth in viscous channel flows. *Journal of Fluid Mechanics*, 252:209–238.

Reddy, S. C., Schmid, P. J., and Henningson, D. S. (1993). Pseudospectra of the orr-sommerfeld operator. *SIAM J. Appl. Math.*, 53:15–47.

Reshotko, E. (1976). Boundary layer stability and transition. *Annual Review of Fluid Mechanics*, 8:311–349.

Reshotko, E. (1994). Boundary layer instability, transition and control. *AIAA Journal*, pages AIAA–94–0001.

Reshotko, E. (1997). Progress, accomplishments and issues in transition research. *AIAA Journal*, pages AIAA–97–1815.

Reshotko, E. (2001). Transient growth: a factor in bypass transition. *Physics of Fluids*, 13:1067–1075.

Reynolds, O. (1883). An experimental investigation of the circumstances which determine whether the motion of water shall be direct or sinuous and of the law of resistance in parallel channels. *Phil. Trans. Roy. Soc.*, 174:935–982.

Roberts, S. and Yaras, M. (2005). Boundary-layer transition affected by surface roughness and free-stream turbulence. *Journal of Fluids Engineering*, 127:449–457.

Robinson, S. K. (1991). Coherent motions in the turbulent boundary layer. *Annual Review of Fluid Mechanics*, 23:601–639.

Roman, K. M. (2002). *The Effect of Selective Roughness and Wake Unsteadiness on the Performance of Low Pressure Turbine Blades*. Master's thesis, University of Cambridge, UK.

Ruban, A. I. (1985). On the generation of Tollmien-Schlichting waves by sound. *Translated from Izvestiya Akademii Nauk SSSR, Mekhanika Zhidkosti i Gaza, Fluid Dyn.*, 5:44–52.

Sakamoto, S., Murakami, S., Kato, S., and Mochida, A. (1993). Unsteady Pressure Field around Oscillating Prism predicted by LES. *Journal of Wind Engineering and Industrial Aerodynamics*, 47:551–556.

Saric, W., Reed, H., and Kerschen, E. J. (2002). Boundary layer receptivity to free-stream disturbances. *Annual Review of Fluid Mechanics*, 34:291–319.

Saric, W., West, D., Tufts, M., and Reed, H. (2019). Experiments on discrete roughness element technology for swept-wing laminar flow control. *AIAA Journal*, 57(2):641–654.

Saric, W., White, E. B., and Reed, H. (1999). Boundary-layer receptivity to freestream disturbances and its role in transition. *AIAA Journal*, pages AIAA–99–3788.

Sarkar, S. (2008). Identification of flow structures on a LP turbine blade due to periodic passing wakes. *Journal of Fluids Engineering*, 130:061103.

Schlatter, P., Brandt, L., de Lange, H. C., and Henningson, D. S. (2008). On streak breakdown in bypass transition. *Physics of Fluids*, 20:101505.

Schlichting, H. (1933). Zur enstehung der turbulenz bei der plattenströmung. *Nach. Gesell. d. Wiss. z. Gött*, MPK:181–208.

Schlichting, H. and Gersten, K. (2017). *Boundary-Layer Theory*. Springer-Verlag, Berlin, Heidelberg.

Schmid, P. J. (2007). Nonmodal stability theory. *Annual Review of Fluid Mechanics*, 39:129–162.

Schmid, P. J. and Brandt, L. (2014). Analysis of fluid systems: Stability, receptivity, sensitivity. *Applied Mechanics Reviews*, 66:024803.

Schmid, P. J. and Henningson, D. S. (2001). *Stability and Transition in Shear Flow*. Springer-Verlag, New York, USA.

Schubauer, G. B. and Skramstad, H. K. (1947). Laminar boundary layer oscillations and the stability of laminar flow. *Journal of Aerospace Science*, 14:69–78.

Schulte, V. and Hodson, H. (1998). Unsteady wake-induced boundary layer transition in high lift LP turbines. *Journal of Turbomachinery*, 120:28–35.

Scillitoe, A., Tucker, P. G., and Adami, P. (2019). Large eddy simulation of boundary layer transition mechanisms in a gas-turbine compressor cascade. *Journal of Turbomachinery*, 141:061008.

Scott, M. R. and Watts, H. A. (1977). Computational solution of linear two point boundary value problems via orthonormalization. *SIAM Journal of Numerical Analysis*, 14(1):40–70.

Sengupta, A., Suman, V. K., and Sengupta, T. K. (2019a). Direct numerical simulation of vortex-induced instability for a zero-pressure-gradient boundary layer. *Phys. Rev. E*, 100:033118.

Sengupta, A., Suman, V. K., Sengupta, T. K., and Bhaumik, S. (2018a). An Enstrophy-Based Linear and Nonlinear Receptivity Theory. *Physics of Fluids*, 30:054106.

Sengupta, A., Sundaram, P., and Sengupta, T. K. (2020). Nonmodal nonlinear route of transition to two-dimensional turbulence. *Physical Review Research*, 2(1):012033.

Sengupta, A., Vadlamani, N. R., and Tucker, P. G. (2017). Roughness induced transition in low pressure turbines. *Presented in AIAA Conference*.

Sengupta, T. K. (1992). Solution of the orr-sommerfeld equation for high wave numbers. *Computers and Fluids*, 21(2):302–304.

Sengupta, T. K. (2012). *Instabilities of Flows and Transition to Turbulence*. CRC Press, Taylor and Francis Group, Florida, USA.

Sengupta, T. K. (2013). *High Accuracy Computing Methods: Fluid Flows and Wave Phenomena*. Cambridge University Press, New York, USA.

Sengupta, T. K., Ballav, M., and Nijhawan, S. (1994). Generation of tollmien-schlichting waves by harmonic excitation. *Physics of Fluids*, 6(3):1213–1222.

Sengupta, T. K. and Bhaumik, S. (2011). Onset of turbulence from the receptivity stage of fluid flows. *Physical Review Letter*, 107(15):154501.

Sengupta, T. K. and Bhaumik, S. (2019). *DNS of Wall-Bounded Turbulent Flows*. Springer Nature, Singapore.

Sengupta, T. K., Chattopadhyay, M., Wang, Z. Y., and Yeo, K. S. (2002). Bypass mechanism of transition to turbulence. *Journal of Fluids and Structures*, 16:15–29.

Sengupta, T. K., De, S., and Sarkar, S. (2003). Vortex-induced instability of an incompressible wall-bounded shear layer. *Journal of Fluid Mechanics*, 493:277–286.

Sengupta, T. K., Kameswara Rao, A., and Venkatasubbaiah, K. (2006a). Spatio-temporal growth of disturbances in a boundary layer and energy based receptivity analysis. *Physics of Fluids*, 18(9):094101.

Sengupta, T. K., Kameswara Rao, A., and Venkatasubbaiah, K. (2006b). Spatiotemporal growing wave fronts in spatially stable boundary layers. *Physical Review Letter*, 96(22):224504.

Sengupta, T. K., Sharma, N., and Sengupta, A. (2018b). Non-linear instability analysis of the two-dimensional Navier-Stokes equation: The Taylor-Green vortex problem. *Physics of Fluids*, 30:054105.

Sengupta, T. K., Sharma, P., Sengupta, A., and Suman, V. K. (2019b). Tracking disturbances in transitional and turbulent flows: Coherent structures. *Physics of Fluids*, 31:124106.

Sengupta, T. K., Singh, H., Bhaumik, S., and Chowdhury, R. R. (2013). Diffusion in inhomogeneous flows: Unique equilibrium state in an internal flow. *Computers and Fluids*, 88:440–451.

Sharma, A. S., Abdessemend, N., Sherwin, S. J., and Theofilis, V. (2011). Transient growth mechanisms of low reynolds number flow over a low-pressure turbine blade. *Theoretical and Computational Fluid Dynamics*, 25:19–30.

Sieg, S. (2000). High Cycle Fatigue and the War Fighter. *Proceedings 5th National Turbine Engine High Cycle Fatigue Conference, Chandler, Arizona, USA*.

Simens, M. (2008). *The Study and Control of Wall-Bounded Flows*. PhD thesis, Dept. of Aeronautics, University Polit/'echnica De Madrid, Spain.

Simens, M. and Gungor, A. (2013). The effect of surface roughness on laminar separated boundary layers. *Journal of Turbomachinery*, 136:031014.

Simoni, D., Ubaldi, M., Zunino, P., Lengani, D., and Bertini, F. (2012). An experimental investigation of the separated-flow transition under high-lift turbine blade pressure gradients. *Flow, Turbulence and Combustion*, 88:45–62.

Smith, C. R. (1993). Use of 'kernel' experiments for modeling of near-wall turbulence. *In Near Wall Turbulent Flows (Eds.: R.M.C. So, C.G. Speziale and B.E. Launders), Elsevier, Amsterdam, Holland*, pages 33–42.

Smith, C. R., Walker, J. D. A., Haidari, A. H., and Soburn, U. (1991). On the dynamics of near-wall turbulence. *Philosophical Transactions of the Royal Society of London A*, 336:131–175.

Sommerfeld, A. (1908). Ein beitrag zur hydrodynamiscen erklarung der turbulenten flussigkeitbewegung. *Proc. 4th Int. Cong. Mathematicians, Rome*, pages 116–124.

Sommerfeld, A. (1949). *Partial Differential Equation in Physics*. Academic Press, New York.

Spalart, P. and Strelets, M. (2000). Mechanisms of transition and heat transfer in a separation bubble. *Journal of Fluid Mechanics*, 403:329–349.

Srinivasan, A. V. (1997). Flutter and Resonant Vibration Characteristics of Engine Blades. *ASME Journal of Engineering for Gas Turbines and Power*, 119:742–775.

Stieger, R. D. (2002). *The Effects of Wakes on Separating Boundary Layers in Low Pressure Turbines*. PhD thesis, University of Cambridge, UK.

Stieger, R. D. and Hodson, H. (2004). The transition mechanism of highly loaded low-pressure turbine blades. *Journal of Turbomachinery*, 126:536–543.

Sundaram, P., Sengupta, T. K., and Bhaumik, S. (2018). The three-dimensional impulse response of a boundary layer to different types of wall excitation. *Physics of Fluids*, 30:124103.

Szèchènyi, E. (1985). Fan Blade Flutter-Single Blade Instability or Blade to Blade Coupling? *ASME Journal*, 126:85–GT–216.

Taylor, G. I. (1936). Statistical theory of turbulence. V. Effects of turbulence on boundary layer. *Proceedings of the Royal Society A*, 156(888):307–317.

Telionis, D. P. (1981). *Unsteady Viscous Flows*. Springer Series in Computational Physics, Springer, Berlin, Heidelberg.

Theofilis, V. (2011). Global linear instability. *Annu. Rev. Fluid Mech.*, 43:319–352.

Theofilis, V., Hein, S., and Dallmann, U. C. (2000). On the origins of unsteadiness and three-dimensionality in a laminar separation bubble. *Philos. Trans. R. Soc. Lond. A*, 358:3229–3246.

Thomson, W. (1887). Stability of fluid motion: rectilineal motion of viscous fluid between two parallel plates. *Philos. Mag.*, 24:188–196.

Tobak, M. and Peake, D. J. (1982). Topology of three-dimensional separated flows. *Annual Review of Fluid Mechanics*, 14:61–85.

Tollmien, W. (1931). Über die enstehung der turbulenz i. *English translation*, page NACA TM 609.

Trefethen, L. N. (1997). Pseudospectra of linear operators. *SIAM Rev.*, 39:383–406.

Trefethen, L. N. and Embree, M. (2005). *Spectra and Pseudospectra: The Behaviour of Nonnormal Matrices and Operators*. Princeton University Press, Princeton, USA.

Trefethen, L. N., Trefethen, A. E., Reddy, S. C., and Driscoll, T. A. (1993). Hydrodynamic stability without eigenvalues. *Science*, 26:578–584.

Tucker, P. G. (2014). *Unsteady Computational Fluid Dynamics in Aeronautics*. Springer Series: Fluid Mechanics and its Applications. Springer, Netherlands.

Vadlamani, N. R. (2015). *Numerical Investigation of Separated Flows in Low Pressure Turbines*. PhD thesis, University of Cambridge, UK.

Vadlamani, N. R., Jefferson-Loveday, R., and Tucker, P. G. (2013). Large Eddy Simulations in Turbines: Influence of Roughness and Free-stream Turbulence. *Flow, Turbulence and Combustion*, 92:543–561.

Vadlamani, N. R. and Tucker, P. G. (2016). Intake lip separation control using plasma actuators. *16th International Symposium on Transport Phenomena and Dynamics of Rotating Machinery*.

van der Pol, B. and Bremmer, H. (1959). *Operational Calculus Based on Two-Sided Laplace Integral*. Cambridge University Press, Cambridge, UK.

Vega, A. and Corral, R. (2013). Physics of Vibrating Airfoils at Low Reduced Frequency. *ASME Journal*, pages GT2013–94906.

Vera, M. (2004). *The Effect of Compressibility on Unsteady Boundary Layers in High-Lift low Pressure Turbines*. PhD thesis, University of Cambridge, UK.

Vieceli, J. A. (1969). A method for including arbitrary external boundaries in the MAC incompressible fluid computing technique. *Journal of Computational Physics*, 4:543–551.

Vogt, D. (2005). *Experimental Investigation of Three-Dimensional Mechanisms in Low-Pressure Turbine Flutter*. PhD thesis, KTH, Sweden.

Volino, R. J. (2002). Separated flow transition under simulated low-pressure turbine airfoil conditions-part 1: Mean flow and turbulence statistics. *Journal of Turbomachinery*, 124:645–655.

Waite, J. J. (2016). *Physical Insights, Steady Aerodynamic Effects, and a Design Tool for Low-Pressure Turbine Flutter*. PhD thesis, Duke University, USA.

Waleffe, F. (1998). Three-dimensional coherent states in plane shear flows. *Physical Review Letters*, 81(19):4140–4143.

Wang, Z. (2003). *Computational simulation of unsteady boundary layer over compliant surfaces.* PhD thesis, National University of Singapore, Singapore.

Wang, Z., Yeo, K., and Khoo, B. (2005). Spatial direct numerical simulation of transitional boundary layer over compliant surfaces. *Comput. Fluids*, 34:1062–1095.

Watmuff, J. (1999). Evolution of a wave packet into vortex loops in a laminar separation bubble. *Journal of Fluid Mechanics*, 397:119–169.

Westin, K. J. A., Boiko, A. V., Klingmann, B. G. B., Kozlov, V. V., and Alfredsson, P. H. (1994). Experiments in a boundary layer subjected to free stream turbulence. part 1. boundary layer structure and receptivity. *Journal of Fluid Mechanics*, 281:193–218.

White, F. M. (2008). *Fluid Mechanics, 6th ed.* McGraw-Hill, New York, USA.

Wissink, J. and Rodi, W. (2003). DNS of a Laminar Separation Bubble in the Presence of Oscillating External Flow. *Flow, Turbulence and Combustion*, 71:311–331.

Wissink, J. and Rodi, W. (2004). *DNS of a laminar separation bubble affected by free-stream disturbances*. Direct and Large-Eddy Simulation V: Proceedings of the fifth international ERCOFTAC Workshop, Kluwer Academic Publishers.

Wissink, J., Rodi, W., and Hodson, H. (2006). The influence of disturbances carried by periodically incoming wakes on the separating flow around a turbine blade. *International Journal of Heat and Fluid Flow*, 27:721–729.

Wu, W. and Piomelli, U. (2018). Effects of surface roughness on a separating turbulent boundary layer. *Journal of Fluid Mechanics*, 841:552–580.

Wu, X. (2010). Establishing the generality of three phenomena using a boundary layer with free-stream passing wakes. *Journal of Fluid Mechanics*, 664:193–219.

Wu, X., Jacobs, R. G., Hunt, J. C. R., and Durbin, P. (1999). Simulation of boundary layer transition induced periodically passing wakes. *Journal of Fluid Mechanics*, 399:109–153.

Wu, X. and Moin, P. (2009). Direct numerical simulation of turbulence in a nominally zero-pressure-gradient flat-plate boundary layer. *Journal of Fluid Mechanics*, 630:5–41.

Wu, X., Moin, P., and Hickey, J. P. (2014). Boundary layer bypass transition. *Physics of Fluids*, 26:091104.

Wu, X., Moin, P., Wallace, J. M., Skarda, J., Lozano-Duran, A., and Hickey, J. P. (2017). Transitional-turbulent spots and turbulent-turbulent spots in boundary layers. *Proc. Nat. Acad. Sci*, E5:292–299.

Wu, X., Vahdati, M., Sayma, A. I., and Imregun, M. (2003). A Numerical Investigation of Aeroacoustics Fan Blade Flutter. *ASME Journal*, pages GT2003–38454.

Yeo, K., Zhao, X., Wang, Z., and Ng, K. (2010). Dns of wavepacket evolution in a blasius boundary layer. *J. Fluid Mech.*, 652:333–372.

Yeung, P. K., Donzis, D. A., and Sreenivasan, K. R. (2012). Dissipation, enstrophy and pressure statistics in simulation at high Reynolds number. *Journal of Fluid Mechanics*, 700:5–15.

Yuan, J. and Piomelli, U. (2014). Estimation and prediction of the roughness function on realistic surfaces. *Journal of Turbulence*, 15(6):350–365.

Zaki, T. A. and Durbin, P. A. (2005). Mode interaction and the bypass route to transition. *Journal of Fluid Mechanics*, 531:85–111.

Zaki, T. A. and Durbin, P. A. (2006). Continuous mode transition and the effects of pressure gradient. *Journal of Fluid Mechanics*, 563:357–388.

Zhang, X. F. (2005). *Separation and Transition Control on Ultra-High-Lift Low Pressure Turbine Blades in Unsteady Flow*. PhD thesis, University of Cambridge, UK.

Zhao, X. (2007). *Computational simulation of wavepacket evolution over compliant surfaces.* PhD thesis, National University of Singapore, Singapore.

Zhou, J., Adrian, R. J., Balachandar, S., and Kendall, T. M. (1999). Mechanisms for generating coherent packets of hairpin vortices in channel flow. *Journal of Fluid Mechanics*, 387:353–396.